IX International conference

Plasma Physics and Plasma Technology

Contributed papers

Minsk, Belarus
September 17 – 21, 2018

B.I. Stepanov Institute of Physics
National Academy of Sciences of Belarus

SPECTRAL INSTRUMENTS

MONOCHROMATORS/SPECTROGRAPHS

- Single and double
- Focal length from 140 mm to 830 mm
- Wide range of detectors and accessories

COMPACT SPECTROMETERS

- Spectral range from 190 nm to 2600 nm
- High-sensitivity
- Multiple optical fibers imaging

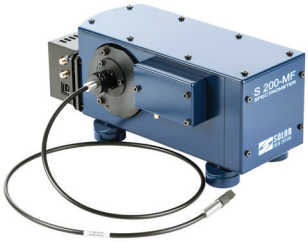

POWERFUL XE LIGHT SOURCES

- Tunable from 250 nm to 2500 nm

WAVELENGTH METERS FOR LASERS AND DIODES

- Spectral range from 190 nm to 1800 nm
- High precision ±3 pm
- Spectrum demonstration and analysis

SOLAR LASER SYSTEMS

SOLAR Laser Systems, 4 Stebenev lane, Minsk 220024, BELARUS,
Fax: +375 (17) 2019596, Phone: +375 (17) 2019590, e-mail: info@solarls.eu, www.solarlaser.com

The National Academy of Sciences of Belarus
B.I. Stepanov Institute of Physics of the National Academy of Sciences of Belarus
Joint Institute for High Temperatures of the Russian Academy of Sciences
Al-Farabi Kazakh National University

IX International Conference

PLASMA PHYSICS AND PLASMA TECHNOLOGY

(PPPT-9)

Minsk, Belarus
September 17 – 21, 2018

CONTRIBUTED PAPERS

Minsk
"Kovcheg"
2018

UDC 533.9(082)

EDITORS:

N.V. Tarasenko, A.A. Nevar, N.N. Tarasenka

COMPUTER PROCESSING:

M.S. Usachonak, V.V. Kiris

CO-ORGANIZERS:

A.V. Luikov Heat and Mass Transfer Institute of NAS of Belarus
Research Institute of Experimental and Theoretical Physics, al-Farabi Kazakh National University
National Nanotechnological Laboratory of Open Type, al-Farabi Kazakh National University
Belarusian Republican Foundation for Fundamental Research
Belarusian Physical Society

SPONSORED BY:

National Academy of Sciences of Belarus
SOLAR Laser Systems
Standa Ltd.
Scientific-Technical Association «Optics and Lasers»

ISBN 978-985-7202-78-2

Advisory Committee

Chairmen: S.Ya. Kilin (Belarus)

V.S. Burakov (Belarus), T. Belmonte (France), V.Ya. Chernyak (Ukraine), M.S. Dmitrijevic (Serbia), S.V. Gaponenko (Belarus), I.E. Garkusha (Ukraine), N.S. Kazak (Belarus), N. Konjevic (Serbia), V.A Orlovich (Belarus), O.G. Penyaz'kov (Belarus), J. Puric (Serbia), R. Soni (India)

International Program Committee

Chairmen: N.V. Tarasenko (Belarus)
V.E. Fortov (Russia)
T.S. Ramazanov (Kazakhstan)

Vice-chairmen: V.M. Astashynski (Belarus)
O.F. Petrov (Russia)
A.E. Davletov (Kazakhstan)

Scientific secretary: A.A. Nevar (Belarus)

Yu.S. Akishev (Russia), A.S. An'shakov (Russia), V.I. Arkhipenko (Belarus), T. Callegari (France), A.N. Chumakov (Belarus), A. DeGiacomo (Italy), V.K. Goncharov (Belarus), K.N. Dzhumagulova (Kazakhstan), I.I. Filatova (Belarus), M.T. Gabdullin (Kazakhstan), F. Krcma (Czech Republic), M. Kuraica (Serbia), H. Kurniawan (Indonesia), D. Mariotti (UK), A.L. Mosse (Belarus), E. Messerle (Kazakhstan), A. Nikiforov (Belgium), I.S. Nikonchuk (Belarus), K. Ostrikov (Australia), N. Parkansky (Israel), G. Paskalov (USA), I.L. Pobol (Belarus), A. Rousseau (France), T. Sakka (Japan), L.V. Simonchik (Belarus), A.S. Smetannikov (Belarus), S. Starikovskaia (France), M. Trtica (Serbia), A.N. Veklich (Ukraine)

Local Organizing Committee

K.A. Akinshau, V.S. Babitskii, N.A. Bosak, A.V. Butsen, E.A. Ershov-Pavlov, A.V. Kazak, A.A. Kirillov, V.V. Kiris, V.V. Kouhar, V.A. Lyushkevich, N.S. Metel'skaya, M.I. Nedel'ko, D.V. Shabrov, I.P. Smyaglikov, N.N. Tarasenka, M.S. Usachonak

TOPICS

1. Fundamentals and modeling of plasma processes, plasma dynamics, transport, optical, and thermodynamic properties of plasmas

2. Electrical discharges and other plasma sources, elementary and near-electrode processes *(arc, spark, barrier, surface, glow, and high-frequency discharges; microplasma discharges and plasma jets, plasma accelerators; electron and ion beam sources)*

3. Non-equilibrium effects and atmospheric pressure plasma processes, plasma in and in contact with liquid

4. Non-ideal and dusty plasmas, fusion and astrophysical plasmas

5. Laser and plasma interaction with surfaces
(laser ablation, modification of materials by laser and plasma treatment; reactions on a surface, sputtering and deposition)

6. Plasma spectroscopy and other diagnostic methods

7. Plasma applications
(plasma synthesis and processing of nanomaterials, plasma deposition of functional coatings, plasma in medicine and biology, plasma in agriculture, plasmas for environmental applications and resource recovery, plasma light sources; plasma in micro- and nanoelectronics, in spectrochemical analysis, plasma chemistry, plasma metallurgy, etc.)

CONTENTS

2. ELECTRICAL DISCHARGES AND OTHER PLASMA SOURCES, ELEMENTARY AND NEAR-ELECTRODE PROCESSES

5. LASER AND PLASMA INTERACTION WITH SURFACES

7. PLASMA APPLICATIONS

1. FUNDAMENTALS AND MODELING OF PLASMA PROCESSES, PLASMA DYNAMICS, TRANSPORT, OPTICAL AND THERMODYNAMIC PROPERTIES OF PLASMAS

DYNAMICAL CHEMICAL MODEL OF LASER INDUCED PLASMA

I. Gornushkin[1], S. Shabanov[2]

[1]BAM Federal Institute for Materials Research and Testing, Berlin, Germany
[2]University of Florida, Gainesville, FL, USA

Laser induced plasma (LIP) is a highly dynamic, short living event which presents significant difficulty for both diagnostics and modeling. The former requires precise spatially- and time-resolved measurements on a micron-nanosecond scale while the latter needs numerous descriptive parameters; many of them can only be obtained from experiment. Diagnostics and modeling should always complement each other for obtaining a truthful picture of LIP.

In this presentation, a newly developed collisional-dominated model will be presented. The model is based on the coupled Navier-Stokes, state, radiative transfer, material transport, and chemical equations. The model incorporates plasma chemistry through the equilibrium approach that relies on atomic and molecular partition functions. Several chemical systems are modeled including Si-C-Cl-N and B-H-Cl systems.

The model is used to study the equilibrium states of the systems as functions of the concentrations of plasma species and plasma temperature. The model also predicts the evolution of number densities of atomic and molecular species in the expanding plasma plume.

References

1. **Shabanov S.V. and Gornushkin I.B.** Appl. Phys. A, 121(2015) 1087-1107.
2. **Shabanov S.V. and Gornushkin I.B.** Appl. Phys. A 122(2016) 676.

ELECTROSTATIC CUMULATION OF HIGH-CURRENT ELECTRON BEAMS FOR TERAHERTZ APPLICATIONS

S. Anishchenko, V. Baryshevsky, A. Gurinovich

Reasearch Institute for Nuclear Problems, Bobruiskaya 11 str, Minsk, Belarus, 220040,
sanishchenko@mail.ru, sanishchenko@inp.bsu.by

The generation of high-power radiation is one of the main goals of vacuum terahertz electronics /1,2/. The progress in this field is strongly connected with the production of relativistic electron beams with ever-increasing density in high-current accelerators /1,2,3/.

A typical high-current accelerator in THz sources consists of axially symmetric cathode and anode /3/. The cathode is hemispherical with a radius of curvature of several centimeters and is separated from the concave anode by tens of millimeters. The vacuum diode produces ~1 kA of total current at ~1 MV applied voltage. The hole in the anode "cuts" only a small central part of the accelerated beam (~10 A), which is guided by magnetic field with the strength ~1 T. Low efficiency of beam use limits applications of such approach.

The second disadvantage of conventional accelerators is high value of an external guiding field (1 T) that results in large dimensions of the whole system. High magnetic fields are necessary to prevent beam expansion due to the Coulomb repulsion. Meanwhile an alternative mechanism precluding beam expansion is already well-known. This mechanism doesn't require external guide field at all. It is based on magnetic cumulation discovered by Bennett /4/. Magnetic cumulation provides the charged-particle beam intensities as high as 10 GW/mm^2 /5,6/, thus enabling the laboratory investigation of the extreme state of matter. However, the large particle energy spread does not permit to use magnetically cumulated electron beams for terahertz radiation sources.

This paper considers one more alternative for high-power electron beam cumulation without use of magnetic field, namely electrostatic cumulation /7/. Occurring in a relativistic vacuum diode with a ring-type cathode, this mechanism doesn't suffer from particle energy spread /7/. Our main task here is to provide a theoretical description of cumulation mechanism and the experimental verification thereof. We will show that electrostatic cumulation provides current densities (>> 1 A/mm^2) sufficient to seed high-power terahertz sources.

It should be noted that electrostatic cumulation was first revealed during modeling the relativistic vacuum diode operation /7/. The qualitative picture of electrostatic cumulation can be described as follows. In a relativistic vacuum diode, explosive electron emission is most intense from the cathode's inner edge Fig. 1. Coulomb repulsion causes the charged particles to rush to the region free

from the beam. As a result, the accelerated motion of electrons toward the anode comes alongside the radial motion to the cathode's symmetry axis. As a result, the high-current beam density increases multifold on the axis of the relativistic vacuum diode as compared to the average current density in the cathode-anode gap. The reported cumulation mechanism is described for the ring-type cathode (the circular cathode with a circular hole). It should be noted that the cumulation mechanism doesn't depend on the hole location, i.e. whether or not the hole axis coincides with the cathode axis /7/.

Fig. 2 shows the results of simulations: the dose absorbed by the anode. The assumed parameters of the cathode are as follows: cathode radius 30 mm, cathode-anode gap 20 mm, and the radius of the inner hole 10 mm. The maximum value of the accelerating voltage pulse is taken equal to 360 kV and its duration is 130 ns. The simulated current density in the region of the central spot on the anode at the moment corresponding to the maximum accelerating voltage is as large as 10 A/mm^2, being 5 times greater than the average current density of the high-current diode. A typical radius of the spot is about 1 mm. Thus, the simulation result indicates the electron-beam cumulation on the axis of a high-current diode with a ring-type cathode.

The undeniable advantage of this cumulation mechanism over a conventional one based on the self-focusing of a high-current beam by its own magnetic field is a very low energy spread of particles in the region of the maximum current density due to the laminar flow of charged particles. In contrast, under the conditions of self-focusing of the beam by its own magnetic field, the flow current becomes appreciably turbulent, and the charged particles acquire a significant momentum. The electron flow in this case is like a compressed relativistic gas with electron temperature of the order of the voltage applied across the diode.

To investigate the cathodes and obtain the information about electron beam parameters, we use a nanosecond pulse-periodic electron accelerator with a compact SF6-insulated high-voltage generator (HVG) as a power supply providing pulsed voltage up to 400 kV in 30 Ohm resistive load with half-height duration of 130 ns and rise time of 30 ns /7/. To obtain integrated full-sized imprints of the electron beam, we use a radiochromic dosimetry film placed 3 mm behind the anode mesh made of stainless steel (the geometrical transparency of the mesh is 0.77); the cathode-anode gap is 20 mm. The dosimetry film enables to obtain information about the total absorbed dose caused by passage of charged particles. After the exposure, the transmission scanning of the dosimetry film using the optical filter is made with EPSON Perfection V100 Photo scanner. The distribution of the absorbed dose over the beam cross section is derived unambiguously from the scanned images and the dose-response calibration curve.

Our first experiments had shown that the intense flow of charged particles on the axis had burned the film through (see Fig. 3) /7/. For this reason, in further experiments we placed 70 μm-thick aluminium foil in front of the dosimetry film to decrease the absorbed dose (see Fig. 3). This enabled us to cut off the flows of both the weakly-relativistic electrons produced at the voltage pulse decay and the cathode plasma. The experiments conducted with one, two, and three foils demonstrated that a sharp increase in the absorbed dose remains in the center. This means that the particle flow consists at the beam axis of high-energy electrons. In the experiments with three foil layers cutting off all electrons whose energy was less than 250 keV, the absorbed dose in the center was almost four times as large as the average dose across the beam cross section, showing a good agreement with the simulation results.

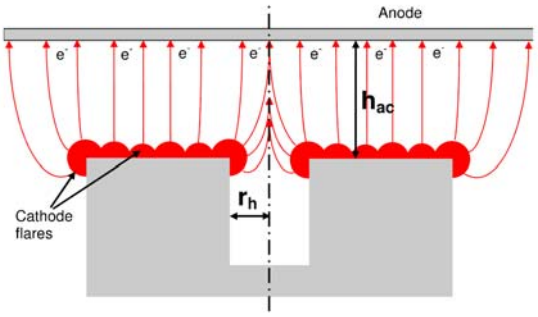

Fig. 1 - Electrostatic cumulation in a relativistic vacuum diode

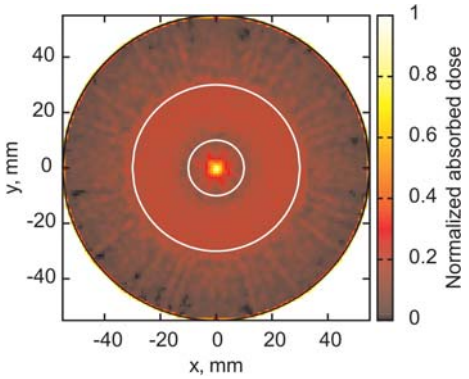

Fig. 2 - Sample of simulated normalized absorbed dose at the anode position for a cathode with outer and inner diameters 60 and 2rh=20 mm, respectively. White circles mark outer and inner cathode diameters

Let us note here that both the simulation and the experiments were performed at maximum accelerating voltage 400 kV and the cathode-anode gap equal to h_{ac}=20 mm. The estimates show that it is possible to achieve the beam current density more than 100 A/mm^2 with the accelerating voltage of several MV. This quantity is several times higher than those obtained in existing high-current terahertz sources producing ~100 kW of radiation power /3/.

In this paper we described the cumulation mechanism of a high-current beam in a relativistic vacuum diode with a ring-type cathode. The basis of this cumulation mechanism is electrostatic repulsion of electrons from the inner edge of the cathode. The simulated values of current density and beam intensity equal to 36 MW/mm^2 and 10 A/mm^2, respectively, qualitatively agree with the experimental data.

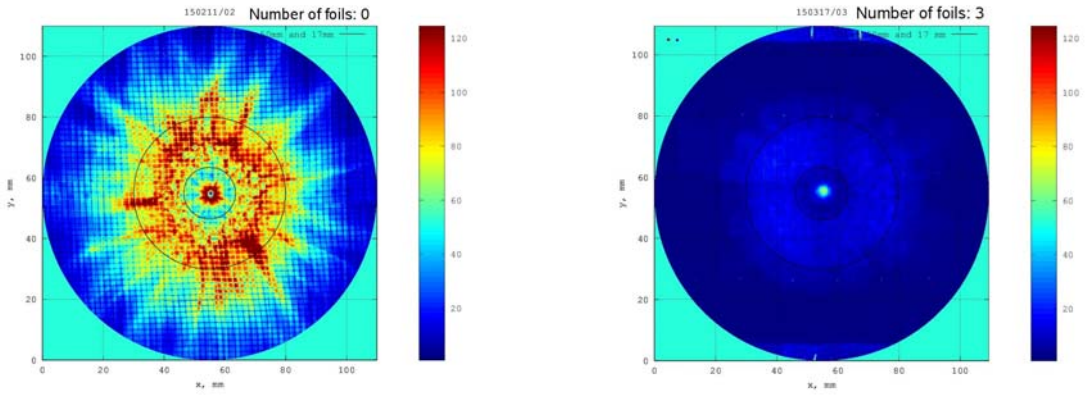

Fig. 3 - Electron beam without foils (left) and with three foils (right)

A very low particle energy spread in the region of maximum current density that is the distinctive feature of the described cumulation mechanism over a conventional one relying on focusing the high-current beam by its own magnetic field. As a result of electrostatic cumulation, a thin relativistic electron flow with a radial width of 1 mm and beam current density of 10–100 A/mm^2 is formed. This quantity is several times higher than those obtained in existing high-current terahertz sources producing ~100 kW of radiated power. As a result, the use of electrostatic cumulation can sufficiently increase the radiation output. One of the main advantages of high-current terahertz sources with electrostatic cumulation is the absence of external magnetics fields resulting in large dimensions of the whole system.

References

1. **Booske J.H.** IEEE Trans. Terahertz Sci. Technol. 1 (2011) 54–75.
2. **Dhillon S.S. et al.** J. Phys. D: Appl. Phys. 50 (2017) 043001.
3. **Garate E.P. et al.** Nucl. Instrum. Methods A259 (1987) 125–127.
4. **Bennett W.H.**, Phys. Rev. 45 (1934) 890–897.
5. **Morrov D.L. et. al**. J. Appl. Phys. 19 (1971) 441–443;
6. **Bradley L.P. and Kuswa G.W.**, Phys. Rev. Lett. 29 (1972) 1441–1445.
7. **Anishchenko S., Baryshevsky V., Belous N., Gurinovich A., Gurinovich E., Gurnevich E., and Molchanov P.** IEEE Trans. Plasma Sci., 45 (2017) 2739–2743; **Anishchenko S. and Gurinovich A.** in Proc. 5th Euro-Asian Pulsed-Power Conf., Kumamoto, Japan, 2014, pp. 1–6.

THREE KINDS OF AMBIPOLAR TRANSPORT FOR GAS DISCHARGE PLASMA

A. Medvedev, P. Pinaev

Institute of Laser Physics SB RAS, Prospect Lavrentyev, 15B, 630090 Novosibirsk, Russia
medvedev@laser.nsc.ru

Introduction Three types of ambipolar transport are sufficient for describing the structure of direct-current atmospheric glow discharge /1/. Ambipolar drift, which plays a special role in maintaining the discharge plasma at moderate pressures /2-4/, becomes, at atmospheric pressures, a key mechanism of transfer of charged particles from the near-electrode layers providing the existence of a discharge without ionization in the bulk /5/. The presence of near-electrode layers results in the fact that the field in the quasi-neutral part of the discharge is always smaller than between the electrodes, outside the plasma pinch. Therefore, the external surface of the plasma pinch in the radial direction will be subject to the action of a force, determined by the energy gradient of the electric field, compressing the pinch. On the other hand, the action of thermal energy leads to the diffusion expansion of plasma. Thus, ambipolar diffusion and ambipolar transport caused by the action of the electric field energy resist each other, determining the plasma pinch radius. A detailed analysis of the results of an experimental investigation of atmospheric pressure discharges in various gases /6-9/ and a comparison with estimates based on three kinds of ambipolar transport of plasma have shown that the distinction of the plasma pinch radii is not more than 20% /5/.

In this paper, in addition to the well-known ambipolar diffusion /10/, ambipolar drift and plasma transport based on the action of the electric field energy are considered. The importance of the mechanisms of ambipolar plasma transport at the formation of a discharge structure in gases of moderate and atmospheric pressures using experimental works as an example is demonstrated.

Three kinds of ambipolar transport To obtain a plasma transport equation (PTE), we use continuity equations, traditional expressions for currents with the drift and diffusion components, without any more other assumptions, taking into account that in low-frequency discharge $\mathbf{div}\,\mathbf{j} = 0$ /11/:

$$\partial n/\partial t - \dot{n} = -\mathbf{div}\left(\mu_a \mathbf{f}\right), \qquad (1)$$

with the force vector acting on the plasma elementary volume:

$$\mathbf{f} = -\mathbf{grad}\left(w_T + w_E\right) + \mathbf{j}/\mu_e\,, \qquad (2)$$

where n are the plasma densities, $\dot{n}$ is the velocity of the bulk processes of

generation and loss of charged particles, $\mu_a = \mu_i \mu_e / (\mu_e + \mu_i)$ is the plasma ambipolar mobility coefficients, μ_i, μ_e are the mobility coefficients of ions and electrons respectively, $w_T = T_e n_e + T_i n_i$ is the thermal energy of the plasma, $w_E = (n_i - n_e)\varphi$ is the energy of the electric interaction of particles or the plasma electric field energy, T_i, T_e are the parameters characterizing the average energy of the components, called the temperature of positive ions and electrons, n_i and n_e are the densities of charged particles, φ is the electric field potential, and $\mathbf{j}$ is the electric current density vector reduced to the electron charge.

Well-known is the first term part in (2) based on the thermal energy w_T, which, at constant temperatures of the components and the strict equality $n_e \approx n_i \approx n$, can be presented in (1) as ambipolar diffusion:

$$\mathbf{div}\left(\mu_a \mathbf{grad}\left(T_e n_e + T_i n_i\right)\right) \approx \mathbf{div}\left(D_a \mathbf{grad}\, n\right),$$

where $D_a = \left(\mu_i D_e + \mu_e D_i\right) / \left(\mu_e + \mu_i\right)$, D_e, D_i are the diffusion coefficients of ions and electrons respectively. Transfer based on the electric field energy, w_E, is observed in plasma with a low-frequency field /12, 13/. The last (with electric current) term in (2) is the major supplier of charged particles to the bulk of the discharge of moderate pressures electrically neutral gases /2-4/ and, according to our assumption, of most atmospheric pressure discharges /5/.

Structure of the gas discharge The basis for describing the structure of the discharge of atmospheric pressure is the assumption that the stationary existence of a pinch is possible only in the event of a breakdown due to the heating of molecular ions and, as a consequence, the absence of dissociative recombination in the volume. Shock-radiation recombination with triple collisions has several orders of magnitude a lower velocity /14/, and diffusion losses with further dissociative recombination at the outer cold boundary of the pinch come to the fore. Another assumption is that there is no ionization in the volume, since charged particles passing through the entire volume from the near-electrode regions are sufficient to compensate for the losses /5/. For example, at atmospheric pressure, the volume loss is a hundredth of a percent of the electron flux. If we talk about the main reason for the absence of ionization in the volume of the atmospheric discharge, then if it were present, because of the sharp dependence of the ionization coefficient on the electric field /15/, the discharge would be unstable by contracting to a spontaneously formed current tube with larges heating. In this case, three kinds of the ambipolar plasma transfer are quite enough for describing low-frequency and DC discharges at moderate and atmospheric pressures. The quasineutral part of the classical

discharge /16-18/ consists of a Faraday dark space (FDS), whose length is on the order of the tube radius, and the positive column (PC) occupying the entire bulk from the anode layer to the FDS. This concept, which is true for pressures of up to 1 Torr for molecular gases and 10 Torr for atomic gases, cannot be used for moderate pressures. In convective lasers with forced gas pumping through the discharge zone at pressures of 10-200 Torr there are fields with two-three times lower ionization in the zone that must be called the PC. An explanation was found using various transport mechanisms providing the input of charged particles from the near-electrode layers to the bulk /19/. In this case, if we use the traditional concepts, at atmospheric pressure the FDS occupies practically the entire bulk of the discharge, where, instead of ambipolar diffusion, charged particles enter the bulk according to other mechanisms of plasma transport, one of which is ambipolar drift /3/. Ambipolar drift determines the transport of charged particles from near-electrode regions along electric current lines at medium /2, 4/ and atmospheric pressures electrically neutral gases /1, 5/. The two other types of ambipolar transport, competing with each other determine the formation of the cross section of the discharge pinch /5/.

Conclusions Thus, the three types of ambipolar plasma transfer presented by the PTE fully determine the particle balance and discharge structure at moderate and atmospheric pressures. In addition, two conclusions follow from the analysis of formation the discharge structure. The interaction of charged particles in plasma, with electric current passing in it, is not limited by their nearest neighbors lying in the Debye sphere. Each particle of the discharge bulk is bound to other ones by electric forces, regardless of the fact where these particles are located: in different areas of the quasi-neutral part or near the electrodes where an uncompensated space charge forms a strong electric field. It has been shown how the pinch radius is formed: due to a charge of the near-electrode layers, by the electric field pressure force, in competition with the thermal expansion of plasma. Another determining factor of the atmospheric pressure discharge is the presence of large particle flows, owing to which losses in the bulk are compensated. According to papers /15, 20/ in which ionization-thermal mechanisms of instability are discussed, moderate and, especially, atmospheric pressures turn out to be a real catastrophe for the ionization mechanism of discharge maintenance in the bulk. High-density plasma generated at negative glow due to ambipolar drift moves in the direction of the anode, rapidly recombining and heating. Recombination leads to the field increase and intensive heating, which determines the changeover to the diffusion regime of losses of plasma particles in the bulk. The stronger the heating, the more stable the discharge. In the zone with the diffusion regime of losses, to compensate for the losses of particles it is sufficient to have a small field

increase, which can be smoothed by heating. In this case the entire pinch zone can be identified as a positive column, and the zone at the outlet from the negative glow, with a low heating and fast field increase, as a Faraday dark space.

Acknowledgements. This work was supported by the Program of the Russian Academy of Sciences no. II.10.1. Project no. 0307-2017-0015 (State Registration no. AAAA-A17-117021750017-0, 17.02.17) and Program of Fundamental Scientific Research of the Russian Academy of Sciences (Project no. № 0307-2018-0014).

References

1. **Medvedev A.E.** Proc. of SPIE, 106141(2018) 106141W-1
2. **Akishev Yu.S. et al.** Teplofiz. Vys. Temp., 18(1980) 266-272
3. **Vysikailo F.I.** Teplofiz. Vys. Temp., 23(1985) 809-811
4. **Ivanchenko A.I., Medvedev A.É.** J. Appl. Mech. Tech. Phys., 32(1991) 9
5. **Medvedev A.E.** EPJ D, 70(2016) 37-47
6. **Arkhipenko V.I., Kirillov A.A.** et al. EPJ D, 66(2012) 252
7. **Staack D., Farouk B. et al.** Plasma Sources Sci. Technol., 17(2008) 025013
8. **Kolesnikov V.N.** Paper of the Ph. Inst. of the RAS, 30(1964) 66
9. **Rutcher A., Wilke Ch.** XI ICPIG Contr. pap. Prague, (1973) 109
10. **Phelps A.V.** J. Res. Nat. Inst. Stand. Technol., 995(4) (1990) 407-431
11. **Medvedev A.E.** Russian Phys. J., 55(4) (2012) 389-393
12. **Shapiro G.I., Soroka A.M.** Pisma Zh. Tekh. Fiz., 5(3) (1979) 129–132
13. **Barkalov A.D., Samokhin A.A.** Preprint IAE, 4147/6(1985) 12
14. **Bates D.R. et al.** Proc. Roy. Soc., A 267(1962) 297-312
15. **Eletskiĭ A.V., Smirnov B.M.** UFN, 166(1996) 1197-1217
16. **Engel A., Steenbeck M.** Elektrische Gasentladungen ihre Physik und Technik., Berlin: Verlag von Julius Springer (1934)
17. **Raizer, Y.P.** Gas Discharge Physics, Berlin: Springer (1997)
18. **Lieberman M.A.**, Lichtenberg A.J. Principles of Plasma Discharges and Materials Processing. Hoboken, New Jersey: John Wiley & Sons, Inc. (2005)
19. **Velikhov E.P., Golubev V.S., Pashkin S.V.** UFN, 137(1982) 117-150
20. **Smirnov B.M.** UFN, 179(2009) 591-604

PLASMA AS A WORKING BODY

A. Medvedev

Institute of Laser Physics SB RAS, Prospect Lavrentyev, 15B, 630090 Novosibirsk, Russia
medvedev@laser.nsc.ru

1. Introduction

It has become clear at the creation of gas discharge powerful systems that particle and energy flows passing through plasma are comparable with the values needed for its maintenance or exceed them considerably. Therefore, regardless of whether we have a powerful gas laser, a plasmatron, or a plasma jet engine, plasma may be considered as a working body. The flows act on the plasma components in different ways, which leads to the emergence of an uncompensated charge and electric fields. An example of this action is passing the electric current with density **j**, known as the gas discharge. The traditional approximation when it is assumed that the density of the space charge $\rho \approx 0$ allows using the Boltzmann equation obtained for gas in the kinetic theory of plasma. For this, it is deemed sufficient to consider the energy of interaction of particles in plasma to be small by comparing the average thermal energy with the energy of interaction of a specific charged particle with other particles in the sphere of Debye length (r_d). It is shown in papers /1, 2/ that in conditions that are typical for gas discharge when $\rho / n \ll 1$ and $(r_d / L)^2 \ll 1$ the interaction area encompasses the charged particles (n) of the entire bulk of size L, and the interaction energy of particles in relation to thermal energy is several orders of magnitude greater than the values determined by the factor $(r_d / L)^2$. However, in this case the use of the Boltzmann equation for microscopic description of plasma is not reasonable. On the other hand, at moderate and atmospheric pressures the energy distribution of plasma components can be considered invariable, which allows remaining within the hydrodynamic approach. In the present paper, conditions for changing from flows of individual components to transport of plasma as a continuum, with the parameters n, ρ, j, thermal energy density nT, and electric field energy $\rho\varphi$, called ambipolar transport /2/, are obtained. On the basis of the equations obtained, low-frequency polarization with the formation of charged layers at the boundaries that is typical for gas discharges is considered.

2. Plasma as a fluid

In gas discharges at moderate and high pressures the charge separation layers of the plasma components become very thin and the collisional relaxation times are sufficiently short, so that in the overwhelming majority of cases each

component can be represented as a continuous medium with an unchanged distribution function. Considering the electric forces, the forces of the gas kinetic pressure and the momentum exchange between the plasma components in collisions, for the selected component of the medium we have a change in momentum per particle with mass *m*:

$$m\left(\partial \mathbf{v}/\partial t + \left(\mathbf{v}\cdot\nabla\mathbf{v}\right)\right) = e\left(\mathbf{E} + \mathbf{v}\times\mathbf{B}\right) - \nabla\cdot\mathbf{p}/n - m\nu\left(\mathbf{v}-\mathbf{v}_0\right)$$

Assuming that the plasma is nonrelativistic (v << c) and isothermal ($\nabla p = kT\nabla n$), the pattern of motion of the particles is stationary, and the velocity of the interesting us particles (**v**) of significantly larger slow particles of the medium ($\mathbf{v_0}$), and large enough to neglect the convective terms, for the velocity and density of the particle flux ($\mathbf{j}$) of the chosen plasma component we will receive:

$$\mathbf{v} = \frac{e\mathbf{E}}{m\nu} - \frac{kT}{m\nu}\frac{\nabla n}{n},\ \mathbf{j} = \mu n\mathbf{E} - D\nabla n, \qquad (1)$$

where $\mu = e/m\nu$, $D = kT/m\nu$ is the mobility and diffusion coefficients, ν is frequency of collisions the particles of the selected component with the other particles. Using expressions for the fluxes (1) and the equation of continuity of particles: $\partial n/\partial t + \nabla n\mathbf{v} = \dot{n}$ ($\dot{n}$ is the velocity of the bulk processes of generation and loss of charged particles), as in the derivation of the diffusion equation, we try to eliminate the electric field, but we will not neglect terms with the spatial charge density and the dependence of the electron mobility on the field. Then, using the Einstein relation $D = \mu T$ (T is expressed in units of electric potential) and the condition for the electric current $\mathbf{div}\,\mathbf{j} = 0$ we obtain the plasma transport equation (PTE):

$$\partial n/\partial t - \dot{n} = -\mathbf{div}\left(\mu_a \mathbf{f}\right), \qquad (2)$$

with the acting on the plasma elementary volume force vector:

$$\mathbf{f} = -\mathbf{grad}\left(w_T + w_E\right) + \mathbf{j}/\mu_e, \qquad (3)$$

where n is the plasma particle densities, $\mu_a = \mu_i\mu_e/(\mu_e+\mu_i)$ is the plasma ambipolar mobility coefficients, μ_i, μ_e are the mobility coefficients of ions and electrons respectively, $w_T = T_e n_e + T_i n_i$ is the thermal energy of the plasma, $w_E = (n_i - n_e)\varphi$ is the energy of the electric interaction of particles or the plasma electric field energy, T_i, T_e are the parameters characterizing the average energy of the components, called the temperature of positive ions and electrons, n_i and n_e are the densities of ions and electrons, φ is the electric field potential, and $\mathbf{j}$ is the reduced to the electron charge electric current density vector.

3. Applicability condition for PTE and estimation of its terms

Application of a divergence operation to the circulation of the magnetic field of the Maxwell equation gives the condition for the total current: $\mathbf{div}\left(\mathbf{j}+\partial\mathbf{D}/\partial t\right)=0$. As follows from /1/, in the low-frequency limit of direct current the plasma polarization is significant, with ε >1. However, since the plasma polarization, as in the dielectric of the capacitor, occurs due to the appearance of charged layers at the boundaries, which in contrast to capacitor, are formed by an electric current flowing through the plasma. In this connection, the current of polarization enter into the current of conduction **j** and in order to estimate the validity of the PTE derivation it suffices to specify the conditions under which $j >> \partial E/\partial t$. Following the assumption that discharge at atmospheric pressures is possible only in a well-heated gas /1/, when molecular ions, in both atomic and molecular gases, remain negligible and the diffusion mechanism of charged particle losses works, thereat using for this case the field distribution /4/, we obtain:

$$\frac{\partial E/\partial t}{j} \approx \frac{(2,4)^2 L\omega}{R^2\eta j} \approx 0.04\cdot\frac{L\nu(GHz)}{R^2\eta\,\tilde{j}(A/cm^2)},$$

where L is the interelectrode distance or the length of the cord in *cm*, ω is the cyclic frequency of the power source, R is the radius of the cord in *cm*, $\eta=(E/p_N)/T_e$ is the energy coefficient, equal to a fraction of a unit in atomic gases, to a dozen in molecular gases /1/, $\nu(GHz)$ is the frequency of the source in *GHz*, $\tilde{j}(A/cm^2)$ is the current density in A/cm^2. Thus, since we made earlier only a single significant assumption $\mathbf{div}\,\mathbf{j}\approx 0$, then up to the microwave range including its lower boundary the plasma motion described by PTE (2), (3) can be regarded as the movement of a single whole. Upon exiting the condition $j >> \partial E/\partial t$, the plasma is described by the motion of individual components.

In a glow discharge of moderate or atmospheric pressure, the plasma transport prevails that is due to the action of the external source; it is described by the current term or by the last term on the right side of the PTE (3). Comparing the current term of the PTE (III) with the diffusion term (I), on the assumption that $\mu_i/\mu_e << 1$, we obtain the ratio of these terms as:

$$\frac{(III)}{(I)} \approx \left[-\frac{d\ln\mu_e}{d\ln E}\right]\left(1-\frac{E/p_N}{T_e}p_N L\right), \qquad (4)$$

where p_N is the neutral density expressed in terms of pressure. The term in parentheses can be presented as $1-U/T_e$, where $U=EL$ is the potential difference for the plasma nonuniformity length. The absence of an electric

current corresponds to the condition $U = T_e$; then the plasma transport is governed exclusively by ambipolar diffusion. The values of the quantities $\left[-d\ln\mu_e / d\ln E\right]$ are the results of processing experimental data and for various gases they are in the range 0.2–0.7 /1/. Therefore, for $p_N L > 10$ *Torr·cm* the current term determined by the electrical energy of the external source prevails. If on the contrary $U << T_e$, then relation (4) becomes equal to $-d\ln\mu_e / d\ln E$. Thus, for low pressures $p_N L << T_e / (E/p_N)$ the current term also remains comparable to the diffusion term.

In the transverse direction to the field at moderate and high pressures the plasma transport due to the energy of electrical interaction of particles is dominant. Defining of the plasma thermal energy by its electronic component and using the well-known expression for the characteristic screening length of an external field $r_D^2 = T_e / 8\pi e n_e$, we obtain the ratio of the energy of electrical interaction of particles (II) to the thermal energy as $\frac{(II)}{(I)} \approx \frac{\rho\varphi}{n_e T_e} = \frac{E^2}{8\pi e n_e T_e} = \left(\frac{E}{T_e / r_D}\right)^2 \approx \left(\frac{r_D}{L}\right)^2 \left(\frac{U}{T_e}\right)^2$. We see that a factor $(U/T_e)^2$ has appeared in addition to the well-known ideality parameter $(r_D / L)^2$ for a current-carrying plasma.

4. Conclusions

Thus, the theory of plasma which was developed on the basis of modeling luminous advertising tubes and the propagation of radio waves in the upper atmosphere and then strengthened by studies of hot plasma with incipient instabilities, various kinds of wave processes, turned out to be completely unsuitable for a plasma that is a working medium with gigantic fluxes of particles passing through it, heat and radiation. Nevertheless, the hydrodynamic representations still remain, but here again the Debye radius ceases to play the role of a criterion in describing the plasma as a continuous medium.

Acknowledgements. This work was supported by the Program of Fundamental Scientific Research of the Russian Academy of Sciences (Project no. № 0307-2018-0025).

References

1. Medvedev A.E. EPJ D, 70(2016) 37-47
2. Medvedev A.E. Proc. of SPIE, 106141(2018) 106141W
3. Ivanchenko A.I., Medvedev A.É. J. Appl. Mech. Tech. Phys., 32(1991) 9-12

TEMPERATURE JUMP VALUE ON THE BOUNDARY OF HEAT SINK PRIMARY ZONE OF THE ELECTRIC ARC

A. Gerasimov, A. Kirpichnikov, F. Sabirova

Kazan National Research Technological University, Kazan, Russia. K. Marx Street, 68, 420015
faridasabirova@mail.ru

Introduction

There is a large amount of material accumulated to date on the T_e distribution in the arc plasma torches, including the Te value as a function of r at the border (in reality, of course, close to the border), stabilizing the discharge of a cylindrical tube, which plays the role of a thermostat for the atomic-ion gas /1-3/.

In other words, the work discusses jump temperature value $T_e(R)$-$T(R)$ at the border of the primary heat sink zone (at r=R where R - radius of the bounding an arc of a cylindrical tube whose walls are maintained at a fixed low enough temperature T(R)).

The relevance of this formulation is due to the fact that at present methods of direct measurement of the temperature of atoms and ions are still not developed enough, while the measurement of the electron temperature or temperature close to it is widely used by spectral analysis methods.

In this paper, this problem is solved in the framework of the known M. Steenbeck channel model /4/ as the most suitable for the analysis of a wide class of problems of maintenance of the gas discharge plasma in the electric and magnetic fields /5, 6/.

System of equations and method of solution

We use the two-temperature channel model arc built in /7/. Referring to the formulas obtained in this work dependencies electron and gas temperatures in the non-conductive zone arc from the current coordinate r

$$T_e(r) = T(R) + \frac{W}{2\pi\lambda}\ln\frac{R}{r} + \left(\frac{W}{2\pi\lambda} + \varepsilon R\right)\cdot\frac{\lambda_e\Psi_0(R) + \lambda_{ai}\Psi_0(r)}{\lambda_{ai}\cdot sR\cdot\Psi_1(r_c)}; \qquad (1)$$

$$T(r) = T(R) + \frac{W}{2\pi\lambda}\ln\frac{R}{r} + \left(\frac{W}{2\pi\lambda} + \varepsilon R\right)\cdot\frac{\lambda_e\left[\Psi_0(R) - \Psi_0(r)\right]}{\lambda_{ai}\cdot sR\cdot\Psi_1(r_c)}, \qquad (2)$$

Where

$$\Psi_0(r)=I_0(s\,r)K_0(s\,r_\kappa)-I_0(s\,r_\kappa)K_0(s\,r);$$

$$\Psi_1(r)=I_1(s\,r)K_0(s\,r_\kappa)+I_0(s\,r_\kappa)K_1(s\,r)=\frac{1}{s}\frac{\partial\Psi_0(r)}{\partial r}.$$

$$s^2=\frac{3}{2}k\,\delta\,\nu\,n_e\left(\frac{1}{\lambda_e}+\frac{1}{\lambda_{ai}}\right).$$

In these formulas, r_c - the radius of the conductive channel, W specific (per unit column length) into the discharge power, $\lambda_e = \lambda_e$ (T) and $\lambda_{ai} = \lambda_{ai}$ (T) coefficients of thermal conductivity of the electronic and atomic-ion gas of heavy particles.

In the latter ratio k - is Boltzmann constant; δ - the proportion of the energy lost in the collision of electrons with heavy particles; ν - the frequency of these collisions; n_e - the concentration of electrons in the discharge. ε in the formulas (1), (2) depends on discharge parameters and selected in each case based on some assumed physical model of interaction of the electron gas with the walls of the cylindrical tube. Case ε = 0; in this case corresponds to the adiabatic conditions for the adoption of the electron gas. Referring to the formula (2), putting in it, we obtain the following fundamental relation, the theory of two-temperature locking arc:

$$\Delta T(R)=T_e(R)-T(R)=\frac{W}{2\pi\lambda_{ai}}\frac{\Psi_0(R)}{s\,R\,\Psi_1(R)}. \qquad (3)$$

Equation (3) can be simplified. We take into account that, in practice, almost always $s\,R>>1$. In this case, simple calculations using the asymptotic representation /8/ functions $I_{0,1}(x)$ and $K_{0,1}(x)$ for large values of the argument, you can get a simple relation

$$T_e(R)-T(R)\approx\frac{W}{2\pi\lambda_{ai}\,s\,R}$$

i.e. to a first approximation by the decomposition of the formula (3) in a series in the small parameter jump in the electron temperature near the boundary limiting the arc of a cylindrical tube with the same input to the discharge capacity of the W, it is inversely proportional to the radius of the tube:

$$\frac{T_e(R_1)-T(R_1)}{T_e(R_2)-T(R_2)}=\frac{R_2}{R_1} \text{ at } \frac{W}{2\pi\lambda}>\varepsilon R_1, \varepsilon R_2$$

$$\frac{T_e(R_1)-T(R_1)}{T_e(R_2)-T(R_2)}\approx 1 \text{ at } \frac{W}{2\pi\lambda}<\varepsilon R_1, \varepsilon R_2$$

Although, of course, the fact that with the growth of R the gap between the electron and gas temperatures on the wall should decrease, that is, the condition must be met

$$\lim T_e(R)\to T(R) \text{ at } R\to\infty$$

is in advance sufficiently obvious physically.

Results and conclusions

Tables 1-2 are represented by the gap value calculated for the different discharge formula amperage values (3). Calculations were made for an argon plasma at atmospheric pressure for two current intensity values I =78 A and I=200 A and various values of the wall temperature. It shows the corresponding experimental results in these tables, published in a series of papers /1-3/. As you can see, there is good qualitative agreement of the results of calculations with experimental data, which increases with decreasing temperature of the wall.

Table 1 – Values $\Delta T(R)$ for I=78 A

	$\Delta T(R)$ for $T(R)$=1440 K	$\Delta T(R)$ for $T(R)$=4000 K
Calculation	7200 K	4700 K
Experimental data /3/	7860 K	5300 K

Table 2 – Values $\Delta T(R)$ for I=200 A

	$\Delta T(R)$ for $T(R)$=4000 K
Calculation	4800 K
Experimental data /3/	6000 K

In conclusion, we note that the results obtained in this study can be used as a simple model for the assessment fairly complex physical processes, and in some engineering calculations, including those relating to the use of low-temperature plasma arcs in the functional coating processes.

References

1. **Asinovskii E. I., Pakhomov E. P., Yartsev Y. M.** Khimicheskie reakcii v nizkotemperaturnoi plasma, Moscow: INKHS (1977) 83-103.
2. **Asinovskii E. I., Pakhomov E. P., Yartsev Y. M.** Teplofizika Vysokikh Temperatur (High Temperature), **1** (1978) 28-36.
3. **Asinovskii E. I., Pakhomov E. P.** Teplofizika Vysokikh Temperatur (High Temperature), **6** (1968) 333-336.
4. **Engel, A. and Steenbeck, M.**, Physics and Engineering of a Discharge of Electric ity in Gases,Vol. 2, Properties of Gas Discharges. Engineering Application (in German), Julius Springer Verlag, Berlin, (1934).
5. **Raizer Yu. P.** Osnovy sovremennoi fiziki gasorazryadnykh processov. Moscow: Nauka, (1980).
6. **Raizer Yu. P.** Fizika gasovogo razryada, Moscow: Nauka, (1987).
7. **Gerasimov A.V. and Kirpichnikov A.P.** Thermal Science, 1 (2003) 101-107.
8. **Dvait G. B.** Tablicy integralov i drugie matematicheskie formuly. (Integral tables and other mathematical formulas) Moscow: Nauka, (1983).

THE DYNAMICS PECULIARITIES OF CARBON EROSION JET FORMED BY ACTION OF NANOSECOND LASER PULSES AT VACUUM

V. Goncharov, K. Kozadaev, M. Puzyrov

A.N.Sevchenko Scientific-Research Institute of Applied Physical Problems of BSU,
7 Kurchatov Str., 220108, Minsk, Belarus, kozadaevkv@bsu.by

Pulsed laser deposition (PLD) processes are widely used to solve a number of practical problems, for example, the application of multi-component and multi-layer nanostructured coatings with promising physical and chemical properties. A special role in this direction of research is played by carbon-containing coatings, a wide range of applications of which is due to the possibility of obtaining different types of hybridization of carbon, as well as its specific electrical, thermo physical and mechanical properties /1, 2/.

The description of the processes occurring in the carbon erosion laser jets (ELJ) is devoted to a number of theoretical and experimental works, however, due to the complexity of the object of their study, the articles, as a rule, are somewhat one-sided, highlighting one or more of the many factors of this phenomenon. This work aims to study the processes of development and decay of carbon erosion torches, based on a vast array of experimental data and taking into account the mathematical model of the dynamics of torches, which is proposed by S. I. Anisimov and B. S. Lukyanchuk /3, 4/. An important role is given to the analysis of own empirical data of the study of spatio-temporal distributions of optical and electrical characteristics of the discussed processes.

The Anisimov-Lukyanchuk model allows us to calculate the dynamics of the vapor-liquid phase transition in an adiabatically expanding vapor-plasma carbon torch, which leads to the formation of a cloud of carbon clusters (with characteristic dimensions of several nanometers). The simulation results are in good agreement with the experimental data /5/, in particular, /6/ it is shown that the deposition of such clusters on different substrates is possible to form carbon and diamond-like films with promising physical properties.

However, as practice shows, the dynamics of the vapor-plasma cloud in this case is even more complex due to the electro dynamic effects in the expanding plasma. The complex nature of the vapor-plasma formation illumination was observed in the study /7/, according to these data, instead of the glow of a spherical vapor-plasma cloud, at different heights above the target, there is a "separation" and an independent advance of the luminous region.

In the conditions of low pressure this effect was explained by the advance of the shock wave front /8/, but such an effect was recorded in a vacuum, which makes us look for other physical mechanisms for its explanation.

The experiments have allowed to find two areas of light emission in the ELJ formed under the action of a laser pulse on a graphite target in a vacuum at a power density of $5.6 \cdot 10^8$ W/cm^2. One zone is stationary and located at the target surface in the area of the laser radiation exposure spot. The other zone of the luminescence moves towards the laser beam at a speed of 10 km/s. This zone is explained by the formation of a moving double electric layer in the laser jet, in the space of which radiation occurs due to the recombination of charged particles. As a result of different time of illumination of individual zones of the ELJ, a ”fixed” glow zone is formed at a distance of about 4 cm from the target surface Fig. 1.

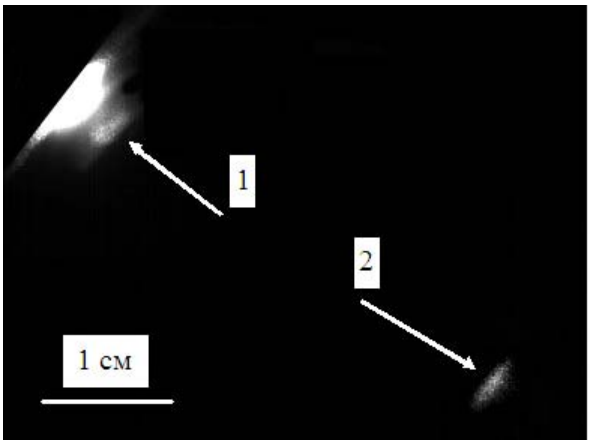

Fig. 1 - Spatial irradiation of the ELJ of a graphite target: 1-glow near the target surface; 2-glow at a distance of ~ 4 cm from the target surface

References

1. **Chrisey D.B. and Hubler G.K.** Pulsed Laser Deposition of Thin Films. New York: John Wiley & Sons Inc. (1994).
2. **Bonelli M., Miotello A. and Mosaner P**. J.Appl.Phys, 93 (2003) 859–865.
3. **Luk’yanchuk B.S., Marine W., Anisimov S.I.** Laser Phys., 8 (1998) 291–302.
4. **Kuwata M., Luk’yanchuk B., Yabe T.** Proc. SPIE, 4065 (2000) 441–451.
5. **Marine W., Luk’yanchuk B., Sentis M.** Le Vide Sci. Tech. Appl., 228 (1998) 440–446.
6. **Luk'yanchuk B.S. [et al.]**. Proc. SPIE, 3618 (1999) 434–452.
7. **Goncharov V.K., Puzyrev M.V.** PPPT8. Cont. papers. 2 (2015) 173–177
8. **Sukhov T.** Laser spectroscopic analysis (in Russian). Novosibirsk: Nauka (1990).

ELECTRON CAPTURE IN THE DENSE NONIDEAL PLASMA ON THE BASIS OF THE EFFECTIVE POTENTIAL

E.O. Shalenov*, M.M. Seisembayeva, K.N. Dzhumagulova, T.S. Ramazanov

IETP, Department of Physics, al-Farabi KazNU, al-Farabi 71, 050040 Almaty, Kazakhstan
*e-mail: shalenov.erik@mail.ru

Introduction

Investigation of the interaction between particles and plasma properties is of great interest in many areas of physics such as atomic and plasma physics. Also, it is important for the development of the plasma technologies. One of the elementary processes in plasma is the electron capture process due to electron and atom collision. The process of the electron capture by an atom was investigated in many studies /1-5, 9/. In this paper electron capture by the hydrogen atom was considered. The neutral hydrogen atom can be transformed into the negative hydrogen ion due to polarization electron capture. The negative hydrogen ion plays an important role in partially ionized plasmas; also it is used for high energy accelerators and for the neutral beam injection systems of fusion devices. In work /5/ the electron capture cross section was theoretically evaluated in the framework of the perturbation theory, where unperturbed linear trajectory of the projectile was considered.

In this work we used the interaction potential between the electron and the atom in partially ionized hydrogen plasmas, which was presented in works /6-8/. This effective potential, taking into account the quantum-mechanical effects of diffraction of particles and plasma screening effects, has finite values at the distance close to zero. It has the following form:

$$\Phi_{ea}(r) = -e^2\alpha\left(e^{-Br}(1+Br) - e^{-Ar}(1+Ar)\right)^2 \Big/ \left(2r^4\left(1-4\lambda_{ea}^2/r_d^2\right)\right), \qquad (1)$$

where $A^2 = \left(1+\sqrt{1-4\lambda_{ea}^2/r_D^2}\right)\Big/\left(2\lambda_{ea}^2\right)$, $B^2 = \left(1-\sqrt{1-4\lambda_{ea}^2/r_D^2}\right)\Big/\left(2\lambda_{ea}^2\right)$. Here, $\lambda_{ea} = \mathrm{h}/\left(2\pi\mu_{ea}k_BT\right)^{1/2}$ is the de Broglie wavelength, $r_D = \sqrt{k_BT/(4\pi ne^2)}$ is the Debye length, k_B denotes the Boltzmann constant, $\mu_{ea} = m_em_a/\left(m_e+m_a\right) \approx m_e$ is the reduced mass of the atom and electron pair, α is the polarizability of the atom. For hydrogen atom it equals $4.5a_B^3$, $a_B = \mathrm{h}^2/\left(m_ee^2\right)$ is the Bohr radius.

Theory and methods

The Bohr-Lindhard method has been applied to obtain the electron capture radius; capture time and electron capture probability. In the Bohr-Lindhard method /2/, it has been known that the electron capture happens when the distance between the atom and moving electron is smaller than the electron capture radius R_{cap}. This electron capture radius is determined by equating the kinetic energy of moving electron and the interaction energy between the electron and the atom.

$$e^2\alpha\left(e^{-BR_{cap}}\left(1+BR_{cap}\right)-e^{-AR_{cap}}\left(1+AR_{cap}\right)\right)^2\Big/\left(2R_{cap}^4\left(1-4\lambda^2/r_d^2\right)\right)=m\upsilon_p^2/2\ , \quad (2)$$

where u_p is the velocity of moving electron, $m\upsilon_p^2/2$ is the kinetic energy of moving electron. The interaction energy provided by the polarization interaction should be greater than the kinetic energy of the moving electron in the frame of the hydrogen atom.

The time of the capture was determined as the time, when electron moves within capture radius. It was found from the ratio of the traversed path of the electron to the velocity of the electron.

$$t_{cap}=\begin{cases}2\sqrt{R_{cap}^2-b^2}\Big/\upsilon_p^2 & \text{for} \quad b\le R_{cap}\\ 0 & \text{for} \quad b\ge R_{cap}\end{cases}. \quad (4)$$

It should be noted that the electron is captured, if the impact parameter is less than the capture radius $b<R_{cap}$. The impact parameter b is the vertical distance between the centers of the moving electron and the atom.

The electron capture probability is defined by the ratio of the collision time to the electron orbital time:

$$P_{cap}(b)=t^{-1}\int_{-t_{cap}}^{t_{cap}}dt\ , \quad (5)$$

Using the electron capture probability, the electron capture cross section was calculated on the basis of the following expression:

$$s_{cap}=2p\int dbbP_{cap}(b)\ . \quad (6)$$

where $t=a_n/v_n$ is the electron orbital time, $a_n=n^2a_B/Z$ is the n-th Bohr radius of the hydrogenic atom, Z is charge number of the atom, $v_n=Zac/n$ is the electron velocity of the n-th Bohr orbit.

In this work the pair collision of impacting electron with atom was considered. The influence of other plasma particles is taken into account by the effective potential (1). The equations of motion of the electron in the field of the motionless hydrogen atom were numerically solved.

Results

Fig. 1 and Fig. 2 show the differential cross section of electron capture obtained on the basis of the perturbation theory (4-6). These figures represent the dependence of the electron capture cross section on the impact parameter for various values of the coupling parameter and density parameter. As one can see, the differential cross section significantly increases with grow of the temperature, and decreases in more dense plasma.

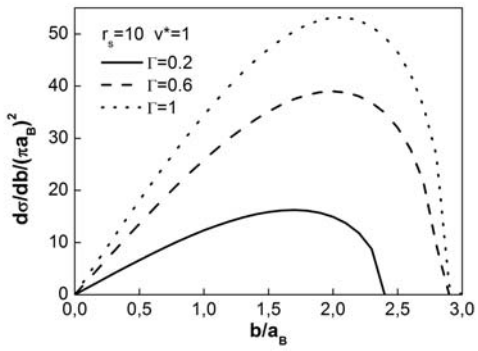

Fig. 1 – The differential cross section for different values of the coupling parameter

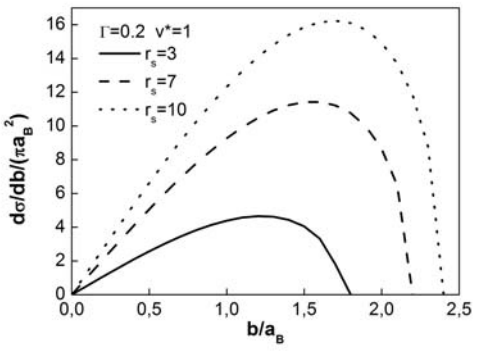

Fig. 2 – The differential cross section for different values of the density parameter

The trajectories of an electron near a hydrogen atom, calculated on the basis of the numerical solution of the equations of motion of electron with initial velocity and impact parameters b, are shown in Fig. 3. In this figure, the hydrogen atom is indicated by a circle.

Comparison of the differential cross section obtained by the perturbation theory and by solving the equation of motion was presented in Fig. 4.

Conclusion

In this paper process of electron capture by the hydrogen atom was investigated. The interaction between the electron and the atom takes into account the screening effect at large distances and the effect of diffraction at small distances.

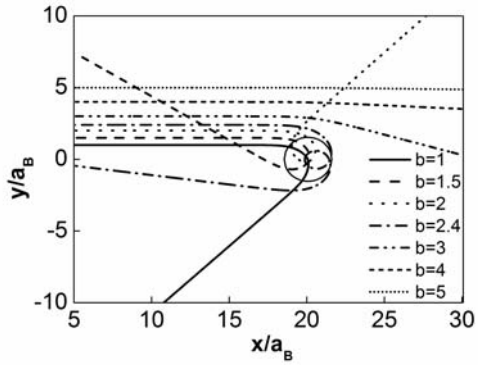

Fig. 3 – The trajectories of the electron near the atom calculated by the equation of motion, $G = 0.2$, $r_s = 3$, $v_x^* = 1$, $v_y^* = 0$

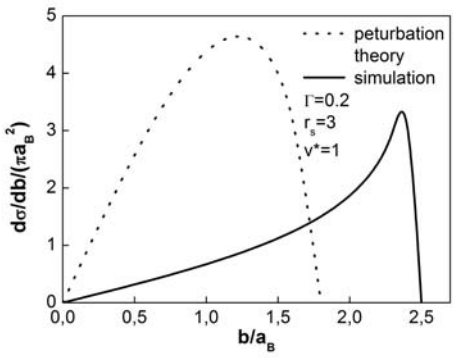

Fig. 4 – Comparison of the differential cross section

The differential cross section was obtained on the basis of perturbation theory and the equation of motion. Results were compared. The differential cross section equals to zero at large values of the impact parameter and grows with an increase in the coupling parameter. These results provide useful information on electron capture process in partially ionized plasma.

Acknowledgments

The authors acknowledge support within the Program BR 05236730 of the Ministry of Education and Science of the Republic of Kazakhstan.

References

1. **Ben-Itzhak I., Jaint A. and Weaver O.L.** J. Phys. B. 26 (1993) 1711.
2. **Brandt D.** Nucl. Instrum. Methods. 214 (1983) 93.
3. **Jung Y.-D.** Phys. Plasmas 4 (1997) 16.
4. **Jung Y.-D. and Akbari-Moghanjoughi M.** Phys. Plasmas 21 (2014) 032108.
5. **Ki D.-H. and Jung Y.-D.** Jour. Chem. Phys. 137 (2012) 094310.
6. **Ramazanov T.S., Dzhumagulova K.N. and Akbarov A.Z.** J. Phys. A - Math. and Gen. 39 (2006) 4335.
7. **Ramazanov T.S., Dzhumagulova K.N. and Gabdullin M.T.** J. Phys. A - Math. and Gen. 39 (2006) 4469.
8. **Ramazanov T.S., Dzhumagulova K.N. and Omarbakiyeva Y.A.** Phys. Plasmas 12 (2005) 092702.
9. **Ryufuku H. and Watanabe T.** Phys. Rev. A. 20 (1979) 1828.

MODELING OF EMISSION CHARACTERISTICS IN A MIXTURE OF MERCURY VAPOR AND ARGON

S. Anufrik, A. Volodenkov, K. Znosko

Yanka Kupala State University of Grodno, 22, Ozheshko Street, 230023, Grodno, Belarus, a.volodenkov@grsu.by

The model for studying of the emission characteristics of a mixture of Hg and Ar depending on the composition, total pressure, and the parameters of the power system when excited by a glow discharge was developed /1/. A simplified four-level scheme of the energy transitions of the mercury atom was used, taking into account the ground level 6^1S_0, the triplet levels $6^3P_{0,1,2}$. The model made it possible to determine the maximum obtainable power of radiation at a wavelength of 254 nm.

There have been numerous theoretical studies of the Ar–Hg low pressure, positive column discharge applicable to the conventional fluorescent lamp. Since inelastic collisions by electrons are the primary source for excitation and ionization, and elastic collisions with heavy particles determine the electron mobility and the gas heating, the electron energy distribution function (EEDF) plays a central role in any model of the fluorescent lamp /2, 3/.

By simultaneously solving the balances together with the kinetic equation the densities of electrons and excited Hg atoms, the electron energy distribution, the resulting mean energy, mobility and various energy transfer rates of the electrons and the ultraviolet radiation output were determined.

This report presents and analyses the macroscopic plasma properties mentioned for a wide range of the wall temperature or the corresponding Hg partial pressure variation, where a good agreement of calculated results with experimental data is obtained.

In the calculations, the following parameters were set. The voltage amplitude is U0 ~ 310 V. The mains frequency is f = 50 Hz. Ballast inductance L1 = 600 mH; ballast resistance R1 = 10 Ohm, capacity between electrodes $C1 = 10^{-8}$ F. Inter-electrode distance d = 40 cm. The radius of the discharge tube is R = 1.1 cm. The concentration of argon atoms is $9.9\ 10^{16}$ 1/cm^3 (partial pressure 3 Torr). When studying the emission characteristics, depending on the composition of the mixture, the concentration of mercury atoms varied within the limits of $1{,}5 \cdot 10^{14}$ 1/cm^3 - $3 \cdot 10^{14}$ 1/cm^3.

Fig. 1 shows the dependence of the radiation power (1) at a wavelength of 254 nm and the power of the heat released in the discharge (2) on the concentration of mercury atoms.

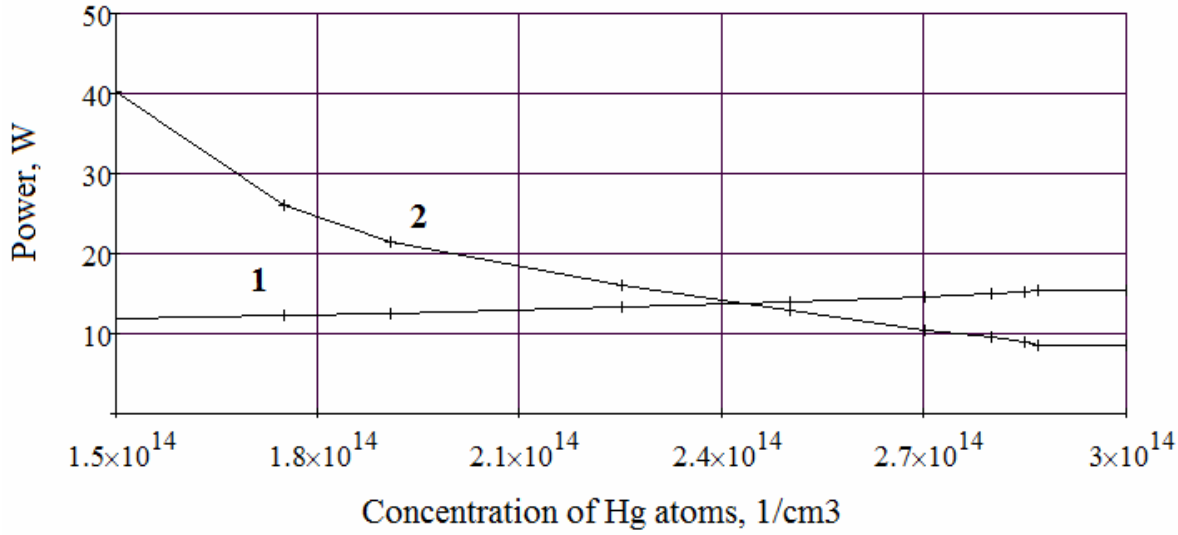

Fig. 1 - Dependence of radiation power (1) at a wavelength 254 nm and the power of heat released in discharge (2), on the concentration of mercury atoms

To construct a closed model of radiation sources for mercury vapor, it is necessary to take into account the dependence of the concentration of mercury atoms on the temperature of the inner surface of the radiator, which is determined by the heat output of the radiator emitted by the radiator and the heat exchange conditions on the external surface of the radiator.

We assume that the emitter has the following parameters: internal diameter D = 2.2 cm; wall thickness d = 0.2 cm; length of the radiator L = 40 cm. The radiator is made of quartz with a coefficient of thermal conductivity λ = 0.0138 W/(cm K). Suppose that we are implementing a mode of operation such as in the established case of the temperature of the inner surface of the radiator is equal to Tin= 43.30^0 C. From the graph of the dependence of the concentration of mercury atoms (partial pressure) on temperature (Fig. 2), we determine that the concentration of mercury atoms is $2.411 \cdot 10^{14}$ 1/cm^3.

According to the graph in Fig. 1, we determine that at such a concentration in the discharge, the heat release power is P = 13.744 W. This power must pass through the walls of the radiator, therefore

$$P = \lambda \cdot \pi \cdot D \cdot L \cdot \frac{(Tin - Tw)}{d}$$

From here, we determine the temperature of the outer wall of the emitter Tw.

$$Tw = Tin - \frac{P \cdot d}{\lambda \cdot \pi \cdot D \cdot L} = 42.5795^0 \text{ C}$$

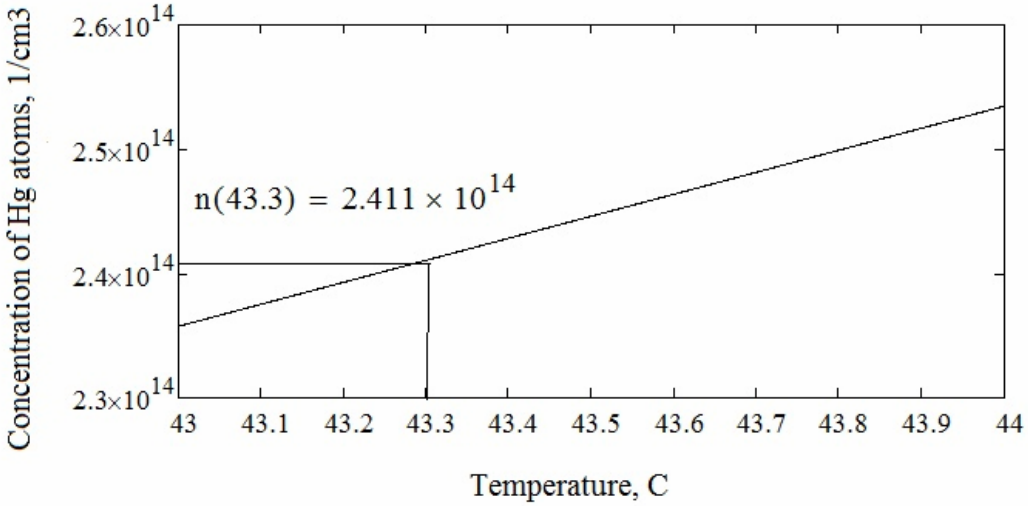

Fig.2 - Dependence of concentration of mercury atoms on temperature

We assume that the heat exchange on the external surface of the radiator is due to the blowing of the air flow with a temperature Tg = 20^0 C at a speed W. The kinematic viscosity of air at this temperature is $\nu = 15.06\ 10^{-2}$ cm^2/s, the thermal conductivity of the air is equal to $\lambda_a = 0.0259\ 10^{-2}$ W/(cm K). The Prandtl number for air at this temperature is equal to Pr = 0.703. We calculate the Reynolds number as a function of the flow velocity W.

$$Re(W) = \frac{W \cdot (D + 2d)}{\nu}$$

According to the data of /4/, the experimental data on the heat transfer in the case of a non-turbulent flow passing through a single circular tube around a single circular tube are generalized by the following formula:

$$Nu(W) = \left(0{,}43 + 0{,}55\left(Re(W)\right)^{0{,}5} \cdot \left(Pr\right)^{0{,}38}\right)$$

Where Nu (W) is the Nusselt number. Then the heat transfer coefficient as a function of the flow velocity W in the stabilized flow region will be equal to:

$$\alpha(W) = Nu(W) \cdot \frac{\lambda \mathrm{a}}{\left(D + 2d\right)}$$

Then the heat flux will be equal to a function of the flow velocity W

$$\mathrm{Pr}(W) = \alpha(W) \cdot \pi \cdot \left(D + 2d\right) \cdot L \cdot \left(T\mathrm{in} - T\mathrm{w}\right)$$

We select a flow rate W such that Pr (W) = P = 13.744 W. This equality will be satisfied at W = 83.56 cm/s. Then Re = 1.443 10^3; Nu = 18.702; $\alpha = 1.863\ 10^{-3}$ W / (cm^2 K): Pt (83.56) = 13.744 W.

Let us consider the case of convective heat transfer on the external wall of the radiator.

The dimensionless Grashof number for air is

$$Gr(\mathrm{Tw}) = \frac{g \cdot \beta \cdot (\mathrm{Tw} - \mathrm{Ta}) \cdot (D + 2d)^3}{\nu^2}$$

To calculate the heat transfer coefficient under natural convection conditions, the following dependence is usually used /4/:

$$Nu(Ta) = B \cdot (Gr(\mathrm{Ta}) \cdot Pr(Ta))^n \cdot \left(\frac{Pr(\mathrm{Ta})}{Pr(\mathrm{Tw})} \right)^{0,25}$$

Where the quantities B, n depend on the product (Gr (Тв) Pr (Тв)) and are given in /2/.

Then the heat transfer coefficient as a function of the air temperature Ta will be equal to:

$$\alpha(Ta) = Nu(Ta) \cdot \frac{\lambda \mathrm{a}}{(D + 2d)}$$

Then the heat flux will be equal as a function of the air temperature Ta will be equal.

$$P\mathrm{т}(\mathrm{Ta}) = \alpha(\mathrm{Ta}) \cdot \pi \cdot (D + 2d) \cdot L \cdot (\mathrm{Tw} - Ta)$$

The above relations enable us to construct a self-consistent model for calculating the emission power of fluorescent lamps.

Based on the developed model, the emission characteristics of a discharge plasma in an Ar-Hg mixture in the ultraviolet region of the spectrum at a wavelength of 254 nm are calculated depending on the parameters of the excitation system, radiator parameters and heat transfer conditions on the radiator surface. It is shown, that the efficiency of conversion, the power received from the network into radiation at a wavelength of 254 nm is ~ 25%. At the same time, the total average radiation power at a wavelength of 254 nm under simulation conditions was ~ 13 W, with a power input of ~ 34 W, and a power consumption of ~ 50 W. It is established, that conversion efficiency and radiation power increase with increasing concentration of mercury vapor, so it is advisable to use natural convection for cooling.

References

1. **Volodenkov A.P.** High Temperature Material Processes, 21, 4(2017) 377-390.
2. **Hagelaar G. J. M.** Plasma Sources Sci. Technol., 14 (2005) 1-12.
3. http://www.codiciel.fr/plateforme/plasma/bolsig/bolsig.php.
4. **Баскаков А. П.** Теплотехника. Москва: Энергоатомиздат (1991).

CALCULATION OF EMISSION CHARACTERISTICS OF XECL EXCILAMPS OF BARRIER DISCHARGE

S. Anufrik, A. Volodenkov, K. Znosko

Yanka Kupala State University of Grodno, 22, Ozheshko Street, 230023, Grodno, Belarus, a.volodenkov@grsu.by

Modeling of electro-discharge XeCl excilamps is discussed. The computer model includes the following modules.

The first is the module of the solving of Boltzmann equation for the electron energy distribution function (EEDF) /1, 2/. This module based on composition of a mixture, on value of a degree of ionization and set *E/N* (*E* - intensity of an electric field in the discharge gap; *N* - full concentration of particles) allows to find EEDF and to define rates of plasma-chemical reactions with participation of electrons, and also to define electron mobility.

For the solving Boltzmann equation ready program Bolsig + /2/ is used, which automatically calculates rate factors of reactions.

Velocity coefficients of reactions involving electrons were determined in the form of tables in which their dependence on the composition of the active medium, electron concentration, reduced electric field strength *E/N* is presented. The excited states were taken into account as separate components of the active medium, since we take into account the superelastic processes. Calculations are presented for a discrete multidimensional array of points. Extrapolation to intermediate values is carried out with the help of cubic splines. In order to be able to investigate the dependence of the emission characteristics on the buffer gas pressure (Ne), the dependence of the three-particle recombination coefficient of xenon (Xe^+) and chlorine (Cl^-) ions on the pressure is calculated.

The second is the module of the solving of system of the equations of plasma-chemical reactions /3/. Models of XeCl-excilamp (halogen HCl) are investigated and analyzed. On the base of these models the program module for solving of system of the equations of plasma-chemical reactions in electro-discharge XeCl-excilamp was developed. The power density of radiation of the excilamps (the power, obtained from unit of volume) is determined by next expression.

$$P = \left[XeCl^*\right] \cdot h\nu / \tau_{sp} \qquad (1)$$

[XeCl*] is concentration of excimer molecules; τ_{sp} - time constant of spontaneous emission.

The third is the module of the solving of the equations of an electric circuit. This module describes work of system of excitation of the volume discharge in active medium. On the total resistance of plasma this module allows to define

time dependence of *E/P*, formed by excitation system in active medium. For excitation of the discharge the system of excitation on the basis of a LC-contour on the lumped capacities has been used (Fig. 1.)

The following designations were used: *C*1 – the storage capacity; *L*1 – inductance of recharging of the storage capacity on peak capacity *C*0; *Rk(t)* – switchboard resistance; *R*pl - discharge resistance; *L0* - inductance of recharging of *C*0 on discharge; *C*d – dielectric capacity, Ce- interelectrode capacitance. The presence of an interelectrode capacitance provides a smaller number of steps in numerical calculations. The length of electrodes *h*=30 cm. The coaxial radiator was used, the value of *d* was 0,2 cm. Distance between electrodes *D2-D1*=2 cm (*D*1=28 cm). Charging voltage *U*ch=*U*1=30 kV has been used. Thus, at carrying out of calculations the equivalent electric circuit is used in Fig. 1b.

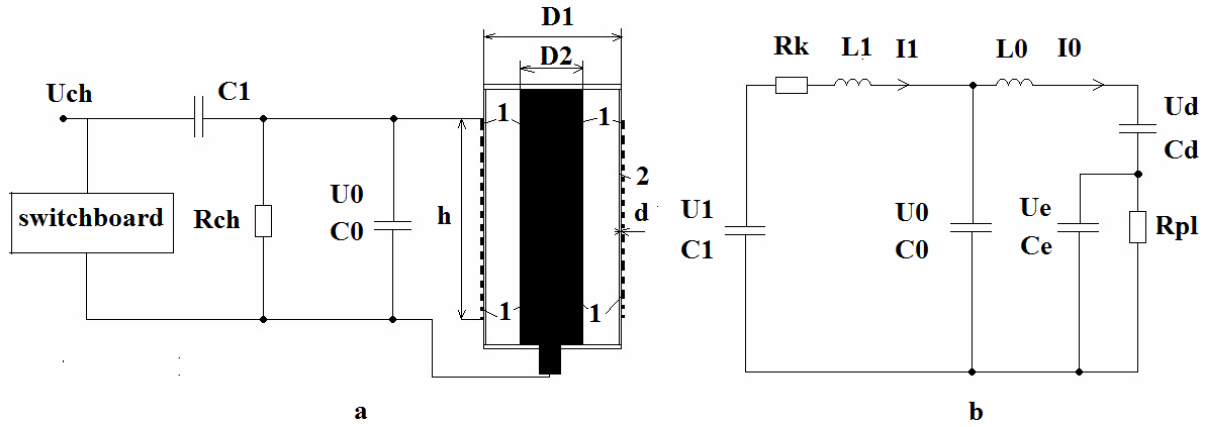

Fig. 1- The system of excitation

During modeling, the harpoon channel for the formation of XeCl molecules was not taken into account.

Simulation was performed at C1 = 2.5 nF; C0 = 2.2 nF; L1 = 5 nH; L0 = 5 nH; Rk = 0.1 Ohm. It was considered that the partial pressure of Xe was 40 Torr, and the partial pressure of HCl was 1 Torr. The charging voltage of the storage tank was 30 kV. Fig. 2 shows the dependence of the energy of spontaneous emission on the total pressure of the mixture.

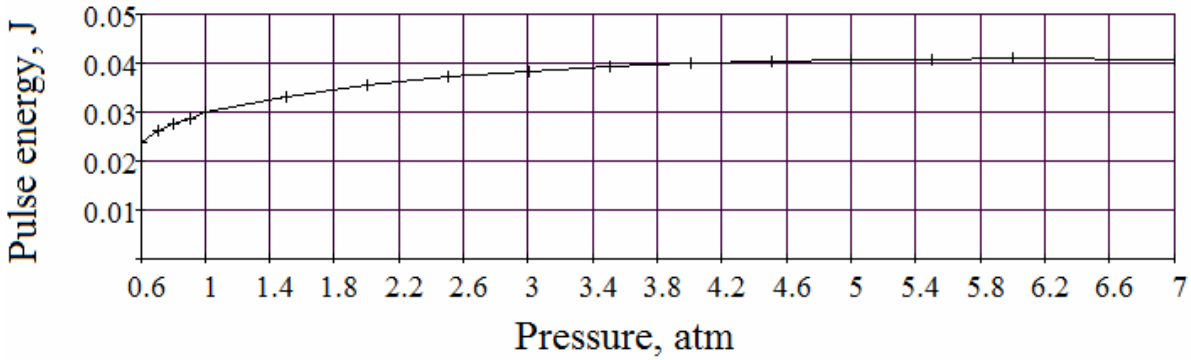

Fig. 2 – The dependence of energy of a pulse of radiation from pressure

Fig. 2 shows the dependence of the efficiency on the total pressure of the mixture.

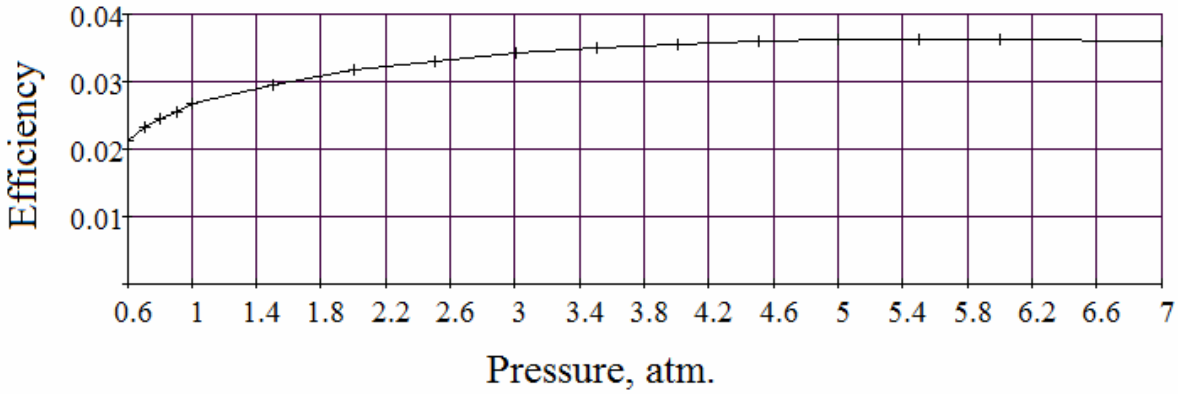

Fig. 3 – The dependence of efficiency of a pulse of radiation from pressure

The energy of the radiation pulse and the efficiency reach a maximum at the mixture pressure of 6 atm, which is due to the fact that the three-particle recombination coefficient reaches a maximum at this pressure.

Table 1 shows the pulse energy and efficiency obtained for different values of C1 and C0.

C1, nF	C0, nF	Energy, J	Efficiency
2	2	0, 041	0,036
2	0,2	0,036	0,04
1	0,2	0,027	0,06
0,9	0,2	0,025	0,062
0,8	0,2	0,024	0,065
0,8	0,4	0,022	0,062
0,7	0,2	0,0217	0,069
0,6	0,3	0,019	0,07
0,4	0,4	0,011	0,061
0,4	0,1	0,011	0,064
0,2	0,05	0,0036	0,04

From the presented dependences it follows that with a storage capacity of ~ 0.7 nF, the greatest efficiency is ~ 0.07.

During modeling, a harpoon channel for the formation of XeCl molecules was taken into account.

The simulation was performed at L1 = 5 nH; L0 = 5 nH; Rk = 0.1 Ohm. It was considered that the partial pressure of Xe was 40 Torr, and the partial

pressure of HC1 was 1 Torr, Total pressure was 1 atmospheres. The charging voltage of the storage tank was 30 kV.

Table 2 shows the pulse energy and efficiency obtained for different values of C1 and C0.

C1, nF	C0, nF	Energy, J	Efficiency
2	2	0, 07	0,078
2	0,2	0.089	0,099
1	0,2	0.069	0,15
0,9	0,2	0,066	0,163
0,8	0,2	0,062	0,174
0,8	0,4	0,059	0,163
0,7	0,2	0,058	0,185
0,6	0,3	0,052	0,192
0,4	0,4	0,031	0,172
0,4	0,1	0,033	0,182
0,2	0,05	0,012	0,13

From the presented dependences it follows that with a storage capacity of ~ 0.6 nF, the greatest efficiency is ~ 0.19. Taking into account the harpoon reaction leads to a significant increase in both pulse energy and efficiency.

Based on the results of the computer simulation of the XeCl excilamp using HCl: Xe: Ne mixtures at a total pressure of 1 atm when excited by an LC circuit, it was shown that the energy of XeCl emission of excilamps is ~ 0.1 J with an efficiency of ~ 37%. The results of experimental studies have shown that the efficiency of the barrier-discharge excilamps is 10% (with the use of HCl) /1/.

The difference between calculation and experiment is the fact that the barrier does not fill the uniformly volumetric volume, but consists of individual threads, which occupy about a half of the total volume. In addition, we believe that the outer electrode is a mesh with a transparency of ~ 60%. and radiation is reflected from the internal electrode with a reflection coefficient of ~ 80%. When these corrections are taken into account, a correspondence between the calculation and the experiment is achieved.

References

1. **Hagelaar G. J. M.** Plasma Sources Sci. Technol., 14 (2005) 1-12.
2. http://www.codiciel.fr/plateforme/plasma/bolsig/bolsig.php.
3. **Панченко А. Н.** Известия вузов. Физика, 42 (1999) 50-66.
4. **Ануфрик С.С.** Вестник ГрГУ серия 2, 1 (2015) 113-123.

INVESTIGATION OF C_2 AND CN BAND EMISSION AS A TOOL FOR DETERMINING THE TEMPERATURE OF ARGON ARC PLASMA

D.P. Ranković[1], M.M. Kuzmanović[1], J.J. Savović[2]

[1] University of Belgrade, Faculty for Physical Chemistry, Studentski Trg 12-16, 11000 Belgrade, Serbia. (ranko@ffh.bg.ac.rs)
[2] University of Belgrade, INN Vinča, Mike Petrovića Alasa 12-14, 11351 Vinča, Belgrade, Serbia.

Abstract

Direct current (*DC*) argon arc with continuous aerosol supply is suitable excitation source for spectrochemical analysis of liquid samples. When 20 % alcohol – water solution was nebulized into the argon plasma, the recorded spectra were dominated by intensive emission of diatomic molecules C_2 and CN. Well-resolved spectral bands of Swan (C_2), and violet system (CN) were used to estimate molecule vibrational and rotational temperature by comparison of experimental and simulated spectra. The obtained rotational and vibrational temperatures were practically the same, and varied from 4500 – 7000 K, depending on the observed radial position.

Introduction

Atmospheric pressure argon plasmas are possibly the most important excitation sources for analytical emission spectroscopy. A specific type of such plasma source is a *U* – shaped argon – stabilized dc arc with continuous – flow sample introduction system. This arc was found to be especially suitable for trace metal analysis. In fact, limits of detection of the *U* – shaped *DC* argon are comparable to those achieved by inductively coupled plasma (*ICP*) sources. Well defined geometry of the arc column and stable arc operation are also suitable for investigation of excitation, ionization and transport processes in the argon plasma [1].

The spectral emission of molecules bands has many applications in the spectroscopy, e.g. for detection of stable molecules, chemical analysis of nonmetal elements, and isotopic analysis. Also, the analysis of molecular spectral emission is a useful diagnostic method for determination of the translational temperature. The C_2 and CN molecules can exist at relatively high plasma temperatures and their spectral bands are of special interest due to its intensive emission in the plasmas containing organic material. In this work, the applicability of C_2 (Swan system), and CN (violet system) emission spectra for

estimation of the temperature of heavy particles (i.e. gas or translation temperature) in an argon arc plasma was investigated.

Experimental

A detailed description of the *U* – shaped dc argon arc with combined gas vortex and wall stabilization, operating at atmospheric pressure was given in our previous paper [2]. The arc source (Fig. 1) consists of electrically insulated segments made of brass. Apart from the central segment, all other segments are water cooled. The water cooled segments have narrow openings for electrodes. The electric arc burns at atmospheric pressure in a horizontal cylinder whose axis is perpendicular to the electrodes. The arc column is stabilized with combined gas and wall stabilization. Aqueous aerosol obtained with glass concentric nebulizer and homogenized by passing through a spray chamber of Scott type, is tangentially introduced into the cavity of the central segment of the arc device to create a gas vortex that spatially stabilizes arc column plasma. Aerosol flow rate and arc current were 2.7 L/min and 7 A, respectively. An ethyl – alcohol water solution (20 % Vol.) was nebulized into argon arc plasma in order to obtain C_2 and CN molecular emission.

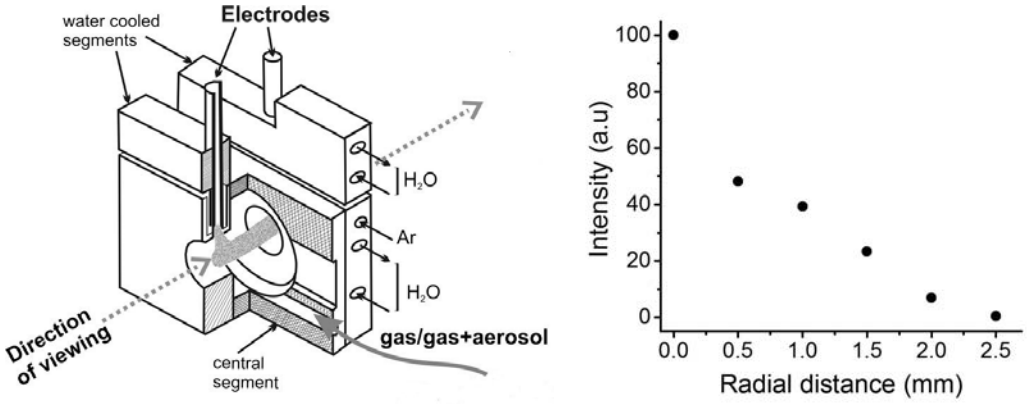

Figure 1. a) A schematic representation of the arc device; b) Radial distribution of C_2 0 – 0 band head intensities

The horizontal part of the arc column was projected by an achromatic lens onto the entrance slit of a Zeiss *PGS* – 2 monochromator. In this way the electrodes and the regions near the electrodes are eliminated from the viewing direction. The reciprocal linear dispersion was 0.73 nm/mm and slit width was 25 μm. Typical dispersion was 7 nm/mm, and FWHM of the instrumental profile was 0.025 nm. The instrumental width was determined by measurements of the appropriate Hg lines emitted from a low pressure pen lamp.

Plasma emission spectra were detected by a back thinned Apogee Alta F1007 CCD camera with enhanced spectral sensitivity up to 200 nm, with low

dark current signal provided by Peltier coolers. The CCD chip active area consists of 1024 x 122 pixels (pixel dimension 12 x 12 μm). For the present spectrograph settings, a detector captures wavelength range of about 8.5 nm.

Results and discussion

Part of the spectrum of (0 – 0) and (1 – 1) bands of C_2 is shown in Fig. 2. The synthetic spectra of Swan system were calculated using the PGOPHER program [3]. Line profile was Gaussian, with FWHM = 0.025 nm. The intensities were normalized to the intensity values of (0 – 0) band head. As it is shown in Fig. 2, *P* and *R* branch are well separated at this resolution, and their intensity ratio is very sensitive to variations in the temperature. The best agreement between the experimental and synthetic spectrum was obtained for a rotational and vibrational temperature of 6400 K. The intensity ratio of (1 – 1) and (0 – 0) band head is not very sensitive to the temperature changes, thus it is unsuitable for determination of the vibrational temperature. Good matching of (0 – 0) band head profile indicates that the self – absorption could be neglected. Intensities of C_2 and CN bands decrease rapidly with shifting of the observed radial position toward the arc column periphery, Fig. 1b. By analyzing the emission spectra of the (0 – 0) C_2 band, the temperature was estimated. For radial positions between 0 and 2.5 mm from the arc axis, estimated temperature was in the 7000 – 4700 K range.

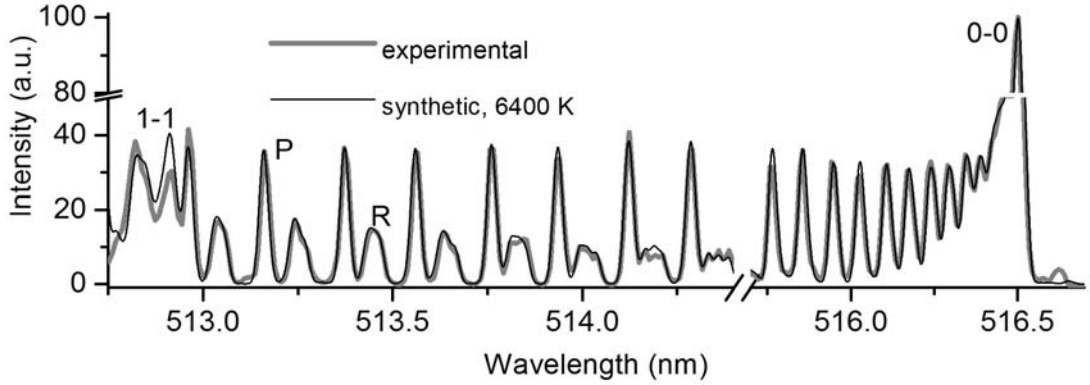

Figure 2. Experimental (obtained at 1 mm radial position) and synthetic ($T_{vib} = T_{rot} = 6400$ K) spectra of $\Delta v = 0$ sequence of C_2.

The applicability of Δv=+0 sequence of CN violet system for determination of the vibrational temperature is demonstrated in Fig. 3. The synthetic spectrum of the violet system was calculated by LIFBASE software [4]. The best matching was observed for $T_{rot} = T_{vib} = 6400$ K. The change of relative intensities of the band heads allowed relatively precise determination of the vibrational temperature, with acceptable low impact of the uncertainty of T_{rot}. Despite a favorable circumstance that four band heads are situated in a narrow spectral

interval (approximately within 3 nm), rotational structure of the sequence is not appropriate for the accurate determination of temperature. As in the case of C_2 spectra, very good matching of the synthetic and experimental band head profiles As in the case of the C_2 spectra, good matching of the synthetic and experimental band head profiles verified that neglecting of the self-absorption was justified.

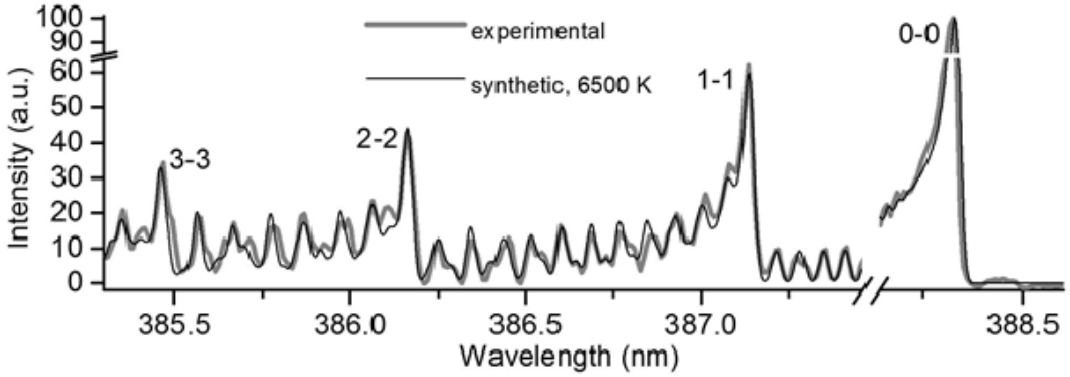

Figure 3. Experimental (obtained at 1 mm radial position) and synthetic (T_{vib} = T_{rot} = 6500 K) spectra of Δν=0 sequence of CN

Conclusion

The applicability of C_2 and CN spectral bands for determination of the rotational and vibrational temperature in the argon arc plasma (containing organic compounds in the nebulized solution) was demonstrated. Comparison of the measured and simulated band spectra showed good matching. Also, both C_2 and CN spectra gave very close temperatures values. Intensive emission of these bands from the arc core can distort the temperature measurements at cooler arc periphery.

Acknowledgements. This research was supported by the Ministry of Education, Science and Technological Development of the Republic of Serbia through the project, "Effects of Laser Radiation on Novel Materials in Their Synthesis, Modifications, and Analysis" (project no. 172019).

References

[1] Savović J., Pavlović M., Stoiljković M., Kuzmanović M., Momčilović M., Vasić V., Spectrochem. Acta, 73 (2012) 62-70.
[2] Ranković D., Kuzmanović M., Pavlović M., Stoiljković M. and Savović J., Plasma Chem Plasma Process, 35 (2015) 1071-1095.
[3] Western C.M., J. Quant. Spectrosc. Radiat. Transf., 186 (2017) 221-242.
[4] Luque J. and Crosley D.R., SRI Int. Rep. MP, 99 (1999) 9.

NUMERICAL SIMULATION OF THE POWDER PARTICLES BEHAVIOUR IN A TECHNOLOGICAL ICP

M. Voronov, K. Nagulin, R. Nazarov, A. Gilmutdinov

Kazan National Research Technical University, K. Marx str. 10, 420111, Kazan, Russia
E-mail: VoronovMV@mail.ru

High enthalpy and plasma density, absence of electrodes resulting in a high purity of the plasma, flexibility of parameters are well known properties of atmospheric pressure ICPs. Because of this the ICPs have found strong practical applications for processing of different substances, including spheroidization of powder particles and production of nanoparticles.

In early stage of ICP simulations, evolution of powders in ICP was simulated within a two-dimensional cylindrically symmetrical (2D) ICP models. In our days three-dimensional non-stationary (4D) models of ICP are developed by few groups and applied for technological ICPs (mostly for simulation of nanoparticle growth), as well as for spectrochemical ICP. However, time of computation of the 4D models is large. For example, the 4D model developed in our group takes 2-3 days for calculation of 10 seconds of the ICP evolution (a simplified model without introduction of the sample in the plasma). This restricts application of the 4D models for practical optimization of the ICP parameters in a wide range. From the other side, our 2D model reaches (for a similar simplified task) the result in about 10 minutes. Therefore the 2D models should not be forgotten yet.

Here we present a 2D model of the technological atmospheric pressure ICP. The model is based on our previous 2D ICP model, which has demonstrated a good agreement with experimental data for a spectrochemical ICP [1-3]. For this work the model is extended: axial component of the electrical current flowing in the load coil is taken into account. This allows simulation of electromagnetically-driven rotation of the plasma around the axis. To check the model in the conditions of technological ICPs, the gas flows in an experimental TICP were visualized. For this an alumina powder was introduced into the plasma; the flows of the glowing alumina particles were detected by a fast video camera. A good agreement between the obtained visualization and the results of the simulations is achieved.

Evolution of the particles of the powder (trajectories, heating and evaporation) is included in the model together with thermal and gas-dynamic load of the plasma by the particles. To calculate the particle trajectories, the 2nd law of Newton is applied to the individual particles. Drag force and gravity are taken into account [4,5]:

$$\vec{F} = m\frac{d\vec{v}_p}{dt} = m\vec{g} - \frac{1}{8}\pi d_p^2 C_D\left(\vec{v}_g - \vec{v}_p\right)\left|\vec{v}_g - \vec{v}_p\right|\rho_g,$$

where $\vec{F}$ is a total force applied to the particle, m is mass of the particle, $\vec{v}_p$ is its velocity, $\vec{g}$ is a gravitational acceleration, d_p is a diameter of the particle, $\vec{v}_g$ is velocity of the surrounding gas, ρ_g is the gas density, C_D is a drag constant of a spherical particle. The following empirical expression is used to estimate C_D as function of Reynolds number R_e [4,5]:

$$C_D = \begin{cases} 24/R_e\,, & R_e \le 0.2 \\ 24/R_e\,(1 + 3/16\,R_e), & 0.2 < R_e \le 2 \\ 24/R_e\,(1 + 0.11R_e^{0.81}), & 2 < R_e \le 21 \\ 24/R_e\,(1 + 0.189R_e^{0.62}), & 21 < R_e \end{cases}$$

The drag force is taken into account at calculation of the particle trajectories and, from the other side, is applied to accelerate the gas, with an opposite sign. In this way a gas-dynamic load of the plasma gas from the particles is taken into account.

For calculation of the particle heating, melting and evaporation, flow of heat to the particle Q is calculated in the model [4,5]:

$$Q = \pi d_p^2 h_c\left(T_g - T_p\right) - \pi d_p^2 \sigma_s \varepsilon\left(T_p^4 - T_a^4\right), \qquad (1)$$

where h_c is a heat transfer coefficient, T_p is temperature of the particle, T_g is temperature of the surrounding gas, σ_s is the Stephan-Boltzmann constant, ε is emissivity of the material of the particle, T_a is an ambient temperature related to a radiation energy transfer. Based on quantity of the received energy, heating or phase change (melting or evaporation) of the particle takes place:

$$Q = \begin{cases} \left(\pi\rho_p d_p^3 c_p/6\right)\dfrac{dT_p}{dt}, & T < T_m \text{ and } T_m < T < T_b \\ \left(\pi\rho_p d_p^3 H_m/6\right)\dfrac{dL}{dt}, & T = T_m \\ \left(-\pi\rho_p d_p^3 H_v/2\right)\dfrac{dd_p}{dt}, & T = T_m \end{cases} , \quad (1)$$

where ρ_p is the particle's density, c_p is a specific heat capacity of the material of the particle, T_m is a melting temperature, T_m is a boiling temperature of the material, H_m is a latent heat of melting, H_v is a latent heat of evaporation of the particle material, L is a mass fraction of the melted material in the particle. In addition to the particle heating, the heat transferred from the gas to the particle (the 1st term in the equation 1) is included in the gas heat equation. In this way cooling of the gas by the particles is taken into account.

In Fig. 1 trajectories of particles in the ICP is presented together with distribution of the gas temperature with different load of the plasma by the particles. Reduction of the temperature at the high plasma load is clearly seen.

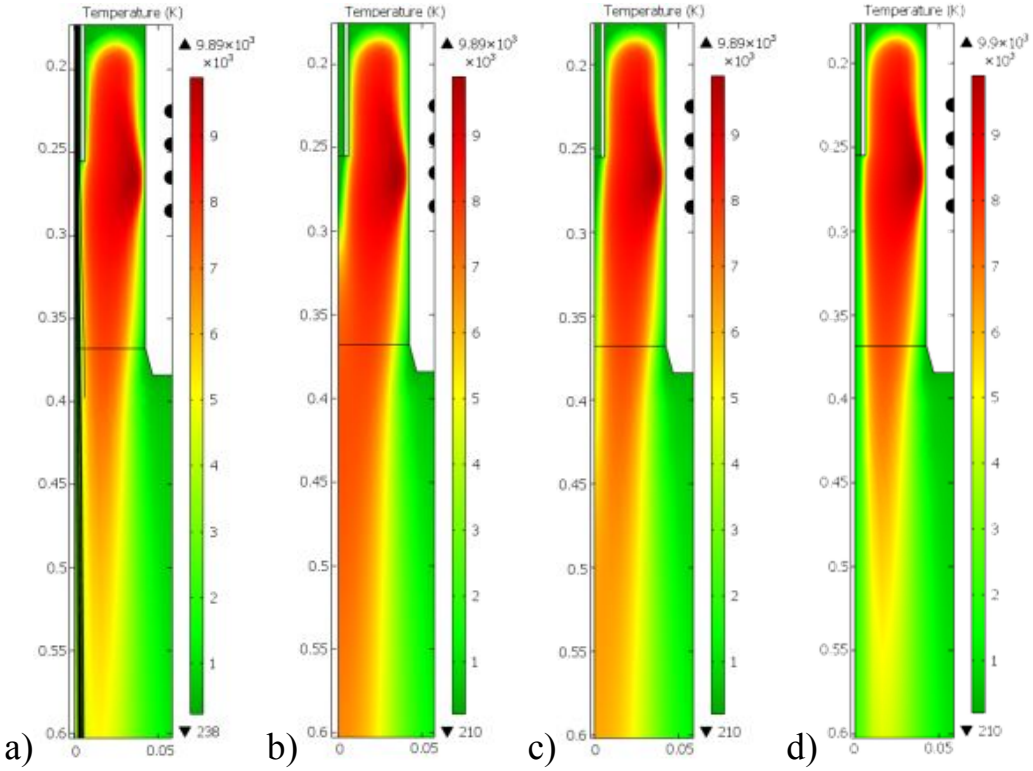

Fig. 1. Trajectories of the particles (a), distribution of temperature in the plasma at the particle load 0 kg/hour (b), 1 kg/hour (c), 10 kg/hour (c).

Acknowledgements. This work is supported financially by the Ministry of Education and Science of the Russian Federation (research grants №14.Z50.31.0023 and 9.3236.2017/4.6), Russian Foundation of Basic Research (contract №18-42-160015\18), and Federal Target Program 1.3 (agreement № 14.578.21.0245).

References

1. M. Voronov, V. Hoffmann, D. Birus, C. Engelhard, W. Buscher, *J. Anal. At. Spectrom.*, 2015, **30**, 2089–2098
2. M. Voronov, V. Hoffmann, C. Engelhard, W. Buscher, *J. Anal. At. Spectrom.*, 2017, **32**, 167–180
3. M. Voronov, V. Hoffmann, W. Buscher, C. Engelhard, *J. Anal. At. Spectrom.*, 2017, **32**, 181–192
4. P. Proulx, J. Mostaghimi, M.I. Boulos, *Int. J. Heat Mass Transfer*, 1985, **28**, No. 7, 1327-1336
5. P. Proulx, J. Mostaghimi, M.I. Boulos, *Plasma Chemistry and Plasma Processing*, 1987, **7**, No. 1, 29-52

VORTEXES IN A TECHNOLOGICAL ATMOSPHERIC PRESSURE ICP PRODUCED BY ELECTROMAGNETIC PHENOMENA

M. Voronov, K. Nagulin, O. Kudimov, A. Gilmutdinov

Kazan National Research Technical University, K. Marx str. 10, 420111, Kazan, Russia
E-mail: VoronovMV@mail.ru

High enthalpy and plasma density, absence of electrodes resulting in a high purity of the plasma, flexibility of parameters are well known properties of atmospheric pressure ICPs. Because of this the ICPs have found strong practical applications for processing of different substances, namely for spheroidization of powder particles, production of nanoparticles (TICPs) and as a source for atomic analysis (SICP). The TICPs are larger than the SICPs, consume more argon and power.

It was computationally found [1-4] that the gas flow has a strong toroidal vortex in a cross-section of the ICP containing its axis (*toroidal vortex*). This vortex is attributed to a compression of the plasma towards the axis by a radial component of Lorentz forces. Direction of rotation of the toroidal vortex prevents undisturbed penetration of the processing substance from the central channel to the hot area of the plasma. Therefore the toroidal vortex should be avoided.

A similar vortex was also found experimentally and computationally in SICP, but explained by gas-dynamical effects [5]. Therefore nature of the toroidal vortex needs clarification.

There is also a rotation of the plasma around the axis that is denoted *axial vortex* here. Obvious reason of this vortex is introduction of a tangential component of the gas flow in the ICP that is used to stabilize it. Additionally there is a tangential component of the Lorentz force exerted to the plasma that can influence on the axial vortex. Therefore the nature of the axial vortex also needs clarification, namely if the vortex produced more by the Lorentz forces or by the swirl component of the input gas stream?

An LTE-based two-dimensional (cylindrically symmetric) stationary model of ICP was developed and applied for the simulation of fundamental properties

of TICPs and SICPs. The model was based originally on existing models of J. Mostaghimi, M. Boulos, P. Proulx *et al* and Lindner *et al*, and have a good agreement with experimental data measured for SICP [6-8]. Now the model is extended based on a work of Xue et al [9], where axial component of the electrical current in the load coil is taken into account. This allows simulation of tangential Lorentz force in the plasma and the corresponding electromagnetically-driven rotation of the plasma around the axis.

The model has already shown a good agreement with experimental results in SICP conditions [7,8]. To check the model in the TICP conditions, the gas flows in an experimental TICP were visualized. For this an alumina powder was introduced into the plasma; the flows of the glowing alumina particles were detected by a fast video camera. A good agreement between the obtained visualization and the results of the simulations is also achieved.

It was found that the Lorentz forces in the induction zone of the TICP are significantly higher than the gas-dynamic pressure. It is the Lorentz force that generates both the toroidal vortex and the axial vortex in the TICP conditions. An opposite situation is found in the SICP. Here the gas inertia dominates over the Loretnz force, which is negligible.

To understand difference between the TICP and the SICP, a similarity laws in an atmospheric pressure ICPs [10] can be used. To scale the ICP source from SICP size to TICP size with conservation of the gas temperature and the gas flow pattern, the following conservation lows should be satisfied: the Reynolds number Re = $\rho v R/\eta = const$, the induction number $I = \mu_0 \sigma \omega R^2 = const$, the Joule number $J = \frac{\sigma |E_0|^2/2}{\rho v C_p T/R} = const$, the Froude number Fr = $f_g/f_l = \frac{\rho v^2/R}{\sigma |Re(\vec{E}_0 \times \vec{B}_0)|} = const$, which is ratio of the gas inertia force and the Lorentz force. The first three numbers can be conserved by adjusting the total gas consumption, RF frequency and the plasma power, respectively. To conserve the Froude number, the authors of the similarity low suggest adjusting the gas pressure. However we are focused on the atmospheric pressure ICPs. Under this condition it is impossible to scale the ICPs without change of the ratio of the forces and, therefore, without change of the flow pattern. Therefore the flow patterns of the TICP and the SICP differ significantly.

Based on the above developed analysis, ways for practical reduction of the toroidal vortex in the TICP are discussed: reduction of the plasma power, increase of the gas flows, increase of RF frequency, reduction of size of the plasma torch.

Acknowledgements. This work is supported financially by the Ministry of Education and Science of the Russian Federation (research grants №14.Z50.31.0023 and 9.3236.2017/4.6), Russian Foundation of Basic Research (contract №18-42-160015\18), and Federal Target Program 1.3 (agreement № 14.578.21.0245)

References

1. J.D. Chase, *Journal of Applied Physics*, 1969, **40**, 318-325
2. M.I. Boulos, *IEEE Transactions on Plasma Science*, 1976, **4**, No. 1, 28-39
3. M.I. Boulos, R. Gagne, R.M. Barnes, *The Canadian Journal of Chemical Engineering*, 1980, **58**, 367-381
4. L. Miao, Yu.M. Grishin, *Science and Education of the Bauman MSTU*, 2016, **8**, 50-66 (in Russian)
5. M. Aghaei, L. Flamigni, H. Lindner, D. Günther, A. Bogaerts, *J. Anal. At. Spectrom.*, 2014, **29**, 249–261
6. M. Voronov, V. Hoffmann, D. Birus, C. Engelhard, W. Buscher, *J. Anal. At. Spectrom.*, 2015, **30**, 2089–2098
7. M. Voronov, V. Hoffmann, C. Engelhard, W. Buscher, *J. Anal. At. Spectrom.*, 2017, **32**, 167–180
8. M. Voronov, V. Hoffmann, W. Buscher, C. Engelhard, *J. Anal. At. Spectrom.*, 2017, **32**, 181–192
9. S. Xue, P. Proulx, M.I. Boulos, *Plasma Chemistry and Plasma Processing*, 2003, **23**, No. 2, 245-263
10. D. Vanden-Abeele, G. Degrez, *Plasma Sources Sci. Technol.*, 2004, **13**, 680-690

INVESTIGATION OF THE SWITCHING ARC IN THE HV GAS-BLAST INTERRUPTERS DOWNSTREAM REGION

Svetlana Averyanova, Eugeniy Tonkonogov

St.Petersburg Polytechnic University, Institute of Energy and Transport System,
averly@yandex.ru

Abstract

The interaction between the switching arc and the gas flow is an important factor for increasing of interrupting ability in the HV gas-blast interrupters. The purpose of this investigation is to study the influence of the downstream region on the interrupting ability through the electric field strength rising. In the paper, the interaction between the switching arc and stream in the region between the nozzle exit and downstream contact is discussed. Numerical calculation of the arc parameters in the vicinity of the current zero in the downstream contact region are presented in comparison with experimental data.

Introduction

The HV gas-blast interrupters interrupting ability depend on the interaction between switching arc and gas flow in three main zones – the upstream, the nozzle throat, and the downstream ones. Main part of the investigations is devoted to the interaction between the switching arc and gas flow in two first sections. The upstream region interest is due to its dominant influence during the dielectric recovery. The nozzle throat region has the dominate influence during the thermal phase of the breakdown.

The influence on the interrupting ability of the process in the region between the nozzle outlet and the downstream arc contact is less investigated. In /1/ was shown that the electric field decrease with the decrease of the current in the region after the shock wave. In /2/ was shown that the arc diameter in the downstream region is remains considerably larger that at the nozzle throat in the vicinity of the current zero. Data that were presented in /1, 2/ has been shown that the flow in the downstream region depends on the Mach number at the nozzle exit and the ratio between the pressure at the nozzle exit and the rated pressure. Combination of these parameters can produce the shock wave in the downstream region. The shock wave placement, intensity and movement has the strong influence on the arc and gas parameters. Therefore, an investigation of downstream region is important in order to increase the HV interrupters parameters such as the rated voltage and the rated short circuit breaking current per break.

The purpose of this investigation is to study the influence of the downstream region to the HV interrupting ability. In the present work, results of a numerical analysis of the downstream region influence on the interruption ability are discussed. The comparison between the experimental /1/ and calculation data of the electric field strength in the downstream region for extinguish arc-chamber are presented.

Gas flow analysis in the downstream region

One of the arc-chamber main parts in the HV gas-blast interrupting is the supersonic nozzle. The schematic diagram of this nozzle is present in the Fig.1. By the arrow lines in the Fig. 1 shows the direction of the flow. The downstream region includes the diffuser part of the nozzle and the unconfined stream region. In the Fig. 1, the unconfined stream region shows as the dotted line.

The flow configuration in the nozzle depends on the pressure ratio between the inlet pressure (p_{in}) and the exit pressure (p_{exit}). Configuration of the out of nozzle flow near the downstream contact depends on the ratio between the pressure at the nozzle exit and the rated pressure. In the HV gas-blast interrupting the pressure ratio is more than 1, but it cannot provide the isentropic flow in the nozzle anyway. It means that in the diffuser part of the nozzle or in the flow out of nozzle, the shock wave can appear. The shock wave position depends on the pressure ratio and nozzle geometry.

For numerical calculations of the shock wave and switching arc interaction were used the time-averaged system of equations including the Navie-Stocks, continuity and energy equations /3/. Ohm's law and models for turbulent viscosity and radiation transfer added differential equations system.

The turbulence model takes into account the turbulence in the shear layer between arc and gas flow produced by two type of instability, such as shear instability and Rayleigh–Taylor instability for steady state /3/. For unsteady state, according to the /3/, was used “freeze”-theory for the kinematical turbulent viscosity. It means that at all moments of time when the current is rapidly falling down, kinematical turbulent viscosity is defined as constant and its numerical value is equal to its stationary value. This assumption provides the turbulent viscosity growth in the vicinity of the current zero.

For the radiation transfer we used “radiation conductivity” approximation, which was presented at the paper /3/. The radiation transfer plays an important role during the maximum current value, but it does not matter in the vicinity on the current zero.

It is known /4/ that axis temperature falling down not evenly after current zero. Therefore, the length where gas has not resistance is the function of time coming from the current zero. So, the arc voltage critical value during the

thermal mode was proportional to the "non-conducting length". The proportional coefficient includes the gas pressure in the "non-conducting length" and time.

Results and discussion

The numerical investigation channel geometry is presented in the Fig. 1. The same geometry data are L_u=6mm; L_d=55mm. The geometry data for nozzle *1* are $\alpha=2^o$; L=15mm, for nozzle *2* are $\alpha=15^0$; L=6mm. The inlet pressure is equal to 4atm, the outlet one is equal to 1atm. Left-hand electrode is in the inlet of the nozzle, right-hand is out of it. The current is changing with time according to the Wail's test with stationary value I_{max}=1.5kA and dI/dt=-5A/μs. Under the given conditions, there are no shock wave in the nozzle *1* and it existing in the nozzle *2*. The numerical investigation data correspond to experimental data given in /1/, where the influence of the shock wave on the electric field strength in the gas-blast interrupter was investigated. In the Fig.1 the vertical lines mark the experimental sections.

The calculation results are shown in Fig. 2 – 4. Fig. 2 shows the limit breakdown voltage calculated curves. In the Fig. 2 the abscissa is the time after current zero. It is seen that the non-conductivity part appearance after 4.77μs after current zero for nozzle *1* and after 11.6μs for nozzle *2*. The RRRV value is equal to 1.2kV/ μs for nozzle *1* and 2kV/ μs for nozzle *2*.

Fig. 3 shows the electric field strength distribution as function of time before the current zero at sections 1 and 5 for the nozzle *1* (see Fig.1). It is seen that inside the nozzle (section 1) the numerical and experiment data are in a good agreement. Out of the nozzle exit (section 5), the numerical electric field strength value is higher than experiment data about 1.5÷2 times in the vicinity of the current zero (t>-15μs). The reason for this difference is that in the numerical simulation the downstream contact is out the numerical area. Because of this there is no the stagnation region before the downstream contact in numerical simulation. The temperature in this region is smaller than in experiment and the conductivity is smaller too. Therefore, electric field strength is higher.

Fig. shows the electric field strength distribution as function of time before the current zero at sections 1 (before the shock wave) and 5(after the shock wave) for the nozzle *2* (see Fig.1). It is seen that inside the nozzle (section 1) the numerical and experiment data are not in a good agreement. The possible reason for this difference is that in the numerical simulation the shock wave is weaker than in the experiment. It placement is out of nozzle and it very weak effect at the gas parameter inside the nozzle. The velocity in the diffuser is higher than in experiment, the temperature is smaller and the electric field strength is higher.

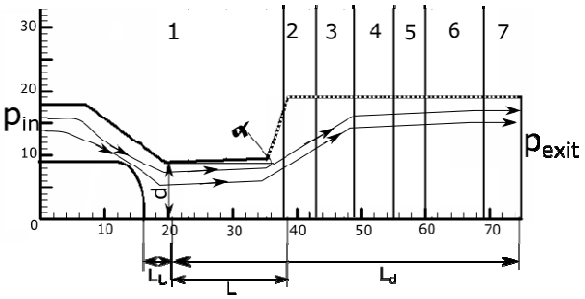

Fig.1 – The schematic diagram of the nozzle

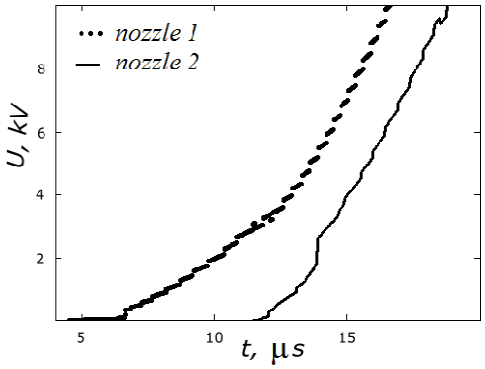

Fig.2 – The limit breakdown voltage as the function of time after current zero

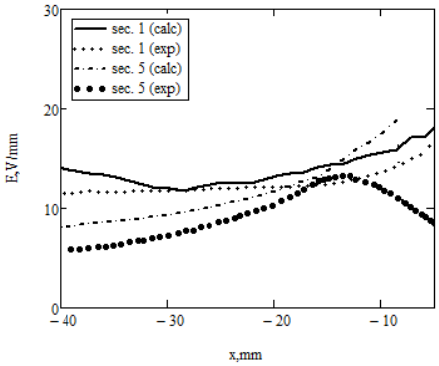

Fig.3 – The electric field strength as the function of time (nozzle *1*)

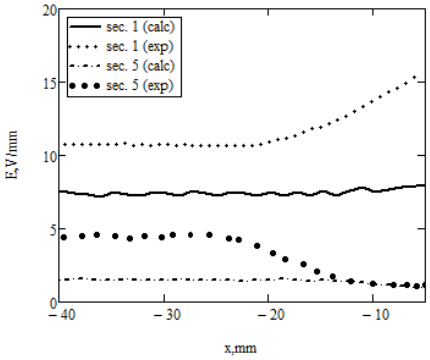

Fig.4 – The electric field strength as the function of time (nozzle *2*)

Conclusion

The conclusions, which were obtained from these investigations, are as follows: the shock wave in the HV gas-blast interrupting has influence with the electric field strength. The non-conductivity part appearance later if the shock wave exists in the HV gas-blast interrupting arc-chamber. The RRRV in this case is higher due to the higher velocity value in the diffuser part of the nozzle. The electric field strength change very slowly in time in the sections that are location after the shock wave.

References

1.**Sturzenegger Ch., et. al**. IEEE Trans., PAS-99(1980), 1957-1963

2. **Kobayashi A., et. al**. IEEE Trans., PS-8(1980), 339-343

3. **Averianova S., et.al**. XV Symposium on Physics of Switching Arc, Brno (Czech Republic), 22-26 Sept. 2003, Vol.1, pp.3-6.

4. **Ragaller K**. Current interruption in high voltage networks. Plenum Press, NewYork, 1978.

INCREASE IN THE SILICON SURFACE ADHESION BY TREATMENT IN ATMOSPHERIC PLASMA

D.A. Kotov, T.A. Kuznetsova, S.A. Nikitiuk, V.A. Lapitskaya,
G. B. Melnikova, S.A. Chizhik, U. V. Zaporojchenko, E. V. Yatsevich

[1]BelarusianStateUniversityofInformaticsandRadioelectronics, 220013, P.Brovky 6, Minsk, Belarus,kotov@bsuir.by
[2]A.V. Luikov institute of Heat and Mass Transfer of National Academy of Science of Belarus, 220072, Minsk, Belarus

Abstract

The silicon wafer surface was processed by atmospheric pressure plasma. Atmospheric plasma treatment resulted in a significant improvement of the surface adhesion. The adhesion was measured as a coefficient of friction. The dependence of the friction coefficient of the silicon on the treatment modes was studied by the atomic force microscope. The use of the atmospheric discharge plasma made it possible to change the surface properties rapidly and at low cost without destroying it.

Introduction

The processes of cleaning the substrate surfaces and their different nature parts, as well as their surface modification before the subsequent technological treatments play an important role in the science and technology. The plasma treatment with dielectric barrier discharge at atmospheric pressure is promising for these purposes. Its most important feature is the combination of the advantages of traditional ion-plasma treatment with a low cost of such processes, as the expensive vacuum equipment is not used in this case.

The changes in surface adhesion of silicon was estimated by the calculations of the forces acting on the cantilever of an atomic force microscope.

Materials, methods and experimental set-up

The experimental complex, which consists of a discharge system, a power supply and a work gas supply system, was used to carry out plasma treatment (Fig 1a).

The plasma stream is formed by dielectric barrier discharge that generated in a coaxial device (Fig. 1b). This discharge system allows the formation of a plasma torch up to 30 mm long, with a processing area of 10 mm in diameter. Argon is used as a plasma-forming gas.

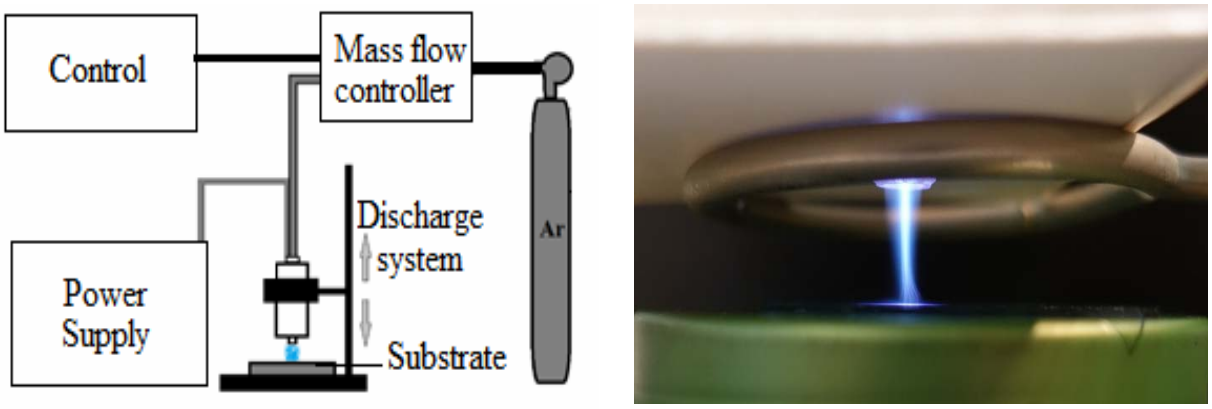

a b

Fig. 1 – Schematic representation of the experimental complex (a) and a photo of the plasma torch (b)

The adhesion value of the surface of monocrystalline silicon was estimated by the determination of the friction coefficient using an atomic force microscope NT-206 /1/.The friction coefficient was calculated using the average value of the silicon probe torsion during its forward and reverse motion, reference probe data and Poisson coefficient. An example of the cantilever stroke for forward and reverse motion on the atom force microscopy is shown in the Fig. 2.

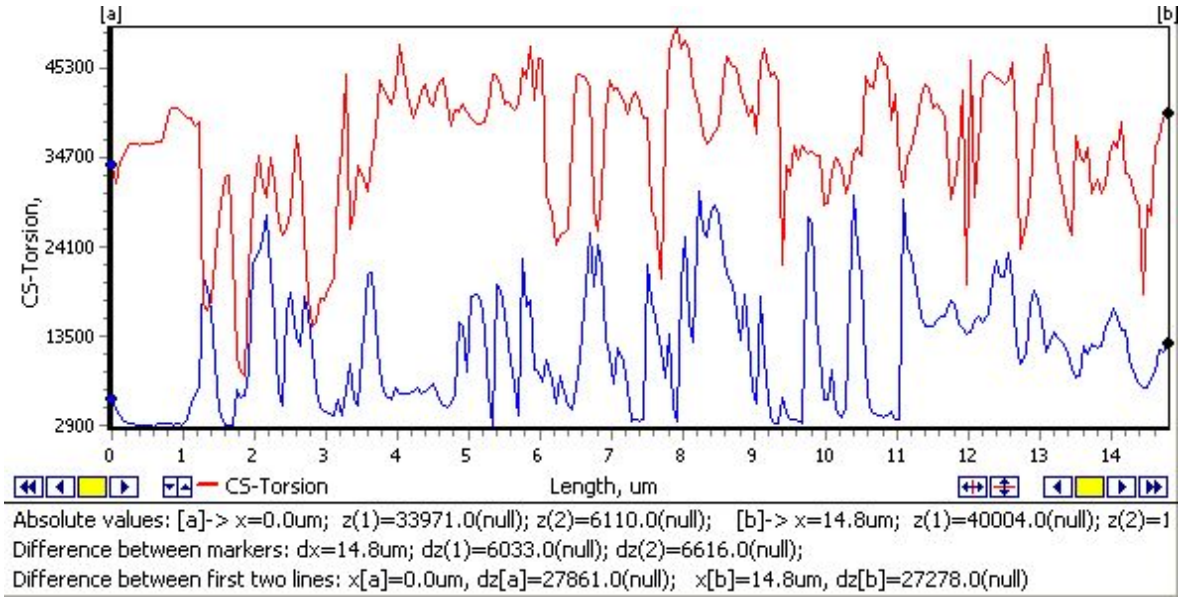

Fig. 2 – Forward and reverse stroke of the cantilever after sample treatment for 4 min

Results and discussion

Surface activation is the appearing of the defects such as the dangling bonds and another that increase a chemically active surface layer. To describe quantitatively the effect of atmospheric discharge plasma on the properties of the silicon surface, the dependence of the friction coefficient on the processing time (at a fixed distance from the plasma source) and on the distance from the plasma source to the processed surface (at a fixed processing time) was studied.

Treatment was carried out at discharge power P ≈ 25 W, plasma gas flow rate S≈300 l/h.

To study the dependence of enhancement capital effect of adhesion on the duration of treatment, the treatment time varied from 1 to 5 min with the step of 1 min. The distance between the end of the discharge system and the sample was 10 mm.

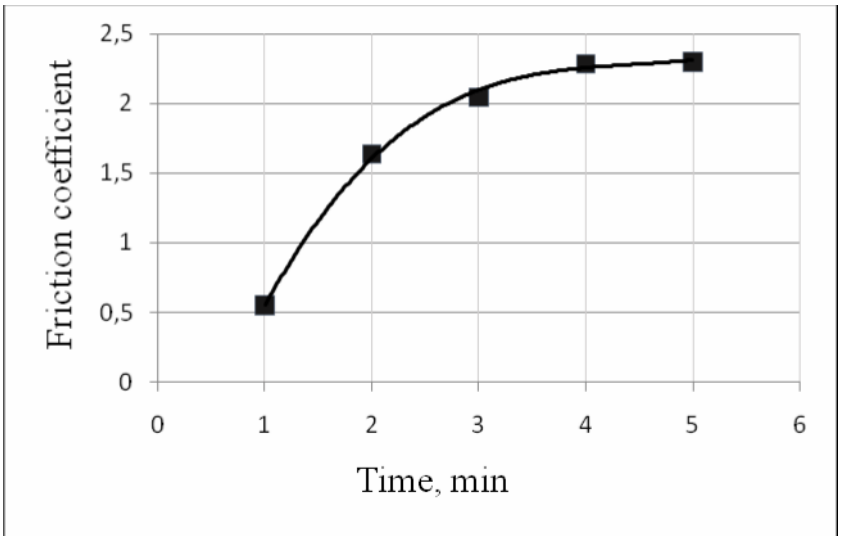

Fig. 3 – Friction coefficient depending on the processing time

As can be seen from Fig. 3 the friction coefficient increases from 0.5 to 2.0 in 3 min in plasma treatment, and then the saturation is observed. Therefore, it is advisable to process the surface of the silicon wafer for no more than 3–4 min.

The dependence of the friction coefficient on the distance between the end face of the discharge system and the sample was studied during processing for 4 min. The distance varied from 5 to 35 mm.

As can be seen from Fig. 4 on the graph there is an extremum. The friction coefficient increases stepwise from 1.2 to 2.25at the removed sample from 5 mm to 10 mm. Then it slowly increases from 2.25 to 2.65at the removed sample from 10 mm to 25 mm. The last one corresponds to the visible length of the

plasma flow. After which the friction coefficient begins to decrease sharply to 1,7at the removed sample to 30 mm.

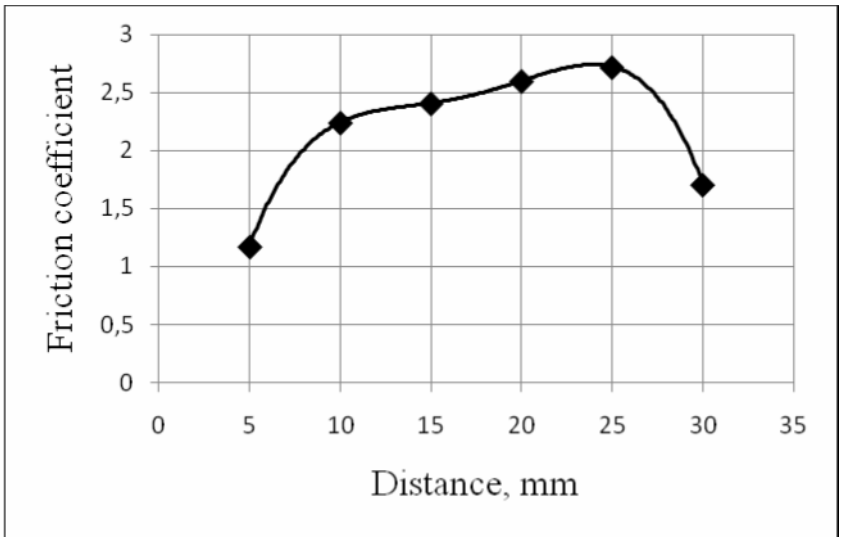

Fig. 4 – Friction coefficient depending on the distance between the sample and plasma source

This indicates different processing conditions along the cross section of the plasma flow. This dependence is probably due to the increase in the number of active particles in the formed flow when the gas-discharge plasma moves from the end of the discharge system.

From point view of maximum adhesion the effective mode of plasma treatment was achieved at the distance range 20–25 mm and processing time more than 3 min.

Acknowledgements. This work was supported by the Belarusian Republican Foundation for Fundamental Research (“Наука-2017”, grant №Ф17-118).

References

1. Методическое пособие по выполнению лабораторной работы «Определение коэффициента трения различных поверхностей МЭМС-акселерометра производства НИИ радиоматериалов» / Минск: БНТУ, 2017. – 12 с.

MATHEMATICAL MODELING OF REACTIVE ION-PLASMA ETCHING

A.V. Abramov, E. A. Pankratova, E. V. Alekseeva, I. S. Surovtsev

Voronezh state technical University, Russia, 20 let Oktyabrya str., 84,
abramovvgasu@yandex.ru

A model of RIE of silicon. The research analysis of reactive ion-plasma etching (RIE) of Si in SF_6 allows adopting following basic provisions: the process of RIE is multistage and reversible at each of these stages; the etching is implemented though the interrelated action of chemically active particles (ChAP) (in SF_6 with atoms of F (ChAP1) and radicals of SF_y (ChAP2) where y =1÷5) and ions /1,2/; the process has first-order kinetics in the concentration of atoms of F (n_F) /3/; ChAP and volatile products are adsorbed at active surface centers (ASC) of Si and on discharge chamber (DC) walls; all ASC on Si have the same characteristics, and their quantity is limited (similar allegations are applicable for ASC on DC walls); only one particle of the etching product or SF_y can be adsorbed on each ASC; the adsorbed particles can are considered as ASC for ChAP; the adsorbed atoms of halogen on ASC of Si do not prevent other particles from adsorbing on them; the mechanism of etching of the adsorbed on Si products of etching is the same as the one of silicon atoms.

In the proposed model, four flows of etching product are considered. The flow I_1 is generated as a result of interaction of ChAP with free ASC of Si and only it defines the velocity of the target process. The flows I_2 and I_3 represent particles formed from etching correspondingly earlier adsorbed particles on Si and DC walls from the flow of etching products I_P, coming from the plasma volume. If the etching occurs in plasma of a complex chemical composition, the velocity of the target process must be expressed in the form of composition of as many elements as many types of ChAP plasma has. For SF_6

$$V_a = V_{aF} + V_{aR}\,\text{a}\,V_{aR} = \sum_{i=1}^{5} V_{ai}\,, \qquad (1)$$

where i is the number of a radical type defined by a quantity of atoms F split off from the SF_6 to the moment of its adsorption on the surface. The first component V_a in (1) results from the action of F and is written in the following form:

$$V_{aF} = \frac{1}{4} b_1^{-1} k_{ma} \omega_m (1 - \Theta_m) n_F u_F\,, \qquad (2)$$

where b_1 is an average number of atoms F, used for etching one atom of Si first leaving the surface; k_{ma} is the probability of chemical interaction of F with free ASC; ω_m is the probability of F getting on ASC of Si; Θ_m is the sum of the

degreesfilling of ASC of Si by the adsorbed etching products (Θ_{mp}) and ChAP2 (Θ_{mR}); u_F is the thermal velocity of F. In line with (2), the component of etching velocity due to the action of particles SF_y*i*-type is expressed as:

$$V_{ai} = \frac{1}{4} b_1^{-1} \omega_m (1-\Theta_m)(1-\Theta_{mR}) n_{Ri} u_{Ri} k_{mi} (d-i) k_i , \qquad (3)$$

where k_i is the fraction of halogen atoms given by the radicals of *i*-type during staying on the surface at the process of etching. Characteristics of n_{Ri}, u_{Ri} and k_{mi} for SF_y the same meaning as n_F, u_F and k_{ma} for F. For dissociative chemisorbtion occurring, SF_y have to interact with two placed around ASC /4/. A variable of $(1-\Theta_{mR})$ helps consider that SF_y cannot be adsorbed on already taken ASC. It is anticipated that the area of the material surface taken by the same ASC or by one adsorbed particle equals $1/\sigma_m$, where σ_m is the average areal density of atoms of the material. Then, $\omega_m=\sigma_{cm}/\sigma_m$,where σ_{cm} is the areal density of ASC. In this case, comparing the velocity of adsorption and desorption of etching products and SF_y on the treated surface and solving an obtained system of equations in reference to Θ_{mp} and Θ_{mR} /5/, we get:

$$\Theta_{mp} = \frac{j_p t_{mp} k_{mp}}{\sigma_m + j_p t_{mp} k_{mp} + \sum_{i=1}^{d-1} j_{Ri} t_{mi} k_{mi}}, \Theta_{mR} = \frac{\sum_{i=1}^{d-1} j_{Ri} t_{mi} k_{mi}}{\sigma_m + j_p t_{mp} k_{mp} + \sum_{i=1}^{d-1} j_{Ri} t_{mi} k_{mi}}, \quad (4\ a, b)$$

where t_{mp} and t_{mi} are the average times of finding adsorbing particles of etching products and of SFy *i*-type on ASC; k_{mp} is the coefficient of adhesion of etching product particles to the material surface when getting on the ASC free from these particles. The equations (4a and 4b) are Langmuir isotherm derivations. Taking obtained remarks and formulas (2) into account, (4a, 4b) the equation (1) is converted into the quadratic one in reference to V_a, solving which we get:

$$V_a = 2V_{a0}\left(\sqrt{1+\frac{S_m}{S_a}}+1\right)^{-1}, \qquad (5)$$

where $V_{a0} = \frac{\sigma_{cm}}{4\sigma_m b_1}\left[k_{ma} n_F u_F + \sum_{i=1}^{d-1} k_{mi} n_{Ri} u_{Ri} (d-i) k\right]$, $S_a = \frac{G\sigma_m P_0 T}{P T_0 k_{mp} V_{a0} t_{mt}}$.

Here G is flow of gas through the DC with a pressure of $P_0 = 10^5$ Pa. The value of V_{a0} is a velocity of target process in the absence of etching product adsorption on the treated surface, and t_{mp} is the average time of etching the layer of adsorbed etching products with the areal density $\sigma_{pm} = \sigma_{cm} \cdot \Theta_{mp}$. This layer is formed as a result of adsorption of only non-saturated particles from the flow I_p. Based on the provisions of the etching model and the fact that the removal of one adsorbed particle of reaction products from the area needs about $(b_2 - b_p)$ halogen atoms, S_a is written as:

$$S_a = \frac{G\sigma_m P_0 T b_1}{P T_0 k_{mp} u_p (b_2 - b_p) \sigma_{cm}} .$$

According to (5), when $S_m << S_a$, the influence of etching product adsorption on the treated surface on the value of V_a can be neglected and $V_a = V_{a0}$. When $S_m >> S_a$, (5) is reconstituted to $V_a = 2\ V_{a0}(S_a/S_m)^{1/2}$. It means that when $S_m >> S_a$, the velocity of etching with the growth of S_m has to decrease at a higher rate comparing to n_F. Calculated with the help of formula (6), the value of S_a with $G = 3\times10^{-3}$ m$^3\times$Pa$\times$ c^{-1}, $P = 2{,}66\times10^{-2}$ Pa, $U_{rf} = 1$ kV, $T = 400$ K, $T_0 = 300$ K, $\sigma_m = \sigma_{cm} = 1{,}35\times10^{19}$ m^{-2}, $k_{mp} = 0{,}05$, $b_p = 1{,}5$, $b_1 = 3{,}0$, $b_2 = 3{,}3$ amounted to 155 mm^2. These conditions correspond to the mode of carrying out the etching which results are presented in Figure 1a. The analysis of (5) considering (6) shows that near the value of S_m that equals S_a the chart must have a curve which can be observed in Fig. 1a.

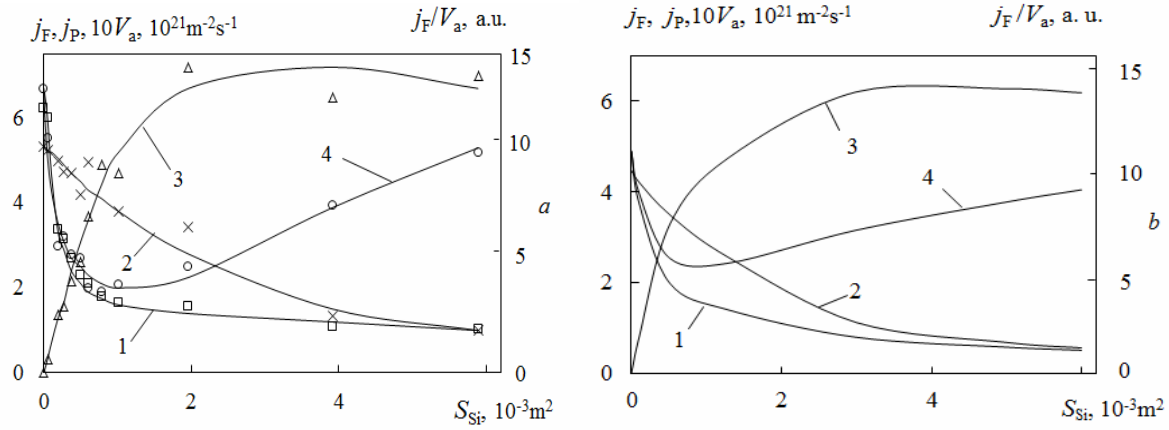

Fig. 1 – Influence of silicon area on etching velocity and density of particle flows. Here: j_F -1, V_a -2, j_p -3, j_F/V_a – 4. Experiment (a), calculation (b)

Calculation of the load dependence. A numerical calculation of dependence of V_a from S_m has been held for the right assessment of the etching model and for receiving analytic expressions. In first step the value of $S_m = 0$. Then the system of differential equations was solved from /5/ for a stationary situation with corresponding attribute values. The values of n_a and n_{Ri} received from solving this system of equations were put in (5) and the velocity of etching was calculated with $S_m \rightarrow 0$. The obtained value of etching velocity was substituted in the system of differential equations which was already solving with a higher value S_m by ΔS_m. Then a cycle repeats $S_m/\Delta S_m$ times. The value of k_{ma} , k_{mi} were set to 0,5 and 0,3 /2/ correspondingly. The results of calculation are presented in Fig. 1b and are in good agreement with illustrated charts in Fig. 1a. Fig. 2a represents calculation dependences which show how the composition of plasma and the rate of silicon surface occupation with adsorbed etching products change with the growth of S_{Si}. The components of V_a defined by the action of F and radicals SF_y (Fig. 2b, curves 1 and 2) behave the same

way as n_F and n_p values. As can be seen the ratio of V_{aR}/V_{aF} gets to the highest point with a certain area of etching and then slowly decreases.

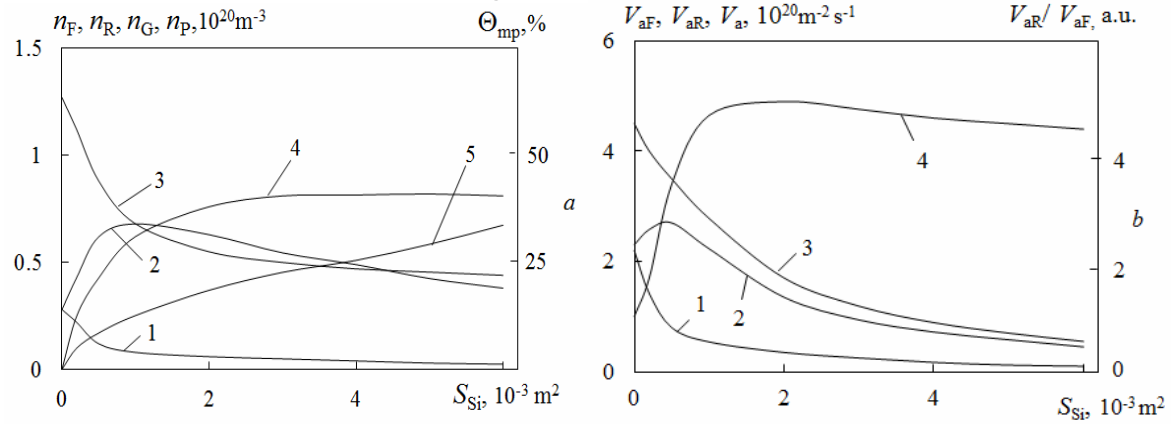

Fig. 2 – Influence of silicon area on composition of plasma, rate of its surface occupation with adsorbed products (a), etching velocity, its components and their ration (b). Here: n_F - 1, n_R - 2, n_g -3 , n_p -4, Θ_{mp}-5 (*a*), V_{aF} - 1, V_{aR} - 2, V_a - 3, V_{aR} / V_{aF} - 4 (*b*). Calculation parameters are the same as for Figure 1*b*

Such a behavior of dependences of V_{aF} and V_{aF} from Si is caused by the character of the atomic concentration change of F and SiF_x particles in the discharge with the growth of S_{si}. The calculations show that at bigger areas of Si the etching in SF_6 must be implemented mostly with SF_y particles. A proposed model of the material etching in chemically active plasma and analytical dependences obtained within this framework allow carrying out numerical calculation not only of velocity but anisotropy and selectivity of RIE with different technological characteristics of its process as well.

Reference

1. Abramov A.V., Abramova E.A., Dikarev Y.I., Surovtsev I.S. Journal of Applied Spectroscopy,Vol.71, No. 5, 2004, P. 715-720.
2. Pauling L. Chemistry: Transl. with English. V. M. Sakharov. Ed. by M. L. Karapet'yants / M.: Mir.-1978. - 683 p.
3. Slovetsky D. I. Heterogeneous reactions in nonequilibrium halogen-containing plasma. Plasma chemistry / / Edited by B. M. Smirnov.- M.: Energoatomizdat.- 1989.- Issue 15.- P. 208-266.
4. Trapnel B. M.W. Chemisorption: Transl. with English. Ed. by A. V. Kiselev / M.: Foreign literature.- 1958.-327 p.
5. Abramov A.V., Abramova E.A., Surovtsev I.S. Mathematical modeling of ITS. Voronezh. VSTA, 2002. №.4. P. 268-272.

SIMPLIFIED NON-LOCAL MODEL OF HOLLOW CATHODE GLOW

V.V. Gorin

MIPT, Kiev Branch, Kiev, Ukraine, vvgorin@gmail.com

Non-local kinetic problems for ionizing electrons appear in modeling of low pressure glow discharge at high electric fields when *E/N* exceeds about 3000 Td. In such fields the equilibrium between accelerating electric force and force of friction for electrons is violated. These electrons are named as "running away". An experimental curves for $\alpha/N(E/N)$ -dependence – reduced 1st Townsend factor on reduced electric field – cut here, because this dependence does not continue being local: ionization here does not depend on electric field in the point of ionization determination, but on electron energy, which is gained from the field along whole path of its motion to the point.

Slow electrons of plasma in glow amount overwhelming majority of all electrons and they allow hydrodynamic description in terms of drift and diffusion of charged fluids. Other most significant charged fluid is ions of plasma. So minimal hydrodynamical system of equations for plasma is:

$$\begin{aligned} &-\Delta\varphi = \frac{e}{\varepsilon_0}(n_i - n_e); \\ &\frac{\partial n_e}{\partial t} + \operatorname{div}\Gamma_e = s; \\ &\frac{\partial n_i}{\partial t} + \operatorname{div}\Gamma_i = s; \\ &\Gamma_e = -D_e\nabla n_e - \mu_e \mathbf{E} n_e; \\ &\Gamma_i = -D_i\nabla n_i + \mu_i \mathbf{E} n_i; \\ &\mathbf{E} = -\nabla\varphi. \end{aligned} \tag{1}$$

But small amount of ionizing electrons needs kinetic (Boltzmann) description in term of *electron distribution function* (EDF). It needs to define the non-local ionization term *s* in the right-hand side of electron and ion balance equations in (1). Generally kinetic equation is formulated in 6D phase space of coordinate and velocity components of electron. Stationary kinetic equation for stabilized state of discharge includes terms with linear differential operator of free electron motion in electric field, also collisional elastic and inelastic terms and a source of ionization (including an external cathode electron source s_c):

$$\begin{aligned} &\mathbf{v}\cdot\nabla f - \frac{e}{m_e}\mathbf{E}(\mathbf{r})\cdot\frac{\partial f}{\partial \mathbf{v}} - \frac{1}{2}\omega_{el}(v)\frac{\partial}{\partial v_i}\left(v^2\delta_{ik} - v_i v_k\right)\frac{\partial f}{\partial v_k} - \int d^3v'\mu(\mathbf{v},\mathbf{v}')f(\mathbf{r},\mathbf{v}') + \omega(v)f = \\ &= \left(s(\mathbf{r}) + s_c(\mathbf{r})\right)\delta^3(\mathbf{v}), \quad f = f(\mathbf{r},\mathbf{v}), \quad \mathbf{E}(\mathbf{r}) = -\nabla\varphi(\mathbf{r}), \quad s_c(\mathbf{r}) = \Gamma_c(\mathbf{r})\delta(\psi_c(\mathbf{r}))\left|\nabla\psi_c(\mathbf{r})\right|. \end{aligned} \tag{2}$$

Here $\psi_c(\mathbf{r}) = 0$ is an equation of the cathode surface.

$\omega_{el} = Nv\sigma_{tr}$, $\omega = Nv(\sigma_{ion} + \sigma_{ex})$. The Dirac 3D delta function here means, that we neglect initial energy of secondary electron in comparison with ionization energy. Formally (see /1/) a solution of (2) can be written as

$$f = \int d^3r' \int d^3v' g(\mathbf{r}, \mathbf{v}; \mathbf{r}', \mathbf{v}') (s(\mathbf{r}') + s_c(\mathbf{r}')) \delta^3(\mathbf{v}'). \tag{3}$$

Combination of solution (3) with additional independent formula

$$s(\mathbf{r}) = \int d^3v\, \omega_{ion}(v) f(\mathbf{r}, \mathbf{v}), \quad \omega_{ion} = Nv\sigma_{ion}. \tag{4}$$

enables to exclude the EDF and derive an integral equation for ionization source in plasma volume /1/:

$$\begin{aligned} s(\mathbf{r}) &= \int d^3r' G_0(\mathbf{r}, \mathbf{r}') s(\mathbf{r}') + \int d^2r' G_0(\mathbf{r}, \mathbf{r}') \Gamma_c(\mathbf{r}'), \\ G_0(\mathbf{r}, \mathbf{r}') &= \int d^3v\, \omega_{ion}(v) g(\mathbf{r}, \mathbf{v}; \mathbf{r}', \mathbf{0}). \end{aligned} \tag{5}$$

To use (5) for calculation the hydrodynamical system (1) is not easy problem, because first we should find the kernel in (5) which is defined through (3) and (2). In /2/ it was shown, how the solution of (2) can be presented through a source term if a solution of the auxiliary equation

$$\left(\mathbf{v} \cdot \nabla - \frac{e}{m_e} \mathbf{E}(\mathbf{r}) \cdot \frac{\partial}{\partial \mathbf{v}} - \frac{1}{2} \omega_{el}(v) \frac{\partial}{\partial v_i} \left(v^2 \delta_{ik} - v_i v_k \right) \frac{\partial}{\partial v_k} + \omega(v) \right) g_1 = \delta^3(\mathbf{r} - \mathbf{r}') \delta^3(\mathbf{v} - \mathbf{v}'), \tag{6}$$

$g_1 = g_1(\mathbf{r}, \mathbf{v}; \mathbf{r}', \mathbf{v}')$.

is obtained. The Green function g is a solution of the integral equation

$$\begin{aligned} g(\mathbf{r}, \mathbf{v}; \mathbf{r}', \mathbf{v}') &= \int d^3r'' \int d^3v'' K(\mathbf{r}, \mathbf{v}; \mathbf{r}'', \mathbf{v}'') g(\mathbf{r}'', \mathbf{v}''; \mathbf{r}', \mathbf{v}') + g_1(\mathbf{r}, \mathbf{v}; \mathbf{r}', \mathbf{v}'), \\ K(\mathbf{r}, \mathbf{v}; \mathbf{r}'', \mathbf{v}'') &= \int d^3v''' g_1(\mathbf{r}, \mathbf{v}; \mathbf{r}'', \mathbf{v}''') \mu(\mathbf{v}''', \mathbf{v}''). \end{aligned} \tag{7}$$

Due to nilpotency of the kernel, the solution is a sum of finite number of integral summands. Function g_1 is a generalized function, the support of which is located in the hyper-surface of total mechanical energy in the phase space:

$$g_1 = C_1'(\mathbf{r}, \mathbf{v}; \mathbf{r}', \mathbf{v}') \delta(\varepsilon(\mathbf{r}, \mathbf{v}) - \varepsilon(\mathbf{r}', \mathbf{v}')), \quad \mathbf{r} \in \Omega, \mathbf{r}' \in \Omega; \quad \varepsilon(\mathbf{r}, \mathbf{v}) = \frac{m_e v^2}{2e} - \varphi(\mathbf{r}). \tag{8}$$

It constitutes a distribution function for fast electrons with total energy ε, eV, which scattered elastically, but before their first inelastic scattering, and emitted with some point source. In /3/ the sufficient conditions for existence of g_1 were formulated. A uniqueness was proved in /2/. Function g constitutes a distribution function for fast electrons from some point source including scattered inelastically also.

In work /4/ it was found significant simplification of these multi-dimensional formulae in the case of diffuse approach: if g_1 is guessed as uniformly distributed along energy hyper-surface:

$$C_1' = C_1(\varepsilon(\mathbf{r}, \mathbf{v})), \mathbf{r} \in \Omega; \quad C_1' = C_1(\varepsilon(\mathbf{r}, \mathbf{v})) \theta(\mathbf{n} \cdot \mathbf{v}), \mathbf{r} \in \partial\Omega; \quad C_1' = 0, \quad \mathbf{r} \notin \overline{\Omega}. \tag{9}$$

In this approach all functions are dependent on total energy, but not dependent on all 6 phase coordinates separately.

Here the diffuse approach is developed further. Two additional

assumptions are made: 1) about non-elastic scattering, and 2) about plasma volume. Thus, not very complicated expressions are found.

1) Non-elastic scattering is slow-angled:

$$\mu(\mathbf{v},\mathbf{v}')=\sum_{a=ion,ex} N v'\sigma_a(v')\delta^{3}\left(\mathbf{v}-\frac{\mathbf{v}'}{v'}\sqrt{v'^2-V_a^2}\right),\quad \frac{m_e}{2e}V_a^2=\varepsilon_a[\text{eV}]. \tag{10}$$

2) Plasma occupies main part of discharge volume, and its electric potential is close to the anode potential.

Under these assumptions one obtains formulae:

$$\begin{aligned}&\widetilde{s}(u)=\int_{-U}^{u-\varepsilon_{ion}} du'\widetilde{p}(u')\widetilde{G}_0(u,u')\widetilde{s}(u')+\widetilde{G}_0(u,-U),\\ &\widetilde{p}(u)=\frac{1}{V_p}\int_{\Omega\cap\{\varphi(\mathbf{r})=u\}} d^2r\frac{1}{E(\mathbf{r})},\quad s(u)=\frac{S_c\Gamma_c}{V_p}\widetilde{s}(u).\end{aligned} \tag{11}$$

It is main integral equation, which defines non-local ionization source. The kernel is defined with formula:

$$\begin{aligned}&\widetilde{G}_0(u,u')=\sum_{i=0}^{M_{ion}}\sum_{k=0}^{M_{ex}} g_{ik}(-u')\frac{w_{ik}}{-u'}\frac{\sigma_{ion}(w_{ik})}{\widetilde{\sigma}(-u')}.\\ &G_0(u,u')=\frac{1}{V_p}\widetilde{G}_0(u,u'),\quad w_{ik}=u-u'-i\varepsilon_{ion}-k\varepsilon_{ex}.\end{aligned} \tag{12}$$

Terms in this sum are defined with recursion relations:

$$\begin{aligned}&g_{ik}:\quad g_{00}(\varepsilon')=1;\\ &g_{0k}(\varepsilon')=\frac{\varepsilon_{0k}(\varepsilon')+\varepsilon_{ex}}{\varepsilon_{0k}(\varepsilon')}\frac{\sigma_{ex}(\varepsilon_{0k}(\varepsilon')+\varepsilon_{ex})}{\widetilde{\sigma}(\varepsilon_{0k}(\varepsilon'))}g_{0,k-1}(\varepsilon'),\quad k=1,\ldots,M_{ex};\\ &g_{i0}(\varepsilon')=\frac{\varepsilon_{i0}(\varepsilon')+\varepsilon_{ion}}{\varepsilon_{i0}(\varepsilon')}\frac{\sigma_{ion}(\varepsilon_{i0}(\varepsilon')+\varepsilon_{ion})}{\widetilde{\sigma}(\varepsilon_{i0}(\varepsilon'))}g_{i-1,0}(\varepsilon'),\quad i=1,\ldots,M_{ion};\\ &g_{ik}(\varepsilon')=\frac{\varepsilon_{ik}(\varepsilon')+\varepsilon_{ion}}{\varepsilon_{ik}(\varepsilon')}\frac{\sigma_{ion}(\varepsilon_{ik}(\varepsilon')+\varepsilon_{ion})}{\widetilde{\sigma}(\varepsilon_{ik}(\varepsilon'))}g_{i-1,k}(\varepsilon')+\frac{\varepsilon_{ik}(\varepsilon')+\varepsilon_{ex}}{\varepsilon_{ik}(\varepsilon')}\frac{\sigma_{ex}(\varepsilon_{ik}(\varepsilon')+\varepsilon_{ex})}{\widetilde{\sigma}(\varepsilon_{ik}(\varepsilon'))}g_{i,k-1}(\varepsilon'),\\ &i=1,\ldots,M_{ion},\quad k=1,\ldots,M_{ex};\\ &\varepsilon_{ik}(\varepsilon')=\varepsilon'-i\varepsilon_{ion}-k\varepsilon_{ex}.\quad M_{ion}=[\varepsilon'/\varepsilon_{ion}],\quad M_{ex}=[\varepsilon'/\varepsilon_{ex}]\end{aligned} \tag{13}$$

The effective cross-section includes electron losses in the walls:

$$\widetilde{\sigma}(\varepsilon)=\sigma_{ion}(\varepsilon)+\sigma_{ex}(\varepsilon)+\sigma_{loss}(\varepsilon),\quad \sigma_{loss}(\varepsilon)=\left(\frac{m_e}{e}\right)^2\frac{q(\varepsilon)}{8\pi V_p N\varepsilon}, \tag{14}$$

$$q(\varepsilon)=2\pi\left(\frac{e}{m_e}\right)^2\left(\sum_{a:\varphi_a+\varepsilon\ge 0}(\varphi_a+\varepsilon)S_a+\int_{-\varepsilon}^{\varphi_{\max}} du(u+\varepsilon)p_1(u)\right),\quad p_1(u)=\int_{\partial\Omega\cap\{\varphi(\mathbf{r})=u\}} dl\frac{1}{|\mathbf{n}\times\mathbf{E}(\mathbf{r})|}. \tag{15}$$

The designations in formulae are (unit system [SI]):

N is gas density; U is voltage; u, φ are electric potential ($\varphi_{\text{anode}}= 0$); σ_{ion} , σ_{ex} are ionization and excitation cross-sections; ε is mechanical electron energy, eV; Ω, $\partial\Omega$ are domain of discharge and its boundary; **n** is an external normal unit vector in the boundary; V_{p} is plasma volume; S_a is area of metal electrode.

From the solution of (11) one can obtain the multiplication factor: an amount of electrons, which appear in discharge volume due to impact ionization (including primary cathode electron), per one cathode electron:

$$m = 1 + \int_{-U}^{\varphi_{\max}} du \tilde{p}(u)\tilde{s}(u). \tag{16}$$

The condition of discharge self-consistency takes a form:

$$m = 1 + \frac{1}{\gamma}. \tag{17}$$

Multiplication factor m is not a function of the discharge voltage U only, but a functional of electric field configuration over whole discharge volume. So, formulae (11) – (17) define a source of ionization s through electric field configuration known. In contrary, system (1) of hydrodynamic equations defines the electric field and density distributions of charged particles in discharge volume. In the aggregate the current-voltage dependence (at given secondary emission factor γ in the cathode) is defined.

To have significant value of multiplication factor the value of electron losses q in (15) must be rather small, – because last term in (14) must not be big in comparison with previous two ones. This property characterizes a hollow cathode geometry configuration, in which cathode walls embrace almost whole volume and prevent electron losses, reflecting electrons due to high negative electric potential. Other way to decrease the loss cross-section is to increase gas density N (or gas pressure P) and diminish electron free path length. It is usual for glow in standard geometry.

The ideas presented here give a hope to calculate real model of hollow cathode in the nearest future.

Acknowledgments. My grateful thank to Prof. V.T. Chemerys, who has found a time to read the text and to give me his comments.

References

1. **Gorin V.V.** European Physical Journal D, 59 (2010) 241–247.
2. **Gorin V.** Journal of Modern Physics, 3(2012) 30, 1647-1662.
3. **Gorin V.V.** Technical Physics, 60 (2015) 11, 1714–1715.
4. **Gorin V.V.** Proceedings of MIPT 5(2013) 4 (20), 185 – 193 (in Russian).

SPECIFIC POWER OF ULTRAVIOLET RADIATION FROM RF MIDDLE PRESSURE DISCHARGE IN A MIXTURE OF INERT GAS AND CHLORINE

A. Golovitskii[1], A. Pelli[2]

[1]St. Petersburg Peter the Great Polytechnic University, Polytechnicheskaya ul., 29, 195251St. Petersburg, Russia. E-mail: alexandergolovitski@yahoo.com
[2]St. Petersburg Peter the Great Polytechnic University, Polytechnicheskaya ul., 29, 195251St. Petersburg, Russia. E-mail: pelli.alexander@gmail.com

Discharges in the mixtures of inert gases and chlorine under middle pressure (1 – 50 Torr) are used as sources of narrow band UV radiation with the output power of several watts to kilowatts /1, 2/. Finding of partial pressure values of mixture components providing maximal values of specific power of UV radiation and its efficiency is very important in design of these sources.

The only relevant experimental investigation of RF discharge in the indicated mixtures /3/ has been carried out for the case where such discharge was proposed as the working medium of luminescent lamps, and its light efficacy has been investigated at nearly constant input RF power (several watts). Maximal value of luminous efficacy was obtained in /3/ in the mixture of Xe and Cl_2 with partial pressure ratio of 100:1, but the lower values of chlorine partial pressure were not investigated. Therefore it was not possible to conclude that the maximal possible UV power has been reached indeed.

The goal of the present work is to estimate the optimal conditions of initial gas filling for the capacitive RF discharge in a mixture of inert gas and chlorine from the viewpoint of maximization of radiative UV power and efficiency. The present work was carried out by a numerical simulation using the models used in of our previous works /4, 5/. The model /4/ describes a low current 1D rf capacitive discharge, and in /5/ it is shown that for RF capacitive discharges with radius/length ratio > 1 it is possible to use 1D modeling for estimation parameters of said discharges instead of much more complicated 2D modeling without notable accuracy losses. The partial chlorine pressure, total gas mixture pressure and RF voltage amplitude were selected as independent input variables for our calculations.

The system of model equation is similar to the given in /4/ (as an example we consider the discharge in a mixture of Xe and Cl_2):

$$\delta n_e / \delta t = -\nabla \Gamma_e + n_e N_{Xe} < \sigma_{i\_Xe} v_e > + n_e N_{Cl2} < \sigma_{i\_Cl2} v_e > - n_e N_{Cl2} < \sigma_a v_e >;$$

$$\delta n_p / \delta t = -\nabla \Gamma_p + n_e N_{Xe} < \sigma_{i\_Xe} v_e > + n_e N_{Cl2} < \sigma_{i\_Cl2} v_e > - n_p n_n \beta_i;$$

$$\delta n_n / \delta t = -\nabla \Gamma_n + n_e N_{Cl2} < \sigma_a v_e > - n_n n_p \beta_i \ ;$$

$$\Gamma_j = -D_j \nabla n_j + z_j n_j \mu_j (E_{ex} + E_x)$$

Here D_j, μ_j, z_j are the diffusion coefficients, mobilities and charge signs of the $j-$th species; subscripts e, p, n correspond to electrons and positive and negative ions; σ_i, σ_a — cross sections for ionization and attachment; E_x – space charge field, $\nabla E_x = 4\pi e(n_p - n_n - n_e)$; $E_{ex} = E_0 \cos(\omega t)$ – external RF field, $E_0 = U_0 / L$; $\omega / 2\pi = 13.56$ MHz; U_0 – RF voltage amplitude chosen to be 200 – 1000 V according to /3,4,5/; L – discharge length. The boundary conditions at $x = L$ и $x = 0$ are: $n_p = n_e = n_n$, $\frac{dn_n}{dr}|_{x=L} = 0$, $\frac{dn_n}{dr}|_{x=0} = 0$.

Excimer molecule concentration N_{XeCl^*} was calculated as: $N_{XeCl^*} = N_M k_{h(M)} N_{Cl2} \tau_{XeCl^*}$. Here $\tau_{XeCl^*} \approx 1.1 \cdot 10^{-8}$ s /6/; N_M — summarized concentrations of metastable and resonant (due to big escape factor) levels of 6s-state of Xe — calculated as $N_M \approx \frac{N_{Xe} n_e \langle \sigma_{0M} v_e \rangle}{n_e \langle \sigma_{Mi} v_e \rangle + N_{Cl2} k_{h(M)}}$; σ_{0M} – total 6s-state excitation cross section; first term of denominator corresponds to the ionization from metastables, and the second one – to the harpoon reaction with Cl_2 molecules. It turned out that the contribution of nonmetastable Xe-states in the building of N_{XeCl^*} is low (< 10%) and drops with the increase of U_0. The specific power of UV radiation (pro cm^{-3}) was calculated as $W_{UV} = N_{XeCl^*} h\nu / \tau_{XeCl^*}$ ($c/\nu \approx 308$ nm).

Initial conditions of external discharge parameters were chosen from previous experimental work /3/. But the results of our calculation showed that the optimal partial chlorine pressures are generally lower than using in /3/. The main results of simulation dependences of W_{UV} and efficiency from external parameters are presented on Fig. 1, 2 (for a fixed total mixture pressure P_0 = 1 Torr) and 3. Obtained results for P_0 = 1 Torr are partially comparable with the experimental data /3/, but our calculations indicate that the optimal values of partial chlorine pressures may range from 0.001 to 0.01 Torr, that is on the whole lower values as in /3/. However, the optimal total pressure, for a given partial pressure ratio, may be significantly more than 1 Torr. The results are presented in Fig. 3. The amplitude of the applied RF voltage was chosen to be constant and was U_0 = 1000 V, the length of the discharge gap was 4 cm. It is shown that the optimal total pressure is about 40 Torr when the partial pressure ratio is 1000:1, and the maximum of W_{UV} under mentioned conditions of RF excitation can reach 0.6 W/cm^3. The last value obtained for the RF discharge corresponds well to ones having been reached for DC /7/ and barrier /8/ discharges

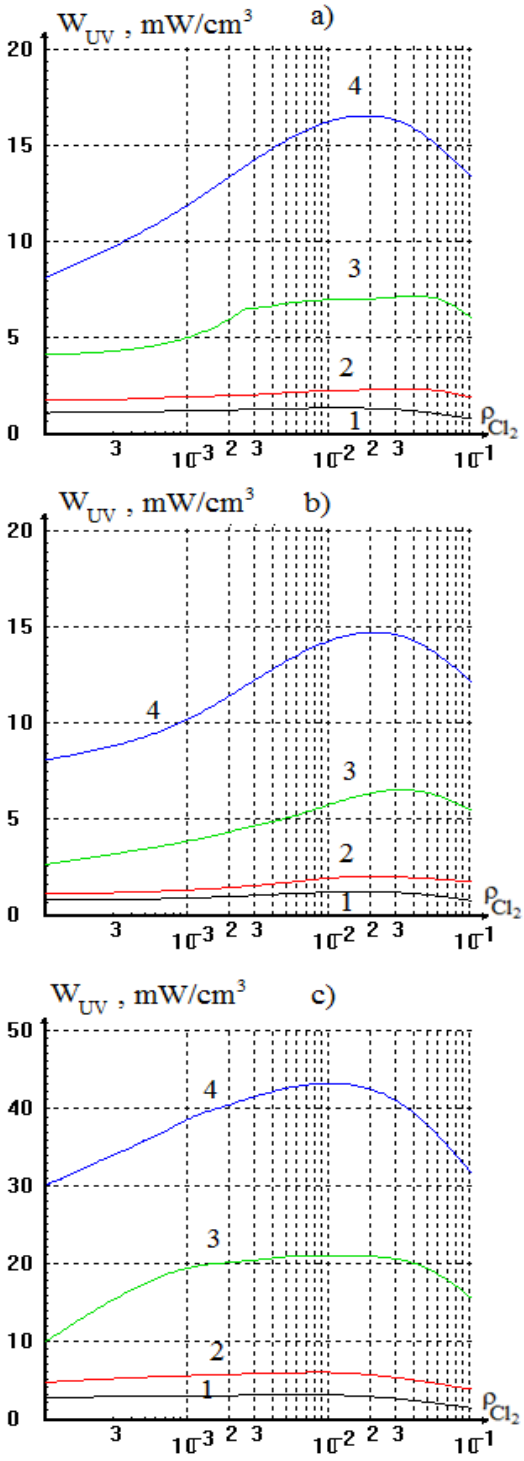

Fig. 1 – Spatially averaged specific UV power W_{UV} (*a*), local values W_{UV} (see /4/) for the discharge center (*b*) and for the discharge periphery (*c*) vs Cl_2 partial pressure; U_0: 200 V (1), 400 V (2), 800 V (3), 1000 V (4); L = 4 cm, P_0 = 1 Torr

The following analysis of results of our simulation showed that:

1).The optimal values of partial chlorine pressures are 0.001 – 0.01 Tor;

2).The maximal value of specific UV power can reach up to 0.6 W/cm^3.

The results of the work were obtained using computational resources of Peter the Great Saint-Petersburg Polytechnic University Supercomputing Center (www.spbstu.ru).

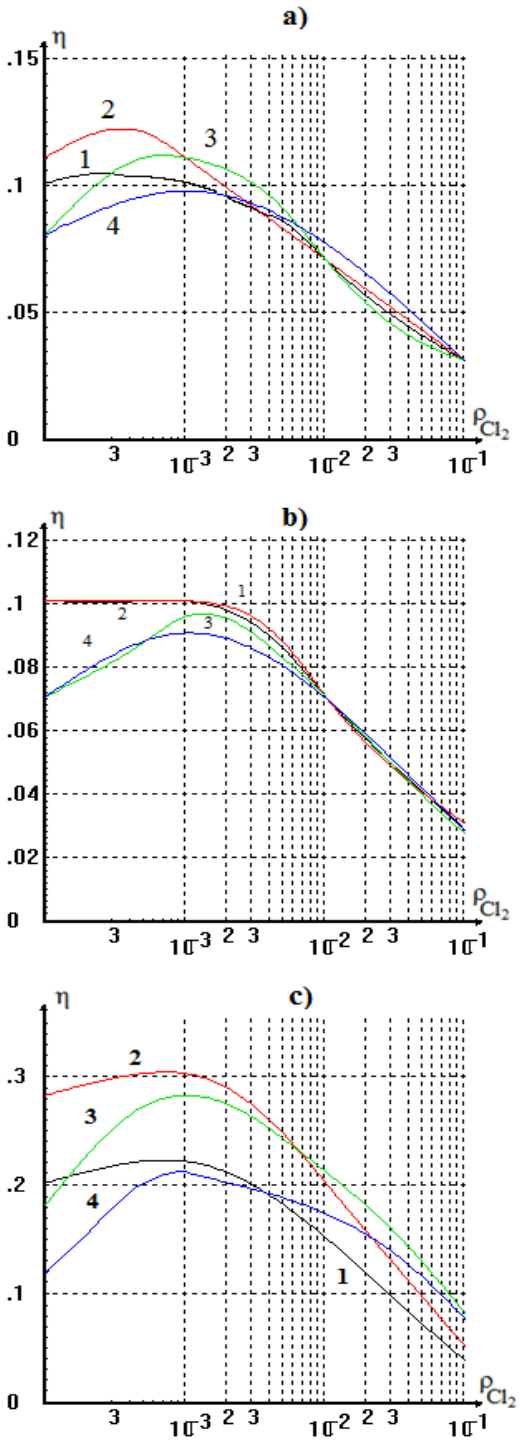

Fig. 2 – Spatially averaged efficiency η (*a*), local efficiencies (see /4/) for the center of discharge (*b*) and for the discharge periphery (*c*) vs Cl_2 partial pressure; U_0: 200 V (1), 400 V (2), 800 V (3),1000 V (4); L = 4 cm, P_0 = 1 Torr

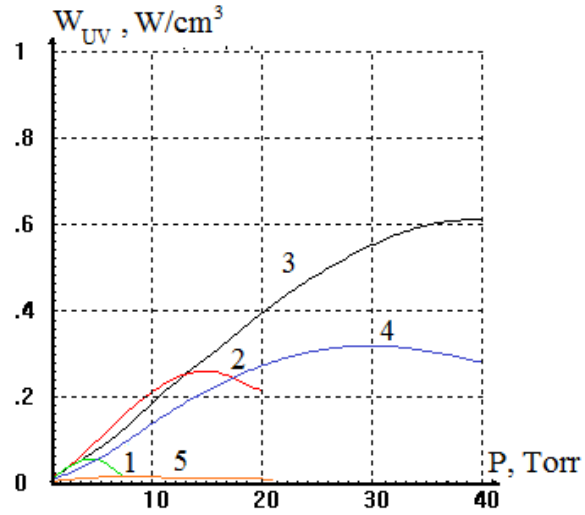

Fig. 3 – Spatially averaged specific power of UV radiation vs total pressure of mixture Xe + Cl_2 in relation: 10:1 (1), 100:1 (2), 1000:1 (3), 3000:1 (4) and 10000:1 (5) with efficiency 3%, 7%, 12%, 12%, and 1% respectively

References

1. **Golovitski A.P.** Tech. Phys., 56 (2011) 361–370.
2. **Skakun V.S., Lomaev M.I., Tarasenko V.F.** et al. Laser and Particle Beams, 21(2003) 115 – 119
3. **Golovitskii A.P**. Tech. Phys. Letters, 24 (1998) 233-234
4. **Golovitskii A., Pelli A.** Proc. of VIII. Int. Conf. Plasma Physics and Plasma Technology. (2015) 31 – 34
5. **Golovitskii A., Pelli A.** // Actual Problems of Electronics Instrument Engineering, 1 **(**2016) 16-18
6. **Smirnov B.M.** Sov. Phys. Uspekhi, 26 (1983) 31 – 45.
7. **Golovitskii, A. P., Lebedev S.V.** Optics and Spectroscopy, 82 (1997) 227-231
8. **Pikulev A. A., Turutin S.L., Sosnin E.A.** Journal of Engineering Physics and Thermophysics 89 (2016) 942-949.

THE NUMERICAL SIMULATION OF A CATHODE SPOT MOTION IN A TANGENTIAL MAGNETIC FIELD

I.Ivanou

Belarusian National Technical University, Republic of Belarus, 220013, Minsk, Nezavisimosty av., 65, iivanou@bntu.by

The vacuum arc burns in the high ionized vapors of the cathode material. This steam environment forms as result of erosion of cathode in cathode spots. The lifetime of the single cathode spot is from tenths to tens of microseconds. A new spot appears at a distance of the radius of the cathode spot r_K or more. Thus, the motion of the vacuum arc cathode spot along the eroding cathode surface is discrete. The cathode spot motion speed reaches 10^2 m/s. The probability of occurrence of a new cathode spot at a distance X greater than the radius of the cathode spot is small and decreases exponentially with increasing $X > r_K$

An external magnetic field is used for stabilization of the arc discharge on the machined surface of cathode and monitoring of the trajectory and the speed of the cathode spot motion. According to existing physical concepts, the reason of the retrograde motion of the cathode spot in an external magnetic field is the "asymmetry of the magnetic field" - the summation of the external and intrinsic magnetic fields on one side of the spot and their subtraction on the other one /1/. This asymmetry leads to the motion of the spot in the direction of the maximum induction of the magnetic field. But this motion is random because it is affected by ionization processes in the near cathode space, the uneven heating of this space and the mobility of the plasma jet itself. Discrete spot motion (the emergence of a new emission center instead of dying one) occurs in a straight line in by jumping. The distance to which the cathode spot moves and the direction of it motion are random variables. The technique for simulation of the trajectory of the single cathode spot motion in the absence of an external magnetic field is given in /2/.

The aim of this paper is to develop an algorithm for calculating the trajectory of the motion of a single cathode spot of a vacuum arc in an external tangential magnetic field as a stochastic process.

MATLAB was used for calculation and visualization of the calculation results. A Cartesian coordinate system was used. The coordinate plane **XoY** was combined with the eroding surface of the cathode, the axis **oZ** was perpendicular to this plane. The current vector ($\boldsymbol{I}$) was perpendicular to the coordinate plane **XoY**, and the magnetic induction vector ($\boldsymbol{B_e}$) was parallel to this one and was directed along the axis **oX**. The direction of the cathode spot motion vector was always perpendicular to the plane in which vectors of the current and tangential

magnetic field lays. The motion of the spot goes in the direction perpendicular to the vector $\boldsymbol{B_e}$. When the vector $\boldsymbol{B_e}$ rotates, the direction of spot motion along the cathode surface will change. The direction of motion of the cathode spot was calculated as random angle of displacement from the ***oX*** axis.

For single cathode spot:

$$X = X_0 - \left(\frac{1}{a}\right) ln(1 - \gamma),$$

where γ – random number from 0 to 1. It is a characteristics of the probability of a new cathode spot appearance at a distance X from the center of the dying one. The coefficient ***a*** is equal to the diffusion coefficient of single spot on electrode surface /2/.

Last equation defines new coordinates of the center of the cathode spot together with the procedure for angular coordinate definition. In this approach, the time parameters of the process are not required. Simulation of the process consists in choosing: a) the direction of the cathode spot motion; b) the distance to which the spot moves in one step. The spot changes its position discretely by the calculated distance.

For realization of this stochastic approach it is necessary to specify a procedure that limits the angular deviation of the spot from the direction of the Lorentz force. An external tangential magnetic field limits an angular coordinate definition of the spot in the direction perpendicular to the magnetic force acting on the current channel. The angle of deviation from the direction of motion is determined by the magnitude of the external magnetic field:

$$\alpha = \frac{\mu \cdot \pi - \frac{\pi}{2}}{d} = \frac{\pi}{d} \cdot \left(\mu - \frac{1}{2}\right),$$

where $d=d(B_e)$ – the positive constant depends on the magnitude of the external magnetic field (indicator of the tangential magnetic field intensity). An angular coordinate definition calculates form the axis which is equal to the vector $\boldsymbol{B_e}$.

The indicator of the tangential magnetic field intensity is determined to use simulation method of /3/. If the angular coordinate at a given value of the external tangential magnetic field is known, it is possible to calculate a new angular coordinate for a new value of the magnetic field:

$$d_2 = d_1 \cdot \left(\frac{B_{e2}}{B_{e1}}\right)^{-b(I)},$$

where *b* is the constant depends on a discharge current.

A program for calculation of the random direction of the cathode spot motion (angle **α**) in the range of ± 90 ° from the direction of the spot motion and for calculation of the one moving step of the spot (dr) has been developed.

The result of the calculation is shown in the figure in polar coordinates.

The graphical distribution of new emission centers relative to the center of the dying cathode spot is showed on figure. As we can see the most of new spots are formed at a distance close to the radius of the spot r_K. Sharp jumps (up to 3.4 radius of spot) are much smaller.

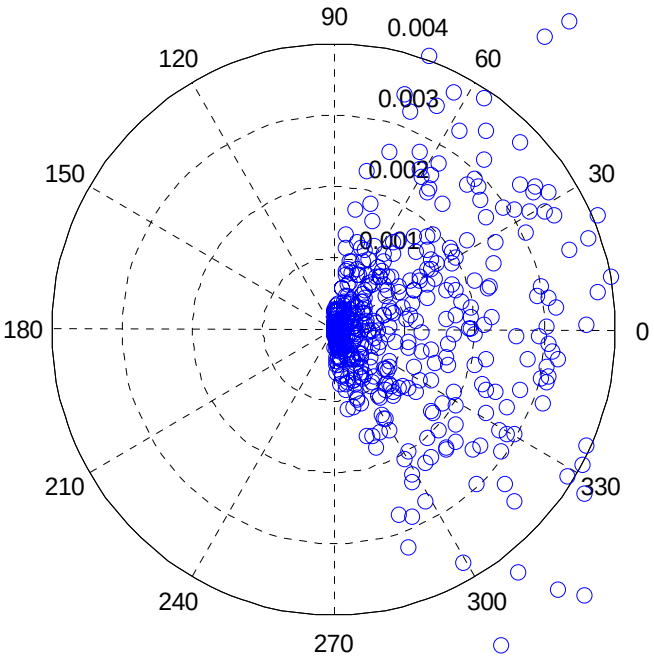

Fig. 1 – The value of the angular and vector coordinates of the new emission center. For the indicator of the tangential magnetic field intensity d = 10 and the number of points of reference N = 500.

Thus, a method for calculation of a cathode spot trajectory in an external tangential magnetic field was developed. This method allows to determine the optimal value of an external magnetic field and to obtain the required trajectory and the velocity of the cathode spot motion, to increase the uniformity of evaporation of the cathode surface and to decrease the droplets in the plasma flow.

This work was supported by state research program «Energy systems, processes and technologies», subprogram "Effective thermophysical processes and technologies" point 2.10.

References

1. Bobrov Yu.K., Bystrov V.P., Rukhadze A.A. Journal of Technical Physics. - 2006.- Volume 76.- vol. 5.- pp. 35 - 41

2. Ivanov I.A. Information Technologies in Education, Science and Production: V International Scientific and Technical Internet Conference, Nov. 2017 [Electronic resource] - http://www.bntu.by/images/stories/mido/ntik5/ivanov1.pdf.

3. Dukhopelnikov D.V. Kirillov D.V., Ryazanov V.A. Electronic Scientific and Technical Journal, 2012, No. 11, p. 21 - 32: [Electronic resource]: http://technomag.edu.ru/doc/482485.html

CHARGED - PARTICLE STOPPING IN A CLASSICAL ELECTRON GAS

Yu.V. Arkhipov[1], A.B. Ashikbayeva[1], S.A. Syzganbayeva[1],
D.Yu. Dubovtsev[1], I.M. Tkachenko[2]

[1]Al-Farabi Kazakh National University, Almaty, Kazakhstan, Yuriy.Arkhipov@kaznu.kz
[2]Universitat Politècnica de València, Valencia, Spain, imtk@mat.upv.es

Phenomena related to the interaction between beams of charged particles with condensed matter and plasmas have been widely studied using different methods of diagnostics. In addition, beams of heavy fast ions are considered as a perspective driver for the inertial fusion.

The plasma polarizational stopping power of heavy ions projectiles is described by the Lindhard formula /1/:

$$\left[-\frac{dE}{dx}\right]^{pol} = \frac{2(Z_p e)^2}{\pi\, v^2}\int_0^\infty \frac{dk}{k}\int_0^{kv} \omega^2 \left(-\mathrm{Im}\,\frac{\varepsilon^{-1}(k,\omega)}{\omega}\right) d\omega, \qquad (1)$$

whose high-velocity asymptotic form was found by Bohr, Bethe, and Larkin /2-4/:

$$\left[-\frac{dE}{dx}\right]^{pol}_{v\to\infty} \cong \left(\frac{Z_p e\omega_p}{v}\right)^2 \mathrm{Ln}\,\frac{2m_e v^2}{\hbar\omega_p}. \qquad (2)$$

This expression is usually employed to diagnose the plasma /5,6/.

The plasma inverse dielectric function (IDF), $\varepsilon^{-1}(k,\omega)$, was determined in /7/ within the moment approach /8/ complemented by some physical observations which permitted to express it in terms of only two characteristic frequencies, which are the ratios of the frequency power moments of the IDF imaginary part:

$$\varepsilon^{-1}(k,\omega) = 1 + \frac{\omega_p^2(\sqrt{2}\,\omega_1\omega + i\omega_2^2)}{\sqrt{2}\omega_1\omega(\omega^2-\omega_2^2) + i\omega_2^2(\omega^2-\omega_1^2)}. \qquad (3)$$

The frequencies ω_1 and ω_2 in (3) can be calculated rigorously as soon as we know the static structure factor (SSF) of the system /7, 8/. Here we employ the following interpolation expressions /9, 10/:

$$\omega_1^2 = \omega_1^2(k) = \omega_p^2\left(1 + k^2 k_D^{-2} + k^4 k_q^{-4}\right), \qquad (4)$$

$$\omega_2^2 = \omega_2^2(k) = \omega_p^2\left(1 + \frac{\langle v_e^2\rangle k^2}{\omega_p^2} - \frac{v_{int}^2 k^2}{\omega_p^2}\right). \quad (5)$$

The interpolation and fitting parameters introduced here are the following:

$$v_{int}^2 = -\frac{4}{15}\frac{\Gamma^{\frac{3}{2}}}{\beta m_e}\left(\frac{-0.9052}{\sqrt{0.6322+\Gamma}} + \frac{0.27243}{1+\Gamma}\right),$$

and k_D^{-1} is the Debye radius, $\Gamma = \frac{\beta e^2}{a}$, $k_q^4\, l^4 = 12 r_s \Gamma^4$, $r_S = \frac{a}{a_B}$, $l = e^2\beta$ is the Landau length, a and a_B are the Wigner-Seitz and Bohr radii, $\beta = 1/k_B T$, k_B is the Boltzmann constant, and T is the temperature. Under the thermodynamic conditions we deal with here, the system is practically a classical plasma so that all magnitudes can be expressed in terms of the plasma coupling parameter Γ, and we may use for the average electron thermal velocity the Vlasov classical form: $\langle v_e^2\rangle = k_B T/m_e$.

We have compared the polarizational losses of heavy projectiles in electron gas calculated within the simplified interpolation version of the modified method of moments /7/ to the results of the latter and to the PIC simulation data /11/ in classical systems, see Figure 1.

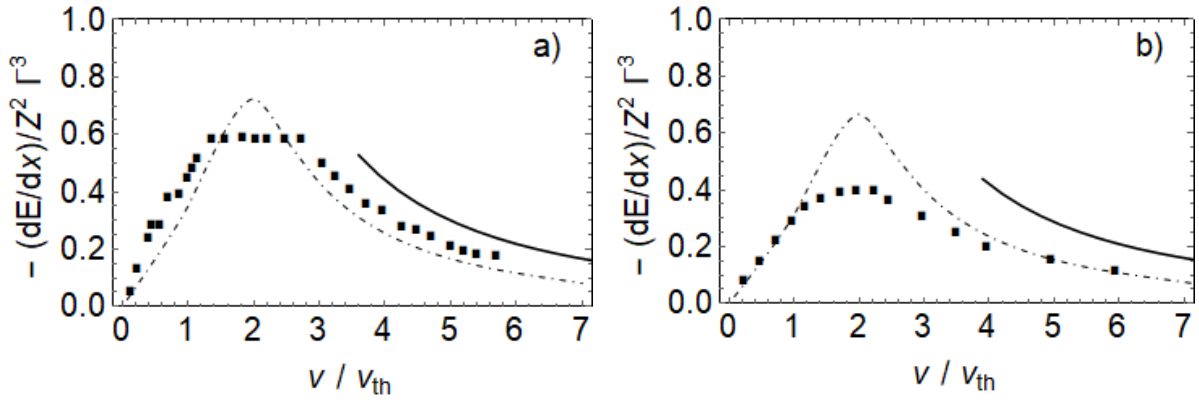

Figure 1: The stopping power (-*dE/dx*) in thermal units, i.e. divided by $3k_B T/l$, plotted vs the beam velocity $v_{th} = \sqrt{k_B T/m_e}$. The dash-dotted line stands for the results of the interpolation model, the solid line represents the asymptotic form (2), the squares display the PIC simulation data /11/. The data describe an ion beam with a charge number of a) $Z = 5$ moving in an electron gas with $n = 1.1 \cdot 10^{20}$ cm^{-3} and $T = 1.6 \cdot 10^5 K$ ($Z\Gamma^{3/2}$ =0.12), b) $n = 1.4 \cdot 10^{20}$ cm^{-3}, $T = 1.3 \cdot 10^5 K$, $Z = 10$ ($Z\Gamma^{3/2}$ =0.354).

Under the above conditions the interaction contribution |*U(q)*| to the frequency

ω_2 is at least an order of magnitude smaller than the kinetic one, *K(q)*, so that the simplified random-phase interpolation form for the frequency $\omega_1(q)$ is perfectly applicable /12/.

We observe that the suggested simplified interpolation approach based on the modified method of moments is capable of describing the energy losses of a charged particle in warm dense effectively classical electron plasmas with a fairly satisfactory precision. Notice that no adjustable parameters were used, and the interpolation-model calculation is practically algebraic. Last year the same interpolation approach was applied to describe the stopping power of two-component plasmas, and we are planning to carry out a comparative study. Our results imply the physical applicability both of the interpolation and the complete modified moment approach.

Acknowledgements. Work supported by the Republic of Kazakhstan Ministry of Education and Science grants AP05132677, AP05132333 and BR05236730/PTsF.

References

1. **J. Lindhard, K.Dan.** Vidensk. Selsk, Mat .Fys .Medd., 28 (1954) 3.
2. **N. Bohr**, Phil. Mag., 25 (1913) 10.
3. **H. Bethe**, Ann. Phys.(Lpz.), 5 (1930) 325.
4. **A.I. Larkin**, Zh. Eksp. Teor. Fiz., 37 (1959) 264.
5. **A. Golubev *et al.***, Phys. Rev. E **57**, (1998) 3363.
6. **A. D. Fertman *et al.*,** Nucl. Instrum. Methods Phys. Res. Sect. B **247**, (2006) 199.
7. **Yu. V. Arkhipov et al.**, Phys.Rev.Lett., 119, (2017) 045001.
8. **Igor M. Tkachenko, Yu.V. Arkhipov, A. Askaruly.** The Method of Moments and its Applications in Plasma Physics (Lambert, Saarbrücken, 2012) 125.
9. **V.M. Adamyan, I.M. Tkachenko**, High Temp., 21 (1983) 307; **J. Ortner, I.M. Tkachenko**, Phys. Rev. E 63 (2001) 026403.
10**. G. Chabrier, A. Y. Potekhin**, Phys. Rev. E 58 (1998) 4941.
11**. D. O. Gericke, M. Schlanges**, Phys. Rev. E 60 (1999) 904.
12**. Yu. V. Arkhipov et al.**, Contr. Plasma Phys., 56, (2016) 403.

COMPARISON OF STATIONARY AND NAVIER-STOKES MODELS OF LASER-INDUCED PLASMA OF ALUMINUM ALLOYS

T.A. Labutin[1], I.B. Gornushkin[2]

[1]Lomonosov Moscow State University, Department of Chemistry,
Moscow, Russia timurla@laser.chem.msu.ru
[2]Bundesanstalt für Materialforschung und -prüfung,
Berlin, Germany, igor.gornushkin@bam.de

Physical processes upon laser ablation of materials are actively studied and modeled. A quantitative description of laser-induced plasma is very important for both fundamental study of this plasma source and development of a robust calibration-free method of laser-induced breakdown spectrometry (LIBS). The current study was focused on experimental and theoretical plasma modeling. The plasma was produced on a surface of an aluminum alloy. The plasma diagnostics was performed including determination of plasma parameters, such as plasma temperature and density of plasma species, and evaluation of plasma homogeneity. We investigated and compared three models of laser-induced plasma: (i) the homogeneous plasma at local thermodynamic equilibrium, (ii) the two-zone heterogeneous plasma approximated by the "hot" core and "cold" periphery (Fig. 1a), and (iii) the hydrodynamic model of expanding plasma (Fig. 1b).

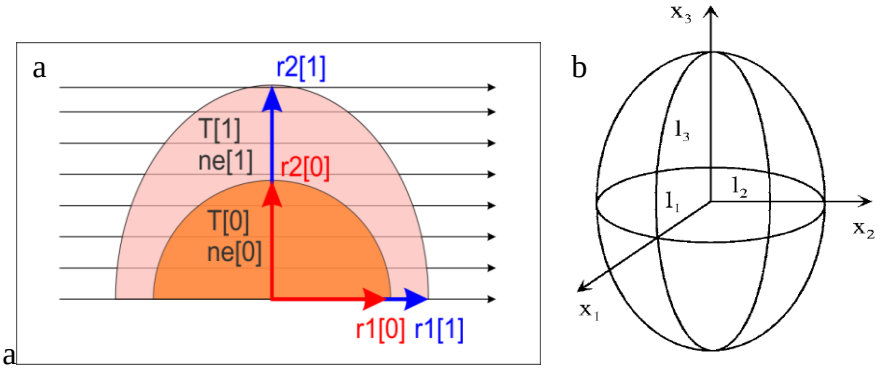

Fig. 1 – Models of laser-induced plasma: a) two-zones one, b) expanding ellipsoid

The use of the model of homogeneous plasma is useful for the description of spectra in a narrow spectral range, where the lines with the similar excitation potentials are present. The more sophisticated models allow for the description of such spectral feature as self-reversed lines or are helpful for the description of plasma evolution.

2. ELECTRICAL DISCHARGES AND OTHER PLASMA SOURCES, ELEMENTARY AND NEAR-ELECTRODE PROCESSES

STRONGLY OVER-VOLTAGE OPEN DISCHARGE IN DEUTERIUM AT LOW PRESSURE AS AN INTENSIVE SOURCE OF RUN-AWAY ELECTRONS WITH ENERGY UP TO 25 KEV

Yu.Akishev[1,2], G.Aponi[1], V.Karalnik[1], A.Petryakov[1], N.Trushkin[1]

[1]State Research Center of Russian Federation TRINITI, 108840, Moscow, Troitsk, Pushkovykh Str., vladenie 12, Russia
[2]National Research Nuclear University MEPhI, 115409, Moscow, Kashirskoe sh, 31, Russia

Strongly overvoltage open discharges in a narrow gap (2-3 mm) between the solid plane cathode and the grid anode are used for generation of the pulsed high-current electron beams with the energy up to several tens of keV. Strongly overvoltage (SO) regime is unstable and the discharge tends to transit into low-voltage (LV) regime with a very high total current. Therefore there is an insistent need in studying of the mechanism of instability of the SO regime which, in fact, is the most of interest from the practical point of view.

We studied this transition by the example of the three-electrode open discharge in D_2 at low pressure (about 0.5-2 Torr) being powered by stepwise voltage with the rise-time of 20 ns and amplitude up to 25 kV. General scheme of the used setup is shown in Fig. 1. The existence of the auxiliary third electrode allows one to get more stable ignition and reproducible operation of the strongly overvoltage open discharge.

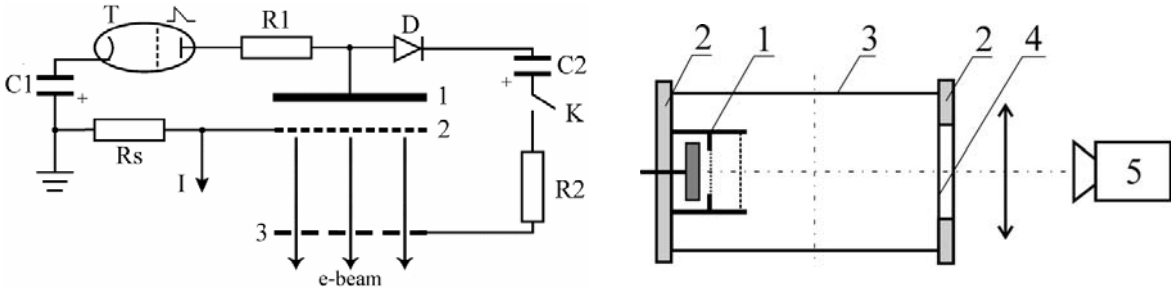

a) b)

Fig. 1 - a) The electrical scheme of the three-electrode system generating a high-current e-beam with the energy up to 25 keV. 1 - the solid cathode; 2 - the grid anode of the main discharge; 3 - the grid anode of the auxiliary discharge; R1 = 56 Ohm, R2 =1 MOhm, Rs = 0.024 Ohm; C1 = 12.5 nF, C2 = 100 μF. b) 1 - the electrode system; 2 – flanges; 3 - quartz tube; 4 - quartz window; 5 - fast multi-frame camera

The physical properties of the SO and LV regimes and transition between them have been explored in detail with the usage of the fast multi-frame camera synchronized with the current and voltage of the open discharge. The experimental data were complemented with the numerical calculations of the SO

regime. The obtained results give more insight into physics of the strongly overvoltage regime of the open discharge generating the pulsed e-beams with their energy up to 25 keV and current up to 150 A.

Fig. 2 shows the Current-Voltage characteristic of the three-electrode open discharge in the overvoltage regime. We found out that this *I-U* characteristic can be satisfactorily approximated by the cubic dependence $I(A) \approx (U-U_0)^3/40$, where $U_0 = 5$ kV.

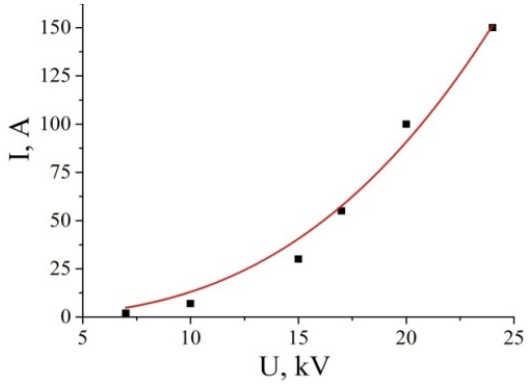

Fig. 2 - The Current-Voltage characteristic of the three-electrode open discharge in the diffuse overvoltage regime. The solid curve is the approximation $I(A) \approx (U-U_0)^3/40$, where $U_0 = 5$ kV. Deuterium, P = 2 Torr, the auxiliary low-current discharge is powered with the voltage U* = 1 kV

As it turned out, the higher applied voltage, the shorter duration of the overvoltage regime which just generates the high-energy e-beam. The experimental data showing in detail the spatial-temporal evolution of the open discharge up to its transition into the low-voltage regime with the high-current cathode spot(s) are presented in Fig. 3. This set of the obtained data is very useful for development of the physical mechanisms which responsible for supporting the strongly overvoltage regime of the open discharge and for its transition into the low-voltage regime.

After close examination of all shots presented in Fig. 3, two important things were revealed. First, the SO open discharge is diffuse and does not constrict – contrariwise, the discharge increases the cross-section and brightness up to the transition into the LV regime. Second, the bright cathode current spot(s) happens after the SO → LV transition and therefore they cannot be a physical reason initiating this transition. Moreover, even if the cathode current spot happens at the SO regime, this spot cannot initiate the streamer (thin current filament) which further could propagate from the cathode towards the anode and eventually shunt the gap, i.e. to form the LV regime. An explanation of this statement is the following - the propagation of streamer (which, in fact, is the ionization wave) towards the anode requires the existence in the gap of an intensive direct ionization of neutral particles by the electron impact. However, the extremely high electric field at the cathode and in the gap in the SO regime (the reduced electric field E/N reaches of the huge magnitude of 10^5 Td and even higher) leads to that the electrons have immediately become the run-away

electrons which have the extremely low efficiency of the impact ionization and therefore cannot support the propagation of the streamer(s).

The numerical simulation of the SO regime showed that the most probable mechanism of the SO → LV transition is a strong gas heating switching-on the intensive thermal ionization which forms the high-conductive plasma in the gap.

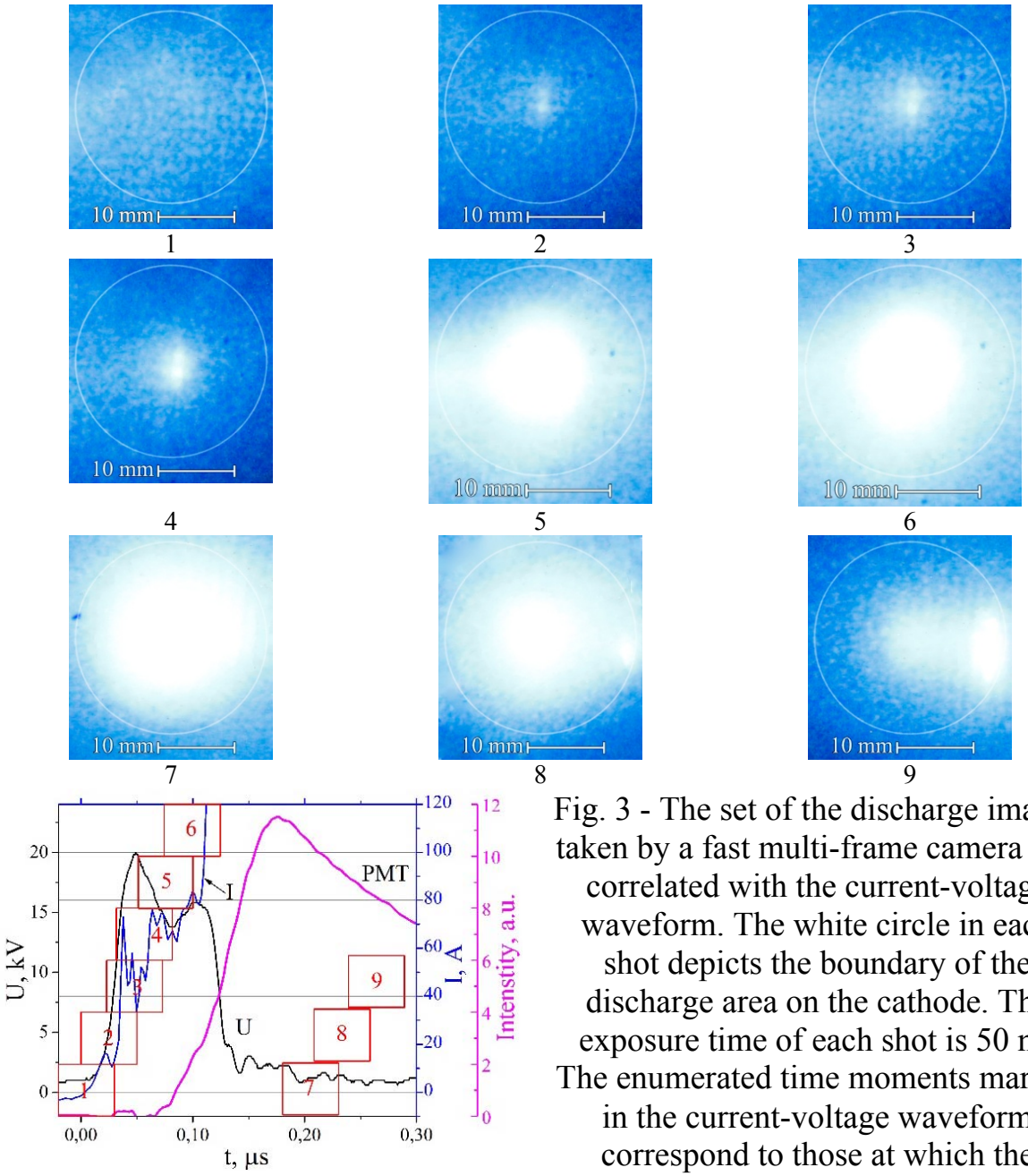

Fig. 3 - The set of the discharge images taken by a fast multi-frame camera and correlated with the current-voltage waveform. The white circle in each shot depicts the boundary of the discharge area on the cathode. The exposure time of each shot is 50 ns. The enumerated time moments marked in the current-voltage waveform correspond to those at which the enumerated images were taken. Deuterium, P = 2 Torr, U = 20 kV, U* =1 kV

Acknowledgement. This work was supported by the Russian Science Foundation (Grant № 16-12-10458).

DEMONSTRATION OF SOLITON STOPPING IN ACOUSTOPLASMA DISCHARGE

A.Abrahamyan

Institute of Applied Problems of Physics, NAS RA, 25 Hr. Nersisyan str.,
0014, Yerevan, Armenia, E-mail: arbel11@mail.ru

Introduction. Modulation of the discharge current creates acoustic vibrations that interact with the plasma and as a result, a new acoustoplasma medium arises /1,2/. Modulation of current can excite acoustic vibrations. The discharge tube is an acoustic resonator. Standing waves are created in the tube. At low modulation frequencies, only longitudinal acoustic modes exist in the tube. As the modulation frequency is increased, the standing non-axial modes are formed in the tube /3/. Plasma and acoustoplasma are self-consistent media, and therefore the phenomena in them (including acoustic ones) should be described by nonlinear equations, i.e. nonlinear acoustics. One solution of the equations of nonlinear acoustics is soliton waves, which can be formed in various media, including plasma /4,5/.

Experiment. The conditions for creating the acoustoplasma and the experimental setup were described in /6/. In this experiment, the xenon pulse lamp IFP-5000 was used as the discharge tube. The internal diameter of the quartz discharge lamp tube is 12 mm. The direct component of the discharge current I_0 = 20-30 mA, the variable component I ~ = 4-10 mA. The pressure of xenon is ~ 100 torr. At this pressure, even at a current of several mA, as a result of thermal contraction, the discharge turns into a thin cord with a diameter of ~ 1 mm.

With DC power, the cord discharge due to Archimedes' force is located in the upper part of the cylindrical tube and represents a straight line (Fig. 1a). When modulating the discharge current due to the acoustoplasma interaction, a standing wave is formed due to reflection from the ends of the tube and the path of the cord discharge is bent. As the depth of the current modulation (modulation depth $M = I \sim / I_0$) increases, different spiral structures appear in the tube, which are stable in time. At frequencies corresponding to the non-axial modes of the acoustic cavity formed by the discharge tube, a spiral is obtained, represented in Fig. 1b. The number of turns of this spiral can be changed by changing the modulation frequency /7/.

The description of spiral structures obtained in plasma can often be found in the literature, but they did not mention their stable state, the possibility of

controlling these structures was not considered, and the acoustoplasma interaction was not considered.

Under certain modulation conditions, ring-stable single-loop turns are formed in the tube. One can obtain one (Fig. 2a) or several (Fig. 2b) of such ring single turns, the rest being a straight line, in spite of the fact that the current is modulated. It can be seen from Fig. 2b following the discharge trajectory that adjacent rings of single turns change the direction of rotation. Two rings connect the straight plasma cordon top. One of the rings goes on the right screw, and the next one, necessarily on the left. If there are several rings, then the next one again on the right screw, etc.

a) b)

Fig.1 - Various trajectories of a cord discharge: a) discharge at a direct current; b) spiral structure in acoustoplasma

Generally. For the non-axial modes, the resultant wave vector has the form

$$k^2 = k_z^2 + k_r^2 \quad (1)$$

where k is the resultant wave vector, k_z is the wave vector along the discharge axis, k_r is the wave vector orthogonal to the discharge axis (circular component). This is also true for acoustic soliton waves.

With an appropriate selection of frequency-amplitude relationships, with the superposition of waves reflected from the ends of the tube, the longitudinal components of the two opposing solitons can be compensated, and the circular components can be made uncompensated. As a result, a standing soliton circular wave in the form of a single turn is formed in the discharge tube with a contracted cord discharge.

In /8/ it is indicated that for the model description of stable vortex structures the term "topological solitons" is used. In the simplest form they are described by the equations "Sinus-Gordon" in the form of "kinks" (loops).

Movement along the positive direction corresponds to "kink", and movement in the opposite direction "antikink." In our case, these are solitons walking along the discharge in different directions. The solutions of the Sinus-Gordon equation are characterized by a topological charge of ± 1. Thus, adjacent rings must have different directions of rotation in order to compensate for topological charges. As a result of the partial annihilation of the multidimensional "kink" and "antikink", we obtain rings in the discharge tube. One-dimensional "kink" and "antikink" would be annihilated entirely.

Usually such a representation is applied to condensed media. The acoustoplasma in its parameters becomes similar to a condensed medium /8/. Therefore, for acoustoplasma, the same consideration can be applied through soliton solutions.

Similarly, in ferromagnets with anisotropy, the simplest configuration of the field is a nonsingular annular vortex.

You can consider a different approach, using the order parameter. The order parameter is a thermodynamic quantity characterizing the long-range order in the medium, which arises as a result of a change in symmetry during the phase transition.

It was experimentally found that under certain conditions, phase transitions can be made in an acoustoplasma during each modulation period /6, 9/. Moreover, it can be done both with a change in the topological connectivity, and without a change in the topological connectivity. Those, oscillations of the order parameter about equilibrium are carried out. Continuous degenerations of the equilibrium states of ordered phases lead to a state in which the order parameters depend on the coordinates. Such inhomogeneous states of the order parameter are usually created by means of external fields. They can exist in the form of different metastable structures (including solitons).

Conclusion. Single turns in the acoustoplasma medium were experimentally obtained. These single turns are identified as stopped solitons. Thus, the formation of solitons and their stabilization in space are possible in a cylindrical discharge tube with an acoustoplasma medium. When reflecting solitons from the ends of a cylindrical discharge tube, it is possible to compensate their longitudinal components while preserving the circular component. It is this phenomenon that leads to the formation of single turns in the acoustoplasma.

The formation of solitons in an acoustoplasma can be described both by the equations of nonlinear acoustics and by changes in the order parameters during phase transitions.

References

1. **GalechyanG.A., MkrtchyanA.R.**Acoustoplasma, Yerevan, Apaga, (2005), 338p. (inrus.).
2. **Mkrtchyan A.R., Mkrtchyan A.H., Abrahamyan A.S**. VII Int. Conf., Plasma Physics and Plasma Technology, PPPT-7, Minsk, Belarus, 17-21 Sept. (2012), Proc., v.1, 3-5.
3. **Skudrzyk E.** The Foundation of Acoustic. Basic Mathematics and Basic Acoustics. N.Y., (1971).
4. **Volovik G.E., Mineev V.P.** Physics and topology, M., (1985). (rus.)
5. **Rudenko O.V., Gurbatov S.N., Hedberg K.M.** Nonlinear acoustics in problems and examples. M., FIZMATLIT, (2007), 176 p. (rus.)
6. **AbrahamyanA.S., Mkrtchyan A.H., Sahakyan Q.G**. VII Int. Conf. Plasma Physics and Plasma Technology, PPPT-7, Minsk, Belarus, Sept. 17-21, (2012), Proc., v.1, 244-247.
7. **Abrahamyan A.S., Abrahamyan K.A., Gevorgyan S.A., Kostanyan R.B**. Control of cord discharge by means of plasma-acoustic interaction. Intern. Seminar "Armenia's conversion potential and ISTC programs", Yerevan, Armenia, October 2-7, (2000), Proc., v.1, 140-142.
8. **MkrtchyanA.R., AbrahamyanA.S., KostanyanR.B., HaroyanK.P., MkrtchyanK.S.**J. Contemp. Phys. (ArmenianAc. Sci.),v.40, N3 (2005), 209-214. (inrus.NASArmenia, Izwesiya, Physica).
9. **Sahakyan Q.G.**The solution of incorrectly posed inverse problems in acoustoplasma. Ph.D.thesis, Yerevan, (2014) (in rus).

PLASMA JET GENERATION FROM HELIUM-AIR GAS MIXTURES IN DC GLOW AND DIELECTRIC-BARRIER DISCHARGES

A. Astafiev [1], A. Kazak [2], M. Pinchuk [1], L. Simonchik [2], V. Spodobin[1], O. Stepanova [3]

[1] Institute for Electrophysics and Electric Power RAS, Dvortsovaya nab., 18, 191186, St. Petersburg, Russia
[2] Institute of Physics of NAS of Belarus, Nezavisimosty Ave. 68–2, 220072, Minsk, Belarus
[3] Saint Petersburg State University, 7–9 Universitetskaya nab, 199034, St. Petersburg, Russia
E-mail: astafev-aleksandr@yandex.ru

Introduction. Sources of atmospheric pressure plasma jets have been becoming an object of intensive study, largely, due to the prospects for their use in biomedical applications. Nowadays, several types of such sources have already developed /1–3/. This paper is devoted to the comparison of two types of atmospheric pressure plasma jets which are based on dc glow /2/ and dielectric-barrier /3/ discharges. The aim of this research is to investigate the formation of the plasma jet depending on the type of the discharge and helium – air mixture proportion.

Generation of plasma jets. The fabricated discharge cells for a dc glow microdischarge and dielectric-barrier discharge (DBD) generation provide the same gas-dynamics conditions due to the identical geometrical sizes. Their design is presented in Fig. 1.

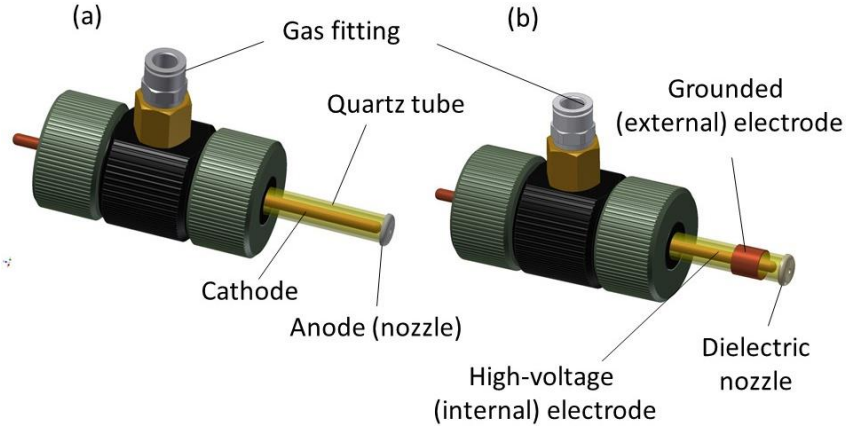

Fig. 1 – The design of the discharge cells for the generation of plasma jets in dc glow (a) and dielectric-barrier (b) discharges

A quartz tube with an inner diameter of 7.5 mm was used as a discharge cell. It was equipped by a cylindrical electrode of 4 mm in a diameter made of copper that was fixed in the center line of the tube. To generate a dc glow microdischarge, it was used as a cathode, and a copper nozzle with the hole of

1.5 mm diameter served as an anode was firmly pressed to the polished edge of the quartz tube so that the interelectrode gap was 0.7 mm (Fig. 1(a)). In the case of DBD, the cylindrical electrode was applied by high voltage, and the second (grounded) electrode made from a copper foil strip wrapped on the outer side of the tube (Fig 1(b)). The outlet of the tube was closed with a dielectric nozzle with a 1.5 mm diameter hole.

Owing to the same geometry of the discharge cells, we provided the same gas dynamics conditions for both discharge systems. The total gas flow rate was equal to 5 L/min. The content of air admixture in a helium flow was varied from 0 till 25%.

To feed a dc glow microdischarge, dc voltage of up to 5 kV was applied to the electrode system through a limiting resistor with an opportunity to change the electrodes polarity. It provides maximum currents up to 40 mA. The discharge currents and voltages were recorded by means of two true-RMS multimeters. In addition, to monitor fast-changing processes, the same values were recorded with an oscilloscope.

In the case of DBD generation, a sinusoidal 26 kHz voltage power supply was used. Electric parameters were measured with a current shunt of 1 kΩ and 1:1000 voltage divider (Tektronix P6015A). A jet current was measured with an additional flat electrode which was grounded with the current shunt of 1 kΩ.

DC glow microdischarge plasma jet. The plasma jet driven by the dc glow microdischarge has been shown not to be formed in the helium flow without air admixture. In this case, the voltage drop across the discharge gap is similar to the observed in /4, 5/. With adding the air admixture, the plasma jet appears and at the increasing of the air content it becomes longer (Fig. 2). At the same time, this leads to the increase in voltage drop, but the current-voltage characteristics (CVC) of the discharge for all the cases are rising at the currents of 5-30 mA (Fig. 3). Solid and dashed lines in Fig. 3 correspond to the different polarity of the electrodes. CVC and the plasma jet formation almost does not depend on the electrodes polarity at different proportion of the helium – air mixture.

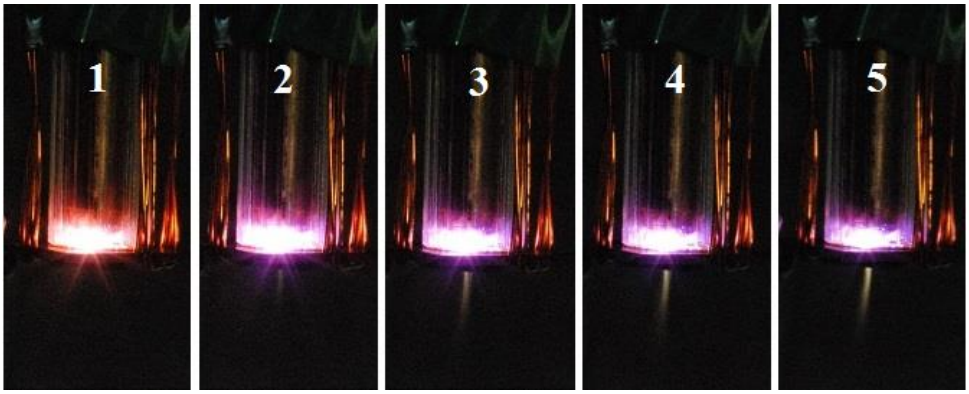

Fig. 2 – 20 mA DC glow discharge in helium–air mixture at the different air

content: 1 – without air; 2 – 1%; 3 – 5%; 4 – 10%; 5 – 25%

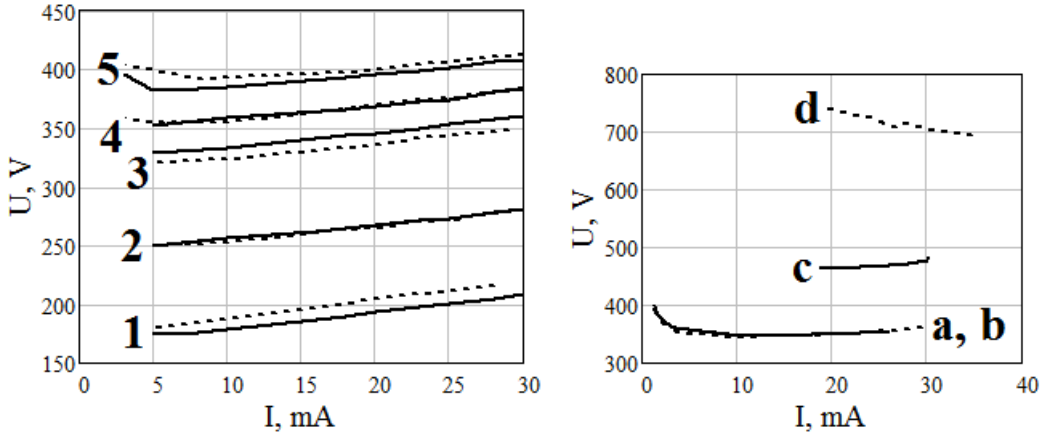

Fig. 3 – Current-voltage characteristics of the dc glow discharge when the electrode inside the tube is a cathode (solid curves) and at reversed polarity (dashed curves): left – in a helium flow at various air content (1 – without air admixture; 2 – 1 %; 3 – 5 %; 4 – 10 %; 5 – 25 %); right – in air (a, b – in a stationary air medium; c, d – in the air flow)

The glow discharges with various electrodes polarities in air are significantly different. Without air blowing through the discharge cell, CVC at both polarities are almost identical (curves **a** and **b** in Fig. 3, right). The discharge voltage drop is similar to the obtained in /6/. When air is blown (at 5 L/min) through the discharge cell, the current-voltage characteristic is shifted at the change of the electrodes polarity (curves **c** and **d** in Fig. 3, right). CVC is falling at the reversed polarity of the electrodes. This indicates nonstationary processes in plasma volume detected by oscilloscope as well.

Comparison with a DBD plasma jet. Fig. 4 shows the discharge and plasma jet images at the discharge current of 6 mA (RMS). The main feature of the DBD plasma jet is that it transfers the current, whereas the dc glow discharge plasma jet current is not detected. The current of the DBD plasma jet is equal to about 3–5 % of the discharge current that is 0.2–0.35 mA. At the same time, it changes along the length of the plasma jet. With the increasing of the air concentration in the helium-air mixture (up to 25%), a fast decrease in a visible jet length and increase in the discharge voltage drop from 1.6 to 1.8 kV has been observed.

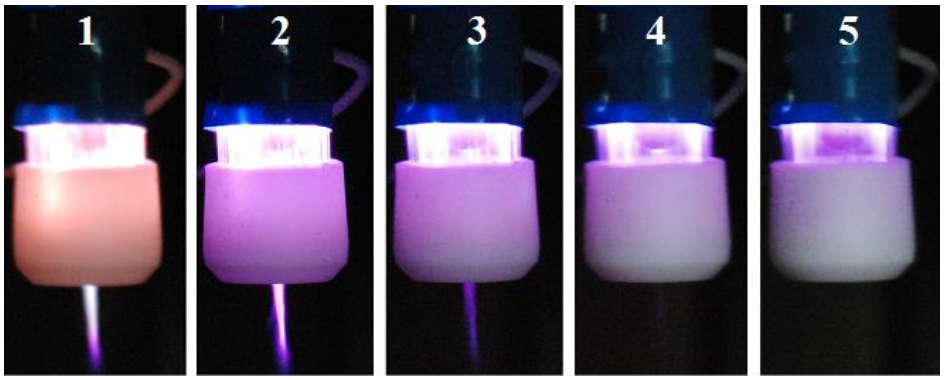

Fig. 4 – Dielectric-barrier discharge in the helium–air mixture at various air content: 1 – without air; 2 – 1%; 3 – 5%; 4 – 10%; 5 – 25%

The studied two types of plasma jets are very different objects. Dielectric-barrier discharge plasma jet transfers a current, but the DC glow discharge plasma jet does not. A visible radiation of the DC glow discharge plasma jet is provided by chemiluminescence of active plasma components which appear at air admixture.

Acknowledgements. This work was supported by the Russian Foundation of Basic Research (project 17-58-04052) and Belarusian Republican Foundation for Fundamental Research (project F17RM-050).

References

1. **Fridman A., Friedman G.** Plasma Medicine. John Wiley & Sons, 2013. 545 p.
2. **Kazak A., Kirillov A., Simonchik L., Nezhvinskaya O., Dudchik N.** // Plasma Medicine, 2017, V 7, № 2, pp. 109-115, DOI: 10.1615/PlasmaMed.2017019263.
3. **Stepanova O., Rybalchenko O., Pinchuk M., Astafiev A., Orlova O., Spodobin V., Kudryavtsev A.** Plasma Medicine 7 (3) (2017) 187-200. DOI: 10.1615/PlasmaMed.2017019064.
4. **Arkhipenko V.I., Kirillov A.A., Safronau Y.A., and Simonchik L.V.** // The European Physical Jouranl D, 2010, V 60, pp. 455–463, DOI: 10.1140/epjd/e2010-00266-5.
5. **Astafiev A., Kudryavtsev A., Stepanova O., Belyaev V., Zamchy R. and Chen Z.** Journal of Applied Physics 123, 083304 (2018). DOI: 10.1063/1.4999551.
6. **A. M. Astaf'ev, A. A. Kudryavtsev**, Technical Physics Letters 40 (9), 816 (2014).

STUDY OF HIGH-POWER BEAMS OF VACUUM SURFACE FLASHOVER OF POLYMER DIELECTRICS AT VOLTAGES UP TO 100 KV: EXPERIMENT AND SIMULATION

R. Emlin, P. Morozov, I. Punanov,V. Lisenkov, E. Shcherbakov

Institute of Electrophysics UD RAS, 620016, Yekaterinburg, 106 Amundsena street
lfd@iep.uran.ru

One of the most important problems in the field of pulsed power thrusters is understanding of mechanisms of generation of high-power high-speed particle beams/1/. An effective method for generation of such beams is high-power vacuum surface flashover at voltages of 100-200 kV. The surface flashover is being investigated by various methods at wide range of pulsed conditions like pulse width, power, energy input etc. Design features of pulsed generators of different types and sizes sometimes in an unknown way affect the parameters of the generated beams and bunches, which makes difficult to compare the experimental results obtained at different setups and complicates the measuring techniques. As the experimental methods become more complex, the development of theoretical models and methods for calculation of plasma bunches parameters depending on the electrical parameters of generators and physical properties of the propellants attract more attention. Like other complex electrophysical processes, high-current surface flashover includes /2,3/ several stages: generation of free electrons and ions by strong electric field, rapid input of energy into dielectric, phase transitions, formation and acceleration of plasma etc.

In this work, we emphasize mainly on aspects, connected with comparative measurements for broad number of parameters of plasma flows, generated by different work materials, as a base for reliable theoretical calculations.

Experimental setup comprised of a nanosecond pulse generator, vacuum chamber and pumps, Faraday cup with measuring circuits, ballistic balances and digital oscilloscope. We used a generator with the following parameters: stored energy is 3 J, impedance is 25 Ω, maximum current is 3.5 kA, pulse duration at matched-load conditions is 25 ns. We used PTFE, polyethylene, polystyrene and PMMA as samples. Also, alkali-halide crystal KCl were tested as model object. The chosen materials have relatively broad range of density, permittivity, heat capacity, thermal diffusivity, molecular weight of the monomer etc. Using of a set of propellants having very different physical properties including materials can significantly increase the reliability of the theoretical results.

Discharge unit has linear electrodes with a gap of 20 mm. We used this electrode configuration of the discharge because of relatively simple pattern of

electrical and magnetic fields distribution around it. It allows us to distinguish the action of different factors on the plasma bunch more clearly. Another advantage of the linear discharge is that the position of the discharge channel is well reproducible from shot to shot (in contrast to coaxial configuration) and the channel has well defined direction relative to the sample. Reproducibility of the results is high also because of good mechanical properties and radiation resistance of the tested materials. For measurement of discharge current we used a current shunt made out of 60 TVO-1 volume-type resistors in parallel.

We obtained waveforms of current and voltage across the discharge gap as the breakdown is initiated both from the anode and from the cathode. Maximal measured current was 3.5 kA. Waveforms of voltage across the gap for PTFE are at the Figure 1. These waveforms show the features of high-voltage stage of the breakdown propagation process, which are related with the difference between mechanisms of anode- and cathode-initiated flashover. Ionization front speed for cathode-initiated breakdown is 1.5 times higher than that for anode-initiated process. This behavior is well explained by the difference in dynamics of electrons emitted from the dielectric in these two configurations.

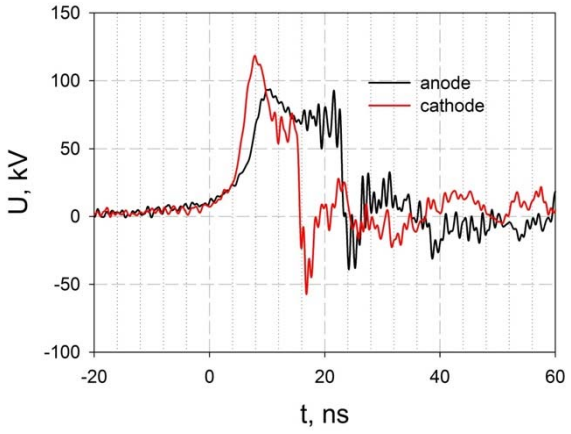

Fig.1 – Waveforms of voltage across the gap for Teflon for cathode (a) and anode (b) initiation of breakdown

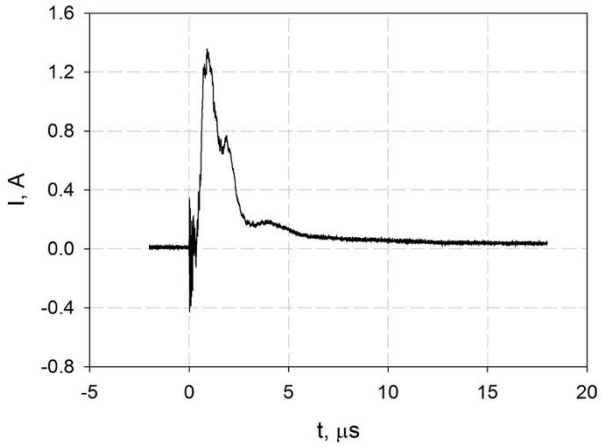

Fig.2 – The waveforms of ion current for a polyethylene specimen

When the discharge is initiated from the cathode, electrons are generated directly in ionizing electric field at the front of propagating conductive area and move to the anode almost without energy loss. However, when the discharge is initiated from the anode, electrons emitted at the front of conductive area move to the anode above partially ionized positively charged surface of dielectric through the region of near-surface ionized gas and create an avalanche of secondary emission electrons.

For measurement of ionic component of current of plasma bunch we used a Faraday cup with magnetic insulation of ion collector. Diameter of the collector is 100 mm. Using of resistive load at the collector (50 Ω) provides relatively good resolution, so we can see several ion peaks in the waveforms of ion current. Waveform of ion current measured at 15 cm from the discharge on PE sample is presented in Fig. 2.

We calculated full ion charge of the bunch using waveforms of current and pre-measured angular distribution of ions. Besides, we measured mass loss per discharge for all the tested materials. If we know value of mass loss per discharge and full charge of ionic component of the plasma bunch, we can calculate ionization degree of the material in the bunch. Values of mass loss, thrust, ionization degree, and energy of the plasma bunch are in Table 1.

The measurements of directional patterns were carried out in two mutually perpendicular planes: in the plane in which a discharge path lies (meridional plane) and in the plane normal to the discharge path (equatorial plane). Faraday cup moves along the arc with radius of 50 cm (distance from the discharge) in steps of 15 degrees. The size of the vacuum chamber (diameter 1.2 m, length 2.5 m) was big enough to avoid the influence of reflected particles on directional pattern. Values of ion current for other points in upper hemisphere (full directional pattern) were found by smooth interpolation of angular distributions of current for equatorial and meridional planes.

As a second method of measuring of directional pattern we used mica targets which absorb the particles ejecting from the discharge area. Four mica plates (150x25 mm) are located in equatorial and meridional planes above the discharge area so that they form two arcs intersecting at the right angle. Each arc approximately corresponds to a spherical sector with radius of 150 mm. Such a location of the targets allows us to estimate the full directional pattern by interpolating with a good reliability.

Thickness of the deposited film was assumed to be proportional to the absorption coefficient of the deposited film. We find this thickness as a logarithm of intensity of transmitted light. Increase of mass of all 4 mica targets accounts for 9 mg. for 30000 shots. Comparison of the directional patterns obtained by the two methods is at Fig. 4. We see that the curves are qualitatively similar which means that the obtained directional patterns and values of full ion charge are reliable enough.

The full charge of ion component and total mass loss allows to calculate ion efficiency, i.e. a share of ions in the whole bunch, and to compare it with the corresponding theoretical estimations.

These patterns demonstrate significant difference in ion current and value of deposited material depending on the azimuth angle. These values abruptly decrease in meridional plane at angles more than ten degrees from the normal.

Optically visible part of the plasma plume in meridional plane tends to converge, whereas in equatorial plane the plume expands. The comparison of this ion patterns with deposit mass distribution on thin mica plates show, that ascattering of charge in equatorial direction is more wide then angular mass dispersion. This is a consequence of more strong scattering of light charged ions (H^+) then more massive molecules. Experimental results of three materials in study collected in Table 1.

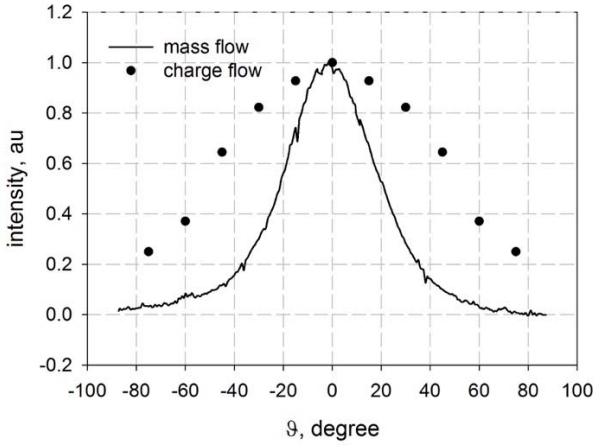

Fig.3 – Angular pattern of plasma bunch, calculated from ion current (dots) and from sediment mass flow (line) for a ceramic barium titanium.

.	Mass consum-ption, μg	Mass consumption, 10^{17}atoms	Thrust pulse, μN*s	Energy of bunch, mJ	Kinetic energy, mJ	charge, μC
Teflon	1,3	0,47	4,7	66	8,5	45
Polyethylene	0,27	0,35	1,8	34	6	35
PMMA	0,46	0,41	1,6	35	5,6	31

We considered that the layer of almost quasi-neutral plasma formed over the surface of the dielectric during the high-voltage phase of breakdown is heated by the Joule heat of a high-current discharge. In these conditions, the dependence of the temperature of this layer on time was calculated by solving the problem of thermal interaction between the plasma and the dielectric. Solving the one-dimensional heat conduction equation in the plasma and the dielectric, we used data of the experimental waveforms as an internal heat source in the plasma. The problem was solved for polyethylene and KCl. The results of calculations for polyethylene are shown in Fig. 4.

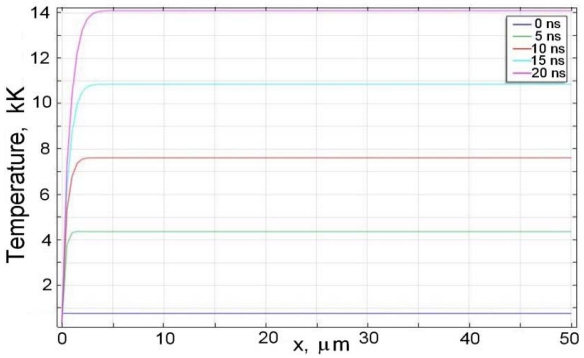

Fig. 4 – Temperature distribution in the plasma of ethylene. X=0 corresponds to the plasma-polyethylene boundary

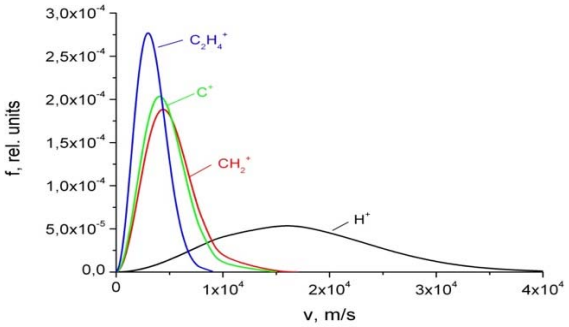

Fig. 5 – The Maxwell velocity distribution of the main ions of the plasma

The calculated Maxwell velocity distributions of the main plasma ions corresponding to a temperature of 14000 K are shown in Figure 5:

It is seen that the average thermal velocities of the main plasma components are in the range of 10^3-10^4 m/s. Hydrogen ions have the highest values, their speed can reach 4×10^4 m/s. The lowest values correspond to ethylene ions, their velocities do not exceed the range of ~10^3 m/s.

Similar calculations were made for all the compounds used. Therefore, the velocities of fast ions ~10^5 m/s observed in the experiments are most likely to be due to the additional influence of electrostatic acceleration, which is to be taken into account in studies /4/ of flashover on liquids in porous ceramic.

Acknowledgements. This work was supported by the Russian Foundation for Basic Research (project 18-08-00185).

References

1.**Burton R.L., Turchi P.J**. Pulsed Plasma Thruster//Journal of propulsion and power, 14 (1998),716 -735.

2. **Punanov I.F., Morozov P.A., Emlin R.V., Cholakh S.O.** Measurement of ion concentration in plasma bunches of nanosecond vacuum surface flashover at 140 kV//Pulsed Power Conference (PPC), May 31 2015-June 4 2015, Austin, TX, USA,IEEE 2015.

3. Морозов П. А., Пунанов И. Ф., Емлин Р. В., Смирнов А. С. Измерение заряда ионной компоненты плазмы, генерируемой наносекундным поверхностным разрядом по поверхности диэлектрика//Известия вузов. Физика, 59(2016), № 9/3.С.106 -110.

4**. Morozov P.A., EmlinR.V., Punanov I.F.** Plasmageneration by a pulsed nanosecond discharge on a surface of porous dielectric saturated with liquid//Pulsed Power Conference (PPC IEEE), June 18 – June 23, 2017, Brighton, England, IEEE 2017.

RECENT RESULTS ON APPLICATION OF NEW TYPES OF LOW PRESSURE GAS DISCHARGES INVESTIGATED AT MEPHI

V. Kurnaev, A. Kaziev

National Research Nuclear University MEPhI
Kashirskoe shosse 31, 115409, Moscow, Russian Federation, kurnaev@plasma.mephi.ru

Different types of low-pressure discharges are now under investigation at Plasma Physics Department and Laboratory of Plasma Surface Interactions and Plasma Technology of MEPhI. The main purpose of our activity is not only to clarify the new type of discharges but also to test these discharges for technological application.

Plasma beam discharge facility with magnetic field was used for detailed characterization of unstable processes occurring during plasma interaction with targets covered with self-sustainable thin dielectric films. A new type of self-oscillation secondary electron discharge SOSED was found. SOSED uses only DC power supplies, but combines the properties of discharges with constant, HF and frequency-pulsed power supply, which extend its practical use as compared to conventional beam-plasma discharges.

This discharge demonstrates possibility of oscillations generation in a broad range of parameters (up to 75 kV (Fig. 1) in amplitude and in 10–100 MHz frequency range).

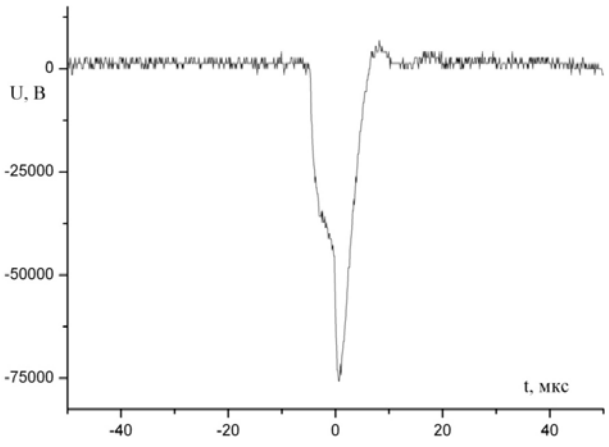

Fig. 1 – High voltage pulse in SOSED at outer circuit inductance L = 180mG

The efficiency of energy transfer from inductance to ion component of plasma is ~ 90%, and ~ 80% of source of negative biasing transforms to ion energy. This effect can be the base for self-oscillatory method of immersion implantation.

Using water-cooled metal resonator, the high current HF self-oscillating discharge with helicon self-oscillation without external source of HF power and antenna is realized.

Plasma beam discharge without magnetic field was also applied for soft etching of carbon based nanostructures and generation of centers of high emissivity.

Some other technological gas discharge devices are shown in Fig. 2a–d.

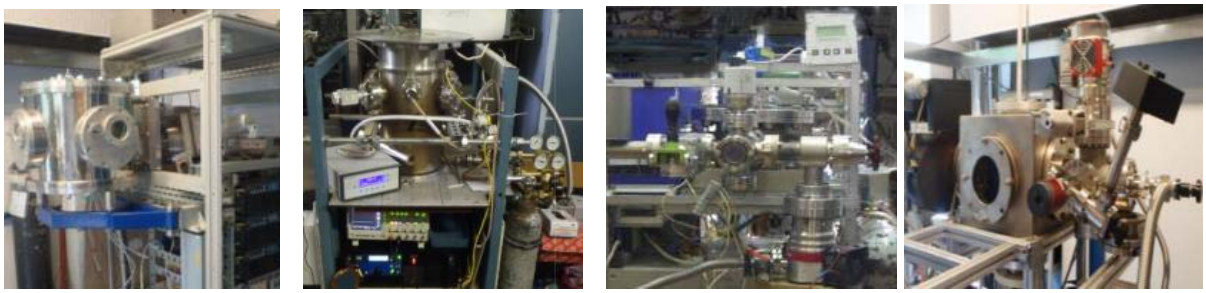

a) b) c) d)

Fig. 2 – Different MEPhI installations with magnetron, anomalous glow and ICP discharges

Despite the wide application of magnetron sputtering systems, in this area there are problems of improving the quality of films and the efficiency of the process of their creation. For this reason, various modifications of the magnetron sputtering technology, differing in the methods of discharge power supply, magnetic field configurations, ion deposition assisted deposition techniques, etc., are being actively developed today. Among these, the most prospective are high power pulsed magnetron discharges and hot target sputtering systems.

Recently /2–8/, the technology of high-rate coating deposition with a hot (liquid) target magnetron has been developed for a number of materials, including Cu, Cr, Si and others. The most prospective approach is to combine high-current impulse magnetron discharge with the hot target gasless sputtering/evaporation. It allows one to greatly enhance the deposition rate without compromising the film quality in comparison to conventional DC, pulsed DC, and HiPIMS regimes.

Some features of magnetron discharge with hot melted cathode are shown in Fig. 3 and Fig. 4. Zone I–IV in Fig. 3 demonstrates different modes of magnetron discharge operation. Zone I corresponds to sputtering of solid target with Ar ions, zone II is target melting, zone III – stabilization of current and voltage, IV is the self-sputtering mode with no working gas used.

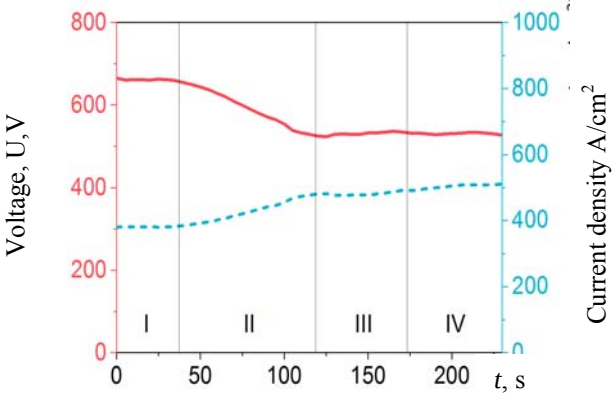

Fig. – 3 Change of magnetron discharge during target melting

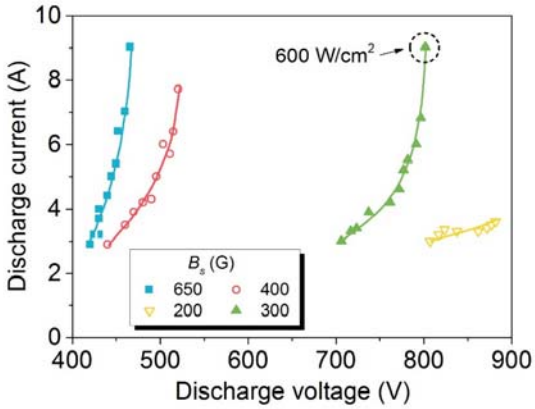

Fig. 4 – Magnetron discharge with liquid cathode parameters for different magnetic fields

The stable pulsed magnetron discharge with melted cathode in self-sputtering mode was realized by applying an additional pulsed voltage (~ 30 ms) to magnetron discharge with melted cathode in self-sputtering mode. The ionization coefficient of this new discharge type is $\alpha \sim 60\%$ at plasma density $n \sim 2\times10^{13}$ cm^{-3}.

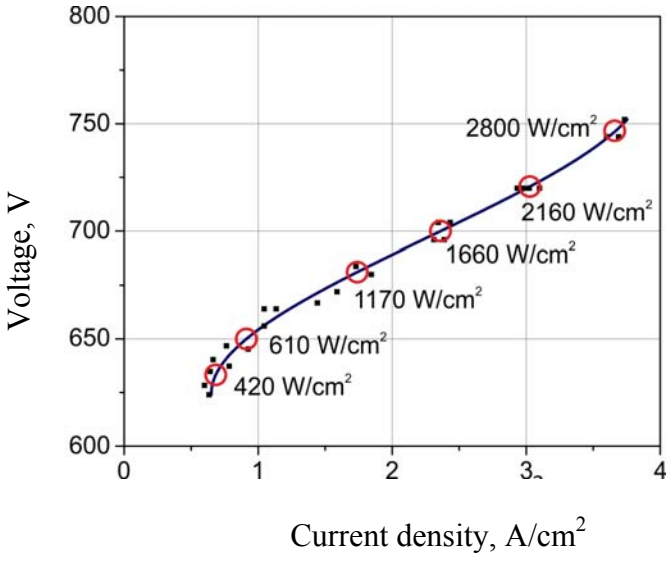

Fig. 5 – Characteristics of pulsed magnetron discharge with liquid cathode

Voltage–current characteristics (peak values measured at 500 μs after the beginning of high voltage pulse) for this discharge are shown in Fig. 5. Target melting stars at $q = 45$ W/cm^2, transition to self-sputtering mode occurs at $q = 70$ W/cm^2.

This new type of pulsed magnetron discharge with liquid cathode was found to give extra high deposition rates of different materials. For example, the deposition rate for Cu ~ 650 nm/min and 30 nm/min for Si that is approximately 30 times higher than that for conventional magnetrons with cold cathode.

Topical applications of high-quality deposition technologies being developed at MEPhI include: creation of protective films on fuel elements of nuclear reactors to prevent steam-Zr reaction in the concept of accident-tolerant fuel; creation of protective wear and corrosion-resistant coatings in automotive technologies; metallization of VLSI; creation of Si-based corrosion-resistant coatings; preparation of transparent thin oxide films (Al_2O_3, ZrO_2, ZnO, etc.) for laser optics; preparation of visible light filters (Al, Zr) on scintillators for X-ray detectors, and many others.

Different methods for plasma-surface modification with above mentioned discharges are being explored /9–11/. For example, the surface of titanium dental implants can be effectively engineered by inductively coupled plasma (ICP) to improve osseointegration time. Different types of surface topology can be prepared and controlled by varying irradiation regimes.

The anomalous glow discharge was used for nitriding of hidden cavities and inner surfaces of tubes.

The surface hardening of materials under low temperatures (without bulk degradation due to unwanted phase transitions) is effectively performed with plasma-immersion ion implantation (PI^3) nitriding technique with ion energies

up to 50 keV. This method ensures high depth of improved hardness combined with low process temperatures. For example, 70-μm nitride layer in VT-22 Ti alloy can be prepared with 25-keV ions after 3 h. This approach is a basis for duplex hardening technology when PI^3 nitriding is followed by magnetron deposition of TiN, and no bulk degradation of material occurs.

ICP discharge has also been used to produce nanostructured W-fuzz.

1. **Visgalov I.V.** Secondary electron instability at plasma surface interactions. Dr.Sci thesis MEPhI (2018).
2. **Tumarkin A. V., Kaziev A. V., Kharkov M. M., Kolodko D. V., Ilychev I. V., Khodachenko G. V.** Surface and Coatings Technology. 2016. Vol. 293. 42–47.
3. **Kaziev A. V., Tumarkin A. V., Leonova K. A., Kolodko D. V., Kharkov M. M., Ageychenkov D. G.** Vacuum. 2018. In press.
4. **Kaziev A. V., Kharkov M. M., Khodachenko G. V., Tumarkin A. V.** Surface and Coatings Technology. Vol. 293 (2016) 48–54.**Stepanova T. V., 5.**
5. **Kaziev A.** 4. **V., Atamanov M. V., Tumarkin A. V., Dolzhikova S. A., Izmailova N. Ph., Kharkov M. M., Berdnikova M. M., Mozgrin D. V., and Pisarev A. A.** Magnetron deposited TiN coatings for protection of Al-Cu-Ag-Mg-Mn alloy // Journal of Physics: Conference Series. Vol. 748 (2016) 012013.
6. **M., Kaziev A. V., Tumarkin A. V., Drobinin V. E., Stepanova T. V., and Pisarev A. A**. Journal of Physics: Conference Series.. Vol. 789 (2017) 012026.
7. **Kaziev A. V., Tumarkin A. V.** International Symposium on Innovation in Materials Processing, Phoenix Jeju, Korea, November 1–3, 2017. Book of abstracts. P. 15**.**
8. **Kaziev A. V., Tumarkin A. V.** International Symposium on Innovation in Materials Processing, Phoenix Jeju, Korea, November 1–3, 2017. Book of abstracts. P. 16
9. **Borisyuk Y.V., Oreshnikova N.M., Mozgrin D.V., Stepanova T.V., Pisarev A.A**., Journal of Physics: Conference Series, 747(1) (2016) 012019,
10. Stepanova T.V., Kaziev A.V., Atamanov M.V., Mozgrin D.V., Pisarev A.A., Journal of Physics: Conference Series, 748(1) (2016) 012013,
11. **Bernt D., Ponomarenko V., Pisarev A**. Journal of Physics: Conference Series, 748(1) (2016) 012006,

ROLE OF EXTERNAL FACTORS IN FORMATION AND DEVELOPMENT OF DIELECTRIC BARRIER SURFACE DISCHARGE IN AIR (recent experimental data)

M.V. Sokolova, V.V. Voevodin, Yu.I. Malachov

National Research University "Moscow Power Engineering Institute"
Krasnokazarmennaya 14, Moscow 111250 Russia,
mvsokolova@mail.ru

The aim of the present work was to analyze the type of the influence of different external factors on electric characteristics and on the structure of surface dielectric barrier discharge (SDBD) in air. The experimental data on the ignition voltages U_0 and dimensions of discharge area L of SDBD that can be found in publications for identical barriers differ much and it prevents their usage in modeling and calculations. For instance, interesting results given in /1,2/ are for a range of ε values but for different barrier materials, whereas the barrier thickness and other experimental conditions are not indicated. Influence of each of these properties separately on SDBD for equal other features is analyzed in present investigation. The dependence of discharge characteristics on such factors as the type of applied high voltage (impulse or sine, impulse form and front steepness and amplitude) and parameters of the dielectric barrier (its material, its thickness, value of dielectric constant ε) were analyzed in present work. The initial voltage U_0 of the discharge appearance, the discharge current I_d, its energy E and the discharge structure were measured for a single strip electrode 1-3 mm wide placed on one side of a dielectric plate 1-5 mm of thickness, while the grounded electrode 60 mm wide has been placed on its reverse side (Fig.1). All electrode edges except one side of the stressed electrode were covered by an epoxy layer.

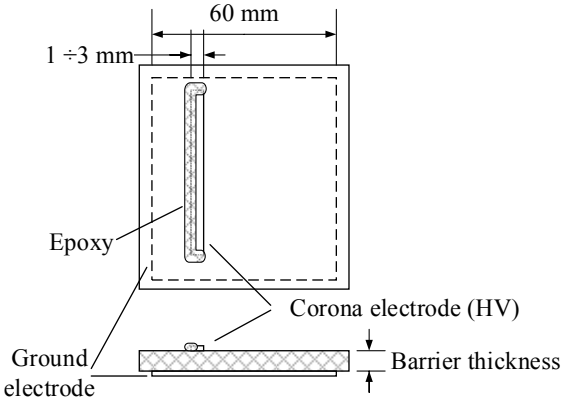

Fig. 1 - Electrode configuration

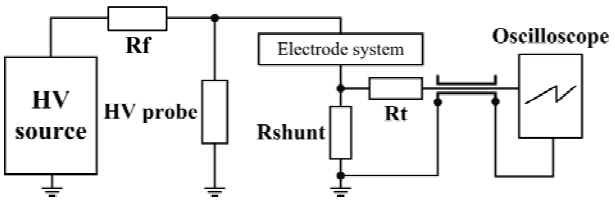

Fig. 2 - Electric circuit

The barrier material was of different kinds of ceramic (Alumina and ceramic on base of MgO with ε = 7- 35) and Plexiglas (ε =2.3). The experiments with single and periodic impulse high voltage (amplitude up to 9 kV, impulse duration 0.5 – 5 μs, impulse front steepness up to 100 V/ns and frequency 14 kHz) were carried on using specially developed high voltage impulse generator. A high voltage probe Tektronix 6015A, measuring resistance R_{sh} and current attenuator D2-31 were used to measure the form and amplitude of the applied voltage and the discharge current (Fig.2). The ignition voltage U_0 of the discharge was defined using the voltage, discharge current and light emission oscillograms for the moment of the current and light emission appearance. The discharge appearance in all cases corresponds to the impulse voltage front. The discrepancy of the measured U_0 values was (10-20)%.

A range of SDBD characteristics in air that were measured in our earlier experiments have been already presented in /3-4/. In the present work an additional recent data are given. All results shown below were achieved in accurately defined conditions. Single impulse voltage U_m = (6.0-8.0) kV (front steepness dU/dt = 70-80 V/ns, R_f = 500 Ohm) was used, barrier thickness was (0.9-1.6 mm) and ε = 2.3 – 35 (ceramic on base of MgO). Measured mean values of U_0 are given in Fig. 3.

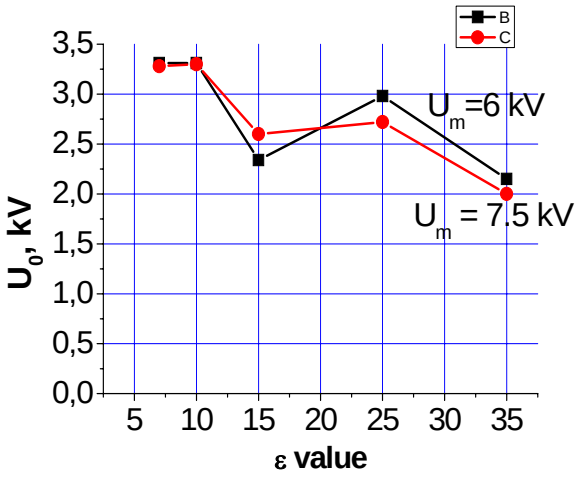

Fig. 3 - Dependence of mean values of U_0 on barrier permittivity ε value

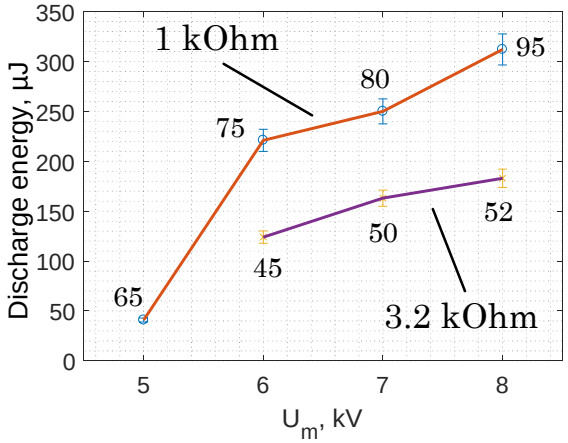

Fig. 4 - Dependence of consumed electrical energy on impulse periodic voltage amplitude U_m

The steepness of the voltage impulse front is known to have an influence on the form of the discharge current impulse form. In Fig. 4 the measured discharge energy E as a function of voltage impulse amplitude U_m is presented for different steepness of voltage impulse front τ_{imp} and two values of R_f. Corresponding steepness values for each amplitude U_m are inscribed in the figure. It is well known that the discharge current in case of a sine voltage consists of a range of pulses of microdischarge currents. Under impulse voltage with nanosecond front duration there is mostly seen a single current impulse

which includes all individual microdischarge current pulses. The present measurements have shown that with the front steepness of the impulse voltage curve less approximately 50 V/ns there appears a set of current pulses instead of a single pulse for the same other conditions. In Fig.5 u(t) and i(t) oscillograms for two values of front steepness of voltage impulse are given for U_m = 6 kV and Alumina ceramic barrier. The result provides a possibility to compare the time of microdischarge formation with the rise time of the applied voltage.

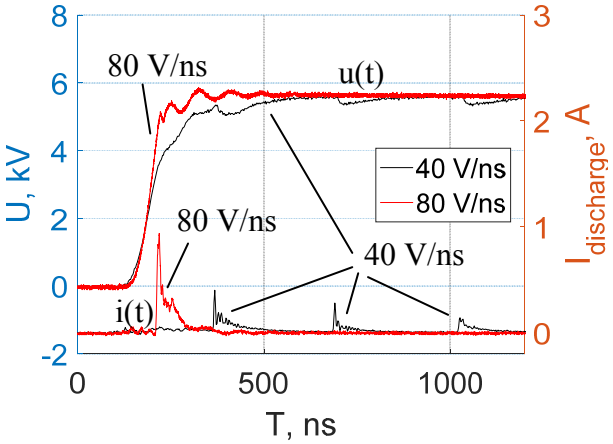

Fig. 5 - Typical oscillogram of the SD currents for different voltage steepness

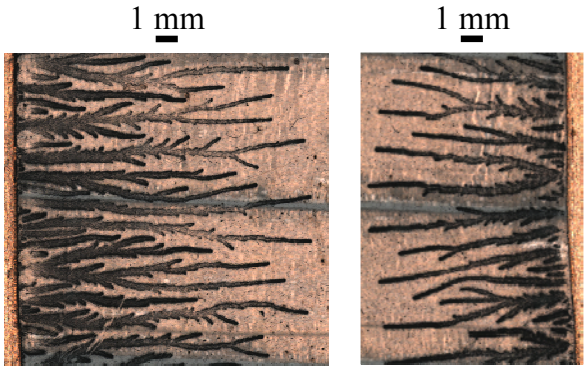

Fig. 6 - Dust figures on Plexiglas barrier for different voltage steepness: 70 V/ns (A) and 40 V/ns (B)

The main attention in present work was paid to the influence of the dielectric barrier characteristics on the structure of the discharge. The experiments with single and periodic impulse high voltage (amplitude up to 9 kV, impulse duration 0.5-5 μs, impulse front steepness up to 100 V/ns and frequency 14 kHz) indicate that the surface discharge structure visualized using different experimental methods, such as photo and dust figure technique, strongly depends on all the above mentioned factors. Dust figures of the charge left on the Plexiglas barrier surface (0.9 mm of thickness) after the discharge under voltage impulse (U_m= +6 kV) with different front steepness are given in Fig.6 and show more powerful and more developed branches of microdischarge channels in case of higher steepness of the voltage impulse front for the same all other conditions. In fig.7 surface discharge images made by Nikon d5200 camera are given for periodic impulse voltage with U_m = +6 kV, f=14 kHz and different voltage steepness dU/dt = 40 and 70 V/ns.

In Fig.8 dust figures of charge left on the barrier surface after the discharge for different ε values of the barrier material and identical all other conditions are presented and demonstrate strong influence of the barrier properties on the discharge characteristics.

Special measurements have shown, that the state of dielectric barrier surface and mostly the possible presence of surface charges can drastically

change the U_0 measured values and the discharge structure. Special attention in the work was paid to get the barrier surface clean from charges, humidity and toner powder that was used to develop the discharge structure.

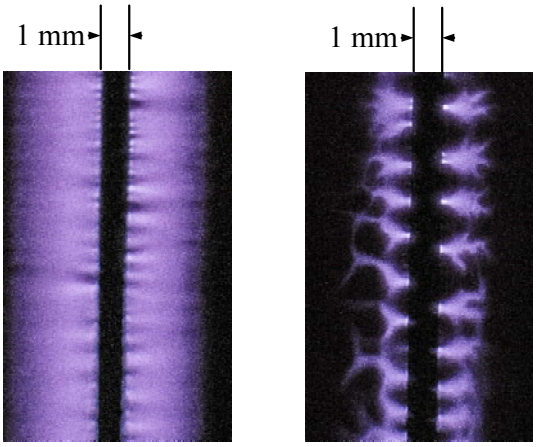

Fig. 7 - SD images for different voltage front steepness: 70 V/ns (A) and 40 V/ns (B)

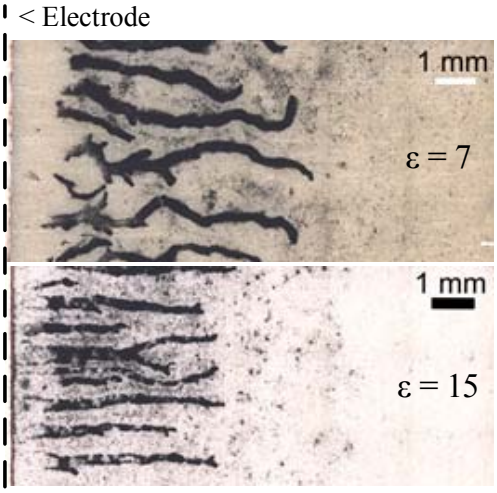

Fig. 8 - Dust figures for different ε values of the barrier material

Conclusions.

The experiments with single and periodic impulse high voltage (amplitude up to 9 kV, impulse duration 0.5 – 5 μs, impulse front steepness up to 100 V/ns and frequency 14 kHz) indicate that the surface discharge electric characteristics especially the U_0 values, and the discharge structure visualized using different experimental methods, strongly depend on wide range of factors, which must be known if the experimental results are used in modeling. The most important influencing factors besides the applied voltage form are the barrier properties and the "memory effect" of the charge left on the barrier surface after previous discharges.

Acknowledgements. Most results of the work were achieved with the financial support of RFBR of Russian Academia of Science (grant 15-08-04384).

References

1. **V.I. Gibalov, G.J. Pietsch,** J. Phys. D: Appl. Phys. 33, 2618 (2000).
2. **V.V. Voevodin, et al.** Russian Electrical Engineering, 88, No. 8, 524 (2017).
3. **M.V. Sokolova, et al.** Book of Contributions of International Conference "The Physics of Low Temperature Plasma" (PLTP-2017), Kazan, Russia, 2017.
4. **M.V. Sokolova, et al.** Book of Contributions of 7th Central European Symposium on Plasma Chemistry, Sveti Martin na Muri, Croatia, 2017.

FEATURES OF THE ACOUSTOPLASMA OPERATING MODE OF GAS DISCHARGE DEVICES

A. Abrahamyan

Institute of Applied Problems of Physics, NAS RA, 25 Hr. Nersisyan str.,
0014, Yerevan, Armenia, E-mail: arbel11@mail.ru

The propagation of an acoustic signal in a tube with a plasma leads to an acoustoplasma interaction. The discharge tube is also an acoustic resonator. Acoustoplasma interaction forms complex superlattices of parameters in the plasma, which can significantly change the parameters of the plasma medium itself. Such environment academician of NAS RA A.R. Mkrtchyan has been proposed to be called an acoustoplasma /1, 2/.

Only gas-discharge plasma with modulated or direct current will be considered below. By modulated current we mean a discharge current containing a direct and a variable component. The ratio of the amplitude of the variable component to the value of the direct component will be called the modulation depth.

The modulation of the discharge current leads to the modulation of the heat release and the pulse simultaneously along the entire axis of the discharge, which results in the appearance of an acoustic wave in a direction that is orthogonal to the axis of the discharge tube. But such a wave in a gas can notexist, it goes into a spiral wave and then breaks down into spiral and longitudinal waves. If the modulation frequency of the current is lower than the frequency of the existence of the spiral waves, then only the longitudinal waves are excited/3/.

Acoustoplasma, as well as plasma without acoustic disturbance, is a self-consistent medium and with the help of control parameters it is possible to control almost all the parameters of the acoustoplasma. Control parameters include gas pressure, frequency and depth of modulation, the magnitude and shape of the variable component of the discharge current.

Figure 1 shows the various processes in the acoustoplasma, the control of which was carried out in our laboratory. Practically for each of the elements of Fig. 1 there is at least one publication. According to the results of the researches by the laboratory staff from 2005 to 2014, 7 Ph.D. dissertations were defended.

A multichannel apparatus for recording measurement results with a record was developed, which allows one to carry out a real experiment once. And then by recording, repeatedly, in a virtual environment, explore the parameters and processes of interest to us.

Methods for processing the results of measurements, which made it possible to process large databases of experimental data were developed. To obtain directly from the experimental data differentials and integrals of the investigated quantities, to obtain, by means of approximations, analytic expressions. Methods for using the theory of catastrophes and for solving incorrectly posed inverse problems in acoustoplasma studies were also developed /4/.

All this set of works allowed us to obtain definite results for all the elements of Fig. Since we conducted the study, in the future the term "management" will be replaced by the term "change".

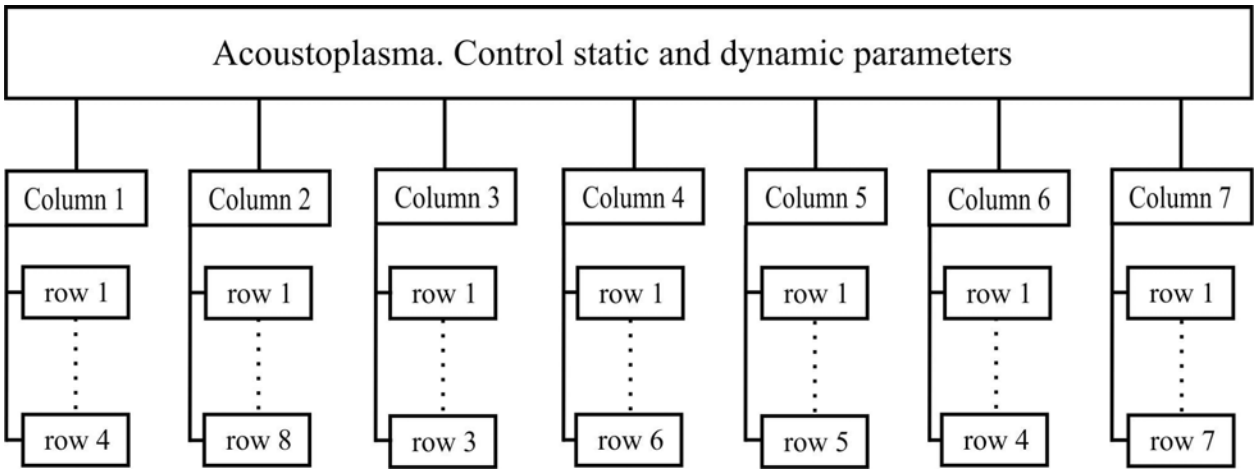

Column 1-change of acoustic parameters in the acoustoplasma medium; row 1-amplification of sound; 2-attenuation; 3-generation; 4-change the speed of sound; Column 2-change of electrical parameters; row 1-direct component of voltage; 2-alternate component of voltage; 3-alternate component of current; 4-phase shift between voltage and current; 5-resistance and conductivity; 6-distribution of charges in space; 7-distribution charges in time; 8-change in time RCL parameters of an equivalent circuit modeling the discharge; Column 3-change of optical parameters; row 1-integrated brightness; 2-change of spectrum lines and bands; 3-generation of strong spectrum lines; Column 4-change of thermodynamic parameters and phase transitions; row 1-temperature; 2-thermodynamic phase transition; 3-non thermodynamic phase transition; 4-speed control of the plasma components; 5-control of acoustic streaming; 6-memory relaxation; Column 5-change in energy parameters; row 1-efficiency; 2-energyinvestigation; 3-energy capacity; 4-luminous efficiency of light sources; 5-stabilization and variation of lasers and light sources; Column 6-change of geometric parameters (sizes and trajectories); row 1-changing the trajectory of discharges; 2-changing of contraction; 3-acoustic turbulence; 4-stop soliton; Column 7-implementation of new types of devices and processes based on acoustoplasma; row 1-development and manufacture of measuring equipment and modernization of the existing one; 2-power sources for acoustoplasma devices; 3-acoustoplasma light sources; 4-acoustoplasma lasers; 5-acoustoplasma magnetrons; 6-acoustoplasma accelerators; 7-acoustoplasma controlling in plasma chemistry.

Fig.1 - Parameters and processes in the acoustoplasma studied in the laboratory

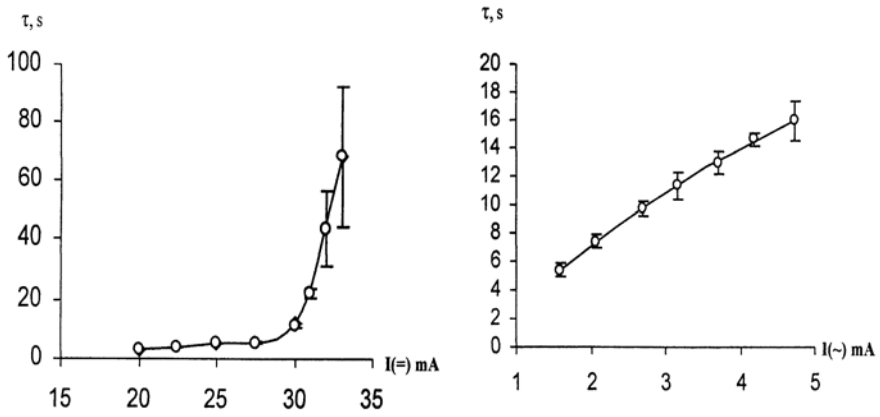

Fig.2 - The dependence of τ: a) on the constant component of the discharge current I_0; P_0 = 200torr; I (~) = 3 mA; b) the variable component of the discharge current I (~) P_0 = 200torr; I_0 = 30 mA

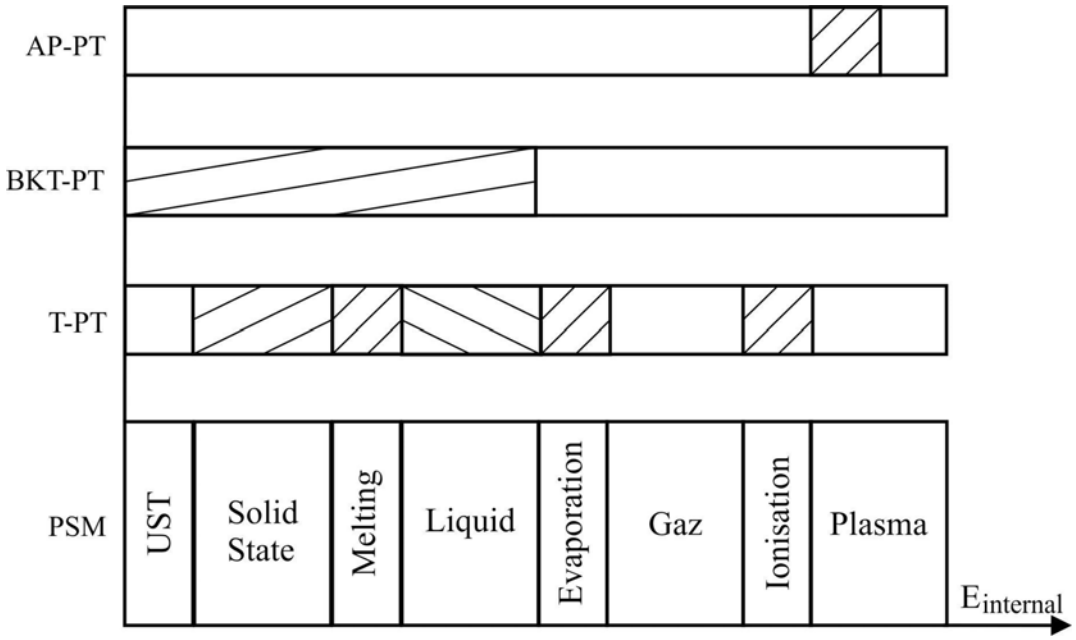

Fig.3 - Diagram of phase transitions. The regions of existence of phase transitions are shaded as slanting lines

Each of the rectangles in Fig. 1 contains a rather large amount of information. For example, in Column 3 row 3, the effect of acoustoplasma memory is obtained.

Fig. 2 shows the dependence of the relaxation time τ of the argon acoustoplasma to the plasma state without an acoustic perturbation after switching off the variable component of the discharge current.

Fig. 3 shows diagrams of phase transitions (PT) for different cases. The abscissa represents the values of the internal energy of the substance in relative units. On the ordinate axis: PSM - the phase state of the substance in the standard representation (UST- ultra small temperatures); T-PT - thermodynamic phase transitions; (Berezisky-Kosterlitz-Thouless phase transitions) /4/ - BKT-PT - topological phase transitions (Nobel Prize in 2016); AP-PT - acoustoplasma phase transitions /5/.

Acknowledgements.I thank A.R. Mkrtchyan for posing many problems, assistance and direct participation in experiments, for a detailed discussion of the results. In part, all of the above studies were financed by Republican grants of Armenia, in part by the Armenia-Belarus grant (2011), in a small share by ISTC A-196 grant.

References

1. **Galechyan G.A., Mkrtchyan A.R.**Acoustoplasma, Yerevan, Apaga, (2005), 338p. (inrus.).
2. **Mkrtchyan A.R., Mkrtchyan A.H., Abrahamyan A.S**. VII Int. Conf., Plasma Physics and Plasma Technology, PPPT-7, Minsk, Belarus, 17-21 Sept. (2012), Proc., v.1, 3-5.
3. **Skudrzyk E.** The Foundation of Acoustic. Basic Mathematics and Basic Acoustics. N.Y., (1971).
4. **Kosterlitz J.M., Thouless D.J**. J. Phys. C, 6(1973), 1181.
5. **Abrahamyan A.S., ChilingaryanR.Yu., Sahakyan K.G**. VII Int. Conf.Plasma Physics and Plasma Technology, PPPT-7, Minsk, Belarus, 17-21 Sept.(2012), Proc., v.1, 197-199.

CALCULATION OF THE ELECTROSTATIC FIELD OF THE CORONA DISCHARGE DURING THE POWDER COATING PROCESS

M. Fazlyyyakhmatov, N. Kashapov

Kazan Federal University, 18 Kremlyovskaya str., Kazan 420008, Russian Federation,
e-mail: mfazlyjy@kpfu.ru

Methods of plasma coating in an electrostatic field have the advantages of easy regulation, possible automation, high efficiency, uniform coating thickness, low substrate wall thickness, and various possible substrate materials /1/.

The object of the study is the process of charging a polydisperse powder-gas mixture in the electrostatic field of the corona discharge.

In the coating process, the powder particles enter the corona discharge region, where ionization of the air by electrons takes place (corona case). Free ions are deposited on the powder particles and impart the charge to them. Powder particles are acted upon by aerodynamic force, electrostatic force and gravity. Under the action of these forces, the powder particles are moved and deposited on a grounded surface (outer corona discharge region). The general equation of motion for the particles can be written as /2/:

$$\frac{\partial u_p}{\partial t} = F_d(u - u_p) + F_g + F_e, \qquad \frac{\partial x}{\partial t} = u_p, \tag{1}$$

where $F_d(u - u_p)$ is the drag force, F_g is the gravity force, F_e is the electric force, u_p is the particle velocity (disperse phase), u is the air velocity (gas phase). The electric force on a charged particle can be given by /3/:

$$F_e = q_p E + \frac{q_P^2}{16\pi\varepsilon a^2}, \tag{2}$$

where $q_P E$ is the Coulomb force and $\frac{q_P^2}{16\pi\varepsilon a^2}$ is the image force. q_P is the particle charge and a is the spacing between the particle and the target.

The image force gives a significant contribution to the electric force only when particles are near the target.

It is usually assumed that the particles are approximately spherical /4/. The typical value for the average particle diameter is from 30 to 40 μm.

To estimate the charge acquired by the spherical particle, Kaptsov /5/ used the Pauthenier and Moreau-Hanot model. According to this model, the limiting charge acquired by the particle is estimated as:

$$q_m = 4\pi\varepsilon_0\left(1 + 2\frac{\varepsilon - 1}{\varepsilon - 2}\right)r^2 E, \tag{3}$$

where E is the electric field strength at the point of particle charging, r is the particle radius, ε is the dielectric constant of the particle.

According to this estimate, the maximum specific space charge is in the range from -1×10^{-3} to -2×10^{-3} C/kg.

The main assumption when calculating the characteristics of the corona discharge is the neglect of the processes occurring in the corona discharge case. Because the corona cover has a small size compared to the outer region.

When calculating the outer corona discharge region, the processes are regarded as stationary and continuous in space.

The system of equations describing the distribution of the field strength and space charge in the outer region of the corona discharge:

$$\begin{gathered} div\bar{E} = \frac{\rho}{\varepsilon_0}, \\ div\bar{j} = 0, \\ \bar{j} = \rho b\bar{E} - \bar{D}grad\,\rho, \\ \bar{E} = -grad\,\varphi, \end{gathered} \tag{4}$$

where $\bar{E}$ is the electric field strength vector, φ is the electric potential, $\bar{j}$ is the current density vector, ρ is the space charge density, b is the ion mobility, $\bar{D}$ is the electric displacement vector.

In the presence of space charges, equation 1 of the system (4) is transformed into the Poisson equation:

$$\Delta\varphi = -\frac{\rho}{\varepsilon_0}. \tag{5}$$

If there are no space charges, equation 1 of the system (4) is transformed into the Laplace equation:

$$\Delta\varphi = 0. \tag{6}$$

To solve the system of equations, the following boundary conditions are given:

1. The potential of the corona electrode is equal to the applied voltage;
2. The potential of a grounded plate is zero;
3. The electric field strength at the surface of the corona electrode is equal to the initial intensity E_0 and does not depend on the intensity of the corona discharge.

For coating, we used a spray gun "START-50" (Fig. 1). Air and powder particles flow through the annular shaped exit 3 of a 15 mm diameter ring. Further, the air-powder mixture moves along the surface of the deflector 2, which is a tubular cylindrical body with a diameter of 5 mm, ending with a flat circular disc of 25 mm in diameter. The thin needle, called the corona electrode 1, is installed in the center of the disk to charge the powder particles.

We solved the two-dimensional task of the distribution of the electrostatic

field in a rectangular area 50×100 cm between the corona electrode and a grounded plate 50 cm long and 25 mm thick. The plate is located at a distance of 25 cm from the corona electrode.

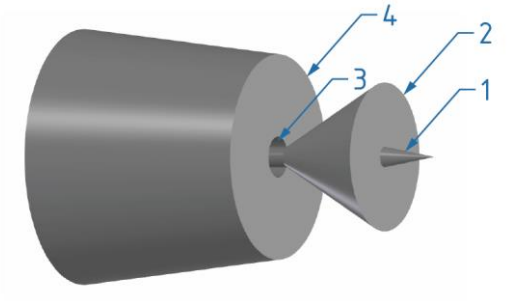

Fig. 1 – The corona spray gun: 1 is corona electrode, 2 is spray nozzle (deflector), 3 is annular shaped exit, 4 is sprayer channel

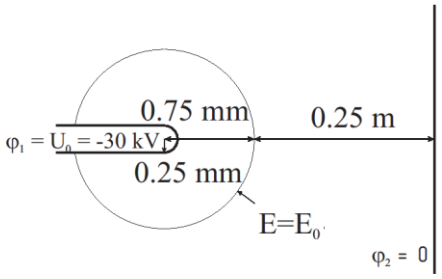

Fig. 2 – Scheme of the calculation area with the assumptions and the boundary conditions

In the model, we used the following boundary conditions:

1. The corona electrode potential $\varphi_1 = -30$ кВ;
2. The grounded plate potential $\varphi_2 = 0$ кВ;
3. The electric field strength at the surface of the corona electrode is equal to the initial intensity E_0.

The assumptions made in the model:

1. The corona electrode is represented by a hemispherical rod with a diameter of 0.5 mm (Fig. 2);

2. The ionization region (corona discharge) where the powder particles are charged is considered to be a spherical region at the end of the rod, with a radius three times the radius of the corona electrode. This assumption was based on photographs of the glowing area of the corona electrode.

Fig. 3 shows the simulation results. The region of high potential of the space charge field with a maximum value of –30 kV is located close to the corona electrode; hence, an ellipsoidal shape of the electric field lines around the electrode is formed.

Fig. 3a shows the distribution of the electrostatic potential in the absence of space charges, Fig. 3b in the presence of space charges. It is seen that the presence of charged particles in the flow region changes the electric field. The effect of space charge is to increase the field near the plate and reduce it near the corona discharge region.

It should be noted that the effect of reverse ionization, which does not adversely affect the quality of the coating, was not considered in this model.

Fig. 4 shows the distribution of the electrostatic potential along the axis of the corona electrode to the surface of the plate.

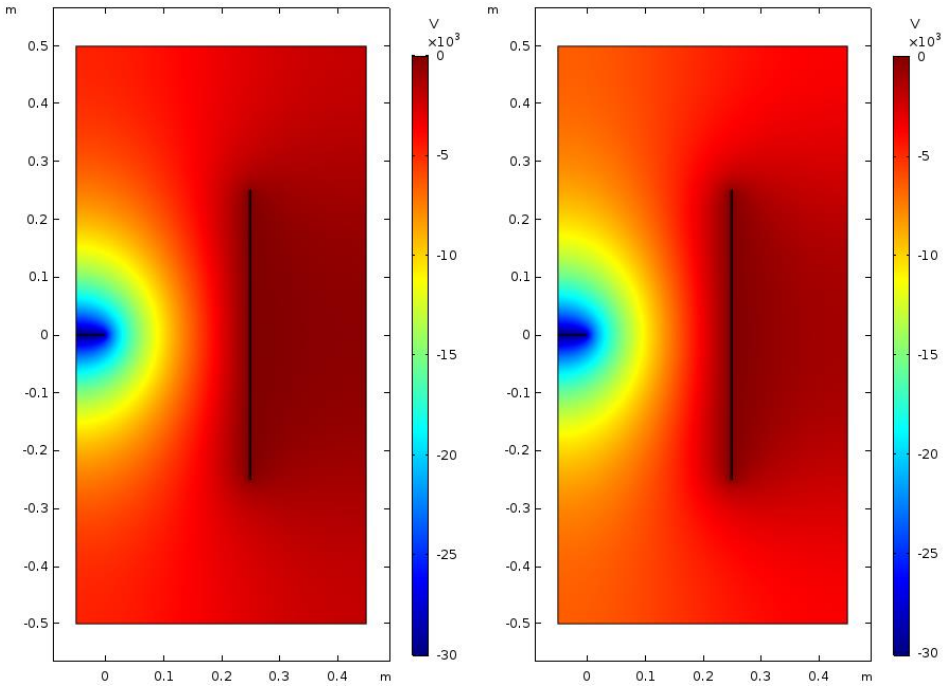

Fig. 3 – Distribution of electrostatic potential: a) absence of space charges, b) presence of space charges

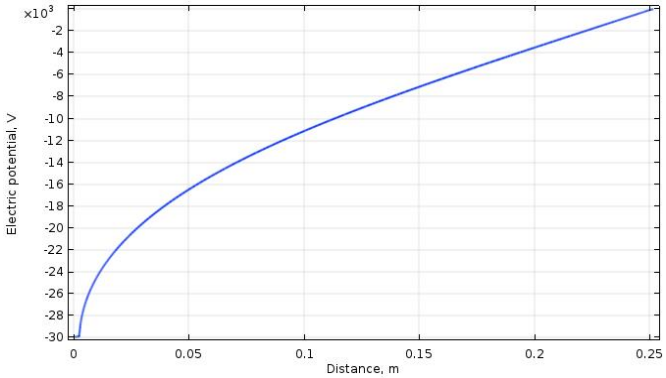

Fig. 4 – Distribution of the electrostatic potential along the axis of the corona electrode

References

1. **Fazlyyyakhmatov M.G., Kashapov N.F.** High Temperature Material Processes, 18(4) (2014) 257–263.
2. **Ye Q., Domnick J.** Powder Technology, 135–136 (2003) 250–260.
3. **Ye Q., Steigleder T., Scheibe A., Domnick J.** Journal of Electrostatics, 54 (2002) 189–205.
4. **Bailey, A.G.** Journal of Electrostatics, 45(2) (1998) 85–120.
5. **Kaptsov N.A.** Corona Discharge and its Application in the electrofilters. Moscow: State-Publishing House of Technical and Theoretical Literature (1947).

STUDY OF ADDITIONAL HEATING OF HELIUM ARC PLASMA AT ATMOSPHERIC PRESSURE BY MILLISECOND-LONG ELECTRIC CURRENT IMPULSE

V. F. Chinnov, D. I. Kavyrshin, M. A. Sargsyan, A. V. Efimov

Joint Institute for High Temperatures of the Russian Academy of Sciences (JIHT RAS)
125412, Izhorskaya st. 13 Bd.2,Moscow, Russia, dimakav@rambler.ru

The need for impulse heating of helium arc plasma at atmospheric pressure to reach electron temperatures above 3.5 eV rises from high transport coefficients of the plasma. Helium thermal conductivity grows rapidly as its temperature increases making it necessary to input more energy to plasma in order to heat it further. Stationary operation of plasmatron at such high load is impossible due to its materials not being able to withstand the heat stress and eroding quickly. The problem of heating the gas with a current pulse when the energy stored in capacitors is discharged rises from the fact that only a small fraction of the energy stored in the capacitors is expended on heating the arc plasma /1/ because the resistance of the external circuit starts to exceed the resistance of the discharge gap, at the resistance of the discharge gap drops as the current in it increases. In order to consider plasma heating as quasistationary, the time of the heating pulse should exceed the characteristic times of establishment of the stationary states for electron heating, stepwise excitation, and ionization of the plasma. Due to high mobility of electrons, their temperature T_e practically "tracks" the current changes in the arc: the electronic subsystem is in thermal quasiequilibrium with the energy flow supplied to the arc. However, equilibrium establishment times in the atomic and ionic subsystems in the range of 3÷4 eV (which is the region of interest to us) exceed by several orders of magnitude establishment time of T_e. The greatest among these times are the times of the first and second ionization. Performed estimations of these times have shown that in order to accomplish the experimental task it will be sufficient to provide electric pulse with duration of about 1 ms with an energy of 1÷2 kJ.

Specific impulse problems were associated with the occurrence of a "double arc" when a breakdown occurred outside the plasma torch channel. At the same time, the voltage on the arc dropped sharply, and the arc itself was not blown through the nozzle into the expanding channel of the plasma torch, and after the pulse passed the discharge did not return to the initial stationary state (it broke off and got extinguished). This problem was solved by spraying the insulating layer of aluminum oxide on the cathode and the nozzle (so that the discharge wouldn’t be able to form anywhere but in the discharge channel).

Thus, the most important technical task of the project was to find the optimal pulse conditions that would ensure the necessary "heating" of the electronic component and avoid electro-and gas-dynamic "disruption" of the discharge. To generate the pulse, a power supply was used, which consists of 20 capacitors 100 μF each connected in parallel. The source made it possible to apply voltage pulses up to 5 kV to the discharge gap. By varying the parameters of pulsed power supply, the geometry of the plasma torch, the flow regime of gas, etc., we were able to achieve stable arc operation with pulse current amplitude up to 2.5 kA and obtain a nearly bell-shaped pulse shape with a width of 1-2 ms /2/. The impulse is superimposed on a stationary burning helium arc with current strength of 200 A. In this experiment, it was possible to effectively control only the source current. It completely determines the arc burning mode and all its properties, and knowing the dependence of the thermal conductivity and electrical conductivity on temperature, and also the temperature dependence on the supplied power, it is possible to estimate all the main characteristics of the discharge within the “channel model” /3/ as a function of the arc current.

The arc zone at a distance of 1 mm from the tip of a tungsten cathode was observed by the methods of optical emission spectroscopy in the wavelength range 200-1100 nm, the observation was carried out through a quartz glass viewing window in the wall of the plasma torch nozzle. The spectrum was recorded using instruments with high-spatial (30-50 μm) and temporal (5-50 μs) resolution: the DFS-452 spectrograph whith the Andor iStar low-exposition ICCD camera at the output. The entrance slit of the DFS-452 spectrograph was set to be narrow and was, as a rule, 20-25 μm, at a pixel size of 25 μm. As a result, the instrumental response function of the system was $\delta_{app} \approx 0.3$ Å, which made it possible to resolve the contours of helium lines, the characteristic widths of which in the investigated mode are of the order of 1 Å and more.

Arc current and voltage measurements were made using the Tektronix TPS-2014B oscilloscope in combination with the Rogowski coil and a shunt with known and temperature-independent resistance, the obtained oscillogram of the arc current is shown in Fig. 1. Temporal variations of the plasma parameters during the pulse are also shown in this figure: the triangles show the relative emission intensities of the atomic and ion spectral lines and the curve shows electron temperature T_e determined using these lines by the relative intensity method /4/. As a result of superimposing a current pulse in 2000A, when the capacitor bank was charged to 1 kV, it was possible to heat the plasma by 0.7 eV, from 3.0 to 3.7 eV.

The contours of atomic helium He I lines are formed mainly due to the quadratic Stark effect, the broadening constants for which is well known /5/. This allowed us to determine from the basis of the entire set of He I lines observed in the experiment the time dependences of the electron density n_e

during the pulse in the near-cathode region. In the stationary arc burning mode at $T_e \approx 3$ eV, the measured n_e was close to the equilibrium value and amounted to $n_e \approx 9 \cdot 10^{16}$ cm^{-3}, but during the pulse it reached $n_e \approx 15 \cdot 10^{16}$ cm^{-3}, which is 1.5 times higher than the calculated equilibrium value, that indicates a jump in pressure in the arc during the pulse. We note that n_e reaches its maximum at atmospheric pressure at $T_e \approx 2.2$ eV and, with further heating, falls due to isobaric expansion.

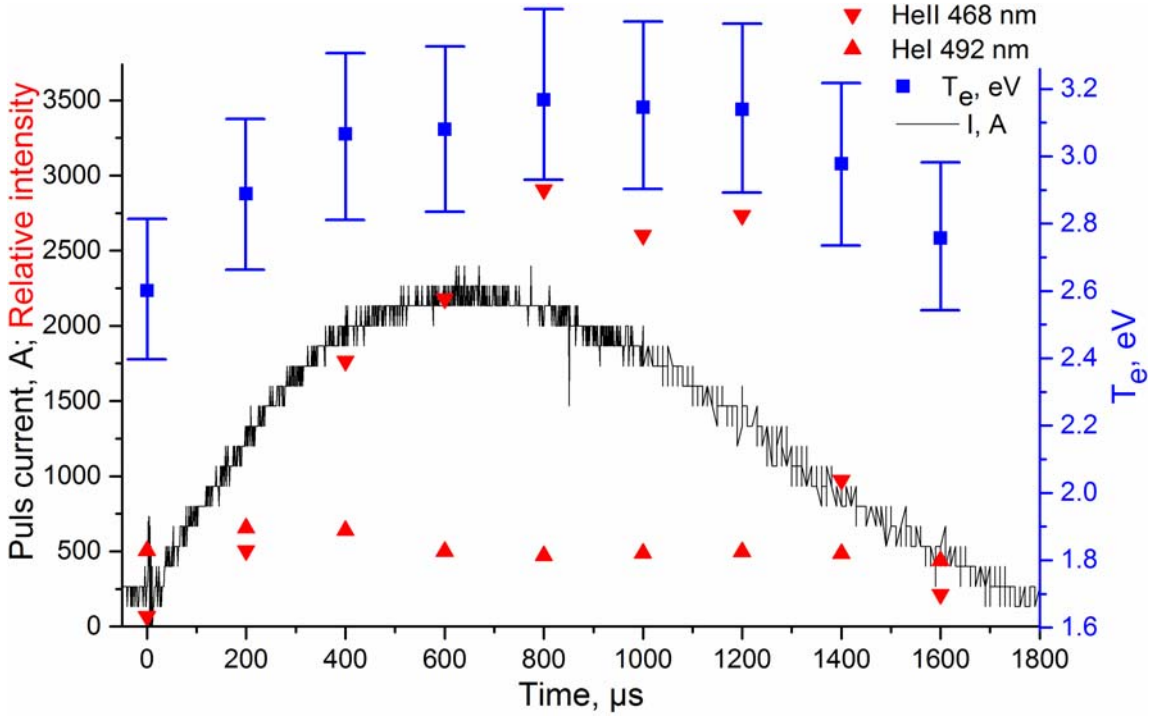

Fig. 1 – Changes in the characteristics of the discharge and plasma during pulse heating of the stationary arc plasma with a current of 200 A

In order to answer the question about which processes are the most important for the plasma object under investigation, we wrote balance equations for the energy (1) and electrons (2) in the arc:

$$\frac{d}{d\tau}\left(\frac{3}{2}n_e k T_e\right) = Ej(T) - \frac{2}{3}\frac{n_e \bar{v}_i \bar{\lambda}_i I}{r^2}\left(1+\frac{T_e}{T_g}\right) - \frac{2m_e}{M}\nu_{ei} n_e \frac{3}{2}k\left(T_e - T_g\right) - Q_{rad} \quad (1)$$

$$\frac{dn_e}{d\tau} = n_1 n_e \beta - n_e^2 n^+ \alpha - 5.8 D_a \frac{n^+}{r^2} \quad (2)$$

where τ is the time, E is the electric field strength, j is the current density, $\bar{v}$ is the average velocity of the thermal motion of the diffusing fraction, $\bar{\lambda}$ is the mean free path, I is the ionization potential of helium, T_g is the gas temperature (the temperature of the heavy particles), m_e is the mass of the electron, M is the mass of the gas atom, ν_{ei} is the electron-ion collision frequency, k is the Boltzmann constant, n_1 is the concentration of atoms, n^+ is the ion concentration,

β is the ionization constant, α is the recombination constant, and D_a is the ambipolar diffusion coefficient. The first term on the right-hand side of equation (1) describes the power supplied by the electric field to the arc and is of the order of ~ 10^6 W/cm^3. Then follows the processes of energy utilization: diffusion losses ~ 10^5 W/cm^3, elastic losses ~10^6 W/cm^3 and radiant losses Q_{rad} ~10^4 W/cm^3. Thus, the bulk of the energy supplied is expended in elastic processes, the contribution of radiation is insignificant. It is important to note that the experimentally determined value of the derivative ~ 10^5 W/cm^3 on the left-hand side of equation (1) is small in comparison with the principal terms on the right-hand side, which is a confirmation of the quasistationary nature of the heating process. Knowing all the terms of the energy balance equation, one can estimate the difference between the electron temperature and the gas temperature during the pulse. It turned out to be approximately equal to 6000 K, which is less than 20% of the absolute value of temperature, from which it can be concluded that the plasma under investigation is close to isothermal.

On the right-hand side of the electron balance equation (2) there are the following terms: the ionization rate by electron impact is ~ 10^{22} 1/cm^{3}s, the rate of three-body recombination is ~ 10^{21} 1/cm^{3}s, the rate of ambipolar diffusion of charges to the channel wall of the plasma torch is ~ 10^{22} 1/cm^{3}s. Thus, under the conditions of this experiment, the ionization process is balanced by a process of ambipolar diffusion, but not by recombination. Aligning the time of ionization τ_i and ambipolar diffusion τ_D, we obtain $\tau_i = 1/n_e \beta \approx \tau_D = r^2/5.8D_a \approx 100$ μs, which is more than an order of magnitude shorter than the pulse time, which again confirms the quasistationary condition of plasma heating.

Acknowledgements. The reported study was funded by the Russian Foundation for Basic Research according to research project № 18-32-00292.

References

1. **Korytchenko K.V., Dovbnya A.N., Volkolupov Yu.Ya., Kosoj A.I., Shkirida S.M. and Chertishchev I.A.** Technical Physics, ISSN 1063-7842. Volume 53, Issue 4 (2008) 415–423. doi: 10.1134/S106378420804004X
2. **Chinnov V.F., Kavyrshin D.I., Ageev A.G., Korshunov O.V., Sargsyan M.A. and Efimov A.V.** Journal of Physics: Conference Series, 774 (2016) 012200 doi:10.1088/1742-6596/774/1/012200
3. **Raizer Yu.P** Gas Discharge Physics. Brelin: Springer-Verlag (1991).
4. **Lochte-Holtgreven W., Ed**. Plasma Diagnostics. Amsterdam: Elsevier (1968).
5. **Konjevic N. and Wiese W.** J. Phys. Chem. Ref. Data., Volume 19, Issue 6 (1990) 1307-1385.

NUMERICAL INVESTIGATION OF PARAMETRS AND ELECTRON HEATING IN DUAL FREQUENCY DIELECTRIC BARRIER DISCHARGE AT ATMOSPHERIC PRESSURE

A. Saifutdinova[1], A. Saifutdinov[2,3], B. Timerkaev[1]

[1]A.N.Tupolev Kazan National Research technical university, K.Marx str., 10, 420008, Kazan, Russia, aliya_2007@list.ru
[2]Kazan Federal University, Kremlevskaya str., 18, 420111, Kazan, Russia,
[3]St. Petersburg State University, Universitetskaya nab., 7-9, 199034, St. Petersburg, Russia, as.uav@bk.ru

1. Introduction

Despite the long history of studies of gas-discharge plasma, in recent years there has been a new surge in the intensive research of its characteristics and the search of ways to control them in order to achieve the optimum properties used in practice. This is due to the fact that the gas-discharge plasma has found a wide range of applications at pressures on the order of atmospheric, which allows us to abandon the use of vacuum technology. Typically, for this purpose, discharges initiated AC voltage applied to the electrodes in a different frequency range. However, in practice it is difficult to achieve independent control and optimization of plasma parameters, initiating it with a single-frequency power supply.

Recently, many scientific groups have begun exploring potential for applications of dual frequency discharge plasmas to mitigate the fore mentioned problems /1-4/. Among which, as an effective method to generate and optimize CAP, the dual radio-frequency (RF) driven dielectric barrier discharge (DBD) with two independent power excitation sources has attracted rapidly growing attention by enabling independent control of plasma parameters and optimization of the discharge for various applications based on the nonlinear frequency coupling effect. However, applications based studies still lack the depth in the theoretical understanding of such discharges which would enable users to alter process parameters in the system to deterministically tailor the resulting plasma parameters. This is largely because the physical and chemical properties critically depend on the dynamics of power dissipation and electron heating mechanisms, whereby the plasma parameters are highly susceptible and influenced primarily by instabilities, mode transitions and associated electron heating variations in the plasma bulk and sheath. It is therefore necessary to gain insight into the electron heating mechanisms in such atmospheric pressure DBD system to bridge the gap in theoretical understanding for specific and targeted application-focused studies.

The role of frequency coupling in the dynamics of plasma ionization and associated mode transitions of atmospheric pressure DBD system are investigated in this work by numerical one-dimensional fluid simulation model.

2. Numerical simulation

The governing equations include the continuity equation of electrons, ions, and neutrals using the drift-diffusion approximation, Poisson's equation and the conservation of electron energy. A detailed description of the set of equations and associated conditions as utilized in this work can be found in work and the references of it.

In this work, a DBD system is considered whereby the plasma is generated between two planar parallel electrodes, and each electrode is covered by an insulating material layer with dielectric constant $\varepsilon = 4$. The distance between two insulating layers is fixed at d = 1 mm. One electrode is grounded, and the other has an applied dual frequency sinusoidal voltage excitation of $V = V_L \cos(2\pi f_L t) + V_H \cos(2\pi f_H t)$. Here, V is the applied voltage signal, V_L, V_H, f_L and f_H are the voltage amplitudes and frequencies of the low and high frequency components respectively. According to previous work from various groups involving dual frequency systems /5/, it is found that dual frequency systems with parameters $f_L / f_H < 0.1$ allows for easier observation of the synergistic coupling effect resulting from the dual applied frequencies. Hence we applied similar operational conditions in our work with a low frequency component of $f_L = 1$ MHz and a high frequency component of f_H = 10 MHz. In this work, we set the total peak voltage at a constant value of V_{total} = 1500 V, and varied the low frequency amplitudes from 100 to 1400 V to study its effect on mode transition and associated electron heating mechanisms. The working gas employed in this work is pure argon which comprises the most elementary of plasma chemistry dynamics, including five species - neutral argon (Ar), three effective excited atomic levels: metastable Ar^m, resonant Ar^r and effective excited Ar^*; two effective excimer levels Ar_2^* and Ar_2^{**} and three kinds of positive ions Ar^+, Ar_2^+ and Ar_3^+ and electrons (e^-). The details of the transport coefficients and chemical reactions can be found in /6/.

3. Results and discussion.

Fig. 1 shows the time averaged electron density (n_e) in the plasma bulk, time and space averaged electron power absorption ($j_e \cdot E$) as a function of the applied low frequency voltage amplitude. From the figure we can see the time averaged total electron production rate has a mild decrement through the variation of the low frequency voltage ratio (V_L =100–700 V and 1000-1400 V), and mild increment through the variation of the low frequency voltage ratio (V_L=700–1000 V).

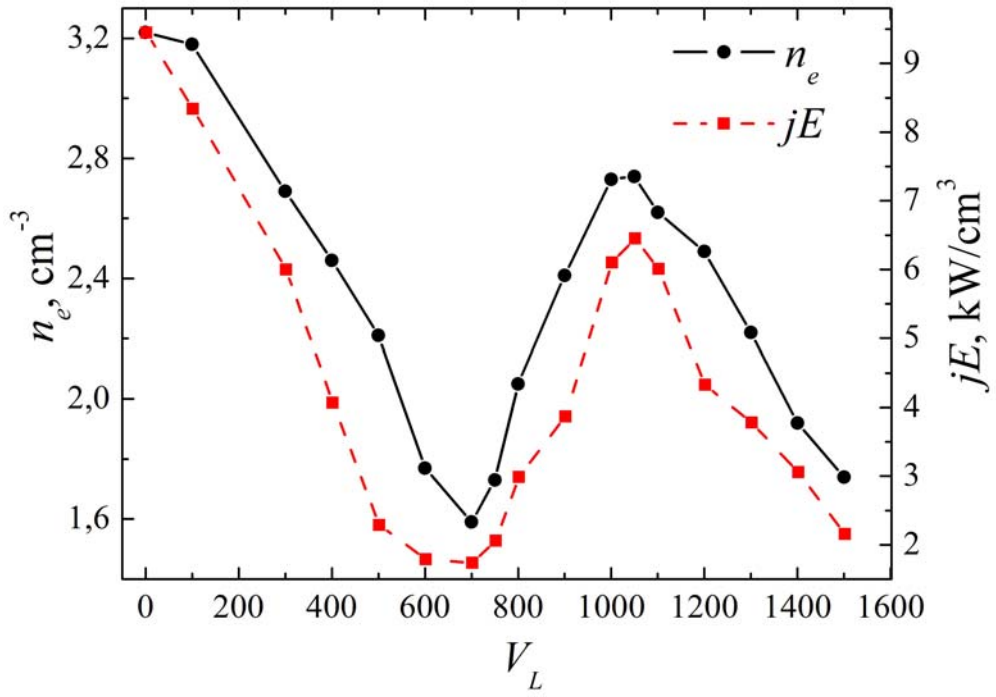

Fig. 1 – Plot of the time averaged electron density (n_e) in the plasma bulk, time and space averaged electron power absorption ($j_e \cdot E$) as a function of the applied low frequency voltage amplitude

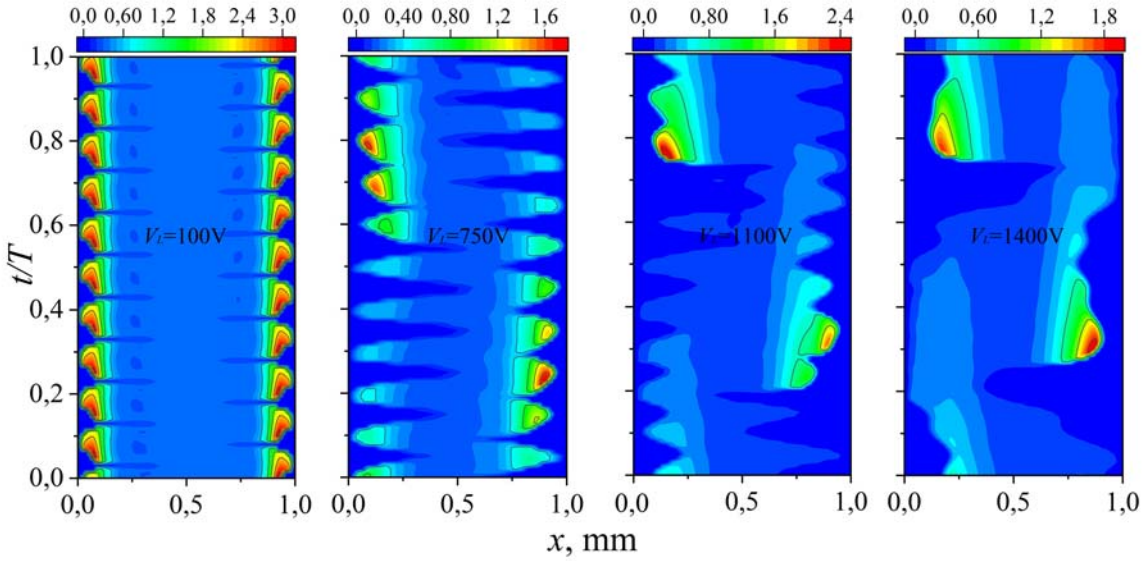

Fig. 2 – Spatio-temporal profiles of electron density with varied low frequency component in the applied voltage ratio in an Ar based atmospheric pressure dual-frequency DBD system

In other words, at a value of 1000 V there is a maximum of the time averaged electron density. Meanwhile, as the contribution due to the low frequency

component in the discharge increases, the sheath motion exhibits faster oscillations. Fig. 2 shows spatio-temporal profiles of electron density with varied low frequency component in the applied voltage ratio in an Ar based atmospheric pressure dual-frequency DBD system.

4. Conclusions.

In summary, in this letter a 1D fluid model has been used to investigate the electron heating mechanisms in a dual frequency atmospheric pressure DBD. We set the total voltage as constant and varied the low frequency component ratio to show that the electrons are mainly heated by the high frequency component in the plasma bulk, and the low frequency component in the sheath due to the sheath motion when the discharge parameters is dominantly controlled by the low frequency component.

We therefore demonstrate potential for independent control of discharge parameters such as electron density and electron energy to a certain extent via non-linear synergistic effect between the two frequencies

Acknowledgements. This work was supported in part by the the Russian Foundation for Basic Research (project no. 18-31-00098 mol_a) and by Russian Federation Presidential Program for State Support of Young Candidates of Sciences (grant no. MK-539.2017.1).

References

1. **Waskoenig J. and Gans T.** Appl. Phys. Lett. **96**, 181501 (2010).
2. **O'Neill C., Waskoenig J., and Gans T**. Appl. Phys. Lett. 101, 154107 (2012).
3. **Yang A. J., Wang X. H., Liu D. X., Rong M. Z., and Kong M. G**. Phys. Plasma. 21, 073507 (2014).
4. **Liu D. X., Yang A. J., Wang X. H., Chen C., Rong M. Z., and Kong M. G.** J. Phys. D: Appl. Phys. 49 (2016).
5. **Boyle C., Ellingboe A. R., and Turner M. M.** J. Phys. D: Appl. Phys. 37, 697 (2004).
6. **Saifutdinov A. I., Saifutdinova A. A., and Timerkaev B. A.** Plasma Physics Reports, 44 (2018), 351–360.

NUMERICAL INVESTIGATION OF DIRECT CURRENT PLASMA TORCH WITH SELF-CONJUGATE HEATING OF ELECTRODES

A. Saifutdinov[1,2]

[1]Kazan Federal University, Kremlevskaya str., 18, 420008, Kazan, Russia,
[2]St. Petersburg State University, Universitetskaya nab., 7-9, 199034, St. Petersburg, Russia,
as.uav@bk.ru

1. Introduction

Plasma spraying, one of the most widely used industrial applications based on thermal plasmas, is commonly employed to provide coatings for protection of materials against wear, erosion, corrosion, and thermal loads /1-4/. Despite its versatility, the limited reproducibility of the processes is a major limitation for its wider application. A major factor for this limited reproducibility is the lack of understanding and control of the dynamics of the arc inside the spraying torch.

A long operation life of a plasma torch is directly related to that of its heavy-duty elements, in particular, electrodes. The thermal state of the surface and the magnitude and character of erosion of thermionic cathodes in high-current plasma torches determine their performance characteristics and working life. The interacting system of electrode and near-cathode plasma is a complicated object of investigation that is characterized by strong spatiotemporal inhomogeneity. Inhomogeneous temperature fields on the surface of thermionic cathodes can lead to the appearance of local overheated zones, evaporation of the cathode material, its cracking and fracture, and a number of other processes and phenomena determining the working life of cathodes.

For these reasons, spatiotemporal analysis of temperature fields on the surface of cathodes generating high-current electric arcs is a topical task. Numerous investigations have been devoted to determination and optimization of plasma torch characteristics. However, despite the considerable progress that has been made in modeling direct-current plasma torches /4–6/, the temperatures of the inner surfaces of plasma torch electrodes are still typically set to be constant and their inhomogeneous heating due to processes at the boundary of arc plasma is ignored.

The present work is devoted to numerical simulation of self-conjugate heat transfer between electrodes and an arc in a dc plasma torch.

2. Model

By applying axisymmetric conditions, the DC plasma torch is modeled as a 2D region. The model was based on the system of Navier–Stokes equations (including the equation of continuity, equations of motion, and equation of heat

transfer in the plasma jet) supplemented by the system of Maxwell equations for the electric and magnetic fields, the differential Ohm's law, and the equations of heat balance in a metal cathode and anode /7/:

$$\frac{\partial \rho}{\partial t} + \nabla\left(\rho \vec{V}\right) = 0, \tag{1}$$

$$\rho\left(\frac{\partial \vec{V}}{\partial t} + \vec{V}\cdot\nabla\vec{V}\right) = \vec{j}\times\vec{B} - \nabla\left[P + \frac{2}{3}\mu\left(\nabla\cdot\vec{V}\right)\right] + 2\nabla\cdot(\mu S), \tag{2}$$

$$\rho c_p\left(\frac{\partial T}{\partial t} + \vec{V}\cdot\nabla T\right) - \frac{dP}{dt} = \nabla\cdot(\lambda\cdot\nabla T) + \vec{j}\times\vec{E} + \frac{5k_B}{2e}\vec{j}\cdot\nabla T - Q_{rad}, \tag{3}$$

$$\nabla\cdot(\sigma\cdot\nabla\varphi) = 0, \quad \vec{E} = -\nabla\varphi, \quad \vec{j} = \sigma\vec{E}, \quad \nabla^2\vec{A} = -\mu_0\vec{j}, \quad \vec{B} = \nabla\times\vec{A}, \tag{4}$$

$$\rho_{c,a} c_{p\,c,a}\left(\frac{\partial T_{c,a}}{\partial t}\right) = \nabla\cdot\left(\lambda_{c,a}\cdot\nabla T_{c,a}\right). \tag{5}$$

Here, ρ, ρ_c, ρ_a are the densities of the gas and the cathode and anode materials, respectively; t is the time; $\vec{V}$ is the velocity vector; $\vec{B}$ is the magnetic-induction vector; P is the gas pressure; μ is the dynamic viscosity; c_p, $c_{p,c}$, $c_{p,a}$ are the heat capacities of the gas, cathode, and anode, respectively, at constant pressure; T, T_c, T_a are temperatures in the plasma channel, cathode, and anode, respectively; $\vec{E}$ is the electric-field strength; λ, λ_c, λ_a are the thermal conductivities of the gas and the cathode and anode materials, respectively; σ is the specific electric conductivity; φ is the electric potential; $\vec{A}$ is the vector potential of the magnetic field; μ_0 is the magnetic permittivity of vacuum; $\vec{j}$ is the total current density; k_B is the Boltzmann constant; e is the electron charge; and Q_{rad} is the temperature-dependent specific radiation power. The computational region consisted of three domains: cathode, anode, and plasma channel. Boundary conditions are presented in Table 1.

Table 1. Boundary conditions

Entrance of plasma channel	$T = T_0$, $\int_{\partial\Omega}\rho\left(\vec{V}\cdot\vec{n}\right)d_{bc}dS = m$, $\vec{j}\cdot\vec{n} = 0$, $\vec{A}\times\vec{n} = 0$;
Cathode working surface	$T = T_c$, $\vec{V} = 0$, $\vec{A}\times\vec{n} = 0$, (6);
Anode working surface	$T = T_3$, $\vec{V} = 0$, $\vec{A}\times\vec{n} = 0$, (7);
Outer boundaries of plasma channel	$\nabla T = 0$, $P = P_0$ $\vec{j}\cdot\vec{n} = 0$, $\vec{A}\times\vec{n} = 0$;
Outer boundaries of cathode and anode	$T = T_0$, $\int_{\partial\Omega}\vec{j}\cdot\vec{n}dS\Big\|_c = I_0$, $\varphi\big\|_a = 0$.

Let us consider in more detail the boundary conditions at interfaces between the arc plasma and electrodes /7/.

1. The boundary between the arc plasma and anode obeys the following condition /5/:

$$\left[-\left(\lambda_a \cdot \nabla T_a \cdot (-\vec{n})\right)\right]_{anode} - \left[-\left(\lambda \cdot \nabla T \cdot (-\vec{n})\right)\right]_{plasma} = \left| j \cdot \vec{n} \right| \phi_a - \varepsilon \sigma_B T^4, \quad (6)$$

which shows that the normal flux of heat to the anode includes components due to the heat conductance from plasma, electron bombardment, and cooling by radiation from a solid. Here, ϕ_a is the electron work function of a metal anode and σ_B is the Stephan– Boltzmann constant.

2. The normal discontinuity of heat flux at the boundary between arc plasma and cathode is described taking into account the heat transfer from the arc to the cathode, heating by ion flux, and cooling by thermoelectron emission and radiation from solid according to the Stephan–Boltzmann law:

$$\left[-\left(\lambda_c \cdot \nabla T_c \cdot (-\vec{n})\right)\right]_{cathode} - \left[-\left(\lambda \cdot \nabla T \cdot (-\vec{n})\right)\right]_{plasma} = j_i \varphi_i - j_e \phi_c - \varepsilon \sigma_B T^4, \quad (7)$$

Here, φ_i the ionization potential of the buffer gas, ϕ_c is the effective work function of the cathode material and j_i and j_e are the ion and electron currents, respectively, defined as

$$j_e = \begin{cases} j_r, & \left(\left|\vec{j} \cdot \vec{n}\right| - j_r\right) > 0 \\ \left|\vec{j} \cdot \vec{n}\right|, & \left(\left|\vec{j} \cdot \vec{n}\right| - j_r\right) < 0 \end{cases}, \quad j_i = \left|\vec{j} \cdot \vec{n}\right| - j_e, \quad j_r = A_r T^2 \exp\left(\frac{-e\varphi_e}{k_B T}\right), \quad (8)$$

where A_r is the Richardson–Dushman constant and φ_e is the effective work function of thermoelectron emission. Numerical experiments were performed with an F4 Metco dc plasma torch with tungsten cathode, copper anode, and argon as the working gas.

3. Results and discussion.

Fig. 1 presents the fields of temperature and plasma-jet velocity (in the arc-plasma channel and near the cathode and anode) at t = 1 s in a plasma torch for a plasma-forming gas-consumption rate of 2 g/s and arc-discharge current of 300 A. It can be seen that the gas temperature in the plasma channel reaches up to 25000 K and the working surface temperature of the tungsten cathode exceeds its melting point and reaches a level of about 4000 K, while the copper-anode surface temperature at the arc spot is slightly above 500 K. In concluding, we have formulated a model of a dc plasma torch with allowance for the self-consistent heating of electrodes.

4. Conclusions.

A DC plasma torch has been modeled and simulated by developing a 2D axisymmetric model of laminar flow and heat transfer coupled to electromagnetic fields. In order to solve the partial differential equations of electric currents and magnetic fields, both in the gas than in the anode region, we have contemplated appropriate boundary conditions in the modeling work.

Lorentz forces and Joule heating effects have been modeled, coupled to the physical model of the plasma torch and finally computed. The results of numerical model calculations showed for the first time that the temperature of the working cathode surface exceeds the melting temperature of cathode material (tungsten). The results can be used in investigations of the erosion of electrodes in modern plasma torches.

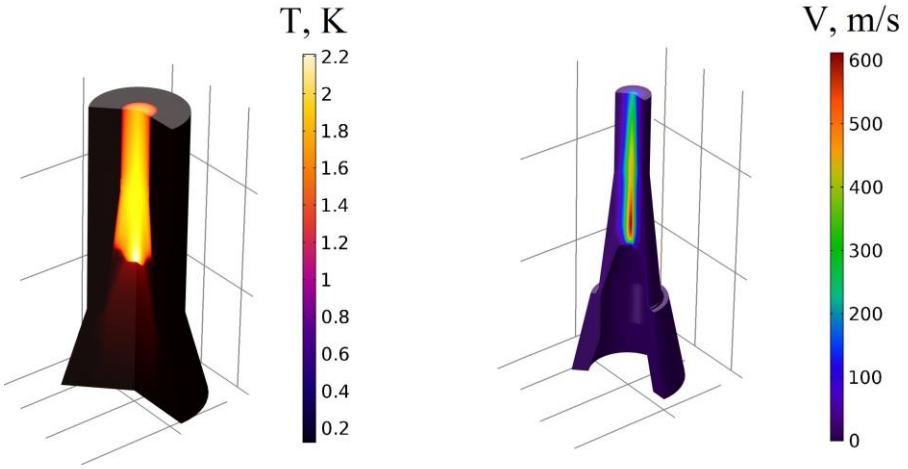

Fig. 1 – Distributions of temperature fields (left) and plasma-jet velocity (right) in plasma torch operating at an arc discharge current of 350 A

Acknowledgements. This work was supported in part by the Russian Foundation for Basic Research (project no. 16-38-60187_mol_a_dk).

References

1. **Zhukov M. F., et all.** Low-Temperature Plasma, Vol. 17: Electric Arc Thermal Plasma Generators (Nauka, Novosibirsk, 1999) [in Russian].
2. **I. A. Glebov and F. G. Rutberg,** *High Power Plasma Generators* (Energoatomizdat, Moscow, 1985) [in Russian].
3. **Frolov V. Ya., Ivanov D. V., and Shibaev M. A.** Tech. Phys. Lett. 40, 676 (2014).
4. **Chazelas C., Trelles J. P., Choquet I., and Vardelle A.**, Plasma Chem. Plasma Process. 37, 627 (2017).
5. **Ramachandran K., Kikukawa N., and Nishiyama H.** Thin Solid Films 435, 298 (2003).
6. **Trelles J. P., Chazelas C., Vardelle A., and Heberlein J. V. R.** J. Therm. Spray Technol. **18**, 728 (2009).
7. **Saifutdinov A. I., Timerkaev B. A., and Ibragimov A. R.** Technical Physics Letters, 2018, Vol. 44, No. 2, pp. 164–166

INFLUENCE OF A CONSTANT MAGNETIC FIELD ON THE UNIFORMITY OF PLASMA GENERATED BY PLANAR ICP SOURCE

A. Yasunas, D. Kotov

Belarusian State University of Informatics and Radioelectronics, P.Brovky 6, Minsk, 220013, Republic of Belarus, alex.yasunas@gmail.com

Inductively coupled plasma (ICP) sources are widely used in the technologies of plasma chemical etching and deposition for low-temperature high-density plasma generation at pressures of 0.05-10 Pa. It is possible to improve plasma treatment uniformity by simultaneous decrease in the operating pressure and increase in the surface being treated by means of ICP source's antenna system geometry, constant gas supply into plasma generation area, and also by means of an external constant magnetic field in a process reactor. In this work it is introduced a research of the influence of a constant magnetic field distribution in a plasma treatment process reactor on the basis of a flat ICP source 200 mm in diameter with a four-spiral helical antenna system, having a discharge gap 55 cm in length, on plasma concentration distribution; a magnetic trap configuration wherein plasma uniformity improves from ±37% to ±24% at a distance of 120 mm from a plasma source was determined.

As was shown in the work /1/ a constant magnetic field has an influence on the operating pressure and the ICP source's plasma concentration. To determine the influence of a constant magnetic field on the ICP source's plasma concentration distribution in a vacuum plant «UVN-630» a stand for measuring plasma concentration distribution over the ICP source's surface at different distances to a plasma source and different magnetic trap configurations was assembled. The measuring stand design is shown in Fig. 1. To measure plasma parameters a single cylindrical Langmuir probe with RF compensation of space charge oscillations was used, a detailed description of this measuring technique is introduced in the work /2/. The measuring probe was fixed on a scanning system, which ensured its movement parallel to the surface of plasma source antenna system. The distance from the plasma source surface to the probe cone scanning surface was: 120 mm, 75 mm and 25 mm, scanning amplitude – 115 mm from the source's axis. A negative bias of 30 V was applied to the probe, ion saturation current was recorded by a micro-ammeter.

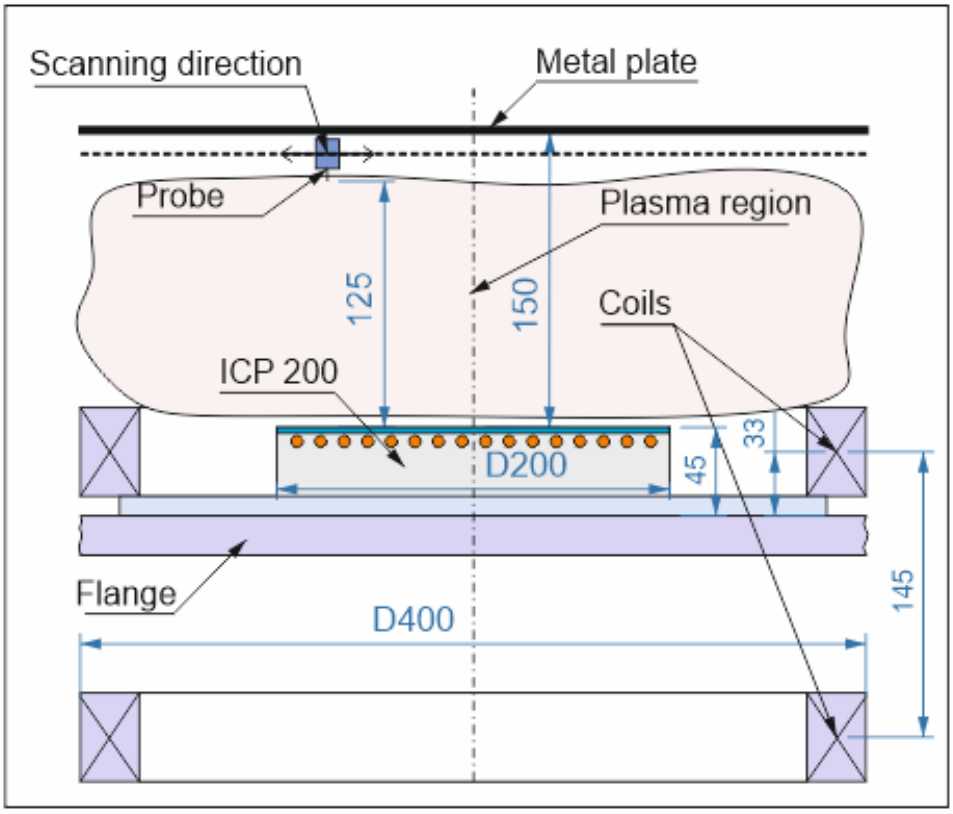

Fig. 1 – Allocation scheme of the devices in the chamber of the vacuum plant «UVN-630»

Fig. 2 represents distribution of ion saturation current on a measuring probe depending on the distance to the process reactor axis – the distance from the ICP source antenna system surface to the probe: 120 mm, 75 mm, 25 mm, pressure – 6 Pa, RF power – 600 W, solenoids are disabled. The graph was constructed from the central axis of the ion source.

All the graphs represent maximum ion saturation current, and, consequently, plasma concentration locates on the source's axis and falls to its edge, what is caused by the diffusion of charged particles from the plasma formation area as a result of their chaotic motion. In order to reduce this effect, it is possible to use magnetic traps of different configurations. In the considered case for the magnetic field formation two solenoids situated behind the ICP source were used (see Fig. 1). Such an arrangement was chosen due to the necessity to use the obtained results in a vacuum plant of the chosen type.

Magnetic field distribution was calculated by finite elements method with the help of program complex COMSOL Multiphysics. Fig. 3 represents a magnetic trap at the current of the lower solenoid equal to 1568 A×turns, and at the current of the upper solenoid - 700 A×turns. We can see an area with zero magnetic field induction on the source's axis, the distance of which from the antenna system surface will be used to describe a magnetic trap and indicated by

H (H=0 mm for this particular case). Table 1 represents main traps configurations where plasma concentration was measured.

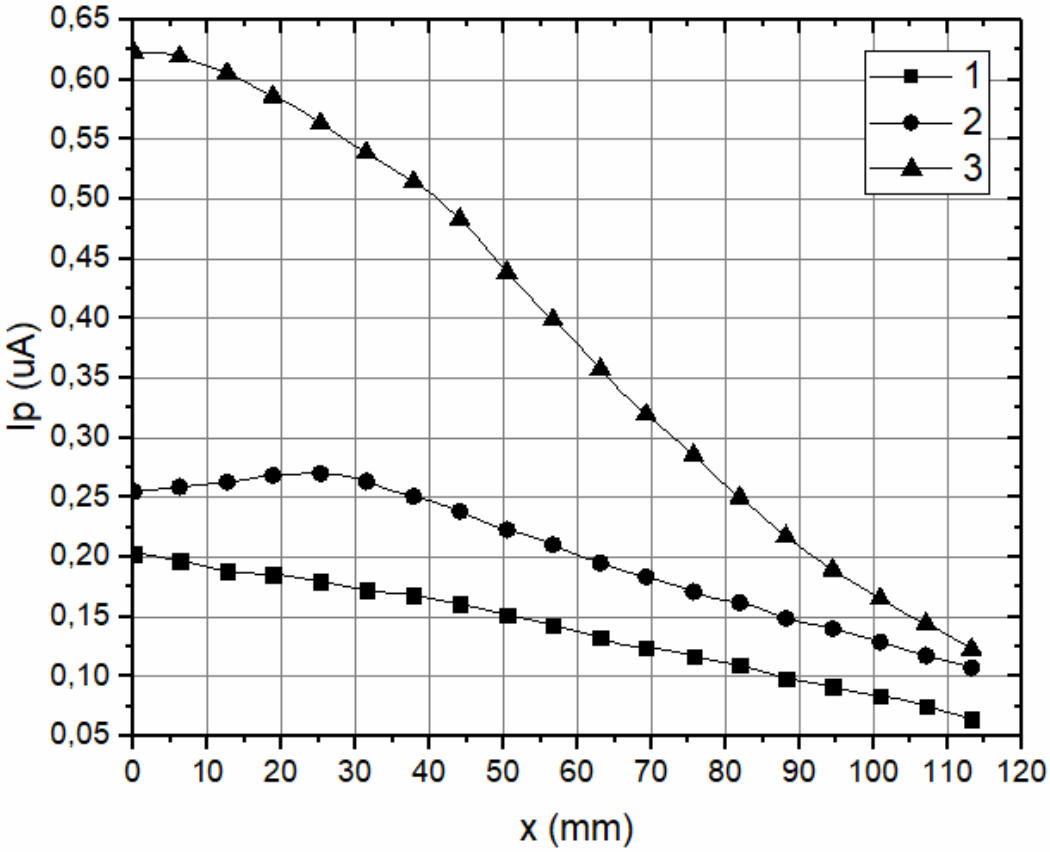

1 – 120 mm; 2 –75 mm; 3 –25 mm

Fig. 2 – Distribution of ion saturation current on a measuring probe for different distances from the ICP source antenna system surface to the probe

Table 1 – Experimental results

	Ion saturation current uniformity, ± %			Distance probe-plasma source, mm	Magnetic trap
№	D220	D200	D150		
1	43	37	24	120	without a magnetic field
2	30	26	14	75	without a magnetic field
3	56	48	26	25	without a magnetic field
4	70	61	34	120	B=0,1-0,3 mT; H = ∞ (2)
5	58	55	42	120	B=0,05-0,2 mT; H = 50 mm (5)
6	35	28	16	120	B=0,2-0,5 mT; H = 25 mm (6)
7	44	38	23	120	B=0,2-0,8 mT; H = -30 mm (11)
8	42	38	24	120	B=0,2-0,4 mT; H = 80-120 mm (12)
9	31	24	12	120	B=0,5-1,5 mT; H = 0 mm (21)

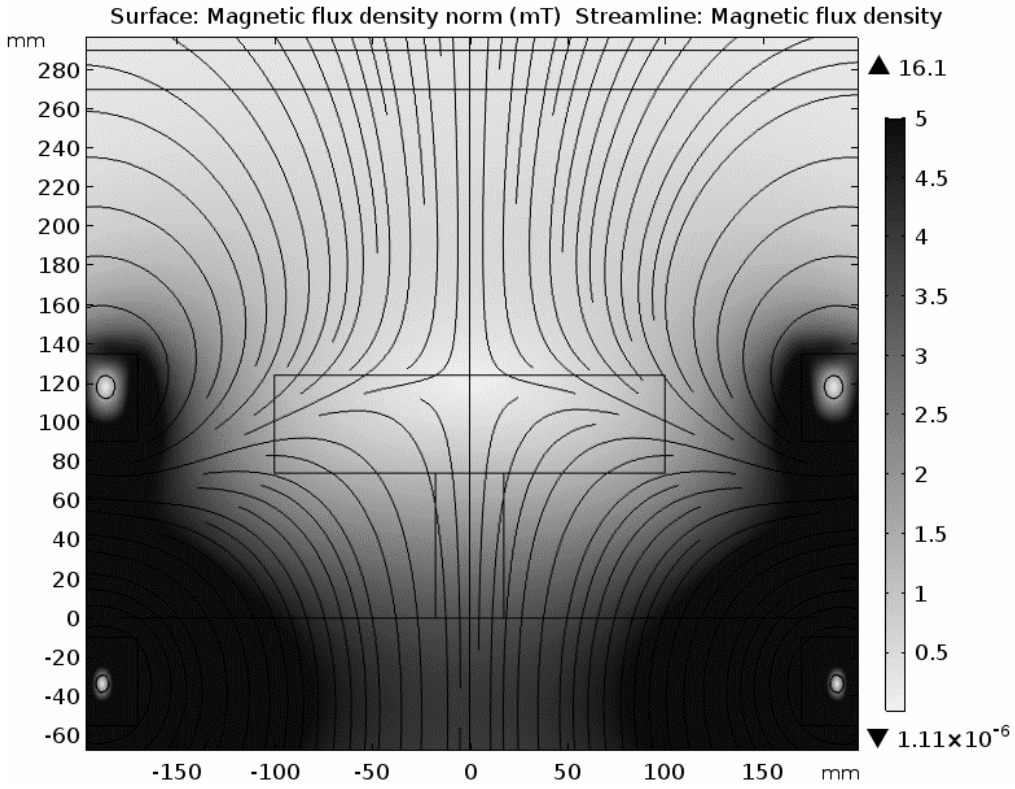

Fig. 3 – Magnetic field distribution in the chamber. Experiment 9 in the table

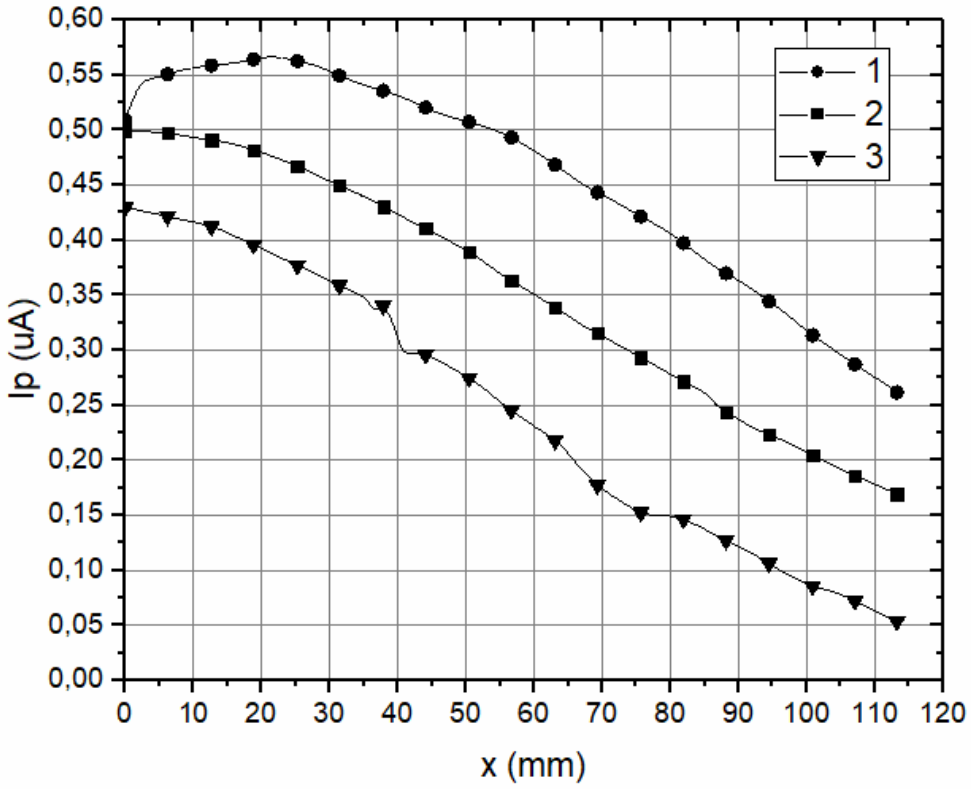

1 – line 9, 2 –line 7, 3 – line 4, in the table 1

Fig. 4 – Ion saturation current distribution on the probe

From the obtained dependencies of the probe ion saturation current density distribution we can see that the maximum plasma concentration locates over the center of the ICP source's antenna system. The most uniform is plasma distribution situated at the distance approximate to the middle distance between the antenna system and the process reactor wall parallel to it.

An introduction of an additional constant magnetic field allows to control the size of the uniform plasma distribution area. So the creation of the magnetic field gradient, where magnetic induction has minimum on the antenna system axis and increases to its edges, allows to increase the uniformity of plasma concentration distribution from 43 % to 31-35 % (experiments 6, 9 in the table 1). The best uniformity is obtained when a magnetic field increases at a distance from plasma source antenna system surface to the measuring plane with 0,01-0,05 mT до 0,7-0,9 mT (experiment 9 in the table 1). And if the gradient change is of the opposite character the plasma concentration distribution uniformity goes down (experiment 5 in the table 1).

A uniform distribution of a magnetic field with the induction lower than 0,8 mT doesn't make significant changes in the distribution of plasma concentration generated by the ICP source, the change in plasma concentration distribution doesn't exceed 1% (experiments 7,8 in the table 1). Fields with the induction higher than 0,1 mT have a significant influence over plasma concentration distribution - deterioration of uniformity from 43% to 70 % in the experiment 4, table 1.

References

1. **Ясюнас А.А.** Влияние распределения магнитного поля на разрядные параметры источника индукционного разряда/ А.А. Ясюнас, Д.А. Котов // «Весці Нацыянальнай акадэміі навук Беларусі», 2014. – 49-53 р.
2. **Yasunas, A.A.** The influence of antenna system configuration on the parameters of the inductively coupled plasma / A. Yasunas, D. Kotov. VII International Conference, Plasma Physic and Plasma Technology, Minsk, Belarus, September 17 –21, 2012., 2012. – 639-642 p.

NUMERIC SIMULATION FOR A SINGLE PULSED PLASMA JET - CAPILLARY DISCHARGE WITH AN EVAPORATING WALL

V.V. Kuzenov[1,2,3], K.V. Polyakov[1], S.V. Ryzhkov[1]

[1]Bauman Moscow State Technical University (BMSTU), 2-nd Baumanskaya, 5, 1, Moscow, 105005, Russia, svryzhkov@bmstu.ru
[2]Ishlinsky Institute for Problems in Mechanics RAS (IPMech), prosp. Vernadskogo, 101, block 1, Moscow, 117526, Russia, kuzenov@ipmnet.ru
[3]*Dukhov All-Russian Research Institute of Automatics (VNIIA)*, Suschevskaya 22, Moscow, 127055, Russia, vik.kuzenov@gmail.com

Despite the importance of *pulsed plasma jets* for different applications (nuclear fusion, propulsion, neutron generator and ion source), the *effect* of multiple-jet *interactions* remains poorly understood. Numerical simulation for interaction of pulsed plasma jets generated by atmospheric capillary discharge is presented. The plasma source is based *on a plasma jet established at the end of a capillary discharge at* atmospheric pressure. *Interaction* between the *pulsed plasma jets* and the shock wave/contact boundary layer is analyzed. Note that the *plasma jet* for magneto-inertial fusion must be *created* in a vacuum environment. Preliminary results on an array of pulsed *capillary discharges* are presented. Main properties of *capillary discharge* plasma are discussed.

Introduction.

A *capillary discharge with* an evaporating wall (CDEW) has been widely investigated /1-7/. It is well known /8, 9/, that upon expiration of a supersonic jet, including CDEW jet formed complex flow structure: in the external flow (or submerged space) and inside the jet appear hanging barrel-shaped compression leaps, waves of rarefaction appear inside the jet, and at the outer boundary of the jet, an expanding mixing layer is formed. Issues "pulse" and "stationary" expiration gas and dense plasma in a gaseous medium devoted a significant amount of work, both theoretical and experimental /8, 9/.

Analysis of the flow of a single pulse jet

Regimes of plasma jet outflow of capillary discharge with evaporating wall have been modeled /4, 6, 7/. The calculation area, when carrying out two-dimensional calculations in the coordinate system r,z and ξ,η, was a rectangle. At the bottom of the figure is the outlet section of the capillary discharge channel. Through this flat surface, the erosive flow of plasma-forming substances flows into the calculated zone. From above it was bounded by a

straight line on which non-perturbing conditions are imposed on the outgoing flow from the calculated region: $\frac{\partial^2 \vec{f}}{\partial x_n^2} = 0$, where $\vec{f} = \{\rho, u, \mathrm{v}, e\}$ and x_n is the coordinate normal to the boundary surface. The spatial position of this straight line is determined from the condition that the perturbations of the numerical solution arising at the upper boundary of the calculated region from the outgoing flow do not distort the flow near the cutoff of the capillary discharge channel. On the right-hand side, the integration region is limited by the symmetry axis, on which the corresponding symmetry conditions for the plasma flow of the capillary discharge are given. On the left side there is a surface that is sufficiently far from the axis of symmetry, so that it can be given boundary conditions corresponding to the conditions at infinity in the unperturbed gaseous medium.

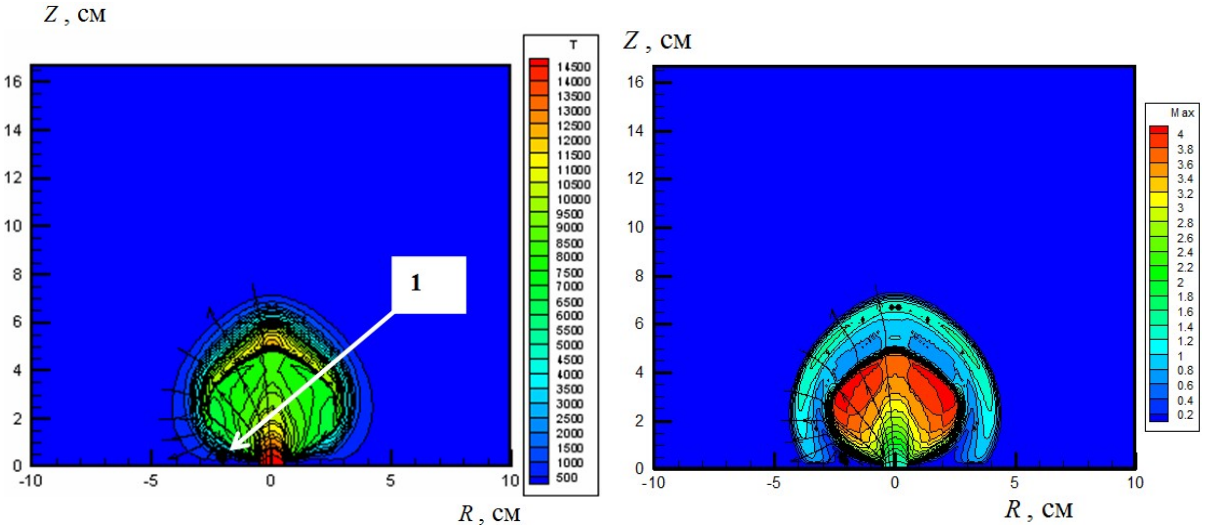

(a) (b)

Fig. 1 – Spatial distribution of the temperature (a) and Mach number (b) in the pulsed jet of the capillary discharge: 1 – the region of the accelerating vortex

Figs. 1-4 show two-dimensional spatial distributions of temperature, Mach number, pressure, and longitudinal velocity at time t = 29.2 μs for W_0 = 2.7 kJ, $d_k = 10$ mm, $P_\infty = 1$ atm

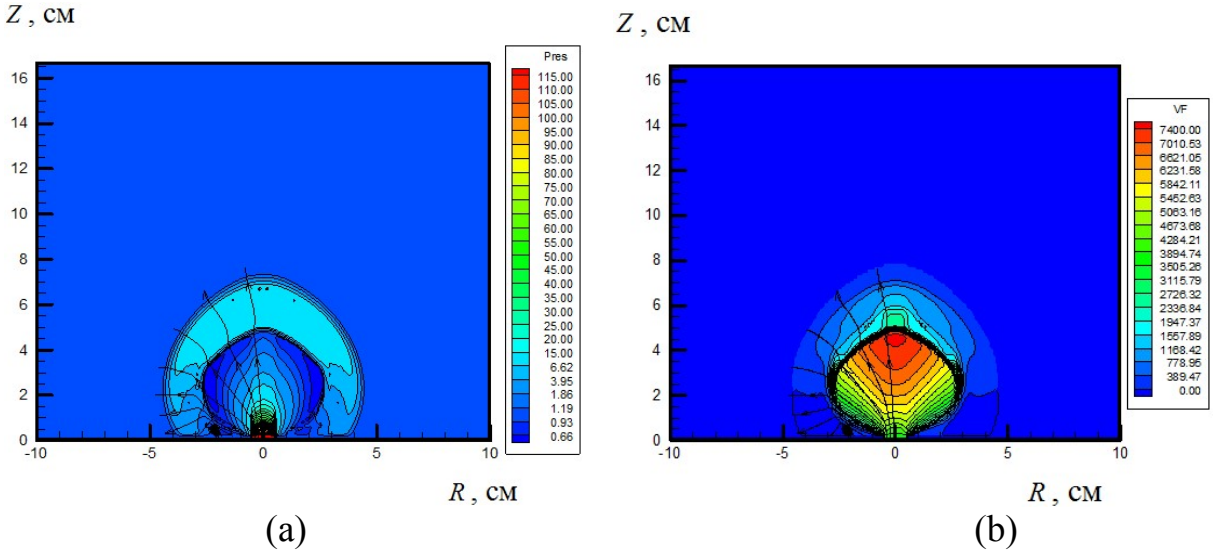

Fig. 2 – Spatial distribution of the pressure (a) and longitudinal velocity (b) in the pulsed CDEW jet

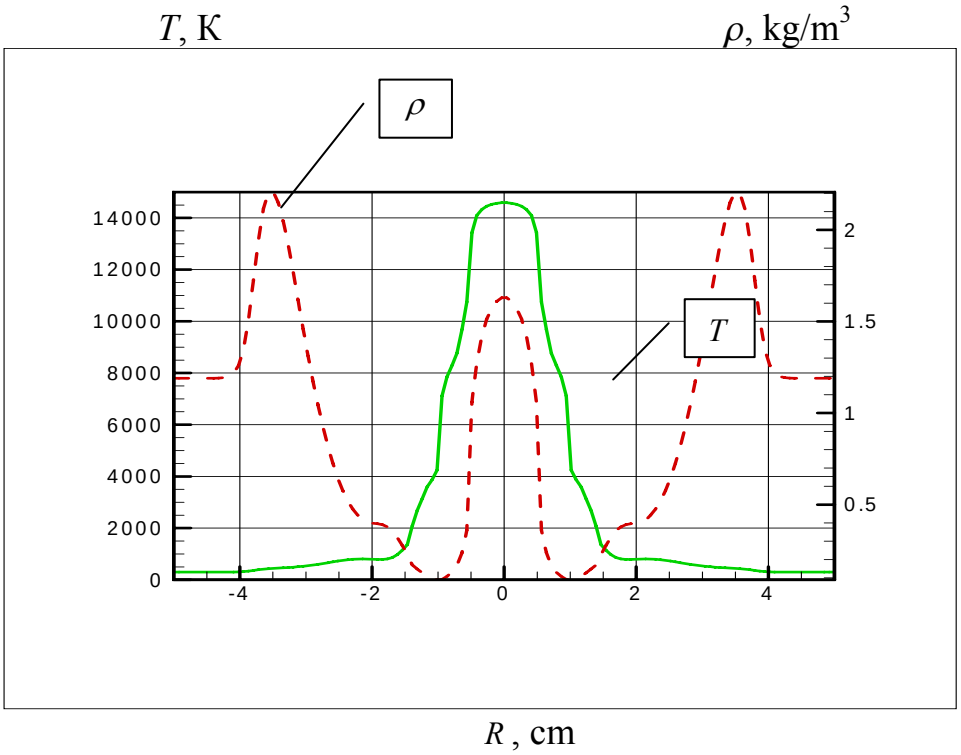

Fig. 3 – Radial distribution of density and temperature in a pulsed jet of a capillary discharge (passing through the center of the accelerating vortex)

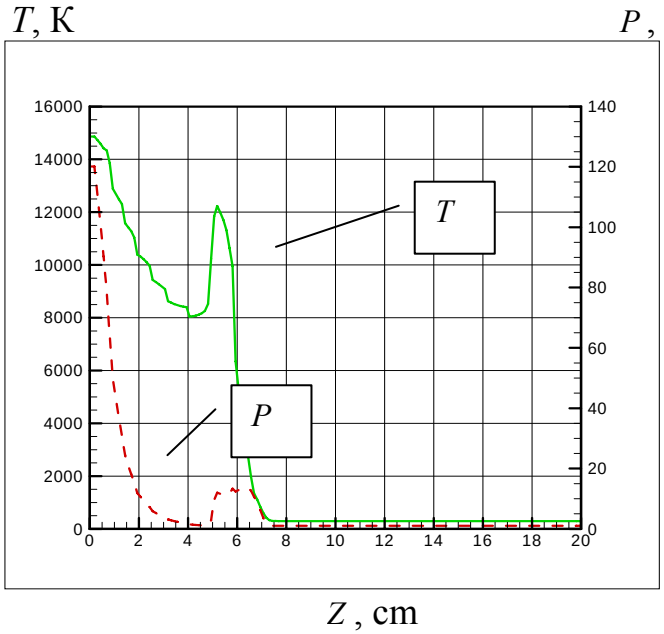

Fig. 4 – Longitudinal distribution of pressure and temperature in a pulsed jet of a capillary discharge (passing through the axis of symmetry of the plasma formation)

Acknowledgements. This work was supported by the Russian Ministry of Education and Science (Project No. **13.5240.2017/8.9**).

References

1. **Sivkov A., Naiden E., Ivashutenko A. and Shanenkov I.** Journal of Magnetism and Magnetic Materials, 405 (2016) 158–168.
2. **Kuzenov V.V., Ryzhkov S.V. and Shumaev V.V.** High Temperature Material Processes, 18 (2014) 99–109.
3. **Kuzenov V.V., Polozova T.N. and Ryzhkov S.V.** Problems of Atomic Science and Technology, 4 (98) (2015) 49–52.
4. **Kuzenov V.V., Ryzhkov S.V., Gavrilova A.Yu. and Skorokhod E.P.** High Temperature Material Processes, 18 (2014) 119–130.
5. **Sivkov A., Ivashutenko A., Shanenkova Y. and Shanenkov I.** Advanced Powder Technology, 27 (2016) 1506–1513.
6. **Kuzenov V.V. and Ryzhkov S.V.** Bulletin of the Russian Academy of Sciences. Physics, 80 (2016) 598–602.
7. **Kuzenov V.V., Ryzhkov S.V. and Frolko P.A.** JPCS, 830 (2017) 012049.
8. **Dulov, V.G. and Lukyanov, G.A.** *Gasdynamics of the Outflow Processes, Moscow: Nauka*, (1984).
9. **Golub V.V. and Bazhenova, T.V.** *Impulse Supersonic Jet Flows*, Nauka, Moscow (2008). (in Russian).

Plasma decay in heated H_2O-containing gaseous mixtures and hydrocarbons after high-voltage nanosecond discharge

M.A. Popov[1], A.Yu. Starikovskiy[2], I.V. Kochetov[3], N.L. Aleksandrov[1]

[1]Moscow Institute of Physics and Technology, Dolgoprudny, 141700, Russia, maksim.popov@phystech.edu
[2]Princeton University, Princeton, NJ08544, USA
[3]SRC RF Troitsk Institute for Innovation and Fusion Research, Troitsk, Moscow, 108840, Russia

Non-equilibrium discharge plasmas generated in water vapor, humid air and other H_2O-containing mixtures are important for atmospheric electricity and discharge applications. Water vapor plasmas are used in technology, with applications ranging from air purification to plasma medicine. Water vapor formation during plasma-assisted fuel oxidation also affects plasma properties in combustible mixtures /1/. Non-equilibrium discharge plasmas generated in gaseous hydrocarbons play an important role in plasma chemical film deposition and synthetic diamond deposition. Electron recombination with hydrocarbon ions is an important mechanism for electron loss and for chemically active species production in plasma-assisted ignition and combustion.

To simulate plasma properties, the rate coefficients for elementary reactions, including the processes controlling the production and the loss of charged particles, are required. Available data on the rate constants for recombination and ion conversion processes in water vapor and hydrocarbon plasmas are not complete /2/. Some rate constants vary greatly with increasing gas temperature. Therefore, it is important to study plasma properties at elevated temperatures in order to obtain information about the rates of elementary reactions with water vapor and hydrocarbon ions.

In this work, the plasma decay was experimentally studied in CH_4, C_2H_6, C_3H_8 and O_2:H_2O and N_2:H_2O mixtures for gas pressures 1-7 Torr and gas temperatures 300-630 K. The rates of plasma recombination depend on the positive ion composition that is dominated by cluster ions for 300 K, whereas simple molecular ions are more important at gas heating. The rates of electron recombination for cluster ions are an order of magnitude greater than the rates for simple molecular ions.

In this work uniform plasma was generated using a high-voltage nanosecond discharge that developed in a gas in the form of a fast ionization wave. The discharge was initiated in a quartz tube with an inner diameter of 42 mm. The high-voltage cone electrode and the grounded ring electrode were separated by a distance of 90 cm. The discharge was ignited by 15 kV pulses (in

the coaxial cable). The pulse full width at half maximum (FWHM) and the pulse rise time were 25 ns and 5 ns, respectively. Electron density was measured in the middle of the discharge gap during the discharge afterglow using a microwave interferometer with a wavelength of 3 mm.

Nichrome wires were reeled up on the quartz tube to heat the gas in the discharge gap. The temperature of the tube surface was measured by a thermocouple. The temperature inside the tube was numerically calculated using the measured temperature on the discharge surface. The energy deposited during the discharge pulse was not enough for additional gas heating, whereas the electron energy in the discharge phase was as large as 10 eV. Electrons were thermalized in the discharge afterglow. Calculations showed that the time of electron thermalization was much shorter than the time of the plasma decay under the conditions studied. It may be concluded that the plasma decayed when the electron temperature was equal to the gas temperature T.

Fig. 1 shows the measured time-resolved electron density for O_2:H_2O mixtures for T = 300 and 630 K. In the experiment, the heated plasma decayed much slower than did the plasma for room temperature. The time it takes to halve the electron density was 0.6 μs for 300 K and 3.7 μs for 630 K. Similar observations were obtained in hydrocarbons and N_2:H_2O mixtures.

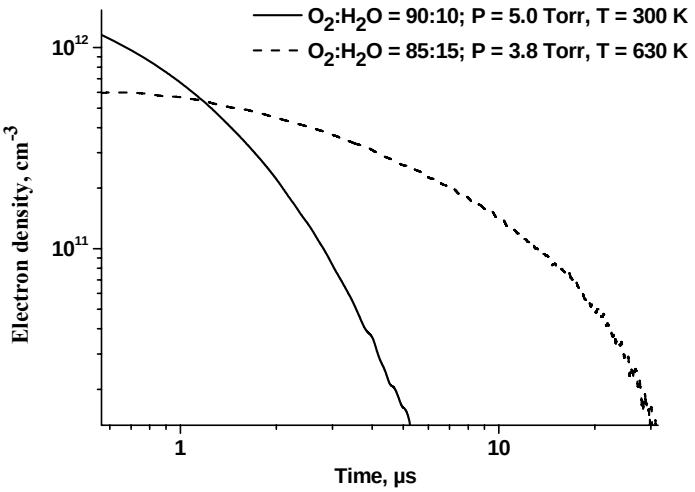

Fig. 1 - Evolution in time of electron density during the plasma decay

There are three possible reasons for the decrease of the plasma decay rate with increasing T. Firstly, the electron-ion recombination coefficient α depends on T as $\alpha \sim T^{-0.5}$. This leads to a decrease in the rate of plasma decay only by a factor of 1.4, much smaller than the decrease in the measured rates when T was increased from 300 to 630 K. The factor of 1.4 is close to the accuracy of our electron density measurements.

Secondly, cluster ions are formed via three-body conversion reactions

$$A^+ + B + M \rightarrow A^+(B) + M,$$

whereas other reactions are binary ones. Therefore, the composition of cluster ions and the effective recombination coefficient depend on the gas number density N that changes with gas temperature and pressure p as $N \sim p/T$ (the equation of state for an ideal gas). To demonstrate this effect, Fig. 2 compares the effective recombination coefficients for various values of T, whereas the values of p were selected such that the values of N were almost the same.

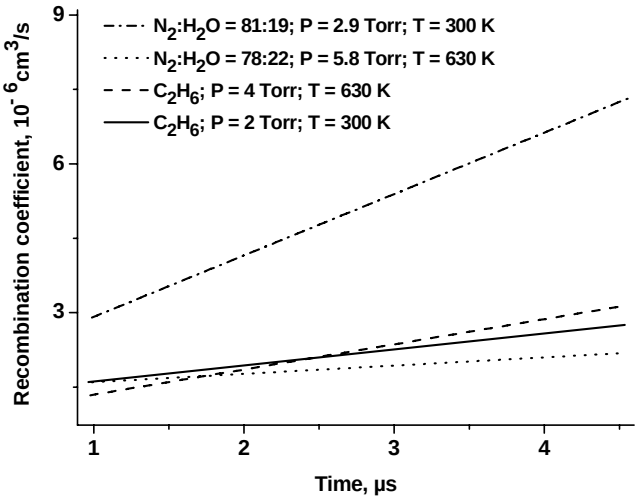

Fig. 2 - Evolution in time of the effective recombination coefficient during the plasma decay

The comparison was made for the plasma decay in pure C_2H_6 and in the N_2:H_2O mixtures. The values of α were determined from the equation

$$1/n_e(t) = 1/n_e(0) + \alpha t,$$

where $n_e(t)$ is the measured electron density and $n_e(0)$ is its initial value. It follows from Fig. 2 that coefficient α is independent of T at N = const for C_2H_6 plasma. However, the influence of gas temperature on the value of α is obvious in H_2O-containing mixtures even at N = const. This is explained by the third reason that the plasma decay rate decreases with increasing T. This reason is a temperature dependence of the rates for the conversion of simple ions to cluster ions. For water vapor ions, this reaction is /3/

$$H_3O^+(H_2O)_n + H_2O + M \rightarrow H_2O^+(H_2O)_{n+1} + M.$$

For instance, the rate coefficient for this reaction at n = 0 is $k = 3.2\times10^{-27}(300/T)^4$. To show this, we simulated the plasma decay in H_2O-containing mixtures under the conditions considered using available data on the rate constants /3, 4/. A system of balance equations for electrons and ions was

numerically solved in a zero dimensional approximation. Fig. 3 compares the calculated electron density histories during the plasma decay in the O_2:H_2O mixture with the measured data. Good agreement is obtained for T = 630 K. Calculations show that here the plasma decay is dominated by electron recombination with O_2^+ ions.

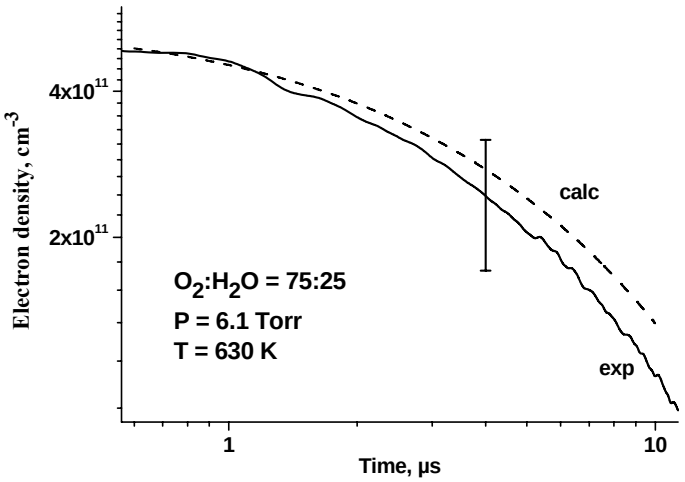

Fig. 3 - Evolution in time of electron density during the plasma decay. Solid curve corresponds to measurements and dash curve corresponds to calculations

In summary, it was experimentally observed that an increase in gas temperature from 300 to 630 K led to a significant decrease in the rate of plasma decay for gas plasma in pure CH_4, C_2H_6, and C_3H_8, and in O_2:H_2O and N_2:H_2O mixtures. The effect of gas temperature on the effective recombination coefficients in the hydrocarbon plasmas was induced only by the change in the composition of cluster ions due to gas number density variation. The effect of gas temperature on the effective recombination coefficients in the O_2:H_2O and N_2:H_2O plasmas was much more profound and was mainly associated with a strong temperature dependence of the rates of water cluster ion formation.

Acknowledgements. This work was partially supported by the Russian Foundation of Basic Research under the project No. 17-02-00481.

References

1. **Anokhin E.M., Popov M.A., Starikovskiy A.Yu., Aleksandrov N.L.** Combustion and Flame, Volume 185, November 2017, Pages 301-308.
2. **Florescu-Mitchell A.I., Mitchell J.B.A.** Physics Reports, Volume 430, Issues 5–6, August 2006, Pages 277-374**.**
3. **Filippov A.V., Derbenev I.N., Dyatko N.A., Kurkin S.A., Lopantseva G.B., Pal A.F. and Starostin A.N.** Journal of Experimental and Theoretical Physics, August 2017, Volume 125, Issue 2, pp 246–267.
4. **Popov M.A., Kochetov I.V., Starikovskiy A.Yu., Aleksandrov N.L.** J. Phys. D: Appl. Phys., 00 (2018) 000000 (11pp).

PREBREAKDOWN CHARACTERISTICS OF WEAKLY IONIZED LIQUID AND GASEOUS MEDIA IN THE STRONGLY NONUNIFORM ELECTRIC FIELD

M. Apfelbaum, R. Syrovatka, V. Vladimirov

Joint Institute for High Temperatures of the Russian Academy of Sciences, Izhorskaya 13 Bldg 2, Moscow 125412, Russia, syrovatkara@gmail.com

1. Introduction

Empiric stationary dependences of the electric current on an applied constant voltage *I(U)* for liquid weakly conductive media were approximated by exponential dependences. For slightly ionized gases, such empirical exponential dependences are known as Nikuradse's curves. They are described in /1/, alongside with similar curves for weakly conductive liquid dielectrics. In /2/, the author analyzes the effect of the prebreakdown electroconvective transport that is formed in weakly conductive liquid dielectrics of the spatial charge on their conductivity and, hence, on such characteristics. In a strongly ionized plasma /3/, the effect both of uniform and nonuniform electric fields on the nonlinearity of the volt–ampere characteristics is approximately the same as in strong electrolytes. In drastically nonuniform prebreakdown fields both in weakly conductive liquids and slightly ionized gases /4/, the most typical among the observed prebreakdown deviations of Ohm's linear law are quadratic.

Theoretically, the exponential growth in conductivity of slightly ionized solid media of a semiconductor type with an increase in the modulus of intensity of the electric field up to the magnitude of electric breakdown was justified by Frenkel /5/. In /5/, an equation of the Arrhenius type was used for the dependence of the volume ionization rate of such media on temperature, taking into account a decrease in the potential of ionization of their neutral particles. It is noteworthy that, e.g., in /4/, the fairly simple, almost identical algebraic Schottky estimates performed earlier were described. For the dissociation constant of weakly conductive liquid dielectrics in /6/, its dependence on the modulus of the intensity of the electric field in the form of the Frenkel exponent was derived, taking into account the decrease in the activation energy of their molecules that are partially dissociated. In /7/, using the methods of physical kinetics, the author obtained a dependence of the dissociation constant of weak electrolytes an analytical and zero Bessel's function on the modulus of electric field intensity of the first order of an imaginary argument (unlike the Frenkel exponent, which grows, according to /8/, almost in the same way under prebreakdown fields).

In /8–10/, macroscopic equations were derived, taking into account the effect in a general case of these processes on the nonlinearity of the volt–ampere

prebreakdown characteristics of weakly conductive liquid dielectrics under study.

In the case of the isothermal regimes implemented for given media in the absence of external heating and for weak Joule heating by the field current of the plane high-voltage capacitor, Frenkel exponential dependence of volt–ampere stationary characteristics on the applied constant voltage theoretically follows from the algebraic equation of the stationary law of charge conservation in a differential form. In the case of a spherical capacitor from this law, we derived in /10/ an ordinary differential equation of the first order for determining the stationary distribution of the electric field potential in its interelectrode gap, which is filled with a weakly conductive liquid such as transformer oil.

In /10/, the analytic solution of this differential equation was also obtained. Under the condition of the equality of the modulus of the potential difference between the capacitor electrodes to the applied constant voltage, it is followed by the expected ohmic linearity of the volt–ampere characteristics in the weak fields and by its quadraticity in the prebreakdown ones for large interelectrode gaps. This theoretic result also agrees well with the prebreakdown empiric curves for weakly conductive liquid dielectrics that were obtained experimentally by different authors. However, in the case of corona discharge in slightly ionized gases /1/, microlevel processes differ markedly from those of weakly conductive liquid dielectrics. Nevertheless, the quadratic dependence for the gases of the type of the quadratic dependence that we obtained fairly long ago for weakly conductive liquid dielectrics /10/ was derived by Townsend /4/, though not in the field of spherical but rather elongate cylindrical condensers with a filamentous internal corona-forming electrode. The Townsend quadratic dependence of *I(U)* for gases is also frequently supported experimentally, with the results described in /4/.

2. Empiric dependence of prebreakdown characteristic in the corona discharge in slightly ionized gases

The slightly ionized gases, like air, called electronegative /4/ are closest in molecular composition and to the type of the prebreakdown dependence *I(U)*, particularly in strongly nonuniform fields, which were described in the previous section, about a weakly conductive liquid dielectric, because of the partial adhesion of their electrons to neutral molecules. Upon the interaction of such media with a strongly nonuniform field of high-voltage electrodes with a type of pin, blade, high voltage wires, or small-size spheres, a corona glow is observed /4/ near these electrodes. In such boundary-layer regions, the electrodynamic characteristics depend on free electrons as well as on positive and negative ions. In the field of a high-voltage corona-forming cathode, the electrons can enter the gas not only through radiation, as they do in weak fields, but also due to the different types of electron emission that are thoroughly described in /4/. Ions in

such gases for the applied prebreakdown fields are formed not only due to the sticking of electrons to molecules, but also due to the shock ionization of the molecules by the free electrons that move in strong fields. In addition, they are formed owing to chemical processes of plasma.

Alongside with the internal zones of discharge adjacent to the corona-forming electrodes, there are also external regions with unipolar charging in the stationary cases /4/. In them, the sign of the forming volume charge upon its establishment coincides with the sign of the charge of the corona-forming electrode. According to /4/ volt-ampere characteristic of the corona discharge in point-plane geometry has the next form:

$$I = \frac{2bU(U-U_c)L}{(r_0+d)^2 \ln\left(1+{}^{d}/_{r_0}\right)}, \quad (1)$$

where U_c is the corona ignition voltage, b is the mobility of ions, d is the interelectrode distance, L is the characteristic size of a grounded counter electrode, r_0 is the radius of coronating edge.

3. Experimental results of prebreakdown characteristic in the corona discharge in air

The experiments were carried out in air at atmospheric pressure. The needle with an edge radius equal to 70 μm was placed above the center of a flat round electrode with a diameter of 100 mm at a distance of 13 mm. In this case, the finite size of the flat electrode can be neglected. High dc voltage of negative polarity was applied to the needle. The flat electrode was grounded. The dc voltage was measured using voltage divider with the voltage ratio of 1 : 1000 and multimeter APPA 505. The error of measuring the dc voltage at the limit of 10 V was equal to ±0.17 V. The current was measured using ammeter with the accuracy class of 0.5. Fig. 1 shows comparison of the experimental data with calculations according to the Townsend theory. The corona ignition voltage was equal to 3.2 kV.

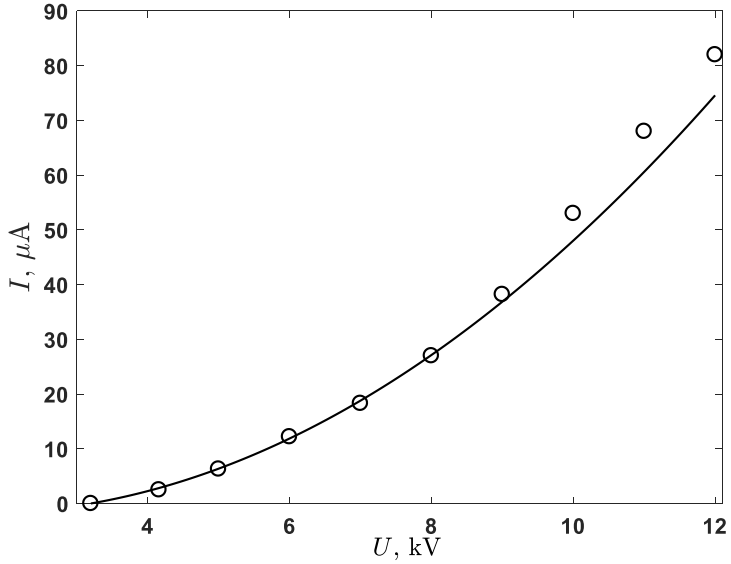

Fig. 1 – The volt–ampere characteristic of the corona discharge of negative polarity: experiment (circles) and theory (solid line)

4. Conclusion

An experimental setup for the investigation of corona discharge characteristics in weakly ionized media was designed and constructed. The measured prebreakdown volt-ampere characteristics for corona discharge in point-plane geometry in air is presented. These experimental results agree with the Townsend theory for the electrodynamics of the outer area of corona discharge.

Acknowledgements. The work was done with financial support of the Russian Science Foundation, grant No. 14-50-00124.

References

1. **Felici N.J.** Direct Current, 2(1971) 90–99.
2. **Felici N.J.** Direct Current, 2(1971) 147–165.
3. **Tonks L. and Langmuir I.** Phys. Rev., 34(1929) 876–922.
4. **Raizer Yu.P.** Gas Discharge Physics. Berlin: Springer (1991).
5. **Frenkel Ya.I.** Zh. Eksp. Teor. Fiz., 8(1938) 1291–1301.
6. **Plumley H.J.** Phys. Rev., 59(1941) 200–209.
7. **Onsager L.** Chem. Phys., 2(1934) 599-615.
8. **Yantovskii E.P. and Apfel'baum M.S.** Zh. Tekh. Fiz., 50(1980) 1511–1520.
9. **Gogosov V.V., Shaposhnikova G.A. and Shikhmurzaev Yu.D.** Prikl. Mat. Mekh., 46(1982) 435–444.
10. **Apfelbaum M.S.** Elektrokhimiya, 11(1986) 1463–1471.

THE EFFECT OF ADDITIONAL GAS BUFFER VOLUME ON THE PARAMETERS OF A GLOW DISCHARGE IN TUBE

S. Fadeev[1], A. Saifutdinov[1,2], N. Kashapov[1], A. Akhmadullin[1]

[1]Kazan Federal University, Kremlevskaya str., 18, 420008, Kazan, Russia,
fadeev.sergei@mail.ru
[2]St. Petersburg State University, Universitetskaya nab., 7-9, 199034, St. Petersburg, Russia,
as.uav@bk.ru

1. Introduction

The glow discharge is used in many areas of modern science and it is the basis of many practical applications (quantum generators, plasma modification of surfaces, thin-film deposition, biological deactivation, spectrometry, etc.). However, some modes of glow discharge remain unexplored. As is known, in a classical cylindrical discharge tube, gas is heated at medium and high pressures and currents. In this case, the neutral particles are displaced into the near-surface (near-electrode and near-wall) regions. In other words, a non-uniform distribution of the density of neutral particles is observed. This fact is one of the causes of contraction /1, 2/. However, in recent years, various complex chamber configurations have been used to initiate discharges in various applications, for example, in plasma chemistry. /3, 4/. In such cells, there are regions buffer volume - without gas-discharge plasma in which the gas remains "cold".

When the values of the currents and the pressure of the critical values at which contraction can occur are reached, most of the particles will be displaced not to the near-wall regions but to the "cold" buffer volume due to a larger temperature gradient compared to the temperature gradient "tube-wall axis." This fact leads to interesting features of discharge burning and extends the range of conditions (values of pressure and current) for the existence of glow discharges with a diffuse positive column.

The aim of the paper was to investigate the influence of the buffer volume on the discharge characteristics in helium in a long cylindrical tube at pressures from 52.5 to 203 Torr and currents from 30 to 200 mA.

2. Experimental setup

To investigate the electrical characteristics and the spatial structure of glow discharge, an experimental setup was developed (Fig. 1). The installation is a tube (1) made of quartz glass (installed vertically) with a length of 24.2 cm and an internal diameter of 2.4 cm filled with helium. Two plane-parallel copper electrodes cooled with water are located at the ends of the tube.

At a distance of 3.6 cm from the cathode is a cylindrical channel with a diameter of 1 cm and a length of 7 cm with a volume of $0.05V_{tube}$, where V_{tube} is

the volume of the discharge tube. At the end of the channel there is a vacuum tap that connects to buffer volume of $5.95V_{tube}$. The buffer volumes (2, 3) is two cylindrical volumes connected to the discharge tube and separated by a vacuum tap. Thus, it is possible to distinguish three buffer volumes connected to the discharge gap with volumes of $0.05V_{tube}$, $0.27V_{tube}$ and $6V_{tube}$.

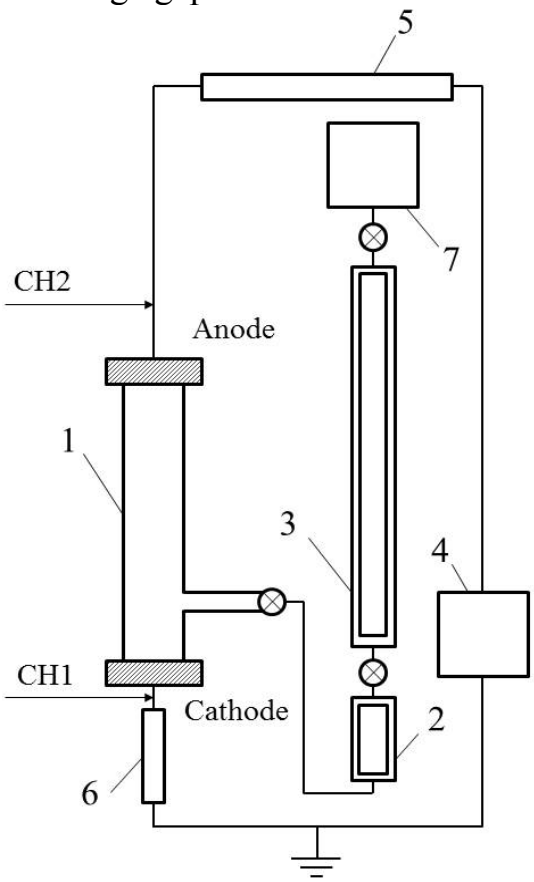

Fig. 1 - The experimental setup (1 – quartz tube; 2, 3 – buffer volumes; 4 – power supply; 5, 6 – ballast resistors; 7 – forevacuum pump)

To supply the discharge, we used a regulated constant voltage source Spellman STR30*6 (0–30 кВ) (4). Positive voltage was supplied to the anode through a ballast resistor placed in series. The cathode was grounded. The source was always operated in current–controlled mode. The total ballast resistance in the electrical circuit was 24.1 kΩ (5, 6). The discharge currents and voltages were recorded by means Rigol DSC2072A oscilloscope. A high-voltage probe ACA-6039 was used to measure the voltage. As a current shunt, a part of the ballast resistance of 1435 Ω (6) with a RP3300A probe was used. The voltage at the discharge was determined by the difference in the readings from the channels of the oscilloscope CH2 and CH1. The measurements of the electrical characteristics of the discharge were implemented in the quasi-stationary mode, that is, by means of soft hand regulating voltage of the supply.

The tube with buffer volume was evacuated to pressures of 10^{-3} Torr in the first stage by means a forevacuum pump. Then helium was injected into the system to the investigated pressure. Buffer volumes (2, 3) were disconnected, and discharge was ignited in a cylindrical tube. The current–voltage characteristic of the discharge was recorded. The connection of the buffer volume with the discharge tube was restored and the current–voltage characteristic was again removed in the second stage.

3. Results and discussion.

The current–voltage characteristics of the glow discharge at different pressures and buffer volumes are shown in Fig. 2. The discharge voltage drop

increases markedly with increasing gas pressure /1, 5/. A normal glow discharge was observed. It was characterized by the increases in the area of the current spot as the current was raised under given pressure. This can be indirectly indicated by the fact that the area of glow near-cathode region increases. A weakly growing part was observed, within the limits of the investigated discharge currents, which was also observed in studies of discharges at atmospheric pressure in work /6/. In the range of currents from 50 mA and higher, a falling part of the current–voltage characteristic is observed, which indicates an unstable regime of discharge burning. The falling region in the current–voltage characteristic is a consequence of the heating of the gas /1/. Therefore, at high pressures and, as a consequence, high power inputs to discharge in the investigated range of currents, the fall is steeper.

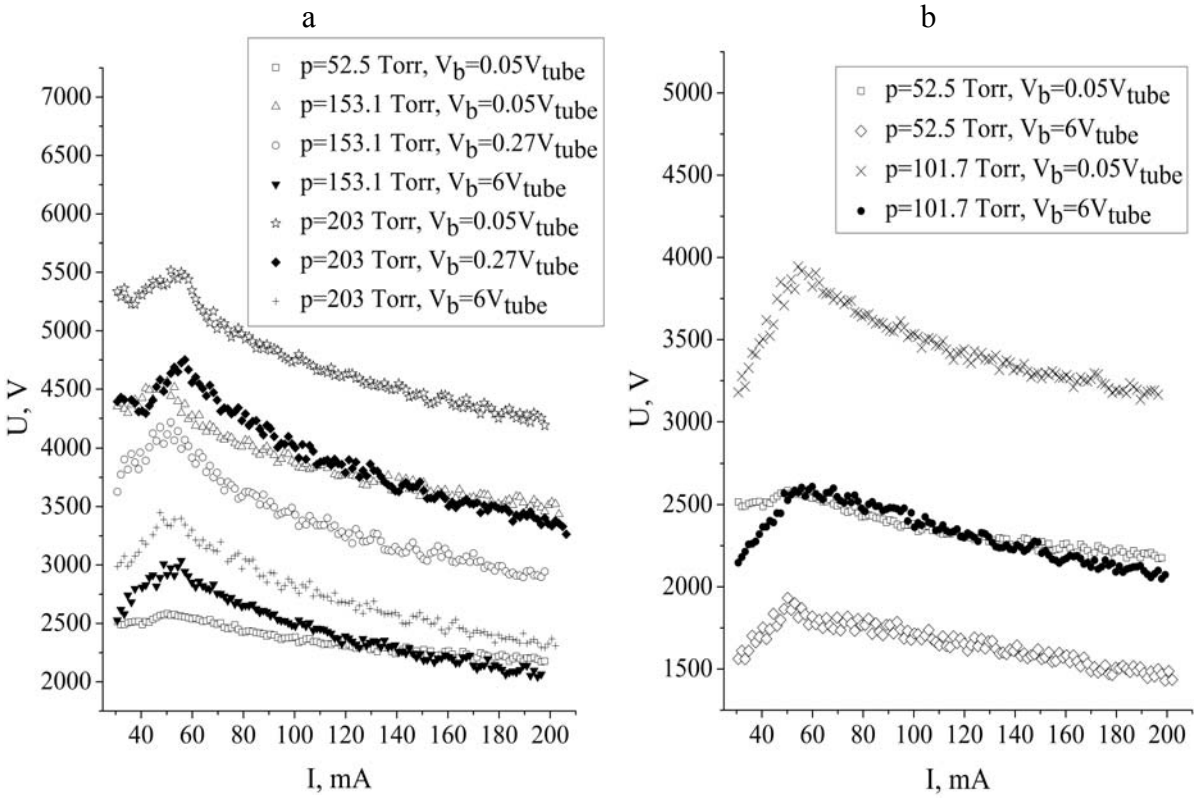

Fig. 2 - Current–voltage characteristic of a glow discharge at different pressures and buffer volumes

As can be seen from Fig. 2, the renewal of the connection between the discharge tube and the buffer volume leads to a drop in voltage on the discharge and a visual increase in the width of the positive column. An increase in the buffer volume leads to reducing the discharge burning voltage. This is due to the fact that the neutral particles are displaced in the “cold” buffer volume due to the temperature gradient and the density of neutral components in the discharge region decreases. This is due to the fact that the neutral particles are displaced in the “cold” buffer volume on account of the temperature gradient and the density

of neutral components in the discharge region decreases. This process can be traced on current–voltage characteristics of the discharge at 52.5 Torr with a buffer volume of $0.05V_{tube}$ and 101.7 Torr with a buffer volume of $6V_{tube}$. The current–voltage characteristics of the discharges practically coincide at pressures differing by a factor of two, which indicates close values of the E/N parameter for these two cases. The presence of a buffer volume leads to more decrease in the discharge burning voltage with increasing pressure. This is due to the temperature increase in the discharge and, as a consequence, more "effective" displaced of neutral particles in the "cold" buffer volume.

4. Conclusions.

We have experimentally investigated the behavior of a glow discharge in a cylindrical tube with non–discharge gas buffer volume attached to it in the pressure range from 52.5 to 203 Torr. Obtained the current–voltage characteristics of a glow discharge in the tube using three different buffer volume connected to the discharge gap. It is shown that by varying the buffer volume, it is possible to vary the parameter E/N and the discharge current density. In this case, using such a simple tool as a buffer volume, it is possible to obtain a glow discharge in helium with a diffuse positive column at sufficiently high pressures.

Acknowledgements. This work was supported in part by the Russian Federation Presidential Program for State Support of Young Candidates of Sciences (grant no. MK-539.2017.1), the Russian Foundation for Basic Research (project no. 16-38-60187_mol_a_dk) and the subsidy allocated to Kazan Federal University for the state assignment in the sphere of scientific activities (11.1300.2017/4.6).

References

1. **Raizer Y.P.** Gas discharge physics. Berlin, Heidelberg: Springer (2011).
2. **Saifutdinov A.I., Fairushin I.I., Kashapov N.F.** JETP Letters, 104 (2016) 180–185.
3. **Gudmundsson J. and Hecimovic A.** Plasma Sources Sci. Technol., 26 (2017) 123001.
4. **Bogaertsa A., Neytsa E., Gijbelsa R., Mullenb J.** Spectrochimica Acta Part B, 57 (2002) 609–658.
5. **Vasilyak L., Polyakov D., Shumova V.** Contrib. Plasma Phys., 53 (2013) 432–435.
6. **Arkhipenko V.I., Kirillov A.A., Safronau Ya.A., Simonchik L.V., Zgirouski S.M.** Plasma Sources Sci. Technol., 18 (2009) 045013.

DYNAMICS OF ONE-ELECTRODE DISCHARGE IN BRANCHED TUBE AT LOW GAS PRESSURE

A. Shishpanov, D. Ivanov, S. Kalinin, A. Meschanov

Saint Petersburg State University, 198504 Saint Petersburg, Peterhof, Ul'yanovskaya str.3
sispanov@mail.ru

Initial stage of a discharge is a gas breakdown may have several forms defined by different mechanisms. In case of non-uniform electric field and low gas pressure the breakdown occurs after ionization wave (IW) propagation /1/. IW is the area of high electric field restricted in space and time, which propagates from high voltage electrode and produces gas ionization. IW occurs during a breakdown in low gas pressure tubes and channels. These waves are excited at low overvoltage; their speed does not exceed 10^8 cm/s and can be easily detected by their optical emission. IW parameters are very sensitive to approaching any grounded conductors; the tube shielding which is a standard way to exclude such external influence results in significant changing in IW front shape and in speed decreasing. More details about tube shielding effect on the breakdown can be found in /2/.

Despite the fact that IW has been extensively studied, there are just few works that concern interfering of separate ionization waves. Authors of /3/ investigated splitting and merging of IW in a tube made of two linear tubes both connected to a ring-shaped tube along the same longitudinal axis being the ring diameter filled with neon at atmosphere pressure. It was found that IW splits in first branching point into two equal fronts that propagated in half-rings with lower speeds than the origin wave did. Speed decreasing was a result of lower electric field strength. In second branching point the two waves merged in one front with higher electric field. The new IW increased in speed and plasma density. There are no similar results for IW accompanying low pressure gas breakdown.

To investigate IW interaction the source of separate waves with high repeatability is required, and this problem can be effectively solved with one-electrode discharge in a long non-shielded tube. This discharge appears after the voltage is applied between one electrode of the tube and the ground while another electrode remains free. As a result, only one IW exists in the discharge volume without return wave and self-sustained discharge. It propagates from active electrode and disappears after approaching the opposite one or after termination of voltage pulse time. The absence of the shield allows to obtain IW with narrow front (optical emission measurements give about 0.1 - 1μs in neon for IW speed ~10^7cm/s) and optical and electrical signals of sufficient amplitude (signal-to-noise ratio >10). One–electrode discharge starts from initial

breakdown between the active electrode and nearest section of the wall. In that moment the peak of optical radiation and peak of current in the electrode circuit are detected /2/. During IW propagation stage the current through the electrode changes slowly and breaks after IW approaches the opposite electrode.

In this work, interactions of IWs were observed in sealed-off Y-shape discharge tube with three electrodes filled with neon at pressure 1 Torr. It consists of two symmetrical channels with the same length (30 cm) and 50 cm long outlet channel. Pulses of positive voltage with amplitudes 1 – 3 kV were applied to two electrodes with repetition rate 0.1 – 5.0 Hz while the third electrode remained free. Initial breakdowns near the electrodes could occur spontaneously with different average statistical delay times (~1ms). To synchronize the breakdowns we used the effect of statistical delay time decreasing under the electrodes illumination with visible spectrum light /4/. Two LEDs with λ = 440 nm irradiate permanently two active electrodes leading to statistical delay time less than 1 μs. Within this time two waves could start from the electrodes and interfere at arbitrary moments. To detect this event four optic fibers were placed in different points. Two of them permanently transmitted the light signal from symmetrical near-electrode points (10 cm from anode) while other fibers were installed in different points of outlet channel and also of the inlet channels. Two photomultipliers (PMT) were connected to the pair of the fibers so that one fiber passes signal from electrode while another fiber transmits light signal from the certain point. IW interfering was detected by statistical accumulation of a number of signals in chosen points. To exclude the disturbance in IW propagation all assembly parts of the fibers fastening as well as elements for Y-tube mounting were made of dielectric materials.

Firstly we examined the breakdown in two channels separately with only one high-voltage electrode. Fig. 1 presents typical IW optical signals which can be detected in all parts of Y-tube including voltage-off channel. This result suggests that IW spreads in each available way after the branching point. IW speed after splitting rapidly decreases on approaching the non-grounded electrode which then results in IW attenuation. As a result, average channel velocities of IW are lower than velocity of initial wave and depend on the channel length.

When voltage pulses are applied to the two channels simultaneously the picture of the IW light signals begins to differ from Fig.1 and depends on time shift between initial breakdowns near the electrodes. Fig. 2 - 4 show several forms of those optical signals. If the time shift between the breakdowns in first and second channel appears to be sufficient for IW transition to the branching point the wave will split into two IWs. One of them goes to the central channel while another IW tends to move to the second active electrode where it meets oppositely directed IW. The result of their interaction may vary depending on

the time shift between two IWs. It is possible to separate several scenarios: amplification, annihilation, partial annihilation.

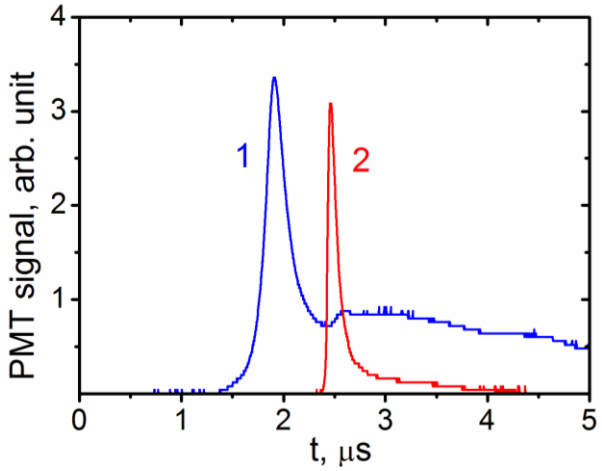

Fig. 1 – IW optical signal in one channel. 1) near anode; 2) 2 cm from branching point

Fig. 2 – demonstrates the early start of IW1 which is approximately 0.5 μs prior the start of IW2 (curve 1 recorded in observation point (1) near the channel anode). Average channel speed of IW1 is about $5 \cdot 10^7$ cm/s which is sufficient to approach the branching point where the wave splits into 2 IWs; one of them interferes with IW2 at the observation point (2) where the curve 2 is recorded. The curve 2 at fig.2 shows the situation where such interaction may lead to amplification of IW

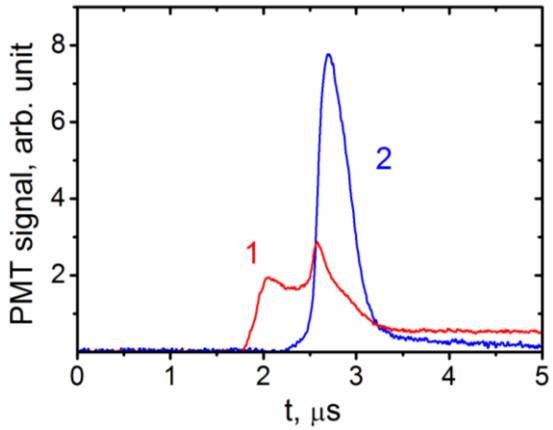

Fig. 2 – IW optical signal in different points: 1) 10 cm from anode of first channel; 2) center of the second channel

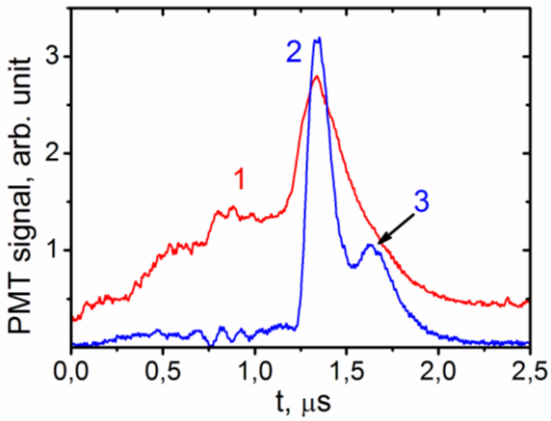

Fig. 3 – IW optical signals from two points in one channel. 1) 10 cm from anode; 2) 2 cm from branching point; 3) repeated weak IW signal

Fig.3 demonstrates optical signals from two points in one channel. Curve 1 corresponds to position of the fiber in 10 cm from the anode while curve 2 depicts IW emission at 2 cm from the branching point. Peaks 1 and 2 correspond to different IWs one of which (1) starts from the channel anode, and second one (2) comes from adjacent channel after splitting in the branching point. The waves interaction appears to be between the observation points and it can be seen as a mere result of the interfering in the form of additional peak at curve 1 corresponding to the resulting IW moving from the anode at Fig.3. At the same

time the picture of the signals was like the one at Fig.4 that was observed for some breakdowns. The fibers transmit optical signals as before, but additional peak is missing. Two peaks presented are not the signal of the same IW because in this case its speed should be about $2 \cdot 10^8$ cm/s which is higher by order of magnitude than in previous breakdowns at the same conditions. Interfering of those waves does not lead to any new signals in observation points that indicate the wave disappearance at a distance between the points.

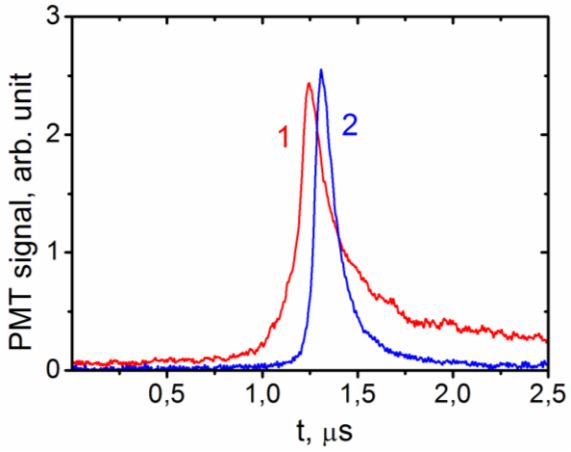

Fig.4 – IW optical signals from two points in one channel. 1) 10 cm from anode; 2) 2 cm from branching point

The result described above shows more complex behavior of IW during interference with another IW when they start with time delay. The experiment confirms IW splitting in branching tube as has been shown in /3/. But apart from that the processes of annihilation, partial annihilation and amplification of IW have also been observed.

Acknowledgements. This work was supported by the Russian Foundation for Basic Research (grant No18-32-00223).

References

1. **Vasilyak L. M., Kostuchenko S.V., Kudryavtsev N.N., Filugin I.V.** Physics – Uspehi (Advances in Physical Sciences), 164 No3 (1994) 263 - 286.
2. **Kalinin S A, Meshchanov A V, Shishpanov A I and Ionikh Yu Z** Plasma Phys. Rep. 44 (2018) 345-58.
3. **Xiong Z., Robert E., Sarron V., Pouvesle J.-M., Kushner M.J.** J. Phys. D.: Appl. Phys. 45 (2012) 275201
4. **Shishpanov A. I., Ionikh Y. Z., Meshchanov A. V.** Opt. Spectrosc. 120 (2016) 929-35.

Modelling the magnetic field of the acceleration channel End-Hall ion source

M. Palmera[1], B. Shandarovich[2], D. Kotov[3]

Belarusian State University of Informatics and Radioelectronics, Str. P. Brovki, 6, 220013, Minsk, Belarus. E-mail: [1]bfcmikep@gmail.com, [2]bazhen.sh@gmail.com, [3]kotov@bsuir.by

In recent decades, the End-Hall ion sources have been used in the optical coating industry for ion-assisted deposition and surface pre-cleaning operations e.g. /1, 2/. The employ of gridless ion sources based on magnetoplasmadynamic thrusters and Hall effect has been beneficial for many applications, because they have a relatively high ion flux density, wide spatial distribution, moderate beam energy levels of approximately 60-200 eV, and its ability to handle either inert or reactive gases. However, as modern manufacturing processes scale to larger systems, higher rates, and larger substrate areas, it has become necessary to increase power capacity of the End-Hall ion sources, reduce form-factor sand significantly improve their service ability and maintenance requirements and, thereby, reduce cost of ownership.

In Hall-effect ion sources, the magnetic field **B** is perpendicular to the discharge current forms a barrier to electron transport from the cathode to the anode at a specific location in space, leading to the increase of the electric field **E** in the plasma at that location, in a direction perpendicular to the magnetic field. This electric field accelerates ions away from the source.

The resulting cross-field configuration generates a current (the Hall current) that direction is perpendicular to the **E**×**B** fields e.g /3, 4/. Most Hall-effect ion sources have an axially symmetric design in which the applied magnetic field and the resulting electric field are such that the Hall current is generate in the azimuthal direction. In this configuration, the anode is at the end of the channel and the exhaust (and acceleration region) is at the other end. In the End-Hall ion configuration, the anode has a conical shape, the acceleration region is close to the anode surface, and the beam divergence is larger.

Magnetic field simulation

For the study of the magnetic field of an ion source (Figure. 1), it is assumed that the field is generated by cylindrical permanent magnets; therefore, the solution will be given by the equations

$$\nabla \cdot B = \nabla \cdot (\nabla \phi) = 0 \qquad (1)$$

where **B** is the magnetic induction field and $\boldsymbol{\phi}$ is the magnetic potential.

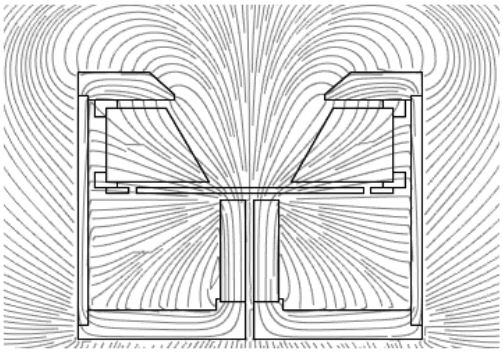

Figure 1. Magnetic field lines configuration in End-Hall ion sources

Rather than being calculated directly from the configuration of permanent magnets, the magnetic field in the discharge channel is obtained from a set of boundary values specified on the domain boundaries. This allows the direct implementation of measured magnetic field data or the deliberate adjustment of the field, which is useful for studying its influence.
The magnetic field lines are described by the stream function $\lambda\ (x, r)$ e.g. /5, 6/, calculated from

$$B_a = \frac{1}{r}\frac{\partial \lambda}{\partial r}, \qquad B_r = \frac{1}{r}\frac{\partial \lambda}{\partial x}, \qquad (2)$$

where *a* and *r* are the axial and radial position coordinates and $\boldsymbol{B_a}$ and $\boldsymbol{B_r}$ are the axial and radial components of the magnetic field. This λ is constant along magnetic field lines ($B \cdot \nabla \lambda = 0$) and usually diverged from anode to cathode. Substituting λ in Equation. (2) in the Maxwell-Ampere, we have

$$\frac{\partial}{\partial x}\left(\frac{1}{\mu}\frac{\partial \lambda}{\partial x}\right) + \frac{\partial}{\partial r}\left(\frac{1}{\mu r}\frac{\partial \lambda}{\partial r}\right) = -rJ_{magnet} \quad (3)$$

where μ is the magnetic permeability and $\boldsymbol{J_{magnet}}$ is the azimuthal current source of the magnet. The solution for this equation is solved numerically.
It is possible to increase the efficiency of ion generation in End-Hall ion source by decreasing the value of the magnetic induction component B_r in the region above the anode. This makes it possible to increase the efficiency of the magnetic trap and to ensure the entry of electrons from the filament-cathode into the plasma formation zone. The value of the component B_a in the plasma formation region should remain high to enhance the ionizing ability of the electrons located there.

Simulations results

In this section presents the magnetic field simulation between reference and developed End-Hall ion sources. The simulation was performed using the free trial version COMSOL Multiphysics software package. The calculation of the magnetic field was carried out in a stationary mode using the Maxwell equation. It is considered that the field distribution is uniform throughout space and is not affected by external fields. During our simulation we were variation the permanent magnets dimension and shape of magnetic poles.
As a result of the simulation, graphs were constructed which show the variation of the values of the magnetic field induction components B_a, B_r on the cylinder surface located at r_1, r_2 and r_3 from the central axis as it shown on the Figure 2.

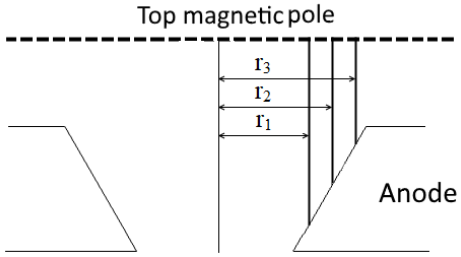

Figure. 2. Schematic of the magnetic field measurements from the central axis at a distance r_1, r_2 and r_3

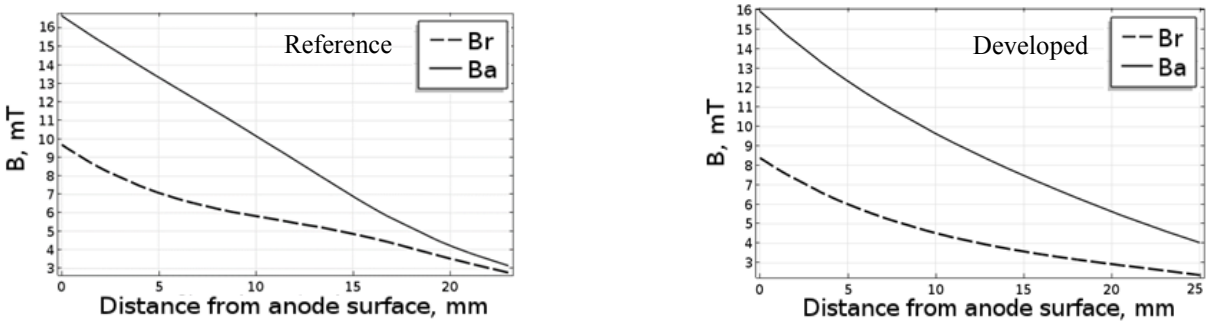

Figure 3. The values of the B_a and B_r magnetic field components for the reference and developed ion sources at the r_1

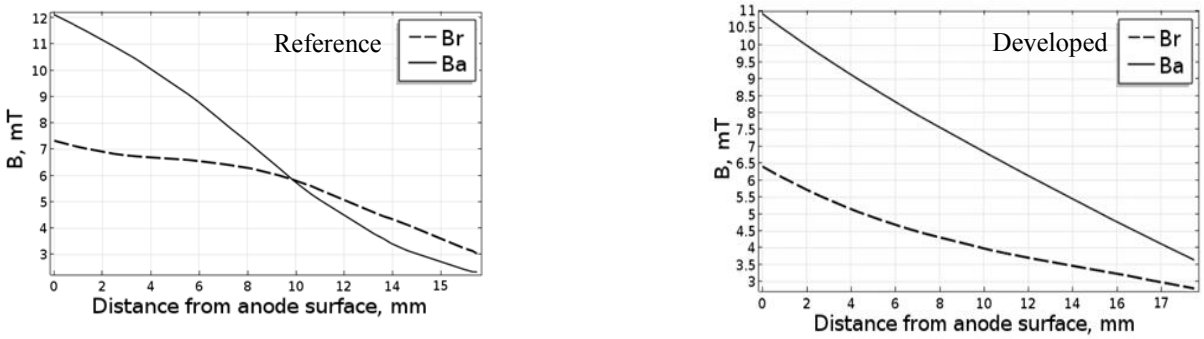

Figure 4. The values of the B_a and B_r magnetic field components for the reference and developed ion sources at the r_2

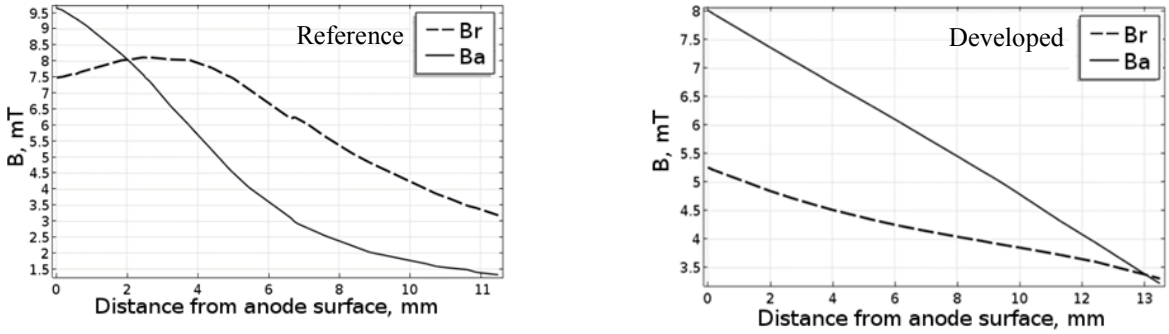

Figure 5. The values of the B_a and B_r magnetic field components for the reference and developed ion sources at the r_3

As can be seen from the figures 3,4 and 5, the values of the B_r component in the region above the plasma formation region decreased by 10-40% without a significant decrease in the B_a component. Moreover, a decrease in the values of the B_r component with a distance from the anode surface occurs more intensively.

Conclusions

The magnetic fields of the reference and developed magnetic system of the End-Hall ion sources are simulated. The values of the magnetic field induction component B_r in the region above the plasma formation zone are decreased. The results obtained indicate expansion of the "channel" for electrons that follow to the anode, increase in “effective surface” of the anode, and, as a consequence, increase in the discharge region. So, there is an increase in the efficiency of the magnetic electron trap for developed End-Hall ion source and, accordingly, an increase in the efficiency of ion current generation.

References

1. **V. V. Zhurin**, U. S. Patent No. 2005/0237000 A1 (2005).
2. **N. Oudini, G. J. M. Hagelaar, L. Garrigues, and J. P. Boeuf**. Numerical Modeling of an End-Hall Ion Source. Adv. Mater. Res. 227, 144 (2011)
3. **D. L. Tang, S. H. Pu, L. S. Wang, and X. M. Qiu**. Linear ion source with magnetron hollow cathode discharge. Rev. Sci. Instr. 76, 113502 (2005).
4. **V. V. Zhurin**. Industrial Ion Sources. Broadbeam Gridless Ion Source Technology (2012)
5. **N. Oudini, G. J. M. Hagelaar, J.-P. Boeuf,L. Garrrigues.** J. Appl. Phys 109, 073310 (2011)
6. **J.P. Boeuf.** Tutorial: Physics and modeling of Hall thrusters J. Appl. Phys 121, 011101 (2017);

STUDY OF ONE-ELECTRODE BREAKDOWN IN LONG DISCHARGE TUBE AT LOW GAS PRESSURE

D. Ivanov, A. Meschanov, S. Kalinin, A. Shishpanov

Saint Petersburg State University, 198504 Saint Petersburg, Peterhof, Ul'yanovskaya str.3
sispanov@mail.ru

In case of a long discharge tube the inter-electrode electric field before the breakdown is essentially non-uniform if the tube length exceeds the diameter. In this case, classical electron avalanches appear only at the initial stage of the breakdown near high-voltage electrode, and could transform into ionization wave (IW) which always propagates from the active electrode /1/. At the moment of initial ionization and the IW formation the existence of another electrode of the tube is insignificant because the electric field strength rapidly decreases toward the tube center becoming zero at a distance of some diameters. Therefore if the tube has infinite length the IW propagation will be restricted to the time of voltage pulse duration and the wave attenuation. The same situation occurs in case of the opposite electrode absence (so called one-electrode breakdown).

The work presents the results of experimental study of the one-electrode breakdown in 800 mm long tube with 15mm inner diameter filled with neon at pressure ~1 Torr. The breakdown was initiated by rectangular pulses with 1 – 2 kV amplitudes of positive polarity and duration of 1ms, which were applied to the one electrode while the opposite electrode remained free. Repetition rate of the pulses ranged from 1 Hz up to single pulse. The tube was used without metal screen but it was distanced from any conducting elements at least by 20 cm. Simultaneous recording of optical emission and current flowing through the active electrode allowed us to detect initial and moving breakdown stages.

The following scenario has been found out. The one-electrode breakdown consists of two main stages: 1) first breakdown between active electrode and wall leading to IW front formation; 2) IW propagation without return wave formation. The breakdown voltage only slightly differs from that of the two-electrode breakdown. The first breakdown appears when the applied voltage is higher than the static breakdown potential. After that the bright peak of intensity (curve 1 at the upper plot of Fig. 1) is detected near active electrode simultaneously with anode current peak (lower plot of Fig. 1). IW forms from space charge remaining after the first breakdown and moves toward the low potential tube area. This motion can easily be observed by recording IW optical emission in different points along the tube. The IW velocity was found to be in the range of 10^6-10^8 cm/s which is in accordance with the results of other works /2, 3/. It is well known that IW interacts with tube wall charging it up to the IW

front potential /3/. Within the propagation time between IW front and the anode the electric current flows through the electrode. This current loops with displacement current. It means that a non-compensated electrical charge must remain in the discharge volume which therefore deposits at the tube wall. This charge was estimated and measured. Its typical value ranges in $18 \cdot 10^{-9}$ - $36 \cdot 10^{-9}$ C depending on the conditions.

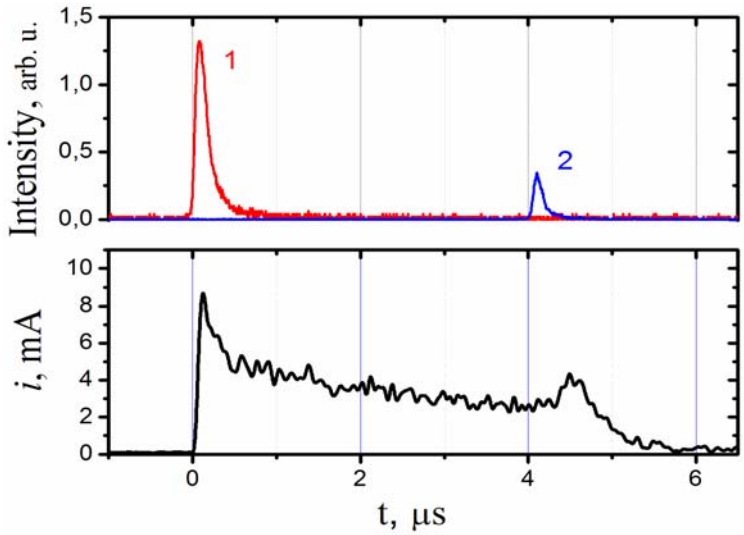

Fig. 1 - Neon 0.6 torr. Upper plot: first breakdown (1) and IW optical signals in 70 cm from the anode (2). Lower plot: current in the anode circuit

After approaching the opposite free electrode, the IW immediately disappears leaving the walls of the tube charged. It was found that in some conditions this charge is sufficient to cause repeated breakdown of gas and generate new IW, which also moves from active electrode after its grounding. Propagation of this wave is also accompanied with current in the anode circuit and movement of the light signal. In such situation the electrode cannot be the source of the charge transported to IW front due to the zero potential, therefore the necessary charge is delivered from the wall from which the first breakdown for the repeated IW starts. This wave passes the tube discharging its wall and finishing the one-electrode breakdown.

Acknowledgements. This work was supported by the Russian Foundation for Basic Research (grant No18-32-00223).

References

1. **Nedospasov A.V., Novik A.E.** ZhTF. 30 (1960) 1329-1336
2. **Vasilyak L. M., Kostuchenko S.V., Kudryavtsev N.N., Filugin I.V.** Physics – Uspehi (Advances in Physical Sciences), 164 (1994) 263 - 286.
3. **Langer R., Garner R., Hilscher A., Tidecks R. , Horn S**. J. Phys. D.: Appl. Phys. 41 (2008), 144011

3. NON-EQUILIBRIUM EFFECTS AND ATMOSPHERIC PRESSURE PLASMA PROCESSES, PLASMA IN AND IN CONTACT WITH LIQUID

PIN-HOLE BASED DISCHARGES IN LIQUIDS: GENERATION, PROPERTIES AND APPLICATIONS

F. Krčma, Z. Kozáková

Brno University of Technology, Faculty of Chemistry, Purkyňova 118, 61200 Brno, Czech Republic, krcma@fch.vut.cz

Electrical discharges generated in liquids or interacting with liquids became a hot topic in plasma chemistry research during the last decade /1, 2/. There are many different discharge (or plasma-liquid) configurations /2/ and new systems are still under development with respect to the specific requirements of selected applications. The physical as well as chemical processes running in these systems are very complex and they are still not fully understood /1/. This contribution focuses on plasma generation directly in the liquid phase in a so called pin-hole configuration.

Generation of the discharge directly under the liquid (mainly water) surface is not so simple because of high water permittivity and generally very dense environment. The breakdown voltage is about 1 MV/cm and thus specific electrode configurations are required /2/. One of such suitable systems is the pin-hole configuration /3-6/ where electric current passing through the liquid is focused in a very small area of about 1 mm2 (pin-hole). Liquid is strongly evaporated there by the Joule heating and electrical discharge is ignited at the bubble surface. Advantage of the pin-hole configuration is that the discharge is ignited in bubbles, so in gaseous phase and thus more or less any power supplies can be used. Discharge reactor can be supplied by DC or AC up to RF range at applied voltage of a few kV depending on the liquid conductivity. The system can be constructed as a batch system (two bigger liquid volumes connected by a small orifice, each part containing one electrode /5/) or one of electrodes can be directly mounted into the pin-hole and the whole system is a pen-like /6, 7/. The liquid conductivity is in the broad range from nearly zero (because of the discharge bubble principle) up to very high conductivities like the physiologic solution (15 mS/cm).

Discharge propagation is dependent on the solution conductivity as well as on the bubble diameter. The discharge is propagating along the bubble surface in the case of small bubbles and low conductive liquids /8/; propagation through the bubble volume is observed in the case of big bubbles /6/. If very short high voltage pulses (sub-nanosecond pulses of tens kV) are used for the discharge generation, streamers propagating directly through the liquid are observed /9/. Similar behavior can be occasionally observed using other supplying systems, as was reported for example in /10, 11/. If a non-pulsed power supply is used, the discharge shows self-pulsing behavior because the bubble containing the

discharge extends its volume up to the critical size and after its cavitation a new discharge is ignited in another bubble /6/.

The plasma-liquid interaction generates many different physical phenomena as well as it produces a lot of different active particles responsible for the consequent bulk liquid phase chemistry /1/. The plasma channel in the bubble usually directly touches the bubble surface and thus the direct interaction of electrons and ions with the liquid leads to mechanical deformation of the bubble surface, local heating followed by evaporation as well as dissociation and ionization of the liquid molecules. The light emitted by the discharge is in the broad range of spectrum including also VUV radiation (mainly of the hydrogen Lyman series) leading to the liquid photo dissociation and photo ionization. These agents together with the discharge thermal effect lead to the further liquid evaporation and bubble extension. When the bubble reaches some critical size it cavitates and a shock wave can be generated /6/.

The chemical active species formed by the electrical discharge in liquids are mainly hydrogen and oxygen atoms and OH radical if the discharge is formed in water solutions. Other active particles can originated from dissociated inorganic salts typically used for the liquid conductivity adjustment, various additives, organic molecules, etc. Moreover, it is possible to add some gas into the pin-hole region and thus change the discharge properties as well as to modify production of chemically active species /12/. These species diffuse into the bulk liquid where they can initiate very complex non-equilibrium chemistry. It must be noted that in the DC systems electrolytic effects must be taken into account, too. Thus combination of physical and chemical effects of the discharge can lead to the broad field of perspective applications.

Removal of various pollutants dissolved in water is the most studied application of all discharges interacting with liquids, i.e. including discharges generated directly in liquids. This application belongs to the bigger group of Advanced Oxidation Processes (AOPs) and uses more or less only active species generated by the plasma-liquid interaction. The decomposition is more or less non-selective and thus very complex solutions can be treated effectively. Synergistic applications of the plasma effect with photocatalysis or sorption were successfully tested besides the simple discharge application /13/. The main problems of these applications are their high energy consumption, limited energy efficiency and mainly formation of huge number of by-products; some of them can be even more hazardous than the original compound /14, 15/. The tests were done using various dyes, pesticides, pharmaceutics, hormones, organic acids and other hazardous pollutants.

Another broad application field is the synthesis of nanoparticles (NPs). The advantage of plasmas generated directly in liquids is that NPs formed by any discharge are very effectively cooled and dissipated into the bulk liquid. Thus

they do not form huge agglomerates. The size can be varied by the discharge conditions setting and the size distribution curve is very narrow. Moreover, if some organic additives are added into the liquid (or if organic liquid is used) the metallic NPs can be covered by very thin organic layers. Thus two processes are completed at the same time – formation of NPs and their surface treatment. The nanoparticles can be formed from the metallic salts dissolved in the liquid /16/ or by the direct sputtering of electrodes /17/ which serve as the NPs material source. The carbon NPs can be formed using organic liquids /18/.

Besides the direct NPs formation, the discharge generated in the liquid phase can also serve as a surface treatment tool for the previously formed nanoparticles /19, 20/.

Not only nanomaterials but also bigger objects can be treated using the electrical discharge in water. The successful application was tested for the surface cleaning of ancient glass objects by another electrode system /21/. Currently, our new system described in /6/ is tested for the surface cleaning of glass and ceramic historical objects.

Plasma in water solutions can be also generated at low power of a few watts. Because of the liquid environment there is a great potential for the biomedical applications. The first successful tests were focused on sterilization and bulk liquid bacterial inactivation. In general, application of plasma-liquid systems is a basis of all plasma medicine topics like sterilization, wound healing, proliferation, coagulation, ablation etc.

The pin-hole discharge can be used also as micro pump. The effect is based on the discharge asymmetry in positive and negative polarity. Thus in DC regime liquid is pumped preferentially in direction to the positive electrode /22/. The preferred pumping direction can be also selected using the asymmetric pin hole (or capillary) as it was described in /23/. The effect can also influence the applications mentioned above.

To conclude, the pin-hole and also other electrical discharges generated in liquids are very effective sources for the strongly non-equilibrium environment combining more physical and chemical processes. Thus they open a new dimension in the wet chemistry followed by a broad field of future applications across classical disciplines.

Acknowledgements. This work was supported by the Czech Ministry of Education, Youth and Sports, project No. LD14014 and under COST Action TD1208 international collaboration.

References

1. **Bruggeman P.J. et al** Plasma Sourc. Sci. Technol. 25 (2016) 053002.

2. **Vanraes P., Nikiforov A. and Leys Ch.** Electrical Discharge in Water Treatment Technology for Micropollutant Decomposition**,** in Plasma Science and Technology - Progress in Physical States and Chemical Reactions, INTECH (2015).
3. **Lukeš P et al** Plasma Chem. Plasma Proces. 33 (2013) 83-95.
4. **De Baerdemaeker F. et al** Plasma Sourc. Sci. Technol. 16 (2007) 341-354.
5. **Kozáková Z. et al** Eur. Phys. J. D 69 (2015) 100.
6. **Krčma F. et al** Plasma Sourc. Sci. Technol. 27 (2018) in print.
7. **Krčma F. et al** Plasma Medicine 6 (2016) 21-31.
8. **Babaeva N. and Kushner M.J.** J. Phys. D: Appl. Phys. 42 (2009) 132003.
9. **Šimek M. et al** Plasma Sourc. Sci. Technol. 26 (2017) 07LT01.
10. **Vanraes P., Nikiforov A. and Leys Ch.** J. Phys. D: Appl. Phys. 45 (2012) 245206.
11. **Ceccato P.H. et al** J. Phys. D: Appl. Phys. 43 (2010) 175202.
12. **Nikiforov A. et al** Plasma Sourc. Sci. Technol. 20 (2011) 034008.
13. **Vanraes P. et al** Water Research 72 (2015) 361-371.
14. **Kozáková Z. et al** Desalination 258(2010) 93-98.
15. **Banaschik R. et al** Water Research 84 (2015) 127-135.
16. **Mariottti D. at al** Plasma Proc. Polym. 9 (2012) 1074-1085.
17. **Ziashahabi A, Poursalehi R. and Naseri N.** Adv. Powder Technol. 29 (2018) 1246-1254.
18. **Xin Y. et al** Vacuum 151 (2018) 90-95.
19. **Galar P. et al** Sci. Rep. 7 (2017) 15068.
20. **Jirasek V. et al** RCS Adv. 6 (2016) 2352-2360.
21. **Hlochová L. et al** Proceedings of HAKONE XV, Brno 2016, 392-395.
22. **Totová I. et al** J. Phys. Conf. Ser. 516 (2014) 012007.
23. **De Baerdemaeker F. et al** Plasma Chem. Plasma Process. 27 (2007) 473-485.

PLASMAS IN LIQUIDS: CHARACTERISTIC FEATURES AND NANOTECHNOLOGICAL APPLICATIONS

V. Burakov, M. Nedelko, N. Tarasenka, A. Nevar, V. Kiris, N. Tarasenko

B. I. Stepanov Institute of Physics, National Academy of Sciences of Belarus
Nezalezhnasti Ave. 68, 220072 Minsk, Belarus, n.tarasenko@ifanbel.bas-net.by

In recent years, liquid-assisted plasma systems based on the electrical discharges generated inside or in contact with liquid have attracted much attention for various technological applications, including synthesis of nanoparticles (NPs) /1, 2/. Electrical discharge between two electrodes submerged in liquid (EDL) has proved to be attractive for the NPs synthesis due to high production rates, versatility and possibility of control over the particle size and size distribution function during the synthesis process. Besides, the non-equilibrium character of plasma in liquids with different temperatures for the plasma species can offer a multitude of possible reaction pathways and realize unattainable by conventional methods strongly non-equilibrium, high energy synthesis processes.

In addition to the discharges generated inside the liquid the gas-liquid interfacial discharges produced in contact with liquid (with liquid electrode) has also become of great interest and importance for nanomaterials synthesis and their functionalization directly in solutions /2/. Usually the discharge in contact with liquid is ignited between an electrode in atmosphere and another immersed into the solution. Igniting the microplasma results in the current flow through the solution and reactions are observed at the anode and cathode. At the anode, oxidation reactions lead to the dissolution of the solid metal into metal cations which are then reduced at the cathode by the microplasma to nucleate metal NPs.

It should be noted that the liquid assisted electrical discharges both within a liquid and at the gas-liquid interface were successfully applied for synthesis of NPs of metals, their oxides and carbides /1, 2/ The capabilities of these methods for synthesis of semiconductor NPs are much less studied. Besides, despite the literature already reports on the possibility of NPs surface functionalization by the plasma in contact with liquid /3/, the exact mechanisms and reaction paths are still not fully known.

In this paper we present the results of our experiments on the application of electrical discharge plasma in liquid for synthesis of carbon and silicon NPs as well as in combination with a laser-induced modification for synthesis of binary SiC and SiGe NPs. In addition, the targeted changes of the NPs properties (surface engineering) could be selectively achieved via microplasma surface treatment of the as-prepared NPs in colloidal solutions. The goal of production

of these particles is their future biomedical and photovoltaic applications.

Both silicon and carbon NPs with size less than 10 nm – so called quantum dots recently have attracted much attention due to their unique properties and broad prospective applications. Silicon NPs (Si-NPs) are characterized by the unique combination of size-dependent optoelectronic properties and biocompatibility, that explains the interest to Si-NPs for the applications in biological imaging and therapy, lasers and light emitting diodes, memory devices, energy source and sensor devices.

Carbon nanoparticles (C-NPs) owing to their excellent biocompatibility, chemical inertness, and size-selective photoluminescence properties may find increasing applications in modern biotechnology as more suitable alternatives to the traditional semiconductor quantum dots.

The synthesis of the silicon based nanocrystalline structures has also received great interest. In particular, silicon carbide nanocrystals are characterized by an enlarged band gap in comparison with silicon; have high thermal and chemical stability, exhibit luminescent properties. Nanostructures based on the alloys Ge_xSi_{1-x} are interesting due to the possibility of adjusting the lattice parameters and the width of the band gap, changing the mobility of charge carriers. Despite some progress in preparation of these structures, the development of new approaches for the controlled synthesis of nanocrystals based on silicon and germanium remains an urgent task.

The two types of plasma-liquid systems used in this work i.e. high-voltage discharge between two electrodes submerged into liquid and gas-liquid interfacial discharge have been described elsewhere /2, 4/. Briefly, a spark discharge (Fig.1a) was ignited between two electrodes, that depending on the required NPs composition could be graphite rods, two silicon plates, or silicon and graphite electrodes immersed in liquid (water, ethanol). The distance between the electrodes during the experiment was less than 1 mm and controlled to maintain the discharge parameters approximately constant. The alternating current discharge was initiated by applying a high-voltage pulse of 8.5 kV. The peak current was about 17 A with a duration of a single discharge pulse of 25 μs.

As the example Fig. 1b presents the TEM image of C-NPs produced by spark discharge between two graphite electrodes in water. It gives the evidence of near-spherical NPs formation with the sizes mainly distributed in the range of 2–5 nm with an average value of 3 nm. The inset in Fig. 1b shows the results of high resolution TEM studies of a separate particle. The presented HRTEM images reveal that particles are monocrystalline and the measured interplanar distances were found to be 2.06 Å that correspond well to the reflections between (111) planes in cubic carbon having diamond-like structure.

The capabilities of the method were extended to obtain silicon and silicon carbide particles. The small nearly spherical Si-NPs with the average size of

about 5 nm were obtained by electrical discharge with silicon electrodes. Analysis of the phase composition showed that NPs with the cubic silicon structure are major in the samples produced by the spark discharge both in water (90 vol.%) and ethanol (95 vol.%) with a small impurity of the oxide phase (SiO_2) in the samples synthesized in water and carbide phase (SiC) in the powder obtained in ethanol.

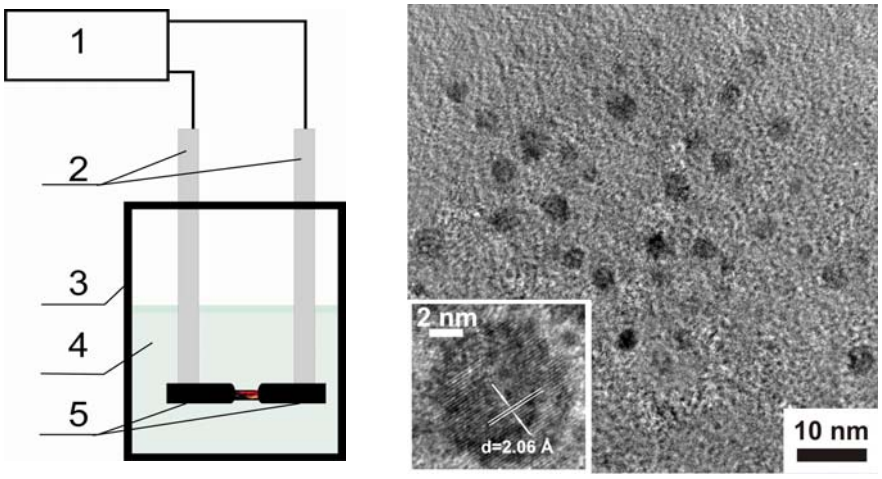

Fig. 1 - (a) Schematic diagram of the setup for NPs synthesis by electrical discharge in liquid: 1-power supply, 2-electrode holders, 3-reactor cell, 4-liquid, 5-electrodes; (b) typical TEM image of carbon NPs generated in water

In the case of the electrical discharge between Si and C electrodes in ethanol, the fabrication of SiC NPs with the dimensions less than 10 nm having a cubic (3C-SiC) internal structure was demonstrated. The synthesized NCs exhibited photoluminescence in blue-green spectral region.

To tailor the surface properties of the synthesized NPs, the prepared colloids were treated by atmospheric pressure two microplasma jets generated over the colloidal solution and coupled to the colloid. It is known that microplasmas generated at the surface of the colloidal solution induce low-temperature liquid-based non-equilibrium chemistry and therefore promote NPs surface functionalization /1,3/. A schematic diagram of the microplasma-liquid system with two plasma jets is shown in Fig. 2a. The discharge in contact with liquid was generated between a stainless-steel capillary electrode served as cathode and the surface of a liquid. The experiments were performed with argon flowing through the capillary tube. The discharge was ignited by applying the high voltage of 3.6 kV using a dc power supply. The discharge current was kept constant in the range of 1 - 5 mA.

To identify the surface functional groups of the initial and plasma treated NPs FT-IR was used. It was found that a different type of surface engineering

can be achieved by changing the liquid media. Typical example for C-NPs is presented in Fig.2. We suggest that the different surface chemistry activated in different solutions could be due to different reactions induced by plasma-electrons at the plasma–solution interface compared to plasma–water surface. Changing the surface groups is believed to be effective in improvement of photoluminescence properties of the synthesized C, Si and SiC NPs.

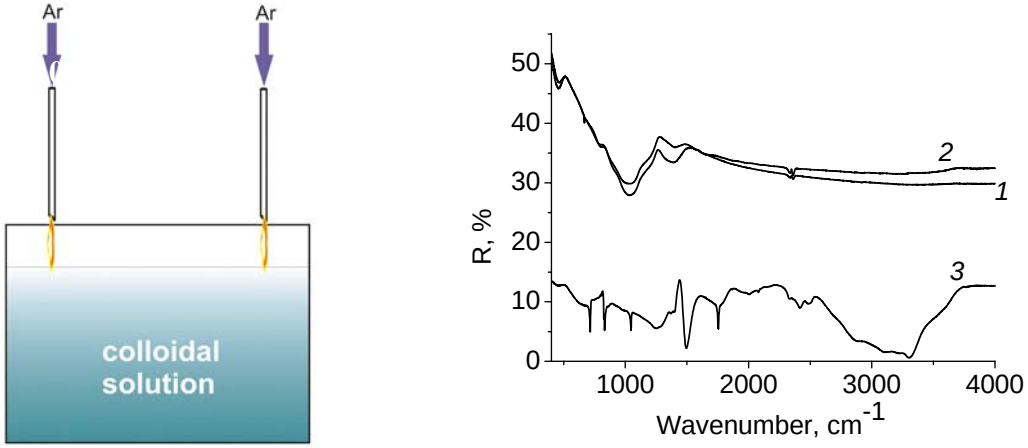

Fig. 2 - (a) Schematic diagram representing the double plasma–liquid system for surface engineering of NPs; (b) FT-IR spectra of as-prepared (1) and plasma processed C-NPs in water (2) and in ammonia solution (3).

Thus, the presented synthesis methods allow the adequate control over the surface characteristics and size distribution, by adjusting the synthesis conditions such as discharge parameters and solution composition.

Acknowledgements The work was supported by the National Academy of Sciences of Belarus under project Convergence 2.4.06 and the Belarusian Foundation for Fundamental Researches under Grant No. F18 MS-020. The authors would like to thank Dr. A.G. Karoza for the FTIR and Dr. A.P. Stupak for the luminescence measurements and fruitful discussions.

References

1. **S. Askari, M. Macias-Montero, T, Velusamy et al**, J. Phys. D: Appl. Phys. 48 (2015) 314002.
2. **V.S. Burakov, V.V. Kiris, M.I. Nedelko et al,** Eur. Phys. J. Appl. Phys 79 (2017) 10801.
3. **D. Mariotti et al,** Adv. Funct. Mater., 22 (2012) 954.
4. **A.A. Nevar, V.V. Kiris, M.M. Mardanian, M.I. Nedelko and N.V. Tarasenko,** High Temp. Mater. Processes. **20** (2016) 251–265

DENSITY EFFECTS IN THE NONEQUILIBRIUM ARC HELIUM PLASMA AT ATMOSPHERIC PRESSURE

L.G. Dyachkov, D.I. Kavyrshin, O.V. Korshunov, V.F. Chinnov

Joint Institute for High Temperatures, RAS, Izhorskaya 13, bd. 2, 125412 Moscow, Russia
dyachk@mail.ru

We report the results of spectral investigations of the occupancy of excited atomic states in the near-threshold region of atmospheric-pressure arc He plasma. This study required complex spectral determination of the main plasma parameters, including the electron concentration n_e and temperature T_e and occupancies n_k/g_k (g_k is the statistical weight of level k) of helium energy levels, which can be established based on the absolute intensities of HeI radiation lines.

Scheme of the experimental setup is shown in Fig. 1. The generator of atmospheric-pressure helium plasma is dc plasmatron *1* with thermionic tungsten cathode *2*, anode channel 4–5 mm in diameter, and an arc with self-stabilizing length. Two viewing windows *3* allow for transverse observation of the arc portion spaced from the cathode tip by 1.0–1.5 mm. In one observation direction, the light flux from the plasmatron passes through lens *4*, as a result of which an image of the plasma object is projected on the observation plane. The image can be scanned with a collimator *5* with an accuracy of 0.2 mm. Then, light is transferred (via optical fiber *6*) to an AvaSpec-2048 spectrometer *7* connected to a personal computer. The second light flux passes through the focusing lens *8* and is fed to a DFS-452 spectrograph *9*, to the output of which a CCD camera *12* is mounted (it is connected to the computer as well). A removable mirror *10* allows one to record the spectra of the reference sources *11* (tungsten, deuterium, or halogen lamp) without disassembly of the plasmatron in order to calibrate the radiation intensity arriving through the spectrograph channel *12*. The schematic also includes a collimator *13* reproducing the construction of the plasmatron viewing window for complete imitation of the optical path of plasma radiation in the experiment. A Toshiba TCD1304DG CCD line array or an Andor matrix camera was installed at the output of the DFS-452 spectrograph; the instrumental function of the DFS–Andor system is $\delta_{ins} \approx 0.3$ Å, which made it possible to resolve the helium atomic line profiles with characteristic widths of 1 Å or more in the studied regimes. The AvaSpec-2048 spectrometer allows one to identify the intensities of individual lines due to simultaneous recording of the spectrum in a wide range (200–1100 nm).

The calibration procedures and Abel transform of the recorded "chord" spectra makes it possible to pass from relative measurements to local values of the absolute intensities of spectral lines and concentrations of radiating atoms and ions of helium.

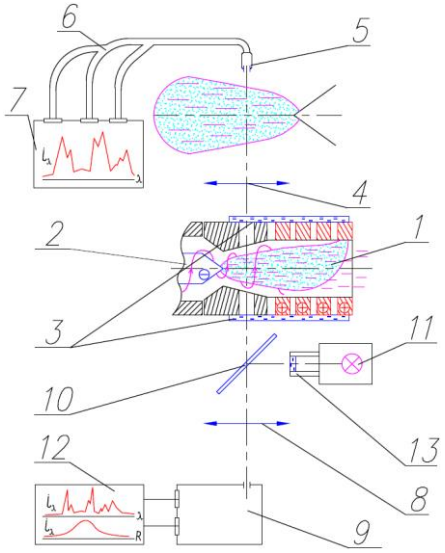

Fig. 1 – Scheme of the experiment : (*1*) dc plasmatron, (*2*) cathode, (*3*) viewing window, (*4*, *8*) lenses, (*5*, *13*) collimators, (*6*) optical fiber, (*7*) spectrometer, (*9*) spectrograph, (*10*) removable mirror, (*11*) reference source, (*12*) CCD camera

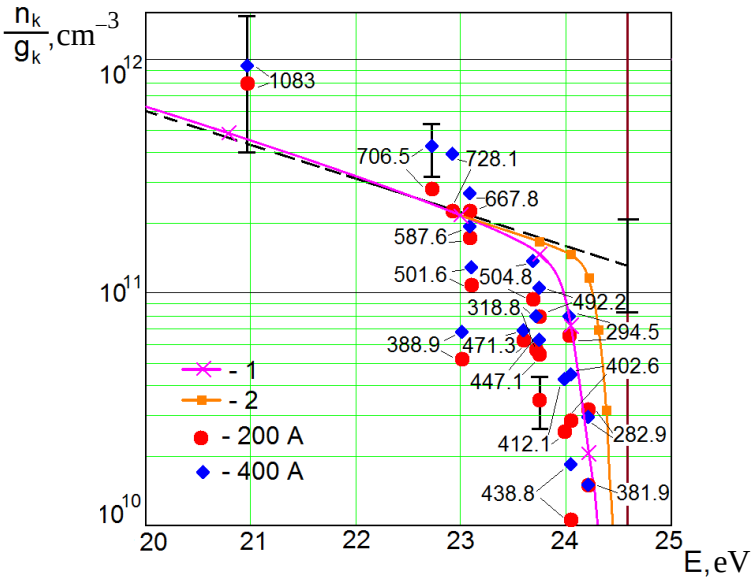

Fig. 2 – Occupancies of the HeI levels in atmospheric-pressure arc plasma at the arc currents of 200 and 400 A depending on the excitation energy; the wavelengths of the HeI lines (in nm) are presented; the dashed line is the ionization equilibrium at $n_e = 9\times10^{16}$ cm^{-3} and $T_e = 3$ eV; (*1*, *2*) calculation based on the MDA with allowance for the density effects by the NI (*1*) and UM (*2*) models. The vertical line is the ionization threshold with the density effects disregarded

Fig. 2 shows the occupancies of HeI excited levels n_k/g_k at arc currents of 200 and 400 A. The occupancy distribution is characterized by strong ionization deviation from equilibrium and, on the whole, is in agreement with the previously obtained experimental data /1–3/. The electron concentration was measured based on the Stark broadening of the series of HeI lines, and the electron temperature was determined by the intensity ratio of ion and atomic helium lines. The values obtained for the central part of the arc channel ($n_e \approx 9\times10^{16}$ cm^{-3} and $T_e = 3.0$ eV) allow a comparison of the spectrally measured distribution n_k/g_k with ionization equilibrium $n_k^0 = n_e^2/K_{k0}(T_e)$, where

$$K_{k0} = \frac{2g_1^+}{g_k}\left(\frac{2\pi m T_e}{h^2}\right)^{1.5}\exp\left(-\frac{I_k}{T_e}\right)$$

is the constant of ionization equilibrium between the kth atomic level and the ion ground state and I_k is the ionization energy of level k.

The dashed line in Fig. 2 corresponds to the equilibrial (with respect to ions) occupation of atomic levels n_k^0/g_k. The experimental occupancies of the ground n_1 (not shown in Fig. 2) and first excited n_2 levels are higher than the equilibrium values, and n_1 exceeds n_1^0 by two orders of magnitude. Similar ionization deviation from equilibrium was previously observed in hydrogen /4/

and helium /5/ plasmas and explained using modified diffusion approximation (MDA) /6/. However, the experimental n_k/g_k values for levels with the ionization energy ≤1 eV are smaller than the equilibrium ones and sharply decrease when approaching the ionization threshold, thus becoming more deviated from the ionization-equilibrium condition $n_k = n_k^0$, which should be satisfied at the upper excited levels, according to the concepts of low-temperature plasma kinetics /6/.

This specific feature of highly ionized plasma can only be due to density effects, leading to the destruction of the excited atomic states in plasma microfields /7, 8/. The superposition of the quasi-static (ion) microfield on the field of interaction between the outer electron and the atomic core induces a potential barrier for this electron. The atomic levels above the barrier top are not implemented; continuous-spectrum states occur instead. The level-implementation probability is determined by the integral of distribution function $P(F)$ of the quasi-static (ion) microfield:

$$w_k = \int_0^{F_k} P(F)dF ,$$

where F_k is the field value for level k at which it is at the top of the potential barrier. Correspondingly, the continuous-spectrum state arises with probability $1 - w_k$. The transition region, in which the spectral lines are gradually replaced with continuum, is extended with an increase in the plasma density (see, e.g., /7, 8/ and references therein).

A simple analytical method to calculate w_k was proposed in /9/. An empirical approximation was given in /10/. However, for any method of calculating w_k, the choice of the F_k value is a critical factor. For this, one of the two simplest models is usually applied: uniform microfield (UM) and nearest ion (NI) /7, 8/. The form of the microfield distribution function is not so important: for example, the calculations with $P(F)$ from /11/ and /12/ yield almost identical results. It is assumed in the UM model that the atom is in a uniform (on the atomic scale) quasi-static electric field formed by all ions; in this case, $F_k = I_k^2/4e^3$, where e is the elementary charge. In the NI model, the atom is in the Coulomb field of the nearest ion, and $F_k = I_k^2/16e^3$ in the case of single ionization. A comparison of the calculation data with the experimental spectra shows /13/ that, for inert gases that are heavier than helium, the best results are provided by the NI model even at the nonideality parameter $\gamma = e^2/r_s T_e \sim 0.1$, where $r_s = (4\pi n_e/3)^{-1/3}$. At the same time, the UM model turns out to be more acceptable for hydrogen plasma /14/. A similar problem for the lightest inert gas (helium) has not been solved.

Fig. 2 shows the calculation results for the occupancies n_k/g_k of the excited HeI states by the MDA method /6/ with allowance for their implementation probability w_n according to /9/ the NI and UM models. The calculation results

by the NI model are in much better agreement with the experimental data compared with the UM model, which yields significantly overestimated occupancies of highly excited HeI states. One can conclude that the NI model is applicable to all inert-gas atoms and, apparently, to all atoms, except for hydrogen.

The calculation based on MDA (with destructions of states in microfields disregarded) yields close-to-equilibrium occupancies of all excited HeI levels, because all these levels are above the "bottleneck" /15, 6/, which, in this case, is between the ground and first excited levels; this is related to the high HeI excitation potential.

Acknowledgements. This work was supported by the Russian Science Foundation grant No. 14-50-00124.

References

1. **Kelleher D.E.** JQSRT, 25(1981) 191–220.
2. **Vitel Y., Bezzari M.El., D'yachkov L.G. and Kurilenkov Yu.K.** Phys. Rev. E, 58(1998) 7855–7863.
3. **Jonkers J., van de Sandle M., Sola A., Gamero A. and van der Mullen, J.** Plasma Sources Sci. Technol., 12(2003) 30–38.
4. **Batenin V.M., Zrodnikov V.S., Roddatis V.K. and Chinnov V.F.** Teplofiz. Vys. Temp., 13(1975) 270–278.
5. **Batenin V.M., Zrodnikov V.S., Roddatis V.K. and Chinnov V.F.** Fiz. Plasmy, 2(1976) 831–837.
6. **Biberman L.M., Vorob'ev V.S. and Yakubov I.T.** Phys.–Usp., 15(1973) 375–394.
7. **Sevastyanenko V.** Contrib. Plasma Phys., 25(1985) 151–197.
8. **Hummer D.G. and Mihalas D.** Astrophys. J., 331(1988) 794–814.
9. **D'yachkov L.G.** High Temp. 35(1997) 811–813; JQSRT, 59(1998) 65–69.
10. **Gavrilov V.E. and Gavrilova T.V.** Opt. Spektrosc., 63(1987) 429.
11. **Hooper C.F.** Phys. Rev., 165(1968) 215–222.
12. **Kurilenkov Yu.K. and Filinov V.S.** Teplofiz. Vys. Temp., 18(1980) 657–667.
13. **D'yachkov L.G., Kurilenkov Yu.K. and Vitel Y.** JQSRT, 59(1998) 53–64.
14. **Kazanskii A.K.** Opt. Spektrosc., 64(1988) 448; 65(1988) 826.
15. **Byron S., Stabler R.C. and Bortz P.I.** Phys. Rev. Lett., 8(1962) 376–378.

PLASMA POWER INTERRUPTION; REVEALING MECHANISMS AND PROCESSES

Joost van der Mullen
Université libre de Bruxelles, 50 av. F.D. Roosevelt, 1050 Brussels, Belgium
jjamvandermullen@gmail.com

The power interruption (PI) technique is a 'powerful' experimental method to get insight in plasma phenomena and time-scales. The procedure is based a sudden disturbance of the Steady State (SS) by dropping the driving power (PI) to zero, after which the plasma is re-ignited (RI). The sequence of PI and RI generates various equilibrium disturbing and restoring mechanisms and insight in phenomena can be obtained by following the response to PI and RI on various system-levels. Of especial importance is the response of the electron gas, {e}. This can be studied via optical emission spectrometry (OES) or better, Thomson scattering (TS). In the 1960s the PI method was applied to arc plasmas /1/.

In this presentation we will discuss PI experiments on various plasma sources. We start with the PI method applied to an inductively coupled plasma (ICP) generated in an atmospheric argon flow /2-4/. In SS the applied power is about 1kW, which results in a robust plasma with a radial size of r ≈ 9mm, an electron density of $n_e \approx 10^{21} m^{-3}$ and electron temperature $T_e \approx 0.8$ eV.

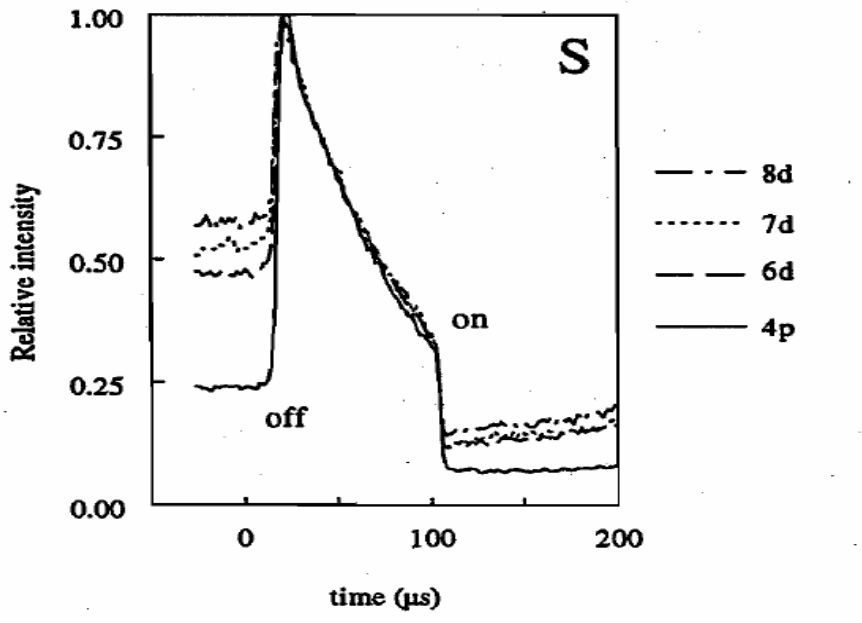

Figure 1, giving the response of 4 Ar- lines as obtained by OES, shows that:
1) at power switch-off (PI) all these lines jump-up in intensity within a few μs,
2) after which they decay in more or less the same time-scale of about 100 μs,
3) the plasma re-ignition (RI) at $\tau_{off} \approx 100\mu s$ shows sharp decreasing intensities,
4) after which a slow increase follows back towards SS values.

The responses found in fig 1 reflect the following changes in {e} /2,3/:
1) Cooling: $T_e \downarrow T_e^*$ the T_e at SS rapidly falls down to a lower T-value at PI,
2) Decay of n_e due to recombination and/or transport (diffusion),
3) Heating $T_e^* \uparrow T_e^{**}$ needed to create new ei pairs; where $T_e^{**} > T_e$.
4) Ionization, the n_e increases and approaches the steady state (SS) value.

Several variations can be applied to the SS plasma settings like the pressure, power, the nature of the plasma gas etc.. Moreover we can play with τ_{off}, the period of PI. It was found /4/ that increasing τ_{off} leads to higher values of T_e^{**}. But the variation in τ_{off} will not change the response of n_e and T_e at PI. These are quite different: the T_e (cooling) responds much faster (*~1μs*) than the n_e-decay by recombination and/or diffusion (τ_{ne} *~200μs*). The latter strongly depends on the plasma conditions; for smaller plasmas we can expect that diffusion will force τ_{ne} to lower values.
The intensities given in fig.1 are scaled to the corresponding maximum values, making clear that, during PI, all lines decay with more or less the same time constant. This supports the idea that the levels are ruled by the Saha balance of ionization and recombination. For the 4p level this reads:

$$e\,(\varepsilon_{fast}) + Ar\,(4p) \leftrightarrow e\,(\varepsilon_{slow}) + Ar^+ + e(\varepsilon_{slow}) \qquad (1)$$

which shows (left to right) that a fast electron ionizes and thus *depopulates* the atom Ar(4p) whereas the opposite *populates* Ar(4p) by 2e recombination. At PI fast electrons will disappear, which explains the upward jump at switch-off. The higher the ionization potential I_p the larger the jump will be.

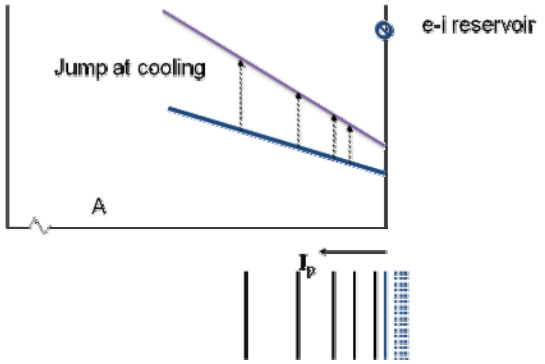

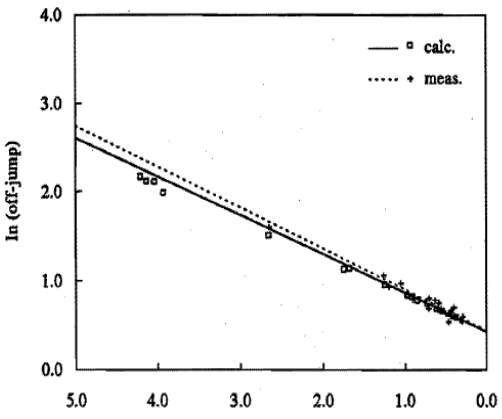

This is depicted in Figure 2a giving $\eta(p)=n(p)/g(p)$, the density $n(p)$ per statistical weight $g(p)$, versus the ionization potential I_p of the level in a semi-log plot. The densities are ruled by the Saha formula (eqn.2) just before and just

after the cooling (PI). The lower graph in fig. 2a corresponds to T_e, the upper to T_e^*. The jumps for four levels are depicted. It is seen that for lower levels (large I_p-values) the jumps are higher. The value of the jumps can be derived from the Saha equation. Before the PI (in SS) the density of level p satisfies

$$\eta^s(p, T_e) = \eta_e\, \eta_+\, h^3/(2\pi m_e\, kT_e)^{3/2}\, exp\,(I_p/\, kT_e) \qquad (2)$$

where $\eta_e = n_e/2$ and $\eta_+ = n_+/g_+$ while $\eta^s(p,T_e) = n^s(p,T_e)/g(p)$ is the Saha density of the states in level p for the electron temperature T_e. Just after PI the Saha density is $\eta^s(p, T_e^*)$, thus eqn. 2 where T_e is replaced by T_e^*. Dividing $\eta^s(p,T_e^*)$ by $\eta^s(p, T_e)$, introducing $\gamma = T_e/T_e^*$, while assuming $\eta_e = \eta_e^*$ and $\eta_+ = \eta_+^*$ gives

$$ln\,\{J(p)\} = 3/2\, ln\,\gamma + I_p/kT_e\,(\gamma - 1) \qquad (3)$$

Here $J(p) = \eta^s(p,T_e^*)/\eta^s(p,T_e) = I(p,T_e^*)/I(p,T_e)$ is the jump at cooling; it is assumed that the jump in densities is the same as that of the intensities (I), which is justified if the plasma is optically thin for the optical transitions under study. This method of plotting the jump $J(p)$ versus I_p directly provides T_e and T_e^*. There is no need for intensity calibration nor transition probabilities.

An example /3/ of such a plot of ln(J(p)) versus I_p is given in figure 2b from which we find that $\gamma = 1.43$ and $T_e = 0.86$ eV; meaning that $T_e^* = 0.61$ eV. However, other methods reveal that the heavy particle temperature in SS is much lower, namely $T_h \approx 3.9$eV. Thus $T_e^* > T_h$ and we have to conclude that after PI the electron temperature does ***not*** fall down to T_h. Apparently the electrons remain heated; this *post-heating* mechanism is however unclear. Evidently it cannot be the EM field since the EM-power is switched-off!

The presence of {e}-post-heating in the ICP was confirmed by performing Thomson scattering (TS) during PI (and RI) /4/.

If we apply PI to a Surface-wave Induced Plasma (SIP) in pure Ar at *low pressure* (~20mbar) we get a different situation in which, due to the low n_e-values, the Saha responses such as given in figs. 1 and 2 are absent. Thus the OES method to determine T_e and T_e^* cannot be used. By applying TS during PI, it was found that the post-heating of {e} is not any longer (clearly) present. However, an addition of a small amount of N_2 or CO_2 to the Ar-SIP again leads to a prominent post-heating /5/. The figure below shows that, due to the addition of 1% of N_2 or CO_2, the T_e^* during PI will stay as high of 70% of the value attained under steady state (SS) conditions, thus $T_e^* \approx 0.7\, T_e$. Since the post-heating cannot be EM in nature; we have to look for other energy sources.

The most likely candidate is the vibrational system of the molecules N_2 and CO_2. The energy distribution of these vibrational levels is an-harmonic; they are separated by energy gaps that decrease for increasing vibrational energy.

This implies that in mutual collisions molecules with high vibrational energy, E_{vib}, will increase further in E_{vib} while those with low E_{vib} will decrease. This so-called upward-pooling via VV collisions leads to the following scenario:
1) In SS the {e} having a large n_e-value will, via electron-molecule collisions, impose their temperature, T_e, on the vibrational distribution function, VDF.
2) At PI, when n_e goes down, the VV collisions between molecules become more important and tend to change the VDF such that the excitation temperature T_{ex}, high in the VDF will increase.
3) This high T_{ex} –value will in τ_{off} be imposed on the {e}, thereby increasing T_e^*.

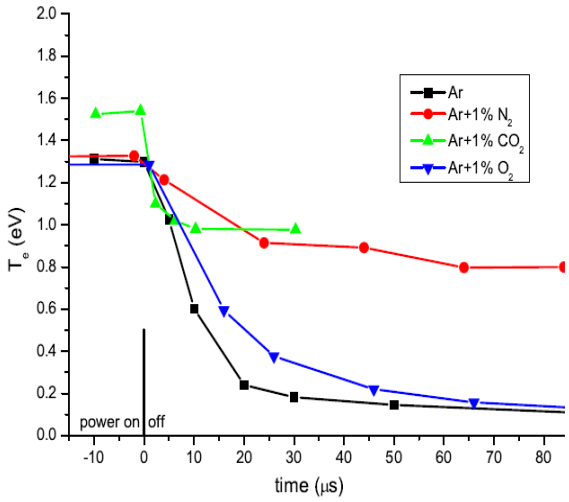

A subsequent stage in the scenario is that:
4) The VV collisions will, during τ_{off}, support dissociation of molecules.
In /6/ it was found that the PI technique applied to microwave plasmas in pure CO_2 indeed leads to more dissociation (CO_2 -> CO+O). The final dissociation efficiency depends on the SS power, the pressure, gas temperature and the repetition rate of PI! As mentioned above, a longer τ_{off} leads to higher T_e^{**} values at RI /4/. This will support the {e} in imposing their temperature on the VDF. For a proper understanding of this frequency-effect /6/ we need more insight in phenomena and time-scales. There is still much work to be done!!

References:

1. **Aleksandrov V.Y. et al.** Opt. Spectrosc. (USSR) **18**, 107 (1965)
2. **Farnsworth P.B. et al.** *Spectrochim. Acta* 42B, 393 (1987).
3. **Fey F.H.A.G.,** thesis http://dx.doi.org/10.6100/IR391169
4. **Sande M.J. van de** thesis http://alexandria.tue.nl/extra2/200210414.pdf
5. **Hubner S. et al**. Plasma Proces. Polym. DOI:10.1002/ppap.201300190 2014.
6. **Britun N. et al.** J. Ph ys. D: Appl. Phys. **51** (2018) 144002 (13pp).

THE DETERMINATION OF THE CONTENT OF METAL IONS IN WATER SOLUTIONS BY USE OF A DC-CURRENT DISCHARGE WITH A LIQUID CATHODE

N. Sirotkin, V. Titov

G.A. Krestov Institute of Solution Chemistry of the Russian Academy of Sciences, 153045, Russia, Ivanovo, ul. Akademicheskaja, d. 1, e-mail: alexsad8@yandex.ru

The quantitative analysis of metal ions in water and aqueous solutions by the method of optical emission spectroscopy of plasma of atmospheric pressure discharges is one of the promising applications of plasma-solution systems /1/. This direction of use of discharges is directly connected with the processes of transferring the components of the solute into the plasma under the action of ion bombardment of the electrolyte cathode. The lines of metal atoms which are present in solutions in the form of cations are detected in the emission spectra. The method has a high sensitivity (up to 10^{-9} g/l /2/), low-power /3/, does not require expensive equipment and allows analysis under atmospheric pressure without using an inert atmosphere. At the same time, a number of studies have noted the dependence of the intensity of the emission lines of atoms in the plasma on the pH of the solution /3, 4/. In addition, the effect of various additives to solutions on the detected line intensities has been established /5/. Analysis of the high salinity solutions this is the most difficult task. The composition of the plasma will be determined by the composition of the electrolyte cathode and the additional electrolytes in the sample will change the emission intensity of the lines of the analyzed metals. Easily-ionizing components of additional electrolytes by transfer processes alter the composition of the gas phase and they lead to a change of discharge characteristics. Thus, it can be expected that the composition of the cathode liquid electrolyte (solution) will affect the intensity of emission lines analyzed metals even at constant concentration of the corresponding ions in solution.

The aims of this work are to perform an experimental study of the effect of the composition of an electrolyte cathode on the emission intensity of metal atom lines and to analyze the possibility of determining the concentration of metal ions in a liquid cathode by the actinometry method of plasma.

Direct current (DC) discharge (i = 40 – 50 mA) was excited by applying high voltage between the surface of aqueous cathode and metallic anode which placed at the position 1–10 mm above the liquid surface /6/. The cell was equipped with a glass trap to collect the condensate formed by spraying the liquid cathode. Water solutions of nickel, copper, barium, magnesium chlorides with concentrations of 10^{-4} – 10^{-1} mol/l were used as cathodes. Solution of sodium chloride (c = 0.05 – 0.5 mol/l) is used as an additional electrolyte.

Atoms of potassium, cations of which in solution were present in a known concentration, were used as a component - actinometer in plasma. The electric field strength in plasma (E) and the cathode voltage drop (U_c) were calculated from dependences of the discharge voltage on the inter-electrode distance. These dependencies are approximated by a linear function with a correlation coefficient is not less than 0.99. The emission spectra of the positive column (λ = 200 – 950 nm) were recorded by the AvaSpec-3648 spectrometer. Gas temperature was found fromthe intensity distribution in the radiation band of N_2 ($C^3\Pi_u \rightarrow B^3\Pi_g$, 0–2) transition as described in /7/. To evaluate the reproducibility of the results were performed five independent measurements. Limits of the confidence intervals were calculated with a confidence level 0.9.

The emission spectrum of the discharge with a liquid cathode containing the Ba^{2+} ions (10^{-4} g/l), K^+ (10^{-4} g/l) ions is shown in Fig. 1. A solution of sodium chloride (c = 0.5 mol/l) was used as background additional electrolyte.

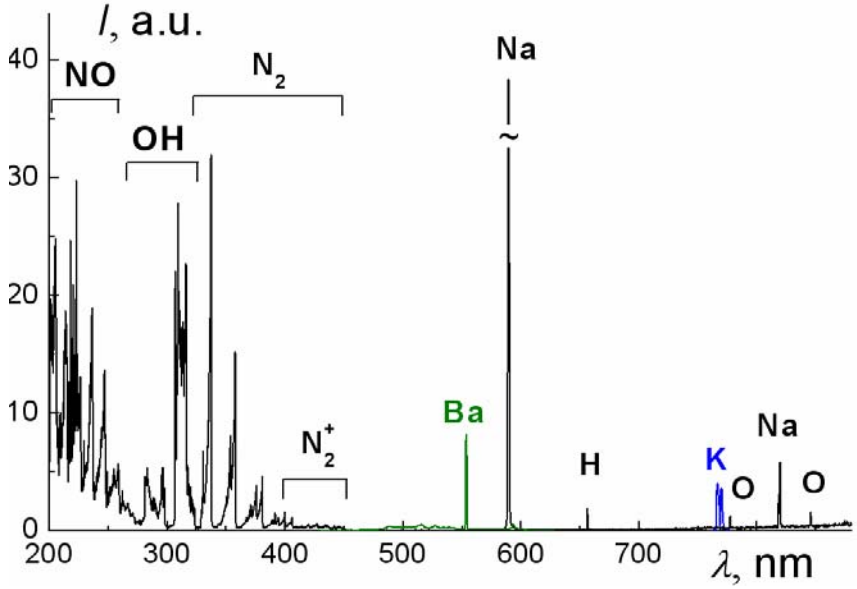

Fig. 1 - The emission spectrum of the discharge (i = 50 mA)

The emission intensities of analysed atoms lines are directly proportional to the concentration of respective cations in the liquid cathode, but the values are significantly various for different concentrations of sodium chloride. The dependences of the relative intensity of Cu atoms emission lines (λ = 324.7 nm), Ni atoms emission lines (λ = 361.9 nm), Mg atoms emission lines (λ = 285.3 nm), Ba atoms emission lines (λ = 553.6 nm) on the concentration of the additional electrolyte NaCl are shown in Fig. 2. Minimum value of the intensity is observed without of NaCl in the solution, the maximum is observed in additional electrolyte concentration 0.05 mol/l. At least there are two reasons of influences of the sodium chloride additive in liquid cathode on the intensity of emission analyzed atoms. First, NaCl additive changes the value of the cathode

voltage drop which in its turn determines the average energy of positive ions bombarding the surface of liquid cathode and the rate of cathode sputtering. Second, the electric field strength in plasma and character of the electron energy distribution function are changed and as a result the rates of excitation of the emitting states by electron impact are altered.

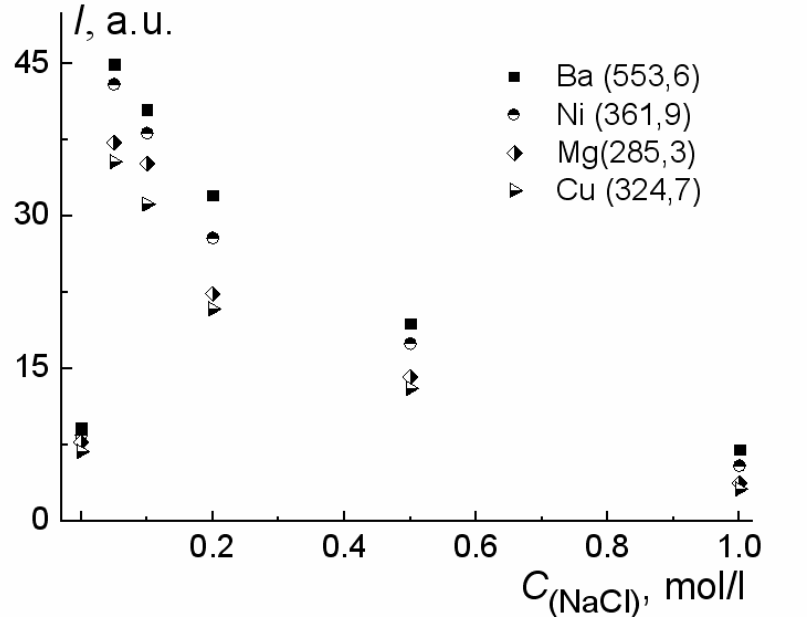

Fig. 2 - The intensities of the analysed atoms lines at various concentrations of sodium chloride in solution

Thus, the presence of any additional cation can affect the reliability of the obtained values of the concentrations of the analyzed ions at the analysis of the solution by the method of emission spectroscopy of plasma.

A possible solution to this problem is to add an aliquot of the metal salt solution to the measured solution and further determination of the number of the atoms of the metal to be analyzed in the plasma by actinometry. In this case, the actinometer was acted upon by the metal atoms. Using the transfer coefficients the concentrations of the corresponding cations in the solution are determined from the known number of atoms of the analyzed metal in the plasma. The actinometric component in the plasma was potassium atoms, the cations of which were added to the solution being analyzed. To determine the concentration of the metals under analysis we used the ratio of the emission intensities of the K atoms (λ=766.9 nm, $4p \rightarrow 4s$), the Cu (λ=324.8 nm, $3d^{10}(^1S)4p \rightarrow 3d^{10}(^1S)4s$) , Ni (λ = 361.9 nm, $3d^9(^2D)4p \rightarrow 3d^9(^2D)4s$).

The results of the analysis of solutions of nickel and copper (II) chlorides are presented in the Table 1.

Table 1 - The concentrations of ions of copper (II) and nickel in solution obtained by the method of actinometry of plasma

Experiment Conditions	$C(Cu^{2+})$, g/l		$C(Ni^{2+})$, g/l	
	input	obtained	input	obtained
i = 50 mA, C_{NaCl} = 0 mol/l	$5 \cdot 10^{-6}$	$(4.8 \pm 0.3) \cdot 10^{-6}$	$5 \cdot 10^{-6}$	$(4.7 \pm 0.4) \cdot 10^{-6}$
i = 50 mA, C_{NaCl} = 0 mol/l	$1 \cdot 10^{-5}$	$(9.5 \pm 0.7) \cdot 10^{-6}$	$1 \cdot 10^{-5}$	$(9.3 \pm 0.8) \cdot 10^{-6}$
i = 50 mA, C_{NaCl} = 0.001 mol/l	$5 \cdot 10^{-6}$	$(4.6 \pm 0.5) \cdot 10^{-6}$	$5 \cdot 10^{-6}$	$(4.9 \pm 0.4) \cdot 10^{-6}$
i = 50 mA, C_{NaCl} = 0.1 mol/l	$5 \cdot 10^{-6}$	$(4.5 \pm 0.5) \cdot 10^{-6}$	$5 \cdot 10^{-6}$	$(4.6 \pm 0.5) \cdot 10^{-6}$

Thus, the method of optical actinometry of atmospheric pressure discharge plasma makes it possible to determine the concentrations of metal cations in solutions oblivious of the presence of additional electrolytes.

Acknowledgements. The study was supported by Russian Foundation for Basic Research according to the research project 16–33–60061 mol_a_dk.

References

1. **Mezei P. and Cserfalvi T.** Sensors, 12 (2012) 6576-6586.
2. **Yang C., Wang L., Zhu Z., Jin L., Zheng H., Belshaw N. S. and Hu S.** Talanta, 155(2016) 314-320.
3. **Shekhar R., Karunasagar D., Ranjit M. and Arunachalam J.** J. Anal. Chem., 81(2009) 8157-8166.
4. **Bencs L., Laczai N., Mezei P. and Cserfalvi T.** Spectrochim. Acta, Part B., 107(2015) 139-145.
5. **Webb M. R., Andrade F. J. and Hieftje G. M.** J. Anal. At. Spectrom., 22(2007) 766-774.
6. **Sirotkin N.A., Titov V. A**. Plasma Chem. Plasma Process., 37(2017) 1475-1490.
7. **Titov V. A., Rybkin V. V., Smirnov S. A., Kulentsan. A L. and Choi H.S.** Plasma Chem. Plasma Process., 26(2006) 543-555.

PLASMA-ELECTROLYTE PRODUCTION OF STAINLESS STEEL POWDER FOR SELECTIVE LASER MELTING TECHNOLOGY

L.N. Kashapov[1], R.N. Kashapov[1,2], N.F. Kashapov[1]

[1] Engineering Institute, Kazan Federal University, 420008, Russia, kashlenar@mail.ru
[2] Laboratory of Radiation Physics, Kazan Physical-Technical Institute of the Kazan Scientific Center of the Russian Academy of Sciences, 420029, Russia

Abstract. Search of new methods for obtaining metallic powders satisfying additive technologies requirements is an urgent task. In the work, studies have been carried out to obtain a 17-4 PH powder in a gas discharge plasma with a liquid electrode. Regularities characterizing the influence of input power, voltage and discharge current on the properties of the powder obtained are revealed. The combustion conditions of discharge are determined, at which minimum oxidation of powder particles is observed.

1. Introduction

Selective Laser Melting, metal three dimensional printing, are increasingly used in industry /1/. This is primarily due to the appearance of new materials for 3D printing of metal and ceramic products. /2/. At the moment, several technologies are known for the production of metal powders for SLM. Disadvantages of these technological productions: a high particle sizes dispersion from 1 μm to 200 μm, which requires additional cleaning and separation, transition difficulty of the plant to the another material production, high energy consumption of the process, the nanometer range controlling and extracting particles difficulty, expensive equipment. Concept of Additive Manufacturing involves individual product geometry, as well as the ability to use a wide range of materials /3/. Next stage in the development of the SLM process is the creation of technologies for the micro and nanopowder production, which are devoid of the above disadvantages. One solution is to use a gas discharge with liquid electrodes /4,5,6/, this method is simple and does not require expensive equipment. Therefore, the aim of the work was to to obtain a 17-4 PH powder in a gas discharge plasma with a liquid electrode.

2. Main part

Our starting point was a survey paper /7/, which describes the main methods of obtaining metal nanoparticles and their oxides. Therefore, the set of possible

variants of studies was greatly reduced, and the experimental setup was optimized.

Fig. 1 shows the functional scheme of the experimental setup, which consists: an electric power supply system 1, an electrolytic bath 2, an electrode system 3, an oscilloscope 4, an additional resistance 5, a voltmeter 6, an ammeter 7 and a thermocouple 8. With electrode system, the distance between the anode and the electrolyte solution was monitored. With oscilloscope 4, the shape of the applied voltage and current was monitored, the ammeter and voltmeter were used to measure discharge current and voltage. The electric power supply system 1 represents a high-voltage DC power source for creating and maintaining electric discharge combustion with smooth regulation of the output voltage in the range from 0 - 3 kV and current 0-10A. Voltage and discharge current were measured by two digital universal measuring devices MMH-930 and APPA 109N, the relative error of measurement is 0.8%.

Burning gas discharge occurs between the metal anode made from stailness steel 17-4 PH and an electrolytic cathode. The anode is a metal cylinder with diameter 5 mm, located above electrolyte surface at height 2 mm. As the electrolytic cathode, aqueous solutions of NaCl and Na_2CO_3 with a concentration of 0.1-1% by weight were used.

When certain current and voltage values are reached, a process of spraying the metal anode is observed. Most of the powder enters the electrolytic cathode and crystallizes. In parallel, there is a process of liquid electrode evaporation. The resulting powder was cleaned by deionized water and dried in a drying oven. The morphology of the powder was studied using a scanning electron microscope, Carl Zeiss EVO 50. The dispersion composition was determined by sieving with a sieve set of sieves of from 10 to 300 microns. The average sieving time was 45 minutes. The microhardness was measured with a PMT-3M device, using the Vickers method. The powder was mixed with cyanoacrylate and pressed into tablets, which were then ground and polished. The resulting microsections were examined at a load of 50 gauss, a holding time of 25 s and 5 prints. Analysis of the chemical composition was determined with the aid of a scanning electron microscope attachment of an energy-dispersive electron-probe spectrometer Oxford Instruments Inca X-act.

The formation of the powder occurs when the surface temperature of the anode reaches the appropriate solidus temperature. When the liquidus temperature is reached, the electrode is melted and large drops of metal are formed. Proceeding from this, the powder can be produced in the temperature range of the liquidus and solidus anode. An increase in temperature will lead to an increase in the productivity of the powder, but with an increase in the particle size of the powder.

The largest amount of powder is obtained by a size smaller than 40 μm.

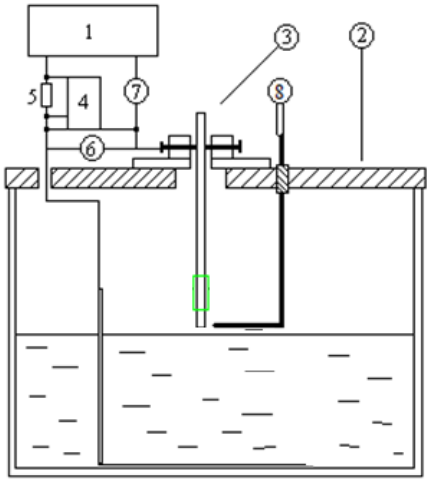

Fig. 1 – The scheme of the experimental setup

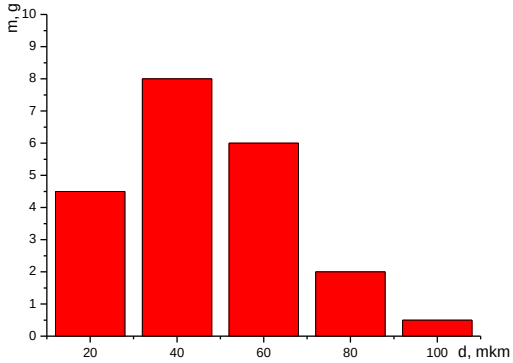

Fig. 2 – Powder distribution histogram

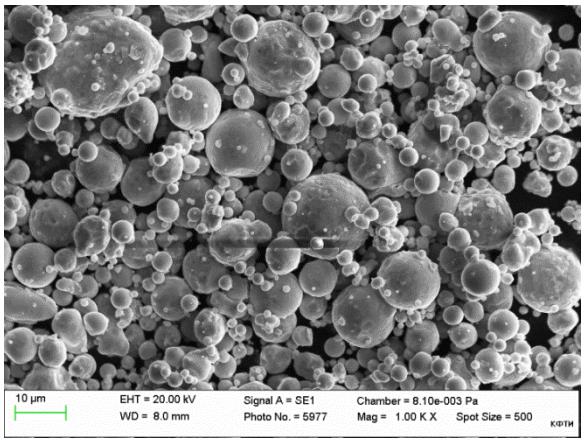

a

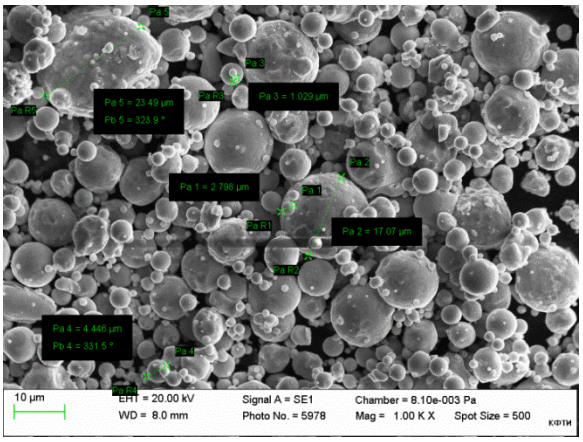

b

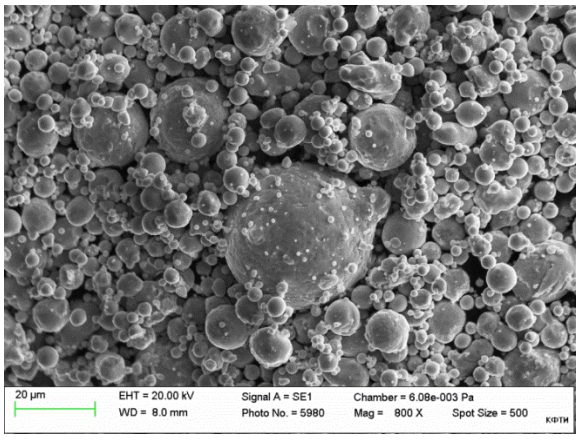

c

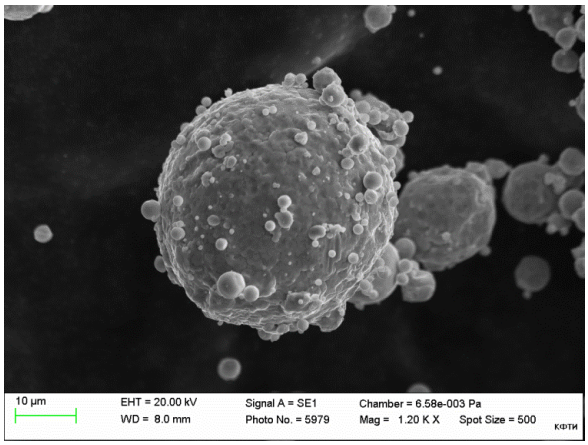

d

Fig. 3 – SEM images of steel powder made by plasma-electrolyte process

Fig. 3 shows SEM images of the resulting powders. The powder has a spherical shape, the smallest particle size is 0.5 μm. The resulting powder is suitable for use in selective laser alloying plants. However, the need for further research related to the increase of the process productivity by increasing the anode area definition and dynamic characteristics of the powder.

The formation of a metal powder occurs as melting result of surface with plasma of gas discharge. The main factors influencing powder production are the power of gas, the amount of thermal energy supplied to the surface of the electrode, and the energy of the ions bombarding the surface of the cathode, the amount of heat withdrawn from the system through the electrode. By changing all of the above factors, it is possible to control the rate of fusion of the electrode surface and the size of the resulting metallic particles.

3.Results

Study of the gas discharge combustion between metal electrode stailness steel 17-4 PH and liquid electrodes have shown the possibility of obtaining a spherical powder with a particle dispersion from 0.5 to 40 μm. Analysis of the obtained SEM photographs shows similarity with the powder obtained by the gas atomization method. Influence of gas discharge parameters on process productivity and size of particles obtained is determined.

Acknowledgements. This work was financed by grant МК-1861.2017.8 allocated by the Council on grants to the President of the Russian Federation for state support of young Russian scientists and for state support of the leading scientific schools of the Russian Federation.

References

1. Journal of Alloys and Compounds, 691, 15.01.2017, 316-322
2. International Journal of Heat and Mass Transfer, 104, 1.01.2017, 665-674.
3. Scripta Materialia, 126, 1.01.2017, 41-44.
4. **Kashapov L.N., Kashapov N.F. and Kashapov R.N.** Journal of Physics: Conference Series, 479, 1, 2013, 012011.
5. **Denisov D.G., N. Kashapov N.F. and Kashapov R.N**. IOP Conference Series: Materials Science and Engineering, 86, 1, 26.06.2015, 012005.
6. **Kashapov L.N., Kashapov N.F., Kashapov R.N and Denisov D.G.,** Journal of Physics: Conference Series, 669, 1, 14.01.2016, 012029.
7. **Hausnerova B., Mukund B. and Sanetrnik D.,** Powder Technology, 312 (2017), 152 – 158.

Laser ablation synthesis of metal oxide nanostructures for photovoltaic applications

E.A. Shustava[1], A.V. Butsen[1], N.V. Tarasenko[1], S. Pashayan[2]

[1] B. I. Stepanov Institute of Physics, National Academy of Sciences of Belarus, 220072 Minsk, Belarus, a.butsen@gmail.com.
[2] Institute for Physical Research, National Academy of Sciences of Armenia, 0203, Ashtarak-2, Republic of Armenia

By using double pulse laser ablation in a liquid (distilled water, ethanol) copper (CuO) and zinc (ZnO) oxides nanoparticles (NPs) promising for solar cells were synthesized. With the applying of absorption spectroscopy, transmission and scanning electron microscopy the optical and structural-morphological properties of the formed particles were studied. The possibility of film layers creating by depositing and assembling colloidal particles in organized structures on the surface of an indium-tin oxide (ITO) substrate was demonstrated.

In the search for new and alternative sources of energy, solar cells are of great interest as the most suitable choice for creating environmentally friendly and efficient energy sources. Increasing the efficiency and reducing the cost of solar cells is one of the most important issues of solar energy.
Materials for photovoltaic elements of the third generation should be effective, stable, produced by environmentally friendly, energy-efficient and low-cost technologies. An important role in solving this problem can be played semiconductor nanomaterials, in particular, metal oxides and silicon quantum dots [1-8]. They are of particular interest as the most promising materials for solar cells in connection with the new optical and electronic properties, attributed due to surface and quantum-size effects. For instance, copper oxide (CuO) is a p-type semiconductor with a band gap energy of 1.5 eV, that is close to an ideal energy gap of 1.4 eV required in solar cells to ensure effective absorption of solar radiation. As it was demonstrated in [6] the introduction of optimal concentration of CuO nanoparticles into solar cells leads to the achievement of an energy conversion efficiency of the order of 40%. Dispersed in a semiconductor polymer, ZnO nanoparticles form the active layer of the solar cell, which is capable of converting up to 40% of the incident photons at a wavelength of 500 nm. [7]. Heterojunctions of solar cells based on inorganic semiconductors can be fabricated using several oxides. For example, devices based on a binary active layer consisting of p-type of CuO NPs and n-type ZnO NPs are known [8]. Typically, thermal annealing and vapor deposition are used to fabricate such heterojunctions. However, the task of developing new more efficient technologies for the synthesis of nanostructures for photovoltaic elements remains urgent.

1. Experimental procedure

For the synthesis of nanoparticles, Nd: YAG laser (LOTIS TII, LS 2134D) operating at double-pulse mode at the fundamental frequency (1064 nm, energy 80 mJ/pulse, repetition rate 10 Hz, pulse duration 10 ns, interpulse delay τ=10 μs) was used. A compressed zinc oxide (ZnO) and copper oxide (CuO) tablets were applied as a targets. The ablation of the targets in ethanol was carried out for 15 minutes. The laser radiation power density on the target surface was 10^8-10^9 W / cm^2. Deposition from the solution of particles onto ITO substrate (Fig.1) was carried out by spin-coating method. Several drops of the colloidal solution were deposited on the substrate of 25x25 mm^2 in size, which was

rotated until the solvent completely dried out, and then the process was repeated until a film of sufficient thickness was formed.

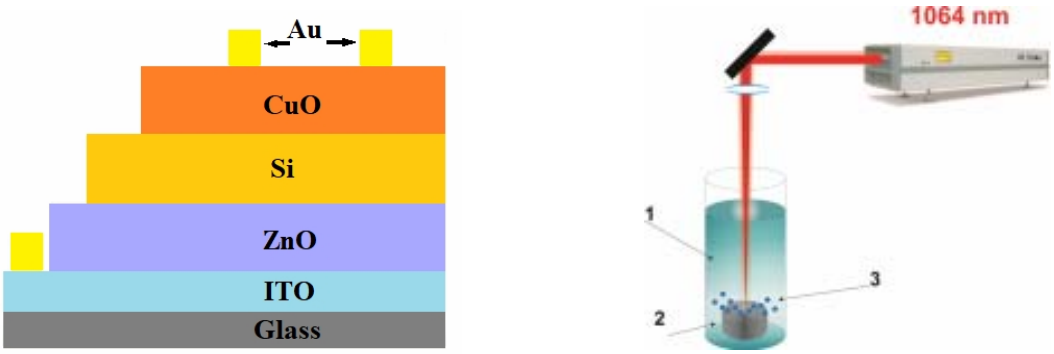

Fig.1 - Schematic diagram of a heterostructural photovoltaic cell (on the left) and an experiment scheme (on the right) for obtaining nanoscale particles during laser ablation in a liquid (1 - cuvette with a solution, 2 - solid-state target, 3 - nanoparticles)

The morphology and structure of the NPs obtained and the deposited structures were analyzed using transmission electron microscopy (TEM), absorption and Raman spectroscopy. Measurements of the absorption spectra were carried out with Cary-500 Scan spectrophotometer at room temperature in the wavelength range from 200 to 700 nm in 1 cm quartz cuvette.

2. Results and discussion

As follows from the results of the TEM investigations, the developed synthesis method makes it possible to obtain spherical NPs with an average size of 5-30 nm. As an example, Fig. 2 shows a TEM image of zinc oxide NPs. Photomicrographs of ZnO particles show groups consisting of separate almost spherical particles. The average particle diameter is in the range of 10-20 nm.

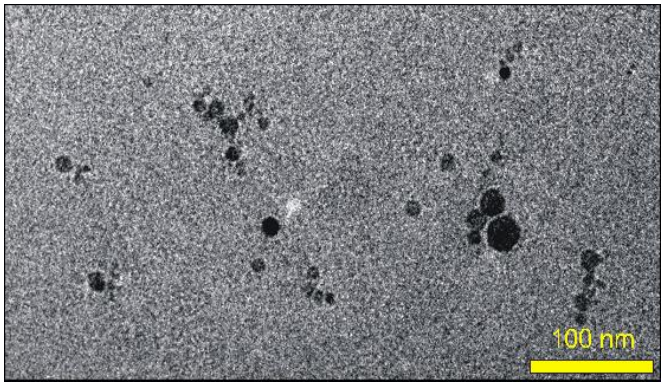

Fig. 2 - TEM images of zinc oxide nanoparticles (right) obtained by laser ablation in distilled water.

A typical absorption spectrum of a colloidal solution of the resulting zinc oxide NPs consisted of a broad band in the UV spectral region with a rapid rise in absorption near the band gap, which is characteristic of semiconductor materials. This type of absorption spectrum with a rise at a wavelength of $\lambda \sim 370$ nm (Fig. 3,) corresponds to the formation of zinc monoxide particles [3].

The absorption spectrum given in the coordinates $(\alpha h\nu)^2$ of $(h\nu)$ allows us to estimate the band gap of a semiconductor. According to the theory of interband optical transitions, in semiconductors in the case of allowed direct transitions, the dependence of the absorption coefficient α on the photon energy hν is expressed as follows [4]:

$$\alpha = A(h\nu - Eg)^{1/2}, \quad (h\nu > Eg),$$

where Eg is the width of the band gap. The coefficient A is inversely proportional to the photon energy. To estimate the band gap Eg, we plot the dependence of $(\alpha h\nu)^2$ vs hν.

Fig. 3 demonstrates dependence $(\alpha h\nu)^2$ vs the photon energy hν for ZnO nanoparticles. The curve is extrapolated by straight lines to the point of intersection with the horizontal axis. The absorption coefficient α was estimated from the measured optical density D and the thickness of the absorbing layer l, using the ratio $\alpha = D/0.43 \cdot l$. As can be seen, the band gap was about 3.0 eV, which is somewhat less than for a massive material (Eg = 3.37 eV). This can be caused both by the size effect and by the formation of defective energy levels near the bottom of the conduction band, for example, due to non-stoichiometry of the ablation process.

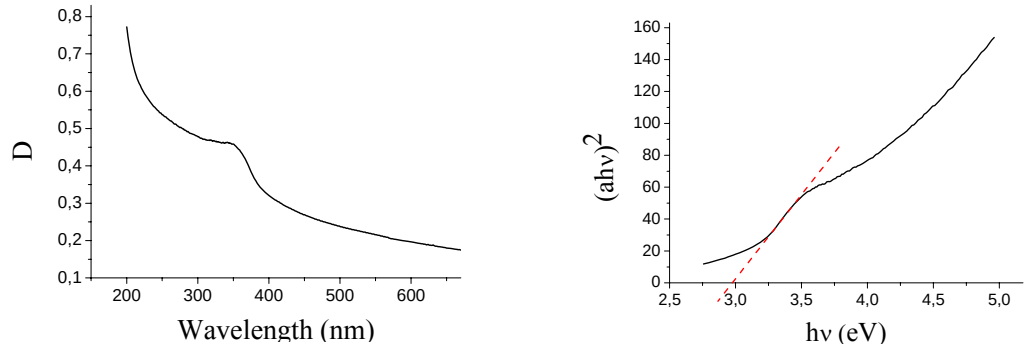

Figure 3 - Absorption spectrum of the ZnO NPs in water obtained by laser ablation of ZnO target (left), and the same spectrum in $(\alpha h\nu)^2$ - hν coordinates (on the right).

A scanning electronic microscope LEO-1420 was used to study the morphology of deposited on ITO structures. Fig. 4 represents surface coated with ZnO. As can be seen, the resulting structure is fairly uniform, the nanoparticle agglomerates do not exceed 50 nm.

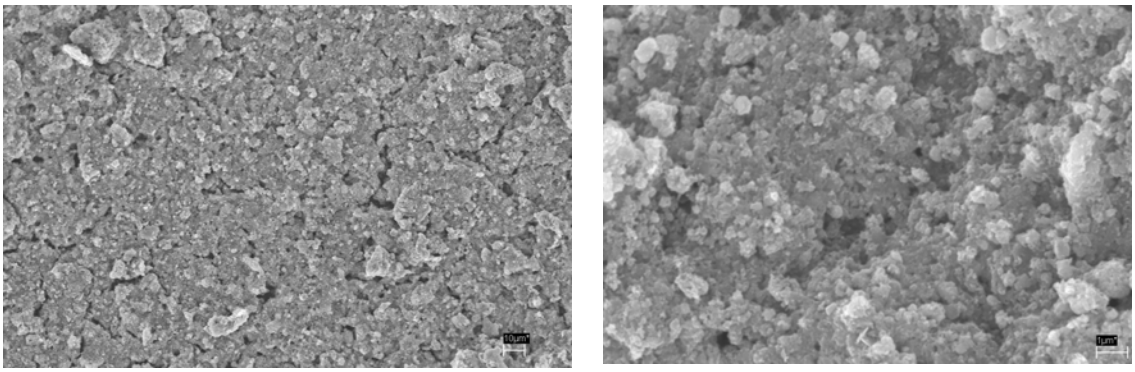

Fig. 4. SEM microphotographs of the structure of ZnO deposited on ITO by the spin-coating method

Conclusion

Thus, the method of laser ablation in liquids can be an effective tool for preparation of metal oxide NPs promising for use in the new generation solar cells. It is shown that the composition, structure, and optical properties of the synthesized particles can be changed by varying the experimental conditions. The possibility of forming film structures by depositing and assembling colloidal particles in organized structures on the surface of an indium-tin oxide (ITO) substrate was demonstrated.

Acknowledgements

This work was supported by the Belarusian Republican Foundation for Fundamental Research (grant No. F17LITG-003).

Literature

1. **Cagataylcli K., Ozenbas M.** Electrochimica Acta, 263, № 10 (2018) 338-345.
2. **Kharel P.L., Zamborini F.P., Alphenaar B.W.** J. Electrochem. Soc., 165, № 3 (2018) H52-H56, doi:10.1149/2.1311802jes.
3. **Kidowaki H., Oku T., Akiyama T., Suzuki A., Jeyadevan B., Cuya J.** Journal of Materials Science Research, Vol.1, №1 (2012) 138-143.
4. **Ibrahem M.A., Wei H.-Y., Tsai M.-H., Ho K.-C., Shyue J.-J., Chu C.W.** Solar Energy Materials and Solar Cells, 108 (2013) 156-163.
5. **Rokhmat M., Wibowo E., et. al.** Procedia Engineering, 170 (2017) 72 – 77.
6. **Wanninayake A.P., Gunashekar S., Li S., Church B.C. and Abu-Zahra N.** J. Sol. Energy Eng., 137(3) 2015.
7. **Beek W.J.E., Wienk M. M., Janssen R.A.** J. Advanced Materials, 16, № 12 (2004) 1009-1013.
8. **Iqbal K., Ikram M., Afzal M. et al.** Mater Renew Sustain Energy, 7: 4 (2018).
9. **Tarasenko N.V., Butsen A.V.** Quantum Electronics, 40, № 11 (2010) 986-1003.

4. NON-IDEAL AND DUSTY PLASMAS, FUSION AND ASTROPHYSICAL PLASMAS

DISSIPATIVE DUST STRUCTURES IN PLASMA: EVOLUTION AND ENTROPY

O. Petrov[1,2]

[1]Joint Institute for High Temperatures, Russian Academy of Sciences, Moscow, Russia, ofpetrov@ihed.ras.ru
[2]Moscow Institute of Physics and Technology, Dolgoprudny, Russia

The dust particles in plasma is quasi-neutral system (dusty plasma) containing micron-sized charged particles of substance with electrical charges up to 10^2-10^5e. Most of the laboratory studies of dusty plasmas are carried out in weakly ionized gas discharge plasmas. As a result of strong interaction of the strongly charged dust particles they may form the open dissipative ordered structures of liquid and crystal types that are different from gas-like or chaotic systems. The laboratory dusty plasma is the unique object for studying the structure, phase transitions and transport properties of the systems of interacting grains on the "kinetic level".

Brownian motion of metal coated grains, suspended in rf gas discharge, was studied under laser radiation action. The radiation could be considered as low entropy radiation. The motion is caused by photophoresis: i.e., absorption of a laser at the metal-coated surface of the particle creates radiometric force which in turn drives the particle. The grains can take sufficiently high electrical charge ($\sim 10^2$-10^5 of electron charge) under the flows of plasma particles. The action of external forces and forces of interparticle interaction combined with dissipative mechanisms in these systems can lead to the self-organization (evolution) of the system, resulting in formation of quasi-stationary crystal- or liquid-like structures. We observed experimentally the active Brownian motion caused by radiometric force at different Coulomb coupling of the charged grains. As a result, we present our studies the evolution of dissipative dust structures strongly coupled systems of charged dust particles driven by low entropy laser radiation.

Acknowledgements. The work was carried out under the support of the Russian Science Foundation (project no. 14-12-01440).

BROWNIAN MOTION OF MACRO PARTICLES IN A TWO-DIMENSIONAL DUSTY PLASMA SYSTEM UNDER DIRECTED EXTERNAL IMPACT. SIMULATION RESULTS

I.I. Fairushin, O.F. Petrov, M.M. Vasiliev

Joint Institute for High Temperatures of the Russian Academy of Sciences (JIHT RAS)
125412, Izhorskaya st. 13 Bd.2, Moscow, Russian Federation, fairushin_ilnaz@mail.ru
Moscow Institute of Physics and Technology (MIPT) 141701, Institutskiy per., 9,
Dolgoprudny, Moscow Region, Russian Federation

The ability to observe the motion of individual particles using a simple optical technique makes dusty plasma /1/ a unique object of study of transport processes, self-organization, phase transitions at the kinetic level. A special place in these studies take works devoted processes occurring under the action of external perturbation /2, 3/. From the point of view of simplicity of observation, two-dimensional systems of dust particles have several advantages. Such a system can formed in the near-electrode zone of the high-frequency capacitive low-pressure discharge. For example, particles of melamine formaldehyde (MF) of micron size can serve as a dust component. To perform external actions on particles, in particular, laser radiation can used. The laser action based on the light pressure force applied to the dust particles in the radiation zone. In addition, the radiation can also heat the surface of the particles and thus cause the appearance of thermophoretic forces acting on the particles. Experimental studies of systems of interacting dust particles in a plasma can also supplemented by their modeling, for example, by methods of molecular dynamics (MD). This makes it possible to reveal even more in detail the regularities of the physical phenomena that occur /4/. This work is devoted to MD simulation of the dynamics of charged dust particles under the action of laser radiation in a two-dimensional system located in a low-pressure gas discharge plasma. The action of the laser is considered as a rendering the force of light pressure to particles in the radiation zone. The round area was filled with particles, the density of the material corresponding to the density of the MF. The particle radius r_d was chosen to be 10 μm, the initial interparticle distance a =1 mm. Temporal integration step was taken equal to one hundredth of the value of the dust component inverse plasma frequency. The value of the particle charge Z_d was of the order of 10,000 electron charges. The particles interact among themselves through the known Yukawa potential:

$$\varphi(r) = \frac{Z_d}{r} exp\left(-\frac{r}{\lambda_D}\right), \quad (1)$$

where λ_D – Debye screening length, which was considered equal to the average interparticle distance a. In the right part of the equation of motion of the particle (2) successively comprises the terms, which determine the magnitude of pair interaction forces, friction forces by neutrals, random Langevin force, radiation pressure force by the laser radiation, and an external force from the confinement, which keeps the system in the predetermined area.

$$m\ddot{\mathbf{r}}_i = -Z_d \sum \nabla \varphi - m\gamma \dot{\mathbf{r}}_i + \mathbf{L}_i + \mathbf{F}_{laser} + \mathbf{F}_{conf.} \tag{2}$$

The light-pressure force module is determined from the following expression /5/

$$F_{laser} = q \frac{n \pi r_d^2 I_{laser}}{c}, \tag{3}$$

where q is the dimensionless factor that is determined by the reflection, transmission and absorption of photons on the particle, n is the refractive index of the medium around the particle, I_{laser} is the intensity of laser radiation proportional of power P, c is the speed of light. Direct action of this force is carried out only in the zone of the laser beam.

One of the main parameters of the 2D plasma-dust system is the effective nonideality parameter /6/.

$$\Gamma_0^* = \frac{3Z_d^2}{2aT_d} \left\{ \left(\frac{\kappa^2}{2} + \kappa + 1 \right) exp(-\kappa) \right\}^{\frac{1}{2}} \tag{4}$$

Here T_d – kinetic temperature of dust particle, and $\kappa = \frac{a}{\lambda_D}$.

In the course of solving equation (2), data on the coordinates and velocities of the particles of the system were obtained. The obtained data were used to calculate the time dependence of the ratio of the mean square displacement of particles to the doubled time:

$$D(t) = \frac{\langle \Delta \xi^2 \rangle}{2t}. \tag{5}$$

For large times, this function takes the value of the so-called effective self-diffusion coefficient /6, 7/. By determining T_d in the laser radiation zone, the nonideality parameter Γ_a^* for this region was calculated.

In Fig. 1 *a)* shows the appearance of the simulated area and displays the trajectories of the particles during 10 seconds at the absence of laser radiation. Fig. 1 *b)* shows the graphs of the function (5) for two mutually perpendicular directions. It can be seen that the function D (t) has a pronounced maximum, which is characteristic for systems of interacting particles /6/. In Fig. 2 shows the particle trajectories in 10 seconds in the case of laser action a) and function (5) at different values of radiation power *b*), *c*) and *d*).

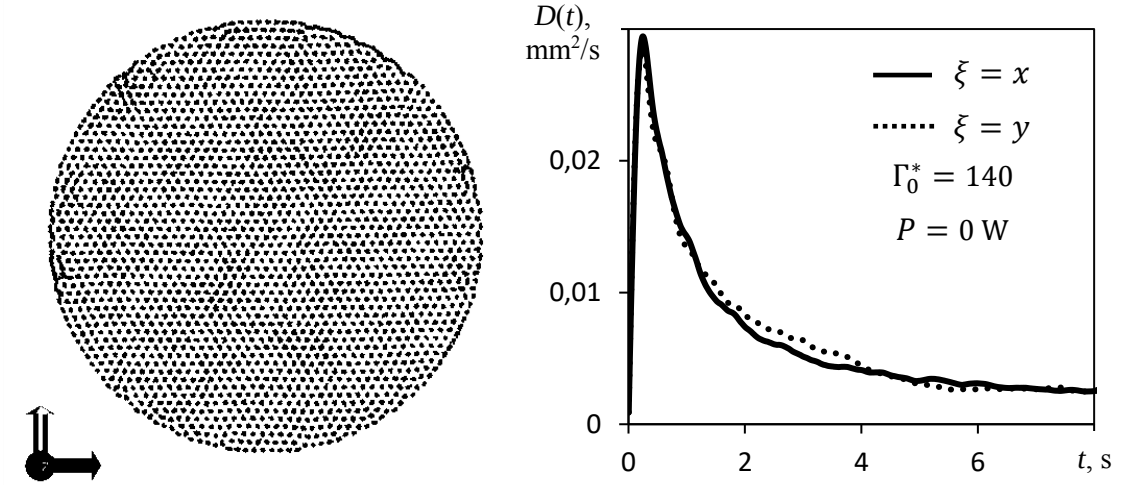

a *b*

Fig. 1.

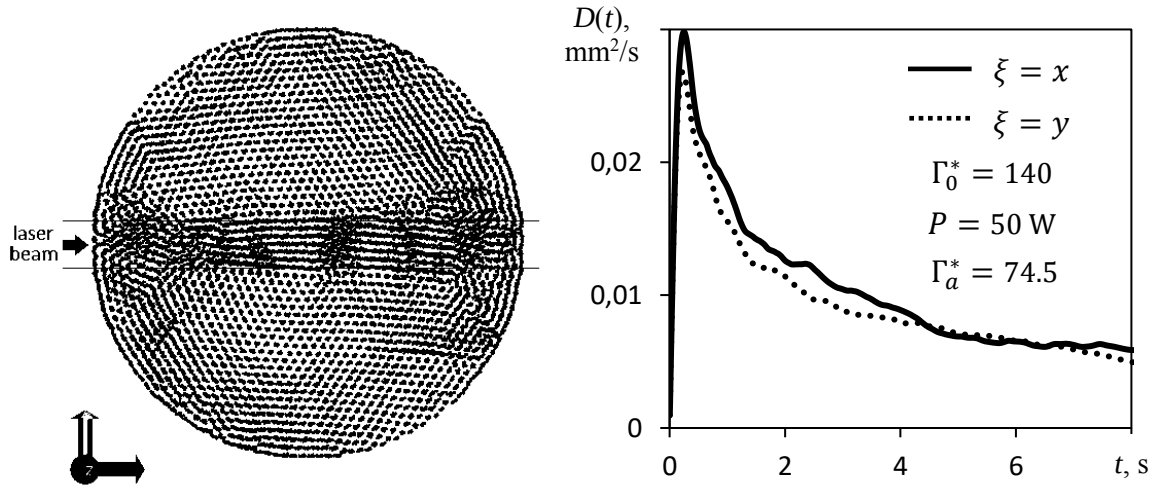

a *b*

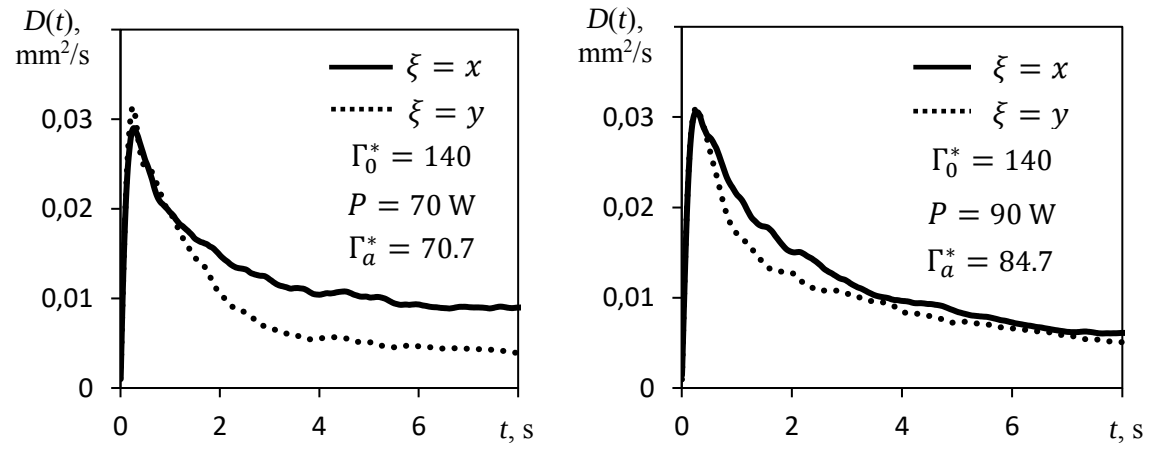

c *d*

Fig. 2.

The steady-state value of the function $D(t)$ increases with increasing radiation power from 50 to 70 W, but it again decreases with increasing power up to 90 W. In this case, this behavior is characteristic only for the direction of the laser beam coinciding with the direction of propagation. The values of the effective parameter of the nonideality of the dust subsystem in the laser action zone are minimal at the maximum values of $D(t)$ and are maximal at the minimum $D(t)$.

Thus, it can be concluded from the simulation that the transfer processes in the plasma-dust system do not depend monotonically on the magnitude of the external action.

Acknowledgements. This work was supported by the Russian Science Foundation, project no. 14-50-00124.

References

1. **Fortov V.E. and Morfill G.E.** Complex and Dusty Plasmas: From Laboratory to Space. Boca Raton: CRC Press/Taylor and Francis (2010).
2. **Vaulina O.S., Repin A.Yu., Petrov O.F., Adamovich K.G.** Journal of Experimental and Theoretical Physics. 102 (2006) 986-997.
3. **Vaulina O.S., Petrov O.F., Gavrikov A.V., Fortov V.E.** Plasma Physics Reports. 33 (2007) 278-288.
4. **Klumov B. A., Rubin-Zuzic M., Morfill G. E.** JETP Letters. 84 (2007) 542–546.
5. **Liu Bin, Goree J., Nosenko V., Boufendi L.** Physics of Plasmas. 10 (2003) 9-20.
6. **Vaulina O.S., Petrov O.F., Fortov V.E.** Journal of Experimental and Theoretical Physics. 100 (2005) 1018-1028.
7. **Fortov V.E., Petrov O.F., Vaulina O.S., Koss K.G.** Journal of Experimental and Theoretical Physics Letters. 97 (2013) 322–326.

MELAMINE-FORMALDEHYDE PARTICLES IN COMPLEX PLASMA

V. Karasev[1], E. Dzlieva[1], A. Gorbenko[1], V. Polischuk[2], S. Pavlov[1]

[1] Saint-Petersburg State University, Universitetskaya Naberezhnaya 7/9, Saint-Petersburg 199034, Russia, e-mail: v.karasev@spbu.ru
[2]ITMO University, Kronvergskiy 49, Saint-Petersburg 197101, Russia

Recently, new applications of dust particles are emerging; there is growing demand for particles with special properties, and for particle-seeded composite materials. DC low pressure glow discharge plasma offer a unique possibility of confinement, control and fine tailoring of particle properties. The interaction between plasma and injected microparticles can also be used as a diagnostic tool for the study of complex plasma /1,2/. In this report we are talking about the processing of monodisperse spherical melamine formaldehyde (MF-R) particles (11.6 ± 0.4 μm in diameter with a density of 1.5 g/cm^3) suspended in neon discharge plasmas. First, we will present the conditions under which the experiment was conducted. Secondly, we will describe the modification of spherical microparticles as a result of this experiment.

Neon discharge tube (the vertical part of the tube h=10 cm; radius R=0.7 cm) has already been used in similar experiments /3-6/. A new problem was to determine the maximum possible particle size for levitation in the discharge tube and to choose the discharge conditions. The largest melamine-formaldehyde particles that could be suspended in DC glow discharge plasmas in this tube were spherical particles 11.6 ± 0.4 μm in diameter. Plasma traps were formed in the discharge tube under the following conditions: Ne, p = 25 ±5 Pa, i = 2.1 ± 0.2 mA. When particles intentionally injected into a discharge from special container, they rapidly acquired a negative charge and densely fill the space in the region of the stratum, in which the vertical electric field is large enough. Without external influence, the microparticles remained trapped for a long time. The dispersion in the mass of the initial particles was small, so the levitation conditions were satisfied for the majority of the injected particles. The particles were exposed to the plasma for a predetermined time (5-40 min) and extracted from the gas discharge tube for further analysis.

The analysis of the modification of microspheres was carried out using the Merlin Zeiss scanning electron microscope. In a scanning electron microscope, a rastering electron beam is used to form an image. The image quality is affected by the charging of an object by electrons, which leads to diffusion of contrast boundaries. To lower the charge of the object (a melamine-formaldehyde particle), we used the mode of low accelerating voltages and small electron beam currents. Dozens of the most successful 2D images with nanometer resolution were used for determination of the particle size with Smart Tiff

(ZEISS) software. A fragment of the image is shown in Fig.1.

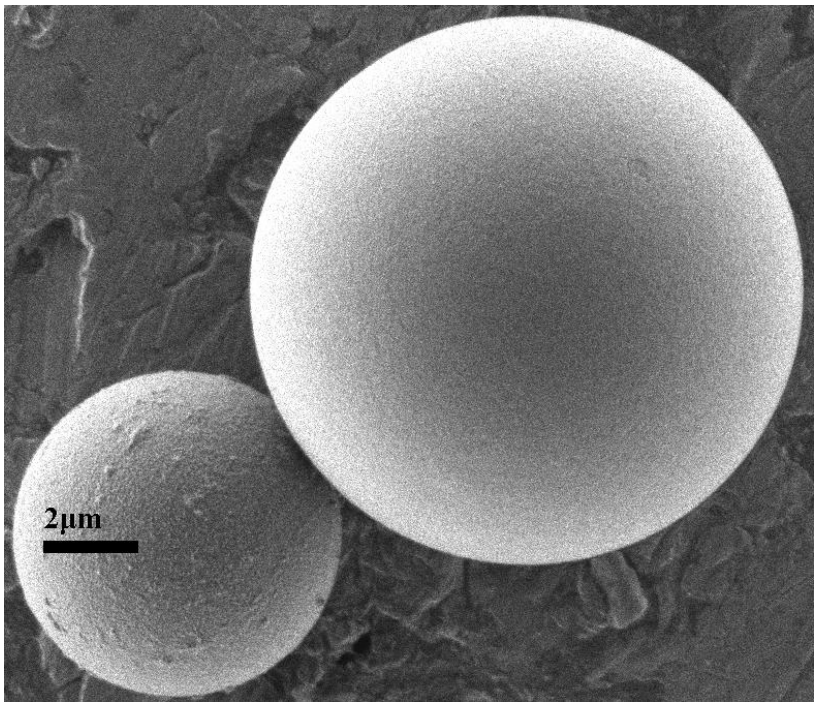

Fig. 1 – A fragment of the electron microscope image. Two spherical particles: the original particle and the degraded particle treated with plasma for 20 minutes

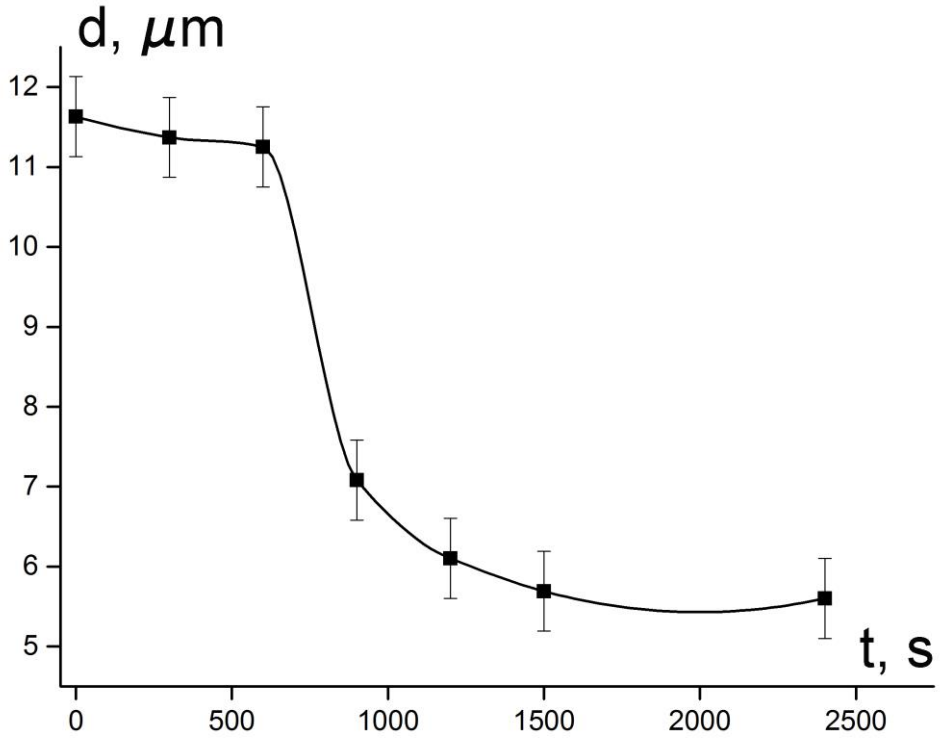

Fig. 2 – Variations in particle diameter depending on the time of residence in the plasma

The second result of the studies was the observed change in the surface morphology, which also became perceptible at exposure times of more than 10 minutes (Fig.3).

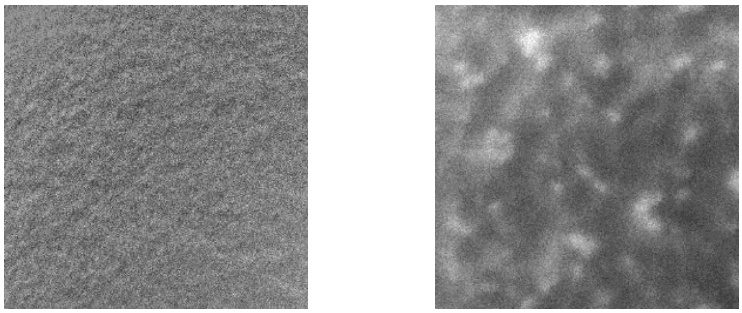

Fig. 3 – Fragments of the electron microscope image. Surface of particles: the original particle and the degraded particle treated with plasma for 20 minutes

For particles that still could be trapped in plasmas in discharge tube from /3-6/, the maximum diameter was determined. The conditions were chosen so that the particles hung up in dust-plasma traps and were under the action of the plasma for 5–40 min. The reduction in particle size and changing of surface morphology which were previously detected for smaller particles (7.3± 0.4 μm) was confirmed. There are still questions about the mechanism of modification of polymer particles in dusty plasmas. In a low-temperature plasma of inert gases, energy of atoms and ions does not exceed hundredths of eV, the melting point of melamine-formaldehyde resin is about 350°C. Comprehensive nanoscale modification of microparticles can be caused by ion flux incident on each particle under condition of maintenance of its stationary charge. Ions are accelerated by an electrostatic field of surface charge, acquire energy of about 10 eV. It is enough to softening the surface layer and knocking out the material. It is also worth noting that reducing the diameter by 50% (25 min) gives a significant change in the negative charge of the particles. Thus, the dusty plasmas can be used for surface treatment of particles, modification of surface morphology and the manufacture of particles.

Acknowledgements. This work was supported by the Russian Science Foundation (RSF) (grant № 18-12-00009).

References

1. Dusty Plasmas: Physics, Chemistry, and Technological Impact in Plasma Processing / Edited by **A. Bouchoule**. NewYork: John Wiley & Sons, (1999).
2. **V.E. Fortov, A.G. Khrapak, S.A. Khrapak, V.I. Molotkov, O.F. Petrov**

Phys. Usp., 47(2004) 447–492.
3. **V. Yu. Karasev, E. C. Dzlieva, V. A. Polishchuk, A. P. Gorbenko, S. I. Pavlov, M. M. Makar and M. A. Ermolenko** PPPT-8 Contributed papers, Minsk, Belarus, II(2015) 312-315.
4. **V. Yu. Karasev, V. A. Polishchuk, A. P. Gorbenko, E. C. Dzlieva, M. A. Ermolenko, and M. M. Makar** Phys. Solid State, 58(2016) 104.
5. **M. A. Ermolenko, E. S. Dzlieva, V. Yu. Karasev,S. I. Pavlov, V. A. Polishchuk, and A. P. Gorbenko** Tech. Phys. Lett., 41(2015), 1199.
6. **V.Yu. Karasev, E.S. Dzlieva, A.P. Gorbenko, I.Ch. Mashek, V.A. Polishchuk, I.I. Mironova** Tech. Phys., 62(2017), 496.

ITER DIVERTOR PLASMA FACING AND NEARBY COMPONENTS DURING TRANSIENT EVENTS

V. Sizyuk[1] andA. Hassanein[2]

Center for Materials under Extreme Environment (CMUXE),
School of Nuclear Engineering, Purdue University, West Lafayette, IN 47907, USA
[1]E-mail: vsizyuk@purdue.edu, [2]E-mail: hassanein@purdue.edu

1. Introduction

A key obstacle to successful magnetic fusion energy production is current limits on our understanding of, and our ability to control, various plasma transient events. Accurate prediction, control, and mitigation of PFC responses to instabilities (e.g., disruption, edge-localized modes (ELMs), vertical displacement events (VDEs), and runaway electrons) are essential for safe and reliable operation of Tokamak fusion devices. While simulation through comprehensive computer models of the HEIGHTS (High Energy Interaction with General Heterogeneous Target Systems) package /1-3/ has successfully enabled investigation of many aspects of plasma-material interaction (PMI) phenomena during transient events, advanced numerical tools and solution methods in an integrated parallel environment are urgently needed to efficiently couple these key areas including plasma/material interaction, boundary-surface and impurity transport, and core plasma in B field dynamic structure to ensure high accuracy of the simulation results while minimizing execution time.

Available experimental data of current tokamak devices and theoretical predictions show that future ITER-like surfaces should be resistant both to steady state heat flux of up to 20 MW/m^2 and to major transient ($\tau = 0.1 - 10$ ms) events of up to 10 GW/m^2. These values are estimates based on the current understanding and extrapolations from existing devices. High particle and heat fluxes can cause high surface sputtering erosion, melt and vaporization erosion, plasma contamination, and possible components failure that can disrupt the expected normal and safe operation of the reactor. The reactor geometry, the magnetic configuration, and the interaction processes in the SOL determine not only heat transport and loads to component surfaces but also play an important role in plasma confinement and control the transition to the H-mode operation.

2. Model details

Our preliminary simulations were significantly improved when the SOL plasma transport problem was divided into the following subtasks: 1) MHD of the escaping core plasma, starting from the last closed flux surface (LCFS); and

2) and MHD of the SOL neutrals (background gas)/4/. Recent investigations have shown that including details of the SOL transport and implementation of various hybrid approaches are very important for better modeling of divertor/wall damage and the evolvedmini plasma evolution to correctly predict components heat loads /5/.

HEIGHTS integrated models are continuously being enhanced to include fine details of various reactor geometries (e.g., ITER, NSTX, etc.) for the 3-D simulation of reactor environment (e.g., Fig. *1*). We developed, for the first time, comprehensive kinetic Monte Carlo model for the simulation of the escaping core plasma and for the prediction of heat load to all plasma-facing components using the entire 3D device geometry. The detailed description of the escaping core particles into the SOL was implemented into the integrated model to be used as the input volumetric power source in the MHD module /3/. Based on the various advantages of the splitting processes used in solution of the transport problem, our upgraded model includes both of the two separated subtasks (i.e., MC and MHD), however, we do not use any fitting parameters or averages from continuum media, i.e., we do not solve Navier-Stokes equations for the escaped core D/T plasma. All the physical processes included into HEIGHTS integrated modules are interconnected. For example, the escaped core plasma particles initiate divertor surface vaporization and further vapor heating leading to the secondary plasma formation. The MHD evolution of the secondary plasma redistributes the density temporal and spatial profiles in SOL and consequently changes the scattering processes and the interactions of the escaping core particles. We simulate the motion of the escaping core plasma as individual particles composed of deuterons, tritons, and electrons escaping along the complex electromagnetic field structure of the entire device. The advantages of our approach are the ability to study various drifts phenomena, to separately divide the contribution of different ions and electrons into components heat loads, and to exclude artificial fitting parameters usually used in the description of anomalous transport properties. The particles motion is

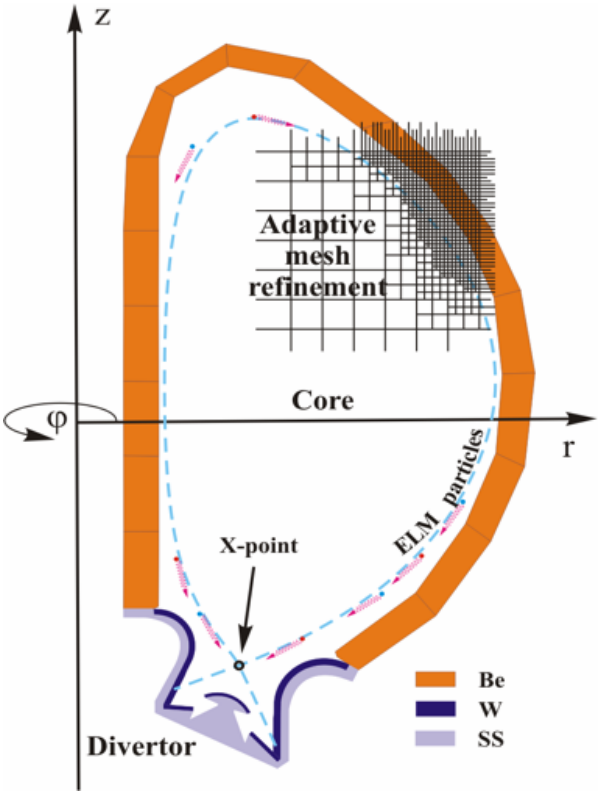

Fig.1 – Model mapping for current ITER design in HEIGHTS

calculated using ab-initio models with simulation of all possible scatterings processes and their probabilities along their path.

To preserve the multiscale approach in our integrated physical and mathematical models and to ensure reasonable accuracy, we used the adaptive mesh refinement (AMR) algorithms with unstructured grid geometry /6/ and applied the TVD-LF method to the quadtree mesh in the finite volume approach. The details of such implementation can be found in Refs. 7. Calculation of these terms is based on the energy deposition into the solid walls following the MC model of the escaping core plasma /7/.The gyrokinetic model determines evolution of the fuel plasma particles (D, T, and e) starting from escaping the LCFS, motion through the SOL including both toroidal rotation and Larmor gyration, and ending in the solid/liquid matter of the tokamak components. The particle evolution included also various possible events: 1) return back into the core plasma, 2) scattering in the SOL from the secondary evolving divertor plasma or from the neutral vapor of the divertor cold vaporized material, 3) penetration into the liquid/solid matter of the component as well as scattering underneath the surface, 4) collisional cascade processes and slowing down inside the target materials. Penetration into the solid matter and scatterings processes under the surface determine the spatial energy deposition in the walls due to the core plasma impact and the resulting appropriate thermal response. Subsequent solution of the heat conduction problems in solid/liquid material provides the resulting vapor amount needed to initiate the MHD evolution of the divertor material. Here we stress that the MC recalculations should be done dynamically, i.e., in parallel to the MHD processes to have accurate energy deposition into the secondary plasma, vapor, and solid wall /3/.

3. Simulation results

The main goal of presented work is, for the first time, to simulate the dynamic interaction of the escaped core plasma particles flow and the resulting secondary divertor plasma during transient disruptions and ELMs in full 3-D real ITER geometry with exact dimensions and to predict details of thermal response and damage to various plasma-facing and surrounding components. These include inner and outer divertor plates, inner and outer reflector plates, inner and outer baffles, inner and outer stainless steel “umbrella” tubes, dome structure, and the lower parts of the inner and outer Be first walls.

Figure *2* shows a comparison between the response of the inner divertor plates, inner W reflector plate, inner SS tube structure, and the W dome. The calculation shown is for 0.1 ms full disruption event. The figure clearly shows that using C as divertor plate will protect nearby components such as the reflector plates, the SS tube structure, and the dome much better than a W divertor plate for the parameters studied in this case. In fact, no potential melting

or vaporization of all these components occurs compared to the case of W divertor plate in which these three components would be damaged. However, the response of these components and others for different disruption parameters and conditions could be different if the divertor plates were made of C instead of W. In addition, the hot-generated less-radiative C plasma may travel farther and damage other components. In summary, analysis of various mitigation and innovative methods to protect the internal components must be studied in detail using full 3-D integrated realistic geometry and design features. These should include pellet injection, massive gas puffing, innovative materials, better design innovation, use of liquid metals, etc. Currently, the ITER design configuration may not be durable to accommodate and survive single unmitigated major plasma instability event. This should be taken very seriously

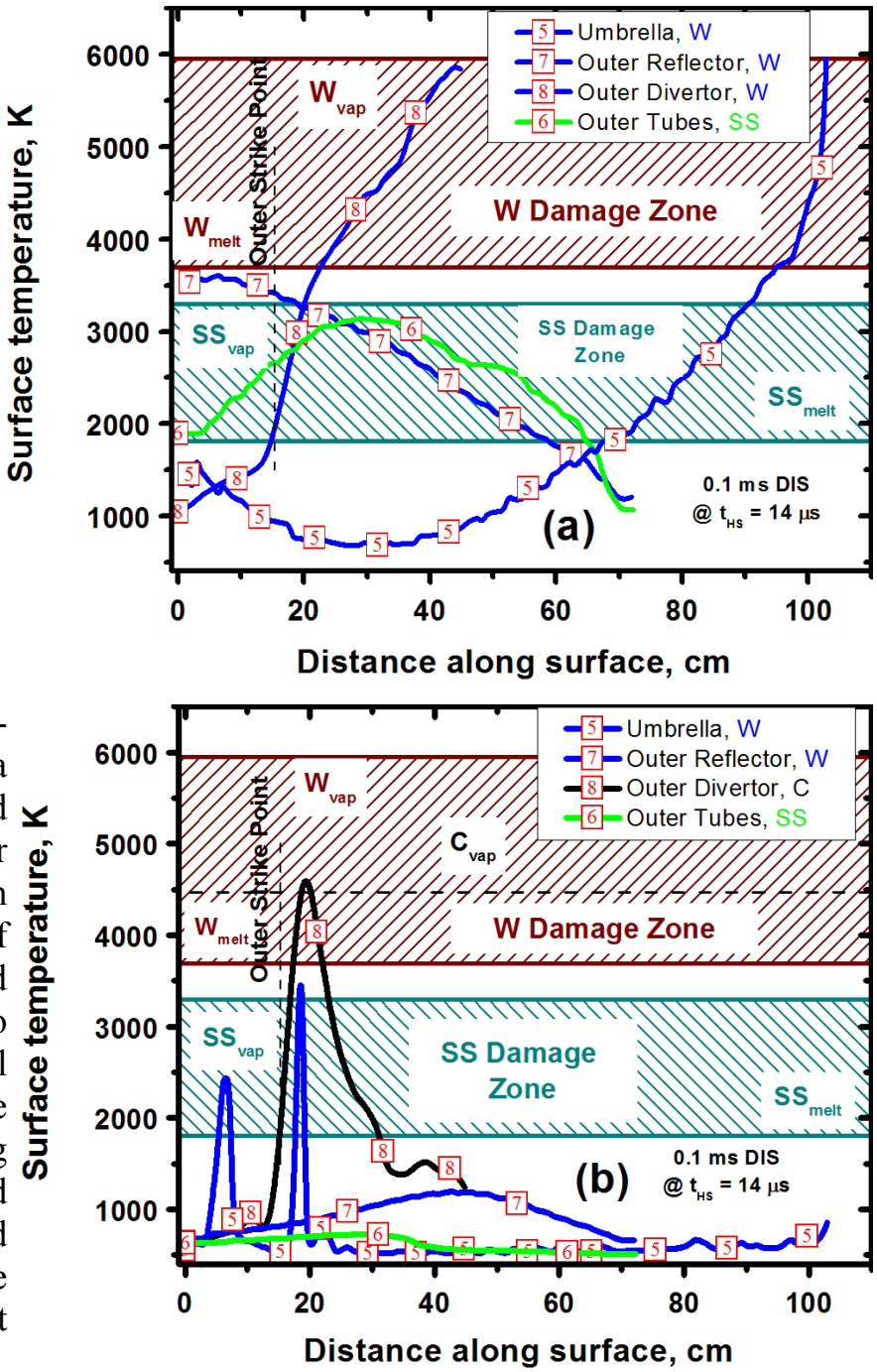

Fig. 2- Response of nearby components (outer reflector 7, outer SS Tube 6, Dome 5) for different divertor plate materials: (a) W divertor 2, 8; and (b) C divertor 2, 8.

and investigated in detail since it has great implication for the success of the tokamak concept and in particular ITER current design as future energy producing devices.

4. Conclusion

In summary, our comprehensive results show, for the first time, that transient events, including even those with longer durations, could cause significant melting and vaporization damage to most interior and hidden plasma-facing and related components, including the first walls that were not directly exposed to the original disrupting plasma particles.The current ITER divertor design may need to be modified or new design may be needed to prevent this damage.

5. Acknowledgment

We gratefully acknowledge the computing resources provided by the Bebop cluster operated by the Laboratory Computing Resource Center at Argonne National Laboratory.This work was partially supported by the National Science Foundation.

6. References

1. **Sizyuk V. and Hassanein A.**Physics of Plasmas, 25(2018) 062508.
2. **Sizyuk V. and Hassanein A.** Physics of Plasmas, 22(2015) 013301.
3. **Sizyuk V. and Hassanein A.**Nuclear Fusion,53(2013) 073023.
4. **Sizyuk V. and Hassanein A.**Nuclear Fusion,50(2010) 115004.
5. **KritzA.H.*et al.***Nucl. Fusion, 51(2011) 123009.
6. **Samtaney R. *et al.***Computer Physics Communications, 164(2004) 220.
7. **Sizyuk V. and Hassanein A.**Journal of Nuclear Materials, 438(2013) S809.

DUST PLASMA IN THE STRATIFIED DISCHARGE IN MODERATE MAGNETIC FIELD

S.I. Pavlov, V.Yu. Karasev, E.S. Dzlieva, L.A. Novikov

[1]Saint Petersburg State University, 199034, RUSSIA, St. Petersburg, Universitetskaya nab., 7/9, e-mail: s.i.pavlov@spbu.ru,

Abstract. In the present thesis we discuss in details the problems of the obtaining of steady dust structures in the trap in standing striation in the glow discharge at a partial magnetizing of the plasma component.

In the experiment the dusty plasma was created in glow discharge in the long discharge tube placed in the magnetic field created by a superconducting magnet. The dynamics of rotation of dust structure at the chosen discharge parameters depending on magnetic induction is measured.

Introduction. One of the methods of studying of complex plasma /1-4/ is the imposing the external influences and observation of reaction of system. The magnetic field is one of productive influences. It strongly impacts on the dc discharge; plasma loses the stability and the instabilities are arises /5-6/.

After the several successful researches of complex plasma in the weak magnetic field, for example /7-10/, the advance of experiments to the area of big magnetic fields was met by difficulties. So, in /11/ the observations in fields up to 40000 G were made but presented only for rf discharge. Researches in striations of the glow discharge showed rich physics, several competing mechanisms playing the dominating role in the different range of magnetic field /12-14/. Several years were required to sequentially explain the physical processes defining rotation of dust structures /15-18/.

Experiment. The experiment was made in the discharge tube placed in the warm hole of a cryogenic magnet in such a way that the first striation from the cathode was in the middle of the conductive solenoid, see Fig.1. The cryogenic magnet consists of the superconducting material solenoid with the height of 20 cm placed in the tank for fluid helium of 20 l which in turn is in the tank for fluid nitrogen of 15 l. Outside of the tank for fluid nitrogen there was a tank which was pumped out by a turbomolecular post to 10-4 Torr. The magnetic field was created in the range from 0 to 1 T. The vector of induction was directed upward.

In the discharge tube with inner diameter of 20 mm and the length of 1,5 m the stratified discharge in neon with the pressure of 0,6 Tor and discharge current of 1,4 mA was ignited. The dust structure in the striation was formed of quartz particles with the size of the levitating particles of 6 microns determined according to. Illumination of dust cloud was carried out by means of a laser

knife which was formed in the warm hole of cryogenic magnet in the area of observed strata by means of periscopic system and the laser of 650 nanometers and 40 mW. The video of dynamics of dust structures was made through the top face window of the discharge tube and through a prism. All measurements were implemented in the solenoid in the distance of 0 – 3 cm from its center.

Fig. 1 – A general view of the cryostat with the cryomagnet; 1 – location of the centre of solenoid; 2 – glass discharge tube. The superconducting solenoid is in the bottom part of the cryostat, its length is 193 mm, the diameter is 146 mm, the diameter of the warm hole is 60 mm

Results. At a zero magnetic field the structure with the diameter about 5 mm and the height about 10 mm having in the average horizontal section about 1000 particles was formed in the striation. At increase in magnetic field up to 800 G the form and number of particles in structure remained.

In the magnetic field dusty plasma comes to rotation. For its quantitative characteristic the projection of the angular velocity of rotation to magnetic induction vector is used. On graphics of Fig.2 the dependence of the projection of angular velocity of rotation of the averages horizontal section of dust structure in the striation on magnetic field is presented. The projection is positive if the vector of angular velocity is directed upward.

When the value of magnetic field achieved 800 G the void which diameter increased with magnetic field was formed in the horizontal section of structure; particles was scattered from the structure. In magnetic field about 2000 G we injected particles; they were not built in. New structure was created only at 2500 G. This structure was created without void.

The growth of an angular velocity of structure in this range of magnetic fields stopped. The angular velocity began to increase only after injecting of new particles.

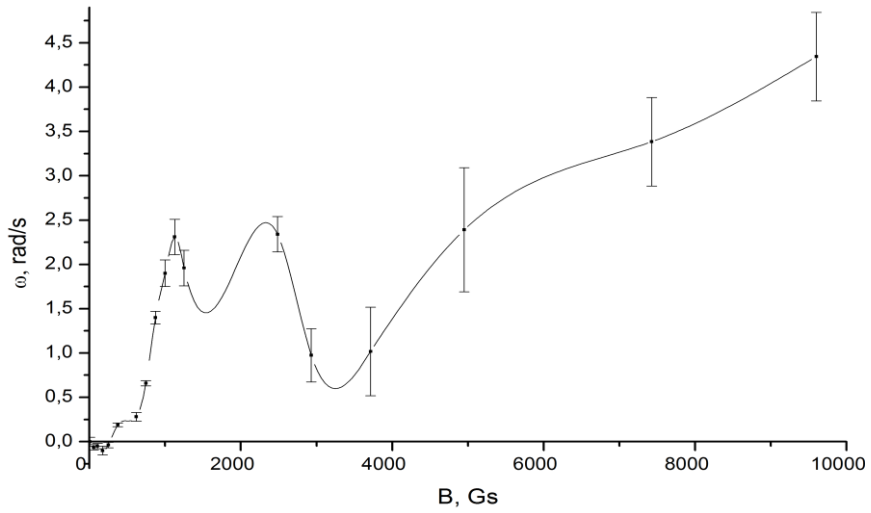

Fig. 2 – The dependence of the projection of the angular velocity of rotation of dust structure to the direction of the magnetic induction on magnetic induction. Conditions: Ne, p=0,6 Torr, i=1,4 mA, polydisperse particles of quartz

The obtained dependence of the projection of angular velocity of rotation in the range of 0 - 1100 G qualitatively repeated the dependences obtained earlier in weak magnetic fields /11-14,16-18/. The value of the negative projection of an angular velocity reaches 0,1 rad/s; inversion of rotation occurs at 300 G. In this range of the magnetic field (less than 300 G) the ion drag force acts as the rotation mechanism; the drag by the rotating gas because of electron eddy current in the striation acts in the magnetic field over 300 G.

At further increasing of magnetic field beginning from 1000 G the angular velocity ceases to grow quickly and tends to the value 3 – 4 rad/s with some deviations; it was observed at several repeated experiments.

Acknowledgements. Work was supported by RSF, grant No. 18-72-10019 in the part of experiments with dust clusters, and grant No. 14-12-00094 in the part of experiments with dust structures.

References

1. **Fortov V.E., Mofill G.E.** Complex and dusty plasmas: from laboratory to space (Taylor & Francis Group, NewYork) (2010).
2. **Tsytovich V.N., Morfill G.E., Vladimirov S.V., Thomas H.M.** Elementary Physics of complex plasmas. (NewYork: Springer) (2008).

3. **Golubovskii Yu.B., Skoblo A.Y., Wilke C., Kozakov R.V., Behnke J., Nekutchaev V.O.** Phys Rev E., 72 (2005) 026414.
4. **Nedospasov A.V.** Sov. Phys. Usp., 11 (1968) 174.
5. **Chen F. F.** Electric Probes. Plasma Diagnostic Techniques (New York: Academic Press) (1965).
6. **Granovskiy V.L.** Curent in Gas (Nauka, Moskva) (1971).
7. **Uchida G., Ozaki R., Iizuka S., Sato N.** Proc. 15th Symp. on Plasma Processing, Hamamatsu, Japan, 21-23 (1998) 152-155.
8. **Konopka U., Samsonov D., Ivlev A.V., Goree J., Steinberg V., Morfill G.E.** Phys. Rev. E 61 (2000) 1890.
9. **Sato N., Uchida G., Kaneko T., Shimizu S., Iizuka S.** Phys. Plasmas. 8 (2001) 1786.
10. **Sato N.** AIP Conf. Proc. 649 (2002) 66.
11. **Dzlieva E.S., Karasev V.Yu., and Eikhval'd A I.** Opt. Spektrosk. 92, 1018 (2002).
12. **Dzlieva E.S., Karasev V.Yu., and Eikhval'd A.I.** Opt. Spektrosk. 98, 621 (2005).
13. **Karasev V.Yu., Dzlieva E.S., and Eikhval'd A.I. et al** Phys. Rev. E 74 (2006) 066403.
14. **Vasiliev M.M., D'yachkov L.G, Antipov S.N., Petrov O.F. and Fortov V. E.** JETP Lett. 86 (2007) 358.
15. **Nedospasov A.V.** Phys. Rev. E 79 (2009) 036401.
16. **Vasiliev M.M., D'yachkov L.G, Antipov S.N., Huijink R., Petrov O.F. and Fortov V.E.** EPL 93 (2011) 15001.
17. **Dzlieva E.S., Karasev V.Yu., Pavlov S.I.** EPL, 110, P. 55002 (2015).
18. **Dzlieva E.S., Ermolenko M.A., Karasev V.Yu., Pavlov S.I., Novikov L.A. and Maiorov S.A.** JETP Letters 100 11 (2014) 703.

FORCED VERTICAL OSCILLATION OF A SINGLE DUST PARTICLE IN A STRATIFIED GLOW DISCHARGE

A. A. Kartasheva[1], Yu. B. Golubovskii[1], V. Yu. Karasev[1]

[1]Saint Petersburg University, Russia, 198504, Saint Petersburg, 3 Ulyanovskaya str,
alexkartasheva@gmail.com

Introduction

The investigation of dust particle oscillations, induced by themselves or by external drive forces, is important for understanding the dynamic processes in dusty plasma systems. For example, the oscillatory motion of dust particles was exploited to obtain insight into the mechanism for the efficient energy transfer between degrees of freedom of the dusty plasma system. In /1/ it was shown that the particle charge fluctuation is the reason for the appearance of forced resonance, which heats vertical oscillations.

Investigation of the dust oscillations is one of the methods used to determine the dust particle charge. In /2/ authors had proposed the method, in which the resonant frequency and damping coefficient of dust particle oscillations in the sheath of rf discharge was used to determine particle charge. The vertical oscillations of the single-layer dust crystal were excited by rf voltage modulation.

In the paper /3/ the experimental method of dust particle charge determination based on the particle oscillations was suggested too. In the experiment the relaxation oscillations of a single dust particle caused by low-frequency discharge current modulation were observed. The calculation of the dust particle charge with the help of the eigenfrequency and damping coefficient was made. In /3/ the theoretical method of the dust particle charge calculation in consideration of the non-locality effect, which occurs in the stratified glow discharge of low pressures and small currents was proposed.

In the present paper, the vertical oscillations of a single dust particle induced by discharge current modulation are investigated in a stratified glow discharge. Amplitude-frequency characteristics (AFC) in dependence on pressure are measured. The AFC measurements for different shapes of modulating signals were made. The quantitative description of the resonance behaviour of the dust

particle based on the theory of the forced harmonic oscillator was made. The calculation of the dust particle charge with the help of eigenfrequency is made. The Q-factor of dusty plasma system is measured.

Experiments and results

The experimental investigation was conducted in stratified glow discharge, which produced in neon in the range of pressures 0.06-0.66 torr and currents 2-3 mA with calibrated monodisperse spherical melamine formaldehyde particles with diameters d=4.10±0.14 μm. The detailed description of the experimental setup was presented in /4/.

The discharge current modulator provides square wave output signals with different on/off ratios α. The current switching from i_1 = 2 mA to i_2 = 2.6 mA leads to the rigid shift of all striations by an order ΔZ = 2 mm. When the current switches back from i_1 to i_2 the striations return to the initial positions. The periodical displacement of the striation excites the vertical oscillation of the dust particle.

The modulation of the discharge current was used to excite the forced vertical oscillations of the dust particle. The frequency of the driving force coincides with that of current modulation. Under the square wave modulation of discharge current, which allowed us to measure the amplitude-frequency characteristic of dust particle oscillations, the driving force takes the form

$$f(t) = \begin{cases} f_{max}\ , for\ \ 0 < t < \alpha T \\ f_{min}, for\ \ \alpha T < t < T \\ f(t + (j+1)T) = f(t + jT)\ \ j = 0,1,2\ ... \end{cases} . (1)$$

Here, f_{min}, f_{max} are the values of the driving force corresponding to the current values i_1, i_2, T is the period, α is the on/off ratio.

AFC of dust particle oscillations were obtained in the range of pressures p=0.06-0.66 torr. The main resonance peaks at the frequency, close to the eigenfrequency of the dusty plasma system, were observed at lowest pressures. Maxima at multiple of the resonant frequencies were obtained /4/.

Discussion.

In the present paper the quantitative description of the experimentally obtained resonance curves is based on the theory of the forced harmonic oscillator. Thus the equation of oscillatory motion of the single dust particle is given by obvious relation $\ddot{z} + 2\beta\dot{z} + \omega_0^2 z = f(t)$, where β is the damping coefficient, ω_0 is the eigenfrequency, f(t) is the driving force given by equation (1). In the case of the square wave driving force the response function is

obtained as the superposition of the response functions of each component in the Fourier series expansion of the driving force

$$A_{sqr}(\omega) = \sum_k \frac{\sqrt{sin^2(k\pi\alpha)}}{k\pi} * \frac{(f_{max}-f_{min})}{\sqrt{\left(\omega_0^2-(k\omega)^2\right)^2+4\beta^2(k\omega)^2}}. \quad (2)$$

In figure 1 the multi-resonance curve is shown at pressure of p= 0.16 torr. The AFC of dust particle oscillations obtained under the square wave discharge current modulation with on/off ratios $\alpha = 3/8$ and $\alpha = 1/2$ at pressure p=0.16 torr were described by equation (2). In fig. 1 a it is observed that the main resonance peak at ν_{res} =22.3 Hz and the subharmonic peak at $\nu_{res}/2$ =11.4 Hz are well described by the theoretical curve. The value of eigenfrequency $\nu_0 = 21.8$ Hz and the damping constant and $\beta = 14\,\mathrm{s}^{-1}$ were determined by fitting the experimental data. In fig. 1 b the AFC obtained under the square wave discharge current modulation with on/off ratio of $\alpha = 1/2$ is shown at pressure of p=0.16 torr. The resonance curve described by equation (2) with the values of $\nu_0 = 21.6$ Hz and $\beta = 17\,\mathrm{s}^{-1}$ shows the main resonance peak at ν_{res} and the subharmonic peak at $\frac{\nu_{res}}{3}$ as expected. One can see that the value of eigenfrequency obtained by fitting the experimental data is of order of 22 Hz and it is invariant in pressure and in shape of modulating signal. The error in measurement of ν_0 is about 12%.

The single dust particle in the striation can be represented as a simple damped harmonic oscillator, which qualitative behavior can be determined by Q-factor value. Q-factor were determined by the following expression $Q_1 = \frac{A_{\max}}{A_0}$, where $A_{\max}$ is the amplitude of the main resonance peak, A_0 is the static zero-frequency offset (see Fig 1, dotted line). At pressure p=0.16 torr the Q-factor value is $Q_1 = 5$.

The eigenfrrequency of this the dusty plasma oscillatory system can be determined by following relation $\omega_0 = \sqrt{\frac{qE'(z_0)}{M_d}}$ ($E'(z_0)$ is the derivative of the electric field profile at point z_0) as suggested in [3,4]. The calculation of the charge of the single dust particle was made using the value of the eigenfrequency obtained through the approximation of the experimental data (fig. 1). The value of dust particle charge number $Z_d = q/e$ is $Z_d = (1.5 \pm 0.4)*10^4$. The dust particle charge determined using our experimentaly obtained data

differs less than 2 times from values obtained for dust particle of the same diameters d=4.10±0.14 μm at pressure p=0.5 torr in /5/. The comparison shows that the experimentally obtained charge number is in good agreement with the value determined through the relaxation oscillations of a single dust particle under the same experimental conditions in /3/.

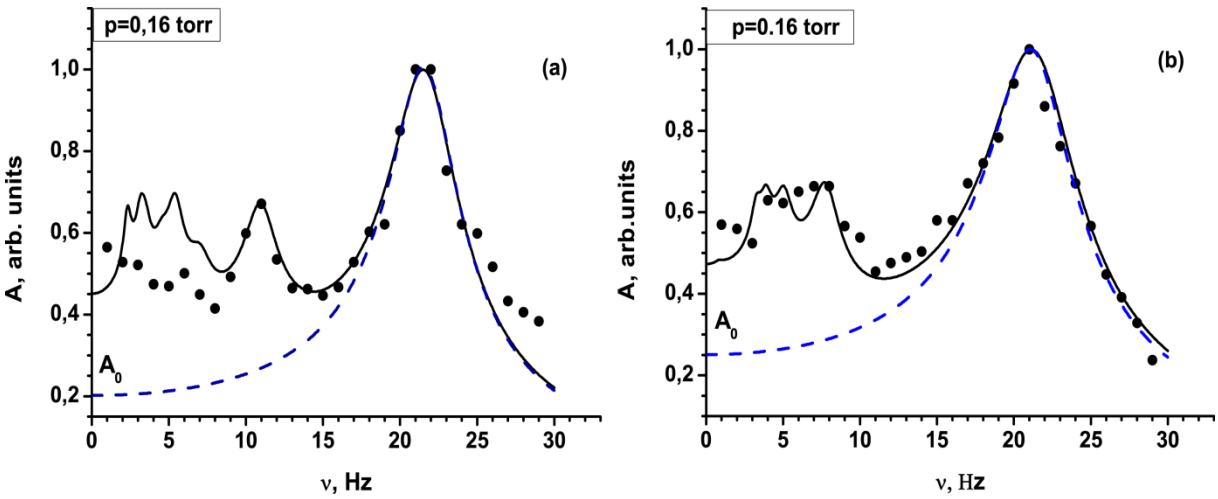

Fig. 1 – AFC obtained under the square wave current modulation with $\alpha = 3/8$ and $\alpha = 1/2$ at pressure p=0.16 torr

The amplitude spectrum is normalized to unity, the symbols represent experimental data, A_0 is the static zero-frequency offset, the solid line corresponds to approximation curve, described by equation (1). The dashed line is the approximation curve, which corresponds to the response function in the case of the sinusoidal driving force /4/.

Acknowledgements. Work was supported by RFBR grant No. 18-32-00685.

References

1. **Norman, G.; Stegailov, V. and Timofeev**, A. Journal of Experimental and Theoretical Physics, 113 (2011) 887-900
2. **Homann, A.; Melzer, A. & Piel**, A. Physical Review E , 59 (1999) R3835
3. **Golubovskii, Y.; Karasev, V. and Kartasheva, A**. Plasma Sources Science and Technology, 26 (2017) 115003
4. **Golubovskii, Y.; Karasev, V. and Kartasheva, A.** Plasma Sources Science and Technology, 27 (2018) 065006
5. **Fortov, V.; Nefedov, A.; Molotkov, V.; Poustylnik, M. and Torchinsky, V**. Physical Review Letters, 87(2001) 205002

Plasma-dust structures in a DC discharge in magnetic field

A. Abdirakhmanov, M. Dosbolayev, T. Ramazanov

Al-Farabi Kazakh National University, Almaty, Kazakhstan
abdirakhmanov@physics.kz

At present, there are several theoretical assumptions that the rotation of the plasma-dust structures in the stratum in a magnetic field can be caused by the presence of a number of irregularities such as the inversion of the radial ion flux, which is related either to the local reversal of the field, or to the onset of recombination on the dust structure; the effect of narrowing current channel /1-2/ and edge effects /3/ In the experiment /2/, a narrowing current channel (insert) is used to reduce the influence of the cathode spot on discharge stability and the formation of standing striations, and its position determines the position of the first standing stratum above the insert, that is, the dust trap, in a convenient place for observation.

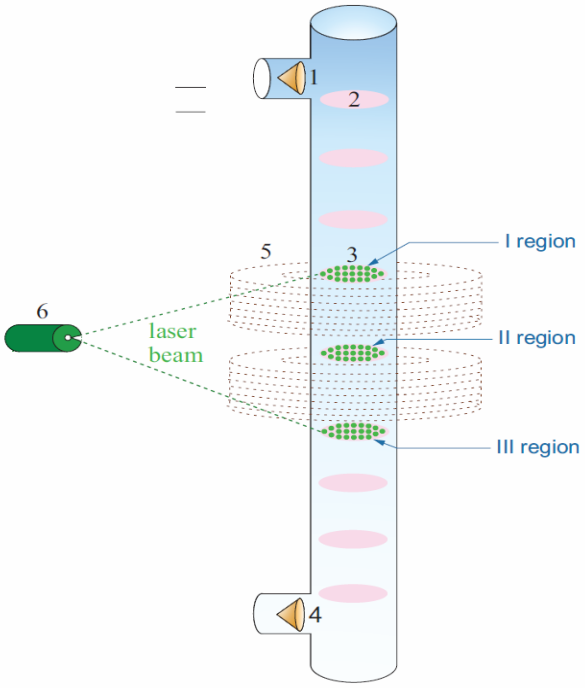

1-anode; 2-strata; 3-plasma-dust structures; 4-cathode; 5-coil; 6-laser;
Fig. 1 - Experimental setup

In this work, the influence of an external magnetic field on the dust structure of a glow discharge suspended in strata without a narrowing current channel (the diaphragm in the form of a cone) was investigated /4/. The results were obtained in the experimental setup for studying the properties of dusty plasma and plasma-dust structures in a glow discharge plasma (Fig. 1). Experimental condition: gas-argon, pressure P = 0.1-0.25 Torr, discharge current i = 0.5-1.5 mA, induction of external magnetic field B = 0-400 mT. As dust particles, polydisperse aluminum with a characteristic size of 1 to 10 μm was used /3/.

The measurement was carried out in three areas, above (I region), under (III region) and between (II region) coils. During the experiment, it was found that the dust structure in the first region rotates only clockwise. In the second region, where the dust structure is located between the two coils,

rotational motion is not detected. The dust structure located at the under the coils rotates counter-clockwise direction.

By the results of the experiment the rotational motion of dust structures was detected, which direction of rotation of dust structures depends on the position of the location of the magnetic coils. The dependence of the average angular velocity of dust structures on the induction of the magnetic field for different regions was obtained.

Acknowledgements. This work was supported by the Ministry of Education and Science of the Republic of Kazakhstan under Grant AP05133536.

References

1. Nedospasov A.V, Motion of plasma-dust structures and gas in a magnetic field // Phys.Rev. E 79, 036401 (2009).
2. Karasev et.all , The Dynamics of dust structures under magnetic field in Stratified Glow Discharges// Contrib.Plasma Phys.56 (2016).
3. Abdirakhmanov A.R., Dosbolayev M.K., Ramazanov T.S. The Gas Discharge Dusty Plasma in a Uniform Magnetic Field// AIP Conference Proceedings 1925, 020007 (2018);
4. M.K. Dosbolayev, A.R. Abdirakhmanov, S.K. Kodanova, T.S. Ramazanov, Zh.A. Moldabekov Plasma-dust structures in the DC discharge // 15th Dusty Plasma Workshop, USA, 2018. - P.58.

DENSITY WAVES IN A STRUCTURE OF CHARGED PARTICLES IN THE ELECTRODYNAMIC TRAP

V. Vladimirov, L. Deputatova, V. Filinov, D. Lapitsky, V. Pecherkin,
R. Syrovatka, L. Vasilyak, O. Petrov

Joint Institute for High Temperatures of the Russian Academy of Sciences, Izhorskaya 13 Bldg 2, Moscow 125412, Russia, syrovatkara@gmail.com

1. Introduction

The investigations of the dust acoustic solitary waves in plasmas were carried out over a period of more than several decades /1-4/. In these works in addition to positive ions and electrons plasmas contain other components, such as negative ions or dust particles. Dust acoustic waves in a dust component were investigated in a complex low-pressure plasma using the analytical and numerical fluid models and kinetic approaches. The main difficulty of this problem is that complex plasma is nonlinear medium where the waves of finite amplitude cannot be considered independently. Nonlinear phenomena in complex plasma are very diverse, due to a large number of different wave modes, which can be sustained. The wave amplitude can reach a nonlinear level because of different processes. This is not necessarily an external forcing, or the wave instabilities – it can also be a regular collective process of nonlinear wave steepening. In the absence of dissipation (or, when dissipation is small enough), nonlinear steepening can be balanced by wave dispersion which, in turn, can result in formation of solitons. When the dissipation is large, it can overcome the role of dispersion and then the balance of nonlinearity and dissipation can generate shock waves.

In this paper for the first time, we experimentally show the possibility of generation and propagation of the density waves in structures of similarity charged dust particles interacting via Coulomb potential in air under normal conditions. Dust particles were confined in the linear quadrupole electrodynamic trap /5/, when the viscosity energy losses are compensated by the energy contribution of the altering electrical fields of the trap.

2. Experiment

Our experimental investigations of excitation and development of the dust particle density disturbances in the similarity charged particle structures were carried out using the linear quadrupole electrodynamic trap (Fig. 1). The trap consists of four parallel steel cylindrical electrodes with a diameter of 3 mm and a length of 30 cm on which the alternating electric potential $U_a \sin(2\pi ft)$ with frequency $f = 50$ Hz was applied. The electrodes were placed at the tops of a square with a side of 2 cm. The phase shift of electric potential between adjacent electrodes was equal to π. At the left end of the trap (Fig. 1) an additional

electrode was mounted, to which a constant electrical potential U = 1 kV preventing the particles escaping from the trap was supplied. The right end of the trap remained open but the end electrode effects /6/ also prevent particle from escaping to the right. The electrodynamic trap was placed in a optically transparent plastic box for protection against air flows. In this paper we used polydisperse Al_2O_3 particles of 10 to 40 μm in size. The particles were positively charged by an induction method on the surface of a flat electrode, to which an electric potential of 10 kV was applied. The electrode was brought to the trap from below and the particles were drawn inward. For video registration of the particles illuminated by a laser beam, the HiSpec 1 video camera was used.

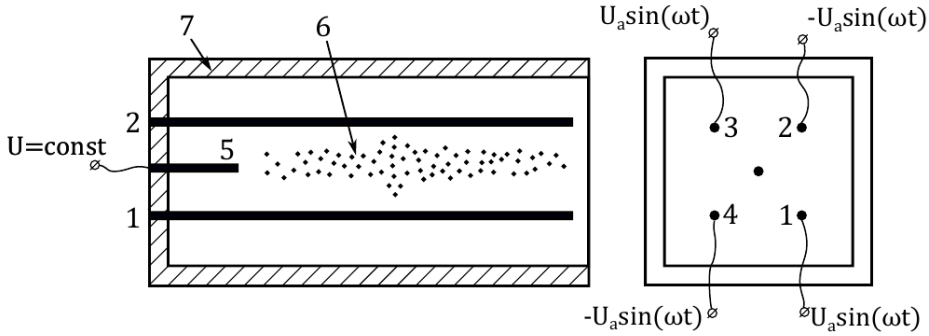

Fig. 1 – The scheme of the trap, front and side views. Notations: 1-4 – the electrodes of the trap, 5–the end electrode, 6–confined particles, 7–optically transparent plastic box

Fig. 2 shows the stable structure of charged dust particles obtained at a voltage U_a = 3.6 kV. The structure oscillates as a whole with frequency f = 50 Hz, the distances between the particles remain constant.

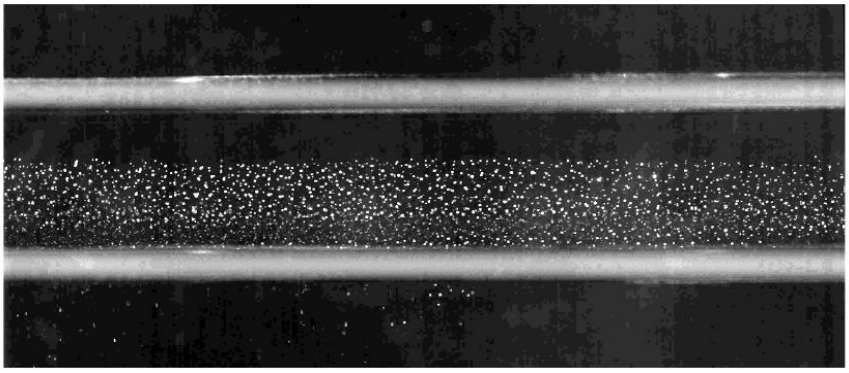

Fig. 2 – Stable structure of charged dust particles in the electrodynamic trap

Density waves can arise in these Coulomb structures after injection of additional particles (Fig. 3). Additional particles were injected into the trap from the surface of the flat electrode (Fig. 3(a)), after which a hump density wave appears in the Coulomb structure propagating to the right edge of the trap at velocity of 4 cm/s (Fig. 3(b)).

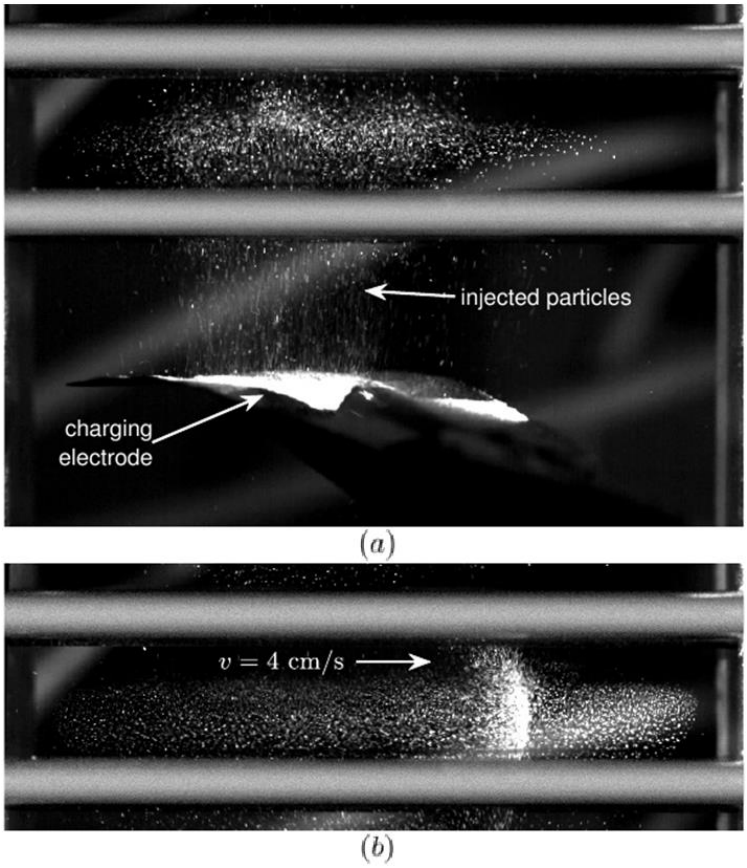

Fig. 3 – The appearance of hump density waves in the Coulomb structure after injection of additional particles

The appearance of density waves can also occur in stable Coulomb structures when the working parameters of the electrodynamic trap were changed, for example, when the voltage on the electrode trap was increased up to 5.1 kV. Then a dust density waves appear in the long dust particle structure (see Fig. 2). During the propagation of such waves, their shape changed insignificantly. The propagation of the density wave in the vicinity of the end electrode is shown in the Fig. 4. The wave propagates toward the end electrode at a velocity of 5.9 cm/s (Fig. 4(a)). After approaching the end electrode for a minimum distance of 1 cm (Figure 4(b)), the wave stops for 0.5 s, after which it started to propagate in the backward direction at a velocity of 4.1 cm/s (Fig. 4(c)). Analogous reflection exists when the hump wave approaches the right end of the trap. This reflection occurs due to the longitudinal electric field, which exists at the boundary of the trap due to curvature of the electric field lines \6\.

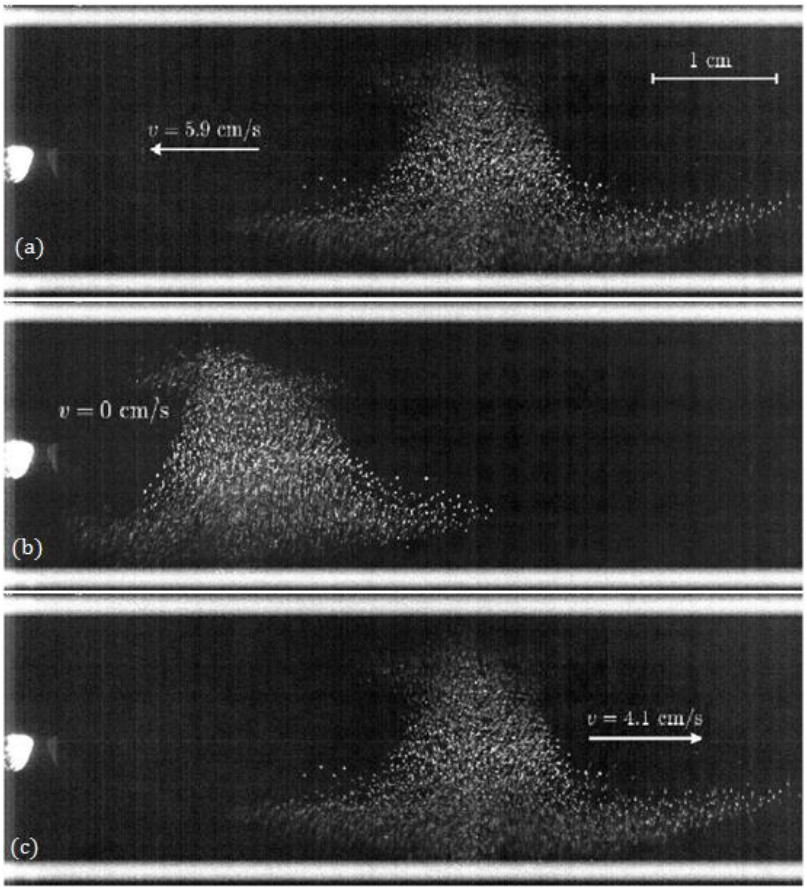

Fig. 4 – Reflection of the wave from the left end electrode (bright spot)

3. Conclusion

In this work, we have demonstrated for the first time the appearance of a density wave in the form of a single hump in a quadrupole electrodynamic trap in air under normal conditions. We have shown that the generation of density waves is possible by adding charged particles to the electrodynamic trap.

Acknowledgements. The work was done with financial support of the program of fundamental research of the Presidium of RAS "Condensed matter and plasma at high energy densities".

References

1. **Bonitz M. and Lopez J.** Complex Plasma. Switzerland: Springer International Publishing (2014).
2. **Fortov V.E., et al.** Phys. Rep. 421(2005) 1–103.
3. **Vladimirov S.V., Ostrikov K. and Samarian A.A.** Physics and Applications of Complex Plasmas. London: Imperial College Press (2005).
4. **Shukla P.K. and Silin V.P.** Physica Scripta, 45(1992), 508.
5. **Vasilyak L.M., et al.** New. J. Phys. 15(2013) 043047.
6. **Lapitsky D.S.** J. Phys.:Conf. Ser., 653(2015) 012130.

5. LASER AND PLASMA INTERACTION WITH SURFACES

Nb-C-N-Fe surface layers synthesis in high speed steel by compression plasma impact

N.N. Cherenda[1], V.V. Uglov[1], V.M. Astashynski[2], A.M. Kuzmitski[2], A. Ya. Leyvi[3]

[1] Belarusian State University, Nezavisimosty Ave 4, 220030, Minsk, Belarus, cherenda@bsu.by
[2] A.V.Lykov Heat and Mass Transfer Institute NAS of Belarus, P.Brovki str 15, 220072, Minsk, Belarus, ast@hmti.ac.by
[3]South-Urals State University, av. Lenina 76, 454080 Cheliabinsk, Russia, leiviai@susu.ru

High energy particle beams such as laser, electron, ion, and laser beams are widely used to modify properties of different materials. The effect of such flows in a mode with melting on heterogeneous systems containing the structure which ensureы certain properties of such systems leads to, as a rule, to dissolution of functional structures and deterioration of the system properties. Thus, a high energy impact on high speed steels results in structure homogenization, namely, dissolving of Fe_3W_3C type carbides /1-3/ and softening of the surface layer. In spite of surface properties worsening such treatment can be used as high temperature quenching. Subsequent annealing allows recovering the structure and obtaining more homogeneous distribution of hardening carbides /3/ than carbide distribution formed by traditional thermal treatment, thus preventing microchipping cutting tools made from high speed steels.

High energy particle beams treatment of the “coating/substrate” system can be used for alloying the substrate material with the coating elements. In particular, treatment of this system by compression plasma flows led to melting of the coating and substrate surface layer, liquid phase mixing and subsequent crystallization under conditions of high speed cooling. The investigation of the phase and element composition of the high speed steel surface layer alloyed by niobium atoms under the action of compression plasma flows was the main aim of this work.

AISI T1 steel samples (Fe 73,9-76,5%, W 17.0-18,5%, Cr 3,8-4,4%, V 1,0-1,4%, Mo 1,0%, C 0,7-0,8%, wt. %) were investigated. Combined treatment was carried out in the following way. At the first stage Nb coating was deposited using the vacuum arc vapor deposition technique with the following operating parameters: the arc current was 190 A, the negative bias voltage on the steel substrates was – 120 V, the deposition time was 10 minutes. The thickness of the coating was ~ 4 μm.

At the second stage the samples were treated by compression plasma flows (CPF) generated in the magneto-plasma compressor of compact geometry. The experiments were performed in the “residual gas” mode, i.e. the vacuum

chamber was filled with nitrogen at the pressure of 400 Pa. The distance between the electrodes and the treated surface of the samples changed from 12 to 8 cm, which corresponded to the energy density of heat flux absorbed by the sample (Q) of 14 and 23 J/cm^2 per pulse, respectively (registered by calorimetric measurements). Treatment was carried out by three or six pulses (n) at the interval of ~ 5 s.

The element composition of the samples modified surface layers was determined by means of the Auger electron spectroscopy (AES) using PHI-660 spectrometer combined with sputtering by Ar ions. Only five elements (C, N, O, Nb, Fe) were taken into account for the concentration determination due to the spectrometer limitations. Therefore AES data can be mainly used for the analysis of elements distribution behavior under different CPF treatment regimes. The determined concentration of the elements does not reflect their real atomic concentration because W atoms (~ 18 %) were not taken into consideration. The phase composition was investigated by means of the X-ray diffraction (XRD) method with the Ultima IV RIGAKU diffractometer in Bragg-Brentano geometry with parallel beams in Cu Kα radiation (λ=0.15418 nm).

The AES data showed the formation of two main sublayers in the analyzed layer after CPF treatment (Fig. 1). The first sublayer is a thin film containing mainly Nb and C. The second sublayer is a steel surface layer alloyed with Nb atoms. The Nb atoms concentration in the steel surface layer decreased with the growth of Q due to the increase of the melted layer thickness and redistribution of the alloying element in it and due to increase or erosion intensity during plasma impact.

One can see that the film contains C, N, O, Nb and Fe atoms. The presence of thin ZrN, TiN or ZrO_2 films on the surface of steel alloyed by Zr or Ti atoms under the action of CPF was observed earlier /4/. The formation of such a film took place due to the interaction of vacuum chamber residual atmosphere gases with alloying elements at the stage of cooling, nitride or oxide formation and subsequent film growth due to diffusion of alloying elements to the surface. Carbon was also observed earlier at the surface but as contamination. In these experiments one can see that carbon is one of the main constituents of the formed film. The ratio of the Nb and C concentration in the surface film (in case of CPF treatment with Q=14 J/cm^2) allows one to assume niobium carbide formation in it (Fig. 1 a and b). Nitrogen and oxygen had diffusion-like profiles in the surface film. Thus, diffusion of these elements took place in carbon-containing film formed earlier. At the same time the cause of the carbon-containing film formation is not clear. The presence of Fe atoms in case of CPF treatment with Q=14 J/cm^2 could be explained by large surface roughness of the sample that appeared after plasma impact.

The growth of Q led to the decrease of the film thickness (Fig. 1c) while the n increase almost did not influence it.

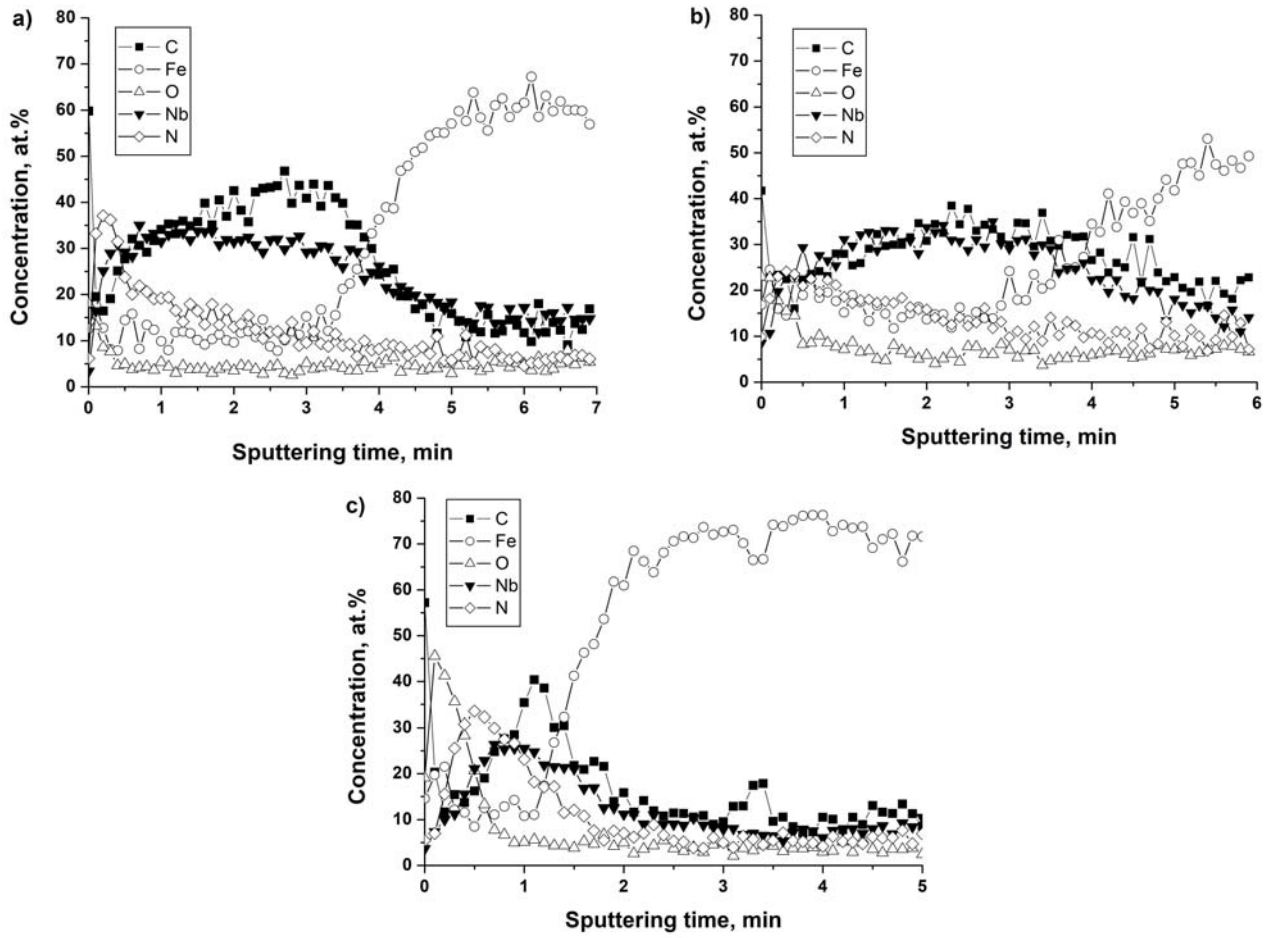

Fig. 1 - AES profiles of elements in the surface layer of the Nb/steel system after CPF treatment with n=3 and Q=14 J/cm^2 (a), n=6 and Q=14 J/cm^2 (b), n=3 and Q=23 J/cm^2

The results of the phase composition analysis are presented in Fig. 2. The XRD data showed that CPF impact on the Nb/steel system led to the dissolution of Fe_3W_3C type carbide and formation of a solid solution (with the alloying elements) on the basis of α-Fe and γ-Fe. The diffraction lines of the α-Fe solid solution are shifted to the area of smaller diffraction angles indicating the presence of interstitial atoms or atoms with a greater radius. The XRD analysis revealed a new phase formation. The position of this phase diffraction lines better corresponds to the position of δ-NbN diffraction lines than to the position of the NbC diffraction lines in spite of the AES data. Both of these phases possess a face centered cubic (fcc) lattice, therefore, the formation of the Nb(C,N) solid solution with fcc lattice can be supposed. One can also see that the position of these phase diffraction lines depends on treatment regimes. In case of CPF treatment with Q=14 J/cm^2 and n=3 diffraction lines shifted to the

position of NbC diffraction lines that could be associated with the carbon increase in the Nb(C,N) phase which correlates with the AES data.

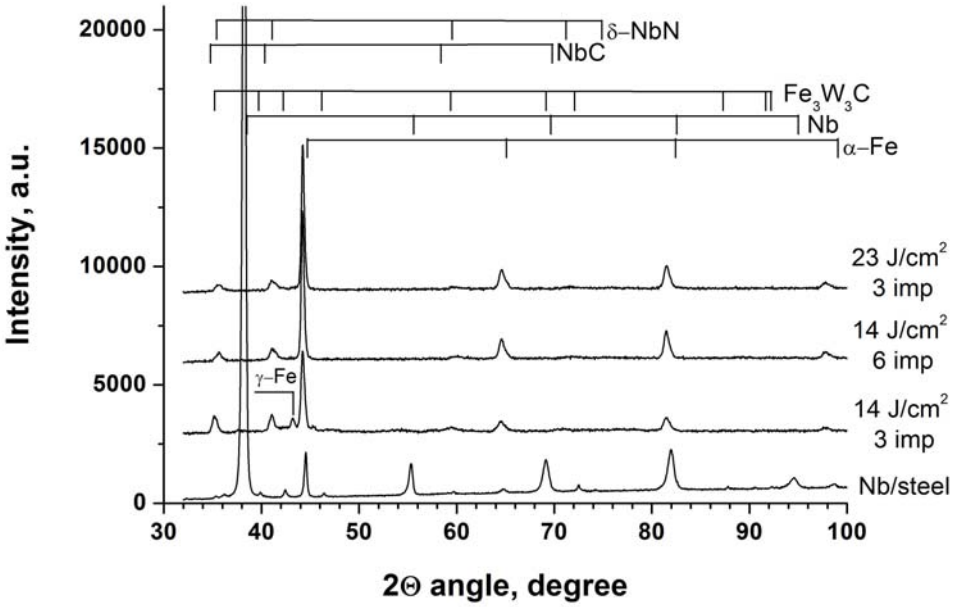

Fig. 2 - XRD patterns of the untreated Nb/steel sample and samples treated by CPF

The findings showed that compression plasma flows impact on the Nb/high speed steel resulted in the formation of two main sublayers in the steel modified layer: the surface film containing the Nb(N,C) phase and the steel surface layer alloyed with Nb atoms. Both the film thickness and Nb concentration in the alloyed steel surface layer were dependent on plasma treatment parameters.

References

1. **Ivanov Yu., Matz W., Rotshtein V., Gunzel R., and Shevchenko N.** Surface and Coatings Technology, 150 (2002) 188-198.
2. **Xian-xiu Mei, Sheng-zhi Hao, Teng-cai Ma, Ying-min Wang and Zhen-min Liu.** Nucl. Instrum. Methods Phys. Res. B 239 (2005) 152-158.
3. **Cherenda N.N., Uglov V.V., Bibik N.V., Gusakova S.V., Astashinskii V.M., Kuzmitskii A.M., and Ukhov V.A.** Journal of Surface Investigation. X-ray, Synchrotron and Neutron Techniques, 5(2) (2011) 305–309.
4. **Cherenda N.N. and Uglov V.V.** Modification of Steels Microhardness by Compression Plasma Flows. In: Handbook of Material Science Research. Editors: Charles Rene and Eugene Turcotte. New York: Nova Science Publishers (2010).

ABLATION PROCESSING OF DENTAL TISSUE BY XeCl LASER

S. Anufrick, A. Volodenkov, K. Znosko

Yanka Kupala State University of Grodno, 22, Ozheshko Street, 230023, Grodno, Belarus,
a.volodenkov@grsu.by

Coherent sources of radiation with high power in the ultraviolet (UV) region of the spectrum are widely used in medicine and various fields of technology.

Laser radiation is widely used in the practical ablative treatment of biological tissues. Studies on ablative effects make it possible to determine the characteristics of radiation, which ensure high efficiency and quality of ablation treatment of biological tissues. Laser ablation has a threshold character, and the magnitude of the threshold depends both on the duration and on the wavelength of the radiation pulse. The report presented below contains the results obtained during the experimental study of the ablation effect on biological objects of radiation from an XeCl electric discharge laser.

The XeCl laser had the system of excitation constructed under circuit of the LC inverter and the unstable telescopic resonator. The maximal value of energy of generation of the XeCl-laser made 30 mJ, thus duration of generation pulse on half-height was 10 nanoseconds.

Ablation influence of ultraviolet radiation on a surface of dental enamel and dental calcium was investigated.

For transportation of radiation of the excimer laser (308 nanometers) the system on the basis of mirrors and lenses has been used which optical circuit is described on Fig. 1.

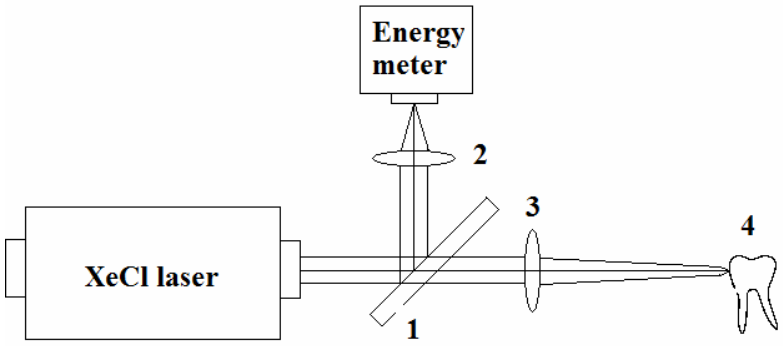

Fig. 1 - Optical schematic model of irradiation

Radiation of the XeCl laser went on a quartz substrate 1. The radiation reflected from a quartz substrate (1), went on focusing lens (2) and got on a measuring instrument of energy (ИМО-2Н) which was used for the control of energy of radiation. Radiation past through a quartz substrate (2) went on

focusing lens (3) and further on the irradiated object (4). Lenses (2, 3) had the antireflection covering for wave length 308 nanometers. Calibration of measuring instrument of energy (ИМО-2Н) which under indications of this device, allows to define energy falling on irradiated object 4 is executed. For this purpose on a place of irradiated object second device (ИМО-2Н) was put.

The focusing lens with a focal length of 235 mm has been used and radiation was focused in an oval spot with average diameter ~ 1 mm. For reception of various values of energy of a pulse of radiation sets of diaphragms and adjustment of value charging voltage were used. Samples of dental tissue were irradiated with a series from 1000 pulses at use of frequency of following of pulses of 2 Hz. Depth of a crater was defined by means of an optical microscope. In Fig. 2 dependence of depth of a crater in dental enamel (1) and dental calcium (2) from density of energy after 1000 pulses is submitted.

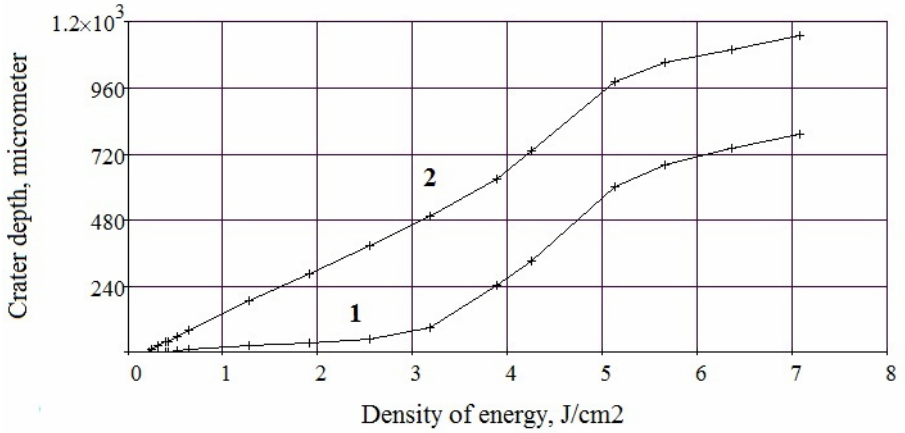

Fig. 2 - Dependence of depth of a crater in dental enamel (1) and dental calcium (2) from density of energy (after 1000 pulses of an irradiation)

The determining factor for depth of a crater is the density of power, therefore in Fig. 3 dependence of depth of a crater on density of power of laser radiation after 1000 pulses is submitted.

From the data, submitted in Fig. 2, it follows that dependence (1) has threshold character and at the density of energy smaller than 0,4 J/cm^2 process of formation of craters in dental enamel is not observed. From data, submitted in Fig. 2, it follows that dependence (2) has threshold character and at density of energy smaller than 0,2 J/cm^2 process of formation of craters in dental calcium is not observed.

From the data submitted in Fig. 3, it follows that dependence (1) has threshold character and at density of power smaller than 40 MW/cm^2 process of formation of craters in dental enamel is not observed. From data submitted in Fig. 3 follows, that dependence (2) has threshold character and at density of power smaller than 20 MW/cm^2 process of formation of craters in dental calcium is not observed.

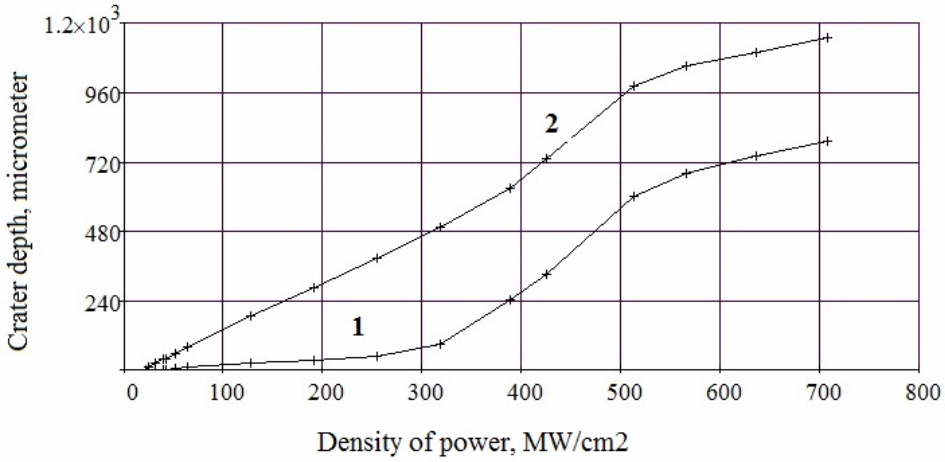

Fig. 3 - Dependence of depth of a crater in dental enamel (1) and dental calcium (2) from density of power (after 1000 pulses of an irradiation)

Then at density of energy more then 0,2 J/cm^2 (20 MW/cm^2) and less then 0,4 J/cm^2 (40 MW/cm^2) the efficient removal of dental calcium takes place without ablation of dental enamel.

From the graphs of the dependencies presented in Fig. 2-3, it is possible to determine at what energy densities the removal of enamel and calcium is most effective. Fig. 4 and Fig. 5 show the dependence of the specific energy of evaporation of tooth enamel on energy density and power density. Fig. 6 and Fig. 7 show the dependence of the specific energy of evaporation of calcium from the energy density and power density. From these dependences it follows that as the density of energy (power) increases, the specific energy of evaporation decreases and, consequently, the more effective removal of calcium and enamel take place.

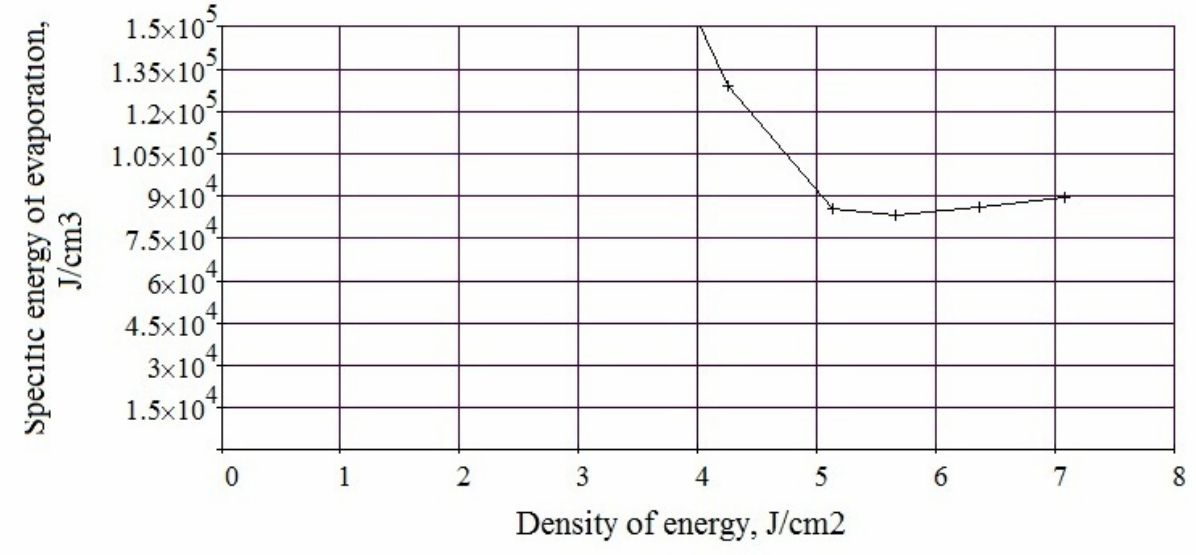

Fig. 4 - Dependence of the specific energy of evaporation of the enamel on the energy density

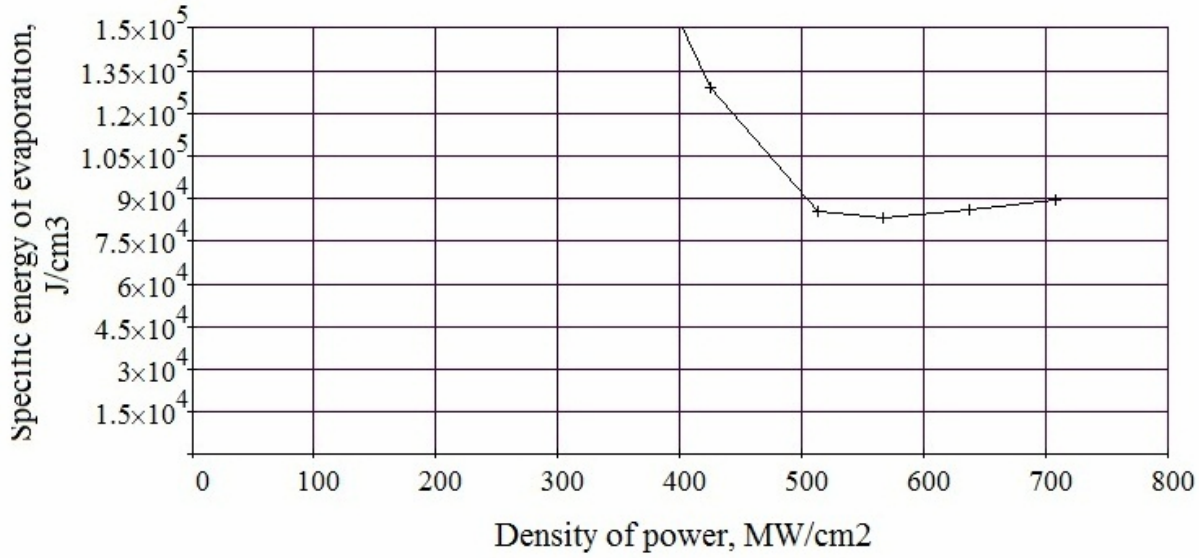

Fig. 5 - Dependence of the specific energy of evaporation of the enamel on the power density

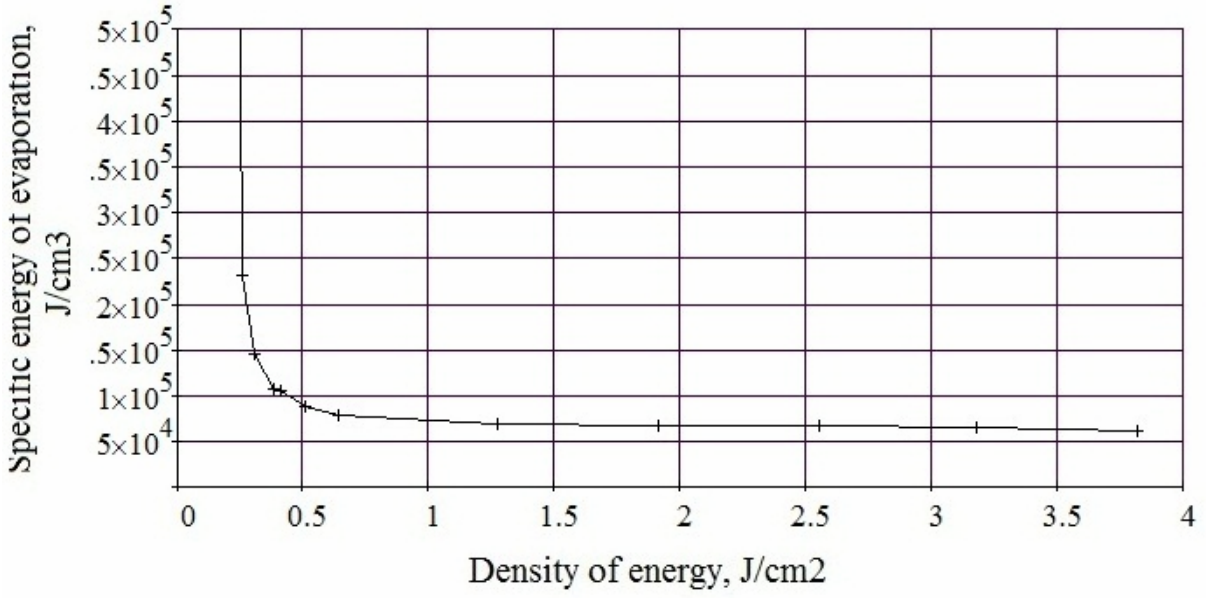

Fig. 6 - Dependence of the specific energy of evaporation of the calcium on the energy density

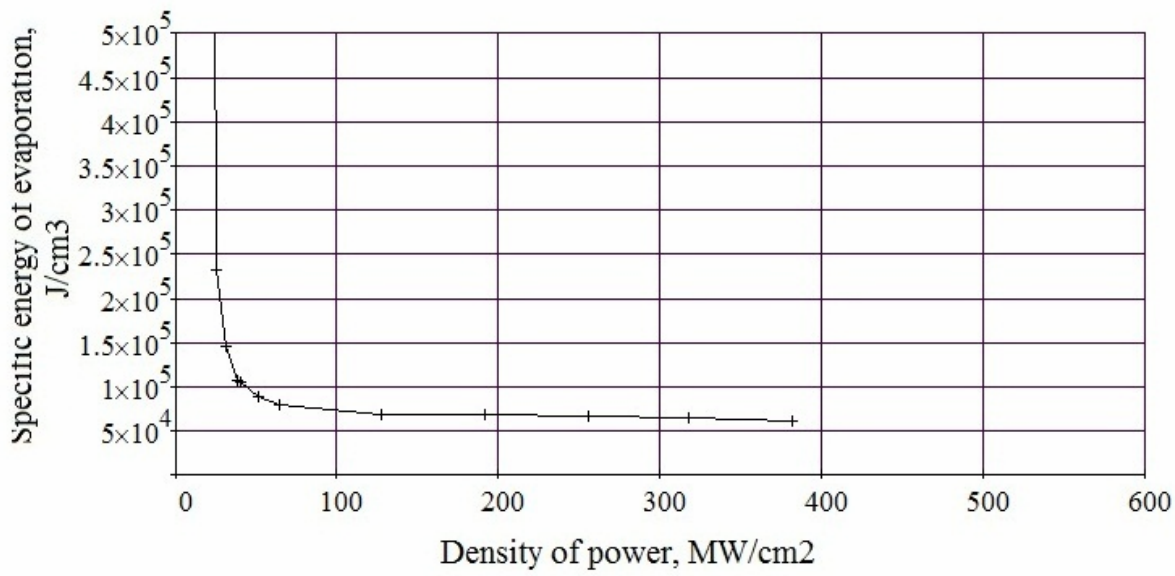

Fig. 7 - Dependence of the specific energy of evaporation of the calcium on the power density

NONEQUILIBRIUM PROCESSES OF INTENSE LASER RADIATION INTERACTION WITH HETEROGENEOUS MEDIA CONTAINING OF NANOPARTICLES WITH PLASMA FORMATION

V.K. Pustovalov[1], A.N. Chumakov[2]

[1]Belarusian National Technical University, Pr. Independency, 65, Minsk, 220013, Belarus, pustovalovv@mail.ru
[2] B.I. Stepanov Institute of Physics, National Academy of Sciences of Belarus, Pr. Independency, 68, Minsk, 220072, Belarus, a.chumakov@dragon.bas-net.by

Nonequilibrium processes of intense laser radiation interaction with heterogeneous media containing of nanoparticles (NPs) are very interesting for laser and plasma modification of different nanostructured materials and media. Laser interaction determines the initiation of various processes preceding plasma formation. Particularly, absorption of intense laser radiation by NPs initiates the following thermal, plasma and hydrodynamical processes, as acoustic waves, evaporation of NPs and ambient medium, dynamics of vapor bubble, shock wave propagation, laser ablation of heterogeneous media, etc, which can initiate optical breakdown and plasma formation in the final moment.

Short analysis of the mentioned processes has been made, taking into account the optical, thermal and heating processes. NPs have different structures (homogeneous, two layered core-shell, multi layered) with shapes (spherical, nonspherical, rod, cubical, others) and produced from various materials – metals (Au, Ag, Al, etc.), oxides (TiO_2, Al_2O_3, Fe_2O_3, etc.), semiconductors (Ge, etc.). Surrounding media can be gaseous (air, etc.), liquid (water, ethanol, etc.), solid (metal, oxide, polymer, semiconductor, etc.). Characteristics and parameters of NPs, their environments and laser radiation, are presented in various studies of the interaction processes of laser radiation with NPs mentioned lower.

Interaction of laser radiation of moderate intensity with NPs includes next set of processes.

1. Absorption of optical radiation by the electron subsystem of the NP metal (material) and plasmonic resonance of metal NPs and resonance Mie of oxide NPs. - Absorption and scattering of light by small particles and optical properties of metal clusters were first time investigated /1, 2/. Optical properties of gold NPs for laser applications in nanotechnology and medicine and characterization of plasmonic and thermo-optical parameters of spherical metallic NPs are presented /3, 4/. Analysis of optical properties of spherical metallic NPs for effective absorption of solar radiation and their heating has been carried out /5/.

2. Nonequilibrium processes of thermalization of electrons and electron-phonon heat exchange after laser pulse action with pulse duration $t_p \sim 10^{-13}$ s are

investigated /6-9/. Temperature dependences of the electron-phonon coupling, electron heat capacity and thermal conductivity under femtosecond laser irradiation and conditions of strong electron-phonon nonequilibrium are presented /6/. The model of electron-phonon coupling and electron heat capacity of metals, including femtosecond optical investigation of electron-lattice interactions in a single metal NP is presented /7, 8/. Modeling of the processes of laser-NP interaction taking into account temperature dependences of parameters is investigated /9/.

3. Thermo-electron emission in the absence and in the process of electron energy exchange with a lattice. – Electron emission from metal surface under action of ultrashort laser pulses has been investigated /7/.

4. Possible Coulomb explosion of charged NP. – Femtosecond laser-induced size reduction of aqueous gold NPs has been studied /10/ in situ and pump – probe spectroscopy investigations revealing coulomb explosion of charged NP because of intensive electron emission from metal surface.

5. Homogeneous and inhomogeneous intensity distributions inside NP. – Extreme light concentration inside plasmonic gold and silver NPs during laser irradiation and their influence on absorption of radiation by NP and following thermal processes has been stated /11/. Local field effects on laser-induced heating of metal NPs have been noted /12/.

6. Heating of spherical NPs in media by short laser pulses and their cooling after the end of radiation action. – Theoretical study of heating of spherical NP in media by short laser pulses has been carried out /13/. Photothermal and accompanied phenomena with gold NPs and laser pulses have been presented /14/. Analytical and computer modeling of thermal processes, light-to-heat conversion and heating of single NPs, their assemblies, and surrounding medium under laser pulse action /15/. External heat conduction transfer produces thermal aureoles around NP and additional scattering of radiation on them. Experimental investigation of nanoscale heating of laser irradiated single gold NPs in liquid has been carried out /16/.

7. Thermal radiation from the heated NP surface. – Thermal radiation and heat conduction from a spherical NP for the application in laser-induced incandescence is investigated /17, 18/.

8. Thermochemical processes (combustion in air, optothermal catalysis, polymerization of the environment, etc.) in the environment. – Heterogenous catalysis mediated by plasmon heating /19/, visible-light-enhanced catalytic oxidation reactions on plasmonic silver nanostructures /20/, degradation of protein in nanoplasma generated around gold NPs in solution by laser irradiation /21/ have been investigated.

9. Vibrations of the volume of a heated NP and acoustic processes in the environment have been investigated on the base of optical studies of dynamics

in noble metal nanostructures /22/.

The processes of interaction of high intensity laser radiation with NPs.

10. Melting processes in the environment. – Gold NPs reshaped by ultrafast laser irradiation inside silica - based glass, studied through optical properties /23/.

11. Processes of vaporization in the surrounding liquid medium. – Excitation of nanoscale vapor bubbles at the surface of gold NPs and cavitation dynamics on the nanoscale together with self-limited growth of laser-induced vapor bubbles around single microabsorbers were investigated /24, 25/.

12. Melting of NP material (surface and complete melting, NP spheroidization). – Optical characteristics of metallic NPs during melting by laser radiation /26/, photothermal reshaping of gold NPs in a plasmonic absorber /27/, laser-induced heating and melting of gold NPs studied by time-resolved x-ray scattering /28/, laser-induced shape transformation of gold NPs below the melting point: the effect of surface melting /29/ have been investigated.

13. Evaporation and growth of a NP under the action of radiation. – Methodological improvement in pulsed laser-induced size reduction of aqueous colloidal gold NPs by applying high pressure /30/, mechanism of laser-induced size reduction of gold NPs as studied by single and double laser pulse excitation /31/, mechanisms of size reduction of colloidal silver and gold NPs irradiated by Nd:YAG laser /32/ have been investigated.

14. Formation of nanostructures under the influence of radiation on NPs. Laser-induced fabrication of hollow platinum nanospheres for enhanced catalytic performances /33/, studies on the interaction of pulsed lasers with plasmonic gold NPs toward nanofabrication /34/ were investigated.

15. Optical breakdown initiated by a NP, formation plasma and shock wave. - Ionization of gold NPs in solution by pulse laser excitation as studied by mass spectrometric detection of gold cluster ions /35/ was investigated.

16. Fragmentation of a NP under the action of radiation. – Fragmentation of colloidal NPs by femtosecond laser-induced supercontinuum generation /36/, photofragmentation of phase-transferred gold NPs by pulsed laser light /37/, experimental and theoretical analysis of photofragmentation of Au NPs by picosecond laser radiation [38] have been investigated.

17. Threshold of laser initiation of various processes are presented /14/.

These processes, especially with plasma formation, can be used for the applications in the synthesis of new materials, characterization and investigation of their parameters and various applications in nanostructured material treatment, laser chemistry, solar energy, etc.

Acknowledgements. This work was supported by the Belarusian State Program “Convergence-2020" (project no. 2.4.02).

References

1. **Bohren C.F. and Huffman D.R.** Absorption and Scattering of Light by Small Particles. Wiley: New York. 1983.
2. **Kreibig U. and Vollmer M.** Optical Properties of Metal Clusters. Springer Series in Material Science. 1995, 25.
3. **Pustovalov V.K. and Babenko V.A.** Laser Phys. Letters, 1 (2004) 516−520.
4. **Pustovalov V.K., Astafyeva L.G. et al**. Solar Energy, 122 (2015) 1334-1341.
5. **Astafyeva L., Pustovalov V.** Nano-Structures & Nano-Obj. 12 (2017) 57–67.
6 **. Lin Z., Zhigilei L.V., and Celli V.V**. Phys. Rev. B, 77 (2008) 075133.
7. **Anisimov S., Kapeliovich B., Perelman T.** JETP, 39 (1974) 375–380.
8. **Del Fatti N, Arbouet A, Vallee F.** Appl. Phys. B, 84 (2006) 175–181.
9. **Pustovalov V.** Laser Physics, 21 (2011) 906–912.
10. **Werner D., Furube A. et al.** J. Phys. Chem. 115 (2011) 8503–8512.
11. **Astafyeva L. and Pustovalov V.** Plasmonics, 10 (2015) 1439–1445.
12. **Bruzzone S. and Malvaldi M.** J. Phys. Chem. 113 (2009) 15805–15810.
13. **Pustovalov V.K.** Chemical Physics, 308/1-2 (2005) 103–108.
14. **Pustovalov V., Smetannikov A. et al.** Laser Phys. Lett., 5 (2008) 775–792.
15. **Pustovalov V.K.** Review. RSC Advances, 6 (2016) 81266 – 81289.
16. **Honda M, Saito Y, Smith N.** Optics Express, 19 (2011) 12375–12381.
17. **Liu F., Daun K., Snelling D. et al.** Appl. Phys., 83 (2006) 355–382.
18. **Martynenko Yu.V. и Ognev L.I.** Technical Physics, 75 (2005) 130–135.
19. **Adleman J, Boyd D., Goodwin, D. et al.** Nano Lett., 9 (2009) 4417−4423.
20. **Christopher P., Xin, H., Linic S.** Nat. Chem. 3 (2011) 467–472.
21. **Takeda Y., Kondow T. et al.** J. Phys. Chem., 110 (2006) 2393−2397.
22. **Hartland G.V.** Chem. Rev., 111 (2011) 3858−3887.
23. **Fan C., Poumellec B. et al.** J. Phys. Chem., 116 (2012) 2647–2655.
24. **Kotaidis V., Dahmen C. et al.** J Chem. Phys., 124 (2006) 184702.
25. **Neumann J, Brinkmann R.** Appl Phys Lett., 93 (2008) 033901.
26. **Pustovalov V. and Chumakov A.** J. Appl. Spectroscopy, 84 (2017) 71–75.
27. **Wang J., Chen Y., Chen X., Hao J. et al.** Optics Express 19 (2011) 14726.
28. **Plech A. and Kotaidis V.** Phys. Rev. B, 70 (2004) 295423.
29. **Inasawa S., Sugiyama M. et al.** J. Phys. Chem. B**,** 109 (2005) 3104−3111.
30. **Werner D., Ueki T. et al.** J. Phys. Chem. C, 116 (2012) 5482−5491.
31. **Muto H, Miyajima K, Mafune F.** J. Phys. Chem B, 112 (2008) 5810−5815.
32. **Pyatenko A., Yamaguchi M. et al.** J. Phys. Chem, 113 (2009) 9078−9085.
33. **Lee H., Kwak J., Jang D.** J. Phys. Chem. C, 118 (2014) 22792−22798.
34. **Hashimoto S, Werner D. et al.** J. Photoch. Photobiol. C, 13 (2012) 28–54.
35. **Shoji M., Miyajima K. et al.** J. Phys. Chem. B, 112 (2008) 1929**–**1932.
36. **Besner S., Kabashin A. et al.** Appl. Phys. Lett. 89 (2006) 233122.
37. **Peng Z, Walter T., et al.** J. Phys. Chem. B, 109 (2005) 15735–15740.
38. **Giammanco F., Giorgetti E. et al.** J. Phys. Chem. C 114 (2010) 3354-3363.

COMPARATIVE STUDY OF THE LASER INDUCED HELIUM GAS PLASMA SPECTROSCOPY WITH SINGLE AND DOUBLE PULSE LIBS

K.H. Kurniawan[1], A.N. Chumakov[2] and K. Kagawa[3]

[1]Research Center of Maju Makmur Mandiri Foundation, 40 Srengseng Raya, Jakarta Barat 11630, Indonesia. E-mail: kurnia18@cbn.net.id
[2]Laboratory of Radiative Plasma Dynamics, B.I. Stepanov Institute of Physics, National Academy of Sciences of Belarus, Independency Ave., 68-2, Minsk, 220072, Belarus. E-mail: chumakov@imaph.bas-net.by
[3]Department of Physics, Faculty of Education and Regional Studies, Fukui University, Fukui 910-8507, Japan. E-mail: k-kagawa@fukuikagakugakuen.com

Despite the well established advantages and popularity of the widely used LIBS for practical and rapid spectrochemical analysis, there are obviously rooms for its further improvements. The need to overcomes the Stark broadening and time mismatching effects for achieving high resolution and highly sensitive detection as well as the demand for the linear calibration line with zero intercept required by reliable quantitative analysis remain the challenging problems for certain important applications. In response to those challenges, we propose in this report a modification of the conventional LIBS by adopting two laser system with He ambient gas simply named "Laser-Induced Plasma Spectroscopy Utilizing He Metastable State (LIPS-He*) method. In this setup, A Nd YAG laser operating at its fundamental wavelength is used to generate the He gas plasma at high energy (60 - 110 mJ), while the third harmonic pulse from the other laser is employed to ablate the sample with certain delay so that the ablated atoms enter the gas plasma when it is sufficiently cooled and free from the initially produced charge particles and be excited via energy transfer from the metastable excited He atoms in the plasma. For comparison, emission spectra of a standard steel sample are measured by this technique and the conventional single pulse LIBS as well as the double pulsed LIBS. The calibration curves obtained by using the (LIPS-He*) technique gives an obviously much better result in terms of the linearity of the calibration curve of Cr. It also has low detection limit of 3 ppm thanks to the low spectral background, with the matrix effect fully suppressed. Finally the excellent emission spectra presented in this report further demonstrate the unusually high resolution in the depth analysis achieved by this new technique

A Comprehensive Review on Metal Nano- Architecture using Laser Ablation Methods in Current Perspective and Future Trends

Ma. Ganjali[1], Mo. Ganjali[2]

[1] Nour Zoha Materials Engineering Group (NMERG) and Materials and Energy Research Centre (MERC), Shadmehr St., No. 1, 4th floor, 1456655695, Tehran, Iran, ganjali.m@gmail.com
[2] Materials and Energy Research Centre (MERC), Emam Khomeini Blvd, Meshkindasht, 31878-316, Karaj, Iran, monireh_gan@merc.ac.ir

Abstract Pulse laser ablation method has been architectured to synthesize metal nanoparticles (MNPs) with unrivaled advantages such as simple, versatile, stabilized, biocompatible, economical, repeatable, and green technique without surfactant for a long term. In medicine, electronics with sensitive effective, it is sufficiently expected to small-scale and ultra-pure particles. Laser parameters (wavelength, intensity, frequency, and exposure time) can also affect shape and size distribution and morphology of the MNPs.

Introduction The metallic nanoparticles (MNPs) nanosized structures has been endlessly fascinating sciences and industries over the last half-century, due to their specific physical and chemical features dedicated to novel possibilities utilized in promising applications such as biotechnology, electronics, photonics, medicine, lithography, photochromic, self-assembling materials, Raman spectroscopy, manufacturing and so on. So both fabrication and applications of the MNP are especially beneficial for today lifestyle.

The most common methods are based on the chemical reduction of metallic ions in solutions leading to benefit results regarding the final size and shape of the MNPs. More applying the nanomaterials is of their higher efficiency and fewer component ingredients leading to higher reactivity with other issues in reactions. The efficiency is inversely correlated to particle radius and this is that more active particles are available with a larger surface area in result from smaller radios. Therefore NPs are sufficiently distinguished from regular materials to nanosized formations with improved features such as optical, physical, and mechanical. Considering all the methods are mainly related to the control of the size, shape, and morphology in nanomaterials, a basic role of the surfactant to fabricate a byproduct is obviously presented which is the most significant disadvantage of the chemical approaches. Hence, scientists must pay significant attention to the selection of an appropriate method to prepare the pure, uniform and homogenous MNPs.

According to solve similar problems, rapid and flexible improvement of laser setup along with particularities of stable and amplified effects and safety and ultimate green eco-friendly products are the main reasons to broadly develop a proper laser ablation method (LAM) born after the invention of the ruby laser in pulse mode in the mid-1960s.

This review comprehensively provides a brief discussion on setup for MNP producing, mechanism, advantages and disadvantage and some common devices to characterize particles using LA method /1-5, 8, 9/.

Method and Mechanism of LAM LAM as a laser-induced effect in liquid, opposite of other wet chemistry approaches, refers to the desired, pure, homogenous and uniform MNPs with narrow size and spectrum and strong control of original materials in liquids. In this concept, the repeatable method is simply performed with relatively economic, biocompatible, promising, reliable, green without chemical toxic and reagents process.

A pulsed laser beam presents a fast ablation of the material from the target surface, while formation and rapid condensation of plasma plume onto a sample are simultaneously performed in a pure liquid. It is considered that homogeneous nucleation of MNPs results in the fine saturation of laser-reduced MNPs in sizes with smaller ranges in solution.

Considerably control NPs generated in alloy, composition ingredient, and lattice shapes are accomplished using photo-mechanical effect by pulsed laser energy. Contrary to the advantages of the LAM in liquid noted above this procedure has one disadvantage including the MNP low formations compared to conventional methods which can also be probably improved under varying the experimental conditions /2-4, 6-8/.

Laser pulses are focused on the target surface to interact with a sample for LAM technique through the present experimental setup shown in Fig. 1. The target can be employed in forms of powder, suspension, or bulk placed into a pure liquid. According to the absorbing of a laser wavelength by the surface of a material, the photo-thermal response made subsequently causes the thermal effect transmitted throughout the target vertically and horizontally, this can be only done if the speed of heat is faster than laser pulse duration. This is that a laser-induced plasma plume, near the surface, successfully leads to a stoichiometric cutting of the substrate, where a magnetic stirrer helps to homogenously fabricate various particles (spherical, rod, wire) due to chemical changes in nanosized forms released into the liquid /2,10/.

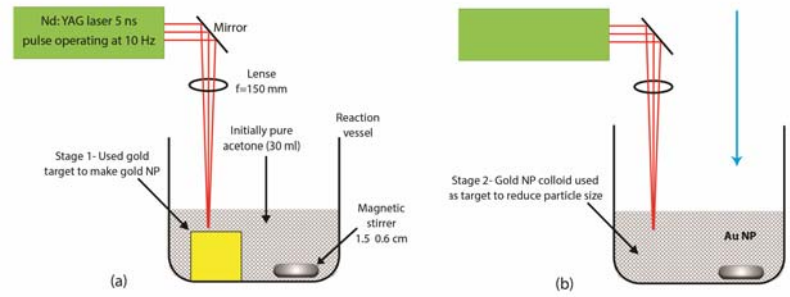

Fig. 1 - A schematic of the MNPs generation by the LAM, (a) with a gold target; (b) to more reduce the Au NPs generated (Updated from /2/)

Although the mechanism of the laser-matter interaction has not still been completely explained, both thermal (the laser-matter interaction) and chemical (related to environment liquids) effects are two mechanisms providing the ablation approach controlled by evaporation, boiling, explosion, and equilibrium phase transition /11/. Nonthermal processes as an over-rapid thermal process are also created through photo-mechanical effect where spallation and fragmentation are two forms of the nonthermal mechanism.

Before starting the experiment, it is a necessity to control quantitatively and qualitatively MNP formation, size, and structure through optimization of the experimental conditions and laser setup (duration time, laser influence, a speed of magnetic stirrer, inner gas, liquid, laser mode) /2/.

Noticeable the laser-induced modification of NPs precisely inhabits to perform undesired phenomena such as agglomeration, deposition, and instability surface plasma resonance (SPR) via two benefit offers: keeping MNPs in dark and cold place and keeping MNPs away from light /1-4/.

Comparison with prior studies, unique physical and chemical Properties of MNPs are characterized by the most common devices i.e., UV-visible spectroscopy, X-ray diffraction, X-ray photoelectron spectroscopy, scanning electron microscopy and transmission electron microscopy. Thus, the stability, both molecular and crystal structures, qualitative and quantitative determination of chemical materials, evaluation the degree of crystallinity, isomorphous changes, grain size, size distribution, and morphology of NPs by the devices listed are continuously evaluated /12/.

Conclusion To conclude several aspects effectively involved in the current review are followed as Discussion about the formation mechanism of the homogeneous and uniform MNPs by a novel method of a laser ablation (LA) in the liquid, Obtaining of stability, and purity of MNPs using several optimizations, Introducing of physical and chemical features of the pure MNPs

by specific devices, i.e., UV-visible spectroscopy, XRD, XPS, SEM and TEM, Explanation of the incomparable advantages and disadvantage of the LAM, Recalling the past and future applications of the MNPs in the numerous industries.

Acknowledgments This work was supported by both Materials and Energy Research Centre and Nour Zoha Materials Engineering Research Group Foundations for Fundamental Research (grant No. 182906).

References

1. **Tarasenko N.V., Butsen A.V., and Nevar E.A.** Applied Surface Science, 247 (2005) 418-422.
2. **Ganjali Ma., Ganjali Mo., Khoby S., and Meshkot M.A.** Nano-Micro Lett., 3 (2011) 256–263.
3. **Ganjali Ma., Ganjali Mo., Vahdatkhah P., and Marashi S. M.** Procedia Materials Science, 11 (2015) 359 – 363.
4. **Ganjali Ma., Ganjali Mo., and Sangpour P.** Journal of Applied Spectroscopy, 80 (2014) 991-997.
5. **Maiman T.H.** Nature, 187(1960) 493–494.
6. **Tsuji T., Iryo K., Watanabe N., and Tsuji M.** Appl. Surf. Sci. 202 (2002) 80–85.
7. **Tsuji T., Kakita T., and Tsuji M.** Appl. Surf. Sci. 206 (2003) 314–320.
8. **Neogy R.K., Rajib N., and Raychaudhuri A.K.** Mater. Chem. Phys. 186 (2017) 478–483.
9. **Marzun G., Levish A., Mackert V., Kallio T., Barcikowski S., and Wagener P.** J. Colloid Interf. Sci. 489 (2017) 57–67.
10. **Christen H.M., and Eres G.** J. Phys. Condens. Matter 20 (26) (2008) 264005.
11. **Andrian H.A. Lutey** J. Applied Physics 114 (2013) 083108 (1-10)
12. **Hamdy Makhlouf A.S., and Barhoum A.** Emerging Applications of Nanoparticles and Architecture Nanostructures, Elsevier publisher, (2018) 575–596.

METAL COATINGS FORMATION BY COMPRESSION EROSION PLASMA FLOWS INTERACTION WITH SURFACES

P.A. Shoronov[1], V.I. Shymanski[2], V.M. Astashynski[1], A.M. Kuzmitski[1], V.V. Uglov[2]

[1]A.V. Luikov Heat and Mass Transfer Institute of National Academy of Science of Belarus, Str. Brovki, 15, 220072, Minsk, Belarus, E-mail: shoronov@hmti.ac.by
[2]Belarusian State University, Nezavisimosty ave., 4, 220030, Minsk, Belarus, E-mail: shymanskiv@mail.ru

In the present work the possibility of metal coatings deposition by erosion compression plasma flows (ECPF) is discussed. The formation of erosion flows occurs due to erosion of the electrodes material in the discharge device. The products of the erosion are accelerated by dense compression plasma flows and reach the surface of a sample placed in the chamber. In the work the coating of tungsten, nickel and copper with synthesized in the air residual atmosphere on the silicon surface. In the work the structure and phase composition of the formed coating are discussed.

The flows of dense (compressed) plasma are widely investigated as effective tool for material structure and properties modification. Such plasma flows are formed by quasi-stationary plasma accelerators during the discharge between two electrodes. These process inevitably followed by the erosion of the electrodes and the products of the erosion are carried away in the plasma stream. So, it can be used for deposition of the eroded material on a substrate. The voltage between the electrodes, residual atmosphere pressure, distance between the electrodes and the substrate are the main factors that determine the effectiveness of the erosion and as a result the structure of the formed coating.

Erosion compression plasma flows were formed in the miniature magnetoplasma compressor in the residual air atmosphere (pressure 1 torr). The radial electrodes in the discharge device were produced from iron, the central electrode was made of copper, tungsten or nickel. So, it allowed to syntheze copper, tungsten and nickel coatings, respectively. The main varied parameters were a voltage between the electrodes which changed from 2.0 to 3.0 kV and distance between the electrodes and the substrate surface changed from 3 to 6 cm. The duration of the discharge in the compressor was about 100 μs. The coating formation was carried out by three pulses. A single crystal of silicon (10×10 mm) with preferred crystallographic orientation (111) or (100) was used as a substrate for the coatings deposition. The structure and phase composition of the formed films were investigated by X-ray diffraction (XRD) with Ultima IV Rigaku diffractometer in the parallel beam geometry using Cu-radiation (λ=0.154178 nm). The thickness of the films was determined by scanning

electron microscopy (SEM) in the LEO 1455 VP microscope on the cross-sections of the samples.

After the ECPF influence on the silicon surface the film from the material of inner electrode were formed. The XRD results provided the information about the phase composition of the films and the varied parameters influence on it. Using a copper electrode, copper films were produced (Fig. 1 and 2).

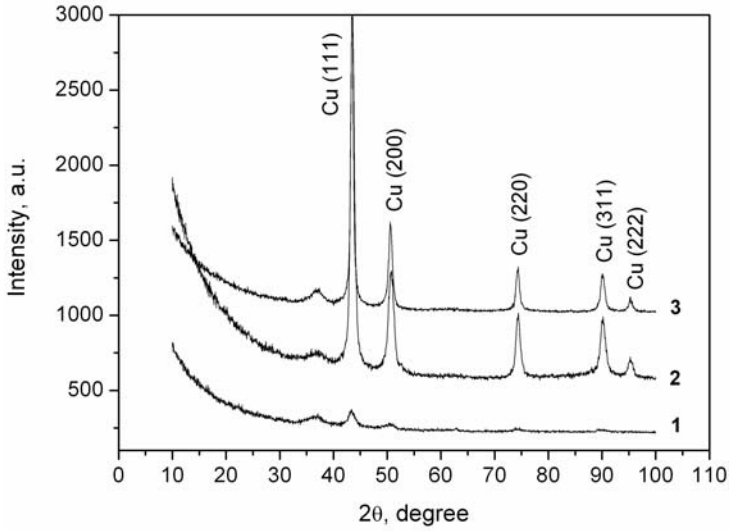

Fig. 1 – XRD patterns of the Cu coatings formed at the voltages 2.0 kV (1), 2.5 kV (2) and 3.0 kV (3)

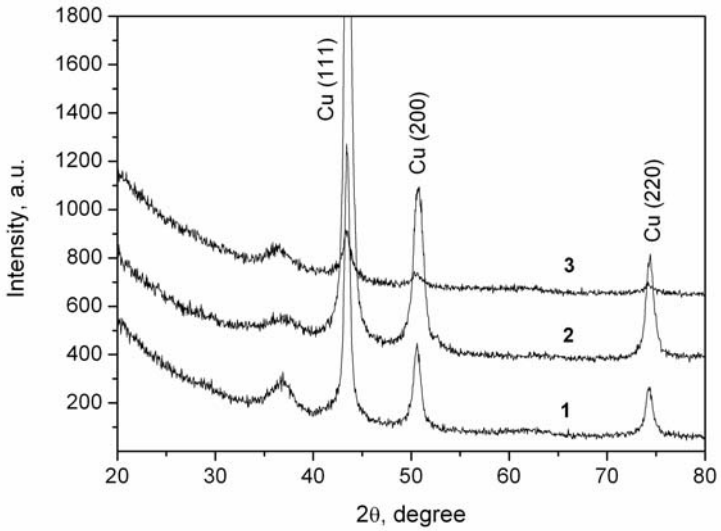

Fig. 2 – XRD patterns of the Cu coatings formed at the voltage 2.5 kV and the electrode-substrate distances 3 cm (1), 4 cm (2) and 6 cm (3)

On the XRD pattern there is a series of the diffraction peaks that indicate the polycrystalline structure of the copper films. The diffraction peaks intensity distribution corresponds to the standard data. Taking into account that the intensity of the peaks depends on the volume fraction of the phase or, in our

case, on the thickness of the films, one can see that the films synthesized at the voltage 2.5 – 3.0 kV (the distance between the electrode and Si substrate was 4 cm) possess manifest crystal structure and thickness. The voltage of 2.0 kV on the electrodes is not enough for the film formation. It is a result of less amount of the eroded material from the electrodes.

The distance between the Si surface and electrode as well as voltage on the electrode influence on the thickness and structure of the formed films. Indeed, the results presented in Fig. 2 show that the most appropriate distance between the electrode and Si surface is 4 cm (at the voltage 2.5 kV). In this case the thickness of the film is the highest. An increase in the distance up to 6 cm results in fall in the thickness due to divergence of the plasma stream and the amount of the eroded material is also decreases. The decrease in the thickness at the distance of 3 cm can be explained by the absence of the eroded material in the compressed area near the electrodes.

The films of tungsten and nickel also were formed by the ECPF influence (Fig. 3 and 4). In the XRD patterns of the W films (Fig. 3) a weak diffraction line of the tungsten (110) was found. Besides, some diffraction lines corresponding to the tungsten oxides also were found in the diffraction angles area 30 – 45 degree. The formation of nickel films is also accompanied by the nickel-based compounds formation. In this case the nickel carbide Ni_3C referred also as hexagonal nickel was found. According to the XRD results purer (without additional phases) nickel film was synthesized at the voltage of 3.0 kV (the distance of 4 cm). But the latter regimes allow to form the coating with a small-grained structure since the diffraction line have a very high width.

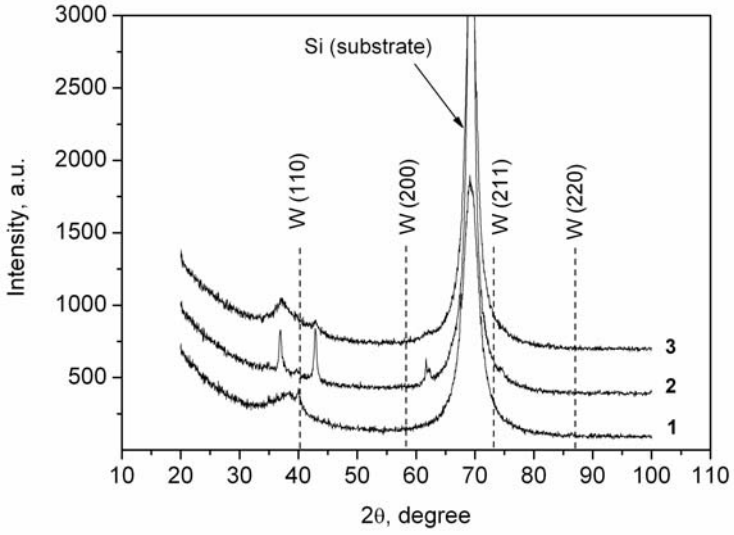

Fig. 3 – XRD patterns of the W coatings formed at the voltages 2.0 kV (1), 2.5 kV (2) and 3.0 kV (3)

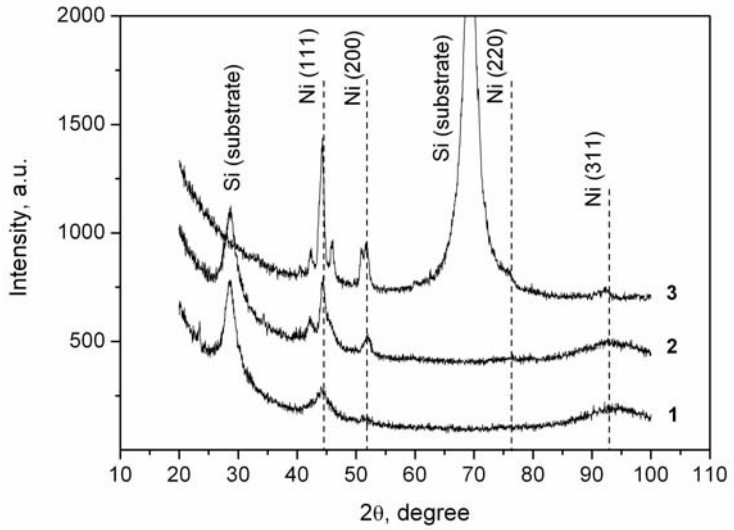

Fig. 4 – XRD patterns of the Ni coatings formed at the voltages 2.0 kV (1), 2.5 kV (2) and 3.0 kV (3)

The SEM results (Fig. 5) showed the thickness of the films formed by the ECPF impact. According to the SEM images the thickness of the tungsten coating is about 130 nm, meanwhile the nickel coating has a thickness of 170 nm (the regimes of the formation are the same). One can see that the coatings have the constant thickness in every section. So, the formed films possess uniform thickness.

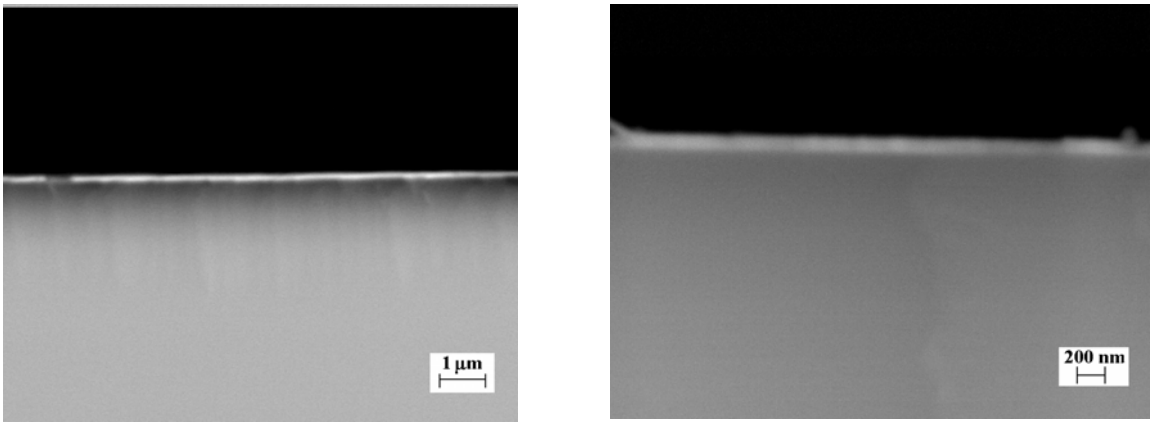

a) **b)**

Fig. 5 – SEM-images of the W coating cross-section (a) and Ni coating cross-section (b). The films were formed at the voltage 3.0 kV

So, in the work the possibility of copper, tungsten and nickel thin (130 – 170 nm) films synthesis on the silicon wafer by erosion compression plasma flows impact in the miniature magnetoplasma compressor was demonstrated.

LASER ABLATION OF SAPPHIRE ON WAVELENGTH 1040 nm

B. Shulenkova[1], E. V. Lutsenko, A.V. Danil'chik, A. Vainilovich

B.I. Stepanov Institute of Physics of National Academy of Sciences of Belarus, 68/2 Nezalezhnasti Ave., 220072 Minsk, Belarus, shulenkovab@gmail.com

Introduction Sapphire, with its combined mechanical, optical, and electrical properties, is a multifunctional, high-performance engineering material. This properties has led to applications of sapphire in optical devices and mass production of sapphire substrate for LED. However, the machinability of sapphire is still an issue, owing to its extreme hardness, brittleness, and chemical stability. As sapphire is inert to most types of wet chemical and dry etching, laser ablation has been proposed as a potential machining method. The interaction of laser pulses with sapphire material has been investigated for many years. The use of lasers for material processing enables fine precision work with minimal, localized, thermal effects such as cracks and heat affected zone /1/.

Recently, femtosecond (fs) laser ablation has attracted considerable attention because of its ability to produce precise, well-defined micrometer-sized structures in materials. This is relevant to LED wafers cutting on chips. The use of fs pulses enables high precision machining with minimal collateral damage due to two main reasons. First, nonlinear nature of the absorption confines any induced damage to the focal volume only. Second, the ionization process is faster than heat conductance to the bulk /2/. From /1,3/, ablation mechanisms are found to be a combination of Coulomb explosions and melt fragmentation, with the latter dominating at high intensities. Considerable work has been reported on the characterization of sapphire scribing and cutting using ultra-short pulses. The effect of the number of pulses and their energy on the surface modification of Sapphire and on the depth and diameter of drilled holes has been investigated /4,5/.

In this work, the ablation of sapphire by femtosecond laser pulses was evaluated under various pulse energies. The quality and morphology of the sapphire surface were investigated by scanning electron microscopy.

Experimental Experiments were performed with an homemade ytterbium-doped femtosecond laser (M2=1.3) with a wavelength of λ = 1040nm, that generated τp=300 fs laser pulses with a maximum pulse energy of Ep=14 mJ at a 62 kHz repetition rate. In the experiments, 400 μm thick polished sapphire substrates were used. The laser beam was irradiated onto a sapphire surface through a 20 x microscope objective lens with a numerical aperture number of 0.40 with beam radius $\omega 0$ = 4.3 μm. The sample was placed on a scanning stage and translated at various scanning speeds under computer control during irradiation. All

experiments were carried out in air at atmospheric pressure and room temperature. After irradiation, the samples were cleaned in an ultrasonic bath. The morphology of the samples surface was examined by scanning electron microscope (SEM) to evaluate the width and depth of the ablation profile, the severity of cracks.

Results and discussion The experiments was conducted at scan speed from 0.4 to 12.5 mm/s. At low laser power (0.1W – 0.3W) and low scan speed width of cuts decreased to 4 μm, but rough and uneven edges observed (Fig 1.). Besides, the melted material was observed around the ablated cuts.

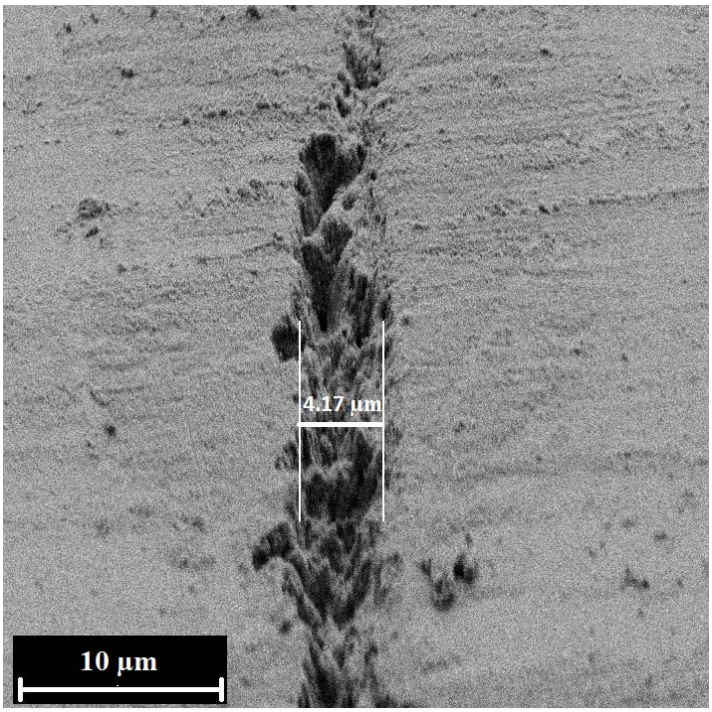

Fig. 1 - SEM image of cut at laser power 0.1W and scan speed 0.4 mm/s

At laser power higher than 0.4 W laser spark in air appears at beam waist and increase of width to 30μm and depth of cuts was observed (Fig.2). Furthermore, removal of material from trench become more severe which leads to material sputtering on larger surface. This sputtered material is effectively removed by subsequent ultrasonic cleaning. Possibly, shockwave generated by spark creates more effective material sputtering. Increasing of scan speed from 0.4 to 12.5 mm/s leads to cuts width and depth increasing.

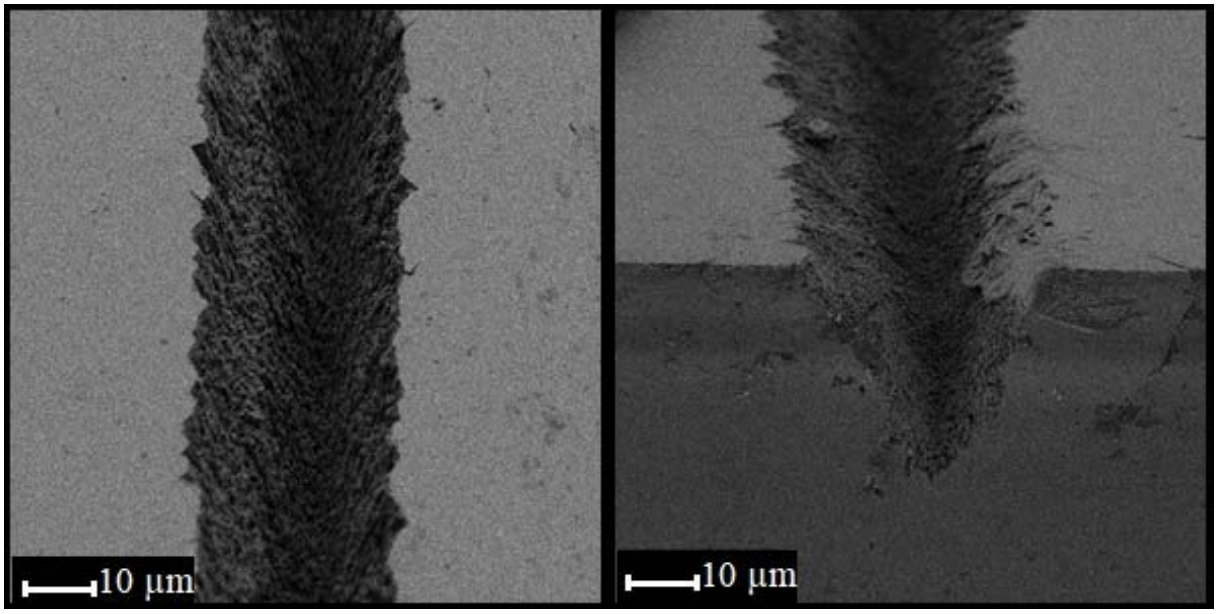

Fig.2 – SEM images of cuts at laser power 0.8 W and scan speed 0.4 mm/s after ultrasonic cleaning

The estimate of ablation threshold fluence of sapphire is given below. The threshold fluences of the Gaussian laser beam can be calculated by measuring the width of the ablated areas versus the pulse energy and extrapolating areas to 0. It is known that for a Gaussian spatial beam profile with a $1/e^2$-beam radius ω_0, a maximum laser fluence φ_0 increases linearly with the laser pulse energy E_p /5/:

$$\varphi_0 = \frac{2E_P}{\pi\omega_0^2} \quad (1)$$

The maximum laser fluence φ_0 can be calculated from the pulse energies in the experiment using Eq.(1).The threshold laser pulse energy can be obtained by an extrapolation to $w^2=0$.

The Fig 3 presents experimental data relation between squared width of cuts and laser pulse energy in logariphmic scale. At E_p from 1.6 to 11.2 μJ one can see smooth growth of width of cuts. Trendline by linear fitting was obtained from dependence of w^2 from $\ln(E_p)$. From graphic, obtained value of threshold laser pulse energy is E_p =1.56 μJ, that corresponds to ablation threshold fluence of 5.36 J/cm^2. Obtained value is comparable to that from /5/.

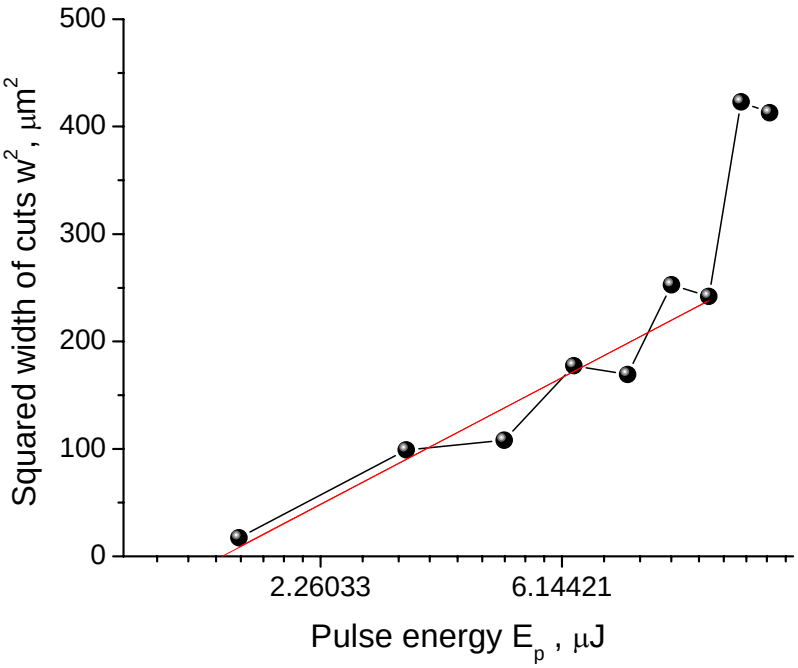

Fig. 3 – Squared width w^2 of the ablated area versus the pulse energy E_p

Conclusion We have demonstrated effective laser scribing of sapphire with width of cuts 15-30 μm depending on laser power. Threshold fluence was estimated 5.36 J/cm2 that corresponds to results of other works. It has been shown that low scan speed and high laser power provide conditions where redeposited material effectively removed from surface in following ultrasonic cleaning.

References

1. Miotello A. and Ossi P. Laser-Surface Interactions for New Materials Production. Springer (2010)
2. **Gattass R.R., Mazur E.** Nature Photonics, 2(2008) 219-225
3. **Puerto D., et al.** J. Opt. Soc. Am. B 27(2010) 1065-1076
4. **Eberle G., et al.** Applied Surface Science, 378(2016) 504-512
5. **Qi L., et al.** Optics and Lasers in Engineering, 48(2010) 1000–1007

Effects of different laser scan speed on surface morphology and chemical composition of nanocomposites Starch/hydroxyapatite coatings

Mina talebi Mazrae Shahi[1], Monireh Ganjali[2]

Materials and Biomaterials institute, 15, 2nd Str., Pakistan Str., Shahid Beheshti Str., Tehran - Iran, iranminamail@gmail.com
Biomaterials group, Nanotechnology and Advanced Materials Department, Materials and Energy Research Center (MERC), 5, Ahuramazda Str., Alvand Str., Argentina Sq., Tehran - Iran, monireh.gan@gmail.com

Dip coated nanocomposites starch/hydroxyapatatite (St/HA) coatings were fabricated on stain steel 316. Laser remelting technique was used to surface modification of dip coated surface. The coatings before and after laser remelting were characterized by using scanning electron microscope (SEM), energy-dispersive spectrometer (EDS).The effects of laser scan speed on microstructure of the laser-remelted nanocomposites St/HA coatings were investigated. It was shown that the increases of laser speed scan are significantly affects on microstructure properties of the coating after laser remelting process. The results show that microstructural correlation in the coatings after laser remelting was much better and denser before laser remelting.

Introduction

Hydroxyapatite (HA) is the bio-ceramic which is used to coat of in order to improving corression and biocompatibility of metallic bioimplants. The hydroxyapatite coating increase the mechanical fixation and bone on growth /1/. Due to the weak mechanical properties of single-phase hydroxyapatite coatings, they can be composited by polymers such polyviniline alchohol (PVA), gelatin and etc. Starch is a natural, semi-crystalline, and very hydrophilic polymer that have a lot of potential for use in the field of medical engineering coating, plating, and thin films refer to a series of processes on different material levels that are performed for a variety of purposes.

Plasma sprays is only commercially available method to coat of HA on biomedical implants. But some defects such as cracking, flaking and scratching due to mechanical bounding between coating and substrate led to delamination of the coating /2/.

In this study, the laser remelting is used to enhance the density and surface quality of dip-coated St/HA nanocomposites by utilizing different laser scan speed is investigated.

Materials and methods

Nanocomposites Starch/HA was prepared by a solution based method. At first starch was slowly added to dionized water. The solution was heated and vigorously stirred at 80° C on a hot plate until the contents were thoroughly mixed. Then Hydroxyapatite nanopowder (nHA) gradually added to solution to prepare St/nHA nanocomposites. It should be mentioned that all the chemicals used in this research are purchased from Merck Company. The stain steel 316L of dimension 10×20×40 was used as the substrate, which the chemical composition of the stainless steel 316 elaborated for this study after quantmetry analysis is shown in Table 1. All specimens were mechanically polished with aqueous slurries of successively finer alumina powder. The surfaces were also cleaned ultrasonically, washed with ethanol and acetone, and then followed by air-dried. A belt-and-pulley-type apparatus has been built and used in this study for dipping the strips into the HA suspensions, and it had a two-way electronic switch to descend and ascend the substrates into (and out of) the dipping suspensions, at constant speeds in the range of 15 to300 mm/rain. In order to increase the thickness of the coating layer, substrates were immersed five times and remain for 5 minutes in the solution and then dried.

Table 1- Chemical composition of stainless steel 316 according to ASTM standard along with chemical elements of samples used

	Fe %	**C % max**	**Si % max.**	**Mn % max.**	**P % max.**	**S % max.**	**Cr %**	**Mo %**	**Ni %**
316	Balance	0.08	0.589	1.1	0.081	0.0416	16.68	2.18	11.7
316 standard	Balance	0.08	0.75	2	0.045	0.03	16-18	2-3 %	10-14

After dip coating, the coated substrates were remelted with a fiber laser (MF-20, Han's Yueming, China) operating at a wavelength of 1.06 μm with a maximum output power of 20 W. The detailed laser remelting parameters are listed inTable 2. The distance between the nozzle and the work-piece surface, and focal length was selected 30 and 12 mm, respectively. The laser beam diameter on the work-piece surface was fixed at 1 mm. To prevent the melted pool from oxidation, Argon gas was used as shielding gas through the coaxial nozzle at 10 L/min.

Microstructure and compositions of the coatings before and after laser remelting were examined by scanning electron micro-scope (VEGA TESCAN, RONTEC, Germany) equipped with X-ray energy-dispersive spectroscopy (EDS).

Table 2 – Parameters of laser remelting

No	Samples	Power (W)	Lasers can speed (mm/s)
1	BL	-	-
2	AL-10	8	10
	AL-20	8	20
	AL-30	8	30

Note: BL and AL indicate before and after laser melting process.

Results and discussion

Phase structure of nHA and nanocomposites starch/HA was performed by Infrared spectroscopy analysis FTIR and is shown in Fig 1 (a). The results confirm the formation of nanocomposite structures. The bands at 565-600 cm^{-1} correspond to ν_4 symmetric P-O stretching vibration of the PO_4^{-3} ion, while the bands at 1042 and 1092 cm^{-1} corresponding to ν_3 vibrational mode of the PO_4^{3-}tetrahedral.The spectra of the two HA powders show bands in the range (1465–1415 cm^{-1}) and at 874 cm^{-1} corresponding to ν_3 and ν_2 vibrational modes of carbonates, respectively. The broad band at 3446cm^{-1}, for starch, is due to the stretching mode of O-H groups /3/.

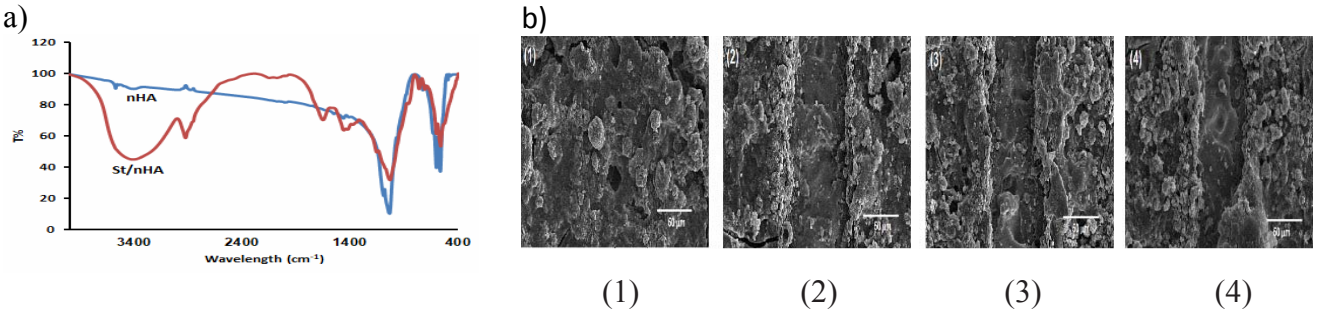

Fig.1 – (a) FTIR of nHA and nanocomposites St/HA and (b) SEM images of St/HA coatings on Ti substrates before and after laser remelting at different laser scan speed; (1) BL; (2) AL-10; (3) AL-20 and (4) AL-30

SEM micrograph of surface coating before and laser remelting is shown in Fig. 1 (b). As it can be seen, there are some cracks on the surface coating before laser remelting. But by increasing energy density or slowing scan speed of the laser, smooth surface because of melting and solidification of material was obtain after laser treatment.

Fig. 2 shows Ca/P molar ratio calculated from EDX results. The Ca/P ratio calculated for samples before and after laser remelting are 1.52, 2.14, 2.16 and 2.24, respectively. The results clearly reveal that by the increasing of laser scan

speed, the starch was vaporized from the molten pool and stimulated the agitation of the molten pool and hence helped the P dissipation. So, the Ca/P ratios of the coating after laser remelting are higher than the coating before heating by laser irradiation. However, it has previously been reported that HA with higher Ca/P ratio has more tendencies to bond to bone /4/.

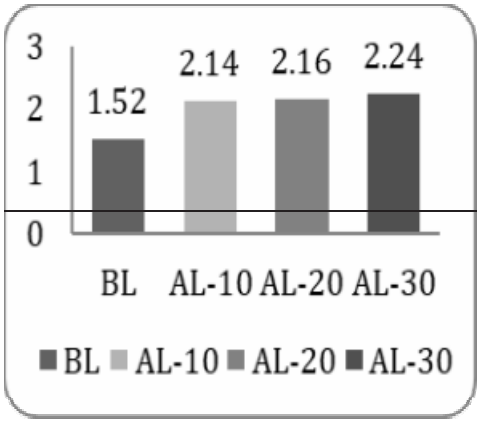

Fig. 2 - EDX results of St/HA coatings on Ti substrates before and after laser remelting at different laser scan speed

Conclusion

Laser surface modification of dip coated St/nHA coatings was performed using fiber laser. Smooth surface and free cracks was performed after laser treatment. Furthermore, increase laser scan speed leads to increase Ca/P ratio.

Acknowledgments

This work was supported by the Materials and Biomaterials Institute for Fundamental Research (grant No. 3902811)

References

1. **Daugaard H., Elmengaard B., Bechtold J.E.** Jensen T. and Soballe K. J Biomed Mater Res A. 92 (2010) 913-921
2. **Demnati I., Grossin D., Combes C., and Rey C.** J of Medical and Biological engineering, 34 (2014) 1-7
3. **Hebeish A., Aly A. A., El-Shafei A. and Zaghlou S.** Egypt. J. Chem., 52 (2009) 73- 89
4. **Ganjali M., Pourhashem S., Vaezi M.R.** Advanced ceramics progress, 1 (2015) 28-33

INVESTIGATION OF CZTS THIN-FILM SOLAR CELLS ON PERLITE GLASS-CRYSTALLINE SUBSTRATES

S. Petrosyan[1], N. Yeranyan[1], A. Musayelyan[1], S. Pashayan[2]

[1] Institute of Radiophysics and Electronics of NAS of RA,
Alikhanyan brother's str.,1, 0203, Ashtarak, Armenia, ashmusa@mail.ru
[2] Institute for Physical research of NAS of RA, Ashtarak, Armenia
svetlana1207@yahoo.com

Abstract Thin polycrystalline Cu2ZnSnSe4 (CZTSe) films were synthesized by selenization of metal precursors Cu, Zn, Sn deposited by magnetron sputtering technique on molybdenum-coated perlite glass-crystalline substrates (PGC). These p-type conductivity layers had a thickness of the order of 1-1.3 μm, a round shape with an average size of 700 nm, and served as a photoactive layer in the thin-film solar cell Mo/CZTSe/ CdS /ZnO/Al: ZnO. Synthesized films used as the photoactive layer for Mo/CZTSe /CdS /ZnO/Al: ZnO solar cells (SC). The conversion efficiency of the created SC is 4.9% and the open-circuit voltage ~ 0.6 V is comparable with the results for more efficient solar cells on glass substrates.

Introduction. In the last decades, an intensive search has been made for materials that allow the conversion of solar energy into electrical energy in the most efficient and minimal expenses. A great progress in this direction (efficiency ~ 22%) was achieved with thin-film solar cells based on copper indium gallium diselenide (CIGS). Mass production of them is strictly limited due to the use of such expensive and rare metals as gallium and indium /1/. Therefore, in recent years, kesterite materials have attracted the attention of researchers for replacing the absorbing layer in the SC structure, in which a new semiconductor compound of the Cu2ZnSn(SexS1-x)4 type (CZTS) /2/. The conversion efficiency of such SC is already around 12.6% /3/. It is known that an important advantage of such solar cells is not only the high coefficient of optical absorption of solar radiation, but also the possibility of selecting the optimal band gap in the interval 1.05-1.6 eV by changing the ratio between the content of selenium and sulfur.

There are various vacuum and non-vacuum deposition technologies for polycrystalline CZTSe layers: electrodeposition /4/, vacuum sputtering /5/, co-evaporation /6/, spray pyrolysis /7/, etc. The most common method for obtaining thin CZTSe films is a two stage process. The first step of it is the formation of metallic precursors on the substrate using one of the above methods, and the second one - the selenization of the resulting metallic layers.

For layer-by-layer deposition of metals, we chose the method of vacuum

magnetron sputtering. To prove the possibility of further integration of such solar cells with building elements, glass substrates have been replaced by substrates made of perlite glass-crystalline material /8/.

The aim of this work was a fabrication of the Cu2ZnSnSe4 compounds based multilayer structures of thin-film SC on PGC substrates and the investigation of such SC conversion efficiency.

Experimental part To fabricate CZTSe thin films by magnetron sputtering, the Cu, Zn and Sn metal layers were sequentially deposited on specially synthesized perlite glass- crystalline substrates with preliminarily molybdenum (Mo) layer-coated. The distance between the target and the substrate was 10 cm, and the base pressure was 10-5 mTorr. During of argon (Ar) injection the pressure was raised to 10 mTorr. At the same pressure, at a working current of 600 mA, a molybdenum layer with a thickness of about 0.5 μm was deposited. Further, the selenization process was carried out during 30 min at a temperature of 450 °C.

For the electrochemical deposition of the CdS buffer layer, cadmium acetate (Cd (CH3COO) 2) was used as a source of cadmium at a concentration of 0.03 M, thiourea (H2NCSNH2) as a sulfur source at a concentration of 0.6 M and ammonium hydroxide (NH4OH) (25%) as a complexing agent with concentration of 5 M /9/. The thickness of the deposited layer was about 65 nm at a temperature of 65-70 °C and a reaction time of 15 minutes. It is known the optimum buffer layer thickness is 40-60 nm /10, 11/. Then, transparent layers of ZnO and ZnO:Al with a thickness of 50 nm and 400 nm, respectively, were deposited by magnetron sputtering. Finally, Ni/Al metal contacts were obtained by thermal spraying.

The morphology of CZTSe thin films was studied using an AFM. The thickness of the layers was measured with the Mitutoyo Surftest SJ-410 profilometer, current-voltage measurements were carried out both without lighting and under standard 1.5AM lighting by Keithley-6340 unit at room temperature. Voltage is varied in the range -0.6 - 1.4 V.

Results and discussion Fig. 1 shows a photomicrograph of one of the selenized at 450 °C CZTSe thin films, obtained by AFM. As can be seen from the figure, the grains are rather dense and have a circular shape that forms after the selenization of the layers as a result of the recrystallization of the Cu2ZnSnSe4 phase. The film thickness is about 1.3 μm, and the average roughness (Ra) of the surface does not exceed 80 nm (Fig. 2). Relatively smooth films can reduce interphase states between the absorbing and the window layers, reducing the dark current. It is known, this is necessary to fabricate a high-quality SC /12/. The average grain size of the film is 700 nm, and the maximum

size is 1.3 μm (Fig.3). The distribution of grain sizes almost coincides with the normal distribution. The grains are small in size, which is apparently due to the small amount of sodium content in the perlite substrate (about 3-4%), which diffuses into the CZTSe layer during selenization and contributes to an increase in the average grain size /13/.

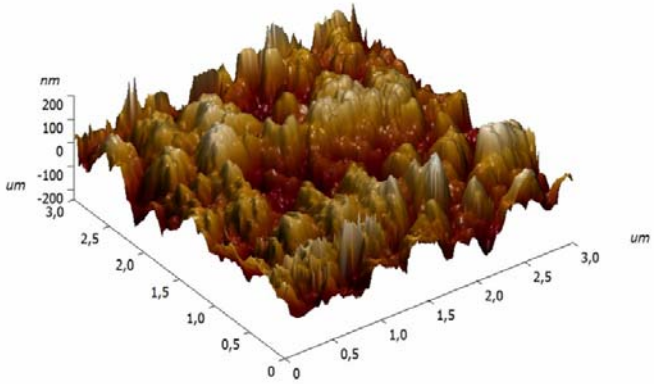

Fig. 1 - 3D AFM-image of thin film CZTSe

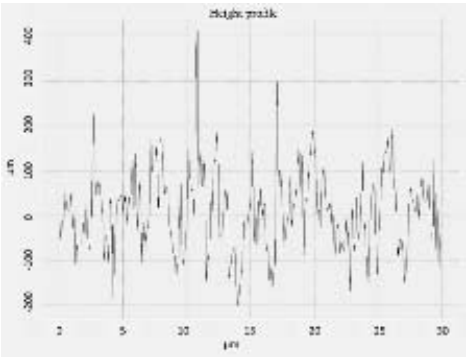

Fig. 2 - The roughness profile of the CZTSe layer.

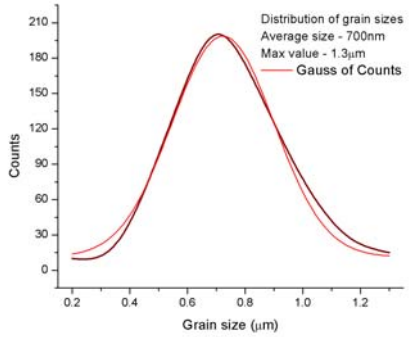

Fig. 3 - Distribution of grain sizes in the film

The current-voltage characteristic (I-V) of the fabricated SC with the best parameters is shown in Fig. 4, and the corresponding parameters of the SC are shown in Table 1.

Table 1 - Morphological and electrical parameters of thin films and a typical CZTSe –based SC

Sample PGC/Mo/CZTSe/CdS/ZnO/Al:ZnO								
From AFM measurements			From I-V characteristic					
Thickness	Ra	The average grain size	R_{sh} (kΩ)	R_s (kΩ)	V_{oc} (V)	I_{sc} (mA)	FF (%)	η (%)
1.3μm	~ 80 nm	700 nm	1.59	5.42	0.598	-9.64	48	4.9

The active area of the SC is 0.5 cm2, and the remaining surface was covered with a Ni/Al contact lattice, which is why a high series resistance is due. The Voc value of the SC is relatively large, while the short-circuit current density Jsc 19.3 mA/cm2 is significantly lower than that of silicon single-crystal SC.

It is our view that the low Jsc values is partly due to recombination at the CZTS-CdS boundary because of the possible appearance of secondary phases on the CZTS surface, a short lifetime of electrons due to recombination at the grain boundary, the absence of an antireflection coating and a non-optimal contact-grid configuration. In addition, as a result of the large series resistance of the SC, the filling factor is below 50%.

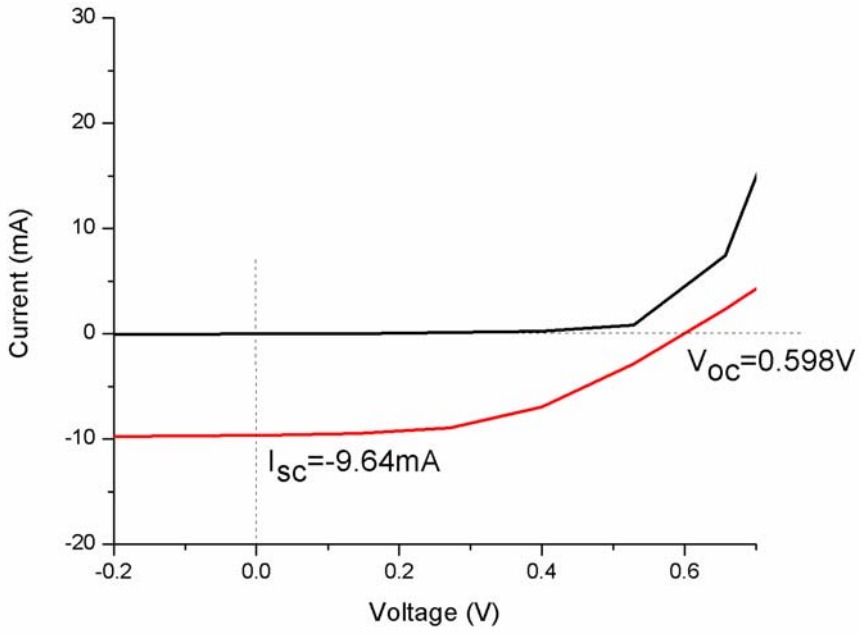

Fig. 4 - I-V characteristic of SC with PGC/MO/CZTSe/CdS/ZnO/Al: ZnO structure

Other factors that define the relatively low efficiency of this SC can be technological growth regimes which has not been fully optimized, the absence of surface treatment of thin films after selenization, and the insufficiently quality of the initial materials used. Elimination of these factors is a task for further work, and the purpose of this work was to clarify the potential opportunities for the fabrication of CZTSe thin-film SC on a perlite glass-crystalline substrate.

Conclusion For the first time, thin-film solar cells with an absorbing CZTSe layer were fabricated on a perlite glass-crystalline substrate coated with Mo. The results show that a two-stage magnetron sputtering method can be

successfully applied to deposition of thin films not only on glass, but also on alternative substrates. According to the morphological analysis, the average grain size should be increased, making it comparable with the thickness of the absorbing layer. The efficiency of the first, not optimized samples of SC, reaches 4.9%. The resulting open-circuit voltage of 0.598 V is comparable to the Voc value for the solar cell with a record efficiency of 12.6%, manufactured by spin-coating using a highly toxic and reactive hydrazine solution /3/. It seems to us that the main reason for the low efficiency is the low value of the fill factor due to the high Rs. In connection with this, the technology of fabrication of SC needs to be improved.

References

1. **M. Green, K. Emry, Y. Hishikawa, et al**, Prog. Photovotaic Res. Appl., 24(2016) 905.
2. **S. Delbos,** EPJ Photovolt., 3(2012) 35004.
3. **W.Wang, M.T. Winklern, , et.al,** Adv. Energy Mater., 4(2014) 1301465.
4. **L. Vauche, L. Risch, et.al**, Prog. Photovolt: Res. Appl., 24(2015) 38.
5. **T. Kato, H. Hiroi, N. Sakai,** 27th Eur. Photovolt. Solar Energy Conf. and Exhib., Frankfurt, Germany (2012).
6. **Y.S. Lee, T. Gershon, et.al,** Adv. Energy Mat., 5(2014) 1401372.
7. **G. Larramona, S. Levcenko,** et.al Adv. Energy Mat., 5(2015) 1501404.
8. **S.G. Petrosyan, A.S. Musayelyan, V.H. Babayan, L.A. Harutyunyan, V.B. Zalesski, et.al**, Eur. Phys. J. Appl. Phys. 62 (2013) 30103–30108.
9. **F. Hergert, R. Hock,** Thin Solid Films 97(2007) 5953.
10. **J.P. Enriquez,X. Mathew,Sol.** Energy Mat. & Solar Cells 76 (2003) 313.
11. **K. Orgassa, U. Rau,** Prog. Photovolt: Res. Appl., 10(2002) 457.
12. **A.M. Hermann, M. Mansour, et.al,** Thin Solid Films, 74(2000) 361.
13. **B.M. Basol, V.K. Kapur, et.al,** Proceed. of the 1st World Conf. on Photovolt. Energy Convers. (1994) 148.

OXIDATION AND SINTERING OF POROUS TITANIUM SURFACE UNDER THE ACTION OF A STATIONARY PLASMA FLOW AND LASER IRRADIATION

A. Chumakov[1], I. Nikonchuk[1], O. Kuznechik[2]
[1]B. I. Stepanov Institute of Physics, National Academy of Sciences of Belarus,
68-2 Nezalezhnastsi Ave., Minsk 220072, Belarus
E-mail: i.nikanchuk@ifanbel.bas-net.by
[2]Powder Metallurgy Institute,
41 Platonova Str., Minsk, 220072 Belarus

Titanium dioxide is promising material for biomedical applications [1] and one of the best semiconductor photocatalyst, which has been extensively studied in recent years [2]. Properties of titanium-based materials depend on the chemical composition and morphology of the surface. Laser and plasma processing are widely studied methods for changing the properties of metal surfaces [3-6]. The main purpose of this work is to reveal an effective modes of oxidation and sintering of the surface layer of porous titanium material under the action of a stationary plasma flow and laser irradiation.

Experimental details

In the present study the multipulse laser irradiation (1–50 Hz frequency, 1064 nm wavelength, and 0.085-200 μs pulse duration) and stationary plasma action ($T_e \sim (7 \pm 1.4) \cdot 10^3$ K, $N_e \sim (1.2 \pm 0.18) \cdot 10^{16}$ см$^{-3}$) were used for oxidation and sintering of porous surface of titanium alloy (0.5 wt. % Fe, 0.15 wt. % N, 0.15 wt. % Cl). Morphology of processed titanium surfaces and composition analysis were examined by methods of Raman spectroscopy, optical microscopy, scanning electron microscopy (SEM) and energy dispersive X-ray micro analysis using microscope MIRA-3 with X-Max extreme silicon drift detector. The emission spectrum of plasma obtained with the compact spectrometer SpectraStar SDH-IV.

Results and discussion

When the surface of the porous titanium alloy was treated by the stationary plasma flow with $7 \cdot 10^3$ K electron temperature and $1.2 \cdot 10^{16}$ см$^{-3}$ electron density, the threshold of initiation of the self-propagating high-temperature synthesis (SHS) was reached within 20-30 seconds, as evidenced by the appearance of a bright glow of the surface that decaying with a significant delay time after the end of the plasma action. Spectroscopic studies of plasma processing revealed a high intensity of continuous radiation and allowed to determine the color temperature in the SHS-reaction zone by spectral pyrometry method [7]. Emission spectrum of the titanium sample under conditions of initiation of self-propagating high-temperature synthesis is shown in Fig. 1.

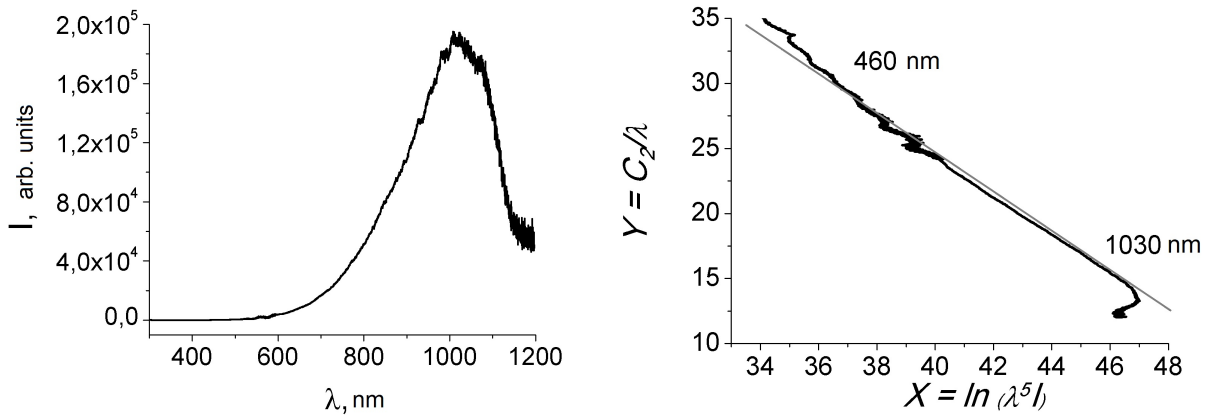

a) b)

Fig.1 Emission spectrum of the titanium sample under conditions of initiation of SHS in ordinary coordinates (a) and in the Wien's coordinates (b)

The spectrum obtained in the Wien's coordinates is straightened out in the range from 460 nm to 1030 nm. Thus, glow of the processed sample in this interval corresponds to the emission of gray body, and its maximum lies in the region λ = 1010 nm, which, in accordance with the Planck's law, is realized at a temperature of 2850 K.

Optical microscopy of the titanium surface treated with plasma revealed fusion of grains and discoloration of the surface onto milky white. Analysis of the Raman spectra of the modified titanium surface (Fig. 2) revealed bands of 235 cm^{-1}, 447 cm^{-1}, 612 cm^{-1}, characteristic of TiO_2 in the crystalline form of rutile, and a less pronounced presence of titanium carbide (674 cm^{-1} band) and TiO_2 in the crystalline form of anatase [8, 9].

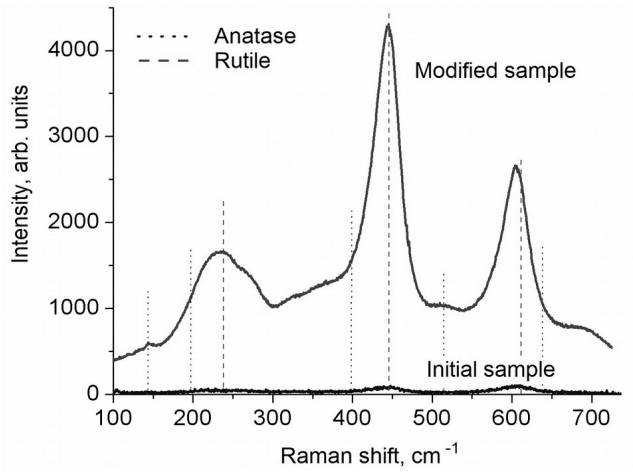

Fig. 2 The Raman spectra of the initial and modified surface of the titanium sample

Laser action (parameters shown at the Table 1) on the titanium samples was accompanied by the formation of a near-surface plasma.

Table 1. Modes of laser irradiation

№	Spot area, м^2	Frequency, Hz	Pulse duration, μs	Power density, W/cm^2
1	$0{,}85\cdot10^{-6}$	25	0,085	$5{,}5\cdot10^{7}$
2	$1{,}77\cdot10^{-6}$	50	200	$1{,}1\cdot10^{4}$
3	$0{,}63\cdot10^{-6}$	25	200	$3{,}2\cdot10^{4}$
4	$1{,}77\cdot10^{-6}$	1	200	$1{,}1\cdot10^{4}$
5	$0{,}38\cdot10^{-6}$	25	0,085	$1{,}24\cdot10^{8}$

Lines of Ti I atoms and the first titanium ions Ti II predominate in typical emission spectra (Fig. 3) of the ablation plasma. The temperature of titanium plasma ~ $1.3\cdot10^4$ K was estimated from the "normal" temperature of the Ti II line at 375.9 nm (excitation energy 3.9 eV, ionization energy of the Ti II ion 13.637 eV), which was calculated in accordance with [10].

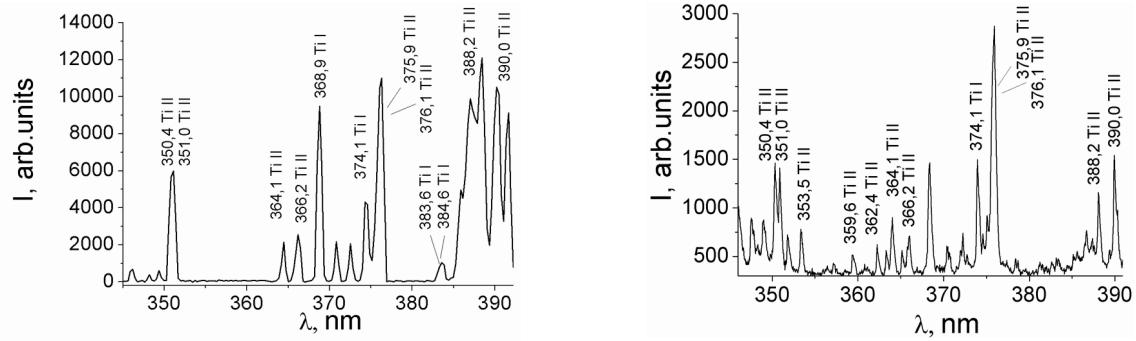

a) pulse duration of 200 μs *b) pulse duration of 85 ns*

Fig 3. Typical emission spectra of the plasma produced by pulsed laser action on titanium.

Scanning electron microscopy of modified samples showed that laser processing with a pulse duration of 200 μs leads to surface melting and nanosecond laser action produces developed structure on the surface with substantially smaller grain and pore sizes compared to the original surface.

Analysis of the elemental composition of the samples with the X-ray microanalyzer EDX X-Max revealed several variations in the chemical composition of the irradiated surface (Table 2).

Table 2. Intensity of X-rays of oxygen and nitrogen

Element	Intensity, pulses/s					
	Initial surface	mode №1	mode №2	mode №3	mode №4	mode №5
O	143	760	911	683	299	641
N	604	298	431	869	773	335

The results of the X-ray microanalysis presented in Table 2 and the analysis of the surface structures by SEM showed that laser action on the porous titanium substrate facilitates its transition in a monolithic state that is characteristic of

metal alloys obtained by casting. It was found that the oxidation of the titanium surface induced by laser irradiation in atmospheric air increases with the increasing of number of laser pulses and has a weak dependence on pulse duration and power density (q ~ 10^4-10^8 W/cm^2). Nitriding of titanium increases with a decrease of repetition rate and power density from 10^4 to 10^6 W/cm^2.

Conclusions

Thus, stationary plasma action (T_e ~ (7±1,4) · 10^3 K, N_e ~ (1,2±0,18)·10^{16} см$^{-3}$) on the sample of porous titanium alloy initiates process the self-propagating high-temperature synthesis at the temperature of T ~ 2850 K, which leads to the partial melting of grains and their sintering on the surface of the processed sample with the formation of TiO_2, mainly in the crystalline form of rutile. Analysis of laser action showed possibility of significantly changing of surface morphology and selectively increasing the content of oxides in the surface layer by varying the modes of laser action on porous titanium alloy. It was found that millisecond laser action are more effective for the nitriding of the titanium, whereas multi-pulse action with nanosecond pulse duration is more suitable for the surface structuring and formation of oxides. It should be noted that laser-induced modifications allows to carry out selective processing of surfaces, while plasma action is more convenient for oxidation of large areas of titanium products.

Acknowledgments

This work is partly supported by the Belarusian Republican Foundation for Fundamental Research (Grant N°T15CO-055) and State program of scientific research "Convergence-2020" (Grant N°2.4.02).

References

1. **Long M., Rack H.J.** Biomaterials, 19 (1998) 1621–1639.
2. **Zaleska A.** Recent Patents on Engineering V.2 (2008) 157–164.
3. **Trtica M. et al.** Applied Surface Science. 253 (2006) 2551–2556.
4. **Lavisse L. et al.** Applied Surface Science. 254 (2007) 916–920.
5. **Bussoli M. et al.** Radiation Effects & Defects in Solids. 163 (2008) 349–356.
6. **Chumakov A.N. et al.** Physica Scripta. T162 (2014) 014016.
7. **Магунов А. Н.** Научное приборостроение. Т.20 (2010) 22–26.
8. **Jing Zhang et al.** The Journal of Physical Chemistry B, 110 (2006) 927 – 935.
9. **Подгорный В.И. и др.** Журнал технической физики, Т.83 (2013) 77–81.
10. **Лохте-Хольтгревен В.** Методы исследования плазмы. М.: Мир (1971).

GENERATION OF GOLD NANOPARTICLES ON ITO GLASS USING NANOSECOND LASER AND THEIR POTENTIAL APPLICATION IN ELECTROCHEMISTRY

E. Stankevičius[1], M. Garliauskas[1], L. Laurinavičius[1], R. Trusovas[1], P. Gečys[1], N. Tarasenko[2], N. Tarasenka[2], R. Pauliukaitė[1]

[1]Center for Physical Sciences and Technology, Savanoriu Av. 231, LT-02300 Vilnius, Lithuania, E-mail: estankevicius@ftmc.lt
[2]Stepanov Institute of Physics of National Academy of Sciences of Belarus, Nezavisimosti Ave. 68, 220072 Minsk, Belarus

In electrochemistry, metal nanoparticles are widely utilized as a functional unit to modify electrode surfaces /1, 2/ in order to develop (bio)sensors and energy production cells /3/ as well as for environmental applications /4/. Metal nanoparticles provide four main advantages over macroelectrodes for electroanalysis: enhancement of mass transport, catalysis, high effective surface area and control over local microenvironment /5/. Nanosized noble metal particles become important for various application fields including biosensors, nanosensors, nanodevices, catalyzes, and nanoelectrochemistry /6, 7/. Particular interests are focused on the synthesis and application of gold nanoparticles (AuNPs) in the electroanalytical and catalytic field due to the ability to enhance the electrode conductivity and facilitate the electron transfer, thus, improving the analytical selectivity and sensitivity /8/.

Indium tin oxide (ITO) films on glass or quartz substrates often used as an electrode surface due to their prominent characteristics such as a good electrical conductivity and wide electrochemical working window /9/, as well as low-cost /8/. ITO electrode modified with Au NPs possesses a faster electron transfer rate and larger current response than the bare ITO electrode /10/, therefore such electrodes could be applied for the creation of highly sensitive and selective future sensors. The modification of ITO electrode with AuNPs faces with the problem of the deposition of colloidal nanoparticles on ITO coating. The immobilization of AuNPs by using binding molecules such as thiols /11/ and silanes /12/ is ideal for glass surfaces /13/, but for ITO coatings this method does not obtain high coverage of AuNPs on the electrode surface. Furthermore, the electroactivity of the AuNPs films fabricated by this method is influenced by the contamination of various chemicals, such as the reactants, surfactant and binder molecules, as well as these methods have the time-consuming complex synthesis procedures. Other AuNPs deposition on electrodes methods as centrifugation /14/ or electrochemical deposition /10/ are more efficient but they are not attractive as they require specific equipment and sample preparation (surface cleaning and chemical modification). Therefore, it is highly desired to develop a

simple and effective method to synthesize AuNPs on a solid support as a highly electroactive electrode /7/. A good alternative strategy for one-step and useful fabrication of AuNPs on ITO electrodes directly can be the thermal treatment of thin gold coatings on ITO glass. These methods have an advantage versus drop-casting deposition or previously mentioned methods as they do not use colloidal solutions and the generation of AuNPs occurs directly on the desired surface. Heat treatment of metal thin films can be performed using thermal annealing furnace /15/ or nanosecond lasers /16/. The main advantages of nanosecond laser processing are the submicron treatment accuracy, the low thermal impact to the substrate and surrounding areas and the selective generation of nanoparticles on desired place and shape of the surface /17/.

The example of SEM images of generated Au NPs when the thickness of the gold coating on ITO glass is 3 nm, 5 nm and 20 nm are shown in Fig. 1 d-f. The micrographs clearly indicate that the size and density of generated Au NPs depend on the gold film thickness.

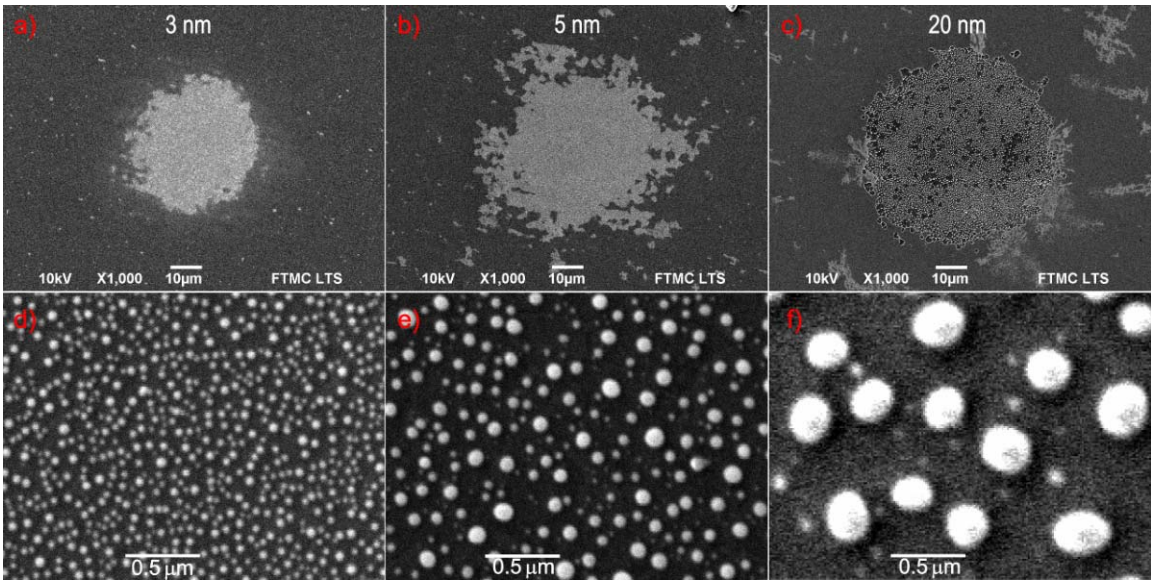

Fig. 1 - SEM micrographs of Au coatings affected by single laser pulse when coatings thickness are 3 nm (a, d), 5 nm (b, e) and 20 nm (c, f). The laser processing parameters in all cases were the same (laser pulse energy – 40 µJ, laser energy density – 505 mJ/cm^2, peak pulse intensity – 14 MW/cm^2, pulse duration – 35 ns, beam diameter – 142 µm)

Here, simple one-step generation of gold nanoparticles on ITO glass using nanosecond laser will be presented and the electrochemical properties of the gold modified ITO electrodes by the detection of the ascorbic acid will be analyzed.

Acknowledgements. E. Stankevičius, M. Garliauskas, R. Trusovas and P. Gečys acknowledge to the Lithuanian Research Council for the financial support of the joint Lithuanian-Belarus project in science and technology "Generation of nanoparticles by laser based methods and formation of structures consisting of nanoparticles by laser" No. S-LB-17-4. N. Tarasenko and N. Tarasenka acknowledge to the Belarusian Foundation for the financial support of Fundamental Researches under Grant No. F17LITG-003.

References

1. **Hernández- Santos D., González- García M.B., and García A.C.** Electroanalysis, 14(2002) 1225-1235.
2. **Campbell F.W. and Compton R.G.** Anal. Bioanal. Chem., 396(2010) 241-259.
3. **Koper M.T.M.** Nanoscale, 3(2011) 2054-2073.
4. **Rassaei L., Marken F., Sillanpää M., Amiri M., Cirtiu C.M., and Sillanpää M.** TrAC, Trends Anal. Chem., 30(2011) 1704-1715.
5. **Yu X., Wang L., and Di J.** J. Nanosci. Nanotechnol., 11(2011) 11084-11088.
6. **Kinge S., Crego- Calama M., and Reinhoudt D.N.** ChemPhysChem, 9(2008) 20-42.
7. **Zhang K., Wei J., Zhu H., Ma F., and Wang S.** Mater. Res. Bull., 48(2013) 1338-1341.
8. **Wang J., Wang L., Di J., and Tu Y.** Talanta, 77(2009) 1454-1459.
9. **Manifacier J.C.** Thin Solid Films, 90(1982) 297-308.
10. **El-Said W.A., Lee J.-H., Oh B.-K., and Choi J.-W.** J. Nanosci. Nanotechnol., 11(2011) 6539-6543.
11. **Brust M., Bethell D., Kiely C.J., and Schiffrin D.J.** Langmuir, 14(1998) 5425-5429.
12. **Okamoto T., Yamaguchi I., and Kobayashi T.** Opt. Lett., 25(2000) 372-374.
13. **Scarpettini A.F. and Bragas A.V.** Langmuir, 26(2010) 15948-15953.
14. **Wu D., Tang X., and Yoon H.S.** J. Nanopart. Res., 17(2015) 184.
15. **Plante M.C., Garrett J., Ghosh S.C., Kruse P., Schriemer H., Hall T., and LaPierre R.R.** Appl. Surf. Sci., 253(2006) 2348-2354.
16. **Ratautas K., Gedvilas M., Račiukaitis G., and Grigonis A.** J. Appl. Phys., 112(2012) 013108.
17. **Lin Y., Zhai T., and Zhang X.** Opt. Express, 22(2014) 8396-8404.

Formation of graphene structures in wood by laser irradiation

R. Trusovas, K. Ratautas, G. Račiukaitis, G. Niaura

Center for Physical Sciences and Technology, Savanorių ave. 231, LT-02300 Vilnius, Lithuania, romualdas.trusovas@ftmc.lt

Graphene is proven as valuable material for the electronics, sensing, energy storage, heat dissipation and other applications. From the discovery of graphene, many of its production methods were being developed. One branch of graphene production approaches is based on laser-induced graphene formation. Laser micro-processing offers production flexibility and scaling opportunities. Operating tightly focused laser beam allows creating of complex graphene microstructures needed for particular applications, such as energy storage, sensing, microelectronics, etc. We present experimental results of laser-induced formation of graphene structures in pinewood. Experiments were conducted using nanosecond and picosecond lasers with a pulse duration of 10 ns and 10 ps, respectively, at the irradiation wavelength of 1064 nm in the hermetic chamber with a nitrogen atmosphere. Raman spectroscopy measurements showed the formation of high-quality few-layer graphene structures with I(2D)/I(G) ratio of 1.10 obtained at an irradiation dose of 662 J/cm^2 utilizing nanosecond laser pulses. Minimum sheet resistance values of laser treated wood was 35 Ω/sq at an irradiation dose of 662 J/cm^2 using nanosecond laser and 179 Ω/sq at an irradiation dose of 584 J/cm^2 using picosecond laser. Sheet resistance measurements showed a correlation with Raman spectroscopy data and revealed a significant decrease in electric resistance for the sample with highest I(2D)/I(G) Raman bands ratio using nanosecond laser irradiation. Modeling of the pinewood surface temperature after pulse laser irradiation revealed substantial higher temperature at the surface in the case of picosecond laser resulting in the laser-induced formation of graphene at smaller irradiation doses comparing with nanosecond laser.

Acknowledgements. This research is funded by the Lithuanian Research Council financial support of the joint Lithuanian-Belarus project in science and technology “Generation of nanoparticles by laser based methods and formation of structures consisting of nanoparticles by laser” No. S-LB-17-4.

GENERATION OF ELECTRIC POTENTIAL AND MAGNETIC FIELD DURING BICHROMATIC LASER IRRADIATION OF TITANIUM TARGET IN AIR

A.N. Chumakov, N.A. Bosak, N.I. Chubrik, A.A. Ivanov

B.I. Stepanov Institute of Physics, NAS of Belarus,
220072 Minsk, Prospekt Nezavisimosti, 68-2; n.bosak@ifanbel.bas-net.by

Introduction. A repetitively pulsed action of laser radiation (LR) makes it possible to vary the air plasma/erosion plasma relationship by increasing a pulse repetition rate to values higher than 5 kHz, which raises the efficiency of both the laser ablation of a target in air /1, 2/ and the generation of a magnetic field /3/. Turning to a double laser pulses action at wavelengths of Nd:YAG laser harmonics extends possibilities of selective plasma formation and target ablation /4/. The aim of the paper is to elucidate the features of generating the electrical potentials and magnetic fields on exposure of a titanium target in air by double laser pulses at the Nd:YAG laser harmonics.

Experimental Setup. The setup includes two Nd:YAG lasers generating at wavelengths of 1064 and 532 nm. The LTI-403 laser (λ_1 = 1064 nm, E = 77 mJ, τ = 20 ns) provides practically the same pulse duration and energy values as the LS-2130 laser does (λ_2 = 532 nm, E = 69 mJ, τ = 20 ns). The setup implements a two-pulse action of LR on a titanium target in air with a controllable time interval between laser pulses and a variable order of their sequence. Negative values of the time shift between the laser pulses shown in the figures correspond to the case of the advancing impact of the short-wavelength LR (λ = 532 nm); the positive values mean that the long-wavelength LR (λ = 1064 nm) is the first to be emitted. The experiments were carried out at the LR power density of $q_{0,532}$= 2,7·10^9 W/cm^2 and $q_{1,064} \le$ 3,8·10^9 W/cm^2 in the irradiation spot of d_n ~ 0.30 mm.

Experimental Results and Discussions. Electrical potentials were measured by using an electric probe /2/. Typical oscillograms of the electric potential on the target surface are shown in Fig. 1. The experimental dependence of the electric potential (U) peak values at the Ti target on the time interval between a double laser pulses of the attacking LR is shown in Fig. 2. The values of the electric potential generated by the action of the 2nd LR pulse on the titanium target vary in the range from 15 to 27 V.

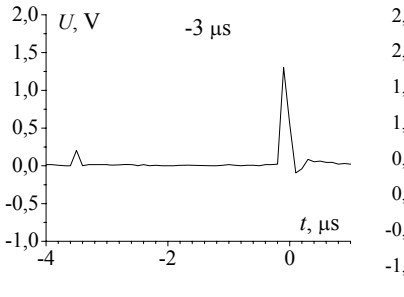

Fig. 1 – Oscillograms of electric potential, U, on Ti target irradiated by double laser pulses (532 and 1064 nm) at a pulse-to-pulse interval of ±3 μs

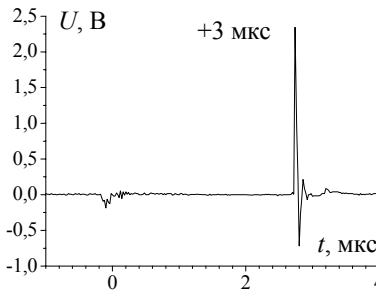

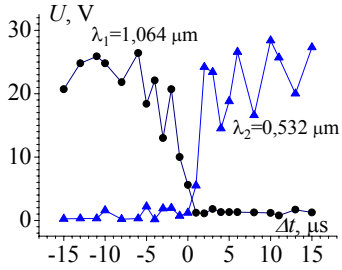

Fig. 2 – Peak values of electric potentials at Ti target irradiated by double laser pulses with interval from –15 to 15 μs

The titanium plasma emission in the visible spectral region was recorded with an FEU-114 photoelectric multiplier (sensitivity spectral range from 0.25 μm to 0.85 μm). The plasma emission was transferred to the photomultiplier input via an optical fiber. A typical oscillogram of the Ti plasma emission and the dependence of the plasma emission lifetime on the pulse-to-pulse interval are shown in Fig. 3.

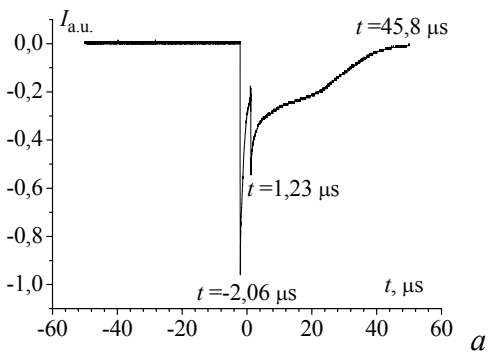

а

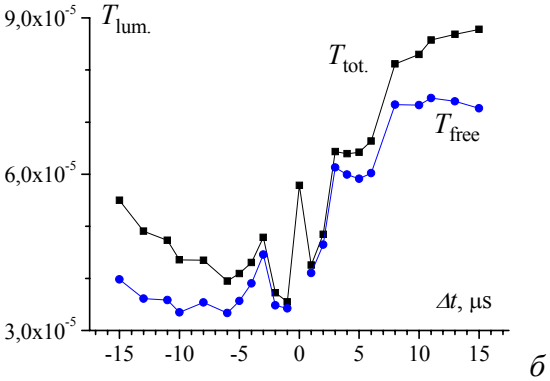

б

Fig. 3 – Oscillogram of titanium plasma emission at a pulse-to-pulse interval of –3 μs (a) and dependence of Ti plasma emission lifetime on the pulse-to-pulse interval (b)

It can be seen that the Ti plasma emission lifetime increases approximately by a factor of two when passing from negative values of pulse-to-pulse intervals to the positive ones. In the region of small time intervals, oscillations in the plasma emission lifetime are observed.

To record magnetic fields, a magnetic probe based on a small inductance coil is used. In Figs. 4 and 5, typical oscillograms from the magnetic probe and the corresponding peak values of magnetic field induction are shown respectively.

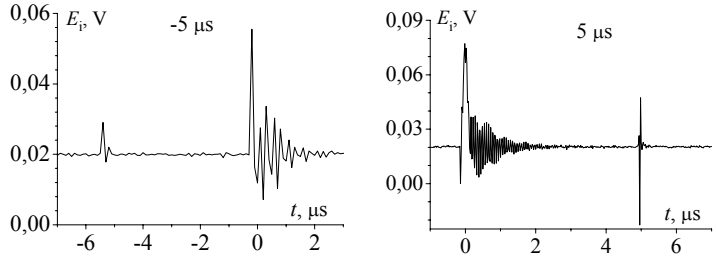

Fig. 4 – Oscillograms of the E.M.F. induced in the magnetic field sensor when irradiating Ti target by double laser pulses at wavelengths of 532 and 1064 nm with the pulse-to-pulse interval of ±5 μs

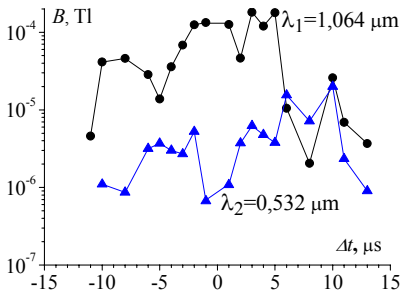

Fig. 5 – Induction of the magnetic field generated by the plasma on exposure of Ti target to double laser pulses with wavelengths of 1064 and 532 nm

The Fourier spectra of the magnetic field pulses at pulse-to-pulse intervals of –3 μs and 3 μs are shown in Fig. 6a and 6b, respectively. The obtained spectra are characterized by the presence of a high-intensity narrow line and a weak wide band in the low-frequency region caused by the oxidation of titanium.

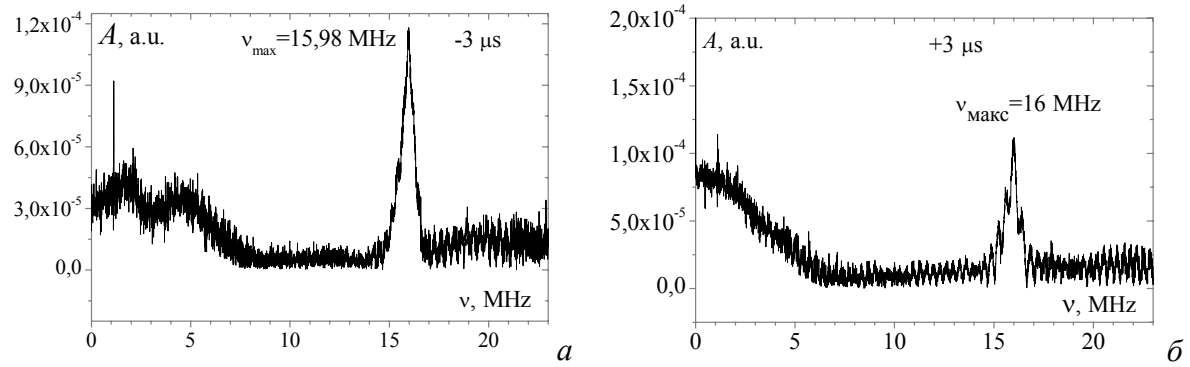

Fig. 6 – Fourier spectra of magnetic field pulses with pulse-to-pulse interval of –3 μs (a) and 3 μs (b)

The half-widths of these lines and the corresponding frequencies as a function of the pulse-to-pulse interval are shown in Fig. 7a and 7b. The half-width of the lines detected in the Fourier spectrum reaches its maximum at a

zero delay between pulses. The dependence of the corresponding frequency on the pulse-to-pulse interval exhibits a plateau at ~16 MHz in the range from −3 μs to 5 μs. Beyond this range, the frequency of the lines in the Fourier spectrum is around ~4 MHz.

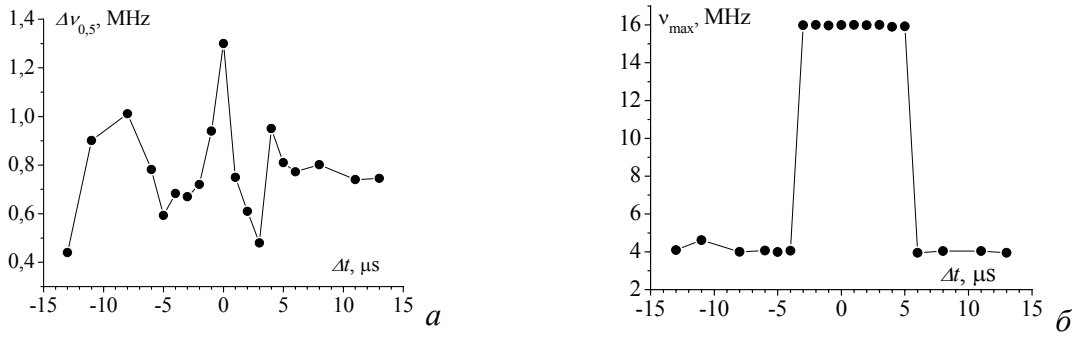

Fig. 7 – The half-widths of the lines in the Fourier spectra of the magnetic field pulses (a) and the values of their frequencies (b) depending on the pulse-to-pulse interval

Generation of the electric potential at the titanium target in air exposed to double laser pulses of radiation with wavelengths of 532 and 1064 nm is more efficient when the 2nd pulse is applied with a time interval from 2 to 15 μs, regardless of the sequence order. Generation of the magnetic field is most effective when the laser plasma is heated by long-wavelength laser radiation with a pulse-to-pulse interval from 10 to 5 μs. The plasma emission lifetime doubles when passing from negative to positive pulse-to-pulse intervals. In the range from −3 μs to 5 μs, the line frequency in the Fourier spectrum of the magnetic field pulses retains its maximum value of ~16 MHz, which indicates the highest velocity of plasma clusters under these conditions.

Acknowledgments. This work was supported by the Belarusian State Program "Convergence-2020" (project no. 2.4.02).

References

1. **Minko L.Ya., Chumakov AN, Bosak N.A.** // Quantum Electronics. 1990. T.17, No. 11, 1480-1484.
2. **Chumakov AN, Avramenko VB, Bosak N.A.** // Journal of Applied Spectroscopy. 2012, T.79, 279-287.
3. **Chumakov AN, Chekan P.V.** // Quantum Electronics. 2015. T.45, No. 3, 224-227.
4. **Chumakov AN, Bosak NA, Panina A.V.** // Journal of Applied Spectroscopy. 2017. 84, No. 4, 595-602.

FEATURES OF TARGET ELECTRIZATION AND GENERATION OF MAGNETIC FIELD IN PROCESS OF BICHROMATIC LASER ABLATION OF NIOBIUM IN AIR

A.N. Chumakov, N.A. Bosak, M.G. Sugak

B.I. Stepanov Institute of Physics, NAS of Belarus,
220072 Minsk, Prospekt Nezavisimosti, 68-2; n.bosak@ifanbel.bas-net.by

Introduction. A high-frequency action of laser radiation (LR) on metals in air makes it possible to vary the air plasma/erosion plasma relationship by increasing a pulse repetition rate to values higher than 5 kHz, which raises the efficiency of both the laser ablation of a target in air /1, 2/ and the generation of a magnetic field /3/. The transition to a double laser pulses action at wavelengths of Nd:YAG laser harmonics extends the possibilities of selective plasma formation and target ablation /4/. The dynamics of plasma and emission spectra of the torch on the surface of the aluminum target at double laser pulses action at a wavelength of 1064 nm with a controlled delay from 0 to 140 μs and a power density of 840 MW/cm^2 were studied by experimental and numerical methods /5/. The aim of this work is to study laser ablation features of a metal with high melting and boiling points such as niobium when it is irradiated by double laser pulses at the first and second harmonics of the Nd:YAG laser and to reveal the features of generation of magnetic and electric field in such conditions.

Experimental setup. The setup consists of two Nd:YAG lasers, generating at wavelengths of 1064 and 532 nm. The LTI-403 laser (λ_1 = 1064 nm, E = 77 mJ, τ = 20 ns) provides practically the same pulse duration and energy values as the LS-2130 laser does (λ_2 = 532 nm, E = 69 mJ, τ = 20 ns). The laser system allows a double pulses LR action on niobium target in air with a controlled time interval between laser pulses and the variable order of their sequence. The negative values of the time shift between the laser pulses shown in figures below correspond to the case of the advancing effect of the short-wavelength radiation (λ = 532 nm); the positive values mean that the long-wavelength radiation (λ = 1064 nm) is the first to be emitted. The experiments were conducted at the LR power density of $q_{0,532}$ = $2.7 \cdot 10^9$ W/cm^2 and $q_{1,064} \le 3{,}8 \cdot 10^9$ W/cm^2 in the irradiation spot of $d_n \sim 0.30$ mm.

Experimental results and their analysis. Measurements of electrical potential were carried out with an electric probe /2/. Typical electric potential oscillograms on the target surface are shown in Fig. 1. The experimental dependence of the electric potential (U) peak values at the niobium target on the pulse-to-pulse interval (time shift between the LR pulses) is shown in Fig. 2. The values of the electrical potential generated by the action of the 2nd LR pulse on the niobium target are subject to oscillations.

To record the magnetic field, a magnetic probe based on a small inductance coil is used. Typical oscillograms from the magnetic probe are shown in Fig. 3, and the corresponding amplitudes of the EMF induced by the magnetic field in the

probe coil under the action of double laser pulses with wavelengths of 1064 and 532 nm are presented in Fig. 4.

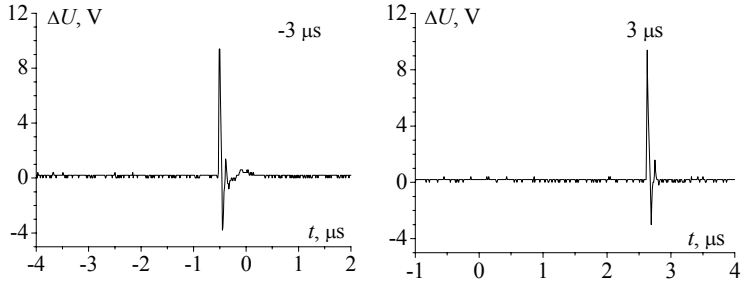

Fig. 1 – Oscillograms of electric potential on a niobium target irradiated by double laser pulses with wavelengths of 532 and 1064 nm at a time interval of ±3 μs

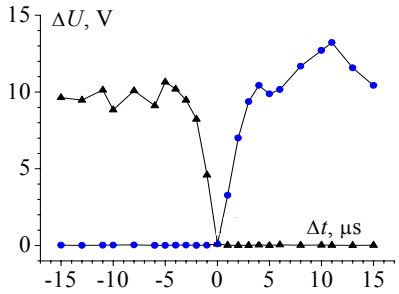

Fig. 2 – Amplitudes of electric potentials at Nb target irradiated by double laser pulses with time shift varying from –15 to 15 μs

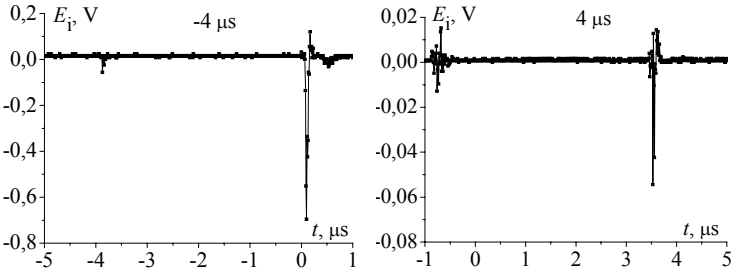

Fig. 3 – Oscillograms of EMF induced in the magnetic field sensor on exposure of Nb target to double laser pulses with wavelengths of 532 and 1064 nm at a pulse-to-pulse interval of ±4 μs

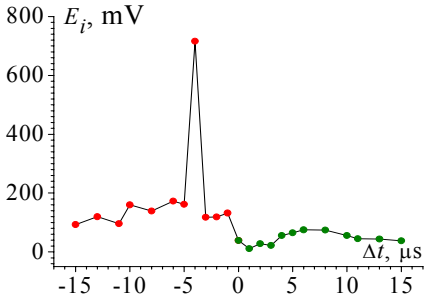

Fig. 4 – EMF induced by a magnetic field in the probe coil under the action of double laser pulses with wavelengths of 1064 and 532 nm on Nb target

The experimental dependence of EMF induced by the magnetic field in the probe coil on the time shift and the order of the pulses sequence (Fig. 4) shows that the maximum EMF value reaches 710 mV at the time shift of $\Delta t = -4$ μs and undergoes oscillations at negative shifts and in areas of approximately constant output around 40 mV.

A luminous laser torch and its variations depending on the time shifts and the sequence order of the laser pulses were investigated using a Canon A 520 camera in a video shooting mode with an exposure time of 500 μs (Fig. 5). A nature of the expansion of near-surface laser-plasma formations under bichromatic double laser pulses of niobium target in air depends essentially on the time interval between the LI pulses. When the pulses coincide in time or a time shift is negative, the plasma front of the torch breaks, which indicates the realization of a low-

threshold air breakdown. With a positive values of the time shift, a continuous mushroom-shaped plasma torch is observed.

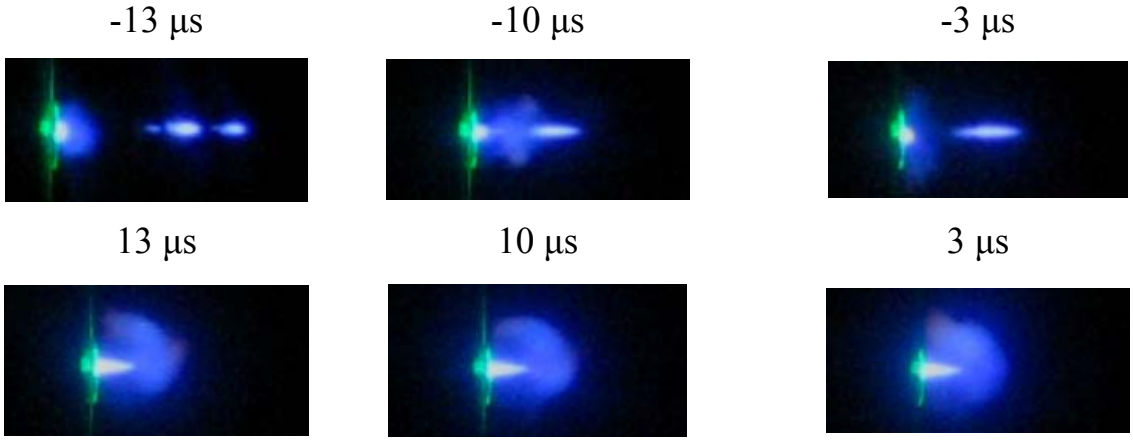

Fig. 5 – Features of the torch structure on exposure of Nb target to double laser pulses in air at $\Delta t = \pm$ 13 μs (a), ± 10 μs (b), and ± 3 μs (c)

The electron temperature in the plasma was calculated from relative intensities of two niobium spectral lines, Nb II 309.4 nm and Nb I 405.8 nm (Fig. 6).

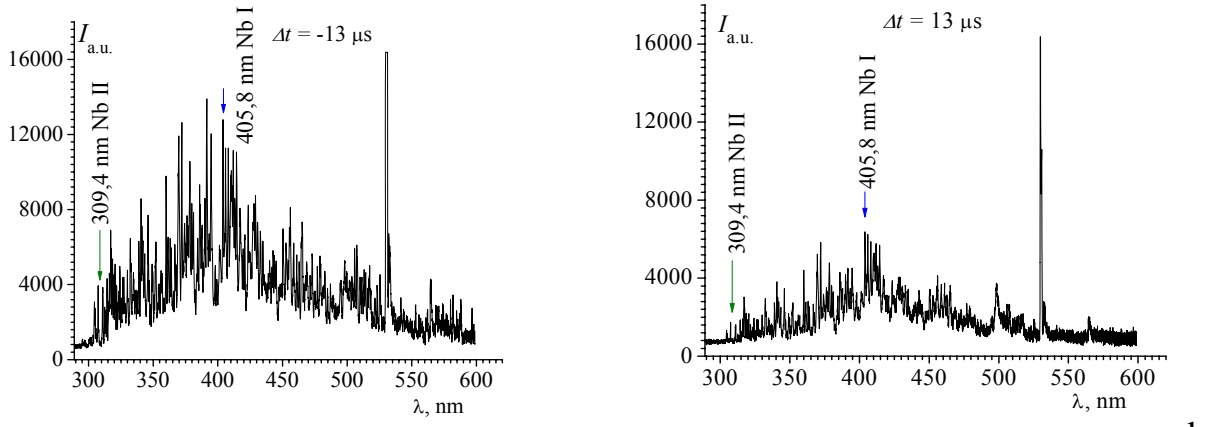

Fig. 6 – Spectra of niobium plasma in air under the action of double laser pulses at two wavelengths with time shifts $\Delta t = -13$ μs (a) and 13 μs (b)

The maximum value of temperature, T_{max} = 11800 K, is achieved with the advancing action of short-wave radiation (λ = 532 nm at a time shift between the laser pulses of $\Delta t = -1$ μs and the minimum value, T_{min} = 7700 K, was observed at Δt = 13 μs (Fig. 7). This is partly due to a rise in the absorptivity of the plasma formation with an increase in the LR wavelength /6/.

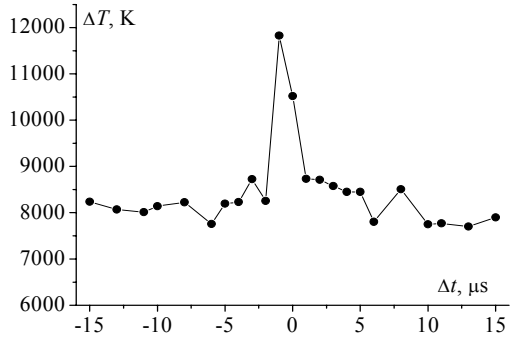

Fig. 7 – Dependence of the niobium plasma temperature on both the time shift and the order of the succession of the double laser pulses

Conclusion. Bichromatic laser irradiation of Nb target results in the enhanced efficiency of target laser ablation because: i) the short-wavelelength LR pulse more effectively heats the target and contributes to the formation of an erosion plasma due to a lower reflection coefficient; ii) the long-wave LR pulse provides a significant heating of the erosion plasma because of the cubic dependence of the plasma absorption coefficient on the wavelength.

Peak values of the electric potential generated by a laser plasma on the Nb target surface depend on both the sequence order of LR pulses and the time shift between laser pulses. They vary from 9 V to 13 V and decrease to 0.1 V in the vicinity of $\Delta\tau$=0 μs. In this case, the electric potential generated on the target surface by the first laser pulse is less by one and a half orders of magnitude than that generated by the second pulse. The magnetic field generated by the plasma multiplies many times at just a small time shift between laser pulses close to $\Delta\tau \tilde{=}$ - 4 μs.

Acknowledgments. This work was supported by the Belarusian State Program "Convergence-2020" (project no. 2.4.02).

References

1. **Minko L.Ya., Chumakov A.N., Bosak N.A.** // Quantum Electronics. 1990. T.17, No. 11, 1480-1484.
2. **Chumakov A.N., Avramenko V.B., Bosak N.A.** // Journal of Applied Spectroscopy. 2012, T.79, 279-287.
3. **Chumakov A.N., Chekan P.V.** // Quantum Electronics. 2015. T.45, No. 3, 224-227.
4. **Chumakov A.N., Bosak N.A., Panina A.V.** // Journal of Applied Spectroscopy. 2017. 84, No. 4, 595-602.
5. **E.A. Ershov-Pavlov, K.Yu. Katsalap, K.L. Stepanov, Ya.A. Stankevich** // Spectrochimica Acta Part B – 2008. – Vol. 63. Pp 1024-1037
6. **Anisimov S.I., Imas Y.A., Romanov G.S., Khodyko Yu.V.** // Effects of high-power radiation on metals. Ed. A.M. Bonch-Bruevich and M.A. Eliashevich. M., ”Science”, 1970. 272 p.

EFFECTIVE REGIMES OF PULSED LASER ABLATION OF MATERIALS AND GENERATION OF PLASMA FLOWS WITH CONTROLLED PARAMETERS

A.N. Chumakov, N.A. Bosak, P.I. Verenich, A.V. Panina
B.I. Stepanov Institute of Physics of the NASB,
68-2Nezavisimosti Ave., Minsk, 220072 Belarus,
e-mail:a,chumakov@dragon.bas-net.by

Abstract. The ablation of a number of materials in air (Al, brass, graphite, silicon etc.) under the action of pulse-periodic laser radiation at the Nd:YAG-laser harmonics is experimentally studied. New possibilities for increasing the efficiency of laser ablation of materials as well as controlling the parameters of near-surface laser plasma using of monochromatic and bichromatic pulsed laser radiation with variable repetition rate of laser pulses are revealed.

1. INTRODUCTION

Laser irradiation of absorbing materials is accompanied by a number of complicated physical phenomena: heating of the target surface, melting of the target and its rapid vaporization. Vapor expanding away from the target at supersonic speed displaces the surrounding air like a piston, forming a shock wave. During of laser irradiation, the optical and thermophysical properties of the surface change (the reflection coefficient, the temperature, the thermal conductivity coefficient) and metal–liquid–vapor–plasma phase transitions occur. In the 50–100 $MWcm^2$laser power density range, the air surrounding the target is heated so strongly that the air itself begins to absorb the incident radiation and the plasma formation process jumps from the target vapors to the air. The air plasma shields the target from the incident laser radiation. Consequently, the energy input to the target and the ablation plasma becomes less effective, which limits the possibilities for laser treatment and laser spectral analysis of materials /1/.

The effectiveness of laser irradiation of materials in air depends not only on the laser power density but also on the wavelength of laser radiation as well as laser pulse repetition frequency /1–5/.Therefore, this article is devoted to an analysis of the possibilities of increasing the efficiency of laser ablation of materials and obtaining plasma flows with controlled parameters using monochromatic and bichromatic pulsed laser radiation with a controlled pulse repetition rate.

2. EXPERIMENTAL

The single pulse and multi-pulse laser irradiation (LI) of a materials at repetition rates $f \leq 50$ kHz was produced by pulsed laser ($\lambda = 1060$nm, $\tau \sim 85$ ns, pulse energy$E = 2–4$ J). The production of singlepulse and periodic pulses was provided using a passive Q-switch with LiF:F^{-}_2 – color centers. The irradiance q

at the target surface was varied over 10^5–10^9W/cm^{2}bymeans of neutral density filters. A vacuum chamber was used for doing experiments at air pressures as low as 2 Pa.

The double-pulse laser irradiation (LI) was produced by synchronizing two Nd:YAG lasers with wavelengths of 1064 and 532 nm (E = 100 mJ, τ= 20 ns) with adjustable time interval between laser pulses. The dependence of the plasma spectra, electron density and temperature of the plasma on the ordering of laser pulses and the inter-pulse time delay during laser exposure of various materials in air was studied. In these experiments, the emission spectra of near-surface plasma and the pressure pulses on the irradiated targets were registered. The SDH-IV spectrometer with a linear CCD detector TCD 1304 AP (Toshiba) was used for registration of plasma spectra. The spectrometer was connected to a computer and a laser system synchronization unit. For registration of pressure pulses on the target and of the LI pulses, a piezoelectric detector synchronized with digital oscilloscope was used. Recoil momenta for different materials were determined by integrating the pressure signal over time.

3. RESULTS

Obtained experimental data shows that excitation of ablation laser plasma in air at atmospheric pressure and below can occur under the following conditions for multipulse laser irradiation.

1. For low laser irradiances ($q \le 2\cdot10^7$W/cm^{2}for $\lambda \sim 1$ μm) applied to metals in single and multipulse modes, independently of the pulse repetition rate. With increasing intensity, $q \ge 5\cdot10^7$W/cm^2, the ablation plasma is weakened because the region where the plasma is primarily formed shifts from the metal vapor into the air still at the front of the laser pulse and because of increased shielding of the target by the air plasma /1, 5, 6/.This sort of physical picture is typical of single-pulse laser irradiation, as well as for series of pulses if their repetition rate does not exceed ~1–5 kHz.

2. For relatively high laser irradiances on metals in gases {$2\cdot10^8 \le q \le 4\cdot10^9$ W/cm^2 for $\lambda \sim 1$ μm on relatively small (~10^{-2} cm^2) irradiation spots} efficient erosion plasma formation occurs only for high pulse repetition rates f > 5 kHz (Fig. 1).

The performed experiments showed that surface ablation plasma is the distinctive feature of high repetition rate (f > 5 kHz) pulsed periodic laser irradiation of metals in air under certain conditions (q ~ 0.1–1 GW/cm^2, $\lambda \sim$ 1 μm, 0.1 < p < 1 atm).The high efficiency of ablation plasma formation for high laser pulse repetition frequencies is of interest for laser spectral analysis /1, 6/.

The sensitivity of analysis for the materials can be significantly improved even with exposure to two laser pulses, separated by a time interval of a few microseconds /6, 7/.

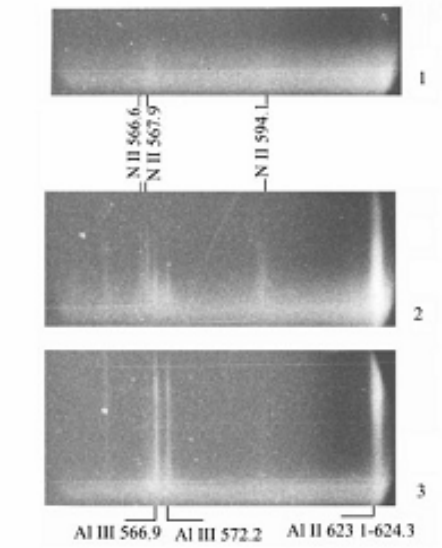

Fig.1 – Fragments of high speed camera spectra of a surface laser plasma on an aluminum target: with an air pressure p = 0.5 atm in the vessel; the pictures were obtained during the first (q = 500 MW/cm^2) (1), second (q = 460 MW/cm^2) (2), and third (q = 520 MW/cm^2) (3) laser pulses at a repetition rate f = 12 kHz with a framing period τ = 8 μs; the bright band at the bottom corresponds to the continuum background near the target surface

Additional benefits in formation and heating of laser plasmas can be achieved by the double-pulse mode irradiation at different wavelengths of the material due to the dependence of the targets reflectance and radiation absorption of plasma on the wavelength of the LI/8/. The performed experiments showed that that the exposure to shortwave LI stimulates the formation of ablation plasma while the infrared LI produces predominantly air plasma (Fig. 2).

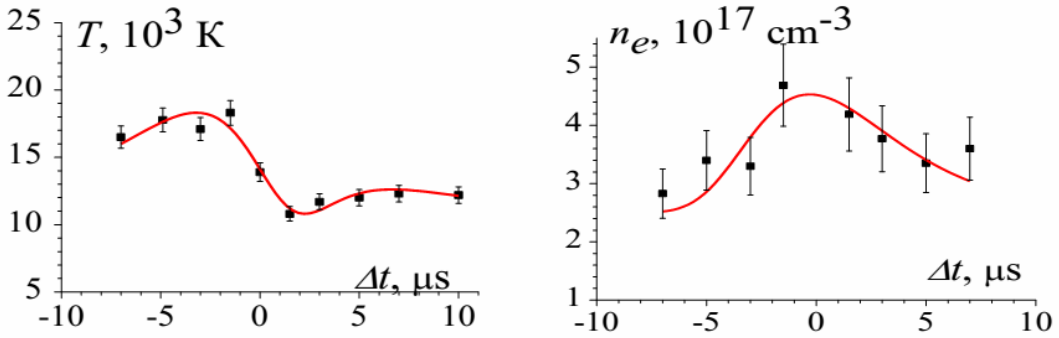

a *b*

Fig. 2 – Dependence of temperature (a) and electron density (b) in the carbon plasma on the timeinterval between laser pulses

It was established that temperature, charged particle density and recoil momentum of a laser-produced plasma are depends on the ordering of the double-pulse laser irradiation of the targets in air at wavelengths of 1064 and 532 nm and on the time interval between pulses(Fig.2).

Investigation of the efficiency of silicon laser ablation in air under double pulses laser irradiation at wavelengths of 532 and 1064 nm with a controllable order of laser pulses and time delay between themwere also carried out (Fig.3).

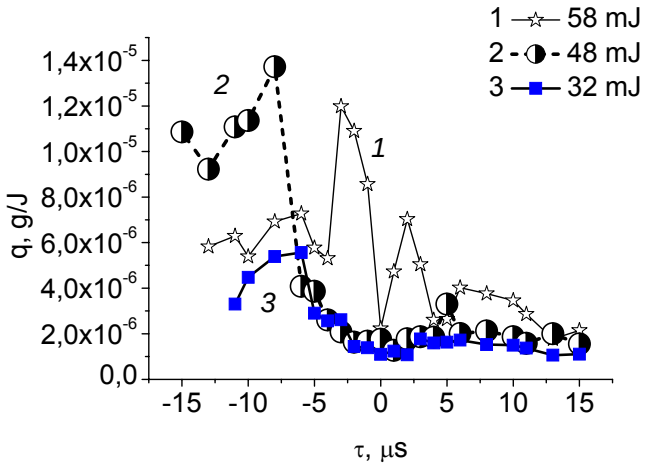

Fig. 3 – Dependence of the silicon specific removal on the time delay between the laser pulses with wavelengths of 532 nm and 1064 nm (negative values of time correspond to the leading action of 532-nm pulses) at three different energy values of 532-nm pulses

A manifold increase in the specific mass removal of silicon has been revealed under irradiation with leading 532 nm nanosecond laser pulses followed by 1064-nm pulses with time delay from 3 to 8 μs.

4. CONCLUSION

Based on optical and spectroscopic studies, we have established thateffective regimes of pulsedlaser ablation of materials in air as well as generation of plasma flows with controllable parametersmay be realized using pulse laser irradiation with a high repetition rate of pulses over 5 kHzor double pulses laser irradiation at wavelengths of 532 nm and 1064 nm with a controllable order of laser pulses and time delay between them. The results obtained can be used to improve the efficiency of laser-induced breakdown spectroscopy method andlaser processing of materials as well as laser–plasma micromotors for aerospace applications.

Acknowledgements. This work was partially supported by the Belarusian State Program “Convergence-2020" (project no. 2.4.02).

REFERENCES

1. L.Ya. Min’ko, A. N. Chumakov, and N. A. Bosak, Sov J Quant. Electron., **17**(11) 1389 (1990).
2. M. L. Petukh, V. A. Rozantsev et al.J. Appl. Spectrosc., **67**, 1097 (2000).
3. S. M. Klimentov et al.,Quant. Electron., **34** (6), 537 (2004).
4. S. M. Pershin,Quant. Electron., **39** (1) 63 (2009).
5. L. Ya. Minko, A. N. Chumakovet al., J. Appl. Spectrosc., **61**, 805 (2000).
5. A.N. Chumakov, V. B. Avramenko, and N. A. Bosak, J. Appl. Spectrosc., **79**, 261 (2012).
7. R. Noll, Laser-Induced Breakd.Spectr.,Springer, Berlin/Heidelberg (2012).
8. A.N. Chumakov, N. A. Bosaket al., J. Appl.Spectrosc., **84** (4) 620 (2017).
9. A. Chumakov, N.Bosaket al., High Temp. Mat. Proc.,**18**(4), 269 (2014).

6. PLASMA SPECTROSCOPY AND OTHER DIAGNOSTIC METHODS

SPECTROSCOPIC MEASUREMENT OF ELECTRIC FIELD IN HELIUM DISCHARGES

M. M. Kuraica

University of Belgrade, Faculty of Physics, P.O. Box 44, 11001 Belgrade, Serbia,
kuki@ff.bg.ac.rs

Introduction In the dipole approximation the selection rules strongly forbid certain transitions between electron energy levels and the appearance of the corresponding atomic lines in the spectra. On the other hand, the presence of the moderate external electric field is sufficient to remove all restrictions with regard to changes in the orbital quantum number and to cause the appearance of the spectral lines that are no usually visible in the spectra. In 1927, Foster /1/ for the first time applied quantum mechanics perturbation theory to the helium atom. In his calculations, considering the external electric filed as a perturbation, he concluded: a) the forbidden lines may appear in helium spectra and b) the displacement of the energy levels, and the shifts of the allowed and forbidden lines in the spectrum are linear functions of the perturbing electric field. The calculation performed by Foster these days represents the standard student problem and it is used in our laboratory as a theoretical background for the solution of the inversed problem and the foundation of the method for the electric field measurements using the shift of forbidden and allowed lines i.e. peak to peak distance between these lines /2/. The proposed method is universal and it doesn't depend on the gas composition, kinetics of the processes in the discharge, gas pressure, temperature, electron density, DC, AC or RF applied voltage etc., because it is based on ab initio calculation.

Experiment The first measurements in our laboratory were performed using Grimm type abnormal glow discharge operating in DC regime at low pressure. These measurements were done using high resolution spectrometer utilizing LOCK-IN technique that enabled low level of noise. The appearance of the forbidden line is depicted in Fig. 1 (a). The newest measurements results performed using monochromator of lower resolution and the iCCD are shown in Fig. 1 (b). As presented in Fig. 1 (b) the lines are shifting in the opposite directions and the distance between them increases closer to the cathode surface where the electric field strength increases. After that, a small amount of hydrogen is added to helium for sake of the independent electric field strength determination using H_β line. This method for the electric field measurements based on the linear Stark effect of hydrogen atom is the previously developed in our laboratory /3/.

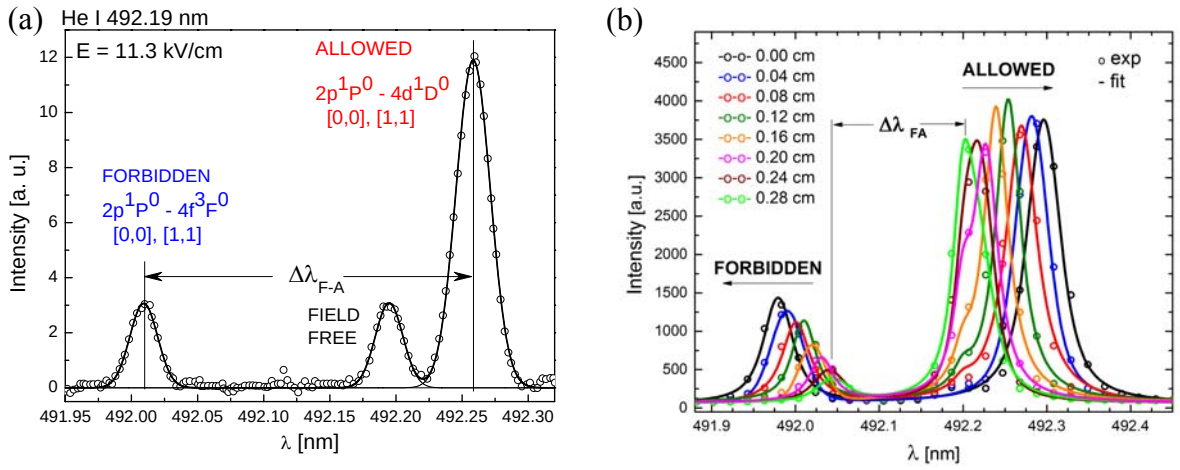

Fig 1 - (a) The part of the spectrum in the vicinity of 492.1 nm detected by LOCK-IN technique, (b) Shifts of the forbidden and allowed line for the rising electric field strengths recorded by iCCD

The plot of the distance between forbidden and allowed He lines in dependence on the electric field strength obtained by H_β line is shown in Fig. 2 (a). These graphs practically represent the calibration curve, due to the independent and reliable electric field determination using hydrogen H_β line.

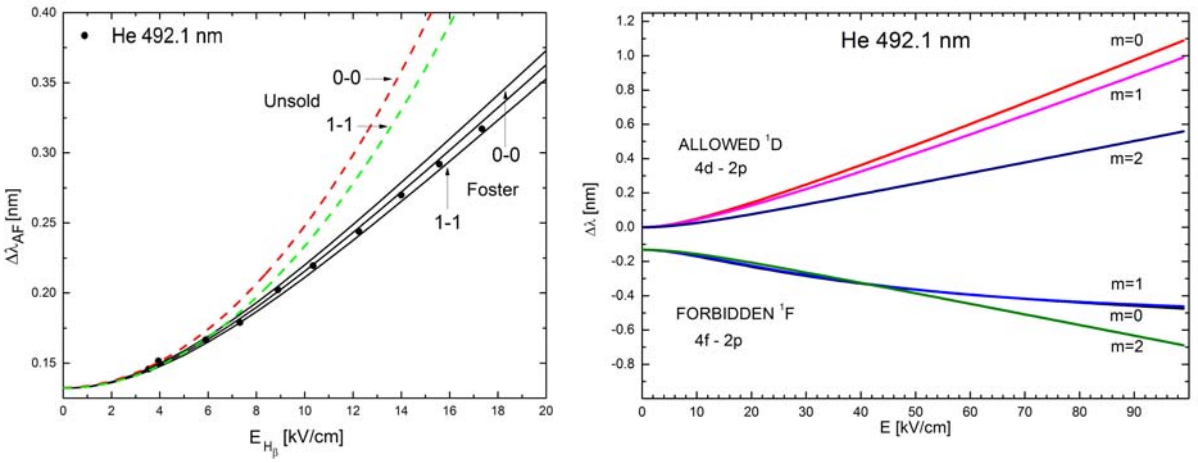

Fig.2 - (a) Comparison of the experimentally obtained values with the quadratic Stark effect (Unsold) and linear Stark effect (Foster). (b) Splitting and shifting of the sublevels of the 492.1 nm line calculated by Foster's perturbation method

On the other hand, the interpretation of the obtained experimental data in a frame of quadratic Stark effect, that is expected for He atom, gave agreement only for the lower electric field strengths, up to 5 kV/cm. For the higher values of the electric field the effect was linear. In order to find the reasons for the discrepancy of the experimentally obtained results and the theory, the perturbation calculation proposed by Foster was repeated. In these calculations,

the electric field was the parameter that was changed in 1 kV/cm steps. Calculation is performed in the basis of the hydrogen wave functions. Therefore, Fig. 2 (b) gives the example of the calculation of the energy level shift for the atomic transitions $2p^1\,P^0$–$4d^1\,D^0$ and $2p^1\,P^0$–$4f\,^1F^0$ i.e. the allowed and forbidden He 492.1nm line components. The comparison of this way the calculated peak to peak distances between allowed and forbidden lines with the experimental results in Fig. 2 (a) demonstrates a very good agreement.

The perturbation calculations are also performed for other two lines around the 402.0 nm and 447.1 nm. It should be noted that all analyzed lines possess substructure originating from the degeneracy of the corresponding electron energy levels with different magnetic quantum number m. Consequently, the emission of the observed He lines consists of two polarized components. For $\Delta m=0$ the light is π polarized, while for $\Delta m=\pm 1$ the light is σ polarized. With the use of the polarizer, one of the components could be blocked. For example, helium line $2p^1\,P^0$–$4d^1\,D^0$ at 492.19 nm consists of two π and three σ components, which is also the case with the forbidden line $2p^1\,P^0$–$4f\,^1F^0$, see Fig 2. b). The mentioned substructure could be observed in the presence of higher electric field.

The proposed forbidden-allowed method is further expanded to eight helium lines, reinterpreted and adopted for the less experienced users /4/. The interpolation polynomials for the calculation of the electric field strength for the measured distance between lines are also given in the named article. If it is not possible to measure peak separation directly, the fitting procedure is proposed. The line fits include all components and the so called field free component that comes from the discharge region without electric field. The fitting method increased the sensitivity of the whole method and allowed measurements of lower electric fields, down to 3 kV/cm. The line fitting is necessary for higher gas pressures.

The method has been tested in the atmospheric pressure DC discharge /5/. The measurement results showed unexpectedly broadened forbidden and allowed line. The line widths exceeded the values that are caused by pressure broadening, which is interpreted by the additional perturbation of the emitter by fluctuating micro-field. It turned out that the amplitude of the fluctuating micro-field is three times higher than the static electric field at the cathode surface. The effect of this type of the broadening of the forbidden and allowed lines is later observed in the other atmospheric pressure discharges in helium.

The number of types and application potentials of atmospheric pressure helium discharges, such as dielectric barrier discharge (DBD) and plasma jets, expanded in the last decade. The information about the electric field strength distribution in these discharges is of key importance for their modeling, and further for the construction and optimization of the plasma reactors based on

these discharges. It came out that the earlier developed method, which was not spotted earlier, became very popular. It doesn't require expensive laboratory equipment; it is easy to use, it is applicable for all discharge conditions and it is non-contact, non-perturbing method.

The experimental results for the spatio-temporal development of the electric field in DBD in helium, formation of the cathode fall region, change of slope of the electric field and the formation of the homogenous discharge, are for the first time obtained utilizing this method /6/. For the situations when the intensities of the helium lines of interest for the allowed-forbidden electric field measurements method are insufficient, the additional method based on the intensity ratio of intensive helium lines is developed which enabled higher measurement sensitivity /7/.

The important conclusions about the propagation of plasma bullets in helium jets are attained by the measurements of the radial and axial distribution of the electric field by the forbidden-allowed method /8/. The obtained profile of the electric field in the plasma bullet has a ring shaped structure. Also, the dependence of the electric field strength on the plasma bullet velocity has been experimentally demonstrated. The obtained experimental results were in good agreement with the modeling outcomes. At the moment, the method represents the standard procedure for the electric field measurements in plasma jets. The results are also compared with the electro-optic probe measurements.

Acknowledgements

This work was supported by the Ministry of Education and Science of the Republic of Serbia through Project 171034.

References

1. **Foster J.S.** Proc. R. Soc. A 117 (1927) 137-63
2. **Kuraica M.M. and Konjević N.** Appl. Phys.Lett. 70 (1997) 1512
3. **Videnović I.R.** et.al. Spectrochimica Acta Part B 51 (1996) 1707-1731
4. **Cvetanović N**. et al. J.Phys. D. Appl. Phys. 48 (2015) 205201
5. **Arkhipenko V.I**. et.al. Appl.Spectrosc. 67 (2000) 910
6. **Ivković S.S.** et. al. J.Phys. D: Appl. Phys. 42 (2009) 225206
7. **Ivković S.S.** et. al. J.Phys. D: Appl. Phys. 47 (2014) 055204 (10pp)
8. **Sretenović G.B.** et.al. Appl. Phys.Lett. 99 (2011) 161 502

INDUCTIVELY COUPLED PLASMA – FROM SPECTROANALYTICAL TO TECHNOLOGICAL APPLICATIONS

A. Gilmutdinov, K. Nagulin, I. Tsivilskiy, M. Voronov

Kazan National Research Technical University, K. Marx str. 10, 420111, Kazan, Russia
E-mail: AlbertGilmutdinov@kai.ru

Key characteristics of an inductively coupled plasma (ICP): high purity, high temperature and rapid gas-phase reactions rate makes it a promising ion source for analytical spectrometry, as well as a useful tool for technological applications for synthesis and post-processing of sub-micron powder materials. Burning ICP is a very complicated process involving interaction of gas-dynamic and electromagnetic forces. Parameters of a plasma torch depend on a set of simultaneous effects: swirled gas flow, design of a torch and inductive coil, applied power, frequency of inducing current, etc. The second it ions make any experimental optimization non-effective, that is why at the very start there was a series of mathematical simulations of both the spectroanalytical and technological ICPs. A digital twin of the ICP verified by a set of experimental works allows to reduce time and material consumes dramatically during the optimization of ICPs.

This work presents results of modeling of 3D transient spectroanalytical ICP with mass-spectrometer interface (ICP-MS) and also a model of technological plasma to produce powders for additive manufacturing.

Developed model is based on a finite element-based solution of coupled system of transient differential equations: Maxwell's equations, Navier-Stokes equations and heat transfer equation. Maxwell's equations are used to obtain spatial-temporal distribution of electromagnetic (EM) fields in zone of interest. Then one should to solve gas dynamics equations taking into account two-way energy transfer: EM energy dissipates in hot gas subsequently increasing its electric conductivity. Then, plasma-induces electric currents increase the EM fields. The solution technique has the following key steps:

- Solve for magnetic vector potential in 3 domains: plasma, coil, air;
- Compute EM fields and inductive current;
- Solve for gas velocity field applying the Lorentz force;
- Solve for heat conduction equation applying Joule heating and radiation loss;
- Compute gas electric conductivity according to Saha ionization equation;

The Maxwell's equations have been written in a complex form in terms of the magnetic vector potential splitted to real and imaginary parts providing the last two partial differential equations of the whole model of ICP. All the equations are solved simultaneously at each time step. Applicability of the continual

approach to solve the Navier-Stokes equations within the vacuum interface is proved by calculating of the Knudsen number which value does not exceed 0.1.

The model does not take into account the gas ionization yet, but first time it provides a comprehensive data on supersonic gas flow pattern inside the vacuum ICP-MS interface. Computed spatial distribution of velocity, pressure and temperature of hot gas flow between two cones in the central longitudinal cross-section of the system and its enlarged view are presented in the picture below (Fig. 1).

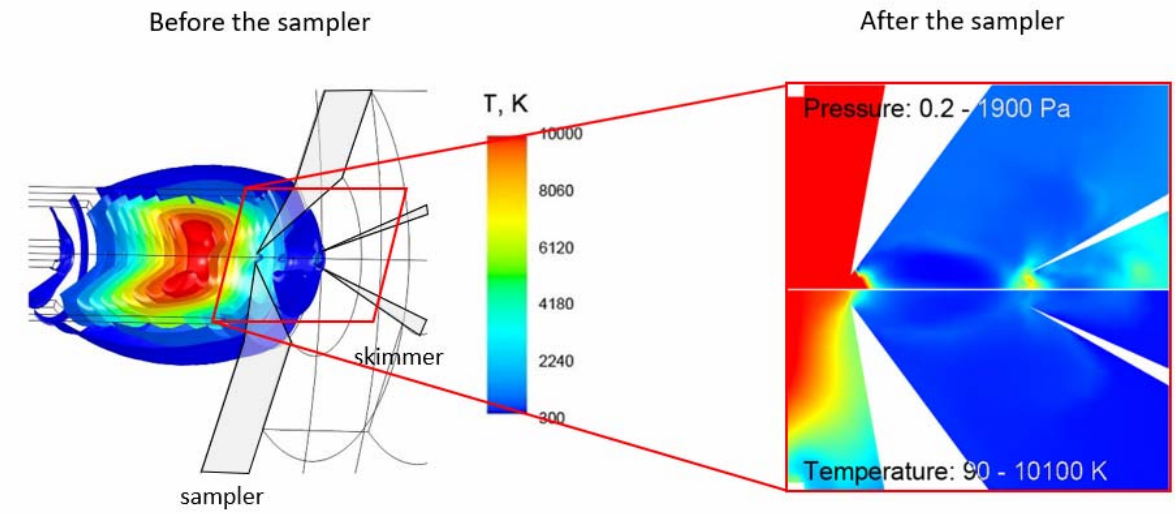

Fig. 1 – Temperature distribution before and after the first vacuum stage of ICP-MS. Pressure pattern shows the location and size of a shockwave

Due to high ratio between ambient atmospheric pressure and the one inside the interface, gas jet forms a typical shockwave of subsonic and supersonic jet streams. The hot gas flow entering the inner space of the interface rapidly accelerates forming shockwave near the boundaries of the region of maximum flow rate. High-pressure zone appears at the distance of 8 mm from the sampler orifice. This zone is a Mach disk producing sharp deceleration of the flow after its length (Fig. 8c). Its position can be estimated from the expression: $h = 2/3 \cdot D \cdot (p_0/p)1/2 = 10.08$ mm, where D is a diameter of the sampler orifice, p_0 is an ambient pressure, p is a pressure on the outlet of the pre-chamber interface. Results of simulation of temperature and velocity in supersonic flow after the sampler cone has been compared to experimental works of Spencer et. al. /1/.The number of “Mach diamonds” formed by the shock waves during propagation of supersonic gas jet inside the interface varies for cold and heated gas conditions.

Numerical simulations first time revealed rapid periodical deflection of the supersonic jet inside the MS-interface along the walls of the sampler cone (that is caused by the asymmetrical rotational way of plasma injection) with the frequency of rotation of the central jet before entering the sampler. This rotation

is visualized by high-speed plasma flow imaging using our plasma-diagnostic experimental complex. According to our estimates, the frequency of the process of plasma jet deflection is about 180 Hz, which agrees well with the results of numerical simulation of hot gas flow dynamics in the interface (168 Hz).

Almost the same approach is applied for simulation of a technological atmospheric pressure ICP (TICP) that is used for production of powders having a spherical shape of particles. In contrary to spectroanalytical ICPs, TICP has larger size, power and gas consumption and a lower operating frequency of EM fields. Evolution of the particles of the powder is included in the model together with thermal and gas-dynamic load of the plasma by the particles. Trajectories of the particles are calculated taking into account the gas-dynamic drag force and the gravity. Processes of heating of the particles within the plasma with the subsequent melting and evaporation are calculated. Heat exchange between the particles and the plasma is calculated during the particle movement. The drag force and the particle heating are taken into account in the plasma equations. In this way the gas-dynamic and the heat load of the plasma from the particles are calculated. Results of simulations are presented in Fig. 2. Spatial temperature distribution within the TICP significantly differs from the temperature pattern inside the spectroanalytical one. Formation of a high-temperature zone near the central inlet tube is caused by a toroidal vortex near the induction zone of TICPs (Fig. 2-c). This vortex introduces some instability, mixes the downstream gas flow and prevents penetrating of the powder particles into the plasma. Commonly the vortex is attributed to an influence of a radial component of Lorentz forces on the ionized gas.

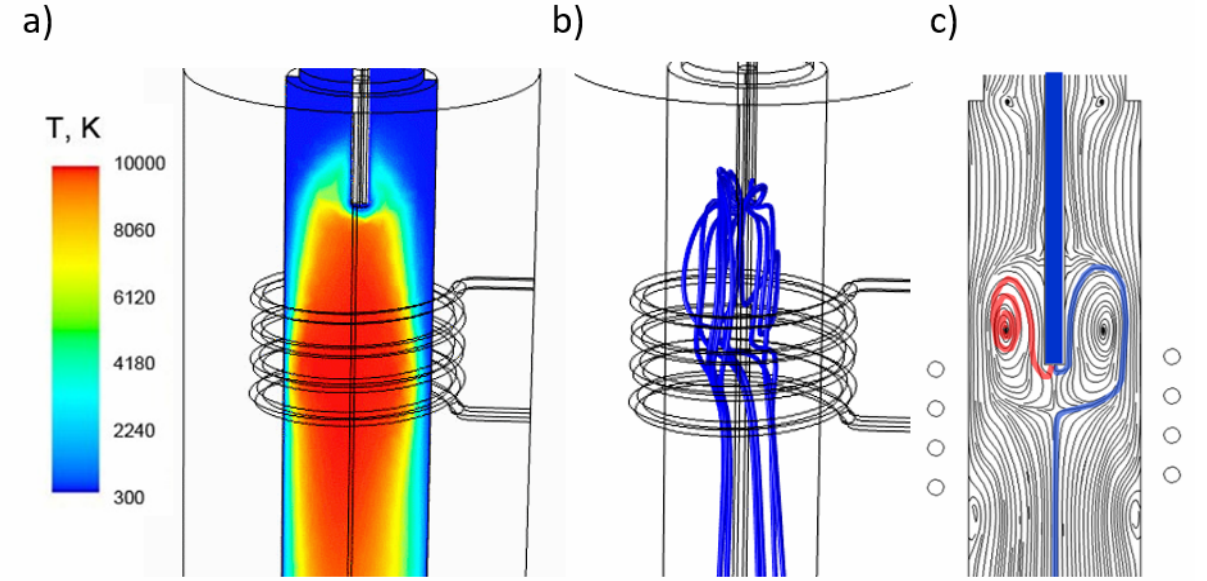

Fig. 2 – a) Temperature distribution in TICP. b) Powder particle trajectories. c) A cross-section of a plasma domain with argon flowlines and particle trajectories: trapped (red) and free one (blue)

Evolution of powder particle shape along its trajectory in TICP has been modelled using the phase field method to track an argon-liquid metal interface (Fig. 3). Particle color corresponds to its temperature and each frame representing its shape is arranged according to x-axis of a temperature plot (Fig. 3-a). Particle sphericity has been estimated as a mean square of its radius. For steel particle having a diameter of 50 μm time of complete melting equals t_{melt} = 0.55 ms and time of spheroidization equals t_{sph} = 1.13 ms respectively. The developed model allows to predict behavior of various powders in the TICP for a variety of operating conditions.

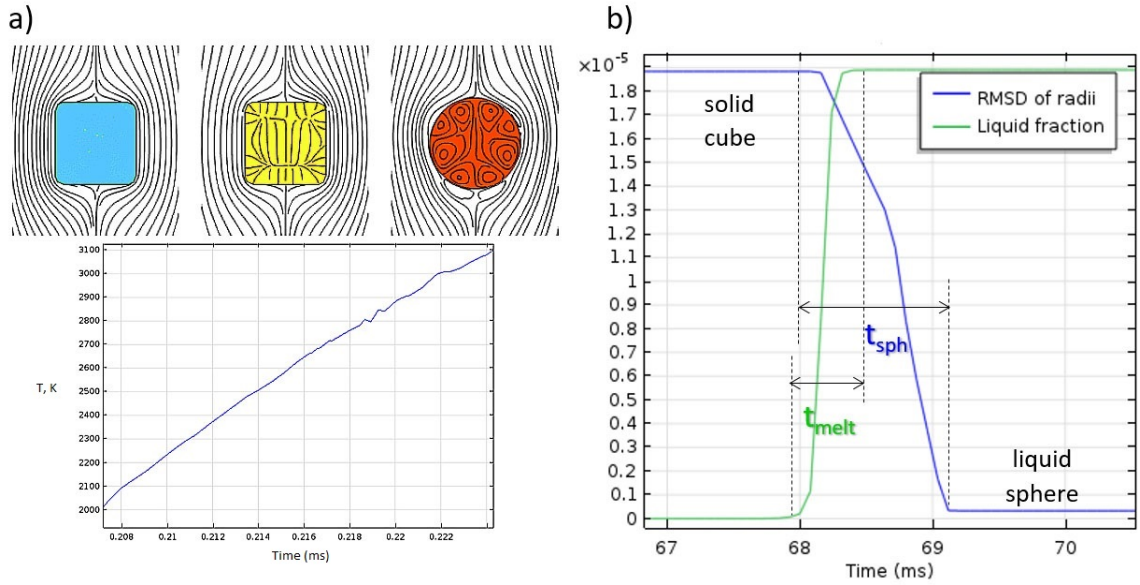

Fig. 3 – a) Evolution of a shape of a 50 μm steel particleduring its heating in plasma (temperature is shown in blue line). b)Particle sphericity and its liquid fraction during the phase change

Acknowledgements. This work is supported financially by the Ministry of Education and Science of the Russian Federation (research grants №14.Z50.31.0023 and 9.3236.2017/4.6), Russian Foundation of Basic Research (contract №18-42-160015\18), and Federal Target Program 1.3 (agreement № 14.578.21.0245).

References

1. **Radicic W., Olsen J., Nielson R., Macedone J., Farnsworth P.**Spectrochim. Acta Part B. 61(2006) 689–695

THE EVOLUTION OF INTENSITY OF FeO BAND, TEMPERATURE AND ELECTRON DENSITY OF LASER INDUCED PLASMA ON THE IRON OXIDE SURFACE

T.A. Labutin, S.M. Zaytsev

Lomonosov Moscow State University, Department of Chemistry,
Moscow, Russia timurla@laser.chem.msu.ru

The systematic registration of optical emission spectra resulting from impact events in the Earth's atmosphere is currently being used for the unambiguous determination of the mechanism of the ablation of astral bodies of natural and industrial origins. From the practical point of view, such research is important for the prediction of possible consequences of a collision of a large body on the order of tens of meters in a diameter with the Earth surface (the so-called "the asteroid hazard") as well as for dealing with the cosmic debris. Moreover, a reliable interpretation of optical spectra makes possible to assess the molecular composition of exoplanet atmospheres (so called "hot Jupiter"), which is one of the "key" to study evolution of planetary atmospheres. The of temperature dependent electronic spectra of diatomic molecules is necessary for such a study, but ab initio calculations of electronic spectra of the very important iron-monoxide (FeO) is extremely complicated. At the same time the modeled data can be supplemented by experimental spectra. The temperature of plasma formed by the meteor entering the atmosphere is close to those one of nanosecond laser-induced plasma on solids at delays of 0.5-10 μs. Thus the laser-induced breakdown spectra can be used for simulation of ablation processes occurring when meteorites enter the upper layers of the Earth's atmosphere. The aim of this work is the investigation of FeO band in laser induced plasma at different delays. The evolution of the plasma in time (the intensity of molecular bands, iron atomic lines, temperature and electron density) was obtained for plasma spectra formed on the surface of model object (iron oxide).

H2 DISSOCIATION IN AR-H2 DISCHARGE OF MODERATE PRESSURE

S. Avtaeva[1]

[1]Institute of Laser Physics, Lavrentyeva 13/3, Novosibirsk, 630090, Russia,
e-mail: s_avtaeva@mail.ru

Hydrogen plasmas can be created in different ways and have a wide range of applications. One of the applications is diamond films deposition. It has been found that high quality diamond films are grown in hydrogen diluted plasma, and that the atomic hydrogen present in these plasmas is essential for getting high-quality films. Argon additive to hydrogen can enhance hydrogen plasma characteristics as the energy of metastable argon states, forming at Ar atom collisions with electrons, can be transferred to hydrogen molecules and then it can initiate dissociation and ionization of H_2 molecules. The high density low pressure hydrogen arc plasma has been used in various applications such as lighting sources, PACVD processes, synthesis of nano-powders, thermionic energy conversion, and electric propulsion. Modern technologies need a large volume discharge technique and diagnostic methods to control characteristics of the plasma.

Generally, atomic hydrogen density can be estimated by OES technique using intensity ratio of atomic hydrogen and argon lines I_{HI}/I_{ArI}. In the most simple case when both species are excited to radiative excited state by a direct electron impact from their ground state, and the excitation cross sections as a function of the electron energy have, for both species, the similar shape and a close threshold, and if principal quenching process, for both excited states, is radiative decay, the density ratio of hydrogen and argon atoms N_H / N_{Ar} is related with the intensity ratio I_{HI}/I_{ArI} according to the following equation /1, 2/:

$$\frac{N_H}{N_{Ar}} = \frac{A_{ki}^{Ar} \nu_{ki}^{Ar} \sigma_{\max}^{Ar} \tau_k^{Ar}}{A_{ki}^{H} \nu_{ki}^{H} \sigma_{\max}^{H} \tau_k^{H}} \cdot \frac{I_{HI}}{I_{ArI}}, \qquad (1)$$

Here A_{ki}, ν_{ki}, $\sigma_{\max}$, and τ_k are transition probabilities, frequencies, cross sections in maximum and life times.

At low pressures in condition of corona equilibrium this rigid requirements are fulfilled. But at moderate and high pressures quenching of the excited state species by atoms and molecules are not negligible and should be taken into consideration /3/. Here the problem of choosing suitable pair of HI and ArI lines for obtaining atomic hydrogen density and H_2 dissociation degree in moderate-pressure arc condition is studied. The Balmer-Serie H_α (656.3 nm) and ArI (750.4 nm) lines are usually taken for this purpose /3, 4/. Also H_γ (434.0 nm) and ArI (811.5 nm) lines were proposed as most suitable /5/ as well as H_α (656.3

nm) and ArI (696.5 nm) /1/. Therefore the using H_α (656.3 nm), H_γ (486.3 nm) and H_γ (434.0 nm) of Balmer-Serie as well as ArI 750.4 nm ($2p_1 \rightarrow 1s_2$) and ArI 811.5 nm ($2p_9 \rightarrow 1s_5$) lines were considered.

The problem of using H_α (656.3 nm) to ArI (750 nm) intensity ratio consists in great difference between excitation threshold energy for radiative states of this lines, namely E_{th}^{Ar}=13.47 eV and E_{th}^{H}=12.09 eV. Therefore at using this intensity ratio it is necessary to know the electron energy distribution function (EEDF) to calculate excitation constants k_{exc} or at least the EEDF at thresholds f_{th} /1/:

$$\frac{N_H}{N_{Ar}} = \frac{A_{ki}^{Ar} \nu_{ki}^{Ar} k_{exc}^{Ar} \tau_k^{Ar}}{A_{ki}^{H} \nu_{ki}^{H} k_{exc}^{H} \tau_k^{H}} \cdot \frac{I_{HI}}{I_{ArI}} \approx \frac{A_{ki}^{Ar} \nu_{ki}^{Ar} \sigma_{\max}^{Ar} f_{thAr} \tau_k^{Ar}}{A_{ki}^{H} \nu_{ki}^{H} \sigma_{\max}^{H} f_{thH} \tau_k^{H}} \cdot \frac{I_{HI}}{I_{ArI}}, \qquad (2)$$

An accurate knowledge of the EEDF is not a simple task. Fig. 1 shows the EEDF in Ar-H_2 mixtures as functions of Ar fraction in the mixture at a fixed reduced electric field *(E/N)* and of *E/N* at a fixed Ar fraction in Ar-H_2 mixture. It is clear the EEDF transforms at variation of mixture composition and very strong depends on E/*N*.

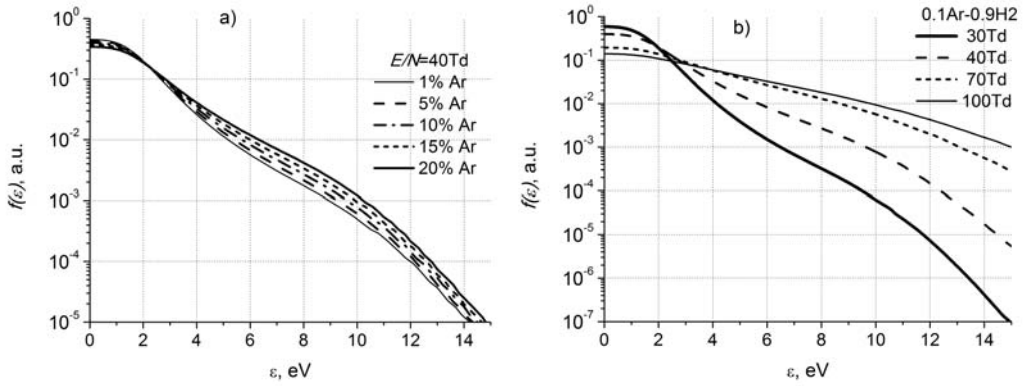

Fig. 1 - The EEDF in Ar-H_2 mixtures as functions of argon fraction in the mixture at *E/N*=40 Td (a) and of reduced electric field at Ar fraction in Ar-H_2 mixture of 10% (b)

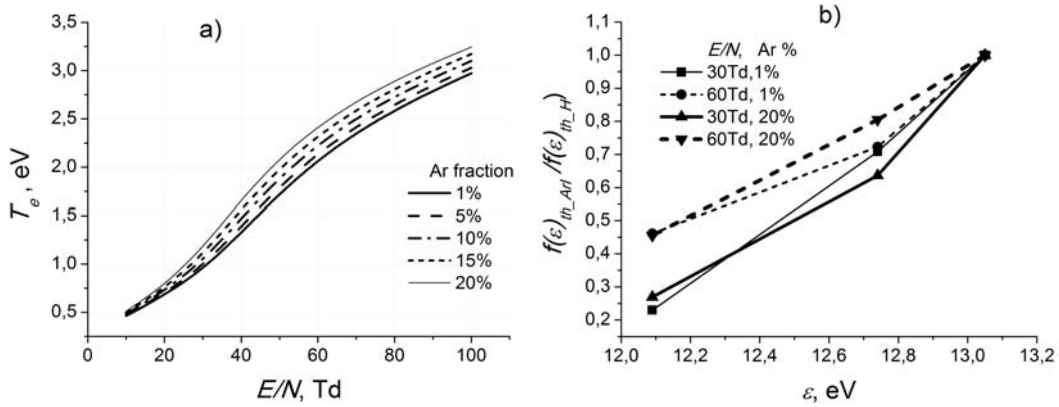

Fig. 2 - The electron temperature as functions of reduced electric field and argon fraction in the mixture Ar-H_2 (a) and ratios of EEDFs at threshold energies f_{thAr}/f_{thH} as functions of the Balmer-Serie H line threshold energy (b); E_{th}^{Ar}=13.47 eV

Fig. 2 show the electron temperature in Ar-H_2 mixtures as functions of reduced electric field and argon fraction in the mixture and ratios of EEDFs at threshold energy for ArI 750 nm line and H lines of Balmer-Serie.

Utilizing H_γ (434.0 nm) and ArI (811 nm) lines is solve the above mentioned problem as difference between excitation threshold energy of the radiative states is very small for this lines, namely E_{th}^{Ar}=13.076 eV and E_{th}^{H}=13.05 eV. But the lower state $1s_5$ of ArI 811 nm ($2p_9 \rightarrow 1s_5$ transition) is metastable and therefore the possibility of the emission re-absorption is great. Also possibility of quenching the excited state by atoms and molecules increases due to life time of H_γ upper level (n=5) is greater (87.1 ns) as compared with life time of H_α upper level (n=3), 10.2 ns.

Here the line intensity ratio technique for estimation of hydrogen-to- argon density ratio and hydrogen molecule dissociation degree in arc discharge in Ar-H_2 mixtures at moderate pressures (2-3 Torr) is analyzed. Ratios of three H lines (alpha, betta and gamma of Balmer-Serie) to ArI 750 and ArI 811 nm lines were analyzed and effect of Ar fraction in the mixture on H_2 dissociation degree was studied. Hydrogen dissociation is obtained with the line intensity ratio technique taking into account difference into excitation energy of the radiative levels. EEDFs in Ar-H_2 mixtures were calculated as functions of the reduced electric field while electron temperatures were estimated using OES technique.

The moderate-pressure discharge in a large chamber (approximately 0.5 m in diameter) is ignited between stainless steel anode and moderate stainless steel cathode assembly; the electrodes were disposed at 90^o angle to each other at distance of 40 cm. The discharge chamber was evacuated up to residual pressure of $2*10^{-5}$ Torr and then H_2-Ar mixture were injected up to 3-3.5 Torr. Ar/H_2 ratio was varied in the range of 0.01-0.15 by adjusting a ratio of gas flow rates. The discharge current was 150 A and voltage was varied in a range of 220-250 V. Radiation of the moderate-pressure arc was collected by a collimated lens, at that the arc column was generally aligned along the optical axis, and then was focused at the fiber optic cable divided in 4 channels to conduct radiation toward a set of four Ocean Optics spectrometers HR-4000. Relative sensitivity of the devices as a function of wavelength was calibrated using the DH-2000-CAL /6/.

Fig. 3 shows typical spectra of the arc discharge plasma in Ar-H_2 mixtures in the wavelength range of 400-800 nm. H_2 dissociation degree k_D calculated after measurement of N_H/N_{Ar} ratio using I_H/I_{Ar} intensity ratio of H_β, H_γ and H_δ lines to ArI (750 nm) according to (2) is shown in Fig. 4a. It is clear, the three ratios give different H_2 dissociation degree; the difference increases with growth of Ar fraction in Ar-H_2 mixture. Fig. 4b presents H_2 dissociation degree calculated with taking into account quenching of the radiative states by Ar atoms and H_2 molecules. One can see, the consideration of quenching allowed getting closed values of k_D for all three intensity ratios, at that the k_D value elevated. The

calculated H_2 dissociation degree increased into 2-3 times when ArI (750 nm) was replaced with ArI (811 nm). The latter can be referred to the emission re-absorption by the metastable state $1s_5$ of Ar.

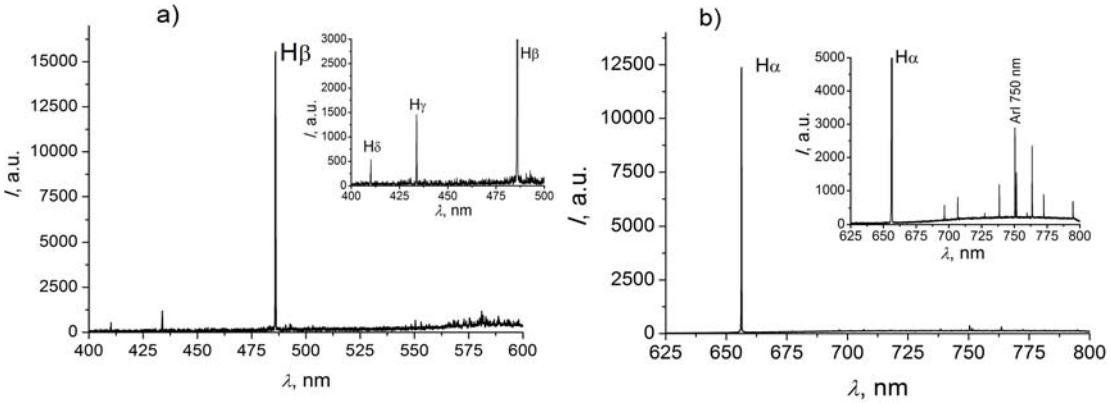

Fig. 3 - Typical spectrum of the arc discharge plasma in Ar-H_2 mixture

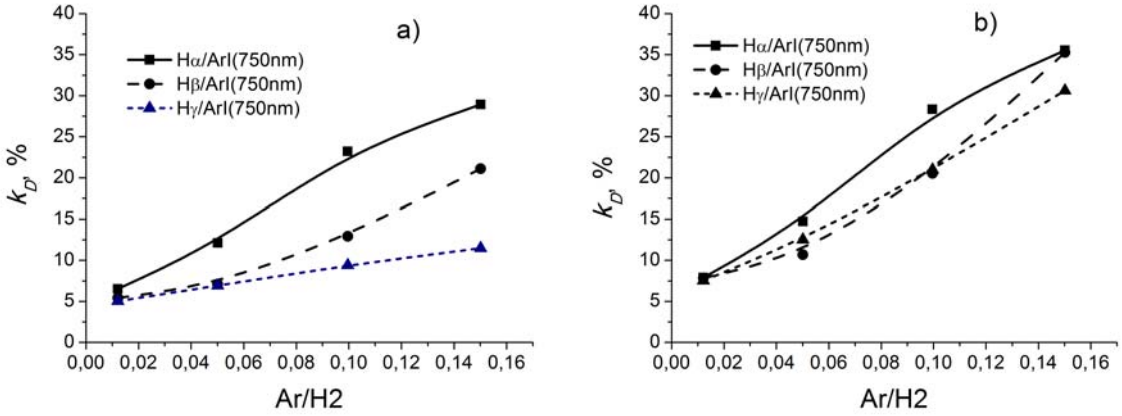

Fig. 4 - The H_2 dissociation degree derived from $I_{H\alpha}/I_{Ar}$, $I_{H\beta}/I_{Ar}$ and $I_{H\gamma}/I_{Ar}$ as functions of Ar/H_2 ratio. P=3.0-3.5 Torr, I=150A, U=223-250 V

It is seen that increasing Ar fraction in Ar-H_2 mixtures results in growth of the H_2 dissociation degree. Rise in H_2 dissociation with increasing Ar/H_2 ratio can be related to contribution of Ar metastable states in H_2 dissociation.

Acknowledgements. The author is very grateful to Dr. V. Gorokhovsky for kindly provided emission spectra of the arc discharge.

References

1. **Avtaeva S.V., Mamytbekov M.Z. and Otorbaev D.K.** J. Phys. D: Appl. Phys., 30 (1997) 3000–3007; High Temperature, 36 (1998) 176-182.
2. **Galtsev V.E. et al.** High Energy Chemistry 17 (1983) 164–166.
3. **Gicquel A. et al.** J. App. Phys., **83** (1998) 7504-7521.
4. **Ma J., Ashfold M.N., Mankelevich Y.A.** J. App. Phys., 105 (2009) 043302.
5. **Radishev D.V.** Optical methods for studying plasma in mw reactors and characteristics of the films produced in them. Thesis, Nizhny Novgorod (2009).
6. **Avtaeva S. et al.** Spectrochimica Acta. Part B, 124 (2016) 25–39.

RELATIONSHIP OF SPECTRAL AND TEMPERATURE CHARACTERISTICS IN AN ACOUSTOPLASMA GAS DISCHARGE

A.S. Abrahamyan*, T.J. Bezhanyan, R.Yu. Chilingaryan

Institute of Applied Problems of Physics, NAS RA, 25 Hr. Nersisyan str., 0014, Yerevan, Armenia, *E-mail: arbel11@mail.ru

In this paper emission spectra of the radiation of a working mixture of a CO_2 laser are presented. The radiation of a CO_2 laser largely depends on the behavior of the nitrogen molecule, which in collisions transfers energy from its metastable level $\{X^1\Sigma_g^+, v = 1\}$ to the upper laser level of the CO_2 molecule (v is the vibrational quantum number). In an electrical discharge up to 50% of nitrogen molecules pass into a vibrationally excited state /1/. In the emission nitrogen spectra, the first and second positive systems (FPS, SPS) and the first negative system (FNS) /2/ for ionized nitrogen are most easily excited.

The emission spectrum of a working mixture of a CO_2 laser (CO_2 : N_2 : He = 1 : 1 : 8) prepared under laboratory conditions (hereinafter laboratory mixture) and the emission spectrum in a working laser with a mixture filled at the factory was studied (in order to increase stability and service life of the mixture in factories use different additives), as well as spectra on specially manufactured tubes.

The emission spectrum of a glow discharge in the region (300-800 nm) was investigated. It is shown Fig. 2 that the emission spectrum of the laser mixture well repeats the emission spectrum of pure nitrogen. Therefore, for the mixture, the radiation energy in the bands FNS (384-428 nm), FPS (575-689 nm) and SPS (350-436 nm) was considered (in relative units). In fact, the bands are a little wider, the areas of the most intense lines of bands are chosen.

The spectra were compared when the discharge was powered by a direct current and in the acoustoplasma mode (when the discharge was powered by a modulated current containing a constant and a variable component). The average current in both cases was the same.

On the discharge tubes of working lasers of the type LG-23 (several Watts in power) and with the factory mixture and the laboratory mixture, the emission spectrum was measured orthogonally in the cathode discharge region. On specially manufactured discharge tubes filled with a laboratory mixture, measurements were taken along the axis of the entire discharge. From the discharge, the radiation from the optical fiber was fed to the computer spectrograph Ocean Optics PC-2000. All tubes were water-cooled with a stable water temperature.

Temperature measurements in the argon discharge were carried out separately on tubes without water cooling /3/. A microwave radiometer with a wavelength of 8 mm was used. Fig. 1 shows the temperature dependence on the discharge axis in argon from the amplitude of the variable component of the discharge current. Graphs are given for three gas pressures in the tube: 25, 200 and 400 torr.

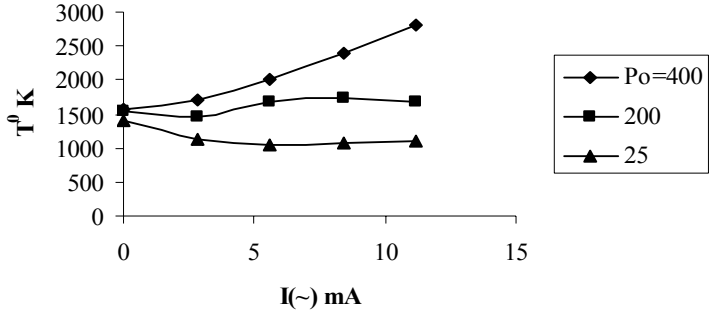

Fig. 1 - Dependence of temperature on the discharge axis on the amplitude of the variable component of the discharge current I (~). The modulation frequency f = 5.4 kHz, the discharge current component constant I_0 = 30 mA

It can be seen from Fig. 1 that only at high pressures the temperature in the discharge begins to increase with the increase of the variable component. This is due to the increasing role of discharge contraction. It should be noted that when contracting in an acoustoplasma with increasing of variable current components, the discharge diameter decreases, and with increasing of constant current components, the discharge diameter increases. In a plasma without an acoustic perturbation (discharge at a direct current) under ordinary thermal contraction with increasing current, the discharge diameter decreases.

At low pressures, the temperature on the discharge axis varies little. With an increase in the variable current components from 0 to 3 mA, the temperature decreases from 1300 to 1000° K, and then remains constant with increasing variable current components up to 12 mA. For large values of the component variable, contraction began, because of which the temperature increased. Thus, in a water-cooled tube, the temperature at the discharge axis is ~ 1000° K, and on a cooled wall ~ 300° K, if the apparent diameter of the discharge is ~ 5-8 mm. We recall that for generation in a CO_2 laser, the temperature of the working mixture should not exceed 800° K. Therefore, the gas pressure in the tube must be less than 25 torr. In addition, because of the best heat transfer, the temperature at the discharge axis of the laser mixture is lower than in argon.

Fig. 2a shows the spectrum of the mixture (CO_2 : N_2 : Ne). In Fig. 2b, the difference spectrum (spectrum of the mixture minus the spectra of CO_2 and He) is presented. It is seen from Fig. 2 that the spectrum of the mixture well repeats

the spectrum of pure nitrogen. Therefore, in the following we consider spectral regions in the bands FNS, FPS and SPS, which are characteristic for pure nitrogen.

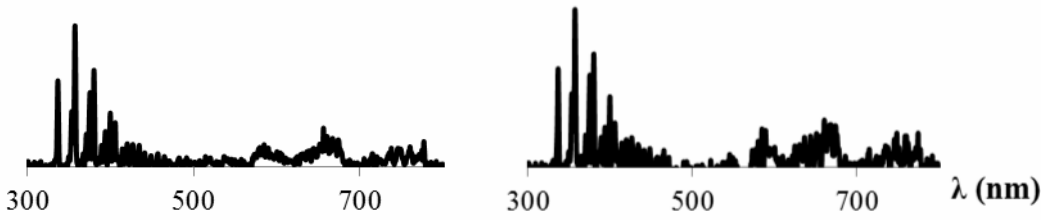

a) b)

Fig.2 - Comparison of the mixture specrtrum (a) and the difference spectrum (b)

We represent the total energy in the spectral band 300-800 nm as ε (300-800), and the total energy in the band, for example FPS, as ε (FPS) = ε (575-689). Then K (FPS) = ε (FPS) / ε (300-800) shows what fraction of the total energy in the band 300-800 nm is the energy of the FPS band. The same is done, accordingly, for the bands FNS and SPS.

Fig. 3 shows the K(FPS) dependence on the discharge current modulation frequency, measured along the discharge (along the entire positive column and cathode region). It can be seen that the fraction of the energy of the FPS band increases insignificantly with increasing modulation frequency.

Fig. 4 shows energy diagrams of the FPS band from the cathode region of working lasers. Index (W) - corresponds to a laser that is filled with a mixture in the factory; index (L) corresponds to a laser that is filled with a mixture (CO_2 : N_2 : He = 1: 1: 8) in the laboratory.

It is seen from Fig. 4 that when the transition to the acoustoplasma mode occurs, the energy shares in the cathode region in the FNS and FPS bands for the laser with the factory mixture increase, and for the laser with the laboratory mixture decrease.

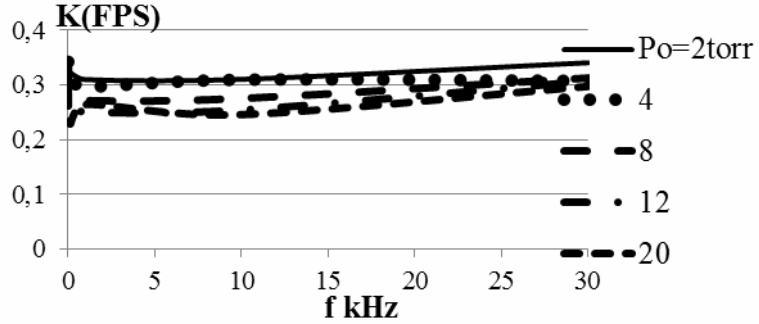

Fig. 3 - Dependence of the energy fraction in the spectrum of the first positive nitrogen system (FPS) on the total energy in the band (300-800) nm on the modulation frequency of the discharge current. P_0 = 2 torr; I_0 = 20 mA; I(~) = 20 mA; Gas mixture (CO_2 : N_2 : He = 1 : 1 : 8)

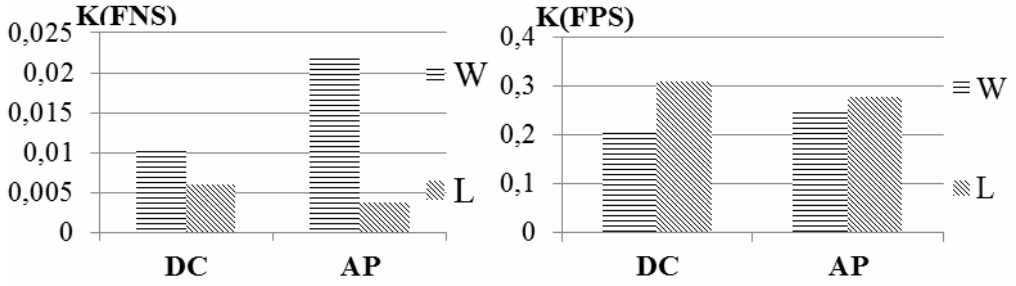

a) b)

Fig.4 - Energy diagrams of the FNS and FPS bands in the cathode region of operating CO_2 lasers. DC - laser powered by direct current, AP - acoustoplasma mode, P_0 = 12 torr, f = 30 kHz, I_0 = 10 mA, I (~) = 8 mA

From a comparison of Fig. 3 and Fig. 4, it can be seen that in the transition to the acoustoplasma mode the behaviour of the cathode region and the positive column is differently. The methods used in the work can be used to determine the parameters of the acoustoplasma discharge by optical methods.

References

1. **Sobelman I.I.** Introduction to the theory of atomic spectra. Moscow, FIZMATLIT, (1963), 640c. (in rus.)
2. **Pearse R.W.B. and Gaydon A.G.** The Identification of Molecular Spectra. 4th ed., London, Chapman and Hall, (1976), 221p.
3. **Abrahamyan A.S., Haroyan K.P., Bagdasaryan E.G., Gevorgyan S.A., Kostanyan R.B., Bezhanyan T.Zh.** Int.Conf.Laser Physycs-2005, LP-2005, October 11-14 (2005), Ashtarak, Armenia, Proc. pp.65-68.

PROBE DIAGNOSTIC OF ARGON ELECTRON BEAM PLASMA

V. Konstantinov, V. Shchukin, R. Sharafutdinov

Institute of Thermophysics SB RAS, Lavrentiev avenue 1, 630090, Novosibirsk, Russia,
konstantinov@itp.nsc.ru

Introduction Thin films have aroused interest for a long time due to their unique properties, which greatly distinguish them from a massive material, primarily due to their conductivity and optical properties. Argon-silane plasma is used for microcrystalline silicon thin films deposition, which are used for solar cells creation /1/. In order to avoid long-term searches for the process parameters at which a film of the required quality is obtained, it is important to have an idea of the gas-phase processes occurring in the plasma and their correlation with the deposited silicon layers. Thus, the investigation of plasmas in such conditions is an actual task.

One of the most common methods of plasma diagnostics is the Langmuir probe /2/. According to the probe characteristic, it is possible to obtain information of the electron temperature and density, plasma potential, and, in general, the electron energy distribution function, which are important characteristics of the plasma.

The purpose of this paper is determination working conditions of an advanced cold plasmatron (prototype) in the forevacuum range of pressures in a reaction chamber, at which obtained plasma parameters are close to the parameters generated by the model of a cold plasmatron /3/.

Experimental setup and technique Experiments were carried out on a low-density gas-dynamical setup at the Institute of Thermophysics of SB RAS. The scheme of the experiment is shown in Fig. 1.

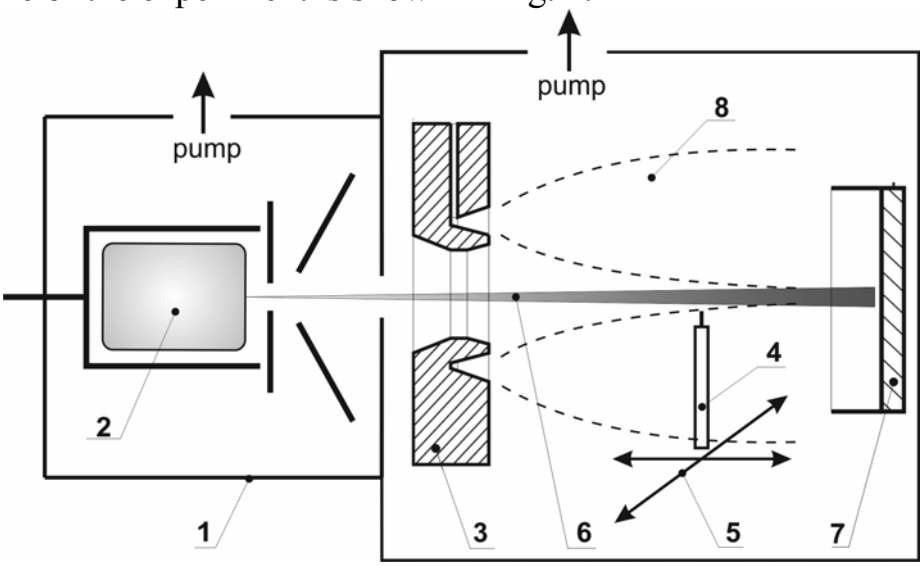

Fig. 1 - The scheme of the experimental setup

A prototype of a cold plasmatron /4/ consisting of an electron gun (1) with a hollow cathode (2) and an axisymmetric supersonic annular nozzle (3), adapt for argon supplying to a working chamber, was used as a plasma generator.

A double Langmuir probe (4) with a diameter of 0.5 mm and a length of 4 mm was used to determine the plasma parameters in this work. The probe was attached to a two-component coordinate mechanism (5) 5 mm below the beam axis to avoid damage from the impact of the primary electron beam (6). The measurement error was no more than 10%.

The beam current was monitored by means of an electron collector (7). Argon was fed into the reaction chamber through the nozzle block and formed a supersonic gas jet (8).

Using a double probe, secondary electrons temperature and density were measured in a free argon jet. The data obtained in the work were compared with the plasma parameters obtained earlier on the model of a cold plasmatron /3/, for which the regimes of deposition for device quality silicon layers were determined /5/ and correlations between the plasma parameters and characteristics of deposited silicon films were obtained /6/.

Results and discussion Fig. 2 shows the secondary electrons temperature and density dependence on the argon flow rate in the electron beam plasma generated by the cold plasmatron prototype at a beam current of 75 mA. The beam energy was 0.6 and 1.0 keV. The pressure varied from 1 to 4 Pa, depending on the flow rate of argon.

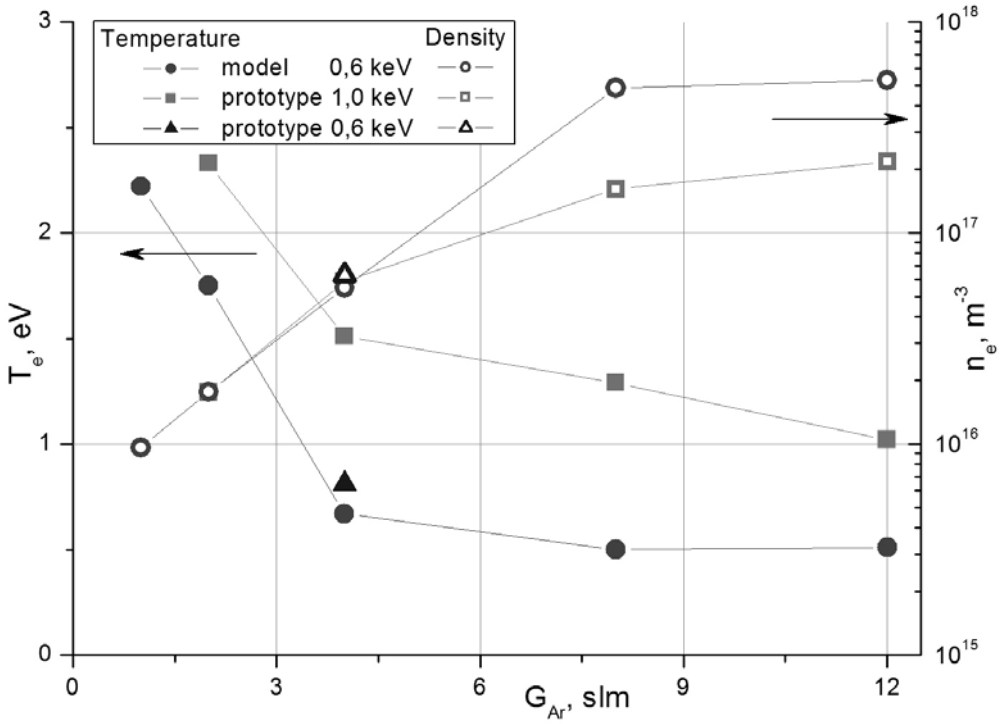

Fig. 2 - Dependence of the temperature and concentration secondary electrons on the flow rate of argon

In both cases, argon flow rate growth leads to electron temperature decreases and density increases.

As was shown earlier /3/, this behavior of the temperature dependence on the flow rate of argon is explained by the scattering and degradation of the electron beam on dense regions of the gas jet. In the case of the model, almost complete scattering of the electron beam is observed, and the electron temperature reaches a constant value. On the prototype, the temperature of the secondary electrons is higher and there is no temperature achievement to a constant value, although the trend of behavior is remaining. This can be explained by the fact that the gas target in both cases is the same in its properties, while the primary beam energy for the prototype is almost twice higher. Such a high-energy electron beam does not completely dissipate on the gas target and creates plasma with a higher electron temperature.

The electron density increases sharply with argon flow rate growth. The smaller secondary electrons density in the case of a prototype with primary beam energy of 1 keV can be explained by the fact that a higher-energy primary beam "flies" through a gas target with less scattering, and correspondingly, a smaller number of newly formed electrons.

To confirm the above assumption about the incomplete dissipation of the primary beam on the gas target, the energy of the electron beam of the prototype was reduced to 0.6 keV. The obtained temperature and the density of secondary electrons are close to those obtained earlier on the model, which confirms the hypothesis of incomplete scattering of an electron beam on a given gas target. Increasing the energy efficiency of the process, consisting in the maximum using of the primary electron beam energy, is possible not only by reducing the energy of the beam, but also by compression the gas target by increasing the pressure in the reaction chamber.

At the same pressure, the electron temperature in the plasma of prototype is substantially higher than in the model, the density is lower, which was explained above by the incomplete scattering of the primary electron beam. As the pressure in the vacuum chamber increases, and as a result, the gas target becomes denser, the temperature of the electrons in the prototype plasma decreases and approaches the value obtained earlier on the model. Density, on the contrary, grows, and even at a pressure of 7 Pa it slightly exceeds the values obtained earlier, and at a pressure of 15 Pa it is more by a factor of 1.6. The obtained difference is in good agreement with the fact that under conditions of complete scattering of the electron beam the number of produced secondary electrons is determined by the energy of the primary electron beam divided by the ionization potential. A similar behavior of the electron density as a function of the pressure is observed in other authors /7/.

The conclusion It is shown that on a cold plasmatron prototype at a primary beam energy of 1 keV it is possible to obtain a dense, cold plasma with parameters close to obtained earlier on the model, which are favorable for the deposition of high quality silicon layers /6, 8/ in the forevacuum range of pressures.

Acknowledgements This study was supported by the Russian Foundation for Basic Research and the Ministry of Education, Science, and Innovation Policy of the Novosibirsk region (project no. 17-48-540665 r_a).

References

1. **Jana M., Das D., Barua A.K.** Solar Energy Materials and Solar Cells. 74 (2002) 407–413.
2. **Huddelstone R. and Leonard S.** Plasma Diagnostic Techniques. New York (1967).
3. **Konstantinov V.O., Khmel S.Ya.** Journal of Applied Mechanics and Technical Physics. 48 (2007) 3–10.
4. **Konstantinov V.O., Sharafutdinov R.G., Karsten V.M.** Contributed papers of V International conference “Plasma Physics and Plasma Technology”. (2006) 276-279.
5. **Sharafutdinov R.G., Khmel S.Ya., Shchukin V.G., Ponomarev M.V., Baranov E.A., Volkov A.V., Semenova O.I., Fedina L.I., Dobrovolsky P.P., Kolesov B.A.** Solar Energy Materials and Solar Cells. 89 (2005) 99–111.
6. **Konstantinov V.O., Sharafutdinov R.G., Shchukin V.G.** PPPT-6. (2009) 413-416.
7. **Parashar A., Kumar S., Dixit P.N., Gope J., Rauthan C.M.S., Hashmi S.A.** Solar Energy Materials and Solar Cells. 92 (2008) 1199–1204.
8. **Alcott G. R.** Plasma deposition of nanocomposite thin films: Process concept and realization. PhD Thesis. Eindhoven (2004).

DETERMINATION OF PARAMETERS OF HELIUM PLASMA JET WITH HYDROCARBON ADMIXTURES BY METHODS OF EMISSION SPECTROSCOPY

R. Kh. Amirov, V. F. Chinnov, D. I. Kavyrshin, M. A. Sargsyan, M. B. Shavelkina

Joint Institute for High Temperatures of the Russian Academy of Sciences (JIHT RAS)
125412, Izhorskaya st. 13 Bd.2,Moscow, Russia, dimakav@rambler.ru

The paper presents the results of spectroscopic investigation of an atmospheric pressured plasma jet generated by a DC plasma torch. Plasma gas is a mixture of helium with a hydrocarbon (propane, butane, methane, acetylene), the ratio of components in which is 3:1 - 5:1. Hydrocarbon is being converted into nanostructures of various morphology from nanotubes and graphene to carbon nano-onions. Resulting product morphology and properties depend on a wide range of parameters such as power input into the arc and ratio between helium and hydrocarbon. The aim of the work is to study the composition and parameters of the plasma by methods of optical emission spectroscopy.

To record the emission spectra, an AvaSpec 2048 optical fiber spectrometer was used. The spectrum of a pure helium plasma jet at atmospheric pressure and 7-8 kK temperature presents itself in the UV band as a set of the strongest atomic He I lines at 318.7, 447.1, 587.5, 587.5, 667.8, 706.5 nm. At the same time, emission intensity of the continuum is small and negligible. The main role in the radiation energy transfer for such plasma should be performed by vacuum ultraviolet lines which correspond to the radiative transitions of the excited atoms to the ground state. However, this radiation turns out to be optically locked due to the high concentration of absorbing helium atoms in the ground state /1/. Thus, for pure helium plasma, radiation does not play a significant role in the energy balance.

The main energy loss mechanism of a helium plasma jet is thermal conductivity. High transport properties of helium /2/ being a low-mass gas also have an effect on the balance of charged particles in plasmas /3, 4/: intensive diffusion losses of charged particles from the arc column lead to the appearance of ionization-type nonequilibrium and of substantial overpopulation of the atomic ground state. Another characteristic feature of helium is a big energy gap between the ground state and the first excited state (about 20 eV), which further aggravates the nonequilibrium of the distribution of helium atoms over excited states. Also, a consequence of high transport properties of helium is the presence of sharp temperature and electron density gradients in the radial direction in the plasma jet /5/. The above factors lead to the fact that the equilibrium-based methods for determining the parameters of the atmospheric pressured helium plasma in the general case turn out to be inapplicable /1-7/, and each specific

study of this kind of plasma objects requires the researcher to develop individual approaches to this kind of research.

When propane-butane is added to the helium arc of atmospheric pressure, lines of the carbon atoms appear in the plasma emission spectrum, the brightest of which being C I 247.9 nm, hydrogen lines H-α and H-β, and a wide range of molecular Swan and CN bands. The spectra recorded at various distances from the outlet of the plasma torch nozzle are shown in figures 1a, b and c.

The spectrum in Fig. 1a, in addition to the atomic helium and carbon lines, as well as molecular bands of carbon compounds, contains atomic copper lines, which were injected into the plasma from the copper walls of the plasmatron channel.

The spectrum in Fig. 1b is extremely saturated and informative. The intensity ratio of the allowed and forbidden components of the He I 447.1 nm line having two peaks, lets us find electron concentration near the plasma torch nozzle outlet /8/, which according to this estimate is $n_e \approx 2 \cdot 10^{16}$ cm^{-3}. The method for determining n_e using the half-width of the atomic hydrogen line H_β /9/, which is also present in figure 1b, confirms the obtained value. The main radiating components here are the molecular bands C_2 and CN. The most interesting for this study are the C_2 bands, which appear at the initial stage of carbon nanostructure synthesis. Intensive and non-overlapping with other radiating components C_2 molecular bands in the wavelength range 440-570 nm allowed us to determine the vibrational T_V and rotational temperature T_R for this molecule. For this purpose, a model was superimposed on the experimentally recorded spectrum, the temperatures set during the calculation were varied to achieve the best fitting of both spectra. Using a set of emission spectra of the C_2 molecule in the wavelength range 440-570 nm at various distances from the nozzle outlet of the plasmatron, an attempt was made to estimate the changes in the vibrational T_V and the rotational temperature T_R along the jet. For this case, an experimental fact was revealed that over the entire observed arc length and, accordingly, in the whole investigated temperature interval of the axial region of the plasma, the emission spectra of the C_2 molecules match each other and differ only by constant factor and correspond to temperatures $T_V = T_R = 5000$ K.

The spectrum in Fig. 1c contains a large set of atomic carbon lines; the analysis of their relative intensities makes it possible to determine the electron temperature T_e in the studied plasma by the "Boltzmann exponential" method /10/. The obtained values of T_e at various distances from the outlet of the nozzle of the plasma torch z are shown in Table 1. Due to the fact that the obtained temperatures turned out to be lower by more than an order of magnitude than the carbon ionization potential (11.26 eV), we can conclude that the measured temperature refers to the hottest region of the plasma stream, namely to its axis.

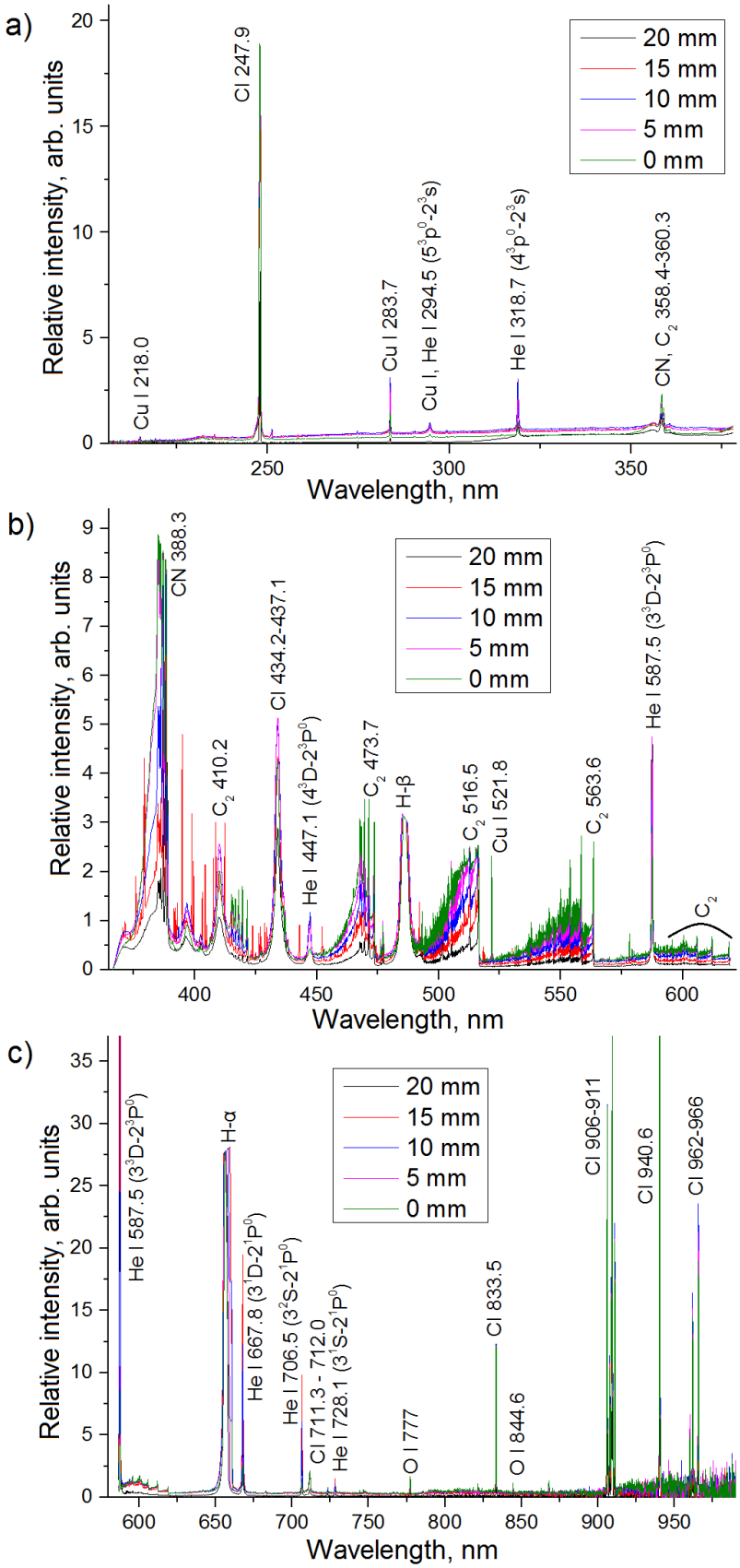

Fig. 1 – Plasma radiation spectra of helium and hydrocarbons mixture at different distances from the plasmatron nozzle outlet

Table 1. Values of T_e at different distances z from the plasma torch nozzle.

z, mm	0	5	10	15	20
T_e, K	7300	7000	6900	6800	6600

As the distance from the plasmatron nozzle increases,T_e is expected to decrease, but for the entire investigated interval it remains above the rotational T_R and vibrational T_V temperatures determined from the emission spectra of the C_2 molecule. This fact indicates that the maximum radiation intensity of C_2 molecules is not achieved at the axis of the jet, but at a lower temperature (5000 K according to the estimates given) at its periphery, where this temperature is realized. It is worth noting that due to the high transport properties of helium, which is a plasma-forming gas, the temperature drop with the radius can be quite sharp, and the distance corresponding to the C_2 radiation maximum is about 1 mm from the jet axis.

Acknowledgements. The reported study was funded by the Russian Foundation for Basic Research according to research project № 18-08-00306.

References

1. **Isakaev E.K., Chinnov V.F., Kavyrshin D.I., Sargsyan M.A.** High Temp., Volume 51, Issue 2 (2013) 141–146. doi: 10.1134/S0018151X13020090
2. **Spitzer L.** Physics of Fully Ionized Gases. Interscience Publishers (1956)
3. **Korshunov O.V., Chinnov V.F., Kavyrshin D.I. and Ageev A.G.** Journal of Physics: Conference Series, 774 (2016) 012199 doi:10.1088/1742-6596/774/1/012199
4. J**onkers J., Marco van de Sandle, Sola A., Gamero A., Joost van der Mullen.** Plasma Sources Sci. Technol., 12 (2003) 30-38.
5. **Chinnov V.F., Kavyrshin D.I., Ageev A.G., Korshunov O.V., Sargsyan M.A. and Efimov A.V.** Journal of Physics: Conference Series, 774 (2016) 012200 doi:10.1088/1742-6596/774/1/012200
6. **Kavyrshin D.I., Chinnov V.F. and Ageev A.G.** Journal of Physics: Conference Series, **653** (2015) 012115 doi:10.1088/1742-6596/653/1/012115
7. **Biberman L.M., Vorobev V.S. and Yakubov I.T**. Kinetics of Nonequilibrium Low-Temperature Plasmas. Berlin: Springer-Verlag (1987).
8. **Suemitsu H., Kazunori I. et al.** J. Phys. B: At. Mol. Opt. Phys., 23 (1990) 1129-1137.
9. **Ochkin V.N.** Spectroscopy of low temperature plasma. Weinheim: Wiley-VCH (2009).
10. **Lochte-Holtgreven W., ed**. Plasma Diagnostics. Amsterdam: North-Holland (1968).

EFFECT OF DELAY ON INTENSITY OF SPECTRAL LINES OF MAIN COMPONENTS OF TECHNOLOGICAL CLAYS AT TWO PULSED EXCITATION.

N. Kurian, S. Anufrik, K. Znosko

Yanka Kupala State University of Grodno, 22, Ozheshko Street, 230023, Grodno, Belarus, kurian90@mail.ry

To determine the qualitative and quantitative composition of substances, various physical methods are used, among which the most promising are the spectral methods. Among them, the highly-informative and expressive method is the method of laser-emission spectral analysis (LIBS) /1/.

The use of the two-pulse excitation regime of the investigated objects significantly expanded the analytical capabilities of the LIBS method. In /2/, the monopulse and two-pulse regimes of plasma excitation are compared. In subsequent experiments /3/, it was shown that when an aluminum alloy was exposed to a double laser pulse with an energy of 50 mJ and a delay of 25 ± 3 μs, the intensity of the spectral lines (Al III 704.2 nm, Al II 624.3 nm) increased by 8-10 times in comparison with the monopulse regime.

In addition to metals, the LIBS method was used to determine the amount of C /4/ and Be /5/ and in soils. In /5/, optimal delays between twin pulses (~0.5 μs) were established at different ablation energies, which allowed reaching of the maximum intensity values of the spectral lines (C I 247.86 nm, Mg I 285.21 nm, Si I 288.16 nm) for soil samples.

Considerable practical interest for manufacturers of ceramic building materials is the research of clays contained in the soil. The analysis of literature sources shows that there are no publications devoted to the optimization of the LIBS method for studying of the composition of technological clays.

The purpose of this paper is to study the effect of the energy of twin laser pulses and the time delay between them on the intensity of the spectral lines of the laser-emission plasma of technological clay.

The objects of investigation were tableted samples of powdered red and white clay of different composition. As shown in /7/, the concentrations of macro- and microelements in red and white clay differ by 3-5 times. Samples preparation were carried out in accordance with the method of MVI. MN 4092-2011 /8/.

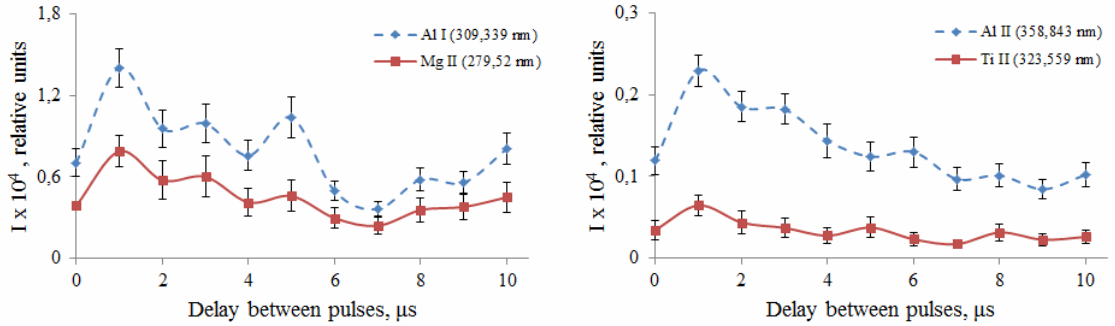

a) E = 17,3 mJ

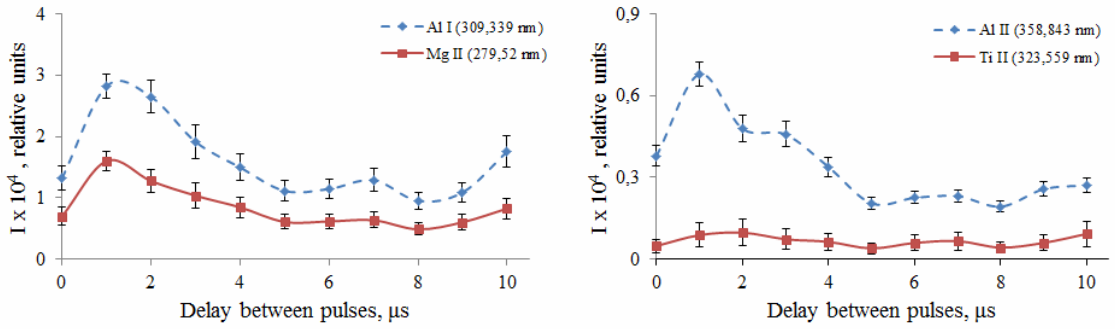

b) E = 30,5 mJ

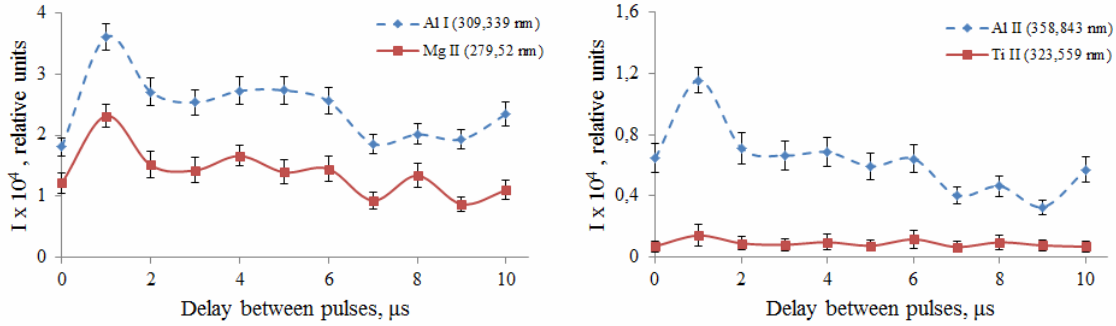

c) E = 45,2 mJ

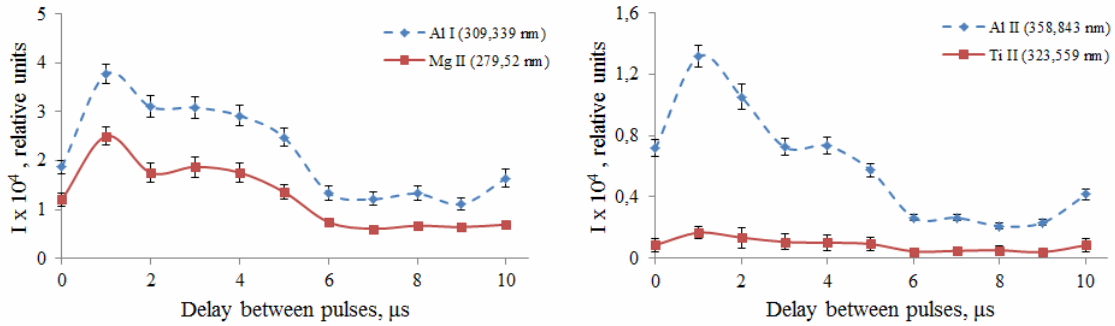

d) E = 61,6 mJ

Fig.1 - Dependences of the intensity of spectral lines Mg II (279.6 nm), Al I (309.4 nm), Ti II (323.6 nm), Al II (358.7 nm) laser-emission plasma of white clay on the delay between the double pulses

Dependences of the intensities of the spectral lines on the delay between twin laser pulses were studied with a laser emission spectrometric analyzer (LIBS) /9/. The delay between the double pulses varied from 0 μs to 10 μs in 1 μs increments. The zero delay corresponded to a single pulse. This range of delays was chosen to analyze the contribution to the emission plasma of its various components. According to /10/, in this time interval, mainly ion emission occurs (0.1-2 μs) and excited atoms (0.5-50 μs).

The sample was tested by five twin laser pulses with a repetition rate of 1 Hz. Under the influence of laser radiation, a laser-emission plasma was formed on the sample under study. Registration of the emission spectra of the plasma was carried out in a direction close to the inverse of the laser beam. The analyzed spectral lines were estimated from the maximum intensity values. For each point on the graphs, 10 series of measurements were carried out. The obtained extremums were subjected to additional experimental verification by an analogous number of measurements. All experiments were conducted in an air atmosphere.

The dependence of the intensity of the analyzed spectral lines on the delay between pulses for samples of red and white clay was investigated. Since the experimental dependences for white and red clay differed insignificantly, the article gives the results of studies of only white clay. Fig. 1 shows the experimental dependences of the intensity of the spectral lines of Mg II (279.6 nm), Al I (309.4 nm), Ti II (323.6 nm), Al II (358.7 nm) laser emission plasma of white clay from the delay between laser pulses with total energy: 17.3 mJ (a), 30.5 mJ (b), 45.2 mJ (c), and 61.6 mJ (d).

It follows from Fig. 1 (a-d), at all energies of the twin laser pulses, the maximum intensity of the spectral lines being analyzed $\lambda_{Al1} = 309.4$ nm; $\lambda_{Mg} = 279.6$ nm; $\lambda_{Ti} = 323.6$ nm; $\lambda_{Al2} = 358.7$ nm is achieved with a delay of 1 μs. The increase of the generation energy leads to an increase in the intensity of the spectral lines at the same value of the time delay. This allows us to conclude that the time delay of 1 μs is optimal. Further, as the delay increases to 10 μs, the intensity of the spectral lines decreases. This may be due to the damping of the luminescence of the ion component of the plasma of the primary pulse. At delays above 10 μs, the intensity of the emission lines is observed, as a consequence of the increasing energy contribution of the second pulse and the emission of excited atoms with increasing temperature plasma.

Analysis of the experimental dependences shows that the transition from single pulses to doubles, with unchanged total energy and optimal delay (1 μs), leads to a twofold increase in the analytical signal. An increase in the energy of twin laser pulses from 17.3 mJ to 61.6 mJ leads to an increase in the sensitivity of the analysis, while the standard deviation decreases from 10 % to 3 %.

Thus, it can be concluded that the increase in the intensity of the spectral lines of the analyzed elements is associated primarily with the additional excitation of the primary plasma by the emission of the second pulse with an optimal delay, rather than with an increase in the amount of the evaporated substance. To study the trace element composition of technological clays by the LIBS method, it is necessary to use twin laser pulses of higher energy with a delay of 1 μs, which will increase the signal level by a factor of 2 times and reduce the standard deviation of the intensity spectral lines Mg II (279.6 nm), Al I (309.4 nm), Ti II (323.6 nm), Al II (358.7 nm) to 3 %.

References

1. **Kremers D., Radiemsky L.** Laser-spark emission spectroscopy Moscow: Technosphere (2009).
2. **Arumov G., Bukharov A., Kamenskaya O., Kotyanin S., Krivoschekov V., Lyash A., Nekhaenko V., Pershin S.** Letters in JTF, 13 (1987) 870-871.
3. **Pershin S.M.** Quantum Electronics, 2 (1989) 325-330.
4. **Burakov V.S., Bohanov A.F., Nedelko M.I., Tarasenko N.V.** Quantum. Electr., T. 33, No. 12, (2003) 1065-1071.
5. **Sattman R.V.** Journal of Physics D: Applied Physics., 28 (1995) 2181-2187.
6. **Corsi M.**, Cristoforetti G., Giuffrida M. Spectrochim. Acta P. B: At. Spectrosc. Vol. 59 (2004) 723-735.
7. **Anufrik S.S., Kuryan N.N., Znosko K.F.**, Belkov MV Journal of Applied Spectroscopy, 85 (2018) 285-292.
8. **Anufrik S.S., Kuryan N.N., Znosko K.F.** Vesnyk GrSU named after. Ya. Kupaly, 8 (2018) 70-81.
9. **Belkov M.V., Raikov S.N.** Science and Innovation, 3 (2013) 17-18.
10. **Goncharov V.K., Kozadayev K.V., Shegrikovich D.V.** Materials 10th International Conference "WITT-2013", September 24-27, Minsk, izd. center Bel. state. University (2013) 29-31.

SOFTWARE-HARDWARE COMPLEX FOR EXPERIMENTAL STUDIES OF CHARACTERISTICS OF ROCKET ENGINE INSTALLATIONS DURING STAND FIRE TESTS

S.A. Grishin[1], V.V.Klimentovski[1], N.S. Niadvetski[1], D. A.Yagodnikov[2]

[1]SSPA"Optics, Optoelectronics and Laser Technology", Minsk, Belarus, grsamail@mail.ru
[2] Bauman Moscow State Technical University, Moscow, Russia, bauman@bmstu.ru

Development of rocket propulsion systems is accompanied by expensive and dangerous fire tests, the effectiveness and accident-free operation of which may be provided by the use of reliable and highly effective means of functional diagnostics and monitoring. Traditional methods and technical means of control currently used in fire tests of propulsion systems are not always effective, and besides they do not provide the necessary level of speed and reliability, which does not allow them to be used for creation of modern control, diagnostic and emergency protection systems. The report presents the results of research works aimed at creation of high-speed sensor devices and software-hardware means for recording and processing of liquid-propellant rocket engines (LPRE) status parameters using non-contact optical, thermal, electromagnetic and other means of monitoring. Characteristics of created software-hardware complex that provides registration and real-time processing of LPRE plume optical radiation spectra, parameters of thermal, vibrational, acoustic, magnetic and electric fields of LPRE plasma flows, as well as regime parameters (flow rates, pressures, temperatures) and videodata of fire tests are presented. The results of studies of combustion and destruction processes of LPRE structural elements, time and amplitude-frequency characteristics of physical fields of LPRE plasma flows, and dependencies of properties of physical fields on engine regime parameters are shown. On the basis of experimental data analysis, selection of diagnostic features was carried out and the possibility of creating emergency protection systems for LPRE with increased speed was proved.

Previous work / 1-4 / showed that the most promising for creation of systems for LPRE technical state monitoring may be utilization of an integrated approach based on simultaneous employment of optical, electrical, magnetic, thermal, acoustic, vibration and other methods and means of control. Taking into account these requirements, a software and hardware complex was developed (Fig. 1 and 2), which provides recording and processing in real time:

• spectra of LPRE plume optical radiation in the wavelength range from 300 nm to 1000 nm;

• values of the strengths and spectra of alternating magnetic (up to 50 A / m) and electric fields (up to 3 kV / m) in the frequency range from 20 Hz to 50 kHz;

• parameters of thermal fields (from 0 ^{o} C to 2000 ^{o} C and more);

• parameters of vibrations and acoustic oscillations:

- vibration amplitude up to 50g in the frequency range - 0.5 Hz to 12 kHz

- sound pressure amplitude up to 146 dB in the frequency range from 2 Hz to 20 kHz,

• regime parameters: pressure and temperature of the oxidizer, pressure drop on the oxidizer washer, fuel consumption, combustion chamber pressure, cooling water flow rate, boost pressure of fuel tanks, etc.

• video data of fire test process.

With the use of the developed complex, fire tests of model LPREs with various types of erosive critical section inserts, cooled combustion chambers and mechanisms for metal powders injection were carried out. During the fire tests, time and amplitude-frequency characteristics of physical fields (Fig. 3), their interrelationships with the processes of destruction of air-gas channel of LPRE and the regime parameters (pressures, flow rates, temperatures, etc.) were investigated; by monitoring characteristics of LPRE physical fields, the processes of particle penetration into the gas path of LPRE and the entrainment of materials during flame erosion of the elements of engine design were examined; diagnostic indicators were revealed. The results of tests and experimental operation of the complex have shown that the dependencies of the parameters of physical fields created by plasma flows on the pressure in the combustion chamber of LPRE can be used as diagnostic features for development of high-speed emergency protection systems for LPRE. It is found that the appearance of characteristic lines on the spectra of LPRE plume optical radiation is a reliable sign of the beginning of erosion and entrainment of materials during flame erosion of LPRE structural elements. As a result of the tests, the following was obtained:

• time dependencies and spectra of physical fields, reflecting the features of LPRE operation modes were registered and analyzed,

• correlation links between parameters of physical fields and regime parameters of LPRE were revealed,

• separate lines were registered against the background of continuous spectra of LPRE plume optical radiation during flame erosion of LPRE structural elements,

• the dependencies of magnetic (electric) fields of plasma flows close to the engine nozzle on pressure in combustion chamber of LPRE are found to be close to linear (correlation coefficient 0.9),

a) b)

Fig. 1 - General view of created software and hardware complex (a) and tested model liquid-propellant rocket engines (b)

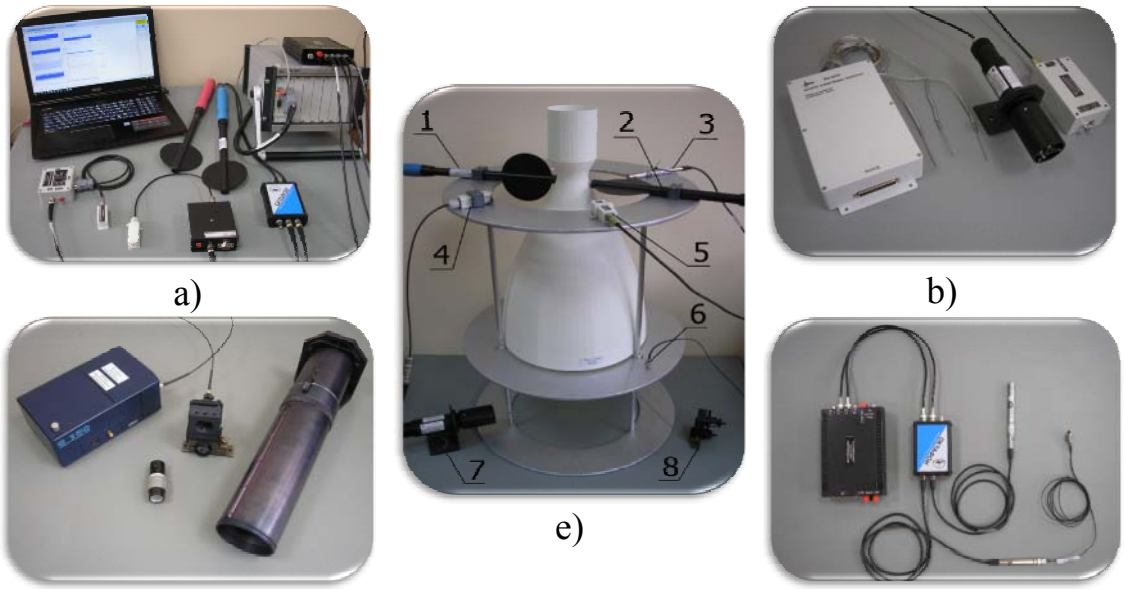

a) b) e) c) d)

Fig. 2 - The main blocks of the software and hardware complex:
a) Block for recording electric and magnetic fields. b) Temperature recording unit. c) Block for recording of optical radiation spectra. d) Vibration and sound recording unit. e) Location of sensors next to LPRE model:
1,2 - magnetic and electric antennas,
3 - microphone and vibration sensor, 4,5 - magnetic and electric field sensors, 6 - thermocouples, 7 - pyrometer, 8 - spectrometer lens.

• an increase of amplitudes of sensor signals and spectral power in certain frequency ranges at the time of injection of metal powders into engine gas path during experimental simulation of the process of flame erosion of LPRE structural elements was revealed,

• it is shown that time dependencies of physical fields parameters and their spectra make it possible to identify the characteristic modes of LPRE operation: the oxidizer valve opening; ignition system switching on and off; fuel supply valve actuation; purging with nitrogen,

• it is shown that parameters of physical fields, the features of their spectra and the dependence on engine regime parameters can be used as diagnostic features for high-speed LPRE emergency protection systems development.

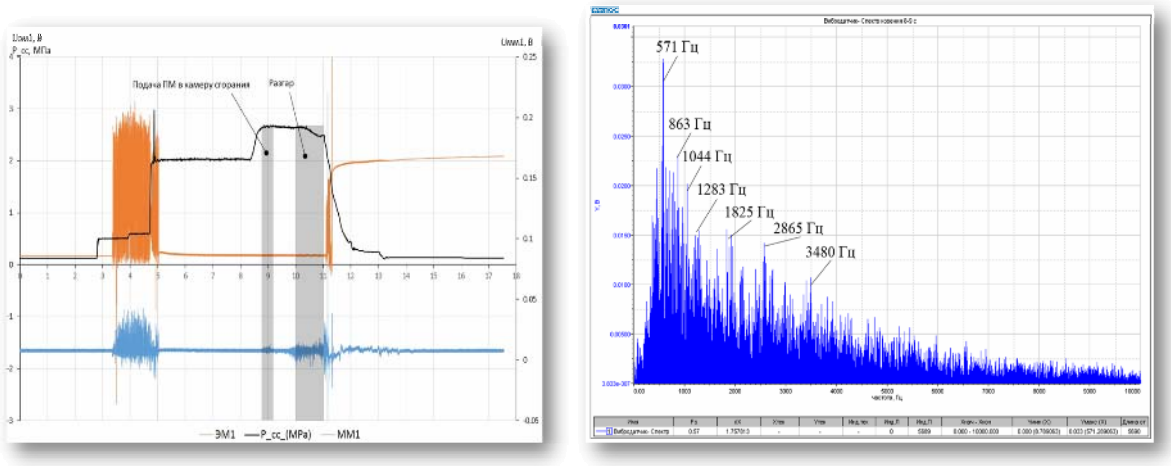

a) b)

Fig. 3 - An example of time dependencies of physical fields parameters (a) and the characteristic spectrum (b) of model liquid-propellant rocket engine.

R&D was carried out within the framework of Russian-Belarusian cooperation on scientific and technical program of the Union State "Monitoring - SG".

References

1. **Hryshyn S.A., Petsiuk A.L., Yagodnikov D.A., Antonov Y.V.** VII International Conference «Plasma Physics and Plasma Technology», 1 (2012) 267-269.

2. **Hryshyn S.A.** VIII International Conference «Plasma Physics and Plasma Technology», **2** (2015) 513-516.

3. **Yagodnikov D.A., Sukhov A.V., Iryanov N.Y., LapitskyV.I.,Grishin S.A, Bunchuk A.A.** Engineering Journal: Science and Innovation **1**(61) (2017) 1-17. (In Russian) http://engjournal.ru/articles/1574/1574.pdf

4. **Yagodnikov D.A., Rudinskii A.V.** High Temperature. **55** №5 (2017) 808–824.

DIAGNOSTICS OF PULSED PLASMA IN THE ACCELERATOR IPU-30

A.B. Tazhen, M.K. Dosbolayev, Zh. Raiymkhanov, T.S. Ramazanov

IETP, Al-Farabi Kazakh National University, Almaty, Kazakhstan. merlan@physics.kz

The experimental setup of IPU-30 assembled in the IETP consists of pulsed plasma accelerator, a plasma duct with a length of 1 m, grounding and protection systems, a control panel and diagnostic equipment. The plasma accelerator is powered by the capacitor bank with a total capacity of 100 μF. The operating voltage varies in the range of 5-14 kV. The schematic diagram and operating principle of the experimental setup are described in detail in references /1, 2/.

In this work, the discharge current was measured by using Rogowski belt. The belt of 400 coils is closed to the resistor R = 12 Ohm. The voltage drop in the resistance is measured by the digital oscillograph LeCroy 354A. One example of oscillograms obtained from the belt is shown in Fig. 1a. Figure 1b shows the dependence of the discharge current on the discharge voltage.

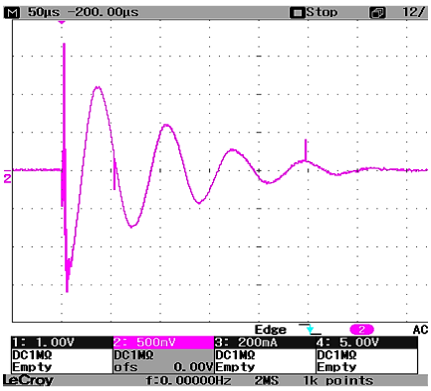

a)

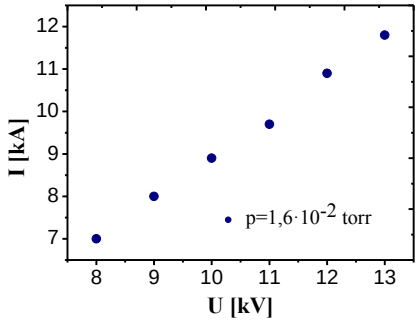

b)

Figure 1. a) The oscillogram of the discharge current, b) the dependence of the discharge current on the discharge voltage

The dependence (Fig. 1b) shows, that when the discharge voltage increases, the electric field between the electrodes increases, which leads to an increase in the ionization process, thereby improving the conductivity of the plasma.

In thermonuclear reactors, the energy density of the plasma flow to the wall after the breakdown of the plasma pinch is several MJ/m^2 /3/. In those conditions the study of the interaction of plasma with protective materials is one of the most urgent problems in thermonuclear research. A wire calorimeter was used to study the energy density of the pulsed plasma flow in the IPU-30. The wire calorimeter is a dielectric frame on which tungsten wires with a diameter of 100

μm are stretched at the same distance of 5 mm. The surface area of the wire is not large, so the wire calorimeter has a high thermal response when interacting with the plasma /2/. In the experiments for the measurement, the wire calorimeter was placed on the path of the plasma flow and covered the entire transverse area of the outer electrode. When a pulsed plasma passes through calorimeter, it gives it energy, the heat is absorbed by the wires, as the result of which, the wires heat up.

The energy density of the plasma flow was calculated by equation 1:

$$Q = \frac{c\rho {S_{\text{П}}}^2}{\alpha\rho_0} \cdot \Delta R. \tag{1}$$

To measure the change in the resistance of the wire calorimeter, it was connected through a shunt to the oscilloscope. In the measurements, we recorded the voltage drop at the shunt of 86 Ohm, the value of which determines the change in the resistance of the wire calorimeter. One of the examples of the oscillograms of the voltage drop on the shunt resistance is shown in Fig. 2. The oscillogram from the calorimeter was divided into two ranges. Range 1 corresponds to Fig. 2a, and range 2 corresponds to Fig. 2b. In Fig. 2a, when the time scale on the oscilloscope is set to 200 μs, one can see the appearance of the oscillation on the curve. The total width of the oscillations corresponds to the lifetime of the pulsed plasma. The difference between Fig. 2b and Fig. 2a, when the time scale on the oscilloscope is set to be long enough, is 2 seconds.

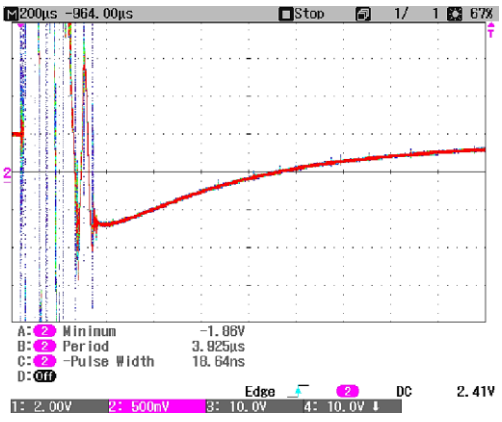

a)

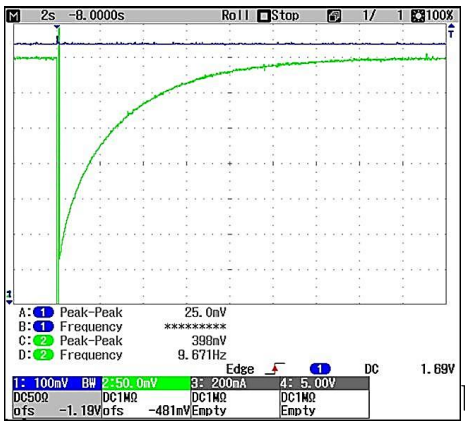

b)

Figure 2. The oscillograms obtained from a wire calorimeter

In the range 2, the wire calorimeter operates as a thermal detector, that is, the change in the voltage drop across the shunt resistance occurs only due to the heating of the wires by the plasma flow. And in the range of 1 there are other effects. In our statements, the appearance of oscillation is due to the redistribution of charges in wires. Based on oscillograms, the energy densities of

the pulsed plasma were calculated depending on the gas pressure and the discharge voltage. The results are shown in Fig. 3a and 3b.

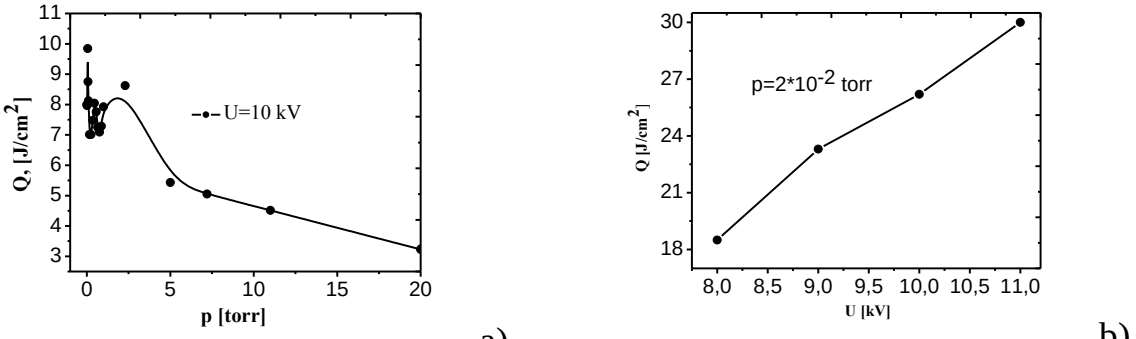

a) b)

Figure 3. Dependences of the energy density of a pulsed plasma a) on the gas pressure and b) on the discharge voltage

The dependence of the energy density of the plasma flow on the gas pressure (Fig. 3a) shows that as the gas pressure increases, the energy density of the plasma flow first increases, then at a certain value of the gas pressure reaches a maximum and decreases with further growth. This behavior of the curve is explained in accordance with Paschen's law. Fig. 3b shows that as the discharge voltage increases, the energy density of the pulsed plasma increases, due to an increase in the ionization energy of the gas.

One interesting phenomenon, the appearance of non-stationary magnetic fields in a pulsed plasma also requires its study. In this work a magnetic probe was used to measure the magnetic field in a pulsed plasma. A magnetic probe consists of 15 coils. The area of the coil section is 7*10^{-6} m^2. For measurement, the magnetic probe is connected to the oscilloscope through an integrating circuit. The integration time of the signal is 25 μs. Some of the examples of the oscillograms obtained from the magnetic probe are shown in Fig. 4.

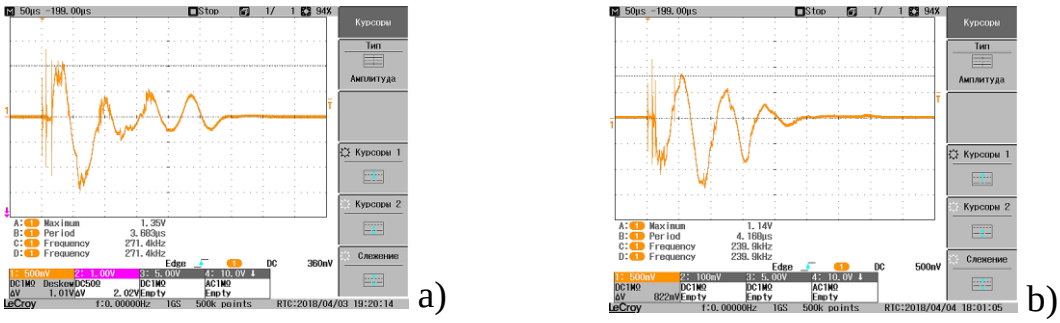

a) b)

Figure 4. The oscillograms obtained from the magnetic probe: U = 11 kV, p = 2*10^{-2} torr, a) magnetic probe in horizontal position, b) magnetic probe in a horizontal position inverted for 180°

To ensure that the magnetic probe is operating correctly, the magnetic probe is located at a fixed distance but in two different positions of the coil. In the first position, the axis of the probe coil was vertically aligned with the electrodes in the interelectrode space, and in the second position, the probe coil was turned upright 180° as in the first position. In this case, we should receive the same signals from the magnetic probe, but the inverse phases, which we obtained in the experiment, are shown in Fig. 4a and 4b.

On the basis of these oscillograms, the values of the magnetic field of the plasma were calculated from the distance in the interelectrode space from the beginning of the end of the outer electrode, Fig. 5a, and from the value of the discharge voltage, Fig. 5b.

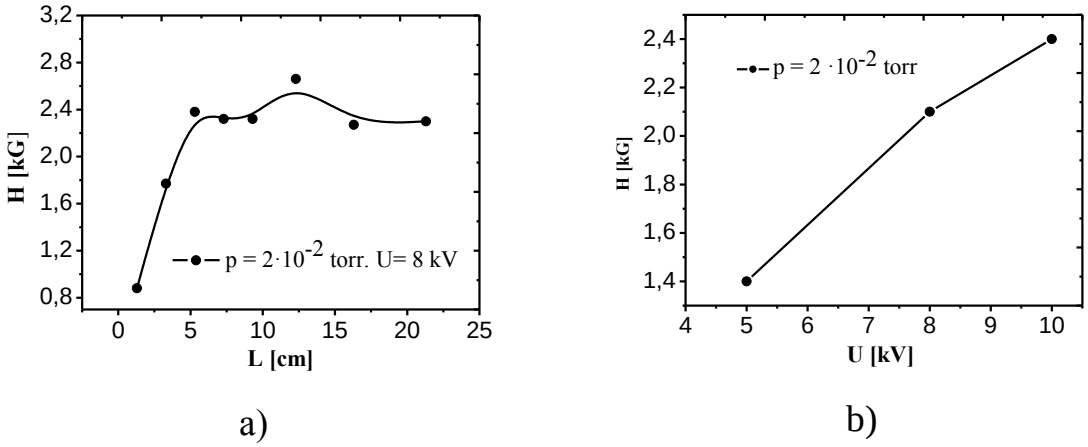

a) b)

Figure 5. a) The dependence of the magnetic field of the plasma on the interelectrode distance from the beginning of the end of the outer electrode, b) the dependence of the magnitude of the magnetic field of the plasma on the discharge voltage

Acknowledgements. This work was supported by the Ministry of Education and Science of Kazakhstan under Grant IRN AP05134671.

References

1. **M.K. Dosbolayev, A.U. Utegenov, A.B. Tazhen, T.S. Ramazanov.** // Laser and Particle Beams, 35 (2017) 741-749.
2. **A.B. Tazhen, A.Kh. Suleimenova, M.K. Dosbolayev, T.S. Ramazanov.** Determination of the energy density of a pulsed plasma flow by means of a wire calorimeter // PEOS. - 2017. - Iss. - P. 510.P.
3. **Flanagan J.C., Sertoli M., Bacharis M., et al.** // Plasma physics and controlled fusion. 2015, Vol. 57. P. 014037.

LUMINESCENCE OF SILICON DIOXIDE WITH REACTIVE ION PLASMA ETCHING

A.V. Abramov, E. A. Pankratova, I. S. Surovtsev

Voronezh state technical University, 82, 20-let Oct. str., Voronezh, Russia,
abramovvgasu@yandex.ru

Studies of luminescence of SiO_2 film observed in reactive ion-plasma etching (RIE) were carried out on a device with a discharge chamber of the RF diode type with a diameter of 120 mm, a detailed description of which is given in /1/. The processed samples were placed on a grounded electrode. The luminescence effect of SiO_2 film on Si was found at RIE in the plasma of SF_6 gas, in which it has the highest intensity. Later it was also found that it is observed less brightly in other fluorinated gases (CF_4, C_3F_8). At the same time the intensity of a luminescence was periodically changing in process of decrease of thickness of a film of SiO_2, that allowed to assume existence of an interference of light. For a research of a range of a luminescent glow a spectral complex of КСВУ-23М was used. In fig. 1 shows an aliasing of emitted spectrums from a surface of the oxidized Si plate going at the moments appropriately to a maximum and a minimum of intensity is shown. It is seen that in the wavelength range (λ) 330 - 650 nm the wide emission band with a maximum is observed at λ = 440 nm (ε =2,81 eV) which intensity does not change over time. In /2/ it is supposed that the luminescence of structure of SiO_2/Si observed at a cathodeluminescence with a maximum energy of 2,7eV is bound to formation of luminescence centers in the field of the interface. Probably, a radiation spectrum presented in Fig. 1 is related to action of the similar centers. This type of luminescence is present in both reactive fluorinated gases and inert ones. Its existence is caused by momentum transfer of ions in oxide volume. The second type of emission is followed by fluctuation of intensity and is observed only in fluorinated gases in the range of 480 - 550 nm with a maximum near 515 nm that visually is confirmed by brightly green color of a luminescent emission. Source of this luminescence is the fluorinated surface of oxide that is confirmed by its fast attenuation at supply of noble gas instead of SF_6 without switching off the discharge. Existence of time of attenuation is explained by physical atomization of the fluorinated SiO_2 layer. At the inverse change of gases the luminescence renews. The fact that the luminescence emission in reactive gas comes from the surface layer of oxide also reflects the alternation of maxima and minima of its intensity which are linked to an interference of light waves demonstrates.

The illustration of the course of the interfering waves entering on the sensor is given in Fig. 2: one - from a surface of the luminescent layer, and the other one - from a demarcation of SiO_2 and Si. The interference maximum condition taking into account loss of a half wave on a demarcation of environments registers as follows:

$$2d\sqrt{n^2-\sin^2\alpha}=(m-\frac{1}{2})\lambda,$$

where d and n respectively thickness and a refractive index of light in SiO_2; α - a corner between a normal to a surface and the direction of a quartz light guide; m - integer numbers.

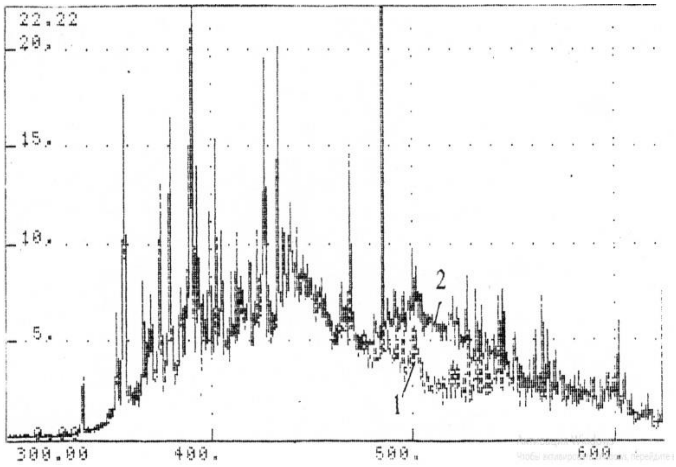

Fig. 1 – Imposing of luminescent spectrums. Gas - SiF_6

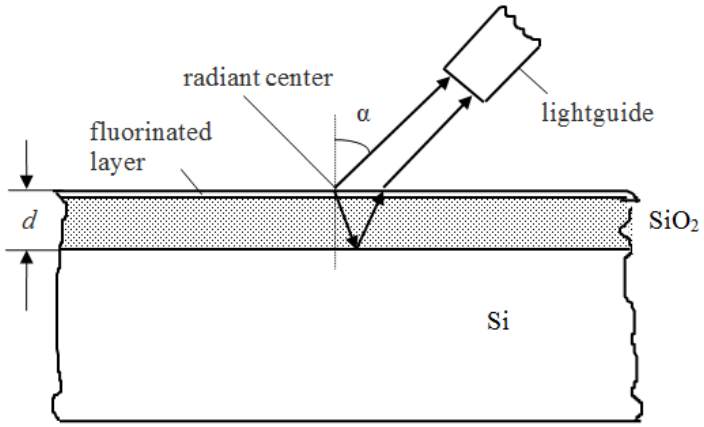

Fig. 2 – Light interference illustration at the expense of the luminescing centers on a layer surface SiO_2

It should be noted that at the plasmochemical etching which is carried out at more high pressure (P), than RIE, luminescence is not observed though concentration of radicals of F (n_F) in the category is higher. It is logical to assume that the factor causing emergence of a luminescence at low P is the ionic bombardment which energy increases with decrease of P of plasma-forming gas. For confirmation of this assumption the experiment in which a wire was stretched over the surface of the oxidized Si plate and on which the negative shift concerning the earthed electrode was made. The increase in the displacement led to a decrease in intensity and to a termination of glow. Thus, this type of luminescence can be considered ionoluminescence. The role of ions can consist in two moments: first, the ionic bombardment leads to in-

crease in a depth of penetration of fluorine into the treated surface, i.e. to an increase in the thickness of the luminescent layer. Secondly, ions are an energy source of exaltation of luminescence centers. Both of these processes play as larger role as energy of ions gets higher. So, for example, the intensity of a luminescent luminescence of SiO_2 in SF_6 at P = 1,33.10-1 Pa with increase in the amplitude of RF voltage (U_{rf}) from 1,0 to 1,8 kV increases approximately six times, while n_F varies slightly.

For increase in a share of interfering radiation in the common luminous flux the green light filter was used, and as the receiver of a light signal photoresistance of ФСК-1 was used. It allowed to trace efficiently dynamics of an interference of a luminescent emission depending on thickness of a layer of SiO_2 which initial thickness in this case was 0,72 μm (Fig. 3). According to the submitted schedule counting rate grows after inclusion of the category during the particular time depending on technological parameters of process. Possibly, existence of building-up period of intensity of a luminescence is bound up mainly with formation on a surface of a plate of the fluorinated layer and a lesser extent with a release of discharge to steady conditions of combustion. This exit is followed by body height of concentration of atomic fluorine in the category which reaches the steady-state value, approximately within a minute. It allowed to trace efficiently dynamics of an interference of a luminescent emission depending on thickness of a layer of SiO_2 which initial thickness in this case was 0,72 μm (Fig. 3). The first maximum to which there corresponds m = 4 was for this reason sheared off and displaced towards larger time of etching. Thickness of oxide corresponding to it was passed during the period of formation of the luminescing layer. Therefore for establishment of a time frame Δt between maxima we take the second and third peaks to which there correspond values m equal 3 and 2. It is equal to ~170 s. On the other hand, using a formula (1) and λ = 515 nm, we find a difference of thickness of a film of SiO_2 (Δd), the corresponding m equal 3 and 2. It appears equal 200 μm. Using the received values Δt and Δd, we receive time which necessary for the complete etching SiO_2 with a thickness of 0,72 μm, it has to take 612 s. This time rather well coincides with experimentally received that demonstrates correctness of assessment of the wavelength corresponding to a maximum of intensity of a luminescent luminescence of a surface of a layer of SiO_2.

It is established that the luminescent emission of SiO_2 grows at increase in temperature of an exemplar for what it was placed on the warm table. In view of the considerable duration of time of etching it was necessary that between a little table and an exemplar the temperature balance is established. It is experimentally established that the thermostimulation of a luminescence gives noticeable effect at a warming up of exemplars to 500-600K, but it can have an adverse effect on characteristics of the processed structures.

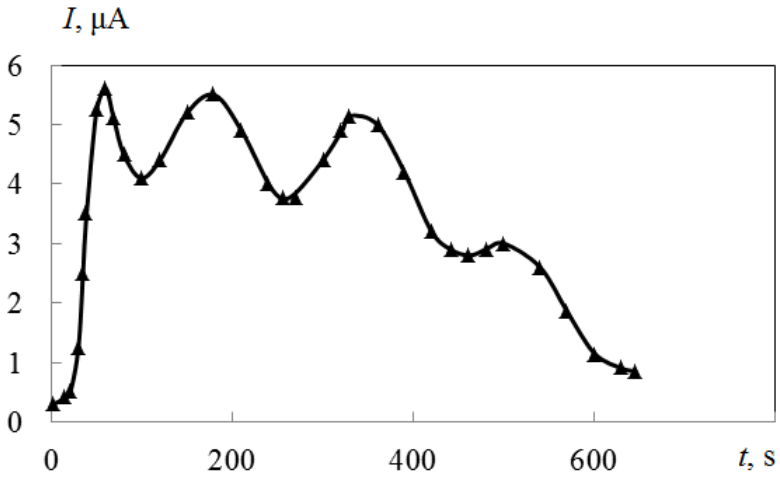

Fig. 3 – Dynamics of luminescence
Gaz-SiF_6; $G = 3{,}1 \cdot 10^{-8}$ $m^3 \cdot Pa \cdot s^{-1}$; $P = 6{,}65 \cdot 10^{-2}$ Pa, $U_{rf} = 1{,}8$ kV.

Using SiO_2 luminescence phenomenon in the course of RIE it is possible to carry out electrooptical checking not only the moment of the end of its etching, but also its thickness. It is also possible to carry out monitoring of the end of etching of layers of other materials lying on SiO_2.

Reference

1. **Abramov A.V., Abramova E.A., Dikarev Y.I., Surovtsev *I*.S.** Journal of Applied Spectroscopy,Vol.71, No. 5, 2004, P. 715-720.
2. **Baraban P. A., Bondarenko A. S., Bondarenko V. P. and ather**. Vestnik St. Petersburg University. Ser. 4. 2011. Issue. 2. P. 24-29.

Optimal Atmospheric Pressure Plasma Jet Parameters for Bacteria Sterilization

A. Jurov[1], U. Cvelbar[2], M. Modic[3], Z. Lj. Petrović[4], N. Škoro[5], K. Spasić[6], N. Hojnik[7], D. Vujošević[8], V. Vuksanović[9], M. Đurović[10]

[1]Jozef Stefan International Postgraduate School, Jamova cesta 39, SI-1000 Ljubljana, Slovenia,
and Jozef Stefan Institute, Jamova cesta 39, SI-1000 Ljubljana, Slovenia, andrea.jurov@ijs.si
[2]Jozef Stefan Institute, Jamova cesta 39, SI-1000 Ljubljana, Slovenia, uros.cvelbar@ijs.si
[3]Jozef Stefan Institute, Jamova cesta 39, SI-1000 Ljubljana, Slovenia, martina.modic@ijs.si
[4]Institute of Physics, University of Belgrade, Pregrevica 118, 11080, Belgrade, Serbia, zoran@ipb.ac.rs
[5]Institute of Physics, University of Belgrade, Pregrevica 118, 11080, Belgrade, Serbia, nskoro@ipb.ac.rs
[6]Institute of Physics, University of Belgrade, Pregrevica 118, 11080, Belgrade, Serbia, kostasp@ipb.ac.rs
[7]Jozef Stefan International Postgraduate School, Jamova cesta 39, SI-1000 Ljubljana, Slovenia,
and Jozef Stefan Institute, Jamova cesta 39, SI-1000 Ljubljana, Slovenia, natasa.hojnik@ijs.si
[8]Center for Medical Microbiology, Institute of Public Health Montenegro, Džona Džeksona bb, 81000, Podgorica, Montenegro, danijela.vujosevic@ijzcg.me
[9]Center for Medical Microbiology, Institute of Public Health Montenegro, Džona Džeksona bb, 81000, Podgorica, Montenegro, vineta.vuksanovic@ijzcg.me
[10]Center for Medical Microbiology, Institute of Public Health Montenegro, Džona Džeksona bb, 81000, Podgorica, Montenegro, milenadjurovic@yahoo.com

Abstract

There are many new alternatives to conventional bacteria sterilisation techniques (heating, filtration, solvents, radiation), such as different plasma sources /1,2/. This research focused on non-thermal atmospheric pressure plasma jet (APPJ) because it's cost-effective, easily transportable, simple to use, and has a low operating temperature thus enabling treatment of heat sensitive surfaces. The experiments were conducted with helium APPJ for four different typical bacteria strains with the focus on finding the most efficient discharge parameters. The analysis that was used on the jet are optical emission spectroscopy and electrical measurements.

1. Introduction

Improving the decontamination of the bacteria is an ongoing process and of great importance in many environments, such as hospitals. As an alternative to conventional techniques, plasma decontamination was proposed. Our choice was an atmospheric pressure plasma in a form of a single electrode jet (APPJ). Atmospheric pressure plasmas have many advantages compared to low-pressure

plasmas, mostly the ability to work without the vacuum system thus reducing the cost of the process and making it possible to treat heat-sensitive materials and hard-to-reach places (e.g. corners, tubes) /3,4/. Because of that we constructed the APPJ and tested its most optimal parameters for bacteria decontamination on four types of bacteria. After finding out which powers and gas flows decontaminated bacteria, the focus shifted onto the diagnostics of the plasma source.

2. Experimental setup

The decontamination effect of the atmospheric pressure plasma jet was investigated on four different types of spore-forming bacteria: *Bacillus stearothermophilus* ATCC No. 7953, *Bacillus subtilis* ATCC No. 6633, *Staphylococcus aureus* ATCC No. 25923, and *Escherichia coli* ATCC No. 25922, of which only the *E. coli* is Gram-negative bacteria. Bacterial cultures were grown overnight on Columbia (COS) agar plates (bioMérieux SA, Marcy l'Etoile, France) at $55^{o}C$ for *Bacillus stearothermophilus* and $37^{o}C$ for *Bacillus subtilis*, S*taphylococcus aureus* and *Escherichia coli.* Bacteria were picked up with a loop and re-suspended in sterile saline to obtain 0.5 McFarland ($1\text{-}2 \times 10^{8}$ *CFU/ml*) initial bacterial suspension.

Small-size APPJ powered by a kHz signal source connected to a low-voltage DC source was used for the treatments. Measurements with the needle type APPJ were conducted with He as a working gas at a fixed distance between the jet and the sample surface (15 *mm*). Bacteria were treated for different gas flows (1 *slm* and 2 *slm*) and with several DC power supply voltages applied (3 *V*, 4.5 *V*, 6 *V*, 9 *V* and 12 *V*). Detailed characterisation of the plasma source was performed employing optical emission spectroscopy and electrical characterization.

3. Results and discussion

After preparing bacteria suspension, we treated them with Helium APPJ under different DC power supply voltages and gas flows. A surface of the suspension was fixed 15 mm under the jet nozzle, and it was fixed for all measurements. The bacteria suspension was placed in a Petri dish that was grounded. The survival curves indicated that He APPJ with higher input power was more effective, meaning that the treatment time for decontamination is shorter for the higher power. Because of that, we focused on the parameters that showed the most optimal sterilization - 2 *slm* gas flow and 12 *V* input voltage.

The plasma source diagnostics was done under the same conditions as the bacteria were treated but the Petri dish was filled with the distilled water. The dish was grounded and the parameters were 2 *slm* and 12 *V*.

First, optical emission spectroscopy was done and the full spectrum is presented in Fig. 1. It contained all the expected species, such as OH, He, N and O atoms and/or molecules. He comes from the plasma itself since it was the working gas used in the experiments, and OH, N and O are present because the experiments were conducted in ambient air and in contact with distilled water. The additional spectrum was obtained for same conditions but with saline instead of distilled water, and it showed no new species meaning that APPJ has no sufficient power for excitation of Na or Cl.

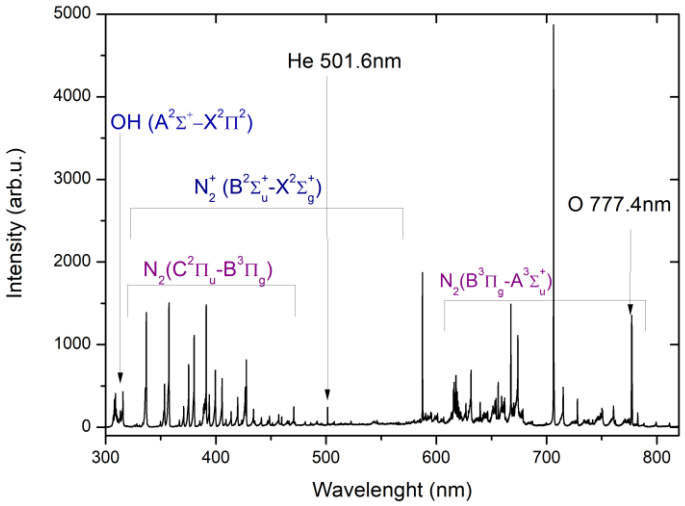

Fig. 1 – OES of He APPJ (1cm from the surface of the distilled water in Petri dish (grounded))

Another set of diagnostics done on the APPJ were electrical measurements from which we obtained average power of the plasma source shown in Fig. 2. These results show no difference in power for 1 and 2 *slm* except for 12 *V* where in the case of 2 *slm* power source gives much higher power.

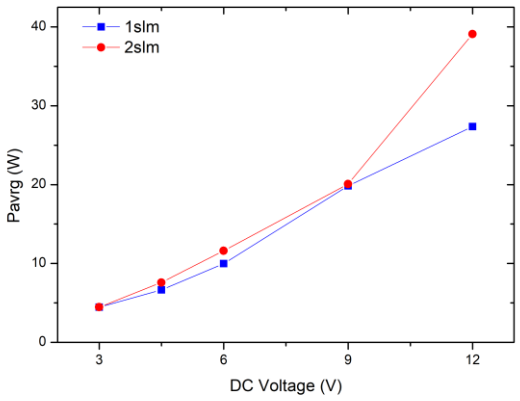

Fig. 2 – Average power for gas flows of 1 slm (blue) and 2 slm (red) and all used voltages (3, 4.5, 6, 9 and 12 V)

4. Conclusions

The decontamination effects of He APPJ were significant but dependent on the type of bacteria, exposure time, and plasma configuration (gas flow and input power). The input power at 3 *V* was not sufficient for bacteria decontamination when the gas flow was 1 *slm*; however, it was enough for decontamination of *S. aureus* and *B. subtilis* with the gas flow of 2 *slm*.

The optical emission spectrum showed that the plasma power was not sufficient enough to excite Na and Cl species, but it exhibits the intensive signature of OH, O and N species. Additional analysis will be done on specific atomic and molecular lines to observe their influence on the bacteria decontamination.

The electrical characterization did not show much difference between gas flows of 1 and 2 *slm* except for the highest input power at 12 *V*. It is still unclear why is there a difference so additional measuremetns will be conducted.

Acknowledgements

This research was a part of NATO Science for Peace Multi-Year Project [SPS 984555], and ARRS project N3-0059.

References

1. **Ehlbeck J., Schnabel U., Polak M., Winter J., Von Woedtke T., et al.** Journal of Physics D: Applied Physics, **44**, 1-33, 2011
2. **Gadri R. B., Roth J. R., Montie T. C., Kelly-Wintenberg K., et al.** Surface and Coatings Technology, **131**, 528-542, 2000
3. **Hofmann S.** *Atmospheric pressure plasma jets: characterisation and interaction with human cells and bacteria*, Eindhoven: Technische Universiteit Eindhoven, 11-30, 2013
4. **Halfmann H., Bibinov N., Wunderlich J., Awakowicz P.** 'A double Journal of Physics D: Applied Physics, **40**, 1-11, 2007

7. PLASMA APPLICATIONS

PLASMA APPLICATION FOR CATALYST PREPARATION

N.A. Savastenko[1], I.I. Filatova[2], V.A. Lyushkevich[2], V. Brüser[3], S.A. Maskevich[1]

[1]Belorussian State University, International Sakharov Environmental Institute BSU, 23 Dolgobrodskaya Str., 220070 Minsk, Belarus, nataliesavastenko@iseu.by
[2]B.I. Stepanov Institute of Physics, National Academy of Sciences of Belarus, 68 Nezavisimosti Ave., 220072 Minsk, Belarus, filatova@presidium.bas-net.by
[2]Leibniz-Institute for Plasma Science and Technology, 2 Felix-Hausdorff-Strasse, 17489 Greifswald, Germany, brueser@inp-greifswald.de

There are three main trends in catalysts preparation using plasmas: synthesis of catalytically active nanoparticles, plasma assisted deposition of catalytically active materials on the support, and plasma modification of catalysts /1,2/. Traditinally, catalysts are subjected to a heat treatment under either inert or reactive atmosphere. Nevertheless, the thermal pyrolysis of catalysts' precursors can lead to an unfavourable morphology of the material. This drawback can be overcome by the replacement of the heat-treatment step by low temperature plasma treatment of precursors. The plasma prepared catalysts or catalysts modified by plasma exhibit a higher activity, enhanced selectivity and better stability, compared to the catalysts prepared conventionally (by heat-treatment).

In this paper, we present our results on the preparation of automotive exhaust catalysts, electrocatalysts, as well as photocatalysts with plasma-assisted methods.

In the field of automotive exhaust gas treatment, one of the most challenging tasks is the development of advanced lean NO_x catalysts, which can chemically convert NO (NO and NO_2) gaseous compounds into molecular nitrogen under oxygen rich conditions as typically present in e.g. diesel exhaust gases /3/. Nanostructured monometallic (Pt, Rh) and bimetallic (PtRh) catalyst samples were synthesized via direct deposition of the respective nanoparticles, which were generated by laser ablation of Pt, Rh metal and PtRh-alloy targets using a pulsed excimer laser ultraviolet light source (Lambda Physik, LPX-100, KrF wavelength 248 nm). The experimental setup employed in the work was described in detail in /4/. The nanoparticles were found to exhibit narrow size distribution centred around 2.5 nm. (Fig. 1). The catalytic activities for synthesized catalyst were tested using a test gas mixture representative of oxygen rich diesel engine exhaust gas in order to assess their capability of lean NO_x reduction. The catalytic activity measurements revealed that under cyclic lean/rich operating conditions the laser synthesized PtRh–SiO_2 catalyst showed the highest activity for NO_x reduction in the low temperature range 100–300°C,

which, at a temperature of 150°C, was found to be a factor of ca. 3 higher than the activity of a monometallic Rh containing reference catalyst prepared by wet impregnation (ablation, Fig. 2). Furthermore, it was shown that the low temperature NO_x reduction activity and the selectivity for N_2 formation of the conventional Rh catalyst can be enhanced by additional laser deposition of PtRh nanoparticles (postablation, Fig. 2).

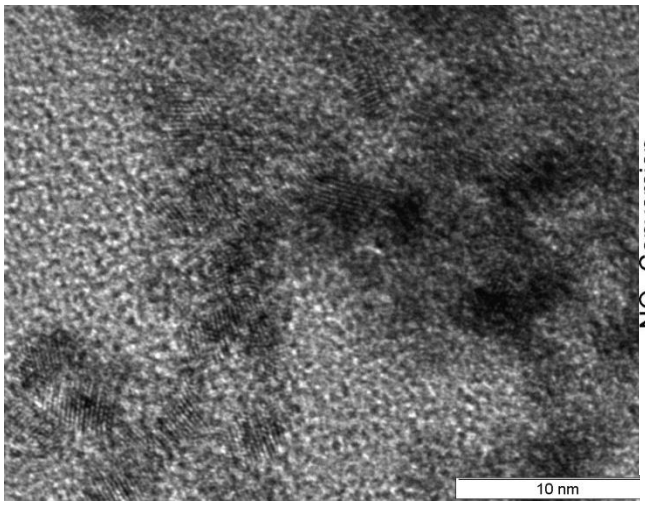

Fig. 1 – High-resolution transmission electron microscopy (HRTEM) images of PtRh nanoparticles generated by laser ablation

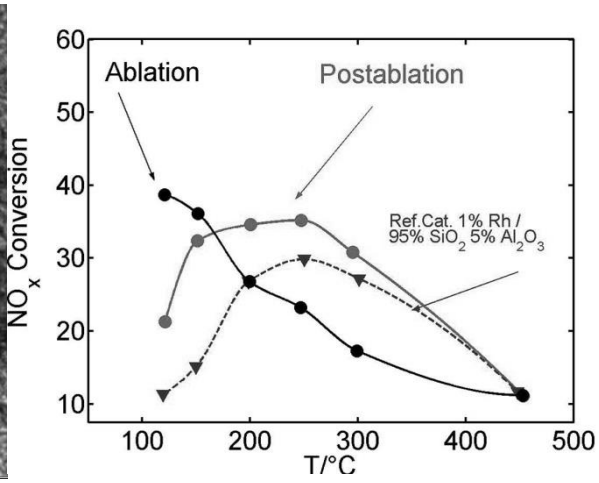

Fig. 2 – Average NO_x conversion within 3 cycles of rich(2sec)/lean(80sec) excursion

As a part of continuing efforts to develop a method of plasma-enhanced preparation of electrocatalysts for oxygen reduction reaction (ORR) we prepared a series of porphyrin- and phthalocyanine-based catalysts and treated them with radio frequency (RF) and dielectric barrier discharge (DBD) plasmas under different conditions to optimize their catalytic activity /5-9/. The activity towards the reduction of H_2O_2 was investigated because it is of practical importance in the field of fuel cell development.

The performance of RF-plasma treated Fe- porphyrin based catalyst (FeTPFPPCl on RF-plasma treated Vulcan) for the H_2O_2 reduction in a fuel cell test is shown in Fig. 4. The performance of reference Pt-based catalyst is also shown. The results are plotted in of power. As it can be seen from the Fig. 3, for the plasma treated electrocatalyst, the maximum power of the fuel cell was 193 mW. It was approximately 1.4 times more than for the fuel cell with reference Pt-based catalyst The experimental details are described in /5/.

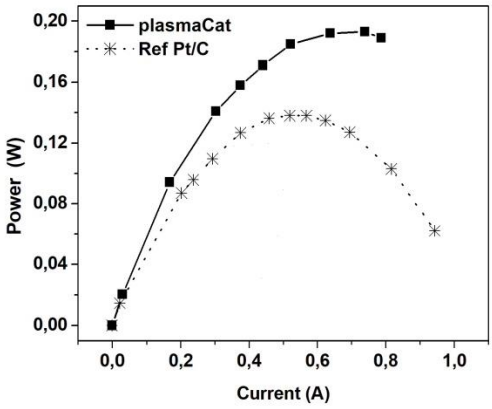

Fig. 3 – Performance of a fuel cell with plasma treated FeTPFPPCl on plasma treated Vulcan (plasmaCat) and Pt on Vulcan (Ref Pt/C) catalysts

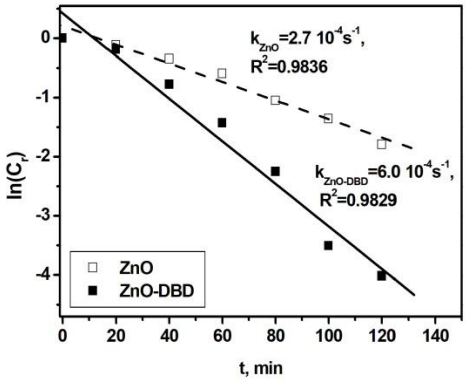

Fig. 4 – Kinetics of the degradation of MO under UV-irradiation with untreated and plasma treated catalysts

Atomic force microscopy (AFM) was applied to investigate the morphological modifications induced by plasma treatment of catalysts. The AFM investigations revealed morphological changes which accompanied the transformation of porphyrin precursor into the catalytic material. The agglomerations of porphyrin molecules on the support were re-arranged after plasma treatment. The height of the agglomeration was reduced. Removed material was re-deposited on the surface of catalyst's support as smaller particles 20–30 nm in height. Such re-deposition can improve the catalyst's performance due to the increased dispersion of catalytically active constituents /5, 6/.

RF- and DBD plasmas were applied to enhance the performance of ZnO-based photocatalysts /10-13/. The performance of untreated and plasma-treated ZnO photocatalysts was investigated for their application for photodegradation of organic pollutants. The photocatalytic activities of plasma treated and untreated ZnO powders were evaluated by measuring the photodegradation of methyl orange (MO) in aqueous solution exposed to ultraviolet (UV) light.

Fig. 4 shows the kinetics of degradation of MO under UV-irradiation with untreated (ZnO) and DBD-plasma treated (ZnO-DBD) catalysts. The semi-logarithmic plots of the concentration data ($\ln(C_r)$ vs time) gave a straight lines. The correlation constants for the fitted lines were calculated to be $R^2 = 0.9836$ and 0.9829 for untreated and plasma treated ZnO, respectively. Therefore, the photocatalytic decomposition can be described by the first order kinetic model /11/. The Fig. 4 clearly indicates plasma treated ZnO to be a better photocatalyst

for MO degradation. The first order rate constants k were found to be 6.0 10^{-4} s^{-1} and 2.7 10^{-4} s^{-1} for plasma treated and untreated ZnO, respectively. The rate of degradation was enhanced about 2.2 times with plasma treated ZnO.
It was found /11/ that different mechanisms might be involved in the decomposition pathway of MO on untreated and plasma treated catalysts. Room temperature photoluminescence (Pl) indicated that plasma treatment resulted in an enhancement of the excitonic (UV) emission and an increase in UV/visible Pl intensity ratio (not shown). Therefore, increasing photocatalytic activity after plasma treatment can be attributed to the increased optical quality of ZnO.

The observed changes in the photoluminescence and photoactivity after plasma treatment were likely caused by oxygen vacancies and surface defects.

In conclusion, the results suggest that RF- and DBD-plasma treatment is very effective way to manipulate catalyst surface properties and to enhance their activity.

Acknowledgements. This work was financially supported by the Belorussian Republican Foundation for Fundamental Research (grant No F17-076) and by the German Federal Ministry of Education and Research (BMBF, FKZ 03F0466E and 03C0339F).

References

1. **Liu C.J., et al.** Appl. Catal. 47 (2004) 95-100.
2. **Vissokov G.P., et al.** J.Mater. Sci. 16 (1981) 1716-1719.
3. **Koenig A**., **at al.** Top Catal. 28 (2004) 99–103.
4. **Savastenko N., at al.** J. Nanopart. Res. 10 (2007) 277-287.
5. **Savastenko N.A., at al.** Energy Environ. Sci. 4 (2011) 3461-3472.
6. **Savastenko N.A. and Brüser V.** Appl. Surf. Sci. 257 (2011) 3480-3488.
7. **Wirth S., et al.** Plasma process. Polym. 8 (2011) 914-922.
8. **Brüser V., et al.** Plasma process. Polym. 4 (2007) 594-598.
9. **Harnish F.**, et.al. J.Power Sources 193 (2009) 86-92.
10. **Savastenko N.A., at al.** J. Appl. Spectroscopy (Rus.) 83 (2016) 757-763.
11. **Savastenko N.A., at al.** High Temperature Material Processes: An International Quarterly of High-Technology Plasma Processes 21 (2017) 127-142.
12. **Savastenko N.A., at al.** Vesti National. Academ. Nauk Belarusi 2 (2016) 57-67.
13. **Filatova I.**I., **at al.** High Temperature Material Processes: An International Quarterly of High-Technology Plasma Processes 19 (2015) 127-142.

APPLICATION OF PLASMA AND RADIO WAVE TECHNOLOGIES IN AGRICULTURE: PROTECTION OF PLANTS, IMPROVEMENT OF PLANT GROWTH AND YIELD

I.I. Filatova[1], V.A. Lyushkevich[1], S.V. Goncharik[1], N.I. Chubrik[1], A.G. Zhukovsky[2], N.A. Krupenko[2], N.G. Poplavskaya[2], J.N. Kalatskaja[3], V. Mildaziene[4], G. Pauzaite[4]

[1]B.I. Stepanov Institute of Physics, NAS of Belarus, Nezavisimosti Ave. 68, 220072 Minsk, Belarus, filatova@presidium.bas-net.by
[2]RUE «Institute of Plant Protection», Mira Str. 2, 223011 Priluki, Minsk District, Belarus
[3]V.F.Kuprevich Institute of Experimental Botany of NAS of Belarus, Academicheskaya Str. 27, 220072 Minsk, Belarus
[4]Vytautas Magnus University, Vileikos str. 8, LT-44404 Kaunas, Lithuania

Applications of cold plasma technologies due to its unique properties (the presence of active particles, low intensity of ultraviolet radiation and of electromagnetic fields etc.) have expanded into a large number of fields. Plasma can exert a stimulating effect on biological objects, acting simultaneously as a sterilizing agent that opens new prospects for the development and use of plasma technologies in agriculture, ecology, food industry /1/ (Fig. 1). At present, the most significant results have been obtained in the field of plasma application for pre-sowing seed treatment that plays an important role in realizing the genetic potential of the seed. The idea of physical methods applying in pre-sowing seed treatment for increasing the productivity of plants is based on the use of mechanisms of adaptation of the biological system in response to the stressor effect. It is shown that physical stressors (including plasma and electromagnetic field treatments) cause changes in the seeds, which persist until their germination /2/. It is assumed that plasma treatment of seeds increases the ability of plants to further cope with biotic and abiotic stress, such as drought and disease /3, 4/. To create a plasma non-toxic gas mixtures are used, usually ambient air and inert gases, that causes high efficiency and environmental friendly of plasma technologies as an alternative to the traditional chemical methods of seed treatment.

In the vast majority of published works, the effect of physical factors is estimated from the analysis of the germination of seeds and the peculiarities of seedling development in the juvenile stage. Investigations of the sowing characteristics of seeds of agricultural plants are carried out mainly in the laboratory conditions that do not allow estimate the effects of plasma treatment on the subsequent stages of plant ontogeny. There is very limited data on the effect of seed treatment on the crop structure, the phytosanitary state of crops

during the growing season, which are necessary to develop technologies for the industrial use of plasma methods in agriculture.

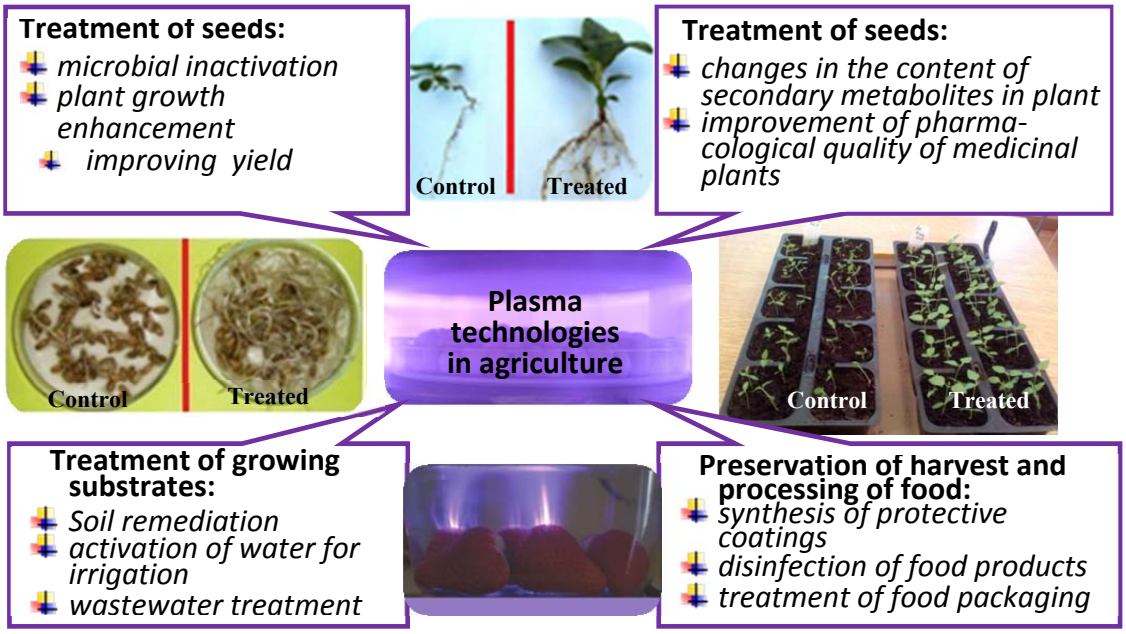

Fig. 1 – Areas of plasma application in agriculture, ecology and food industry

Several type of discharges (glow, corona, microwave, RF, dielectric barrier discharges etc.) at low and atmospheric pressure are used for seeds modification. But despite the fact that plasma sources of atmospheric pressure are more technologically (no vacuum is required), the use of low-pressure plasma is more preferable for careful non-thermal processing of seeds, ensuring their effective disinfection due to direct contact with charged particles /5, 6/.

In this paper, the prospects of seed treatment with cold plasma and RF electromagnetic field for effective cultivation of some agricultural, ornamental, medicinal and woody plants are considered both in laboratory and field tests /6–10/. The effect of treatment on seed germination, plant resistance to common diseases and accumulation of secondary metabolites is discussed.

The treatments with physical stressors were performed in the B.I. Stepanov Institute of Physics of the NAS of Belarus. The sowing qualities and phytosanitary condition of agricultural seeds were studied in RUE "Plant Protection Institute". The sowing characteristics of number of perennial plants were tested in vitro in the Kaunas Botanical Garden (Vytautas Magnus University, Lithuania). The experimental conditions for seed treatment in RF (5.28 MHz) plasma and radio frequency electromagnetic field (EMF) were reported in detail in /6, 7/. The level of accumulation of active oxygen species in dry seeds was measured by electron paramagnetic resonance (EPR). Some results obtained in laboratory and field experiments, are shown in Fig. 2.

Plasma and radio-wave treatment stimulated the germination of seeds with reduced germination (spring wheat, maize), improved the morphophysiological characteristics of seedlings /8/. In the case of perennial crops, the germination of plasma-treated seeds can be increased up to 50% in comparison with untreated samples /9/. Seed treatments also changed the dynamics of germination and drastically shortened the time necessary for germination of 50% of all germinated seeds of perennial plants (black mulberry, Smirnov's rhododendron, purple Echinacea, Norway spruce, etc. /7, 9/). Longer-term observations (during 4–17 months from sowing) revealed that perennial woody plants grown from the treated seeds of all experimental groups developed better: they exceeded the control plants in height, had greater total leaf surface area, the number of leaves, the biomass, and the weight of the roots /7, 9, 10/.

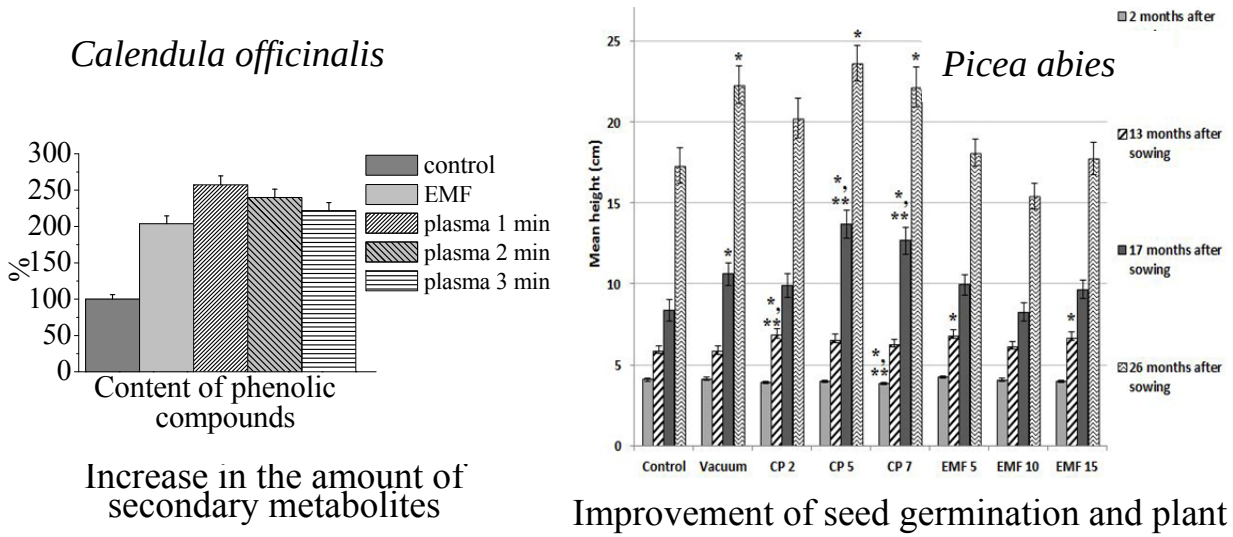

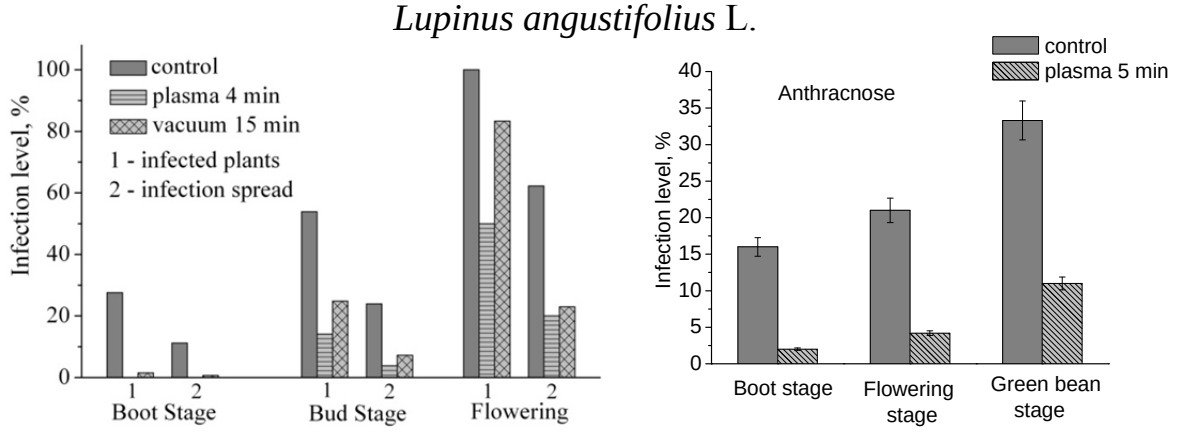

Fig. 2 – Some outcomes obtained as a result of laboratory and field experiments with a number of annual, perennial woody and medicinal plants /6–10/

Pre-sowing seed treatment reduced the development of diseases of agricultural crops during the growing season, in particular, the infection of narrow-leaved lupine with one of the most dangerous diseases – anthracnose. Plasma treatment inhibited the development of anthracnose up to the flowering stage. Thus, seeds treatment with physical stressors can contribute to the stability of plants to phytopathogens during the growing season, which allow optimize the use of chemicals at various stages of plant ontogenesis. From the analysis of the effectiveness of various regimes of pre-sowing treatment of maize seeds, it was revealed that seeds treatment with electromagnetic field for this culture can act as an inducer of increasing the plant resistance ensuring preservation of the physiological quality of the seeds during storage and maintaining the growth rate of plants or their survival /11/.

Plasma and radio-wave treatment of seeds promoted the increase of crop yield and the improvement of its structure. It was revealed that, due to a decrease in the level of seed infection, stimulation of field germination and plant resistance to phytopathogens during the vegetative period, the spring wheat grain yield increased depending on the treatment regime by 4-6%, maize – by 1.5 - 2.0%, narrow-leaved lupine – by 20-28% compared with the control plants.

It has been established, for the first time, that pre-sowing treatment with RF plasma and EMF of seeds of perennial and annual medicinal plants causes stable changes in metabolic processes at the subsequent stages of development and allows increasing the content of medicinal substances in plant. We observed in particular a drastic increase in the amount of cichoric acid (relative amount in leaf extract increased 2.7-fold, amount per plant – 3.8-fold for treatment by EMF 5 min), vitamin C (amount per plant increased up to 1.9-fold for treatment by EMF 5 min and EMF 15 min), and radical scavenging activity (up to 2.1-fold in case of EMF 5 min) in *Echinacea purpurea* leaves /10, 12/.

The treatment of seeds enhanced the content of phenolic compounds (including flavonoid and ascorbic acid) in the inflorescences of *Calendula officialis* L. The total amount of ascorbic acid was considerably higher in comparison to the control in all treated seed groups. The amount of the main secondary metabolite of *Calendula officinalis* – phenolic compounds was increased even more – by 100% after EMF treatment and by 160% as a result of plasma treatment during 1 min. It was established that seed treatment with RF plasma and EMF induced substantial changes of the amount of izoflavones in leaves of *Trifolium pretense.*

Seed treatment with physical factors induced significant changes in the amount of anthocyanins in maize seedlings that was increased up to 2.1-fold in roots, and up to 1.3 fold in leaves in comparison with control. The change in the content of anthocyanins in plant cells is one of the strategies of metabolic adaptation of biological system to the action of stress factors of different nature,

in particular environmental stresses including drought, wounding, pathogen infection and insect attack.

Thus, it is shown that seeds treatment with physical factors such as non-thermal plasma and electromagnetic fields induce not only changes in germination and plant growth but also causes stable changes in metabolic processes at the subsequent stages of plant development, contributes to the height and increasing the biomass of seedlings of the second year of cultivation up to 50%, allows increasing the crop yield, stimulates the accumulation of some pharmaceutically important secondary metabolites in plants.

Acknowledgements. This work is partly supported by the State Committee on Science and Technology of the Republic of Belarus and Belorussian Republican Foundation for Fundamental Research (grant No Ф17ПАКГ-001).

References

[1] Cold plasma in food and agriculture: fundamentals and applications. Ed.: **Misra N. N., Schlüter O., Cullen P. J.** – Elsevier. 2016. – 367 p.
[2] **Yin M. Q. et al.** Plasma Sci. Techno, 7 (2005) 3143–3147.
[3] **Huang, M. J.** J. Shanxi Agri. Sci., 38 (2010) 22–25.
[4] **Jiang J. F et al.** Plos one, 9 (2014) 1–6.
[5] **T. Nishioka et al.,** Biocontrol Sci. 19(2) (2014) 99–102.
[6] **Filatova I.I., Azharonok V.V., Goncharik S.V. et al.** J. Appl. Spectrosc., 81 (2014) 250–256.
[7] **Mildaziene V. et al.** Bioelectromagnetics, 37 (2016) 536–548.
[8] **I.I. Filatova et al.** Proc. of 31st ICPIG, July 14-19 (2013), Granada, Spain: http://www.icpig2013.net/papers/127_2.pdf.
[9] **Pauzaite G. et al.** Plasma Processes and Polymers, 15 (2017) 1700068.
[10] **Mildaziene V. et al.** Plasma Processes and Polymers, 15 (2017) 1700059.
[11] **Kalatskaja J. N., Laman N. A., Filatova I. I., et al.** Proc. of the NAS of Belarus. Biological series, 1 (2018) 7–19 (in Russ.).
[12] https://www.advancedsciencenews.com/natural-medicine-plasma-technology-come-together-new-research.

PLASMA BASED IMMOBILIZATION OF CATALYSTS FOR CHEMICAL SYNTHESIS

V. Brüser[1], S. Peglow[1], Y. Hu[2], T. Werner[2], M. Beller[2], A. Kruth[1]

[1]Leibniz Institute for Plasma Science and Technology, Felix-Hausdorff-Str. 2, 17489 Greifswald, Germany
[2]Leibniz Institute for Catalysis, Albert-Einstein-Str. 29 a, 18059 Rostock, Germany

In chemically catalyzed processes, a distinction is made between homogeneous and heterogeneous catalysis. Homogeneous catalysis refers to catalytic reactions where the catalyst is in the same phase as the reactants. Soluble catalysts are used for synthesis in liquids. Heterogeneous catalysis is the alternative to homogeneous catalysis, where the catalysis occurs at the interface of two phases, typically gas-solid or liquid-solid.

Homogeneous catalysis is often highly efficient, but separating and recovering the catalyst from the product is usually difficult. Heterogeneous catalysts, on the other hand, offer the possibility to be recovered and then recycled back into the catalytic cycle by standardized efficient separation methods, such as e.g. filtration. Application examples for homogeneous catalysis are chemical processes, such as hydroformylation, hydrogenation, cyclization or photochemical water splitting. Homogeneous catalysts can be converted in heterogeneous catalysts by immobilization onto solid substrates as SiO_2, carbon, Al_2O_3 or other materials.

Plasma surface treatment methods are suitable for catalyst immobilization. In our previous work various dye sensitized titania catalysts were used for visible light driven photoelectrochemical water splitting experiments. The dyes were immobilized onto titania substrates by encapsulation with a plasma polymerized allylamine (PPAAm) coating. As dye supports nanopowdered [1, 2] and magnetron sputter-deposited [3] titania semiconductor materials were used. The stability of the Ru dye (N3 ((2,2‘-bipyridine-4,4‘-dicarboxylate)$_2$Ru(NCS)$_2$)/semiconductor assembly was found to be significantly improved by application of a PPAAm nanoconfinement for the sensitizer at the titania surface.

Also PPAAm encapsulation for Ir dye [Ir(pyb)$_2$(dcbpy)][PF_6]/titania catalyst assemblies has been shown to drastically enhance the photoefficiency [4]. The optimum thickness for the polymer layer is found to be between 20 and 50 nm. At smaller layer thicknesses the stability of the catalyst assembly may be compromized whereas at thick layer thicknesses, the mass transport of the electrolyte to the catalytic sites is likely to be hindered. The encapsulated Ir dye is found to outperform the Ru-based dyes by more than twice of the IPCE (Incident Photon to Current Efficiency) value. Ideality factors for the dye/titania

assemblies with 50 nm PPAAm encapsulation show that recombination is smallest for the Ir dye-sensitized TiO_2 layer as compared to the photocatalyst assembly sensitized with commercial N3 dye.

In this study amorphous hydrogenated carbon (a-C:H) thin films were employed for the immobilization of phosphorous based catalysts onto SiO_2 support. The SiO_2 support was impregnated with phosphonium salt by a wet chemical method.

A critical issue with immobilized catalysts is leaching. Leaching means that the catalyst separates from the support and goes into solution. This reduces the proportion of catalyst on the support. When reusing the catalyst/support assembly its catalytic activity is less than before. The better the adheasion to the support, the more often it can be reused.

For the immobilization of the catalysts on the support materials by encapsulation in a-C:H coatings, a PECVD process (Plasma Enhanced Chemical Vapor Deposition) was used. The sample was dispersed on a sample holder in a vacuum chamber of the plasma deposition device ("Piccolo", Plasma Electronic GmbH, Neuenburg). The PECVD process was carried out at a pressure of 15 Pa in a gas atmosphere having the composition $Ar:CH_4$ = 1: 1 and at 600 W RF plasma power (13.56 MHz). The deposition time was 25 min.

The immobilized P-based catalyst was used for ethylene carbonate synthesis experiments by the reaction between ethylene oxide and carbon dioxide. It could be shown that the immobilized catalyst can be reused three times without significant loss of efficiency. Only at the fourth and fifth run, the ethylene carbonate yield decreased.

The phosphor-based catalyst could be successfully immobilized onto SiO_2 support by PECVD process with allyl alcohol as precursor.

Table 1 Recycling experiments with five runs with P-catalyst immoblilized on SiO_2, catalyst loading 1 mol%, yields were determined by ^1H NMR using mesitylene as the internal standard.

Entry	Yield/ %
1st run	90
2nd run	90
3rd run	89
4th run	45
5th run	27

Acknowledgements. We are grateful to the BMBF (FKZ 03XP0060D) for funding this work as part of the "Materialien für eine ressourceneffiziente Industrie und Gesellschaft – MatRessource" initiative. Further, the authors

acknowledge financial support from the Phosphor-Campus: Leibniz-WissenschaftsCampus Phosphorforschung Rostock.

References

1. **Kruth A., et al.** ChemSusChem 6 (2013) 152-159.
2. **Karnahl M., et al.** ChemCatChem 6 (2014) 82-86.
3. **Kruth, A., et al.** J. Phys. Chem. C 117 (2013) 3804-3811.
4. **Kruth, A., et al.** J. Photochem. Photobiol., A 290, no. 0 (2014): 31-37.

Study of the influence of the reflex discharge radial electric field on the propagation of the plasma flow of substances modeling the components of spent nuclear fuel

N. Antonov, G. Liziakin, R. Usmanov, Ya. Murzaev, A. Gavrikov, V. Smirnov

Institute for High Temperatures of the Russian Academy of Sciences, Izhorskaya st. 13 Bd.2, Moscow, Russia 125412, antonovnickola@gmail.com

Introduction

The development of nuclear power industry requires updating technologies related to the processing, transportation and storage of spent nuclear fuel (SNF) and radioactive waste. To date, among the processing methods under development it is possible to highlight gas-fluoride, pyroprocessing and plasma separation approaches. The plasma separation concept /1-6/ can be divided into 3 main stages: a transformation of solid substance into a low-temperature plasma flow, a separation of chemical elements by groups of masses in a special configuration of the electric and magnetic fields in a buffer plasma (buffer plasma is required to compensate the space charge), a deposition of separated substances into collectors. The study of the plasma stream motion characteristics in the crossed electric and magnetic fields in a buffer plasma is an urgent task for the developed nowadays method of SNF plasma processing /1-6/.

When the experimental units of a laboratory setup (plasma source and buffer discharge) are combined, the question of their mutual influence on the distribution of the electrostatic potential and on the trajectory of the ions inside the separation chamber arises. It is necessary to provide a sufficient electric field intensity and to form a certain electrostatic potential profile in the buffer plasma for the effective separation /4/. The results of the experimental study of the reflex discharge and the lead plasma flow (injected along the magnetic field lines and simulating the "heavy" SNF component) mutual influence are presented in this paper.

Experimental setup and results

An experimental setup plasma separation of substances includes the following main units (Fig. 1): a vacuum chamber (it is a cylinder with a diameter of 0.8 m and length of 2 m), magnetic coils (magnetic field intensity is up to 2 kG), a system of an electrostatic radial potential distribution formation (reflex discharge and end electrodes) /7,8/, venting and a pressure control systems (buffer gas is argon), a model substance evaporation and ionization unit (it is a plasma source based on the non-sustained arc discharge with an incandescent cathode /9/). In the experiments described in this paper, no buffer RF plasma generation system was used.

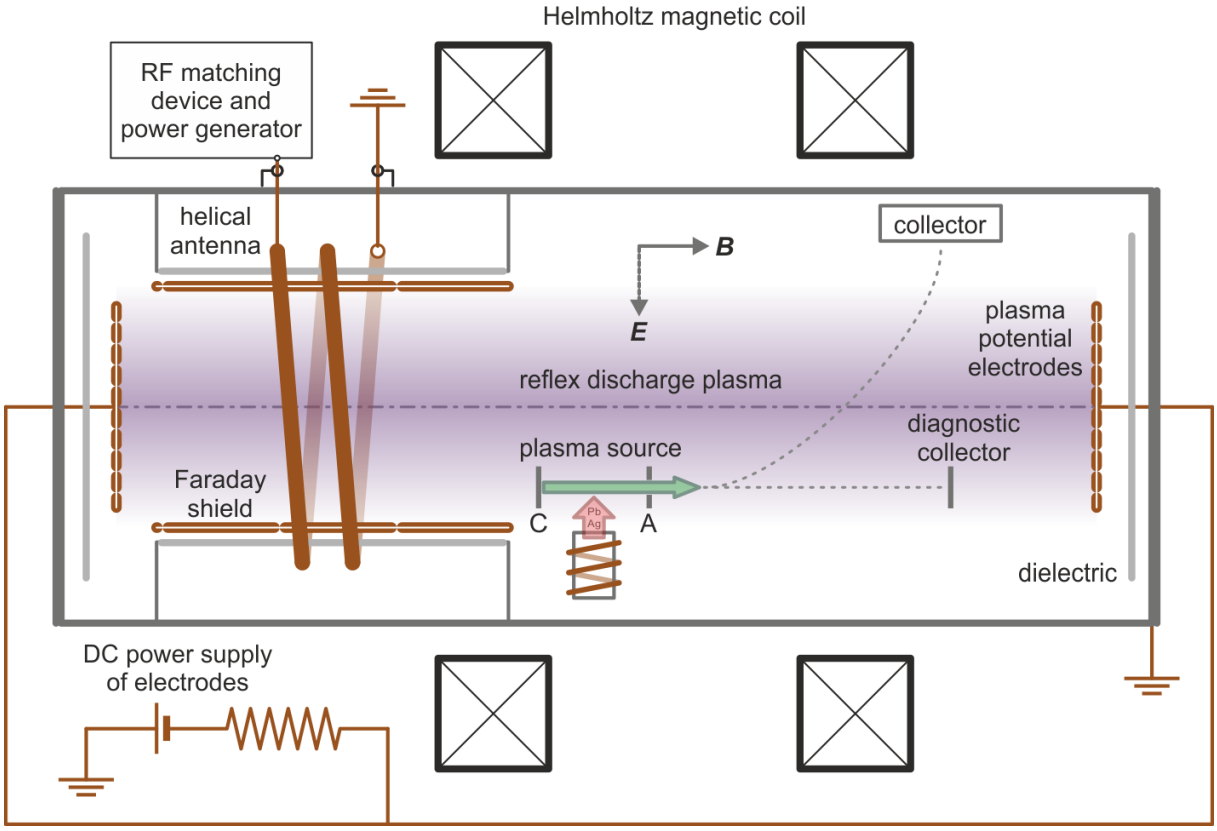

Fig. 1 – A scheme of the experimental setup

The experiment was carried out as follows. Initially, a reflex discharge between a system of the electrodes in the form of truncated cones and a grounded shell of the vacuum chamber was initiated. Argon gas pressure was 0.4 mTorr. The characteristic value of the magnetic field intensity was 1.3 kG, and potential of the end electrodes was about -1200 V (discharge current was about 200-450 mA). The plasma density on the reflex discharge axis was at a level of 10^{10} cm^{-3}. Potential measurements were performed using the floating probe method. The potential difference between the cathode and the anode of the plasma source was maintained at 18 V level (discharge current was about 14 A) /9/. The cathode was grounded. It should be noted that a dielectric material was placed on the outer surface of the hollow anode. In the absence of a dielectric element the anode potential is reproduced along the magnetic field lines. This potential shields the radial electric field of the reflex discharge. Further, in a stationary operation mode of the plasma source, the current of ions coming to the collector was measured in the presence of the reflex discharge and without it. The axis of the plasma source was located at a distance of about 17 cm from the axis of the reflex discharge. The diagnostic collector, which potential was about -50 V, was located at a distance of 540 mm from the hollow anode. The results of the measurement of the plasma source and the reflex discharge mutual influence on the potential radial distribution inside the

separation chamber are shown in figure 2. Measurements were carried out at a distance of about 340 mm from the anode. It can be seen from the figure 2 that the plasma flow has a significant influence on the radial potential distribution. This is due to a significant difference between the reflex discharge plasma density ($\sim 10^{10}$ cm^{-3}) and the plasma density of ionized matter stream ($\sim 10^{12}$ cm^{-3}). It can be seen from Fig. 2, that the cathode potential is efficiently reproduced on the plasma source axis. This leads to the formation of a potential well for the ions of a model substances. It is also worth noting that the radial electric field near the plasma source reached a value of about 10 V/cm.

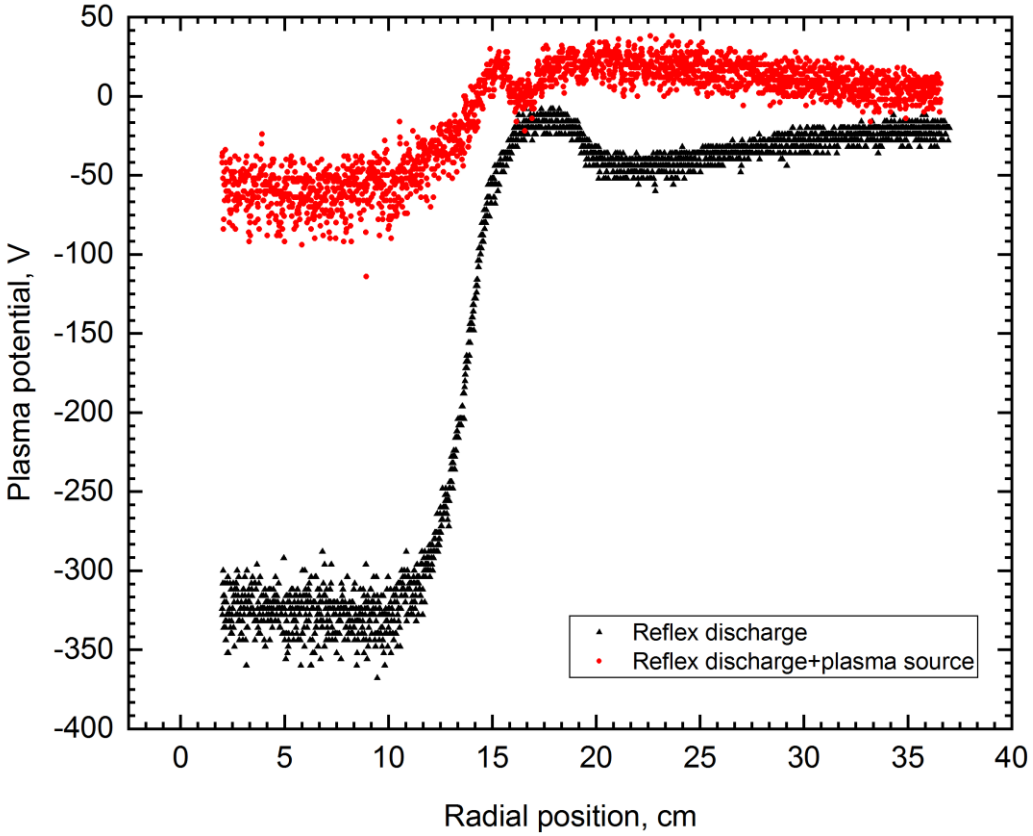

Fig. 2 – The radial distribution of electrostatic potential in the joint operation of the reflex discharge and the plasma source

The ion current in the absence of a reflex discharge was close to 60 mA, and at the discharge initiation the detected current decreased to 8 mA (reflex discharge current was 250 mA). It was concluded from a ratio of the two current values that the efficiency of deflection due to the influence of the electric field formed by the end electrodes of the reflex discharge in the buffer plasma was near 87%. It must be emphasized that the ions current value coming from the reflex discharge buffer plasma in the absence of the lead plasma stream was less than 1 mA. So we have neglected the influence of this factor. An increase of the reflex discharge current (increase of the plasma density) leads to an increase of the deflection efficiency. So at the reflex discharge current of about 450 mA, the

deflection efficiency reaches 95% (the total ion current in the absence of a reflex discharge was 63 mA, and with a reflex discharge was 3.3 mA).

Conclusion

The influence of the radial electric field formed in the reflex discharge argon plasma on the lead plasma stream was studied. The possibility of the plasma stream injected along the magnetic field lines deflection was demonstrated. As part of the research, it was shown, that along the magnetic field lines, based on the thermionic cathode, its electrical potential was reproduced. This underlines the importance of the geometric parameter ratio in the combination stage of the experimental setup units. It should be noted, that the buffer plasma density is an equally important parameter that affects the deflection efficiency.

Acknowledgements. The study was supported by the Russian Science Foundation (project No. 14-29-00231).

References

1. **Zhil'tsov V.A. et al.** Atomic Energy, 101(2006) 755–759.
2. **Bardakov V.M., Kichigin G.N., Strokin N.A. and Tsaregorodtsev E.O.** Technical Physics, 55(2010) 1504–1508.
3. **Gavrikov A.V., Sidorov V.S., Smirnov V.P. and Tarakanov V.P.** Journal of Physics: Conference Series, 946(2018) 012172.
4. **Smirnov V.P., Samokhin A.A., Vorona N.A. and Gavrikov A.V.** Plasma Physics Reports, 39(2013) 456–466.
5. **Papernyi V.L. and Lebedev N.V.** Plasma Physics Reports, 40(2014) 78–82.
6. **Ohkawa T. and Miller R.L.** Physics of Plasmas, 9(2002) 5116-5120.
7. **Liziakin G., Gavrikov A., Usmanov R., Timirkhanov R. and Smirnov V.** AIP Advances, 7(2017) 125108.
8. **Liziakin G.D., Gavrikov A.V., Murzaev Y.A., Usmanov R.A. and Smirnov V.P.** Physics of Plasmas, 23(2016) 123502.
9. **Antonov N.N., Gavrikov A.V., Smirnov V.P., Liziakin G.D., Usmanov R.A., Vorona N.A. and Timirkhanov R.A.** Journal of Physics: Conference Series, 946(2018) 012171.

PLASMA TREATMENT AS AN APPROACH TO CONTROL BIOCOMPATIBILITY OF POLYLACTIDE MATERIALS

T.S Demina[1,2], A.B. Gilman[1], T.A. Akopova[1]

[1]Enikolopov Institute of Synthetic Polymer Materials, Russian Academy of Sciences, 70 Profsoyuznaya str., 117393, Moscow, Russia, e-mail: detans@gmail.com
[1]Institute for Regenerative Medicine, Sechenov University, 8-2 Trubetskaya st., Moscow, 119991, Russia

Plasma treatment is one of the most effective and powerful tool to control surface properties of materials, especially ones tailored for biomedical applications. A possibility of varying plasma treatment conditions allows to control surface chemistry, morphology and properties in a wide range. Polylactide-based materials are widely used for tissue engineering due to their biocompatibility, biodegradability and high mechanical properties. However, the surface of such materials suffers of hydrophobicity and a lack of specific functional groups to support cell adhesion and growth.

This research was aimed to investigate an effectiveness of DC discharge treatment of various polylactide-based materials as a direct approach to modify its surface properties or as a tool to preliminary activate it for further immobilization of different bioactive components. Film samples and non-woven mats made of poly(L,L-lactide) or its graft-copolymer with chitosan and gelatin were treated at an air pressure of 10-20 Pa and a discharge current of 50 mA for 60 s. Chemical structure, morphology and wettability of surface layer of native samples and treated by DC discharge at the cathode and anode were evaluated using X-ray photoelectron spectroscopy, scanning electron microscopy and contact angle measurements. Effect of plasma treatment on further immobilization of hyaluronic acid and collagen onto the samples were investigated as well.

Acknowledgements. The reported study was funded by RFBR according to the research project № 18-32-00901.

References

1. **Demina T.S., Gilman A.B., Zelenetskii A.N.** High Energy Chemistry 51(2017) 302–314.
2. **Demina T., Zaytseva-Zotova D., Yablokov M., Gilman A., Akopova T., Markvicheva E., Zelenetskii A.** Surface and Coatings Technology 207(2012) 508–516.

Experimental and theoretical study of plasma-based formation of free-standing N-graphene

D. Tsyganov[1], N. Bundaleska[1], A. M. Botelho do Rego[2], A. M. Ferraria[2], E. Tatarova[1]

[1]Instituto de Plasmas e Fusão Nuclear, Instituto Superior Técnico, Universidade de Lisboa, Lisboa, 1049, Portugal
[2]Centro de Química-Física Molecular and IN, Instituto Superior Técnico, Universidade de Lisboa, 1049, Portugal

Abstract. *In situ* direct synthesis of free-standing nitrogen-doped graphene structures was achieved in a single step method by employing microwave plasma at atmospheric pressure conditions. The technique is based on injection of nitrogen-containing precursor together with hydrocarbon in the reactive plasma environment. Nitrogen gas and ethanol were used as source of both nitrogen and carbon.

Introduction. Nitrogen doping proved to be an effective way of tailoring the properties of graphene, which in turn widen its practical application /1/. The addition of nitrogen atom impurities into pristine graphene increases the electrochemical activity of N-doped graphene (NDG) due to creation of "active sites". NDG can be used directly as a catalyst in oxygen reduction reaction or as a support for the metal catalyst; it is also of great interest for fuel cells, lithium ion batteries, solar cells and sensors /2/.

There are numerous synthesis methods for graphene and NDG, as chemical vapor deposition (CVD), bottom-up syntheses, wet chemical methods, plasma methods etc. To this end, plasma techniques are applied for both the initial synthesis of graphene and for its post processing /1, 3/. The reactive plasma medium can provide fixation of different chemical species to the graphene structure, thus making the plasma an effective doping tool.

In this study, a surface-wave driven microwave type plasma working at atmospheric pressure has been used for direct selective synthesis of NDG structures. Ar was used as a background gas, while ethanol and N_2 gas were used as carbon and nitrogen precursors, respectively. Optical emission spectroscopy (OES) was applied to detect the emission from the plasma and to estimate the gas temperature. The synthesized material was analysed by SEM and XPS. A chemical kinetic model describing the ethanol decomposition in the argon plasma environment previously developed was further updated for ethanol-nitrogen mixture. The resulting distributions of the produced species along the discharge give insight into the main mechanisms of solid carbon formation.

Experimental setup. A surfatron-based setup was used to create a surface wave induced microwave plasma at atmospheric pressure conditions (Fig. 1) /4/. A 2.45 GHz generator, whose output power was fixed to 2 kW, provides the

microwave power. The discharge takes place inside a quartz tube reactor, which is inserted downstream vertically and perpendicularly to the waveguide wider wall. The quartz reactor comprises two sections; a small one with internal and external radii of 0.75 cm and 0.9 cm, respectively, connected via conical section to the large tube with internal and external radii of 2.15 cm and 2.3 cm. The vaporized precursor, i.e., ethanol molecules is injected in the plasma together with N_2. The background argon flow is kept constant at 1200 sccm; the ethanol partial fluxes were varied in the range 30-35 sccm. To test the direct NDG synthesis in the plasma, nitrogen gas flow was injected to the reactor at Q_{N2}=10, 30, 50. The synthesized nanostructures were captured by a Hurricane Cyclone system followed by a methanol trap.

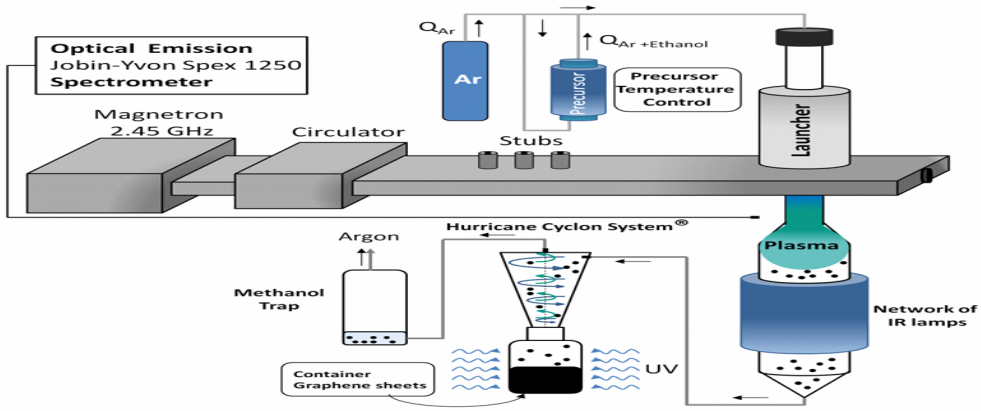

Fig. 1 – Scheme of experimental setup.

The plasma emission spectra in the visible range (230-750 nm) was detected. The emission spectrum of argon/ethanol/nitrogen plasma reveals the presence of new molecular and atomic species such as CN (violet system, $B_2\Sigma \rightarrow X_2\Sigma$), C_2 (Swan system, between 450–570 nm, $A_3\Pi g \rightarrow X'_3\Pi u$), C atoms (247.9 nm), the hydrogen Balmer-alpha line Hα (6563 Å) and several Ar lines. These species are formed because of ethanol and N_2 dissociation.

SEM images of NDG samples synthesized at 2 different conditions are shown in Fig. 2. The samples contain only graphene-like sheets and indicate a more compact structure than the one of pure graphene sheets.

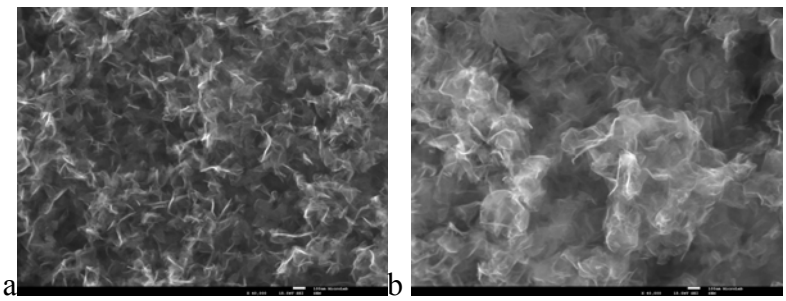

Fig. 2 – SEM images of NDG samples at
a) Q_{Et} = 30 sccm, Q_{N2} = 30 sccm; b) Q_{Et} = 30 sccm, Q_{N2} = 50 sccm.

Relatively small amount of nitrogen was detected with XPS. The N 1s region was fitted with one peak, in the center at a binding energy 401.2±0.2 eV, corresponding to graphitic nitrogen. The quantitative analysis shows that the relative atomic concentration of nitrogen incorporated in the graphene scaffold is 0.23% for the conditions Q_{Et}=30 sccm, Q_{N2}=30 sccm. The relative atomic concentration of incorporated oxygen is 2.8%.

Theoretical model. The model is based on a set of non-linear differential equations describing plasma thermodynamics and chemical kinetics. The model predictions were validated by experimental results. In order to account formation of nitrogen-carbon spaces in the outlet gas stream, 200 additional reactions and 10 new spaces were included /5/. The wall temperature axial profile was experimentally determined and fitted by an analytical expression.

Results and discussion. Hydrocarbon-like CxHyOz and nitrogen molecules dissociate in the plasma environment via a series of dehydrogenation reactions giving rise to various species such as CxHy, NxHy, CN, HCN, N, H (Fig. 3).

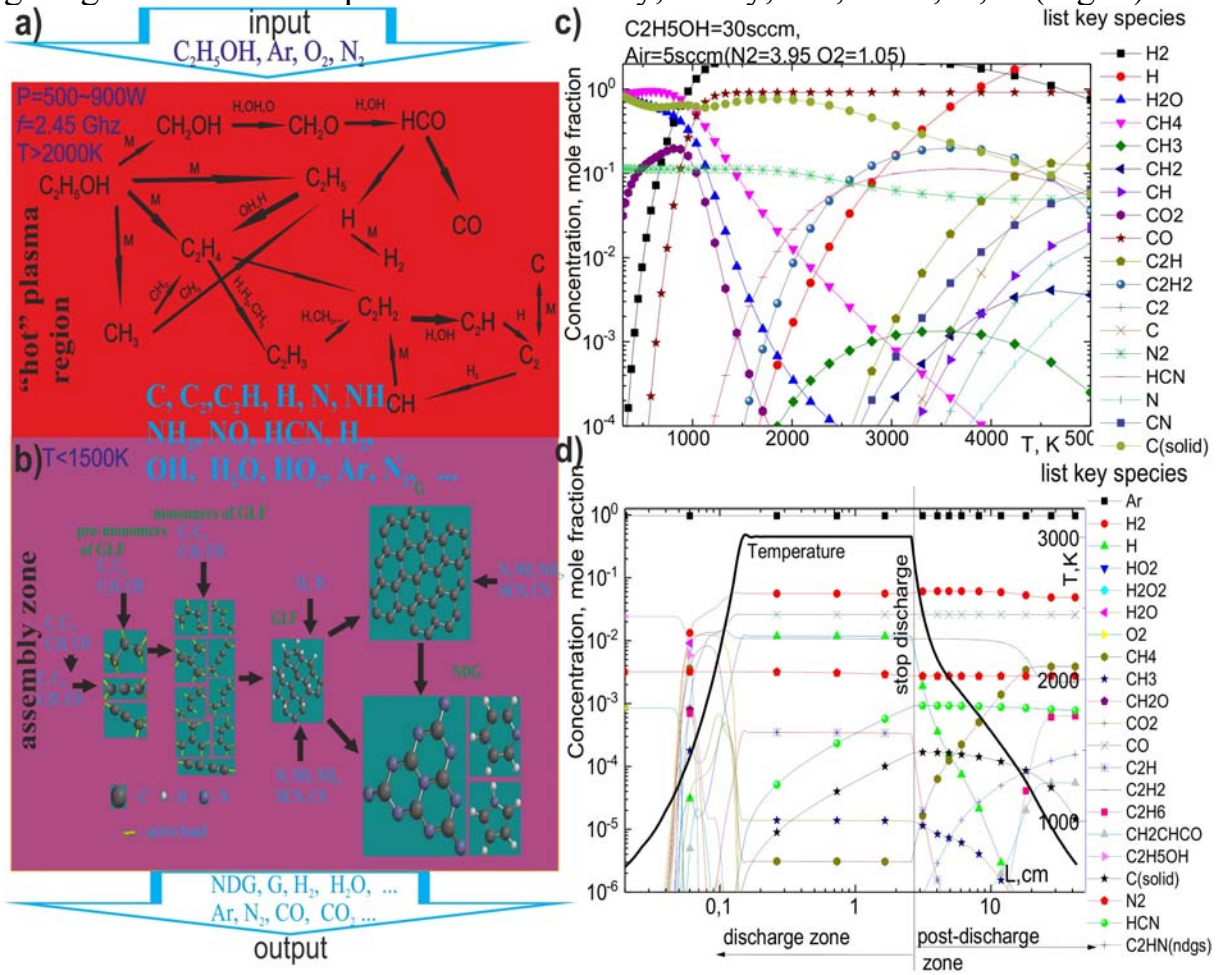

Fig.3 – (a) Scheme of the main processes in "hot" plasma zones, (b) typical processes that occur from the formation of the nuclei (the pre-monomer of graphene-likes forms (GLF)) to graphene (G) and NDG, (c) Simplified equilibrium diagram for main ethanol decomposition products and (d) Evolution of the species concentrations in the discharge and the afterglow

The initiation of the nucleation process is complicated and challenging to understand and describe. The formation of the nuclei - "the birth" - as the first and the most important step in the growth of graphene and NDG structures was never available for observation, and this initial stage of growth was completely devolved to theoretical modelling.

Smaller carbon species (C, C_2, C_2H, CH) form monomers, which further grow into GLF structures. The available H atoms migrate between islands of graphene, and form H_2 molecules, which simply evaporate. Some of the new-formed in the plasma species such as N, NH_2, NH_3, CN, HCN, as well as bigger clusters of graphene-like structures, attach to the island clusters at its edge and create NDG sheets. This hypothesis is not in contradiction with the experimental and theoretical results.

Conclusions. A successful direct synthesis of NDG structures applying microwave-driven plasma reactor at atmospheric pressure was achieved. The method is a simple, rapid, environmentally friendly single-step technique for selective synthesis of graphene / NDG nanostructures. It is also non-disruptive and does not employ harsh chemicals, metal catalysts or substrates. The developed chemical kinetic model provides insight into the processes of precursor's decomposition and formation of the main output products.

Acknowledgements. This work was performed under de framework of the PEGASUS (Plasma Enabled and Graphene Allowed Synthesis of Unique nano-Structures) project, funded by the European Union's Horizon research and innovation programme under grant agreement No 766894 and partially supported by Portuguese FCT - Fundação para a Ciência e a Tecnologia, under Project UID/FIS/50010/2013.

References.

/1/ Xuewan Wang, Gengzhi Sun, Parimal Routh, Dong-Hwan Kim, Wei Huangb and Peng Chen, Heteroatom-doped graphene materials: syntheses, properties and applications, Chem. Soc. Rev., 2014, 43,7067

/2/ Yanhong Lu, Yi Huang, Mingjie Zhang, and Yongsheng Chen, Nitrogen-Doped Graphene Materials for Supercapacitor Applications, Journal of Nanoscience and Nanotechnology Vol. 14, 1134–1144, 2014

/3/ A Dias, N Bundaleski, E Tatarova, F M Dias, M Abrashev, U Cvelbar, O M N D Teodoro and J Henriques, Production of N-graphene by microwave N2-Ar plasma, J. Phys. D: Appl. Phys. 49(2016) 055307 (9pp)

/4/ E. Tatarova, J. Henriques, A. Dias, M. Abrashev , N. Bundaleska, N. Bundaleski, A.M. Botelho do Rego, A.M. Ferraria, E. Kovacevic, U. Cvelbar, E. Valcheva, J. Berndt, E. Felizardo, L.L. Alves, B. Gonçalves, "Towards large-scale in free-standing graphene/N-graphene sheets", *Scientific Reports* **7**, Article number: 10175 (2017), doi:10.1038/s41598-017-10810-3

/5/ N.M. Marinov A Detailed Chemical Kinetic Model for High Temperature Ethanol Oxidation. Int J Chem Kinet. 31. 1999. 3. P.183.

INACTIVATION COMPONENTS PRODUCTION MECHANISMS OF AN AIR DC PLASMA JET

V.I. Arkhipenko, A.V. Kazak, A.A. Kirillov , L.V. Simonchik, V.V. Shkurko*

B.I. Stepanov Institute of Physics of NAS of Belarus, 68-2 Nezavisimosty Ave., 220072, Minsk, Belarus, a.kirillov@dragon.bas-net.by
*Graduate School of the National Academy of Sciences of Belarus, 1 Knorina Ave., Minsk, Belarus

1. Introduction

A special place among the promising sources for biomedical applications of the atmospheric pressure nonequilibrium plasma is occupied by plasma jets that allow objects processing of various shapes and sizes outside a closed discharge volume /1/. Plasma jets sources are distinguished by the type of gas discharge, the configuration of the electrodes, and the composition of the working gas. Examples of such sources are generators of plasma jets based on high frequency and microwave discharge, barrier discharge, arc discharge and other types of discharges /2, 3/.

The working gas of plasma jets supported by alternating or pulsed-periodic voltages with frequencies from kilohertz to gigahertz is usually an inert gas or an inert gas with small additions of molecular gases, which is associated with the difficulty of generating a discharge in a molecular gas. They require high-voltage power sources, which imposes certain requirements for their safe operation. The low-temperature plasma jets of molecular gases based on a self-pulsating spark discharge or on a microdischarge with a hollow cathode have a significant drawback in the large content of electrodes in the plasma jet, which limits their use in medicine.

"Cold" plasma jets based on a direct current atmospheric pressure glow discharge (APGD) have a number of advantages: the possibility of using both inert and molecular working gases; simplicity of the device; small erosion of electrodes /4, 5/. The paper studies the production mechanisms of the main bactericidal components of “cold” air plasma jets generated by the APGD.

2. Experimental setup

Plasma jets based on the APGD are generated in a two-electrode gas-discharge chamber with an internal diameter of 8 mm and an interelectrode gap of about 1 mm at an air flow rate of 5 l / min from a 30 mA DC source (Fig. 1). The plasma-forming gas flows through specially constructed channels in the cathode to the gas-discharge cell, passes through the discharge region and forms a plasma jet through the central hole of 1.5 mm at the exit from the anode. As a

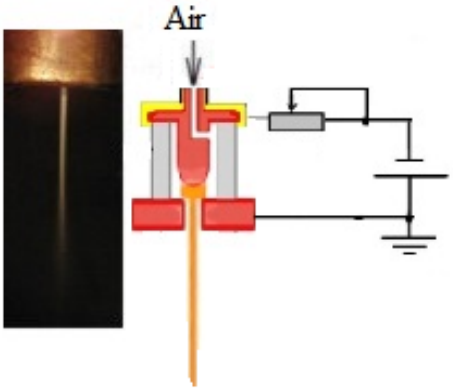

Fig.1. Photo air plasma jet and scheme of discharge device

result, a glow of plasma jet of 2-3 mm in diameter and several centimeters in length is observed.

Emission spectra of the jets were recorded using a diffraction monochromator MDD 500x2 in two directions: first, in the direction of the plasma jet-chamber along the observation line passing through the hole in the anode and coinciding with the axis of the jet, secondly, along the line of sight orthogonal to the axis of the jet with the recording of the spectrum of the jet part located 1 cm below the edge of the anode.

In Fig. 2 spectra are presented with the same intensity unit. It is easy to see that in the case of axial observation (Fig. 2a), the spectrum corresponds to the APGD emission endowing the decisive contribution to the detected radiation of the jet.

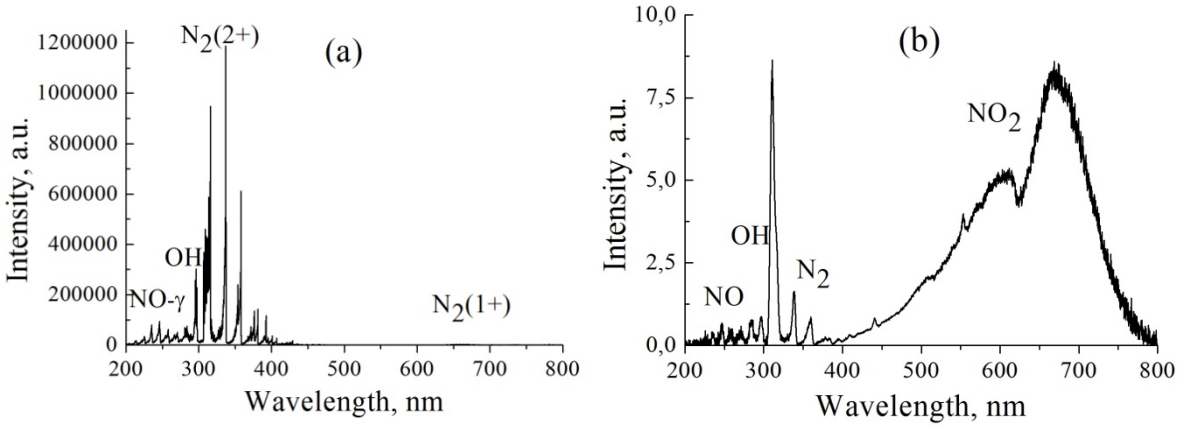

Fig. 2. The emission spectra observed along (a) and transverse (b) axis

The gas and vibrational temperatures of the APGD were determined using the vibrational-rotational bands of the second positive nitrogen system N_2 ($C^3\Pi_u - B^3\Pi_g$) and reached 1600 K and 2850 K respectively. The temperature in the plasma jet was measured using an isolated chromel-alumel thermocouple K-type with a wire diameter of 0.3 mm. When removed from the anode, the gas temperature decreases from 520 K to 318 K (45 C) at a distance of 4 cm due to mixing with the ambient air in turbulent mode with the number Re = 3000.

The emission spectrum of the jet contains bands of electron-vibrational transitions of nitrogen molecules, hydroxyl OH, oxide and nitrogen dioxide (Fig. 2b). It was shown in /4/ that the main bactericidal components of air plasma jets generated by the APGD are oxygen and nitrogen containing components: NO, NO_2 and HNO_2.

The concentrations of bactericidal components were determined by the methods of absorption IR spectroscopy. Absorption spectra were recorded in the spectral range 600-4000 cm^{-1} using the infrared Fourier spectrometer Nexus (Thermo-Nicolet) with the gas cuvette 186-0305 (Perkin-Elmer).The optical path of the gas cuvette was 135 cm. The gas was taken to the cuvette using a

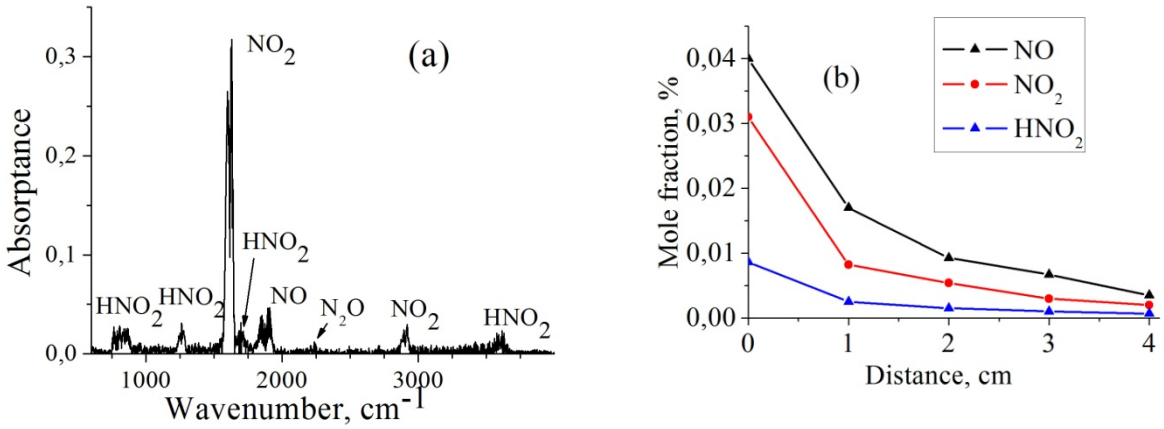

Fig. 3. The absorption spectrum at a distance of 1 cm from the anode (a) and the bactericidal components concentrations dependence on the distance from the anode (b)

3.5 mm diameter tube that was placed on the axis of the jet parallel to the gas flow. Concentrations of the bactericidal components of the jets were determined by comparing the experimental and calculated absorption spectra calculated using the HITRAN spectral data base.

3. Results and discussion

The main nitrogen monoxide production takes place in the nonequilibrium plasma of the APGD, where N, O, and OH are produced in plasma-chemical reactions involving electrons. Taking into account the measured gas temperature of 1600 K and the typical density of ~ 10^{12}–10^{13} cm^{-3} and average electron energy of 1 eV for discharge in molecular gases at a current of 30 mA /6/, analysis shows that these processes are more effective than thermal dissociation of nitrogen, oxygen and water molecules. In addition, an insufficiently high temperature in the discharge leads to a very low reaction rate of oxygen atoms with nitrogen molecules. Therefore, the NO production can not be correctly described within the framework of the Zeldovich thermal mechanism and requires kinetic analysis taking into account plasma-chemical reactions.

The equilibrium constant for the reaction of oxidation of nitric oxide to nitrogen dioxide $NO+\frac{1}{2}O_2 \rightleftarrows NO_2$ is 0.0085 at the temperature of 1600 K and exceeds 1 at the temperature below 800 K. Therefore, conditions for thermal

dissociation of nitrogen dioxide molecules are provided in the active zone of the discharge. The increase in NO_2 concentration begins with a decrease in temperature downstream in the discharge chamber and continues in the jet.

The NO_2 production in the three body chemiluminescence reaction $NO+O+M \rightarrow NO_2+M+h\upsilon$ with the participation of NO and O is accompanied by intense emission of the jet in the spectral range of 400-800 nm (Fig. 2a). Nitrous acid molecules, decaying in the reaction $HNO_2 + M \rightarrow OH + NO + M$, are less thermally stable than nitrogen dioxide molecules. Therefore, the formation of nitrous acid occurs at low temperatures outside the APGD zone.

Due to the high rate constants of hydroxyl OH reactions with the products of plasma-chemical reactions, the concentration of OH decreases sharply when its formation ceases. Therefore, at a distance of 4 cm from the hole, OH is practically absent. For the same reason, hydroxyl OH could not be detected with the help of the absorption spectroscopy technique we used, since the absorption spectrum was recorded after the gas was taken into the cuvette and placed in a Fourier spectrometer.

The absence of a noticeable concentration of ozone in the jet is apparently caused by the following reasons. Due to the low bond breaking energy, O_3 begins to be produced in the stream at a low temperature, i.e. after NO and NO_2. The fast three body reaction of NO_2 formation "takes away" the oxygen atoms necessary to produce O_3. The nascent ozone molecules die in collisions with molecules of nitrogen monoxide and nitrogen dioxide, already having a significant concentration.

Acknowledgements. This work was supported by the Belarusian Republican Foundation for Fundamental Research (grant No. F17IC-030).

References

1. **Weltmann K.-D., Metelmann H.-R., Woedtke Th.** Europhysics News, 47(2016) 39–42.
2. **Graves D.B.** Physics of Plasmas, 21 (2014) 080901.
3. **Fridman A., Friedman G.** Plasma Medicine. New York: John Wiley & Sons (2013).
4. **Kirillov A.A., Paulava A.V., Safronau Y.A., Simonchik L.V.** Applied Physics, (2013) 52–55 (in Russian).
5. **Kazak A.V., Kirillov A.A., Simonchik L.V., Nezhvinskaya O.E., Dudchik N.V.** Plasma medicine, 7 (2017) 109 –115.
6. **Arkhipenko V.I., Kirillov A.A., Safronau Y.A., Simonchik L.V., Zgirouski S.M.** Eur. Phys. J. D 66 (2012) 252.

DEPOSITION OF DOUBLE-LAYER COATINGS FOR PREPARING COMPOSITE MEMBRANES WITH SYPERHYDROPHOBIC PROPERTIES

L. Kravets[1], M. Yarmolenko[2], A. Rogachev[2], R. Gainutdinov[3], N. Lizunov[1]

[1]Joint Institute for Nuclear Research, Flerov Laboratory of Nuclear Reactions, Joliot-Curie Str. 6, 141980 Dubna, Russia
[2]Francisk Skorina Gomel State University, Sovetskaya Str. 104, 246019 Gomel, Belarus
[3]Shubnikov Institute of Crystallography of FSRC "Crystallography and Photonics" Russian Academy of Sciences, Leninskii pr. 59, 119333 Moscow, Russia
E-mail: kravets@jinr.ru

The present paper describes the possibility of double-layer superhydrophobic coating formation on a porous substrate by the electron-beam sputter deposition of the polymers. As a porous substrate a poly(ethylene terephthalate) track-etched membrane (PET TM) with a thickness of 9.5 μm and pore diameter of 250 nm (pore density of 2×10^8 cm^{-2}) was used. Ultra-high molecular weight polyethylene (UHMW-PE) was used for sputtering to form the first hydrophobic layer on the membrane surface and polytetrafluoroethylene (PTFE) was used for sputtering to form the second superhydrophobic layer.

The electron-beam generator with filamentary cathode which allows to form beams with current density of 0.01-0.03 A/cm^2, energy E = 0.8-1.6 keV is used as the electron source. The deposition process of coatings was produced at initial pressure of residual gas in the vacuum chamber $\approx 4\times10^{-3}$ Pa. The growth rate in the deposition process was monitored by quartz crystal microbalance. Powders from UHMW-PE ($M_w = 5\times10^6$; density = 0.93 g/cm^3, Foresight Global FZE) and PTFE (density = 2.15 g/cm^3, Aldrich) were used as target materials without additional drying before application.

The characteristics of the original membrane and membranes with the deposited polymer coatings were determined by different procedures. The amount of the deposited polymer on the membrane surface was defined by the gravimetric method. The gas flow rate through the membranes was determined at an adjusted pressure drop by a float-type flow meter. From the obtained data, the effective pore diameter was calculated using the Hagen-Poiseuille equation. The microstructure of membrane samples was studied by a scanning electron microscope Hitachi SU-8020 (Japan). Morphology of the membrane surface was studied by an atomic force microscope NTEGRA Prima (NT-MDT, Russia). The surface properties were characterized by values of the contact angle measured with an Easy Drop DSA100 instrument (KRUSS, Germany) and the software Drop Shape Analysis V.1.90.0.14 using deionized water as a test liquid.

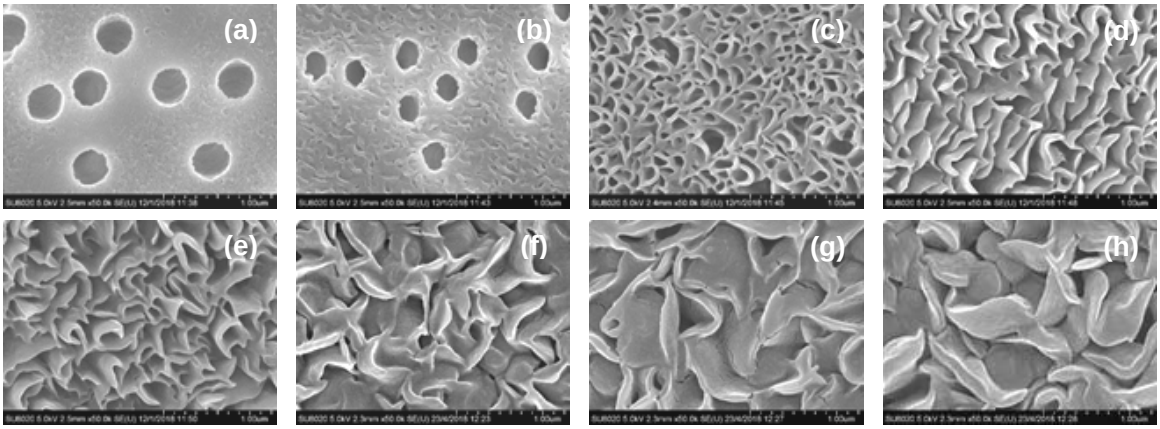

Fig. 1 – SEM images of the (a) original PET TM and membranes with applied coating of UHMW-PE with a thickness of (b) 100, (c) 200, (d) 300, (e) 500, (f) 700, (g) 900 and (h) 1200 nm

The investigation of the deposition process of UHMW-PE coating on the PET TM surface shows that, as the thickness of the deposited polymer coating increases, the effective pore diameter decreases. Reduction of the effective pore diameter of composite membranes (CMs) means that the pore diameter in the deposited polymer is less than the pore diameter of the original PET TM. Electron microscopic examination of the CMs surface (Fig. 1) has shown that for the membrane with the UHMW-PE coating of 100 nm (Fig. 1b) there is a slight decrease in the pore diameter on the surface. The surface of the deposited polymer coating has a slightly pronounced roughness. As the thickness of the deposited UHMW-PE coating increases, the pore diameter on the membrane surface decreases. So, the decrease in the pore diameter for the membrane with a coating thickness of 200 nm (Fig. 1c) is more significant. The deposited coating of the polymer thus acquires a mesh shape and becomes more roughness. Further increase in the thickness of the applied UHMW-PE coating leads to the formation of an ordered rough morphological structure on the membrane surface (Figs. 1d-1h). The effective pore diameter of the CMs is significantly reduced in these cases. From the electron microscopic data, it also follows that the pore diameter on the backside of the composite membranes remained unchanged, thereby implying that the polymer is not deposited in part of the pore channels. The electron-beam sputter deposition of a UHMW-PE coating on the PET TM surface thus leads to the formation of CMs having an asymmetric (tapered) shape of pores; the pore diameter remains unchanged on the untreated side of the membrane and significantly decreases on the modified side. This result correlates with the data obtained in our study of the modification of track-etched membranes by plasma polymerization /1, 2/.

Study of the morphology of CMs surface using AFM confirms the conclusion that during the UHMW-PE coating deposition on the PET TM surface there is a development of its roughness. Thus, for the original

membrane, the mean square deviation (R_{ms}) surface profile calculated for all scan points with an area of 5×5 μm^2 equal to 58.9 nm. The relatively high value of roughness is due to the presence of pores on the membrane surface, and the method of manufacturing the track-etched membranes, including chemical etching. The presence of pores has a more noticeable effect on the value of roughness. This is indicated by the determination of such parameters as the average height of the peak of the roughness (R_{pm}) and the average depth of the cavity of the roughness (R_{vm}) of the middle line of the surface profile. Evaluation of these parameters for the original membrane leads to the following results. The R_{vm} value is 52.1 nm, while the R_{pm} value is 30.8 nm, which is much lower.

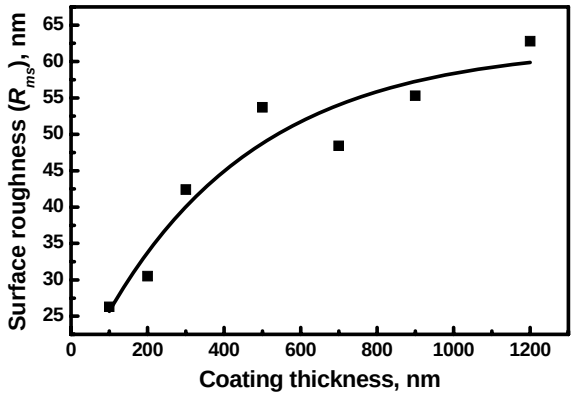

Fig. 2 – Plot of surface roughness of deposited UHMW-PE coating as a function of its thickness

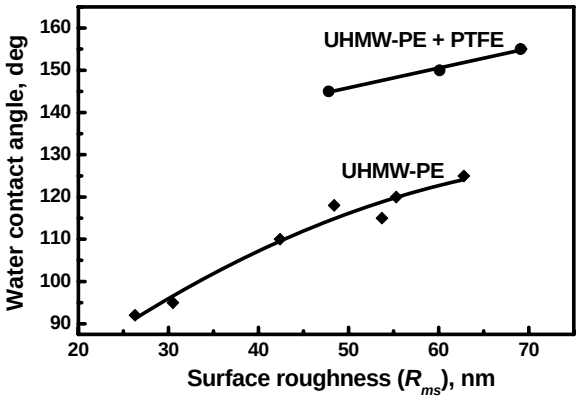

Fig. 3 – Plot of contact angle values of the CMs surface as a function of coatings roughness

Deposition of UHMW-PE coating on the surface of PET TM leads to a change in its surface roughness. The studies show that at the coating thickness of 100 nm surface smoothing is observed. The R_{ms} values decreases for this CM. This result is explained by the formation of a polymer in the pore channels at a certain depth from the entrance and the overlapping of pores on the membrane surface. However, the increase in coating thickness leads to increased surface roughness (Fig. 2). The R_{ms} values for the CMs markedly grow. The increase of R_{ms} value of the membrane surface during deposition indicates that the UHMW-PE coating has a more developed surface compared to the surface of the original track-etched membrane and the value of the surface roughness depends significantly on the duration of the deposition process.

The study of the surface properties of composite membranes shows that the deposition of UHMW-PE coating on the PET TM surface leads to substantial hydrophobization. If the original PET TM has the water contact angle (CA) of 65°, whereas the membranes with UHMW-PE coating have the CA from 92° to 125°, depending on its thickness as well as on the surface roughness (Fig. 3). This change is due to the development of roughness of the deposited coating having hydrophobic properties with an increase in its thickness. Therefore, the

application of the UHMW-PE coating on the surface of the PET TM thus leads to the formation of CMs consisting of two layers, one of which is the original PET matrix characterized by a medium level of hydrophilicity. The second layer deposited by means of UHMW-PE electron-beam sputtering in vacuum is hydrophobic in nature.

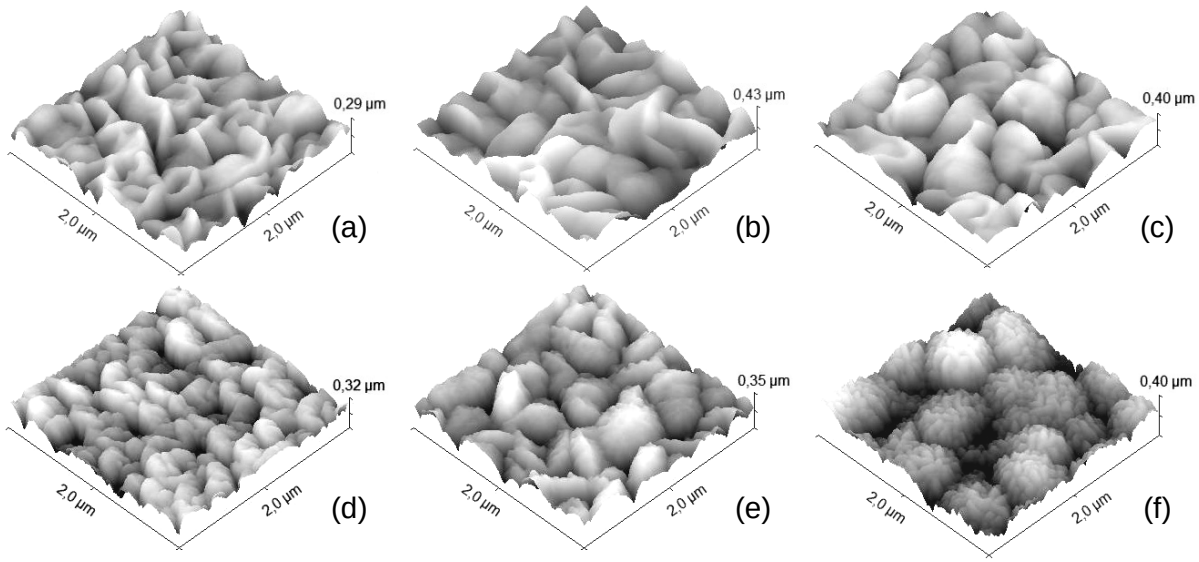

Fig. 4 – AFM scan images (2×2 μm^2 area) of applied on the PET TM surface UHMW-PE coating with a thickness of (a) 700, (b) 900 and (c) 1200 nm; (d-f) the same CMs with additionally applied second PTFE coating with a thickness of 100 nm

Formation on the CMs surface the second layer with a thickness of 100 nm obtained by electron-beam sputter deposition of the PTFE results in formation of superhydrophobic coatings. The values of water contact angle for this type CMs are 145°–155° (Fig. 3). It can be explained by the lower surface energy of the fluoropolymer and also by more significant development of the roughness of PTFE coating (Figs. 4d-4f) compared to the UHMW-PE coating (Figs. 4a-4c). In addition, in this case we observe formation of polymer particles with hierarchical structure (Fig. 4f).

Acknowledgements. This work was performed in the frame of collaboration between the JINR, FLNR (Dubna) and GSU (Gomel), contract no. 4783-5-18/21. We are grateful to Russian Foundation for Basic Research (grant No. 17-08-00812) for financial support.

References

1. **Kravets L.I., Dmitriev S.N., Altynov V.A., Satulu V., Mitu B., Dinescu G.** Rus. J. Electrochem., 47 (2011) 470–481.
2. **Kravets L.I., Dmitriev S.N., Goryacheva T.A., Satulu V., Mitu B., Dinescu G.** Membr. Membr. Technol., 1 (2011) 126–138 (in Russian).

COMPARISON OF DIRECT PLASMA GASIFICATION AND COMBINED THERMOLYSIS-PLASMA PROCESS

A. Liavonchyk, V. Sauchyn, S. Shabunya, D. Skamarokhau, N. Kurbanov

A.V. Luikov Heat and Mass Transfer Institute of the National Academy of Sciences of Belarus, Minsk, 15 P.Brovka str. ita1661@gmail.com, v.sauchyn@gmail.com

Introduction During human life a significant and constantly growing waste stream with a predominant organic part appears. Problem of environmentally friendly and economic method of the waste recycling is still not solved. One of such methods is waste processing with thermal plasma /1-4/, which means complicated organic substances decomposition up to two and three atomic gases forming in conditions of partial oxidizing and further its utilization. Non-organic part of the wastes can be melted into homogeneous slag. The other proposed way is combined thermolysis-plasma technology, which greatly simplifies the process control, gives an opportunity to work with materials of different fractions and to obtain useful co-products with little change in the technology.

Experimental Experimental facility for direct plasma processing is described in details in /5/. For the combined process reactor STR-10 /6/ was connected to the plasma reactor, which was described in /7/. Firstly, material enters the pyrolysis reactor, where it is divided into a gas mixture and a carbon residue, which can be processed separately. Wood saw and tire scrap were selected as model materials.

Results and discussion According to results of thermodynamic calculation for wood and tire scrap and data in the literature /2, 4/ composition of obtained gas varies slightly in temperature range of 1200-2000K. Reaction speed grows with the temperature increase. Data from /4/ was used to estimate maximum size of the particle that can be treated in the reactor. It was found out, that the size of wood particle should not exceed 4 mm. It was proved in the experiments too. Estimated energy costs for conversion of wood and tire scrap and its evaporated fractions in different media are presented in Fig. 1.

Thermodynamic calculations performed for air-steam gasification of wood showed that if the oxidizer is in exceed, there is a maximum of hydrogen concentration and a minimum of water concentration at temperature of 1000K. For practical use mass fraction of the material should be not less than 0,5, mass fraction of steam – not more than 0,25.

Experimental studies of direct gasification of tire scrap showed that size of a particle should be much less than for wood due to the absence of oxygen in the material. It takes more time to complete all the process of the conversion. Our estimations showed that the size should be not more than 0,7 mm and

experiments proved that 1 mm size is too big to be treated in the reactor.

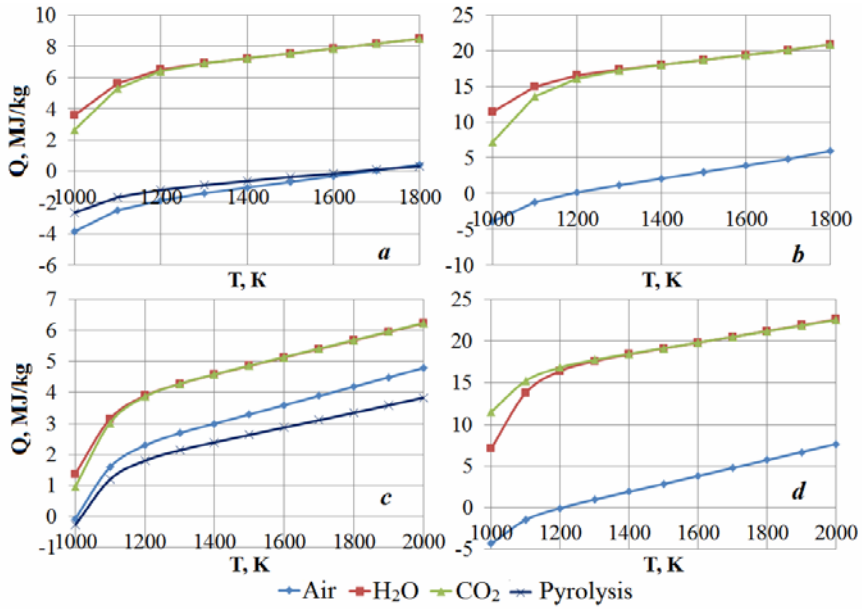

Fig. 1 – Estimated energy costs for wood (a) and rubber (b) conversion and its vapourized fractions (c, d) in different media

Experimental research of direct gasification with addition of water steam into the reactor showed, that the construction should be significantly changed to avoid condensation on the cover of the reactor.

The second stage of the research was study of combined process. Only evaporated fraction was subjected to the high temperature processing.

Results of wood saw pyrolysis in STR-10 are described in /7/. Approximate elemental ratio for the evaporated fraction was determined as C:H:O=21:56:12. Material size was 5 mm. Material and the plasma gas flow rate was selected to get the excess of oxygen of 1-1,05. The air flow through the plasma torch was 2,88 kg/h, flow rate of nitrogen in the screw reactor 0,61 kg/h, material feed rate 3,2 kg/h, the residence time of the material in screw reactor - 15 minutes, the reactor temperature 500°C.

Experiment results of wood processing correlate with the calculation. It should be noted that a small amount of soot is formed. Apparently, it is the carbon dust carried from the screw reactor and carbon produced in the plasma unit. The results of thermodynamic calculations and experiments for wood gasification in air are shown in Table 1 and for tire scrap in different media – in Table 2. Lower heating value (LHV) of gas is estimated on the basis of concentrations of combustible gases.

Experiments with rubber chips of 5 mm size were carried out. On the basis of results published in /6/ approximate elemental ratio for evaporated fraction was determined as C:H=4:5. Sulphur was not taken into account. It was

proposed to supply water or CO_2 in the screw reactor to improve mixing of the material and oxidizer. Water feed rate was chosen from 0 to 2,5 kg per 1 kg of vaporized fraction of material. During the experiments material feed rate was 1,5 – 2,6 kg/h, average mass fraction of vaporized was 62%.

Table 1 - Results of calculations and experiments for wood gasification in air

	Direct gasification		**Combined gasification**	
	Calc., % vol.	Exp., % vol	Calc., % vol.	Exp., % vol
H_2	31	28	36,5	29,8
CH_4	1	1	0	0
CO_2	6	4	3,7	5,8
CO	32	33	36	34,2
N_2	30	32	23,8	30
Others	0	2	0	0,2
Total	100	100	100	100
LHV, MJ/m^3	7,7	7,5	8,5	7,5

Table 2 - Results of calculations and experiments for tire scrap gasification

Gas	**Direct gasification**		**Combined gasification**							
	Air		Air		Air+H_2O		Air+CO_2+H_2O (in excess)		Air+CO_2(in excess)	
	Calc., % vol.	Exp., % vol	Calc., % vol.	Exp., % vol	Calc., % vol.	Exp., % vol	Calc., % vol.	Exp., % vol	Calc., % vol.	Exp., % vol
H_2	13,0	10,5	17,4	17,2	46,4	37,9	22,1	24,5	5,3	4,9
CH_4	0,0	1,2	0,0	0,2	0,0	0,5	-	0,1	-	0,1
CO_2	1,0	5,1	0,6	5,0	3,0	4,1	13,5	13,2	35,7	31,6
CO	26,4	16,1	23,5	16,4	21,4	21,3	31,1	28,9	23,1	29,6
N_2	59,6	65,3	56,4	59,1	29,1	34,5	33,3	30,8	35,9	28,5
Other	0,0	1,8	2,1	2,1	0,1	1,7	-	2,5	-	5,3
Total	100,0	100,0	100,0	100,0	100,0	100,0	100,0	100,0	100,0	100,0
LHV, MJ/m^3	4,7	3,6	4,8	4,0	7,7	7,0	14,3	13,7	13,4	10,8

Comparison of the results of calculations with experimental data showed good agreement for the wood and greater divergence for rubber. It should be noted that in the case of rubber the problem of mixing the material and oxidizing agent was not fully solved. For air-water gasification optimum parameters were found out: 0,63of water per 1 kg of gas mixture, energy consumption: 1,4-1,5 kW·h/kg of total gas mass in the reactor, air feed rate: 1,25 kg per 1 kg of gas mixture. For mixed media CO_2 should be preferably supplied in excess.

Conclusions Comparison of wood conversion with two methods showed, that for dispersive (not more than 4 mm) material the results are very similar, but combined technology provides possibility to work with the material of bigger fraction size. For rubber (tire scrap) this point is of great importance.

For rubber combined process is more preferable as the material does not contain oxygen. Furthermore, it is much easier to add different oxidizing agents (water, CO_2) in combined process and thus provide mixing of the material and oxidizer and preforming the conversion process in desirable gas medium.

Optimal parameters of air-water combined gasification of tire scrap were found out.

Experimental studies of gasification of organic materials have shown that combined process can be used for the material of larger size than direct plasma gasification. Combined technology allows addition of different agents to the conversion providing to choose the necessary composition of syn-gas. It also showed better results for conversion the materials without oxygen. Addition of CO_2 significantly increases the LHV of the syn-gas.

Acknowledgements. The research was supported by HMTI, and we express our gratitude to Dr. I. Jamaikina who made all the gas analyses for us.

References

1. **Ducharme C.** M.S. Degree in Earth Resources Engineering Thesises. Columbia University (2010).
2. **Hrabovsky M.** High Temperature Material Processes. Vol. 10, №4. (2006) 557-570.
3. **Heberlein J. and Murphy A**. Journal of Physics D: Applied Physics (2008), No. 41, p. 1-20.
4. **Hrabovsky M.** Progress in Biomass and Bioenergy Production/ Edited by Dr. Shahid Shaukat. – InTech, (2011) – Ch.3. – P. 39-62
5. **Liavonchyk A.I., Sauchyn V.V., Khvedchyn I.V.** Proceedings of 22 Int. symposium on plasma chemistry. Belgium, Antwerp. 2015 July 5-10.
6. **Lozhechnik, A. and Sauchyn, V.** Journal of Engineering Physics and ThermophysicsVol. 89, Issue 6,(2016), p. 1482–1486.
7. **Liavonchyk A., Morozov D., Sauchyn V. and Dalholenka H.** CYSENI 2018. Proc. of annual conf. of young scientists on energy issues. [CD]. Kaunas: Lithuanian Energy Institute. 2018 May 23-25.
8. **Liavonchyk A., Khvedchyn I., Sauchyn V., Dalgolenka H. and Lozhachnik A.** Proceedings of 24th European Biomass Conference and Exhibition. Amsterdam. 2016 June 6-9.

LOW-TEMPERATURE OZONE GENERATOR BASED ON DIELECTRIC BARRIER DISCHARGE FOR WATER TREATMENT

O.V. Shchebetun, V.V. Krasnyj, O. Chechelnizkij, A.V. Taran, A.S. Lozina

Institute of Plasma Physics, NSC "Kharkiv Institute of Physics and Technology"
Kharkiv, Ukraine alex.schebetun@gmail.com

Abstract

The paper presents a device for ozonizing water based on a plasma reactor using dielectric barrier discharge (DBD). The design feature of this device is to obtain high ozone concentration with low air flow rate (0.2-0.3 l/min) at atmospheric pressure. The concentration of ozone comprised 28-35 mg/l. When oxygen was supplied at purity 90-92%, the ozone concentration reached 100-120 mg/l. Stabilization of the obtained parameters is achieved by cooling the ozone reactor with a thermoelectric module based on the Peltier element.

Keywords- ozone, dielectric barrier discharge; water treatment, microorganisms Staphylococcus aureus, E. coli.

1. Introduction

Nowadays, various plasma technologies are widely applied in medicine due to their ecological compatibility, relatively low energy consumption, etc. Ozone technologies based on barrier discharges at atmospheric pressure are used for sterilization and disinfection purposes. But there is a lack of portable compact devices for domestic needs capable of quickly saturating water with ozone to a concentration necessary for its disinfection and further use. The dose of ozone necessary for disinfection of water is 0.5-5 mg/dm^3, depending on the content of organic substances in water, and the duration of contact of water with ozone is 5-20 minutes. For effective disinfection of drinking water, it is necessary to introduce a dose of ozone sufficient to provide a residual concentration of dissolved ozone 0.4 mg/dm^3, which should be maintained for 4 minutes /1/.

Low-temperature ozonator based on reactor with dielectric barrier discharge (DBD) operated in water solution has been developed. Such a device can be used for disinfection of various surfaces by ozonated water, cosmetology procedures, for washing hands in urgent and purulent surgery, food processing (vegetables, fruits), etc.

2. Experimental setup

The device for preliminary water purification is made as a portable device

(Fig.1) and includes the following main units and elements: ozone reactor with a cooler (Fig. 2), built-in 20 liter capacity, two compressors, power unit, high voltage source, destructor, a pump for injecting ozone into water and further mixing the water-ozone mixture.

The ozone reactor is made on the basis of flat electrodes with glass-enamel dielectric coatings ($\varepsilon \approx 5$), with cooling by a thermoelectric module. This type of reactor is described in more detail in /2/. Switching power supply with a frequency of 0.5 kHz, 10 kV and a power of 200 watts is used. The output concentration of ozone is 30-35 mg/l with air flow rate of 0.25 l/min and is controlled by an integrated spectroscopic meter.

The device is built on the principle of the formation of ozone from the oxygen of the air exposed to a barrier electric discharge. Air intake is carried out by the compressor. After that, the air enters the container with silica gel, where it drains. Further through the destructor enters the barrier discharge of the reactor. The output ozone-air mixture is injected by a water pump into the water tank using the Venturi effect. Next, there is a mixing of the water-ozone mixture and its further saturation with ozone.

Fig. 1 – The device for preliminary water purification

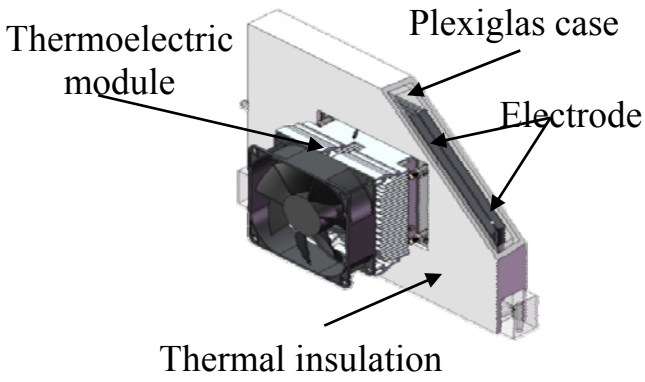

Fig. 2 – The ozone reactor with a cooler

3. Results and discussion

The ozone concentration in water was determined using an automated stand equipped with MDR-2 monochromator and photoelectric multiplier (PMT), where ozonized water circulated through the optical system with two quartz lenses. The excess ozone, which was collected over the water in the vessel, was blown to the environment through the destructor filled with activated carbon. During experiments, productivity of ozonator and temperature of the water was changed. The results of the measurement were recorded on a PC.

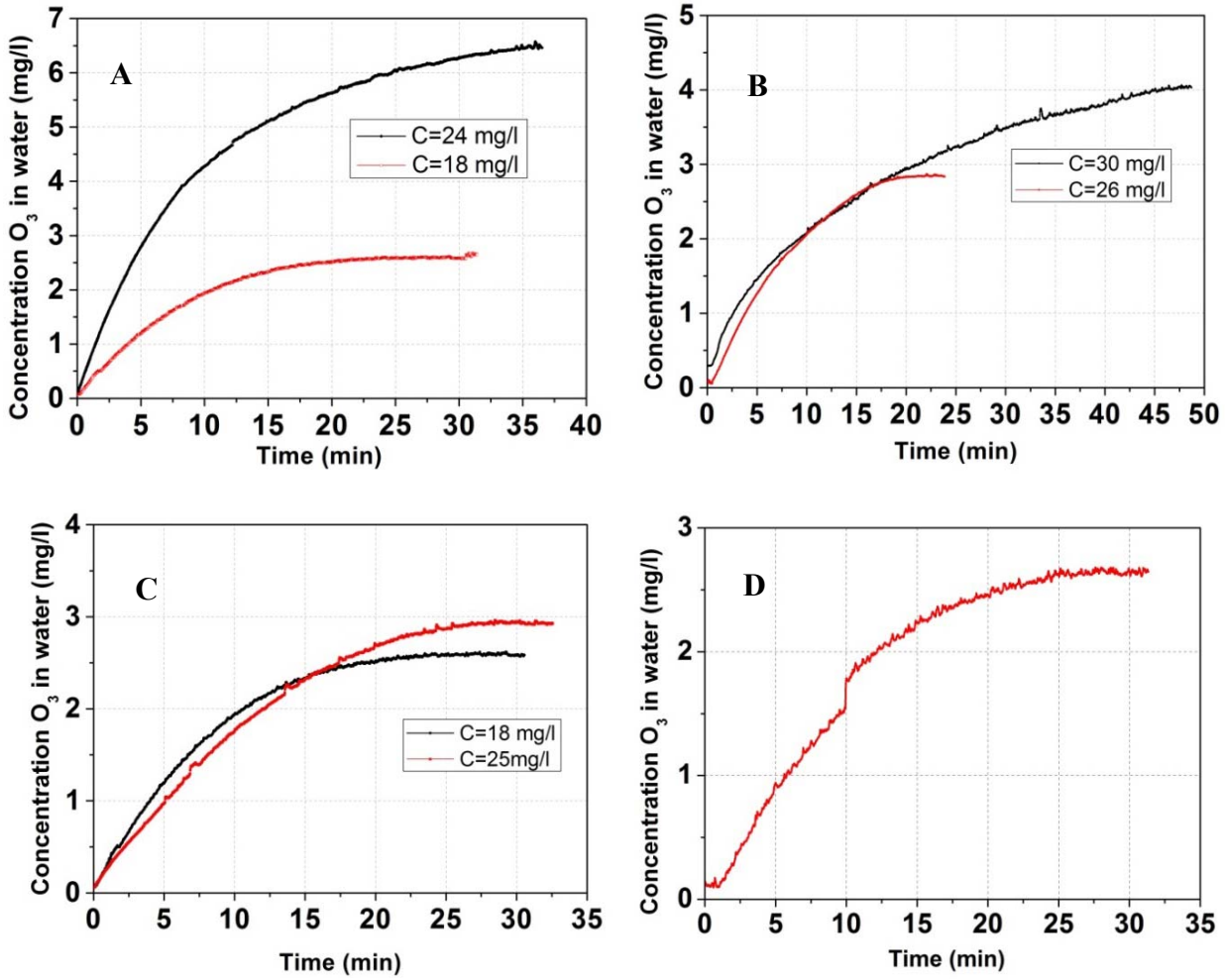

Fig. 3 – Time dependence of ozone concentration in water

It was established that with input O_3 concentration of 24 mg/l the saturation of water took place in 38 min and ozone concentration in water comprised 6.5 mg/l. With an inlet concentration of 20 mg/l for 30min, ozone concentration in water comprised 2.8 mg/l (Fig.3a). With input ozone concentration of 26 mg/l, the saturation of water occurred in 25 min and ozone concentration in water was 2.8 mg/l, whereas with an inlet concentration of 30 mg/l for 46 min it comprised 4.0 mg/l. (Fig.3b).With input ozone concentration of 18 mg/l the saturation of water took place in 30 min and ozone concentration in water comprised 2.6 mg/l. With an inlet concentration of 25 mg/l for 32 min, ozone concentration in water comprised 2.9 mg/l (Fig.3c). In Fig. 3d, the water saturation took place in 31 min, and the O_3 concentration in water was 2.7 mg/l.

A set of experiments were carried out on eliminating various test-cultures from preliminary polluted medical instruments by using ozonized water. Table 1 presents the results of disinfection treatment of medical equipment.

Table 1 – Inactivation of test-cultures in ozonized water

Test - culture	O3 mg/l in water	T°C in water	Kill time (min)
E.coli 055 K 59№3912/4	1.8	18	2
Staphylococcus Aureus	1.8	18	2
Pseudomonas Aeruginoza	6	10	5

As it seen from the Table 1 /2/, the test-cultures of E.Coli 055 K 59№3912/4 and Staphylococcus Aureus ATCC№25923 were eliminated from the surface of medical equipment during 2 min of processing in ozone-aqueous media at 1.8 mg/l ozone concentration and at a temperature of 18^{o}C. Test cultures of Pseudomonas Aeruginoza 27/99 were destructed at 6.0 mg/l and at 10^{o}C during 5 min.

Conclusions

Compressor type ozonator built on the principle of ozone formation from air oxygen under the action of dielectric barrier discharge with flat electrodes have been designed. Experiments on ozone saturation with tap water have been carried out. The ozone concentration at the output of generator comprised 20 to 30 mg/l and depends on the blow down rate and on the reactor power applied to the plates. The ozone concentration in the aqueous solution varies from 2.5 to 6 mg/l with a water volume of 10 liters and with air flow rate through the reactor 0.2-0.4 l/min, respectively. Various test-cultures were eliminated from the surface of medical equipment in ozonized water produced by compressor-type ozonator.

References

1. **Dolina L.F**. New methods and equipment for disinfection of sewage and natural waters.Dnepropetrovsk from the "Continent", 2003, (st.25).
2. **Taran V.S, Chechelnizkij O.G, Krasnyj V.V, Shvets O.M.** J. Probl. At. Sci. Technol. 1(2011), 161 – 163.
3. **Shchebetun O.V., Taran V.S., Krasnyj V.V., Lozina A.S., Chechelnitskyi O.G.** Device for disinfection and pre-sterilization of products. The patent of Ukraine No. 92922 of 10.09.2014.

INFLUENCE OF PARAMETERS OF GAS-JET PLASMA-CHEMICAL METHOD ON DEPOSITION RATE AND STRUCTURE OF SILICON FILMS

R. Sharafutdinov, V. Shchukin, V. Konstantinov

Institute of Thermophysics SB RAS, Lavrentiev avenue 1, 630090, Novosibirsk, Russia, molkin@itp.nsc.ru

Films of microcrystalline silicon cause an increased interest of researchers in connection with their unique properties that distinguish them from amorphous silicon. First of all, this is increased conductivity and a lower level of degradation in the structure of the solar cell under sunlight illumination. A number of physical and chemical methods for depositing thin-film coatings have been developed, allowing them to be deposited on various substrates. One of the first and well-studied methods of depositing thin films is sputtering the target, carried out by various methods, such as magnetron, radiofrequency or sputtering with a direct current /1/. The most promising methods of depositing thin films are plasma-chemical methods using remote plasma, where precursors are introduced at some distance from the plasma source, which reduces the negative influence of high-energy ions on the surface of the growing film. Examples of such processes can serve as: electron-cyclotron resonance, corona discharge, inductively-coupled plasma, expanding thermal plasma /2, 3/. Another method for depositing thin films using a remote plasma is the electron beam plasma, in particular, monosilane plasma is used for deposition of silicon films /4, 5/. However, the main industrial method for depositing silicon layers in the solar cell structure is PECVD, which provides very low deposition rates at 0.3 nm/s /6/.

This work is devoted to the development of a new high-speed deposition method. The production of thin films of microcrystalline silicon with high deposition rates is ensured by the unique features of the gas-jet plasma-chemical method. The first of these consists in raw material feeding into the process in the form of a supersonic jet, which ensures the rapid delivery of the activated particles to the substrate. The second is that the used electron beam has a large number of electrons for effective activation and dissociation of gas molecules.

Plasma generator, named cold plasmatron, consisting of an electron gun 1 with a hollow cathode 2 was used to generate an electron beam 3. The nozzle block 4, which is a Laval nozzle system, was used for supplying working gases. The electrode configuration of the discharge system of the electron gun included a hollow cathode, an anode 5 and accelerating electrode 6 (extractor). The electron beam was formed by applying a potential to the extractor, relative to the anode /7/. The silicon-containing gas monosilane (SiH_4) and the diluent gas argon (Ar) were supplied to the reaction vacuum chamber by means of a nozzle

block in the form of a supersonic jet. Upon interaction of the gas jet molecules with the electron beam, a low-temperature high-density electron beam plasma was formed, which contains chemically active particles. The particles, having reached the substrates arranged on the heater, formed a silicon film /5/.

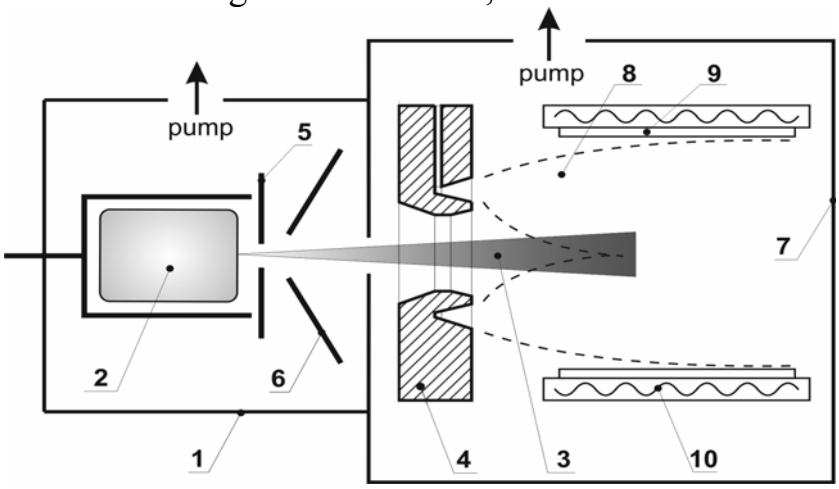

Fig. 1 - The scheme of the experimental setup

Determination the crystallinity of the deposited silicon layers was carried out by processing Raman spectra. A spectrometer with a triple monochromator T64000 manufactured by Horiba Jobin Yvon was used in this work. To obtain data on the crystallinity, the Raman spectrum was decomposed into three Gaussian peaks /8/, and for small crystallinity values, the method of subtracting the spectrum of the amorphous phase /9/ was used. To determine deposition rates, films thicknesses on the LEF-81 "Microscan" scanning ellipsometer and the near-infrared reflection spectra (800-2000 nm) were measured on a UV-3101 PC Shimadzu spectrophotometer.

In the course of the work, the influence of various parameters of the gas-jet plasma-chemical method on the degree of crystallinity and deposition rate of silicon films was investigated. As the substrate for deposition, Corning EAGLE 2000 glass, having a size of 150 × 150 mm and a thickness of 0.7 mm was used. The parameters were studied along the symmetry axes: along the gas flow and across it. Fig. 2 shows the longitudinal distributions of crystallinity (a) and the deposition rate (b) of silicon films as a function of the substrate temperature, which was set by means of a heater. Fig. (c) and (d) show the same dependences, but obtained in cross section perpendicular to the gas flow on the axis of the substrate.

As can be seen from Fig. 2a, as the substrate temperature increases, the degree of crystallinity increases, both in absolute value and in length. Moreover, when passing from room temperature to 100°C, a sharp jump in the length of the crystallinity zone occurs, and further growth is absent, while the absolute value is slightly increased. More noticeable is the effect of temperature on the width of

the crystallinity zone. As can be seen from Fig. 2c, only at 170°C crystalline material precipitates practically on the entire area of the substrate, and at temperatures of 100°C or lower, the crystalline material is formed only in a narrow region, of the order of 30 mm, at the center of the substrate. It can be concluded from Fig. 2b and 2d that as the temperature increases, the deposition rate increases.

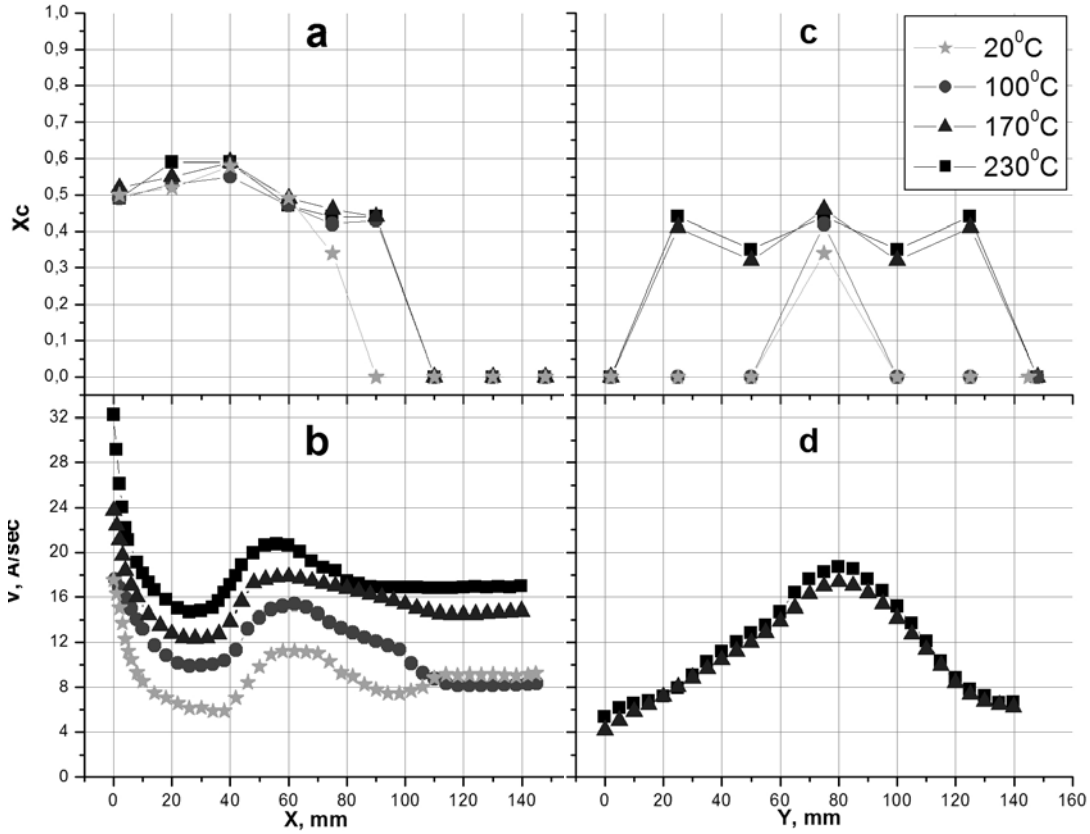

Fig. 2 - Distribution of crystallinity (a, c) and deposition rate (b, d) of silicon films over the substrate surface as a function of the deposition temperature

Thus, to obtain films of microcrystalline silicon at high deposition rates over large areas, it is necessary to maintain a sufficiently high temperature, determined by the thermal stability of the substrate. It can be concluded that the proposed method is also suitable for depositing microcrystalline silicon films on low-temperature flexible plastic substrates such as polyethylene naphthalate (PEN) or polyethylene terephthalate (PET), with deposition rates several times higher than those achieved in industrial production of thin-film silicon solar cells.

Acknowledgements This study was partially supported by FASO Russia (project no. 01201350443 "Fundamental Thermophysical Problems in the Growth of Crystals and Films").

References

1. **Behrisch R.** Sputtering by Particle Bombardment. Berlin: Springer (1981).
2. **Van de Sanden M.C.M., Severens R.J., Kessels W.M.M., Meulenbroeks R.F.G. and Schram D.C.** J. Appl. Phys. 84 (1998) 2426–2435.
3. **Zhang J.L., Yu S.J., Ma T.C.** Vacuum. 65 (2002) 327-333.
4. **Ohshita Y., Yamaguchi K., Motegi H., Yamaguchi M.** Journal of Crystal Growth. 237–239 (2002) 1394–1398.
5. **Sharafutdinov R.G., Khmel S.Ya., Shchukin V.G., Ponomarev M.V., Baranov E.A., Volkov A.V., Semenova O.I., Fedina L.I., Dobrovolsky P.P., Kolesov B.A.** Solar Energy Material & Solar Cells. 89 (2005) 99-111.
6. **Terakawa A.** Solar Energy Material & Solar Cells.119(2013)204–208.
7. **Shchukin V.G., Konstantinov V.O., Morozov V.S.** Technical Physics. 63 (2018) 888–893.
8. **Das D., Jana M., Barua A.K., Chattopadhyay S., Chen L.C., Chen K.H.** Japanese Journal of Applied Physics. 41 (2002) 229-232.
9. **Smit C., van Swaaij R.A.C.M.M., Donker H., Petit A.M.H.N., Kessels W.M.M., van de Sanden M.C.M.** Journal of Applied Physics. 94 (2003) 3582-3588.

WETTABILITY AND ELECTRET PROPERTIES OF PLASMA-TREATED POLYTETRAFLUOROETHYLENE FILMS

M.Yu. Yablokov[1], D.E. Temnov[2,3] S.M. Kulemina[2], A.A. Kuznetsov[1]

[1]Enikolopov Institute of Synthetic Polymer Materials, Russian Academy of Sciences, Profsoyuznaya Str. 70, 117393 Moscow, Russia
[2] Herzen State Pedagogical University of Russia , 6 Kazanskaya st., 191186, St. Petersburg, Russia
[3] Saint Petersburg National Research University of Information Technologies, Mechanics and Optics, Kronverkskiy prospekt, 49, 197101, St. Petersburg, Russia
E-mail: yabl1@yandex.ru

Abstract Plasma treatment of polytetrafluoroethylene (PTFE) films by direct current glow discharge was used for polymer surface modification. In this study we examined the relationship of wettability and electric charging of plasma-modified polymer films.

Introduction Treatment of polymer films by low-temperature plasma is a very effective method for enhancement of their properties such as wettability and adhesive strength /1/. The changes in plasma-modified polymers take place within a surface layer with thickness not exceeding 100 nm as estimated by different authors. At the same time the bulk of polymer remains intact, retaining the inherent mechanical and physicochemical properties. We have shown earlier that the direct current glow discharge treatment of fluorine-containing polymers leads to the significant hydropilization and improvement of adhesion properties and also to appearance of stable surface charges /2,3/. Recently we showed the existence of correlation of wetting, adhesion and electret properties of PTFE films, modified by direct current glow discharge /4/.

Important question is the stability of properties of plasma-modified polymer films. One of the most significant problems is the stability of wetting. Hydrophobic polymer surfaces after plasma treatment become hydrophilic, and this hydrophilicity is lost with time. This process is called “hydrophobic recovery”, and the nature of this process is not yet known.

In this contribution we report on the investigations of the dynamics of wettability and electric charging of plasma-modified polymer films, and treat hydrophobic recovery as the result of relaxation of surface charges on polymer surface. The relaxation is considered not only as the process of leakage of the electrical charge gained by the polymers under plasma treatment, but as the relaxation of polarized dipole groups, formed under electric field in glow discharge.

Experimental Samples of the PTFE film of 40 μm thickness ("Plastpolymer", St. Petersburg, Russia) were used in the study. The procedure for film modification by DC discharge is detailed in /2/. Two symmetrical parallel plate aluminum electrodes of 18 cm in diameter with 5 cm distance between electrodes – cathode and anode, were used. The polymer samples were placed on the bottom electrode of the two electrode system. Working plasma gas was air, pressure of 10–15 Pa and a discharge current of 50 mA, treatment time 60 s. Surface properties were characterized by values of the contact angle measured with an Easy Drop DSA100 instrument (KRUSS, Germany) using deionized water as a test liquid. The electret potential was measured by the compensation technique using a dynamic capacitor. The experimental setup and the procedure of measurement are detailed in /5/. From the measured value of electret potential (U), the effective density of the surface charge (σ) was calculated by the equation $\sigma = \varepsilon_0 \varepsilon U/L$. In this equation, ε_0 is the electric constant and L is the thickness of the polymer film. Dielectric permittivity of the samples was taken to be $\varepsilon = 2$. The spectra of thermostimulated depolarization (TSD) of PTFE films were obtained on a TSCII device (Setaram, France) in helium atmosphere with heating rate of 9 K/min. The currents were measured by a Keithley electrometer 6517E.

Results and Discussion Water droplets on pristine and plasma-treated PTFE films are shown on Fig. 1. Plasma treatment leads to drastic changes in wettability: PTFE surface from hydrophobic (contact angle θ=110º) becomes hydrophilic (contact angle θ=33º).

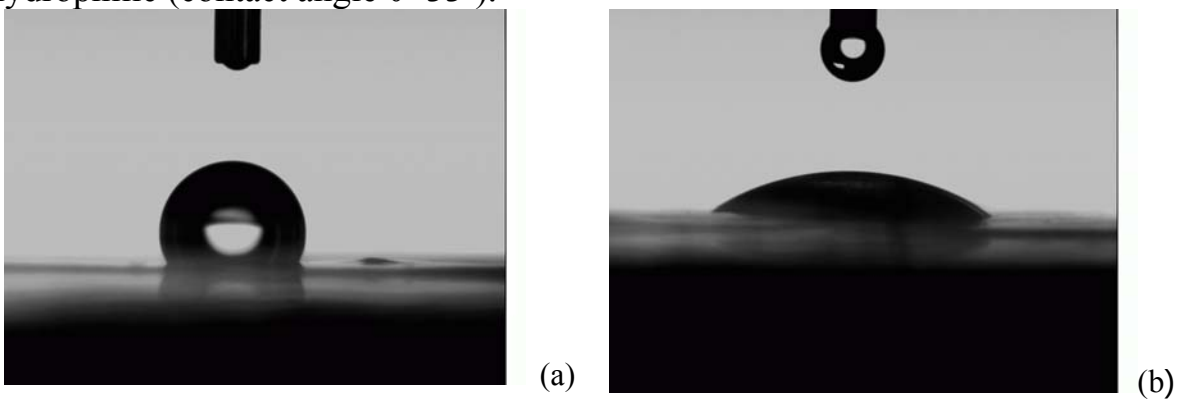

(a) (b)

Fig. 1 - Water droplets on PTFE films: (a) pristine polymer film, contact angle of water θ=110º, (b) polymer film treated at the anode, contact angle of water θ=33º

Plasma-treated PTFE films were stored on the air with relative humidity of 50%. Wettability and electret properties of polymer films were measured simultaneously. The experimental data on changes in contact angle of water (**θ)**

and effective surface charge density (**σ**) for the PTFE films are shown on Fig.2. It can be seen that the plasma treatment of the films at the anode is more effective for wettability enhancement, than at the cathode.

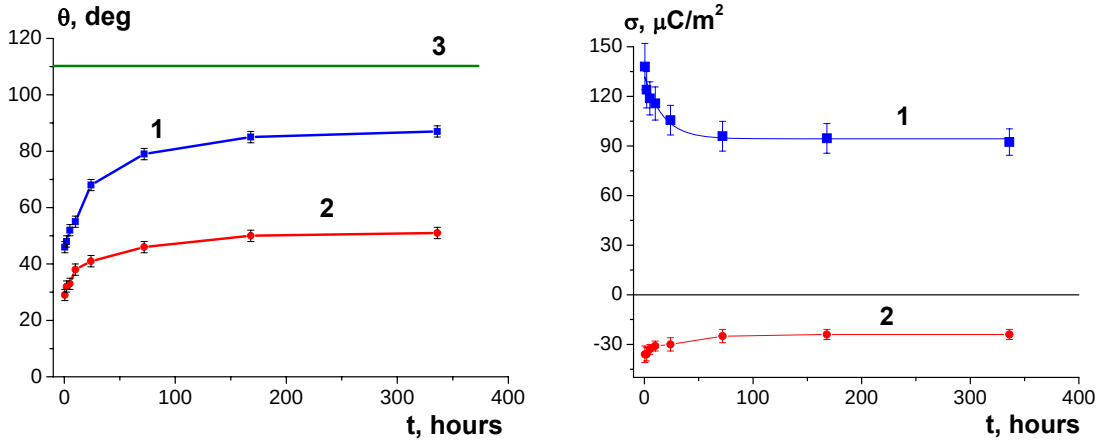

(a) (b)

Fig. 2 - Storage time dependencies of contact angle θ (water) of PTFE films (a) modified at the (1) cathode and (2) anode. (3)- contact angle of pristine PTFE film. Storage time dependencies of effective surface charge density σ of the PTFE films (b) modified at the (1) cathode and (2) anode

After modifying PTFE film at the anode, the effective density of negative charge increases to –36 μC/m^2, whereas the film treated at the cathode acquires a positive surface potential, equal to 140 μC/m^2. Pristine PTFE film had a small negative surface potential and the effective charge density σ = –15 μC/m^2. TSD currents of glow-discharge treated PTFE films are shown on Fig.3.

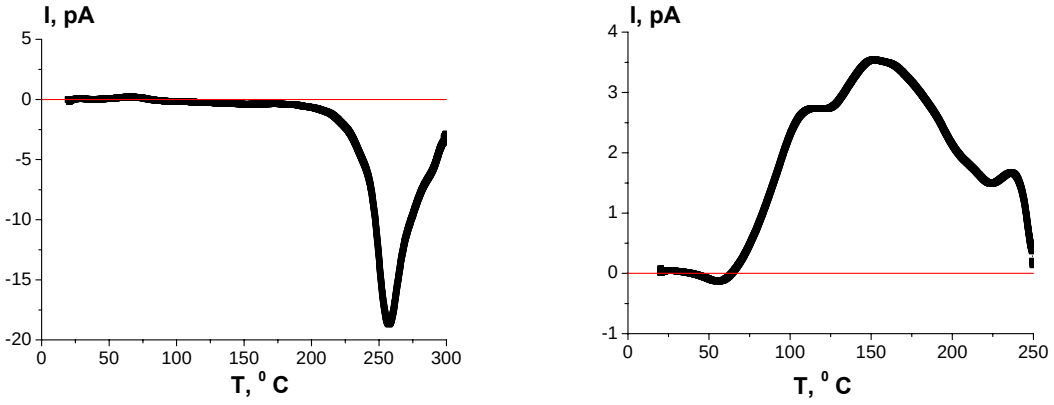

(a) (b)

Fig. 3 - Temperature dependence of depolarization currents glow-discharge treated PTFE films (a) at the anode (b) at the cathode

It is known that the experimentally determined value of the effective surface charge density is an integral characteristic of the electret state and is the sum of homo- and heterocharges. For both TSD curves maximums of currents with different polarity are observed. Major high-temperature peaks on the curves obviously belong to relaxation of homocharges, which are injected into the polymer surface during DC discharge treatment. Low-temperature minor peaks may be attributed to heterocharge, connected with orientation of polar groups during plasma treatment of polymer film. These polar groups are formed during oxidation reactions and oriented in electric field in the surface layer during polymer plasma modification. So, the nature of the DC discharge-induced electret state in the polymer film may be associated not only with the charges, but also with oriented dipoles on the surface.

Polymer films, stored at room temperature, show simultaneous time dependencies, characterizing the increase of hydrophobicity and charge decay Fig. 2. Surface charge decay curves during polymer heating are presented in Fig. 3. Thus, relaxation of electrets charges of PTFE films, treated by direct current glow discharge, can account for hydrophobic recovery, observed after storage of plasma-modified films. The observed relaxation should be considered not only as the process of leakage of the electrical charge gained by the polymers under plasma treatment, but also as relaxation of polarized dipole groups, formed under glow discharge treatment in PTFE films.

It was shown that experimental values of time dependence of contact angle (θ) and effective surface charge density (σ) for the plasma-treated PTFE films correspond to the theoretical model of wetting of charged polymer films /6/.

Thus, to ensure high and stable wettability of polymer films processed in plasma, stabilization of electret charges are necessary.

References

1. **Baldan A.** Journal of Materials Science, 39 (2004) 1–49.
2. **Richkov D., Yablokov M., Richkov A .** Appl. Phys. A, Mater. Sci. Process., 107 (2012) 589–596.
3. **Gilman A., Piskarev M., Yablokov M., Kuznetsov A.** Russ. J. General Chem., 85 (2015) 1302–1310.
4. **Yablokov M., Piskarev M., Gilman A., et al.** High Energy Chem., 49 (2015) 207–210.
5. **Yablokov M., Kechekyan A., Gilman A., Ozerin A.** Nanotechnics, 2(26) **(**2011) 86–88.
6. **Bormashenko E., Multanen V., Chaniel G. et al.** Colloids & Surf. A, 487 (2015) 162–168.

DENSE NON-THERMAL PLASMA IN HEAT AND MASS TRANSFER INTENSIFICATION AND ENERGY GENERATION

E.Agarwal[1], Iu.Bosneaga[2], M.Bologa[2]

[1]University Dimitrie Cantemir, Chisinau, MD-2028, Republic of Moldova
[2] Institute of Applied Physics, Chisinau, MD-2028, Republic of Moldova
E-mail: iubosneaga@gmail.com

Dense non-thermal plasma is a perfect instrument for heat and mass transfer intensification and energy generation - mainly because the flux of the ionized gas, being placed in the magnetic field, becomes a dirigible one.

The issue of minimal high-potential energy consumption for dense "cold" (non-equilibrium, non-thermal) plasma generation - is a decisive one for ensuring high final cost-efficiency. We elaborated and apply a powerful tool for optimization based on thermodynamics, which is especially efficient for energy management optimization. It is based on thermodynamic analysis and ensures obtaining of optimal solutions (technologies) - with the extreme indices, which are maximally close to the respective thermodynamic limitations. The main parameter for optimization is the resultant increment (gain) of free energy ΔG (Gibbs's energy). Maximal gain of free energy ΔG, ensured by the technology, corresponds to the optimal solution. All the relevant factors are taken into account for the calculation of the resultant gain of free energy ΔG, inclusively ones referred to the eventual ecological damage.

Generation of the dense non-thermal ("cold") plasma in an energy-efficient way - is determinant for attaining of significant results. We consider several methods for energy-efficient dense non-thermal plasma generation: impulse microwaves (frequency range - approximately 1 - 9 GHz); dielectric barrier discharge (DBD); short (nanosecond) high voltage impulses; radionuclides (mainly coming from the spent nuclear fuel re-processing).

Non-thermal plasma is essentially non-equilibrium one because the ion (and neutrals) temperature remains low, electron temperature being high ($T_e >> T_{ion} = T_{gas}$). The relative number of ionized particles (molecules, atoms and radicals) is proportional to the electron temperature and defines the intensity of the desirable magneto-hydrodynamic action.

Energy-efficient methods of non-thermal plasma generation

Microwaves are one of the best methods of obtaining dense cold plasma /1/: the higher is the frequency and applied power, the higher is the grade of non-equilibrium and plasma density. For the most typical microwave discharges plasma density (i.e., the concentration of free electrons n_e) is rather large, respectively electron plasma frequency

$$\omega_{pe} = (n_e e^2 / m_e \varepsilon_0)^{1/2} \quad (1)$$

is sufficiently high and surpasses the cyclic frequency of microwave generation ω ($\omega<\omega_{pe}$). So, the frequency of the electromagnetic field remains smaller than the plasma frequency, and this corresponds to the condition of effective (high) absorption of microwave energy by plasma. Also should be mentioned the advantages of microwave discharge plasma - as electrodless and which could be easily maintained at relatively high (inclusively, atmospheric and higher) pressure - especially when **impulse microwaves** are applied.

The other two methods of non-thermal plasma generation - **DBD and short (of order - nanosecond) high voltage impulses** - could be treated as of the same (as compared with microwaves) mechanism of action - because periodic short impulses could be presented as the sum of simple oscillating functions, namely sines and cosines (i.e., decomposed in Fourier series) - of "microwave" range frequencies. So, for the generation of the non-equilibrium (non-thermal) plasma it is not obligatory to use *harmonic* high frequency oscillations. The same effect can be obtained as a result of application of the short (nano- and, eventually, pico-second) high voltage impulses. In this case plasma parameters can be controlled through the amplitude, duration and duty ratio of impulses. The main differences come from the hardware design, which appears to be more complex in the case of microwaves (see Fig. 1).

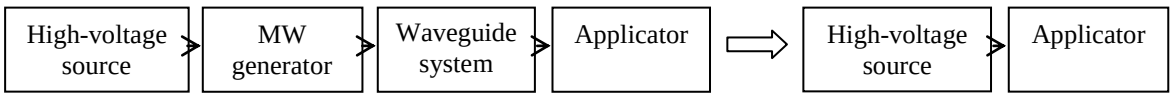

Fig.1 – The scheme of microwave plasma installation as compared with high voltage impulses variant

Radionuclides seem to be the most attractive instrument for non-thermal ("cold") plasma generation - because dense plasma of necessary ionization grade could be obtained without any consume of high-potential (free) energy - but due to accumulated in radionuclides nuclear energy. All three (α, β, γ) ionizing factors could be used, depending on the case. Of special interest are radionuclides coming from the spent nuclear fuel re-processing - strontium-90 (Sr^{90}) is a good example. Strontium-90 is practically "pure" beta emitter with E = (0,546 MeV & 2,28 MeV) and is one of the most abundant isotopes of uranium fission (about 4.5% of the total nuclear daughter products). Chemical instability of strontium (it manifests extreme reactivity with oxygen and water) can be annihilated - by a thin layer of aluminum oxide (Al_2O_3) coating, or by its transforming into strontium titanate. (Strontium titanate is chemically stable and insoluble - due to its special stability quality it is used as a diamond simulant). Besides ionization of gas components, radionuclides (it is especially characteristic for α and β emitters) - additionally - ensure kinetic action

(momentum) in the direction of emission (propagation). The final value of this total momentum depends on the radioactivity and quantity of the radionuclide(s) used (and, of course, on the grade of construction's optimization).

Example of wind (éolien) magneto-hydrodynamic power generator

The moving ionized atmospheric air ("ionized wind") can generate electricity directly, without any mechanical transformations - due to magneto-hydrodynamic effect: magnetic field applied perpendicular to ionized air flux causes Lorentz force which separates moving charges:

$$\boldsymbol{F} = Q\,[\boldsymbol{vB}] \qquad (2)$$

On Fig. 2 is presented schematically the wind MHD power generator.

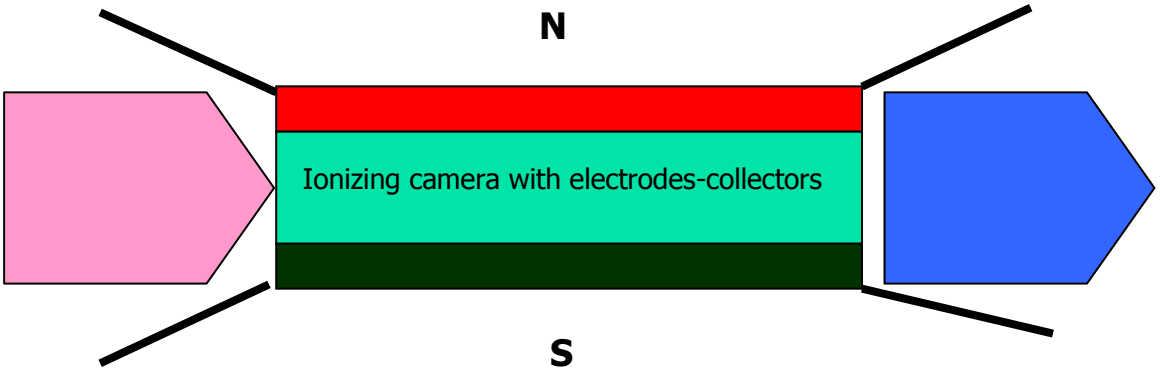

Fig.2 – The scheme of the wind (éolien) MHD power generator. No moving parts. Charge separation occurs under the action of the Lorentz force $\mathbf{F} = Q\,[\mathbf{v}\times\mathbf{B}]$. The main ionizing agents – radionuclides, which are placed in the ionizing camera

Example of magneto-hydrodynamic steam condensation improvement

Cold plasma can be used in heat and mass transfer intensification. Nowadays most of the electric power is generated by means of thermodynamic cycles which predominantly use steam turbines. Respectively, evacuation of the waste heat through water vapor condensation is an extremely widespread, economically and ecologically sensitive technological process. The main feature of the proposed technology of dirigible energy-efficient condensation - transformation of the neutral water vapour from the output of the turbine into cold (non-equilibrium) plasma of sufficiently high density. Such "activated" flux of steam allows transformation of a part its thermal and kinetic energy into electricity - due to the relevant magneto-hydrodynamic (MHD) cycle. As a result of magnetic field application (perpendicular to vapour flux) there appears Lorentz force (2) which separates charges.

Additional power production is beneficial itself, but it is more important that for condensation there will be necessary to absorb much less amount of

heat. As a collateral positive effect, in the presence of the proper catalysts, there can be achieved partial water dissociation - with obtaining desirable products (H_2, O_2, H_2O_2) on the electrodes-collectors.

In dependence of the applied methods of dense plasma generation, the components of the "steam" plasma (molecules, atoms, radicals - and their electric charges) vary, the dominant remaining hydroxyl radicals (OH), hydroxide ions (OH^-), hydrogen atoms (H) and their ions (H^+), oxygen atoms (O) and their ions (O^+, O^-).

Table 1 – Dissociation and ionization energies of water vapour and descendant products

Molecule, radical, atom type	**H_2O**	**HO**	**O_2**	**H_2**	**H**	**O**
Bond (dissoc.) energy, *eV (kJ/mol)* &respec.rad.λ (λ_{max} dissociation limit)	$H_2O + h\nu \rightarrow$ OH + H 5,19 (498,7) λ_{max}= 239,1 nm	$HO + h\nu \rightarrow$ O + H 4,45 (427,8) λ_{max}= 278,9 nm	$O_2 + h\nu \rightarrow$ O + O 5,12 (493,6) λ_{max}= 242,4 nm	$H_2 + h\nu \rightarrow$ H + H 4,49 (432,1) λ_{max}= 276,3 nm	N/A	N/A
Ionization energy (for atoms, molecules), *eV*	$H_2O + h\nu \rightarrow$ $H_2O + e$ 12,61	$HO + h\nu \rightarrow$ OH^+ 18,9	$O_2 + h\nu \rightarrow$ $O_2^+ + e$ 12,08	$H_2 + h\nu \rightarrow$ $H_2^+ + e$ 15,42	$H + h\nu \rightarrow$ $H^+ + e$ 13,60	$O + h\nu \rightarrow$ $O^+ + e$ 13,62

As it comes from the Table 1, ionization energy (for plasma atoms, molecules, radicals) exceeds the dissociation one practically in all cases. It means that the concurrent processes of inevitable positive ions' recombination (transformation into neutral particles - due to electrons' re-absorption) cause dissociative recombination - a process where a positive molecular ions recombine with electrons, and, as a result of energy emission, the neutral particles - mostly molecules - dissociate. So, ionization means also dissociation.

Without any doubt, the presence of charged particles additionally contributes to facilitation of water vapour condensation (through stimulation of nucleation) and consequent reduction of resistance to phase transition.

Improved cold plasma magneto-hydrodynamic steam condensation is particularly beneficial for Nuclear Power Plants - because of the possibility to use additionally the spent nuclear fuel for cost-efficient cold plasma generation. (Spent nuclear fuel is always easily accessible directly on the Nuclear Power Plant's site, and it disposes of - both useful - ionizing and thermal potentials).

References

1. **V.Azharonok, I.Filatova, Iu.Bosneaga, M.Bologa, O.Shedikova.** "Non-thermal plasma sterilization in RF and MW discharges". Romanian Journal of Physics, Volume 56, Supplement, 2011, p.62-68.

THE CONTACT PROPERTIES AND CHEMICAL STRUCTURE OF POLY(ETHYLENE TEREPHTHALATE) FILMS MODIFIED BY DIRECT-CURRENT DISCHARGE

M.S. Piskarev, A.B. Gilman, A.A. Kuznetsov

Enikolopov Institute of Synthetic Polymer Materials, Russian Academy of Sciences, Profsoyuznaya Str. 70, 117393 Moscow, Russia
E-mail: mikhailpiskarev@gmail.com, plasma@ispm.ru

It is known that poly(ethylene terephthalate) (PET) films are widely used for insulation of wires and cables, windings of electric motors, as well as in the composition of laminates for slotting high voltage electrical machines. In recent years, polymer films have been used in solar cell elements, and the laminate on their base serves as the back panel of the devices. The use of such laminate in comparison with the alternative three-layer PVDF/PET/PVDF structure (PVDF – poly(vinylidene fluoride) allows to improve the electrical insulation properties, reduce the penetration of moisture, and significantly reduce the cost of the element. Apparently, this explains the interest shown at the present time to study the process of modifying the contact properties of the PET films surface.

This paper presents a study of the surface modification of poly(ethylene terephthalate) films by DC discharge.

The industrial PET films of PETLAIN BT 1010 E ("Superfilm", Turkey) were used in the experiments. The films of 40μm in thickness were modified by DC discharge using the setup and procedure described in detail in /1/. The film samples were placed at the anode or cathode, the working gas was filtered air. The plasma treatment was carried out at a pressure of ~10 Pa, discharge current of 50 mA, and treatment time of 50 s. The surface properties were characterized by contact angles of wettability θ) measured using two test liquids - water (deionized) and glycerol with an Easy Drop DSA100 instrument (KRUSS, Germany) and the software Drop Shape Analysis V.1.90.0.14 (error ±1°). Measurements were made both directly after modification of the films and after storage for 14 days under ambient conditions. The values of the total surface energy (γ), and its polar (γ^p) and dispersion (γ^d) components were calculated from the experimental θ values /2/.

The chemical structure of the films was studied by the method of X-ray photoelectron spectroscopy (XPS). The XPS spectra were obtained using “PHI 5500VersaProbeII" photoelectron spectrometer. The experiments were performed in an ultrahigh vacuum of 5×10^{-8} Pa using monochromatic AlK_α radiation (hν=1486.6 eV, power 50 W), the diameter of the analysis area was 200 μm.

The original PET film has the following values of the contact angles of water and glycerol: $\theta_w = 80°$ and $\theta_{glyc} = 73°$. It was established that the increase in the plasma treatment time leads to a rapid decrease in θ values for the first 30–40 s, and then the curves gradually reach a plateau with increasing the treatment time to 50 s. The Table 1 presents the experimental data on θ_w and θ_{glyc} as meas-

ured after PET films treatment at the anode or cathode, and after storage for 14 days in air under ambient conditions. The calculated values of the total surface energy, its polar and dispersion components are also given.

Table 1. The changing in the contact angles and surface energy of PET films modified by DC discharge at the anode and cathode (10 Pa, 50 mA, 50 s), and after storage for 14 days

Sample	Storage time, day	θ, deg		Surface energy, mJ/m^2		
		θ_w	θ_{glyc}	γ	γ^p	γ^d
Initial	–	80	73	26.5	12.4	14.1
Treated at the anode	–	12	10	71.6	55.0	16.6
	14	46	40	52.4	34.3	18.1
Treated at the cathode	–	10	9	72.2	55.8	16.4
	14	56	50	44.6	27.6	17.0

It can be seen that the plasma treatment leads to hydrophilization of the PET film surface, and. the θ values for the films treated at the cathode and anode are almost identical. As a result of plasma treatment, the γ and γ^p values increased by factors of ~2.7 and more than 4.5, respectively. After storage of the films for 14 days under ambient conditions, θ_w and θ_{glyc} increased to a greater extent for the films modified at the cathode, although the films remained hydrophilic in both cases ($\theta_w < 60°$).

The chemical composition and structure of the initial PET film and the films modified at the anode and cathode were studied using XPS. Their survey spectra showed that the initial PET is characterized by the major lines C1s and O1s. Fig. 1 depicts the C1s spectra of (a) the initial film and the films modified at (b) the anode and (c) the cathode, and fig. 2 shows the respective O1s spectra. Deconvolution of the complex C1s peak of the initial film (Fig. 1a) revealed the following peaks: (*1*) the one characteristic of the C–C bond of aromatic ring at 284.8 eV, (*2*) the peak due to C–O bond at 286.5 eV, (*3*) the peak corresponding to the O=C–O at 288.9 eV. Note that there is a π–π* satellite at 290–292 eV indicating the aromatic nature of the polymer. The O1s spectrum of the initial film (Fig. 2a) exhibits two peaks at (*1*) 531.6 and (*2*) 533.2 eV due to O=C–O and C–O groups, respectively.

The modification of the PET film at the cathode leads to a noticeable change in the chemical structure of the film surface. For a sample modified at the cathode, the position of the peaks in the spectra of C1s (Fig.1b) and O1s (Fig.2b) persists, however, their appreciable broadening is observed. The peak corresponding to the π-π * transition in the aromatic ring of the polymer is shifted to the region of lower energies. The spectrum shows an increase in the second peak, which indicates an increase in the amount of oxygen-containing C–O groups in the polymer. The ratio of the peaks in the spectrum of C1s also changes (Table 2). Similar changes are observed in the O1s spectrum – the intensity of the second peak corresponding to the C–O groups increases markedly.

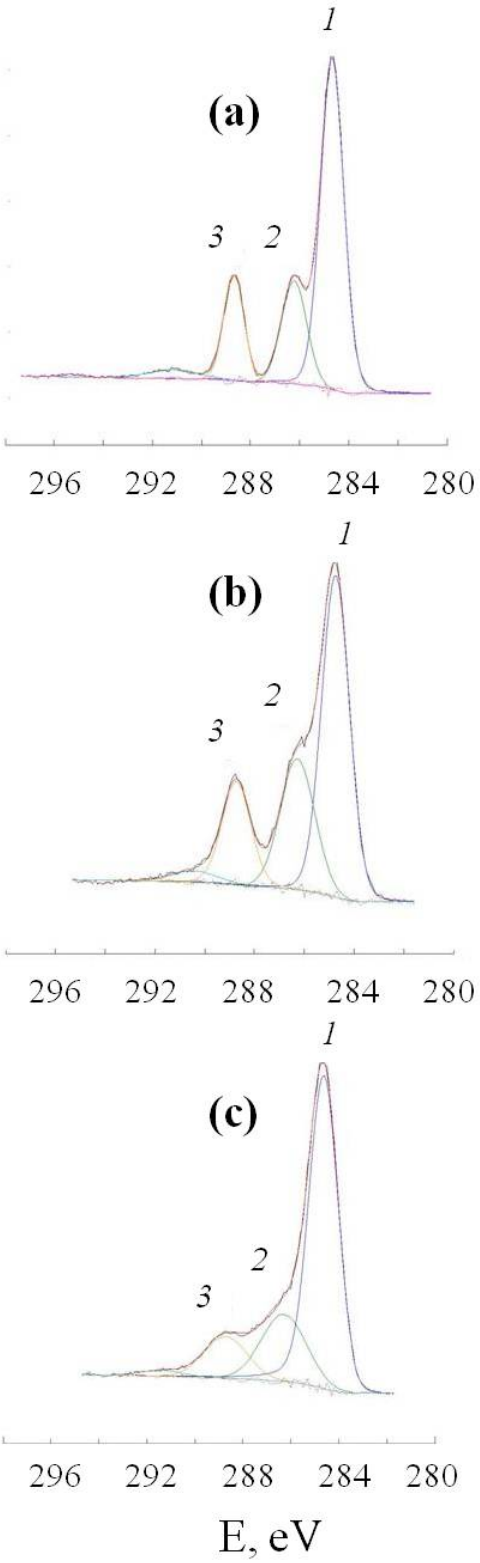

Fig. 1. C1s XPS spectra of (a) the initial PET film and the films modified at I = 50 mA for 50 s at the (b) cathode and (c) the anode

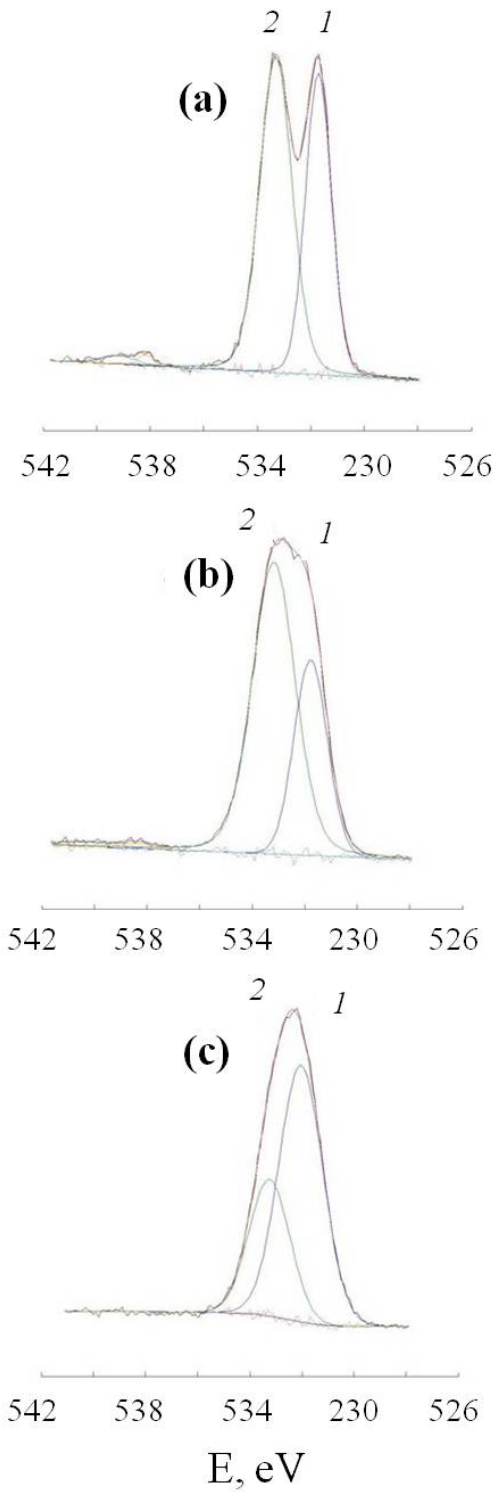

Fig. 2. O1s XPS spectra of (a) the initial PET film and the films modified at I = 50 mA for 50 s at the (b) cathode and (c) the anode

Table 2. Deconvolution of the C1s peak of the initial film and the films modified at the cathode and anode

Sample	Deconvolution of C1s peak, %			Deconvolution of O1s peak, %	
	C–C, E=284.8 eV	C–O, E=286.5 eV	O=C–O, E=288.9 eV	O=C–O, E=531.6 eV	C–O, E=533.2 eV
Initial	63	20	17	43	57
Treated at the cathode	56	26	18	33	67
Treated at the anode	65	21	13	67	33

Probably, in this process the amount of O=C–O groups in the polymer structure decreases, and the amount of C–O group associated with the oxidation of precipitated products increases (Fig. 2c). This assumption confirms the O1s spectrum, shown in Fig. 2c. It is seen, that the intensity of the peak at 531.6 eV (O=C–O) decreases, whereas the peak at 533.2 eV (C–O) appreciably broadens. The ratio of structures in the polymer in this case is shown in Table 2. This assumption confirms the O1s spectrum, shown in Fig. 2c. It is seen, that the intensity of the peak at 531.6 eV (O=C–O) decreases, whereas the peak at 533.2 eV (C–O) appreciably broadens. As a result, despite the similarity of the elemental composition of such a film with the original, the chemical structure of its surface significantly differs.

On the basis of the results obtained, it can be concluded that the modification of PET films by DC discharge at the anode and cathode results in significant hydrophilization of the surface, which persists for a long time. According to the XPS data, this effect can be explained by significant changes in the chemical structure of the film surface. For the film surfaces modified at the cathode and anode, the increase in the quantity of oxygen-containing C–O groups is observed. However, the chemical structure of the surface treated at the anode differs, apparently, due to the etching of the film occurring by discharge process, followed by the deposition of products on this surface.

Acknowledgements. We are grateful to Russian Foundation for Basic Research (grant No. 18-32-00901) for financial support (XPS method).

References

1. **Demina T.S., Drozdova M.G., Yablokov M.Y., Gaidar A.I., Gilman A.B., Zaytseva-Zotova D.S., Markvicheva E.A., Akopova T.A., Zelenetskii A.N.** // Plasma Proc. Polym., 12 (2015) 710–718.

2. **Wu S.** Polymer Interfaces and Adhesion. N.Y.: Marcel Dekker. 1982.

CALIBRATION-FREE ANALYSIS OF ZOOPLANKTON BY LASER-INDUCED BREAKDOWN SPECTROSCOPY (LIBS)

N. Sushkov[1], N. Lobus[2], S. Zaytsev[1], A. Popov[1], T. Labutin[1]

[1]Lomonosov Moscow State University, 1/3 Leninskie gory ul., Moscow 119234, Russia, nikolaisushkov@yandex.ru
[2]Shirshov Institute of Oceanology of the Russian Academy of Sciences, 36 Nakhimovsky Prospekt, Moscow 117997, Russia

It has recently been discovered that Kara Sea copepods accumulate trace elements like lithium, arsenic and uranium [1]. Moreover, determination of Mg/Ca, Sr/Ca and other element ratios in biota provides insight into environmental conditions [2]. Application of LIBS for the analysis of plankton samples is limited by the absence of suitable CRMs. Therefore, a calibration-free (CF) approach [3] is of a great interest for the solution of this problem. This study was focused on determination of ratios between Li, Na, K, Mg, Ca, Sr, and Al in zooplankton.

Initially, we compared harmonics of a Nd-YAG laser (532 nm, 355 and 266 nm) for sampling of pelleted plankton specimens. The 2nd harmonic (532 nm) prevented reliable measurements with a sufficient signal-to-noise ratio due to the formation of big craters with a relatively low plasma emissivity, and the 3rd and 4th harmonics provided a much higher lines intensity in plasma spectra. We used a 0.5–4 μs time interval to ensure local thermodynamic equilibrium in nanosecond laser plasma following literature data. Temperature and electron density were calculated from CN molecular bands in the 383 nm region, hydrogen (H_α and H_β) and magnesium (at 383 and 517 nm) atomic lines. We selected lines for CF calculation free from self-absorption and spectral interferences with the use of a synthetic spectrum (an approximation of light transport in a homogeneous plasma).

Temporal evolution of the plasma was traced over 0.5–3 μs delays. Minimum level of disturbing factors was observed at early delays (0.5–0.75 μs), which is not surprising given generally low plasma temperature, low line intensity and reproducibility of spectra owing to the features of the object under investigation. Analytical measurements were performed with the smallest possible gate width to minimize the influence of plasma variations. Accuracy of the results was proved by common ICP-OES analysis. At the moment, the proposed method for the determination of element ratios in animal tissues is suitable for their semi-quantitative determination.

Acknowledgements. The reported study was funded by RFBR according to the research project № 18-33-01297.

References

1. **Lobus N.V.** Oceanology, 56(2016), 809–818.
2. **Marali S. et al.** Palaeogeography, Palaeoclimatology, Palaeoecology, 484(2017) 109–128.
3. **Ciucci A. et al.** Applied Spectroscopy, 53(1999), 960–964.

TEMPERATURE MEASUREMENT ON ANODE SPOT ON THE METAL SURFASE BY THE SPECTRAL METHOD

L. M. Simonyan, Ya. L. Kats

National University of Science and Technology "MISIS", 119049, Moscow, Leninskiy pr. 4.
e-mal: lsimonyan@misis.ru

An investigation of the metal surface temperature on being affected by plasma-arc discharge is of an interest in connection with its influence on processes of evaporation, condensation, dissolution of gases, refining, melting and crystallization and, finally, on performance attributes of metals and alloys.

Complexity of the metal surface temperature measuring underneath an arc and especially in an anode spot is connected with high error, introduced by arc radiation. In the paper /1/, interference filters have been used for separating arc radiation and the surface in order to find «transparence windows» and to carry out temperature measurements without an impact of the arc radiation.

With spectral methods /2/, it is possible to separate radiation of the arc and the metal since their nature is different: the surface radiation of heat provides continuous spectrum, while the arc radiation the line ones. The problem is reduced to finding «transparence windows» spectral interval in the spectra, in which the arc continuum intensity may be neglected in comparison with that of the metal thermal radiation.

Measurement procedure and results

Temperature of anode surface (iron) in the reduced pressure arcs. Experiments have been implemented at pressures about 10 Pa, discharge current strength of 150 and 220 A in the atmosphere of argon. Radiation of the object has been directed on the slit of a PGS-2 high resolution spectrograph by means of special optical devices. Line spectra has been identified on a SP-2 spectroprojector, «transparence windows» have been defined, and photometric densities of selected areas have been measured by an MD-100 microdensitometer and recorded on a K201 logger.

In order to simultaneously observe continuous spectrum over all discharge gap, including anode (iron) and cathode (tungsten), a tenfold decreased vertical arc image has been pointed to the slit of the spectrograph so that the slit coincided with the discharge axis. The width of the investigated section was 0.2 mm, the height was 40 mm. The measurements have been carried out in a wave-length interval, at which continuum intensity was minimal (240– 450 nm). Parts of the spectrum free of lines (340 and 440 nm) have been chosen for determining temperature of anode (melt) and cathode. Fig. 1 represents the

typical distribution curve of continuous component of spectrum along the discharge axis. The left maximum corresponds to the glow area of anode (melt), the right one to that of cathode. The discharge glow area itself is placed between them. One can see that continuum of the discharge spectrum at the discharge current of 150 A is sufficiently weak and is not able to influence essential on results of measuring of the anode and cathode temperature.

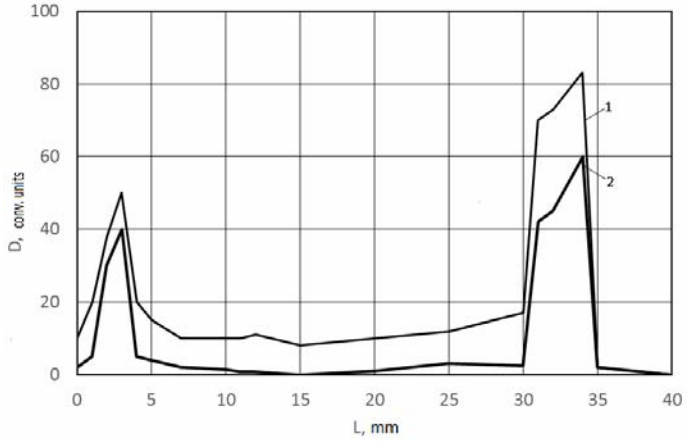

Fig. 1 – Distribution of photometric density along the discharge axis (10 Pa, 440 nm): 1– 200 A; 2 – 150 A

The temperature of the tungsten cathode has been determined by intensity of its radiation[1]. Using the tungsten cathode as an internal standard, we defined temperature of the anode. At the discharge current of 150 A, maximal temperature values of the iron melt surface and cathode has amounted to 3031 and 3160 K, respectively. The obtained values don't contradict to the available literary data.

Relation between the temperature of the body and intensity of its radiation is expressed by Plank's law, or in Wien's approximation for real body ($T\lambda \leq 2000$ K·μm):

$$b(\lambda,T) = \varepsilon(\lambda,T)\cdot b_0(\lambda,T) = \varepsilon(\lambda,T)\cdot c_1\lambda^{-5}\exp\left(-\frac{c_2}{\varepsilon(\lambda,T)}\right) \quad (1)$$

where $b_0(\lambda,T)$ is spectral brightness of the blackbody; $\varepsilon(\lambda,T)$ – spectral radiant emittance; T is temperature, K; λ is wavelength, μm; $C_1=2hc^2=3.74\ 10^{-16}$ W/m^2; $C_2=hc/k=1.438\text{-}10^{-4}$ μm·K; h is Planck's constant; c is velocity of light; k is Boltzmann's constant.

The temperature of outer surface of the hollow tungsten cathode has been calculated by relative background intensity at two wavelength values (340 and 440 nm):

[1] Radiant emittance of tungsten is known for temperatures from 300 to 3000 K and in a wide wavelength interval, which allow measuring the tungsten cathode temperature by radiation intensity at different wavelengths (Ebert G. Abridged reference book on physics. Moscow : GIZFML, 1963. 551 pp.)

$$\ln\frac{b_1}{b_2} = \ln\frac{\varepsilon_1}{\varepsilon_2} - 5\ln\frac{\lambda_1}{\lambda_2} - \frac{c_2}{T_k}\left(\frac{1}{\lambda_1} - \frac{1}{\lambda_2}\right) \quad (2)$$

According to calculation, the temperature of the tungsten cathode has been estimated as 3160 и 3317 K at the discharge current of 150 A and 220 A correspondingly. The temperature of anode (iron melt) T_a has been determined by relative intensity of cathode and anode radiation b_k/b_a at the wavelength of 440 nm using T_k, computed from the formula (2):

$$\frac{\ln b_k}{b_a} = \frac{\ln \varepsilon_k}{\varepsilon_a} - \frac{c_2}{\lambda}\left(\frac{1}{T_k} - \frac{1}{T_a}\right) \quad (3)$$

Value ε for iron practically doesn't depend on temperature and is equal to 0.45 at a given wavelength value. At the discharge current of 150 A, the liquid iron surface temperature was 3031 K. The error is as higher, as the values of temperature and equivalent wavelength $\lambda_{eq}=(\lambda_1\lambda_2)/(\lambda_1+\lambda_2)$ are higher. In our conditions, ΔT is 50–100 K.

Temperature of metal surfaces at atmospheric pressure

The series of spectral investigations of the melting surface of refractory metals under conditions of plasma heating in atmosphere of argon at general pressure of 0.1 MPa and current of 225 A and higher have been implemented.

Optical arrangement of temperature measurement along the side surface of cylindrical tungsten rod is presented in Fig. 2. Results of measurements of the temperature distribution in a heating zone (along the entire length of the tungsten rod of 50 mm in length and 25 mm in diameter) are sown in Fig. 3.

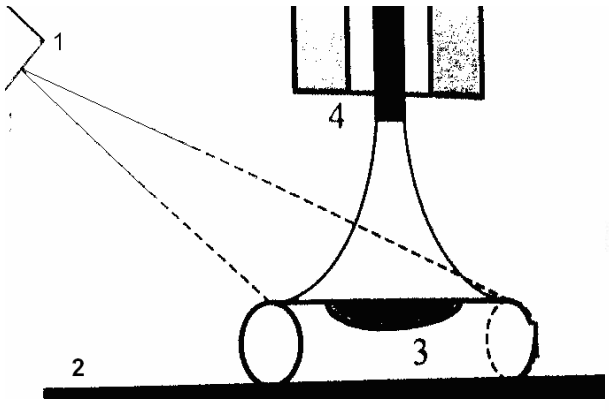

1 – object-glass; 2 – substrate-anode; 3 – metal sample; 4 – plasmotrone-cathode.

Fig. 2 – Optical arrangement of the temperature measurement along the side surface of cylindrical rod

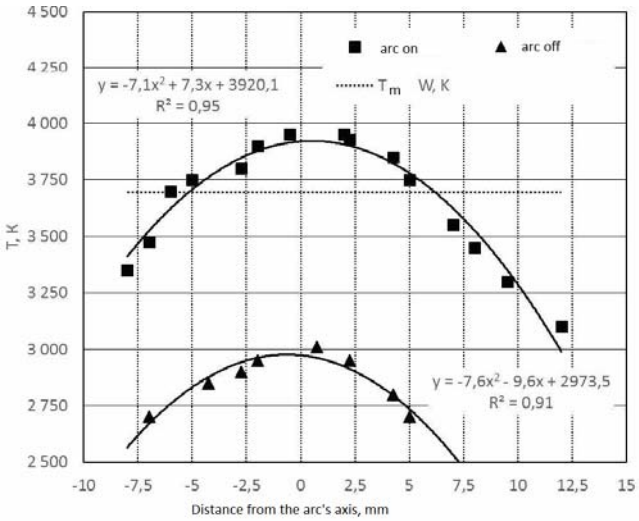

Fig. 3 – Temperature distribution along the tungsten rod. I = 225 A, U = 20 V

It is obtained that maximal temperature in the center of the metal equals to 3975 K; on the metal surface, temperature within a radius of 10 mm exceeds melting temperature of tungsten (T_m=3693 K). When the arc is cutting off, metal is instantly becoming hardened. In Fig. 3 one can see that the melt surface temperature lessens from 4000 to 3000 K. The maximal temperature on the axis is still high (3000 K), but it is essentially lower that the tungsten melting temperature (3693 K).

In conditions under consideration, maximal temperatures for iron and nickel in the plasma heating zone are close to the boiling-point (T_b), as it is shown in the Table.

Metal	T_m, K	T_b, K	T_{max}^*, K
Fe	1811	3145	2960
W	3693	5953	4120
Zr	2125	4613	4040
Ni	1728	3073	3590

*– results of measurement

Reaching the boiling-point for refractory metals (W, Zr) requires the greater power contribution.

Conclusion

It is shown that in the wavelength range of 240-450 nm, there exist «transparence zones» in spectra of the arc plasma in argon; they may be used for measuring the melt surface temperature directly in the process of plasma-arc heating. It was obtained that the melt surface temperature in an anode spot depends slightly on the total pressure and current strength, but essentially depends on the melt features and can reach the boiling-point.

References

1. **Zhukov M. F., Kozov N. P., Pustogarov A. V. et al.** Near-electrode processes in the arc discharges. Novosibirsk : Nauka, 1982. 157 p.
2. **Magunov A. N.** Spectral pyrometry. Moscow : FIZMATLIT, 2012. 248 p.

SURFACE METALLIC NANOSTRUCTURES FOR PHOTOACOUSTIC FIBER-OPTIC TRANSDUCERS SYNTHESIZED BY LASER PLASMA CONDENSATION

A.P. Mikitchuk, K.V. Kozadaev

Department of Radiophysics and Computer Technology, Belarussian State University, Minsk 220045, Belarus, e-mail: m.helenay@yandex.by

Wideband ultrasonic signals are widely investigated as powerful diagnostic tool for advanced applications, for example, biomedical high-resolution high-contrast imaging and nondestructive analysis /1/. Number of studies of ultrasonic transducers have been conducted because ultrasonics offers very high-resolution diagnostics due to the relatively small speed of sound within the most part of liquids and solids (ultrasound waves are typically characterized by the optical-scale wavelengths even in the sub-gigahertz frequency range). But there are some limitations for effective ultrasonic transducers design. Conventional transducers based on piezoelectric effect typically allows bandwidths only up to tens of megahertz. Moreover, such transducers are quite bulky. Furthermore, the attenuation of ultrasonic wave is higher than 100 dB/mm in the frequency range exceeding gigahertz /1,2/. Thus, the thickness of absorption layer on the surface of an optical fiber should be minimized. Additionally, a tiny transducer is only suitable variant because it should be place directly on the object under test. Fiber-optic transducers based on the photoacoustic effect are comparatively small (optical fiber core diameter is less than 10 μm), flexible and movable. Moreover, they are characterized by high electromagnetic immunity, dielectric design and chemical durability. Metallic nanostructures, which are formatted on the surface of an optical fiber edge by laser plasma condensation, can potentially provide very high absorption (up to 90%) within the thickness of nanoparticles (NPs) monolayer. Photoacoustic transformation of the modulated optical signal in the acoustic waves takes place due to periodical thermal expansion/contraction.

In this paper, we present theoretical investigation of absorption of laser radiation within metallic NPs monolayer on the surface of the optical fiber edge.

Optical characteristics of surface metallic nanostructures. In general, surface nanostructures can be synthesized by means of chemical deposition /3/, optical assisted deposition in liquid media /4/, and laser plasma condensation /5,6/. The procedure of NPs formation within the ablation flare allows the expulsion of the atmospheric gases, which in turn provides the direct synthesis of chemically pure NPs of noble metals without an oxide/hydroxide shell /7/.

A frequency domain simulation by means of the CST Microwave Studio Student Edition is performed for the modelling of optical characteristics of a

metal NPs monolayer on the surface of an optical fiber edge. The unit cell of the NPs monolayer is simulated as follows. The unit cell contains two infinite osculating parallelepipeds, one of them is the solid substrate and another is the surrounding medium. NPs is placed on the surface of the solid substrate (fiber edge), so the whole NP volume is located within the surrounding medium. The representation of the structure and scattering parameters is shown in the Fig. 1.

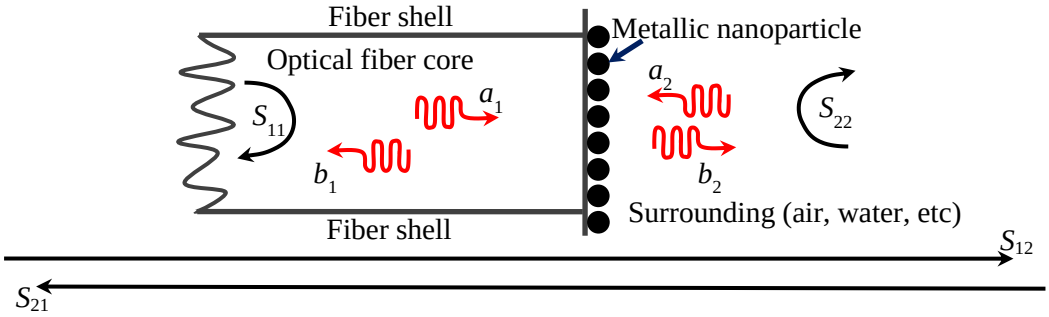

Fig. 1 – Simulation layout of the nanostructure based on the metal NPs monolayer on the fiber edge

For effectiveness of the photoacoustic transformation of the modulated optical signal in the acoustic waves due to periodical thermal expansion/contraction, it is necessary to fulfil the following conditions: 1. Commercially available cheap laser with up to GHz-range frequency response (405, 445, 450, 510–530 nm semiconductor lasers are studied theoretically); 2. Wide peak in the absorption spectrum (full width at the 90% maximum exceeding 25 nm is studied); 3. High absorption value at the spectral peak (more than 50% is studied).

Semiconductor lasers allow easy and effective coupling with optical fiber. In this work, optical loss coefficient is calculated from optical scattering parameters. Optical loss in the nanostructure are calculated as loss associated with energy dissipation. It is shown earlier that Au NPs monolayer on the optical fiber edge allows the most effective transformation of the modulated optical signal in the acoustic waves within wide ranges of sizes (from 10 to 30 nm) and surface occupation densities (from 35 to 70%) /8/. In particular, it is possible achieve optical power up to 60 mW at the wavelength of 520 nm in the optical fiber. Absorption peak for nanostructures based on Ag NPs monolayer on the optical fiber edge is observed near the wavelength of 445 nm. Absorbtion coefficients are less than to 30%. But it is possible achieve optical power up to 1800 mW at the wavelength of 445 nm in the short optical fiber pigtails /8/.

Fig. 2 shows regions of nanostructure parameters, which provide the most effective absorption of the laser radiation (1 denotes region for Ag NPs within the air surrounding, 2 denotes region for Ag NPs within the water surrounding). It is necessary to note, that thin protective coatings can be deposited on the NPs monolayer.

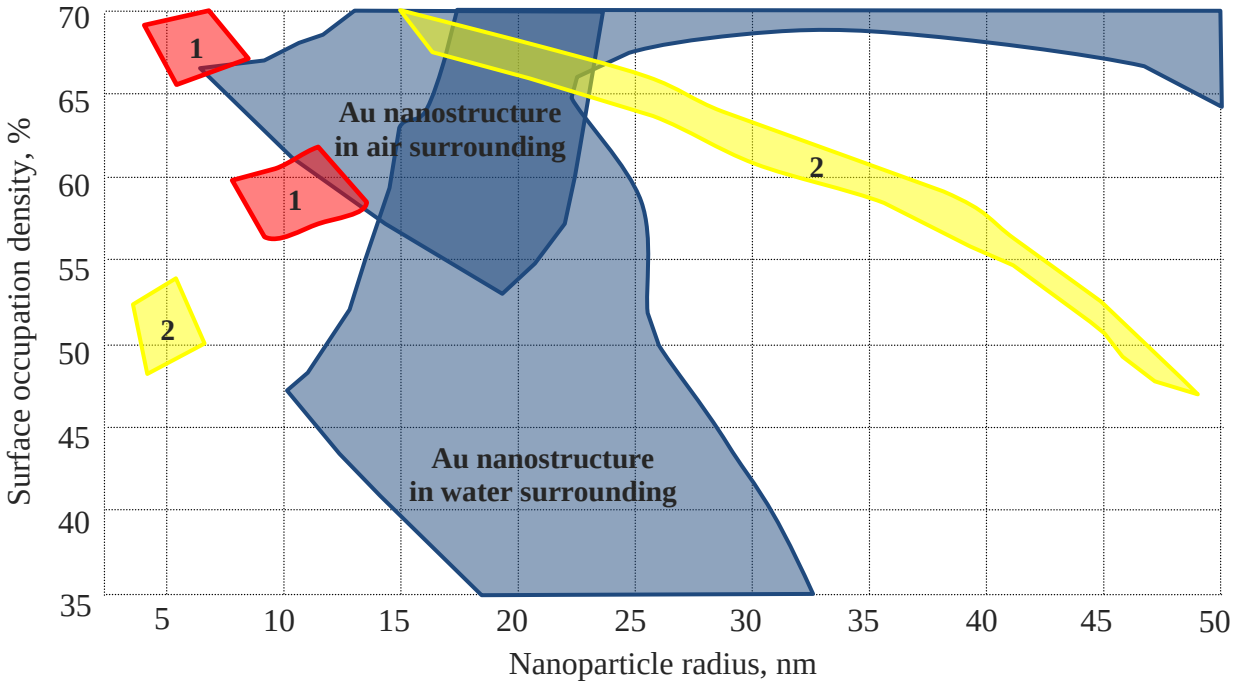

Fig. 2 – Regions of parameters, which provide the most effective absorption of the laser radiation by surface nanostructures (1 for Ag NPs in the air surrounding, 2 for Ag NPs in the water surrounding)

It is shown that Au NPs monolayer on the optical fiber edge allows the most effective transformation of the modulated optical signal in the acoustic waves within wide ranges of sizes (from 10 to 30 nm) and surface occupation densities (from 35 to 70%).

References

1. **Nan Wu, Ye Tian, Xiaotian Zou, Xingwei Wang** Proc. SPIE, 8694 (2013) 86940.
2. **Smith R., Arca A., Chen X., Marques L. ,Clark M., Aylott J., Somekh M.** Phys.:Conf., 278 (2011), 012035.
3. **Ortega-Mendoza J.G., Chavez F., Zaca-Moran P., Felipe C., Perez-Sanchez G.F., Beltran-Perez G., Goiz O., Ramos-Garcia R**. Opt. Expr., 21(5), 6509 (2013).
4. **Bishop C.A.** Vacuum deposition onto webs, films and foils (Elsevier: Amsterdam, 2016).
5. **Kozadaev K.V.** J. of Eng. Phys. and Thermophys, 87(3), 704 (2014).
6. **Kozadaev K.V.** Instr. and Exp. Techn., 59(6), 863 (2016).
7. **Goncharov V.K., Kozadaev K.V., Mikitchuk A.P.** High tem. mat. proces.: an intern. quart. of high-technol. plasm. proces. 18(3) 217 (2014).
8. **Mikitchuk A.P., Kozadaev K.V.** 26th Int. Symp. “Nanostructures: Physics and Technology” (Minsk, Belarus, June 18–22), 99 (2018).

COMPOSITE MEMBRANES WITH TWO HYDROPHOBIC LAYERS OBTAINED BY PLASMA POLYMERIZATION

L. Kravets[1], N. Lizunov[1], A. Gilman[2], V. Satulu[3], B. Mitu[3], G. Dinescu[3]

[1]Joint Institute for Nuclear Research, Flerov Laboratory of Nuclear Reactions, Joliot-Curie Str. 6, 141980 Dubna, Russia
[2]Enikolopov Institute of Synthetic Polymer Materials, Russian Academy of Sciences, Profsoyuznaya Str. 70, 117393 Moscow, Russia
[3]National Institute for Laser, Plasma and Radiation Physics, Atomistilor Str. 409, 077125 Magurele-Bucharest, Romania
E-mail: kravets@jinr.ru

The synthesis and characterization of the polymer bilayer composite membranes (CMs) prepared by deposition of nanosized films onto one side of a porous substrate using a plasma polymerization were performed. Polypropylene track-etched membrane (PP TM) with thickness of 10.0 μm and pore diameter of 300 nm (pore density of 10^8 cm^{-2}) was used as a porous substrate. To produce the membrane, PP-foil 'Torayfan' T2372 (Toray Co., Japan) was irradiated by xenon ions accelerated at the cyclotron and then subjected to physicochemical treatment using the method described in /1/. The deposition of the polymer films onto the membrane surface was conducted by RF-discharge (13.56 MHz, 100 W) generated at a working pressure of 0.7 Pa established by a mixture of argon, used as the feed gas, with hexamethyldisilazane (HMDSN) vapors used as a precursor. The deposition time was varied. The schematic diagram of the setup and the processing procedure are described in detail in /2/.

The surface morphology of the membranes was characterized by scanning electron microscopy (SEM) and atomic force microscopy (AFM), the surface properties were studied by measuring the water contact angles, and the chemical structure was investigated by X-ray photoelectron spectroscopy (XPS). The measurements of the current-voltage characteristics of the membranes were carried out with a direct current regime in the voltage range of –1 to +1 V using a PC-controlled potentiostat 'Elins P-8S' (Russia) with a scan rate of 50 mV/s. A two-chambered cell with Ag/AgCl electrodes, containing a water solution of potassium chloride of identical concentration on both sides of the membrane was used for this purpose.

The investigation of the CMs formation process shows that, as the thickness of the deposited polymer layer increases, the pore diameter on the membrane surface decreases. When the process is carried out for 5 min, the thickness of the polymer layer of hexamethyldisilazane (PPHMDSN) is 150 nm, which causes a slight decrease in the diameter of pores, which remain open (Fig. 1b). In the case of a membrane with a thickness of the deposited layer of

300 nm, the decrease in pore diameter is more significant (Fig. 1c), which causes a significant decrease in the gas permeability (Table 1). After the processing for 20 min, the thickness of the polymer layer is 600 nm, and the SEM studies show that it covers the pores almost completely (Fig. 1d). A further increase in time to 30 min results in a thickness of the polymer layer of 900 nm, which completely covers the pores on the surface of the TM (Fig. 1e). The examination of a transverse chip of such a membrane shows (Fig. 1e, inset) that the pores in the layer of the deposited polymer are markedly narrowed, and the average pore diameter in the mouth is about 20 nm.

Table 1. Change of the membrane characteristics after plasma treatment

Characteristics	Original membrane	Modified membrane (min)			
		5	10	20	30
Relative increase in the mass (%)	—	2.5	4.4	10.0	13.5
Thickness of the deposited layer (nm)	—	150	300	600	900
Air flow rate at $\Delta P=10^4$ Pa (ml/min cm^2)	280	255	240	195	15
Effective pore diameter (nm)	300	295	290	275	130
Water contact angle (deg)	120	100	98	97	96
Surface roughness, R_{ms} (nm)	34.7	21.9	19.5	17.0	13.8

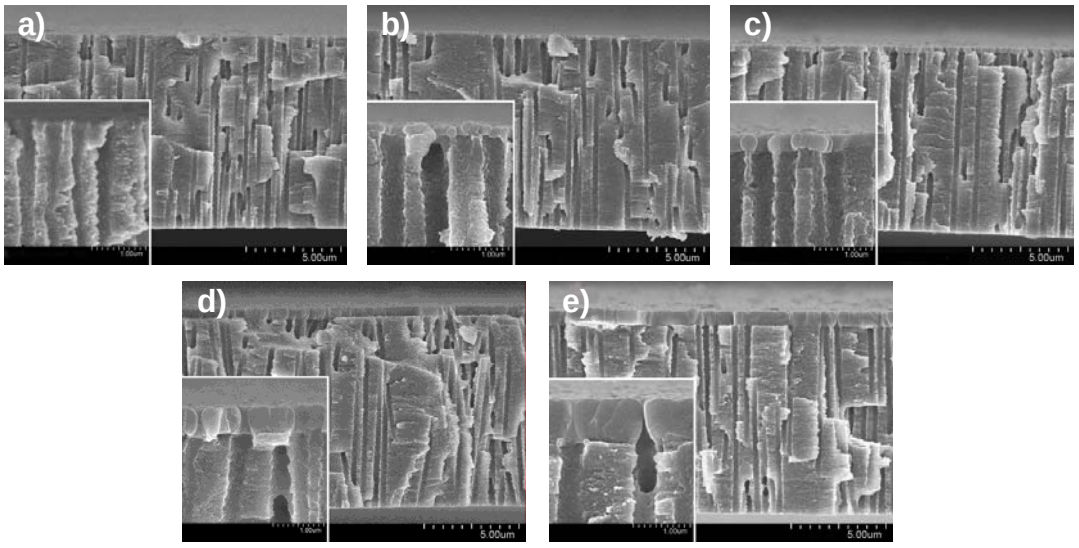

Fig. 1 – SEM images of the surfaces and cross-sections (insets) of the original PP TM (a) and membranes with applied layer of PPHMDSN with a thickness of 150 (b), 300 (c), 600 (d) and 900 nm (e)

The study of the surface morphology of modified membranes by means of AFM shows that, in the course of the coating deposition, a change in the roughness occurs on the surface of PP TM. For the original membrane, the standard deviation (R_{ms}) of the surface profile with respect to the baseline is 34.7 nm. The observed relatively high value of this quantity is associated with the

method of obtaining TM involving chemical etching in the environment of a powerful oxidant. The PPHMDSN film deposition by plasma leads to a smoothing of the irregularities, so the value of R_{ms} for the modified samples is markedly reduced. For example, the deposition of the film with a thickness of 150 nm leads to a decrease in the R_{ms} value to 21.9 nm, whereas with a thickness of 300 nm, this value decreases to 19.5 nm (Table 1). The comparison of the surface properties of the original PP TM and the modified membranes shows that a decrease in the value of water contact angle from 120° to 98° is observed after the deposition of the PPHMDSN film; however, both CMs layers are hydrophobic.

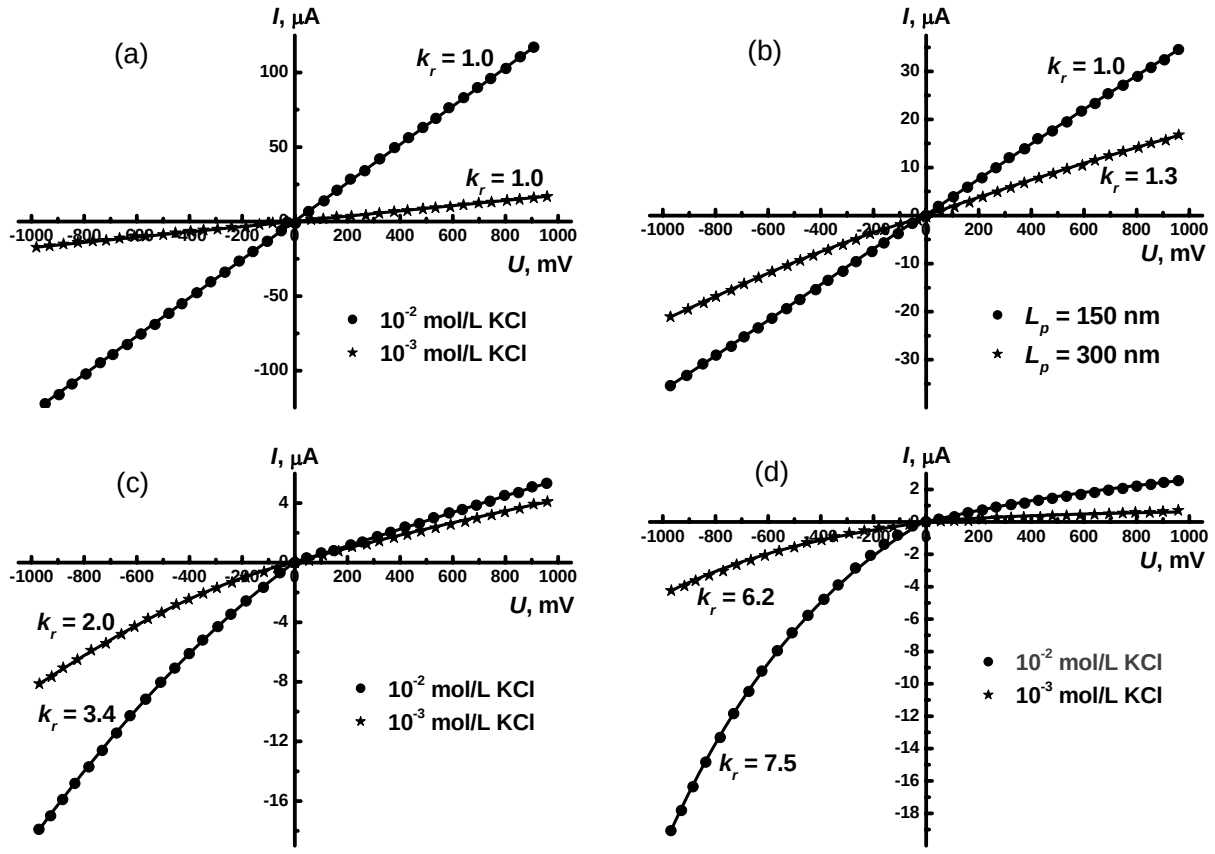

Fig. 2 – Current-voltage characteristics of original PP TM (a) and membranes with applied PPHMDSN layer having a thickness (L_p) of 150 and 300 nm in KCl solution at a concentration of 10^{-2} mol/L (b); and PP TM with applied PPHMDSN layer having a thickness of 600 (c) and 900 nm (d) in KCl solution at a concentrations of 10^{-2} and 10^{-3} mol/L

The XPS spectra of PPHMDSN polymer films exhibit peaks associated with carbon, silicon, nitrogen, and oxygen atoms. The deconvolution of the C1s spectrum indicates the presence of C–Si (283.5 eV), C–C, C–H (284.5 eV), and C–N, C–O (286.0 eV) bonds, whose concentration is 90.9, 6.1, and 3.0%, respectively. The deconvolution of the Si2p spectrum shows the presence of next bonds: Si–C (100.3 eV), Si–N (101.6 eV), and Si–O (102.4 eV) with

concentration of 91.1, 6.2, and 2.7%, respectively. The presence of oxygen-containing chemical groups means that a part of the carbon and silicon atoms is in the oxidized state, which is inherent in polymers produced by plasma polymerization.

The measurement of the current-voltage characteristics shows that the electrical conductivity of PP TM with a 150-nm-thick layer of PPHMDSN, for which the pore diameter at the surface and the effective pore diameter hardly change, does not depend on the current direction (Fig. 2b), but only results in a decrease in the current value. This could be connected with the existence of an interface between the original membrane and the polymer layer. The deposition of layers with a higher thickness leads to a conduction asymmetry in CMs, i.e., a rectifying effect that consists in the difference in currents of opposite directions (Figs. 2b-d). So, the rectification coefficient for a membrane with a PPHMDSN layer of 300 nm thick in a KCl solution with a concentration of 10^{-2} mol/L is 1.3, whereas in the case of KCl concentration amounting to 10^{-3} mol/L, this coefficient is 1.2. In the case of a deposited PPHMDSN layer with a thickness of 600 nm, CM exhibits the formation of conical pores with a considerable decrease in their diameter at the mouth (Fig. 1c). The rectification coefficient for such a membrane in the KCl solution with a concentration of 10^{-2} mol/L is 3.4, whereas in the KCl solution with a concentration of 10^{-3} mol/L, the coefficient is 2.0. The deposition of the layer with a thickness of 900 nm leads not only to a decrease in the current but also to an increase in the rectification coefficient: in KCl solution with a concentration of 10^{-2} mol/L, k_r = 7.5, whereas in the solution with a concentration of 10^{-3} mol/L, k_r = 6.2. The main reason for the conduction asymmetry occurring in CMs of this type consists in the change in the pore geometry and in a substantial decrease in the pore diameter in the deposited polymer layer (Fig. 1e), which leads to the difference in the resistance of the system with change in the current direction.

Acknowledgements. This work was performed in the frame of collaboration between the JINR, FLNR (Dubna) and NILPRP (Bucharest), contract no. 4648-5-17/21. We are grateful to Russian Foundation for Basic Research (grant No. 17-08-00812) for financial support.

References

1. **Kravets L.I., Dmitriev S.N., Apel P.Yu.** Collect. Czech. Commun., 62 (1997) 752–760.
2. **Kravets, L., Dmitriev S., Lizunov N., Satulu, V., Mitu B., Dinescu G.** Nucl. Instr. Meth. B, 268 (2010) 485–492.

UNIFIED POWER SUPPLY UNIT FOR ACOUSTOPLASMA DEVICES

A.S. Abrahamyan*, T.J. Bezhanyan, R.Yu. Chilingaryan, H.T. Hovhannisyan

Institute of Applied Problems of Physics, NAS of Armenia,
25 Hr. Nersisyan str., 0014, Yerevan, Armenia
*E-mail:arbel11@mail.ru

Usually, for the supply of gas-discharge lasers and gas-discharge lamps of solid-state lasers, a constant, a variable (LF, HF, SHF) and a pulsed current /1/ is used.

When the discharge is powered by a modulated current containing a constant and a variable component, an acoustic field appears in the discharge, caused by the variable current component and coinciding with it in frequency. This acoustic field interacts with the plasma in the discharge tube, the discharge tube is behaving like an acoustic resonator. As a result, the plasma passes into a new - acoustoplasma state. In the acoustoplasma state, the plasma parameters can differ considerably from the plasma parameters without an acoustic perturbation /2, 3/.

The architecture of modern laser tubes and power supply units (PSUs) does not take into account the specifics of acoustoplasma interaction. The specificity of the acoustoplasma discharge is such that during the period of modulation of the discharge current the ohmic discharge resistance can vary from several tens of kOhm to several MOhm, short-term current and voltage surges several times higher than the average values over the modulation period.

Particularly serious requirements are imposed on the PSU of an acoustoplasma gas-discharge laser. The average voltage at the discharge is 5-10 kV, the input power is hundreds of watts, and the modulation frequency should vary from very low frequencies to several tens of kHz. The power supply unit for the acoustoplasma magnetron should provide a stable mode of operation with a discharge current change from 150-200 mA with a change in the discharge resistance from values close to a short circuit to values close to idling.

Therefore, for acoustoplasma gas discharge devices, a unified power supply unit was developed capable of providing different depths of modulation of the discharge current at different frequencies.

The PSU is designed to supply lasers, magnetrons, gas-discharge light sources, plasma chemical reactors and other gas-discharge devices with both direct current and modulated current containing constant and variable components.

It works stably with significant fluctuations in the active and differential resistances (tested in short-time idle and short-circuit modes), with overloads in energy input, voltage and current. In addition, the PSU undergoes minimal changes (changing the high-voltage (HV) transformer and multiplier) for magnetron discharges or for discharge tubes of different designs, different lengths and different gas compositions, both independently with a separate tube and as part of a modular laser, when feeding individual modules.

Fig. 1 shows a schematic diagram of the developed PSU.

The mains power supply (1) Fig.1 provides a constant voltage of 300 V for power supply and +15 V for power supply of the control part. The control input of the pulse-width modulator (PWM converter) (2) is fed with a modulating frequency signal (6). PWM converter frequency is 50 kHz. At the output of the PWM converter there are powerful HV transistors providing power to the transformer and the voltage multiplier (3). A small resistive ballast (4) serves to protect the discharge tube (5) from overload and is much smaller in magnitude than the average value during the modulation period of the negative differential resistance (when the DC power is applied, the ballast resistance must be greater than the negative differential resistance). Reducing ballast resistance significantly increases the efficiency of the power supply.

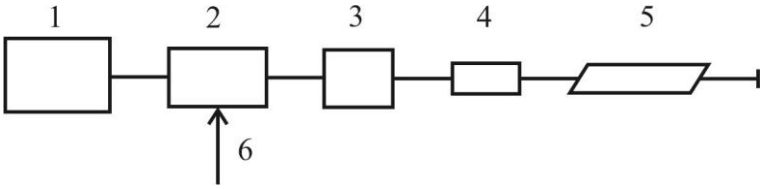

Fig. 1 – Diagram of supply of acoustoplasma discharge. 1 - power supply; 2 - pulse-width modulation voltage converter and power amplifier; 3 - high-voltage transformer and voltage multiplier; 4 - resistive ballast; 5 - magnetron; 6 - the modulating signal

Fig. 2 shows the diagram of voltage at different points in the circuit.

A diode voltage multiplier is connected to the secondary winding of the transformer. The capacitors of the multiplier are selected in such a way that the output high voltage after the multiplier at the input of the resistive ballast (pos.4 Fig. 1) contains the constant and variable components (diagram 3 of Fig. 2) and the component variable repeats the frequency and shape of the modulating signal curve. This voltage is applied to the discharge tube.

Fig. 3 shows the circuit diagram of the power supply unit. The PWM converter is assembled on a TL494 chip. Resistance R1 - changes the clock frequency. The external generator G specifies the frequency and depth of modulation, which is determined by the amplitude of the signal of the generator

G and the position of the engine R2, which determine the duration of the PWM pulses at the zero level of the signal of the generator G (i.e., the level of the constant component of the discharge current). The keys on the transistors VT1 - VT4 through the transformer decouplings T1 and T2 control the high-voltage transistors VT5 and VT6. The primary winding of the T3 transformer is connected to a half-bridge inverter (VT5, VT6, C1, C2).

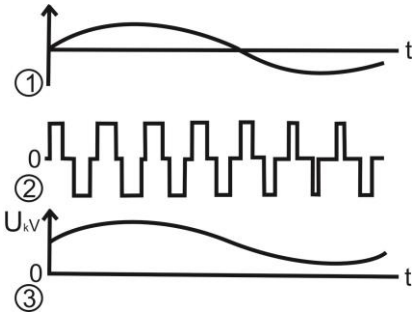

Fig. 2 – Power supply voltage diagrams. 1 - modulating signal; 2 - signal on primary winding of HV transformer; 3 - voltage at the output of the HV multiplier

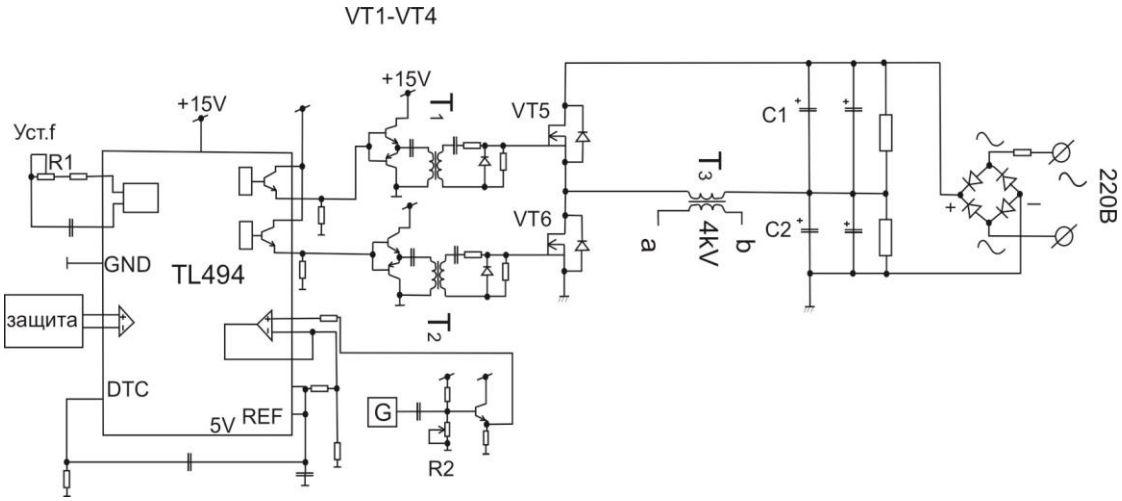

Fig. 3 – Diagram of the power supply unit (without multipliers). The pulse amplitude on the primary winding is 150 V, and on the secondary side it is ~ 4 kV for the laser (and 1.5 kV for the magnetron)

For short laser tubes (the length of the discharge gap is <0.4 m), a doubler of voltage is sufficient.

For long discharge tubes, a multistage full-wave /4/ multiplier is used (Fig. 4), which allows the output voltage to be 15-20 kV at currents of 20-30 mA.

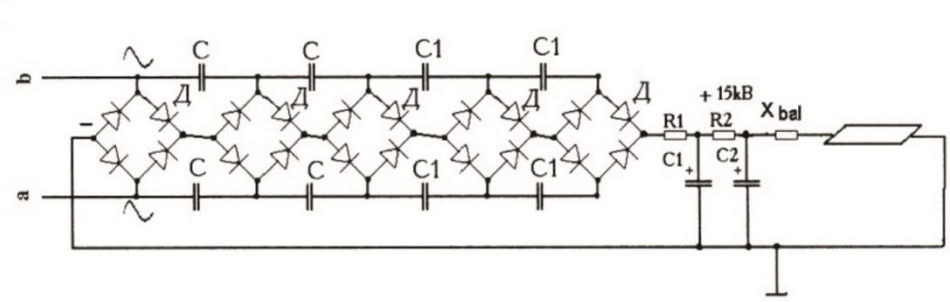

Fig. 4 – Full-wave multiplier

The manufactured power supply units had the following parameters:

- Modulated high voltage output, kV - up to 20
  Modifications (3-4 kV)
- Output power, W - 400
- Supply voltage, V - 220
  Modification – onboard network, V 27
- Frequency range of output modulation
  high-voltage, kHz - 0 - 10
- Modulation depth change, % - 0 - 50
- The form of the discharge current - is a sine or any other

The described power supply can be used in various areas not related to acoustoplasma, for example, in geophysics (electrical prospecting), biophysics (the effect of slowly varying electric and magnetic fields over large areas), etc.

References

1. Reference book on lasers. In 2 volumes. v.1, M., Energia, (1978), 504c.
2. **Mkrtchyan A.R., Mkrtchyan A.H., Abrahamyan A.S**. VII International Conference Plasma Physics and Plasma Technology, PPPT-7, Minsk, Belarus, 17-21 Sept. (2012), Proc., v.1, 3-5.
3. **Abrahamyan A.S.** Features of the acoustoplasma operating mode of gas-discharge devices. In this Proc.
4. **Severns P., Bloom G.** DC impulse converters for secondary power supply systems. (rus; Moscow, Energoatomizdat, (1988), 294 p.).

INVESTIGATION OF THE DEVELOPED ACOUSTOPLASMA MAGNETRON IN THE SPUTTERING MODE

A.S.Abrahamyan*, T.J.Bezhanyan, R.Yu.Chilingaryan, A.S. Hakobyan, H.T. Hovhannisyan, A.H.Mkrtchyan, V.V.Nalbandyan

Institute of Applied Problems of Physics, NAS RA,
25 Hr. Nersisyan str., 0014, Yerevan, Armenia
*E-mail: arbel11@mail.ru

The experimental results for a developed cylindrical planar acoustoplasma magnetron (a diode with magnetic izolation) are presented /1,2/.The difference between the acoustoplasma discharge and the discharge at a constant current is described in /3, 4/. The acoustoplasma is created in the discharge by the interaction of a plasma created by a modulated discharge current containing a constant and a variable component with acoustic vibrations. The parameters of the acoustoplasma, including the magnetronacoustoplasma, can differ from the plasma parameters without acoustic perturbation.

The manufactured magnetron had a ferrite-barium magnet ring with dimensions D_{out} = 45 mm, D_{in} = 18 mm, ring height h = 10 mm, magnetic induction ~ 0.3-0.5 Tl. The diameter of the central core d = 7 mm, height h = 12 mm.

The plasma torus had an external diameter of 26 mm and an inner diameter of 12 mm. The anode was a ring with a diameter of 50 mm made from a 6 mm copper rod. The distance from the anode to the cathode could be varied from several mm to several cm.

The region of localization of a strong magnetic field was located at a distance of 0-4 mm from the cathode. When the cathode was displaced for long distances, the discharge became unstable, space charge pulsations began.

A specially designed power supply unit was used to supply the magnetron /5/. The average current of the magnetron discharge is 0.1-0.15 A (the current density at the cathode surface is ~ 20 mA / cm^2). Voltage at the discharge is of 150-300 V. Parameters for DC power supply and in acoustoplasma mode were compared.

Fig. 1 shows the work of the magnetron when deposited on a glass substrate.It is seen how the stream of sputtered particles "hits" the glass substrate. The diameter of the torch of the sputtered material is ~ 4 cm, the height of the glow of the torch is 8-10 cm. It can be seen from Fig. 1 that the intensity of the torch is more typical for a plasmatron than for a magnetron.

The formation of a narrow torch is associated with the focusing action of the anode loop of small radius.

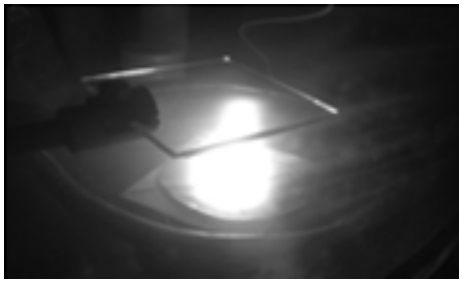

Fig.1 – The work of the manufactured magnetron

As a result of ion acceleration after the passage of the anode loop, it is possible to obtain such a large energy of the sputtered particles that the deposition layer is destroyed, i. e. at the same time, an etching of the sprayed particles takes place. This energy is less than the standard implantation energy.

Fig. 2 shows a scheme for measuring ion and electron currents with two grids. Such a scheme allows to measure more exactly the collector current and avoid the parasitic effect of modulating the voltage on the anode on the collector current.

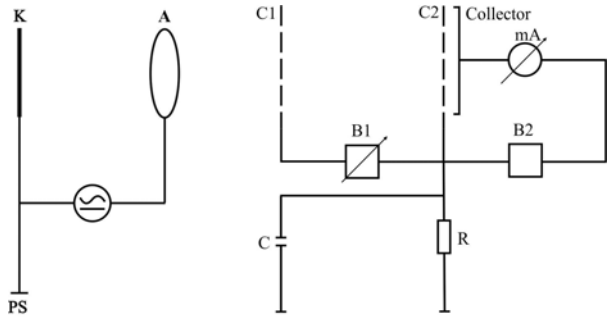

Fig. 2 – Scheme of measuring the strength of ion and electron currents in experiments with an acoustoplasma magnetron. K–sputtered cathode, A-anode, C1-first grid, C2-second grid, Collector-collector, mA-microammeter, B1–battery1, B2–battery2, PS-discharge power source, R, C-resistance and leakage capacitor

Fig. 3 shows the change in the ion current (with a voltage on the first grid>0, in this case the field between the grids 1 and 2 slows the electrons) and electron current (voltage on the first grid <0, the field between grids 1 and 2 slows the ions). Fig. 3 also shows the expression of the approximating curve. It can be seen from Fig. 3 that the collector current becomes purely ionic only after the voltage that detains the electron is ~ 8V.

M is the depth of modulation of the discharge current (the ratio of the variable component to the direct),I_0 is the value of the direct component.

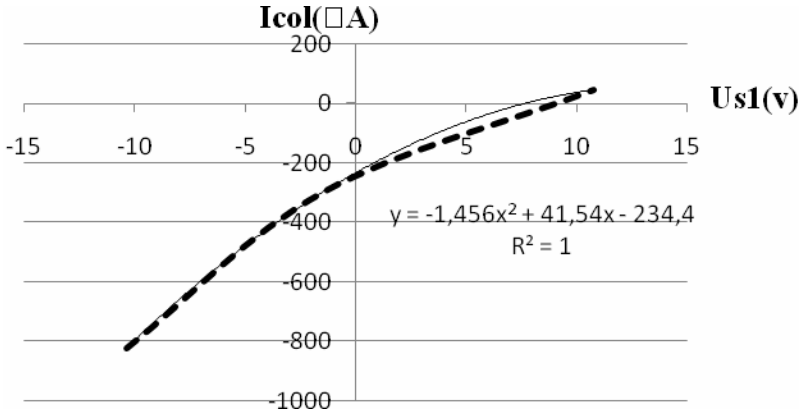

Fig.3 – Ion and electron currents to the collector in the acoustoplasma mode: f = 1.25 kHz, M = 0.25, I_0 = 0.15 A, U_{s2} = -1.5 V, U_{s1} = -10.4 / + 10.8 V

Conclusion

- A cylindrical planar acoustoplasma magnetron was developed.
- The small radius of the anode loop allows focusing and further acceleration of the ionic component of the sprayed material. The possibilities of focusing and its aberration are shown.
- The characteristics of the magnetron are compared when supplied with DC and in acoustoplasma mode (AP) (with a modulated current supply containing direct and variable components).
- The radiation pattern of the particle flow from the sputtered cathode is significantly narrowed (the angle at the level of 0.5 from the maximum in the directivity pattern in existing magnetrons is ~ 100°, and in the developed magnetron ~ 50° in the DC mode and ~ 40° in the AP mode).
- The current-voltage characteristic for the AP regime at a buffer gas pressure of 0.5 Pa is increasing, and at a buffer gas pressure of 10 Pa is decreasing. For the DC mode at 0.5 Pa - increasing, and at a pressure of 10 Pa - parallel to the axis of the current, i.e. When the discharge current changes, the voltage remains constant.
- At a cathode power density of 95 W / cm^2, when the anode-substrate distance is changed from 2 to 4 cm in the DC mode, the sputtering speed decreases by a factor of 3.4, and in the AP mode by a factor of 2.3. With a power density of 75 W/cm^2, respectively, 3.3 and 2 times. With a power density of 55 W/cm^2, respectively, 3.8 and 2.5 times. With a power density of 40 W/cm^2, respectively, 12.5 and 4.7 times. Thus, with increasing distance from the anode to the substrate and decreasing power density (i.e., discharge current), the AP mode becomes increasingly advantageous.

- A scheme is proposed for measuring the strength of ion and electron currents in experiments with an acoustoplasma magnetron, taking into account the specificity of the acoustoplasma discharge.
- Graphs of ion and electron currents on the substrateare shown.

References

1. **Mkrtchyan A.H., Mkrtchyan A.R., Abrahamyan A.S., Nalbandyan V.V.** Method of acoustoplasma sputtering in vacuum.The patent of Armenia N3086A, 27.10.2016.
2. **Mkrtchyan A.R., Abrahamyan A.S.** The First Russian CrystallographicCongress, Moskow, November 21-26 (2016),Thesis, p.177.
3. **Mkrtchyan A.R., Mkrtchyan A.H., Abrahamyan A.S**. VII International Conference Plasma Physics and Plasma Technology, PPPT-7, Minsk, Belarus, 17-21 Sept. (2012), Proc., v.1, 3-5.
4. **Abrahamyan A.S.** Features of the acoustoplasma operating mode of gas-discharge devices. In this Proc.
5. **Abrahamyan A.S., Bezhanyan T.Zh., Chilingaryan R.Yu., Hovhannisyan H.T.** Unified source for power supply of acoustoplasma devices. In this Proc.

FORMATION OF COMPOSITE MEMBRANES WITH HYDROPHILIC POROUS SUBSTRATE AND HYDROPHOBIC TOP LAYER

M.Yu. Yablokov[1], L.I. Kravets[2], V.A. Altynov[2], R.V. Gainutdinov[3]

[1]Enikolopov Institute of Synthetic Polymer Materials, Russian Academy of Sciences, Profsoyuznaya Str. 70, 117393 Moscow, Russia
[2]Joint Institute for Nuclear Research, Flerov Laboratory of Nuclear Reactions, Joliot-Curie Str. 6, 141980 Dubna, Russia
[3]Shubnikov Institute of Crystallography of FSRC "Crystallography and Photonics" Russian Academy of Sciences, Leninskii pr. 59, 119333 Moscow, Russia
E-mail: yabl1@yandex.ru

In the present paper, we describe the synthesis and characterization of polymer composite membranes with hydrophilic porous substrate and hydrophobic top layer. To prepare such type of composite membranes a polytetrafluoroethylene-like (PTFE-like) thin film has been deposited on one side of a poly(ethylene terephthalate) track-etched membrane used as a porous substrate. PTFE-like layers were deposited by electron-beam dispersion of solid polymer in vacuum. The electron source was a filament electron gun; the initial pressure of residual gases in the reaction chamber was ~10^{-3} Pa; the emission current 10 mA and the electron energy 1.2 keV. The target was a PTFE plate of 10 mm in thickness and 35 mm in diameter (Plastopolymer, St. Petersburg). The schematic of the setup and the treatment procedure detail are described in /1/.

The characteristics of the original membrane and membranes with the deposited polymer layers were determined by different procedures. The amount of the deposited polymer on the membrane surface was defined by the gravimetric method. The gas flow rate through the membranes was determined at an adjusted pressure drop. Gas consumption was measured by a float-type flow meter. The effective pore diameter was calculated using the Hagen-Poiseuille equation from the obtained data. Surface topography of the membranes was studied using a NTEGRA Prima (NT-MDT, Russia) atomic force microscope (AFM). Measurements were made in the dynamic mode to obtain a three-dimensional image; the scan area for each sample was 5×5 μm^2. The surface properties were characterized by values of the contact angle measured with an Easy Drop DSA100 instrument (KRUSS, Germany) using deionized water as a test liquid.

The characteristics measured for the original PET TM and the membranes with a polymer layer obtained by electron-beam dispersion of PTFE are shown in Table 1. Standard deviations of values were calculated after triplicate experiments. As it follows from the given data, the deposition of the PTFE-like layer on the PET TM surface leads to a gradual increase in mass of the sample

with the increasing time of the process. The thickness of the membrane increases, and the effective pore diameter decreases in this case. Thus, during deposition for 4.5 min, the thickness of PTFE-like layer reaches 150 nm and the effective pore diameter decreases by 55 nm. In the case of membrane treatment for 7 min, the thickness of the deposited PTFE-like layer is 250 nm and the effective pore diameter decreases by 75 nm. A decrease in the effective pore diameter of the composite membranes means that the pore diameter in the deposited polymer layer is much smaller than that of the original PET TM.

Table 1. Changes in the membrane characteristics with a PTFE-like layer on the surface

Parameters	Original membrane	Modified membrane (min)	
		4.5	7.0
Relative increase in the mass (%)	—	2.9 ± 0.1	4.2 ± 0.1
Thickness of deposited layer (nm)	—	150 ± 5	250 ± 5
Air flow rate at $\Delta P=2\times10^4$ Pa (ml/min cm^2)	300 ± 5	125 ± 3	85 ± 3
Effective pore diameter (nm)	250 ± 7	195 ± 5	175 ± 5
Water contact angle (deg)	65 ± 1	115 ± 1	140 ± 1

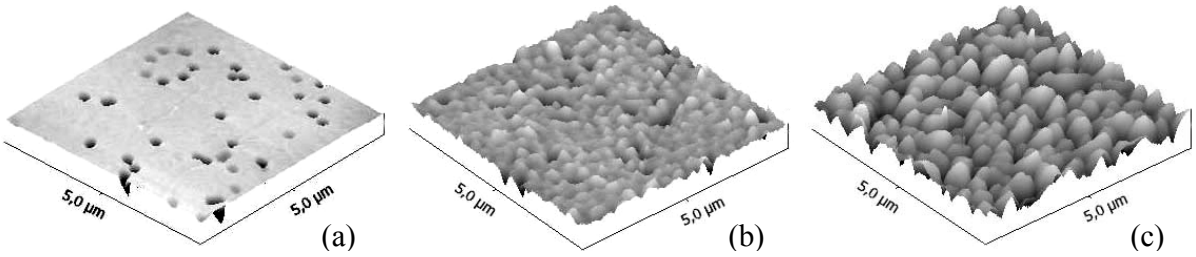

Fig. 1 – AFM images of the surface of the original PET TM (a) and the membranes after deposition of the polymer layer by electron-beam dispersion of PTFE for 4.5 (b) and 7 min (c)

Study of the surface of the modified membranes using AFM (Fig. 1) shows that only an insignificant reduction of the pore diameter on the membrane surface is observed for the membrane treated for 4.5 min (Fig. 1b). The membrane pores are open in this case. In contrast, for a membrane treated for 7 min a PTFE-like layer on the treated side covers the membrane pores (Fig. 1c). The essential reduction in the effective pore diameter for this membrane suggests that PTFE-like polymer is deposited mostly on the pore surface, with the pore shape being altered. According to AFM data, the pore diameter on the back side of the modified membranes remains practically unchanged in our experiments. This means that the electron-beam deposition of the PTFE-like layer onto the PET TM surface leads to a change in the pore geometry, namely, the pores acquire an asymmetric shape. Moreover, the AFM data show that the deposited PTFE-like layer has globular character (Fig. 2a and 2c). The globules,

constituting the porous system of the layer, are polymer nanoclusters with an irregular shape. Determination of a particle size shows that with increasing deposition time of PTFE-like layer, the size of the deposited particles increases. For example, the average particle size of the deposited polymer during the process for 7 min is ~ 300 nm, and their maximum size reaches 500 nm (Fig. 2b). During the process for 15 min, the average size of PTFE-like globules is 400 nm, and their maximum value reaches 700 nm (Fig. 2d).

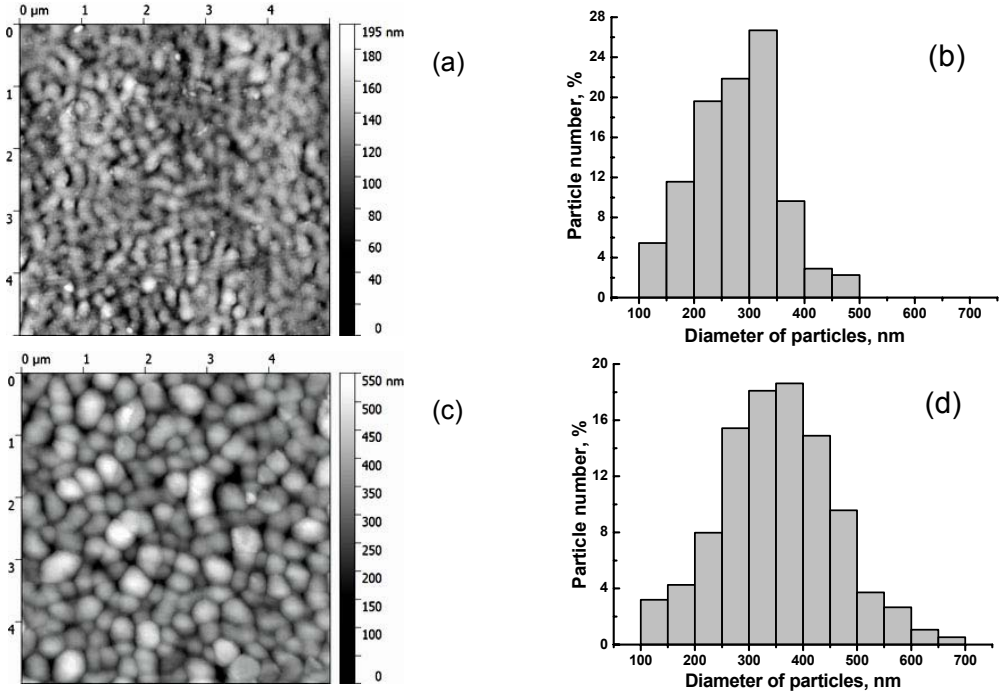

Fig. 2 – AFM images of the PET TM surface after deposition of PTFE-like layer with the thickness of 200 (a) and 500 nm (c); histograms of the particle size distribution for these PTFE-like layers (b and d)

The study of the wetting properties of the membranes has shown that the deposition of the PTFE-like film leads to substantial hydrophobization of the membrane surface. The original membrane has the water contact angle (θ) of 65°, whereas the PET TM with a PTFE-like layer on the surface has θ = 115° for the membrane treated for 4.5 min, and 140° for the membrane treated for 7 min. An increase of contact angle can be explained by increasing of the surface roughness /2/. So, for the membrane with 150-nm PTFE-like layer, the surface roughness (R_{ms}) is 13 nm. Deposition of the 250-nm polymer film leads to increasing of the R_{ms} value up to 30.5 nm and after deposition of the 500-nm film, the R_{ms} becomes equal to 70 nm.

The chemical structure of the polymer obtained by the electron-beam dispersion of PTFE was determined using X-Ray Photoelectron Spectroscopy (XPS) measurements. Analysis of the XPS spectrum of the PTFE-like layer shows the presence of the peaks corresponding to carbon and fluorine atoms.

Theoretically, the fluorine to carbon atomic ratio in PTFE is equal to 2. In the polymer layer obtained by electron-beam dispersion of PTFE, this ratio is 1.8, indicating the detachment of a certain amount of fluorine atoms during the deposition. A detailed analysis of the C1s spectrum (Fig. 3a) shows that it has a complex pattern due to the presence of C–C bonds (284.8 eV), CF_2 (292.1 eV), C*−CF (287.5 eV), C*F−CF (289.8 eV) and CF_3 (293.9 eV). Presence of (−CF_3) groups indicates the existence in the polymer layer macromolecules with short chains.

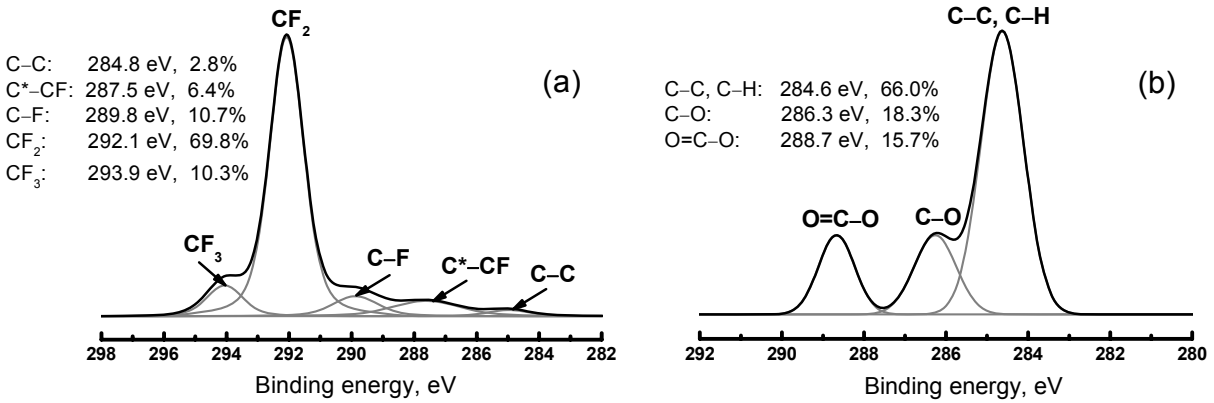

Fig. 3 – Carbon (C1s) spectra of the polymer obtained by electron-beam deposition of PTFE-like coatings (a) and the original PET TM (b)

Figure 3b shows the detailed structure of the carbon C1s peak for the original PET TM. The peak consists of three sub-peaks belonging to the C–C and C–H bonds (284.6 eV), to the C–O bond (286.3 eV) and to the O=C–O bond from the ester group (288.7 eV). Thus, the deposition of the PTFE-like layer onto the PET TM surface leads to the formation of the composite membranes consisting of two layers, one of which is the original PET matrix bearing terminal carboxyl groups on the surface and having an average level of hydrophilicity. The other layer deposited by electron-beam dispersion of PTFE has hydrophobic properties. Membranes of this type can be used in various separation processes, such as desalination of water, pervaporation, reverse osmosis, micro- and nanofiltration.

Acknowledgements. This work was supported by the Russian Foundation for Basic Research (grant No. 17-08-00812).

References

1. **Kravets L.I., Gilman A.B., Yablokov M.Yu. et al.** High Temp. Mater. Proc., 19 (2015) 121–139.
2. **Quere D.** Ann. Rev. Mater. Res., 38 (2008) 71–99.

INFLUENCE OF ELEMENTAL COMPOSITION ON THE OPTICAL PROPERTIES OF $Ti_{1-x}AL_xC_{1-y}N_y$ COATINGS PREPARED BY REACTIVE MAGNETRON SPUTTERING

I.M. Klimovich[1], V.A. Zaikov[1], L.V. Baran[1], V.V. Vorob'ev[2], A.M. Rogov[2], F.F. Komarov[1,3]

[1]Belarusian State University, Nezavisimosti ave. 4, Minsk, 220030, Belarus, imklimovicih@gmail.com, zaikov@bsu.by, brlr@mail.ru
[2]Kazan Physical-Technical Institute, Russian Academy of Sciences, Sibirskiy tract 10/7, Kazan, 420029, Russia, slavik.ksu@mail.ru, alexeyrogov11@gmail.com
[3]Sevchenko Research Institute of Applied Physics Problems, Kurchatov st. 7, Minsk, 220045, Belarus, komarovF@bsu.by

$Ti_{1-x}Al_xC_{1-y}N_y$ films were studied by energy dispersive X-ray analysis, scanning electron microscopy, atomic force microscopy, and optical spectroscopy. The results of investigation have been shown that solar absorptance coefficient $\alpha_s = 0.51$ and emittance $\varepsilon = 0.44$ correspond to the $Ti_{0.72}Al_{0.28}C_{0.34}N_{0.66}$ film, $\alpha_s = 0.59$ and $\varepsilon = 0.43$ correspond to the $Ti_{0.38}Al_{0.62}C_{0.32}N_{0.68}$ film, and $\alpha_s = 0.66$ and $\varepsilon = 0.31$ correspond to the $Ti_{0.51}Al_{0.49}C_{0.37}N_{0.63}$ film.

1. Introduction

Spectrally selective functional coatings prepared by plasma deposition processes are used as a solar absorber for solar thermal convertors and as a thermal control material for spacecraft applications /1, 2/. In this report, a systematic investigation has been made to determine optical characteristic of the $Ti_{1-x}Al_xC_{1-y}N_y$ films depending on elemental composition.

2. Experimental

Prior to deposition the substrates were cleaned by ion etching in argon plasma at $6.0 \cdot 10^{-2}$ Pa, at the discharge current of 20 mA, the discharge voltage was 2.4 kV, the cleaning time was 5 min.

$Ti_{1-x}Al_xC_{1-y}N_y$ coatings were deposited onto the glass and silicon substrates by a reactive magnetron sputtering technique. The deposition experiments were performed in an argon–nitrogen-acetylene plasma at $7.0 \cdot 10^{-2}$ Pa. The target-to-substrate distance was maintained at 80 mm. The discharge current was 1.5 A, the deposition temperature was 220 ◦C, the bias voltage was - 90 V, and deposition time was 20 min. Pressure, discharge current, substrate heating and bias potential were kept constant throughout the coating

deposition process. $Ti_{1-x}Al_xC_{1-y}N_y$ films with different elemental composition were deposited using various Ti-Al mosaic targets. The schemes of Ti-Al mosaic targets are shown in Fig. 1.

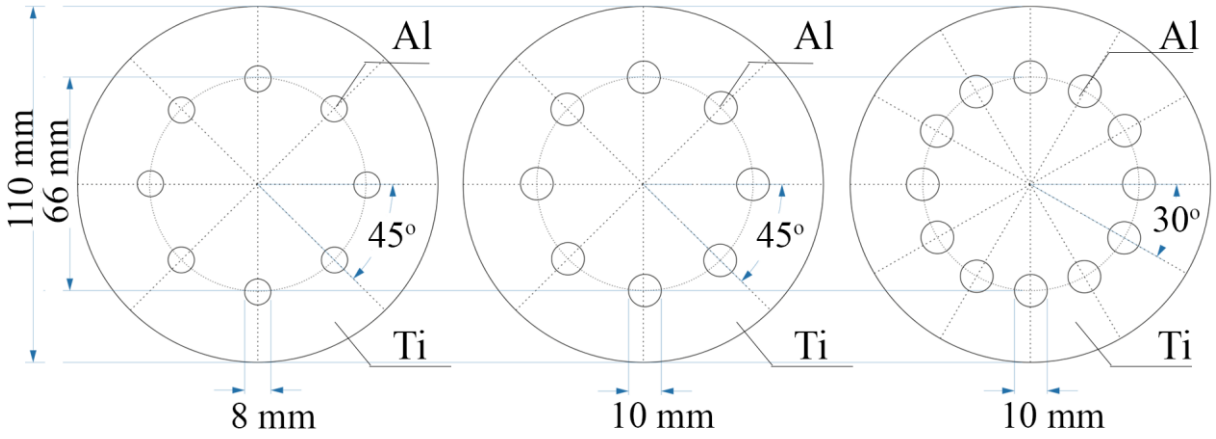

a b c

Fig. 1 – The schemes of the Ti-Al mosaic targets:
a) target no.1 with the lowest Al/Ti ratio; b) target no.2; c) target no.3 with the highest Al/Ti ratio

Microstructure of the $Ti_{1-x}Al_xC_{1-y}N_y$ coatings was studied by scanning electron microscopy (SEM) using a Merlin Carl Zeiss microscope. Elemental compositions of the films were determined by energy dispersive X-ray spectra (EDS). The surface roughness parameters (the average S_a and root-mean-square S_q) were measured by atomic force microscopy (AFM) with a Solver P47 Pro microscope.

Solar absorptance coefficient α_s and emittance ε of the films under study were calculated according to following formulas /3/:

$$\alpha_S = \frac{\int_0^\infty A(\lambda)P_\lambda^i\,d\lambda}{P_\lambda^i d\lambda} = \frac{1}{S}\int_0^\infty A(\lambda)P_\lambda^i d\lambda \quad (1)$$

$$\varepsilon = \frac{\int_0^\infty \varepsilon(\lambda)P_\lambda^{bb}(T)d\lambda}{\int_0^\infty P_\lambda^{bb}(T)d\lambda} \quad (2)$$

Here P^{i}_{λ} and $P^{bb}_{\lambda}(T)$ denote the incident spectral solar radiant power (or intensity, irradiance) and the temperature dependent, spectral blackbody radiant power respectively. The spectral absorptance, $A(\lambda)$, and spectral emittance, $\varepsilon(\lambda)$, were determined from optical measurements of reflectance and transmittance spectra in wavelength range of 0,36-25 mkm.

3. Results and discussion

The results of EDS measurements of $Ti_{1-x}Al_xC_{1-y}N_y$ coatings are presented in Table 1. Fig. 2 shows SEM images of $Ti_{1-x}Al_xC_{1-y}N_y$ coatings.

Table 1 – The elemental composition of $Ti_{1-x}Al_xC_{1-y}N_y$ films

Sample	Target no.	Elemental composition, at. %						(Al+Ti)/(C+N)
		Ti	Al	C	N	O	Ar, Si, Cu, etc.	
$Ti_{0.72}Al_{0.28}C_{0.34}N_{0.66}$	1	47.39	17.94	10.42	18.56	4.02	1.67	2.25
$Ti_{0.51}Al_{0.49}C_{0.37}N_{0.63}$	2	19.72	19.10	18.28	30.25	6.41	6.24	0.80
$Ti_{0.38}Al_{0.62}C_{0.32}N_{0.68}$	3	19.40	32.23	12.78	26.62	2.62	6.35	1.31

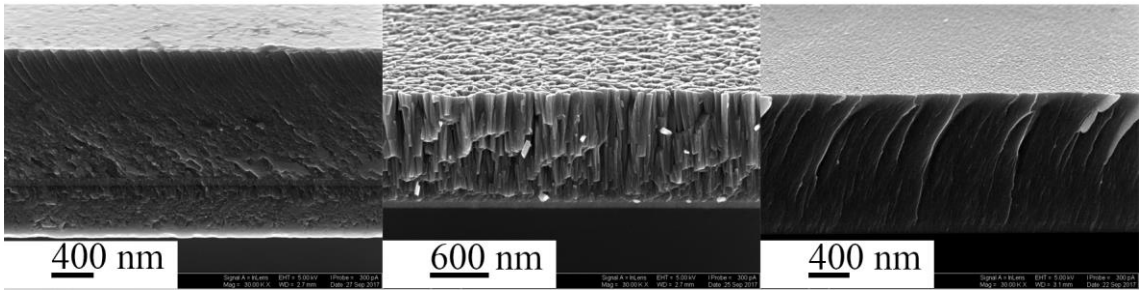

a b c

Fig. 2 – SEM images of $Ti_{1-x}Al_xC_{1-y}N_y$ coatings:
a) $Ti_{0.72}Al_{0.28}C_{0.34}N_{0.66}$; b) $Ti_{0.51}Al_{0.49}C_{0.37}N_{0.63}$; c) $Ti_{0.38}Al_{0.62}C_{0.32}N_{0.68}$

There are impurities of the aluminum alloy AK1.0 (Si, Cu, Mg, Mn, Fe, Na), oxygen and argon in the $Ti_{1-x}Al_xC_{1-y}N_y$ films composition. The oxygen concentration in the coating can be due to the coating microstructure peculiarities. The presence of argon is associated with the implantation of argon ions into the growing film.

SEM images are shown in Fig. 2. $Ti_{1-x}Al_xC_{1-y}N_y$ coatings of different elemental composition have dissimilar microstructure type: $Ti_{0.72}Al_{0.28}C_{0.34}N_{0.66}$ has a mixed granular-columnar structure type, $Ti_{0.51}Al_{0.49}C_{0.37}N_{0.63}$ has a columnar structure with voids between columns, and $Ti_{0.38}Al_{0.62}C_{0.32}N_{0.68}$ has a fine-grained microstructure. It should be noted that the coating $Ti_{0.51}Al_{0.49}C_{0.37}N_{0.63}$ with voids between the columns has the largest atomic oxygen concentration.

The results of thickness, surface roughness and optical characteristic

measurements are shown in Table 2.

Table 2. The thickness h, the average S_a and root-mean-square S_q surface roughness, the solar absorptance α_s, the emittance ε, and the ratio α_s/ε of $Ti_{1-x}Al_xC_{1-y}N_y$ films

Sample	h, mkm	S_a,nm	S_q,nm	α_s	ε	α_s/ε
$Ti_{0.72}Al_{0.28}C_{0.34}N_{0.66}$	1.87	1.04	3.30	0.51	0.44	1.15
$Ti_{0.51}Al_{0.49}C_{0.37}N_{0.63}$	1.16	8.88	11.07	0.66	0.31	2.14
$Ti_{0.38}Al_{0.62}C_{0.32}N_{0.68}$	1.42	1.38	1.74	0.59	0.43	1.39

$Ti_{0.72}Al_{0.28}C_{0.34}N_{0.66}$ film of the largest thickness was formed from target no.1 with the smallest Al/Ti ratio. The results of AFM investigations are in good agreement with the results of SEM.

The experimental spectroscopic data and calculation results have been shown that the lowest solar absorptance coefficient ($\alpha_s = 0.51$) and highest emittance ($\varepsilon = 0.44$) correspond to the $Ti_{0.72}Al_{0.28}C_{0.34}N_{0.66}$ coating with a thickness of 1872 nm, the solar absorptance coefficient of 0.59 and emittance of 0.43 correspond to the $Ti_{0.38}Al_{0.62}C_{0.32}N_{0.68}$ coating with a thickness of 1416 nm, and the highest solar absorptance coefficient ($\alpha_s = 0.66$) and lowest emittance ($\varepsilon = 0.31$) correspond to the $Ti_{0.51}Al_{0.49}C_{0.37}N_{0.63}$ film with a thickness of 1157 nm.

4. Conclusion

Sputter mosaic Ti-Al targets have been found to be good means of varying the deposited coatings composition. It has been found that the film composition can be varied to lower the α_s/ε ratio by decreasing the aluminum-to-titanium ratio in the target.

References

1. Jyothi J. et al. Design and fabrication of spectrally selective TiAlC/TiAlCN/TiAlSiCN/TiAlSiCO/TiAlSiO tandem absorber for higherature solar thermal power applications // Sol. Energy Mater. Sol. Cells. 2015.
2. Brogren M. et al. Titanium–aluminum–nitride coatings for satellite temperature control // Thin Solid Films. 2000. Vol. 370, № 1–2. P. 268–277.
3. Brogren M. et al. Ti_xAl_yN coatings for temperature control of spacecraft // EUROPTO Conf. on Adv. in Opt. Interf. Coat. 1999. Vol. 3738. P. 493–501.

EXPERIMENTAL INVESTIGATION OF ELECTRICAL AND MAGNETIC FIELD PARAMETERS OF MODEL LIQUID-PROPELLANT ROCKET ENGINES PLASMA FLOWS DURING STAND FIRE TESTS

S.A. Grishin[1], V.V. Klimentovski[1], N.S. Niadvetski[1], D. A.Yagodnikov[2]

[1] *SSPA"Optics, Optoelectronics and Laser Technology", Minsk, Belarus, grsamail@mail.ru*
[2] *Bauman Moscow State Technical University, Moscow, Russia, bauman@bmstu.ru*

Liquid-propellant rocket engine (LPRE) is highly energy intensive complex technical object. It operates in severe conditions and may be exposed to substantial mechanical and thermal stresses during operation. Usually it is designed for operation on such important facilities as spacecrafts, aircrafts and special machinery. Malfunction of such engine can lead to significant loss of property and even to destruction. Implementation of continuous engine technical status and operating mode monitoring may reduce probability of this scenario. Such monitoring requires development of multichannel registration systems, that can enable analysis of heterogeneous parameters, which can characterize engine technical condition and operating mode. Meanwhile existing contact methods of liquid-propellant rocket engine status diagnostics such as monitoring of propellant mixture components flow rates, pressures, temperatures cannot provide response speed and reliability necessary for development of advanced engine diagnostics, control and emergency shutdown systems. Also contact sensors require that possibility of their installation must be provided by engine design, and engine design modification is not allowed in many cases. Moreover, operational environment not always will allow mounting sensors in close proximity to such engine units. Therefore search for innovative and particularly for non-contact and fast-responding techniques for liquid-propellant rocket engines health and operating regimes monitoring is of current concern. Such techniques can be based, specifically, on investigation of parameters of alternating electrical and magnetic fields, originating during engine operation.

Most of propellant mixtures for LPRE burn at temperatures of 2000-4000 K. In the flame front ionization processes take place and exhaust gas flows contain uncompensated electric charges. Charged particles appear to be ions, soot particulates and charged particles, originating at early stages of engine structural elements destruction or flame erosion. Parameters of alternating electrical and magnetic fields originating in proximity to engine, depend upon charged particles distribution within plasma flow and also upon the pattern of their motion, which, in turn, are related to engine design features, engine technical condition and operating modes. Revelation of such correlation may enable to utilize it for development of non-contact electromagnetic techniques

for rocket engine technical status and operating mode monitoring and emergency shutdown systems.

SSPA“Optics, Optoelectronics and Laser Technology” has developed hardware-software means for multiparameter monitoring of complex technical objects /1/. These hardware-software means were used for investigation of parameters of physical fields originating during stand fire tests of various types of model liquid-propellant rocket engines at Bauman Moscow State Technical University testing stand as shown in Fig. 1 and Fig. 2.

Parameters of alternating electrical and magnetic fields in proximity to the engine, engine plume optical radiation spectra, engine body temperatures and vibrations, acoustic noise produced by the engine during operation, as well as test procedure videodata were registered simultaneously.

Also testing stand nominal measuring tools were used for registration of propellant mixture components flow rates, pressures and temperatures at various parts of testing stand gas-dynamic scheme. Fig. 3 shows erosing insert of engine nozzle critical section after fire test execution.

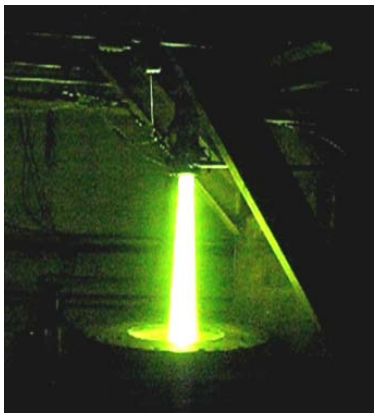

Fig. 1 – Model liquid-propellant rocket engine stand fire test process

Fig. 2 – Example deployment of sensors in proximity to liquid-propellant rocket engine

Fig. 3 – Erosing insert of nozzle critical section after fire test execution

Deployment of alternating electrical and magnetic field sensors and electrical and magnetic antennas in proximity to liquid-propellant rocket engine is shown in Fig. 4 and Fig. 5. Fig. 6 shows working window of dedicated computer software in alternating electrical and magnetic fields registration mode.

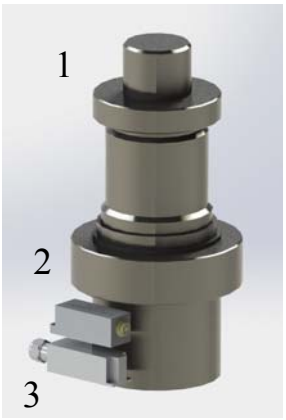

1 - LPRE; 2 - electrical field sensor; 3 - magnetic field sensor
Fig. 4 – Deployment of alternating electrical and magnetic field sensors in proximity to LPRE

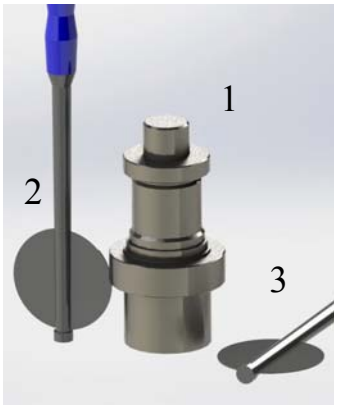

1 - LPRE; 2 - magnetic antenna; 3 - electrical antenna.
Fig. 5 – Deployment of electrical and magnetic antennas in proximity to LPRE

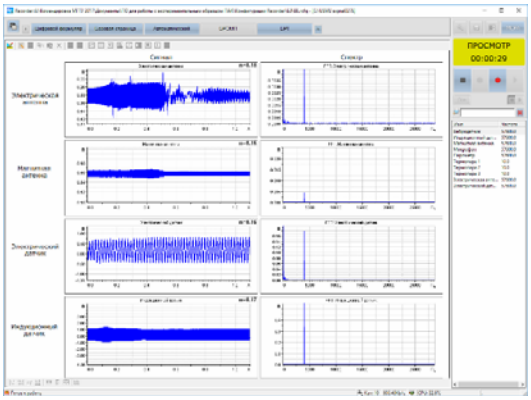

Fig. 6 – Working window of dedicated computer software in alternating electrical and magnetic fields registration mode

Propellant mixture for tested liquid-propellant rocket engines consisted of kerosene and oxygen. Basic parameters of model liquid-propellant rocket engines operation were as follows: pressure in combustion chamber, $P_к$ – 1…3 MPa; oxidizer (gaseous oxygen) flow rate, $m_о$ – 0.10…0.30 kg/s; fuel (kerosene) flow rate, $m_г$ – 0.10…0.30 kg/s; oxidizer excess coefficient α – 0.2…2.0; individual test start-up duration, t – 1…30 s. Fig. 7 and Fig. 8 show example oscillograms of registered signals, acquired by alternating electrical and magnetic fields sensors, superimposed on profiles of pressure variation in combustion chamber of liquid-propellant rocket engine.

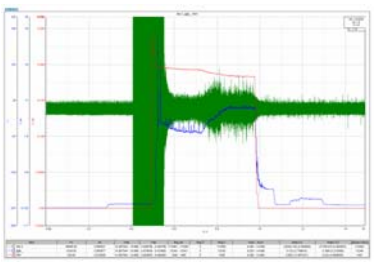

Fig.7 – Profile of pressure variation in combustion chamber of LPRE and oscillogram of signal from alternating electric field sensor

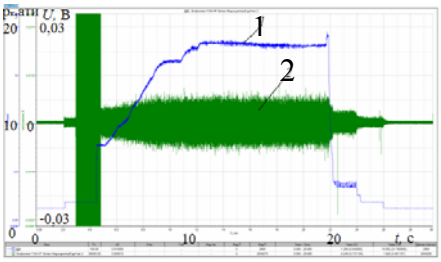

Fig. 8 – Profile of pressure variation in combustion chamber of LPRE (1) and oscillogram of signal from alternating magnetic field sensor (2)

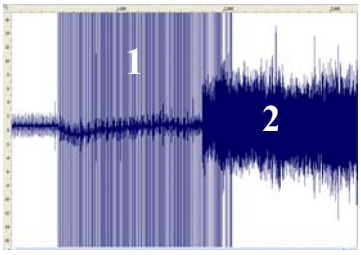

Fig. 9 –- Enlarged fragment of signal oscillogram from alternating magnetic field sensor

Oscillograms of signals, acquired by alternating electrical and magnetic fields sensors, superimposed on profiles of pressure variation in combustion

chamber of liquid-propellant rocket engine, show specific engine operation phases: valves opening and closing (for oxidizer, fuel feed, nitrogen purging valves), electrospark ignition system switching on and off, increase of pressure in combustion chamber and its stabilization. The largest signal was registered during electrospark ignition system operation.

Fig. 9 shows enlarged fragment of signal oscillogram, acquired from alternating magnetic field sensor, where phases of electrospark ignition system operation (1) and appearance of noise-like signal (2), associated with the beginning of burning process can be seen.

Analysis of measurement data, achieved during tests, shows that amplitudes and spectra of alternating electrical and magnetic fields, registered in proximity to tested liquid-propellant rocket engines, presence and intensity of spectral lines in LPRE plumes optical radiation, depend upon the phase and modes of operation of the engine. The same applies to engine body frames vibrations and also to acoustic noise, produced during engine operation. Comparison of the data, achieved with the help of developed hardware-software means for multiparameter monitoring of complex technical objects, with information, achieved from testing stand nominal measuring tools, revealed correlation between LPRE operating modes and parameters of alternating electrical and magnetic fields, registered in proximity to tested liquid-propellant rocket engine. In particular, near-linear dependence of amplitude of oscillation of electrical and magnetic fields on pressure in combustion chamber of LPRE was revealed. The results, achieved during tests, show that signals acquired with the help of developed hardware-software means and their correlation with LPRE modes of operation may be utilized as diagnostic indicators for development of fast responding LPRE health monitoring, control and emergency shutdown systems.

Conclusions

Investigations carried out show that measurement information, acquired with the help of developed hardware-software means can be used for revelation and exploration of correlations between rocket engine technical status and modes of operation and parameters of alternating electrical and magnetic fields, originating in proximity to the engine during its operation, which, in turn, may be utilized as diagnostic indicators for development of specialized fast responding automated rocket engine monitoring, diagnostics and emergency shutdown systems.

References

1. **Hryshyn S.A., Klimentovski V.V.,** VIII International Conference «Plasma Physics and Plasma Technology», **2** (2015) 517-520.

DEPOSITION OF FILM COATINGS WITH TITANIUM AND SILVER NANOPARTICLES BY MEANS OF COMBINED MAGNETRON-LASER PLASMA

A.P. Burmakou, O.R. Lyudchik, V.N. Kuleshov, A.V. Stoliarov

Belarusian State University, 4, Nezavisimosti avenue, 220030, Minsk, Belarus.
E-mail: Burmakov@bsu.by; KuleshovV@Yandex.ru

Introduction

Combination of laser and magnetron plasma creates potential possibilities for obtaining coatings with improved properties. The main feature of this combination is the simultaneous use of two plasma streams, which differ significantly in energy and time characteristics. The effectiveness of the use of magnetron-laser technology was demonstrated by the example of the creation of protective coatings with low coefficient of friction based on carbon, for the deposition of nanosized films, cermet structures, composite coatings, the production of solid lubricants /1-4/. Recently, interest has grown in such structures as dielectric film coatings with the inclusion of a nano-sized semiconductor or metallic phase, for example, silicon nanocrystals in a silicon dioxide matrix, as well as silicon or germanium nanocrystals in an Al_2O_3 or $SiGeO_2$. Nanostructures with particles of Au and Ag introduce great possibilities because of the effective absorption of light due to surface plasmon resonance (SPR). To form structures such as an array of metal particles in a solid-state dielectric matrix, magnetron-laser deposition was not used. The purpose of this work was the formation of such structures based on the matrix TiO_2 with particles of Ti or Ag.

Experiment and results

The technique of magnetron-laser deposition of the TiO_2 oxide matrix with Ti and Ag nanoparticles is realized using a vacuum unit, the main structural elements of which are shown in Fig. 1.

A magnetron sputter (cathode diameter 5 cm) formed a TiO_2 film coating on the substrate at an argon-oxygen gas mixture with pressure of 0.8 Pa and the values of $X = 40$ mm, $Y = 70$ mm, $\varphi = 25^{\circ}$. The oxygen consumption was controlled by an optical system using a small-size spectrometer. The laser plasma was formed by a two-pulse laser on YAG:Nd^{3+}. The wavelength was 532 nm, pulse frequency 2 Hz, duration 12 ns. Scanning of the beam along the surface of the target was carried out with the help of prisms of total internal

reflection. The radiation power density on the target was 2,0–2,5 GW/cm^2. The deposition time of the coatings was 27 min.

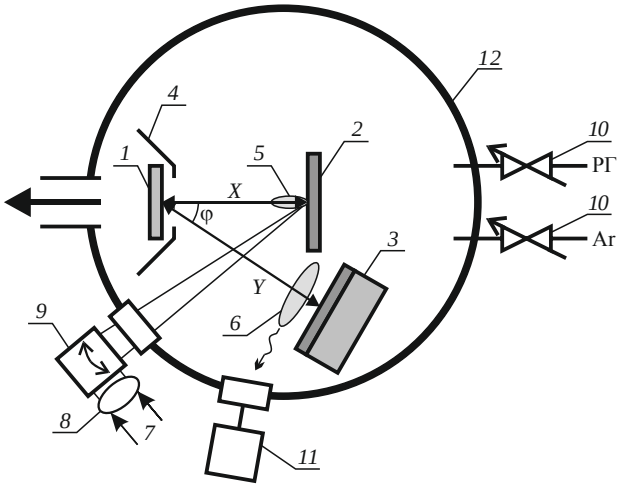

Fig. 1 – Scheme of realization of the technique of combined magnetron-laser deposition: 1 - substrate, 2 - laser target, 3 - magnetron, 4 - screen, 5 and 6 - laser and magnetron plasma, 7 - laser beam, 8 and 9 - focusing lens and scanning device, 10 - controlled puffing of argon and oxygen, 11 - sensor of the optical system of the oxygen flow control, 12 - vacuum chamber

A significant effect on the characteristics of the plasma of a magnetron discharge is exerted by the potential of the metal screen in front of the substrate (element 4 in Fig. 1). The potential value +(20-30)V leads to a significant increase in the density of excited atomic particles in comparison with the case of a grounded screen. Near the surface of the substrate, the OI line intensity has grown almost 6 times, the TiI lines 3 times, the ArI lines 2.5 times. This resulted in an increase in the deposition rate and uniformity of the coating over the thickness.

The characteristics of the laser plasma are affected by the time delay between the laser pulses in the two-pulse generation mode. It is established that such a delay increases the intensity of ion lines by 1.5-2.0 times with a delay in the interval 0.2-0.6 microseconds.

The simultaneous existence of the magnetron discharge plasma and the pulsed-periodic laser plasma leads to a change in the characteristics of the magnetron discharge. After the appearance of the laser plasma, a glowing magnetron discharge for a time of 5-30 μs passes into the arc by a sharp increase in the current and a decrease in the voltage /5/. A cathode spot arises on the surface of the magnetron cathode. A consequence of this effect of the laser plasma on the magnetron discharge is the additional contribution of the arc discharge found in /5/ to the radiation of the combined-flux plasma. In addition, there is also an additional contribution of the arc discharge to the drip phase of

the laser erosion flow. This is confirmed by the results of the analysis of coatings by the method of scanning electron microscopy. In the formation of Ti matrix structures with Ag particles, when the laser target was silver, and the cathode of the magnetron was titanium, Ti particles with a particle size of the order of 1 μm were found in the coating in addition to the metallic Ag particles. The detected titanium particles are not purely metallic. They contain oxygen in weight percent less than for the TiO_2 compound.

The optical and structural properties of TiO_2 coatings with Ti and Ag particles were studied by optical, scanning electron microscopy, spectrophotometry and atomic force microscopy.

The transmission and absorption spectra of films with Ti and Ag particles are significantly different.

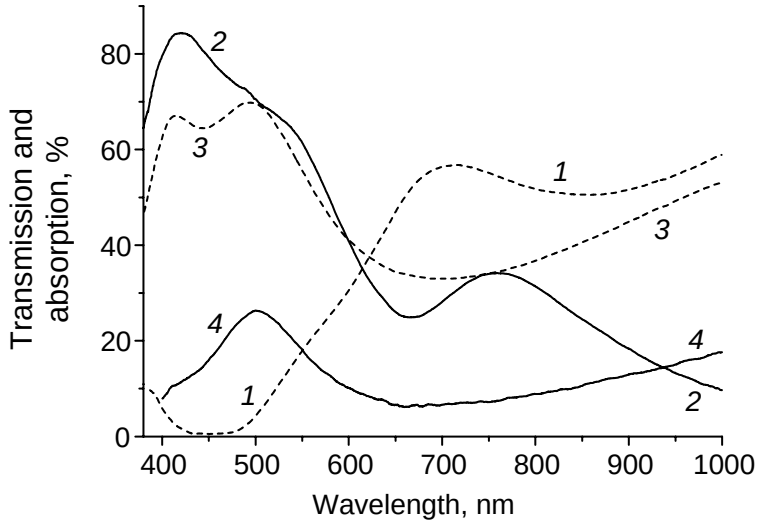

Fig. 2 – The transmission (1) and the absorption (2) for the structure Ag in TiO_2, the transmission (3) and the absorption (4) for the structure Ti in TiO_2. Substract is glass

For Ti in TiO_2 film like in the TiO_2 the interference structure of the reflection and transmission spectra is observed, which corresponds to a sufficiently high transparency of the coating. Absorption varies little and amounts to 15-18%. For film Ag in TiO_2 in the range of 400-500 nm there is a significant absorption and a very low transmission of about 1%. This feature is most likely due to SPR. The maximum optical density of the coating is about two in the range 430-440 nm. Measurement of optical characteristics for 1 year has shown their stability. Using the results of /5/, where the dependence of the wavelength of the absorption maximum on the diameter of the silver particles is presented, it is possible to estimate the characteristic size of the Ag coating particles in TiO_2. In our case this size is about 50 nm.

The AFM images of the surfaces of the structure of Ti in TiO_2 and Ag in TiO_2 are shown at Fig. 3. The processing of planar AFM images showed that the predominant particle size of Ti in the TiO_2 matrix lies in the range of 50-150 nm

with a surface density of 10-15 per 1 μm^2, and Ag particles in the TiO_2 matrix in the range of 20-60 nm with a surface density of 90-150 at 1 μm^2. The film thicknesses are close to 200-250 nm. As in Fig. 2, these structures were obtained under the same conditions. However, the structure of particles and their surface density are significantly different.

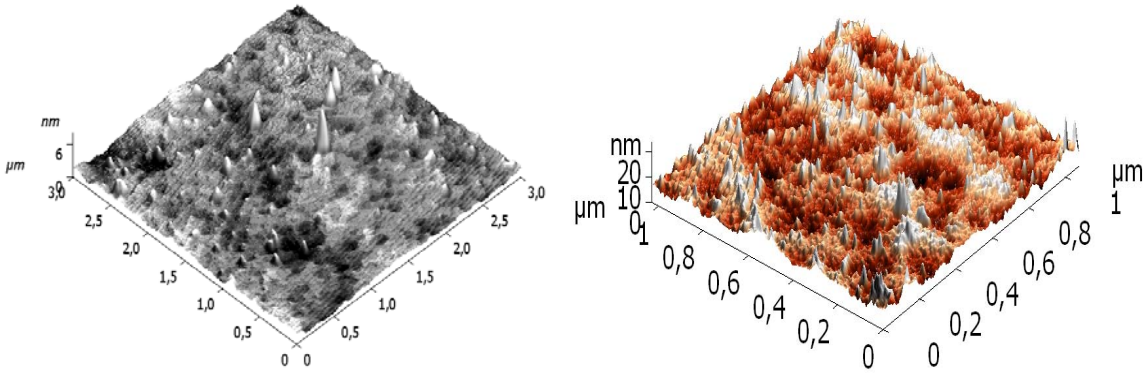

Fig. 3 – 3D AFM images of film Ti in TiO_2 (left) and Ag in TiO_2 (right)

Conclusions

Combined magnetron-laser plasma makes it possible to form coatings, which are an array of nanosized metal particles distributed over the thickness of the dielectric oxide matrix. On the example of Ti and Ag particles in the TiO_2 matrix, the conditions for the realization of the procedure are determined. For the structure of Ag in TiO_2, an absorption band in the visible region due to surface plasmon resonance is observed.

References

1. **Voevodin A. A., Capano M. A., Safriet A. J., Donley M. S., Zabinski J. S**. Applied Physics Letters, 69(1996) 188–190.
2. **Krzanowski J. E., Nainaparampil J. J., Phani A. R**. Journal of Vacuum Science Technology A, 21(2003) 1829–1836.
3. **Jelinek M., Kocourek T., Zemek J., Novotný M., Kadlec Ja**. Applied Physics A, 93(2008) 633–637.
4. **Jelínek M., Kocourek T., Kadlec Ja., Zemek J**. Laser Physics, 19(2009) 149–153.
5. **Бурмаков А.П., Кулешов В.Н., Прокопчик К.Ю.** Инженерно-физический журнал, 89(2016) 1281–1287.
6. **Крутяков А.Ю., Кудринский А.А., Оленин А.Ю**. Успехи химии, 77(2008) 242-269.

GRAFTING OF NATURAL POLYMERS ONTO POLYMER FILMS ACTIVATED BY DC DISCHARGE

I.S. Melnikov[1,2], M.S. Piskarev[2], T.S Demina[1,2,3], A.I. Shpichka[3], N.N. Veryasova[3], Yu.S. Sotnikova[1,2], D.A. Kulagina[1,2], E.V. Istranova[3], A.B. Gilman[2], P.S. Timashev[3], T.A. Akopova[2]

[1]Moscow Aviation Institute (National Research University), Moscow, 3, Orshanskaya st., 121552 Moscow, Russia, e-mail: support-rubick@yandex.ru
[2] Enikolopov Institute of Synthetic Polymer Materials, Russian Academy of Sciences, 70 Profsoyuznaya str., 117393, Moscow, Russia, e-mail: plasma@ispm.ru
[3]Institute for Regenerative Medicine, Sechenov University, 8-2 Trubetskaya st., Moscow, 119991, Russia; e-mail: detans@gmail.com

Polymer materials are widely used for biomedical applications ranging from catheters, heart valves, stents to biodegradable scaffolds for tissue engineering. In all cases strict requirements to materials properties are applied starting from common microscopical characteristics (3D architectonics, mechanical properties, etc.) to aim-targeted features, such as specific bioactivity and biodegradation rate. A fabrication of polymer materials with desired structure and properties requires a lot of compromise between polymer characteristics and processing technology and, thus, almost leaves no possibility to control surface properties, which are critical for medical application. Plasma treatment is a well-known and highly promising approach for direct modification of surface properties of biomaterials /1−3/. Variation of processing parameters, such as discharge type, a nature of working gas, duration, etc., allows to control surface properties, chemistry and morphology in a wide range. Another promising approach of plasma treatment of materials for medical applications is using it as a tool for surface activation prior further immobilization or grafting of bioactive components onto the materials /4/. Deposition of bioactive components, such as proteins and polysaccharides, onto surfaces of materials based on synthetic polymers is highly desired to control their biocompatibility. For example, chitosan is one of the widely used natural polymers to be immobilized onto various surfaces to control their compatibility with various cell lines or blood components. This polysaccharide is a biocompatible, biodegradable and could effectively act as site for binding of bioactive components, drugs or cell attachment.

This research aims to evaluate an effectiveness of direct current (DC) discharge treatment of polymer films such as poly(ethylene terephthalate) (PET) and poly(L,L-lactide) (PLLA) as surface activation method for immobilization of chitosan and collagen onto the film surfaces.

Commercially available PET films (PETLAIN BT 1010 E, «Superfilm»,

Turkey) and PLLA films casted from 5 wt. % solution of poly(L,L-lactide) (Sigma-Aldrich, USA) in CH_2Cl_2 were treated by DC-discharge (50 mA) at the anode or at the cathode using a residual air as working gas (~10 Pa) for 60 s /5/. Then, untreated and plasma-treated films were incubated within either 0.25 wt.% collagen (type I) or 1 wt.% chitosan (molecular weight of 60 kDa, degree of acetylation of 0.1) solutions in 1% acetic acid for 2 hrs at 37°C. The films were carefully washed with water (bidistillate) and dried in a dust-free chamber at RT.

The surface properties of native films as well as coated films were characterized by contact angle (θ) measurements with an Easy Drop DSA100 instrument (KRUSS, Germany) and the software suite Drop Shape Analysis V.1.90.0.14 using two test liquids (bidistilled water and glycerol). The values of work of adhesion, the total surface energy (γ), and its polar (γ^p) and dispersion (γ^d) components were calculated according to /6/. Figure 1 shows results of contact angles measurements of untreated and plasma-treated PET and PLLA films after immobilization of chitosan and collagen, respectively. Measurements of contact angles showed that wettability of untreated films even after the incubation in chitosan or collagen solutions was similar to native PET or PLLA film indicating the absence of any chitosan/collagen grafting onto untreated polymer surfaces. The contact angles of wettability of chitosan/collagen-coated films were close to values determined on model films casted of chitosan (68°) and hydrolyzed collagen, i.e. gelatin, (63°) and significantly higher than angles obtained on plasma-treated films prior incubation /5/.

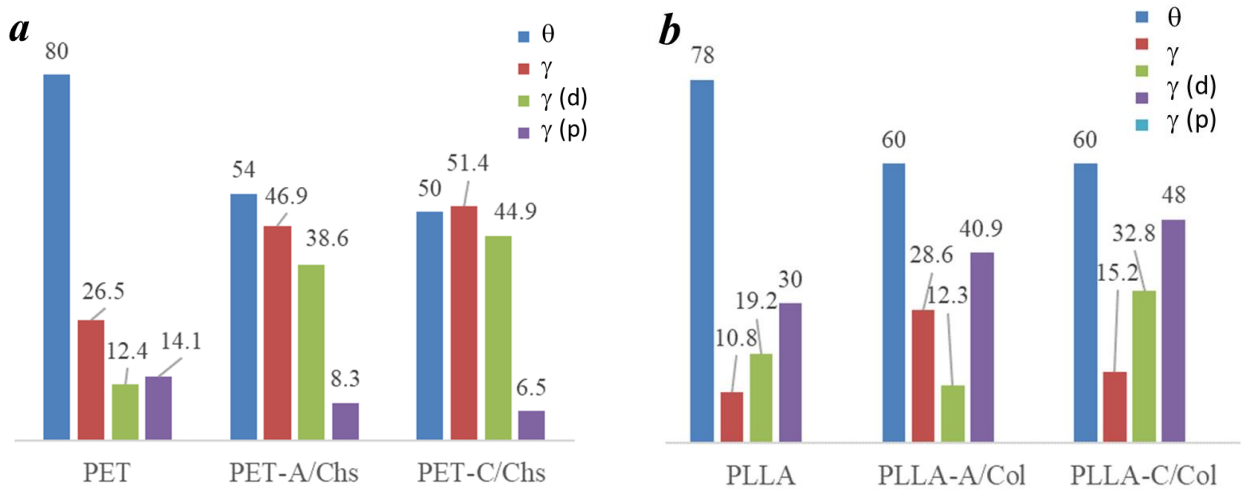

Fig. 1 – Effect of plasma treatment on surface properties of the PET and PLLA films coated by collagen (b) without (PET or PLLA) or after treatment on the anode or the cathode (PET-A/Chs or PLLA-A/Col). Water contact angle (θ±1°) air/water, %; total surface energy (γ) and values of its dispersive (γ^d) and polar (γ^p) components, mJ m^{-2}

The MTT-assay using 3T3 fibroblast cell line and LDH-assay using human mesenchymal stromal cells showed no notable cytoxicity of the films because the lowest cell viability detected was above 70%. Scanning electron microscopy revealed that the PLLA film coated by collagen after the preliminary plasma treatment at the anode ensured the best adhesion and proliferation of human mesenchymal stromal cells (Fig. 2) compared to native and cathode-treated PLLA films.

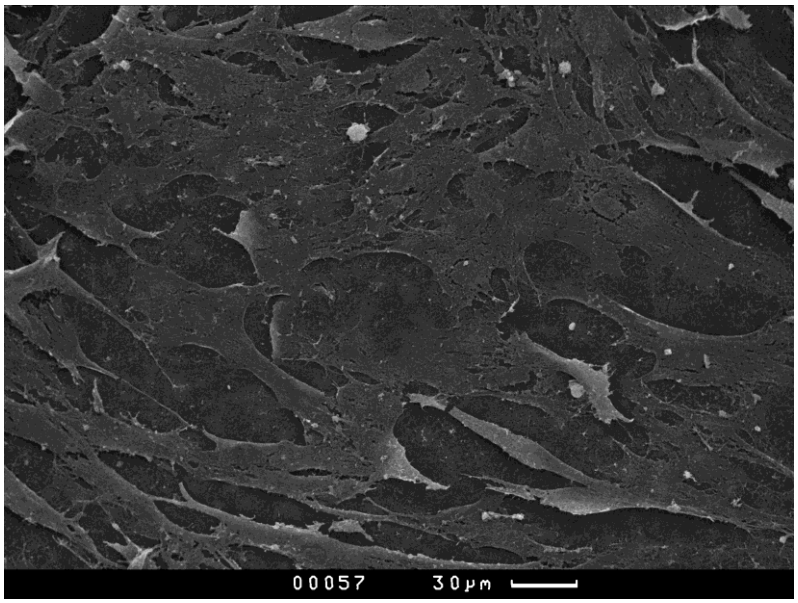

Fig. 2 – Scanning electron microscopy of human mesenchymal stromal cells cultured on the collagen-coated PLLA film treated at the anode

Thus, DC discharge plasma treatment of poly(ethylene terephthalate) and poly(L,L-lactide) films allowed to effectively activate their surface prior immobilization of chitosan and collagen onto the film samples, and, thus, to enhance their surface properties, including ability to support adhesion and proliferation of human mesenchymal stromal cells.

Acknowledgements. The reported study was funded by RFBR according to the research project № 18-32-00901 and partially by 17-34-80151 (biological testings).

References

1. **Chu P.K., Chen J.Y., Wang L.P., Huang N.** Materials Science and Engineering R 36(2002) 143–206.
2. **Demina T.S., Gilman A.B., Akopova T.A., Zelenetskii A.N.** High Energy Chemistry 48(2014) 293–302.

3. **Demina T.S., Gilman A.B., Zelenetskii A.N.** High Energy Chemistry 51(2017) 302−314.
4. **Kudryavtseva V., Stankevich K., Gudima A., Kibler E., Zhukov Y., Bolbasov E., Malashicheva A., Zhuravlev M., Riabov V., Liu T., Filimonov V., Remnev G., Klüter H., Kzhyshkowska J., Tverdokhlebov S.** Materials and Design. 127(2017) 261−271.
5. **Demina T., Zaytseva-Zotova D., Yablokov M., Gilman A., Akopova T., Markvicheva E., Zelenetskii A.** Surface and Coatings Technology 207(2012) 508–516.
6. **Wu S.** Polymer Interfaces and Adhesion, New York: Marcel Dekker, 1982.

REGULATION OF THE PHASE COMPOSITION AND STRUCTURE OF CARBON COATINGS BY PLASMA METALS DOPING METHODS

A.S. Rudenkov, A.V. Rogachev, D.G. Piliptsov, E.A. Kulesh

Francisk Skorina Gomel State University, 246019,
Belarus, Sovetskaya str., 104, e-mail: rudenkov@gsu.by

The properties of the carbon coating are mainly determined by the phase ratio sp^3/sp^2, the phase dispersion, which are largely unambiguously determined by the choice of the method and technological formation regimes /1-4/. Thus, any data on carbon coatings must be correlated with an accurate description of the deposition conditions, including the materials and technologies used (sample preparation, carbon plasma sources operation regimes, geometric parameters of the working chamber, etc.). It is known that doping with metals and their compounds is an effective technological method to achieve multi-functionality and improve the properties of carbon-based coatings /5-7/. In this connection, it is of scientific and practical interest to study the regularities of the influence of plasma doping conditions and regimes, to develop effective technological methods to control the properties of carbon coatings not only by selecting the alloying element and varying its concentration, but also by changing the energy of the deposited ions and carbon atoms due to the interaction of carbon plasma and the ionized stream of the doping element. By varying the regimes of the metal plasma flow generation, one can change the energy of atoms and carbon ions, thereby controlling the phase composition and properties of the deposited coating.

The formation of metal-carbon coatings was carried out by simultaneous deposition of carbon from a plasma source of a pulsed cathode-arc discharge with a graphite cathode and a metal from the flow generated by a magnetron sputtering system, as well as from an arc discharge plasma. Coatings were deposited on silicon substrates. Ti, Cu, were used as alloying metals which are chemically active to carbon.

Synthesis of coatings was carried out by sequential performing of the following basic operations: cleaning and heating of the substrate using an ion source "Radical" (working gas – argon, $P_{Ar} = 10^{-1}$ Pa, current – 0,2 A, accelerating voltage 2 kV, solenoid current – 3 A, processing time 15 minutes); deposition of doped carbon coatings from a particle stream generated by a pulsed cathode-arc source of carbon plasma (5000 pulses, pulse repetition rate – 20 Hz, discharge voltage 350 V) and magnetron sputtering of metal (working gas – argon, residual pressure – 10^{-1} Pa, the discharge power is 40, 120, 200, 280 and 400 W, the energy of argon ions is ~ 300 eV). Doping of carbon

coatings with metal from an electric arc discharge (EDI) plasma was performed with the arc current equal to 50, 60, 70, 80, 90 A.

The phase composition of the carbon coatings was determined by analyzing the Raman spectra (RS) with a Senterra spectrometer with the exciting radiation wavelength of 532 nm and power of 10 mW. The recorded spectra were decomposed into D- (~ 1400 cm^{-1}) and G-peaks (~ 1550 cm^{-1}) by the Gauss method. The analysis results of are presented in Table 1.

Table 1 – Parameters of Raman spectra of carbon coatings doped with metals from the plasma generated by a magnetron sputtering system (MSS) and plasma of the electric arc source (EAS).

Sample	lasing regime		doping element concentration *, at. %	G-peak position*, cm^{-1}	I_D/I_G*
	MSS, W	EAS, A			
C	–		–	1562,8	0,50
C+Ti	40	50	0,55/3,05	1557,0/1560,8	0,55/0,73
	120	60	0,35/3,71	1555,5/1559,2	0,69/0,84
	200	70	2,11/4,68	1555,0/1556,3	0,80/0,86
	280	80	2,41/5,41	1551,9/1558,2	0,89/0,96
	400	90	2,64/7,35	1554,8/1559,4	1,01/1,01
C+Cu	40	50	1,02/5,28	1555,1/1554,1	0,69/0,93
	120	60	1,43/6,32	1553,7/1555,0	0,85/1,05
	200	70	2,24/6,91	1553,6/1556,6	1,04/1,06
	280	80	4,74/7,43	1548,5/1556,1	1,48/1,08
	400	90	6,35/8,45	1551,8/1557,2	0,64/1,09
*MSS/EAS-for corresponding lasing regimes of metal plasma					

It is stated /8, 9/ that the increase in the I_D/I_G ratio and the shift of the corresponding peaks in the low-frequency area can be explained by the increase in the content of sp^2 -hybridized carbon atoms. The narrowing of G-peak width, in its turn, is interpreted by the increase in the degree of sp^2-clusters ordering /10/. In addition, according to formula (1) [11], the decrease in the size of sp^2-clusters also leads to the increase in the ratio I_D/I_G :

$$I_D/I_G=c(\lambda)/L_a, \quad (1)$$

and with the clusters size less than 2 nm

$$I_D/I_G=c'(\lambda)\cdot L_a^2, \quad (2)$$

where I D and I G – the intensities of the corresponding peaks;

$c(\lambda)$ – proportionality coefficient (nm);

$c'(\lambda)$ – proportionality coefficient (nm^{-2});

L_a – graphite grains size (nm).

Compared to the single-component coatings in the Raman spectra of metal-doped layers, irrespective of the choice of the method for generating metal plasma fluxes and carbon coatings, the ratio of the intensities of D- and G-peaks varies significantly. The positions of D- and G- peaks shift to low wave numbers, which, with the increase in the I_D /I_G ratio, indicates the increase in the sp^2 phase content and is proved by X-ray photoelectron spectroscopy /12, 13/. There is an increase in the ratio I_D/I_G, both as in the case of the increase in magnetron power, and with increasing arc current in the case of electric arc evaporation of the metal, which indicates the decrease in the size of the sp^2 clusters. In the case of doping by magnetron sputtering method with the further increase in the concentration up to 6,35 at. % and power up to 400 W, the I_D/I_G ratio falls, which can be explained by the increase in the number of sp^2 –clusters with the size less than 2 nm and is proved by atomic force microscopy /13/.

It is stated that at approximately equal concentrations of the doping element (Ti – 2,64/3,05 at. %; Cu – 4,74/5,28 at. % for MSS/EAS) the Raman spectra of metal-carbon coatings formed by magnetron sputtering are characterized by a higher I_D/I_G ratio (for C+Ti 1,38 times and for C+Cu 1,59 times), less width of G-peak (Ti – 169,8/190,8 cm^{-1}, Cu – 149,6/182,4 cm^{-1}) in comparison with the Raman spectra of carbon coatings formed during electric arc evaporation of a metal. The complex of the established facts allows us to state that the metal alloying of carbon coatings using a magnetron contributes to the increase in the number and size of sp^2-clusters to a greater extent than at electric arc evaporation. It should be noted that, regardless of the doping method used, copper doping of carbon coatings leads to the maximum increase in the number of carbon atoms with sp^2-conjugated bonds.

In the majority of cases, close I_D /I_G ratios for different doping methods are observed for different doping metal concentrations in the coating. In both methods of plasma doping, when the technological regimes are changed (the increase of the magnetron power and arc current), the increase in the flux density of metal plasma particles occurs, which, in its turn, leads to the increase in the number of inelastic collisions between the metal and carbon particles. This process is accompanied by the decrease in the energy of carbon ions in the carbon plasma flow due to scattering on atoms and ions of the metal, which, in its turn, reduces the formation probability of the sp^3 phase of carbon at deposition on the substrate. In addition, the number of ions and metal atoms bombarding the coating during the growth process increases. Such plasma treatment activates the diffusion processes in the coating, which leads to the appearance of sp^2-clusters of smaller sizes and stimulates phase transformations of $sp^3 \rightarrow sp^2$ due to the energy dissipation of carbon particles because of two plasma flow interactions.

Acknowledgements. The research was carried out with the financial support of the Ministry of Education of the Republic of Belarus in the framework of the task 4.1.02 of the GPIS "Physical Material Science, New Materials and Technologies".

References

1. **Robertson J. et al.** Material Science and Engineering, 37 (2002) 129–281.
2. **Grill A.** Surface and Coatings Technology, 95 (1997) 507 – 513.
3. **Angus, J.C.** Science, 241 (1998) 913 – 921.
4. **Robertson J.** Physical Review Letters, 68 (1992) 220 – 223.
5. **Bull S.J.** Diamond and Related Materials, 4 (1995) 827 – 836.
6. **Donnet C.** Surface and Coatings Technology, 100 (1998) 180 – 186.
7. **Grill A.** Wear, 168 (1993) 143 – 153.
8. **Cloutier M. et al.** Diamond and Related Materials, 48 (2014) 65 – 72.
9. **Druz B. et al.** Diamond and Related Materials, 13 (2004) 1592 – 1602.
10. **Varade A. et al.** Procedia Engineering, 97 (2014) 1452 – 1456.
11. **Ferrari A.C., Robertson J.** Physical Review B, 61 (2000) 4095 – 4107.
12. **Пилипцов Д.Г. и др.** Проблемы физики, математики и техники, 12 (2012) 33 – 36.
13. **Руденков А.С.** Проблемы физики, математики и техники, 24 (2015) 26 – 32.

PLASMA REACTOR FOR LIQUID ORGANICWASTE TREATMENT

A.Essiptchouk[1], G. Petraconi[2], F. Miranda[2], F. Caliari[2], A. Marquesi[2], L.Charakhovski[3]

[1]Instituto de Ciência e Tecnologia, UNESP – Univ Estadual Paulista, 12247-004 São José dos Campos, SP, Brazil alexei.essiptchouk@gmail.com
[2]Technological Institute of Aeronautics, 12228-900, ITA–DCTA, São José dos Campos, SP, Brazil petrafilho@gmail.com
[3]A.V.Luikov Heat and Mass Transfer Institute, National Academy of Sciences of Belarus, Minsk, Belarus leonidsh.hmti@gmail.com

The application potential of thermal plasma for the incineration of solid, liquid and gaseous hazardous waste is well known, /1/. In the last decades of the last century the environmental pollution has become a worldwide problem due to the significant increase of municipal, industrial (including radioactive materials) and hospital waste. Among these, liquid wastes with a high content of organic material call for greater attention due to the possibly contamination of the environment (by releasing wastewater effluents) to affect the health of humans besides unbalance the bio systems.

There are many reactor geometries to induce chemical reactions in treated liquids by using plasmas with different operating principles /2/, which can be applied by three approaches /3/: (i) direct discharges in liquids; (ii) discharges in the gas phase over a liquid, including when a conductive liquid work as an electrode and (iii) discharges in multiphase environments (discharges in bubbles, or foams, sprayed liquid).

The organic liquid waste is generally incinerated in cement plants (as inexpensive fuel) or in a conventional burner in a furnace, /4/. Many efforts have been made to find effective methods for treating liquids of various types with the efficient removal of contaminants and without forming greenhouse effect gases (dioxins or ozone depleting gases) that harm the environment. For this purpose, plasmas outside the thermodynamic equilibrium and thermal plasmas were studied /2/.

Recently, the application of the submerged in-liquid plasma has been intensively studied for the treatment of liquid wastes with elevated content of organic material as well as for the remediation and treatment of water, /5/. Remediation of chemical residues, in addition to water treatment, requires the study of the interaction processes between plasma and liquid environment.

Here, a plasma-chemical reactor for the treatment of liquid waste with elevated content of organic matter is presented. The reactor can be equipped with conventional air/oxygen as well as water vapor plasma torches. The principal advantages of the reactor are:

- high local temperature of the plasma jet and low temperature of the treated liquid, which diminishes corrosion of the reactor wall;
- elevated quenching rate (10^6-10^7 K/s) preserves high concentration of radicals produced in discharge (O, OH, H, O_3, H_2O_2, O_3) to promote advanced oxidation processes for decontamination of aqueous effluents and suppress its recombination;
- high turbulence, induced by plasma jet, contribute to intense mass transfer from plasma to liquid;
- UV radiation;
- off-gas treatment system (cooling, filtration, and neutralization)embedded to the reactor.

Organic contaminants (for example in wastewater effluents) cause serious human health and environmental problems due to their high chemical oxygen demand (COD), low biodegradability, and toxicity.

The plasma chemical reactor with the direct contact between plasma and solution is shown in Fig.1. The reactor principal parts are: bottom (1) and top (2)vessels, mist eliminator (13)and entrance to heat exchanger (12) to cold produced gas. The reactor is equipped with thermocouples (15). The liquid waste injected to the top of the reactor (10) and drained from the reactor bottom, passes through additional heat exchanger projected to maintain the temperature of liquid. The plasma torch is attached to the bottom flange (7) with the plasma jet injected directly to the solution, axially to the draft tube (8), placed above the torch, for many purposes: maximize the liquid recirculation inside the reactor, increase agitation between plasma gas and treated liquid and residence time. Thus the reactions occur nearly liquid-gas boundary, while bulk temperature of the solution remains relatively low.

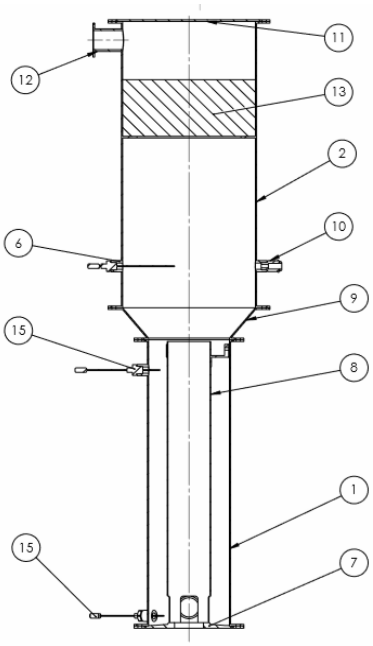

Fig. 1 - Schematic drawing of plasma chemical reactor

Table 1. Elemental analysis of glycerol, %m/m

Water	15,50
Carbon	25,80
Hydrogen	7,73
Nitrogen	0,20
Oxygen	52,00
Sulfur	1,89

The ability of submerged thermal air plasma for destruction of organic contaminants was investigated. A crude glycerol (by-product of diesel production) was used as contaminant. An elemental

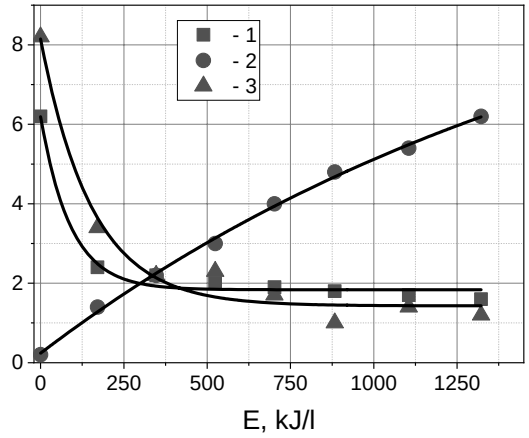

Fig. 2 - Effect of SIE on acidity (1); electrical conductivity of liquid, mS/cm, (2); dissolved O_2, mg/L

analysis is presented in Table 1. The heat of combustion is 12,32 MJ/kg (LHV) and 13,96 (HHV). The experiments were carried out at arc current 80-150 A, arc voltage 110-150V with plasma forming gas (air) flow rate of 200 l/min. The reactor working volume was 13 l. Thermal efficiency of the system was 40-50% for the liquid recirculation flow-rate of 0,35 l/s. For that conditions the nominal temperature of the treated liquid was 45°C.

The glycerol at elevated amounts intensely produces foam in contact with water. Thus in the experiments we use small amounts of contaminant so the foam appearance does not disturb the experiment dynamics.

To characterize the glycerol degradation a specific input energy (SIE), E,

$$E(t) = \frac{1}{V}\int_0^t \phi I(t)U(t)dt$$

and a degradation efficiency, η,

$$\eta = \left(1 - \frac{c_t}{c_0}\right) \times 100$$

were defined. Here, V is the treated liquid volume; ϕ is the reactor thermal efficiency; $I(t)$ and $U(t)$ are temporal variation of the arc current and voltage, respectively; c_t and c_0 are the Chemical Oxygen Demand(COD)at treated and initial conditions, respectively.

Fig.2 shows the effect of SIE on principal characteristics of the treated liquid. For our working conditions, the acidity and quantity of dissolved oxygen

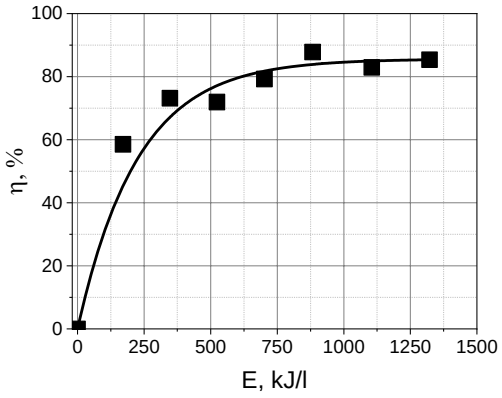

Fig. 4 Effect of SIE on glycerol degradation efficiency

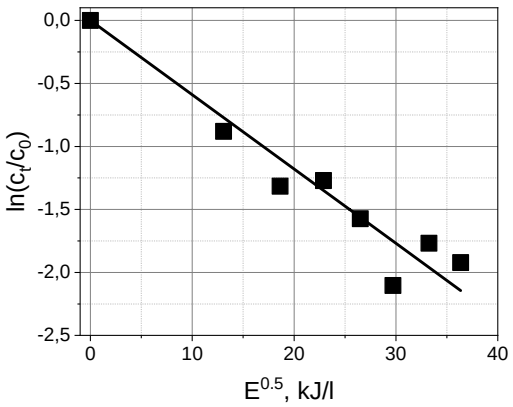

Fig. 4 Kinetic plots of glycerol degradation

diminishes exponentially and after 800 kJ/l attain its limiting values.However, the electrical conductivity of liquid keep grooving. A generation of the arc plasma jet is unaffected by the liquid's properties.

Submerged thermal plasma provides direct thermal and oxidizing contact between plasma, oxidizing gas, and organics in solution. The Fig. 3 shows that after 30 min treatment (1322 kJ/l)the concentration of organic materials decreases up to 15% (η = 85%).All organic are decomposed significantly in the plasma reactor. Therefore, submerged thermal plasma has significant ability for organic removal from solutions.

An overall reaction constant, k,and reaction order, n, of the glycerol degradation were estimated.Taking into account that the reactive species production rate is linearly depends on enthalpy of plasma discharge the degradation can be presented in the form

$$\ln\frac{C_t}{C_0} = kE^n$$

Plotting the degradation relation logarithm versus specific input energy (see Fig. 4) and making fitting it can be possible to obtain the values of k and n. For this particular case the reaction order is n=0.5 and overall reaction constant k=0.059.

Thus the plasma chemical reactor for liquid waste treatment was developed and successfully tested in the treatment of water contaminated with crude glycerol. It was found that the energy input 1000 kJ/l permits to decay 80% of contaminant by effectively utilizes the low pH and high-temperature environment.

Acknowledgements. This work was supported by the São Paulo Research Foundation, Brazil, (grant No 2016/11728-3). We thank Miss Vanessa Rodrigues Pereira for his technical assistance in this work.

References

1. **J. Heberlein and A. B. Murphy**J. Phys. D: Appl. Phys. 41 (2008) 053001
2. **P. J. Bruggeman et al.**Plasma Sources Sci. Technol. 25 (2016) 053002.
3. **P. Vanraes, A. Y. Nikiforov, and C. Leys** Electrical Discharge in Water Treatment Technology for Micropollutant Decomposition. London: InTech (2016)
4. **M. Mabrouk, M. Marchand, A. Russello, J. M. Baronnet, and F. Lemont**Plasma Chem Plasma Process (2015) 35:45–60
5. **Safa, S., Soucy, G**. Int. J. Environ. Sci. Technol. (2014) 11:1165–1188

ELECTROLYTIC PLASMA POLISHING OF TITANIUM IMPLANTS

S.I. Bahayeu, I.P. Smyaglikov

Physical and technical institute of NAS of Belarus, 220141 Minsk, Kuprevicha str., 10,
ltm.plasmoteg@gmail.com

Investigation of the electrolyte-plasma polishing of implants made of titanium alloys have been carried out. The electrolyte composition is developed and treatment modes are found, which ensure low roughness, gloss and surface purity. It is established that electrolyte-plasma polishing of VT6 alloy leads to a decrease of aluminum and vanadium concentrations in the surface layer from 7.3 and 2.1 at. % to 3.5 and 0.1 at. %, respectively.

A different surface morphology of implants is required depending on their purpose. For example, high surface purity is needed for tooth crowns, movable joints of the musculoskeletal system and cases of artificial heart valves. For dental pins, on the contrary, a developed surface with a high roughness is needed, which promotes the fusion of bone tissue with the implant. To obtain smooth polished surfaces, various methods of mechanical, chemical and electrochemical polishing are traditionally used. Electrolytic-plasma polishing (EPP) is a promising method of treatment. EPP has several advantages over traditional processing methods [1]:

– the surface cleaning and polishing take place in a single process;
– absence of force and thermal effects on the product;
– the use of inexpensive and low-toxic components of electrolytes.

To date, many technical solutions have been found for the EPP of titanium and its alloys. Various aqueous solutions based on fluoride-containing compounds, such NH_4BF_4, Na_2SiF_6, KF, NH_4F [2–4], are proposed for the polishing of titanium. Unfortunately, these electrolyte compositions are suitable only for EPP of titanium of grade VT1-0. In the case of VT6 and VT16 alloys, only partial polishing of the surface takes place, therefore, it is necessary to further improve the technology of EPP of titanium alloys.

An analysis of the available information on the EPP of various metals has shown that additive of a complexing agent into the solution greatly affects the result of the treatment, especially in the case of polishing of metal alloys. Therefore, for EPP of titanium alloys, it is necessary to select a complexing agent that can effectively bind to complexes with all the metal ions (Ti, Al, V, Mo) contained in the processed alloys. Metal ions can form complex compounds with fluoride ion, EDTA (ethylenediamine tetra-acetic acid) and pyrocatechol. In this row, the use of pyrocatechol seems promising, since it forms the most stable complex compounds with all metals, in comparison with other

complexing agents. Since pyrocatechol forms a complex compound with vanadium at pH 4.7-7.0 [5], citric acid was added to the electrolyte to regulate its pH. Thus, the following electrolyte was developed: potassium fluoride – 4 wt. %, ammonium fluoride – 1 wt. %, citric acid – 0.4 wt. %, pyrocatechol – 0.4 wt. %. Based on the obtained experimental data, the developed electrolyte provides a good quality of surface treatment of titanium alloys.

When the concentrations of chemical compounds in the electrolyte exceed those recommended, there is a significant reduction in the quality of processing due to the prevalence of metal etching and, as a consequence, the disappearance of the surface gloss. As a result, most mechanical scratches are removed, but pitting etching of the surface is observed because of the increased chemical activity of the solution. When the concentration of salts is lower, the stability of the process is reduced and the processing time is increased, the polishing effect of the surface is not fully achieved.

For the EPP of titanium, it is necessary to maintain the temperature of the solution within 70–85 °C. At lower electrolyte temperature, the workpiece instead of polishing is heated to form a black coating on its surface. At higher temperatures, the electrolyte is sprayed and its chemical activity increases. As a result the surface remains mat. The dependences of the surface roughness parameter Ra on the operating voltage at different electrolyte temperatures and polishing time of 3 minutes are shown in **Fig. 1**.

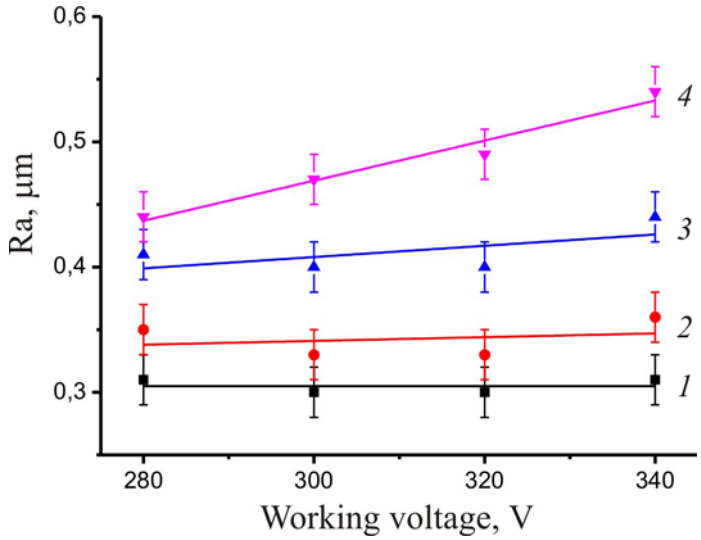

1 – 65 °C; *2* – 75 °C; *3* – 85 °C; *4* – 95 °C

Fig. 1. Dependence of the surface roughness parameter Ra on the working voltage at different electrolyte temperatures.

It is clear that Ra strongly depends on the electrolyte temperature T_{el}. The higher the T_{el}., the worse the surface is polished. In the temperature range of 65–75 °C, the operating voltage does not affect the parameter Ra. At T_{el}.= 85–95 °C,

Ra increases with increasing the voltage at the electrodes. The obtained dependences are explained by the fact that during the EPP process, when the temperature of the electrolyte decreases, the current density at the electrodes increases and, consequently, the etching rate of the metal increases. For the EPP of titanium and its alloys, the optimum working voltage is in the range of 260–330 V. At lower or higher operating voltages, a white-gray coating forms on the surface, the surface gloss disappears, and the roughness increases.

Dependences of the surface roughness parameter Ra of samples ща titanium alloy VT6 on the processing time at different electrolyte temperatures and operating voltages of 300 V are shown in **Fig. 2**. As can be seen from the figure, the duration of the EPP process affects nonlinearly the surface roughness. For all the considered values of voltage and temperature, 90% of the change in Ra occurs during the first 3–4 minutes of the EPP process. Further processing results in a slight decrease in Ra. From the point of view of the ratio of energy costs and surface quality, it is advisable to carry out the EPP of titanium alloys for no more than 3-4 minutes.

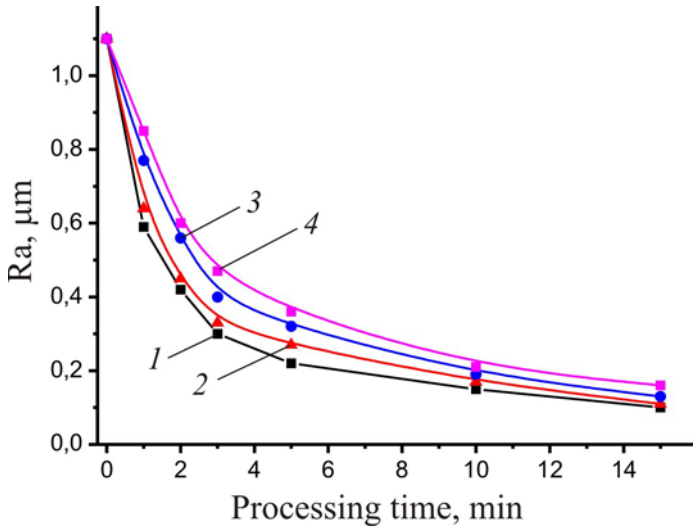

1 – 65 °C; *2* – 75 °C; *3* – 85 °C; *4* – 95 °C

Fig. 2. Dependence of the surface roughness parameter Ra on the processing time at different electrolyte temperatures.

Due to various physicochemical processes, accompanying electrolytic-plasma polishing, the surface chemical composition is changed. The elemental composition of the surface layer of titanium samples treated by different methods, determined by X-ray photoelectron spectroscopy (XPS), is shows in Table 1. It can be seen from the table that along with the alloy elements (Ti, Al, V), oxygen is present on the initial surface due to a natural oxide film. The chemical treatment of titanium leads to an increase in the Al content from 7.3 to 9.1 at. %, while for V the concentration decreases from 2.1 to 1.1 at. %.

Table 1. Elemental composition (at. %) of VT6 alloy surface layer.

Эле-мент	Время обработки, мин						
	Исходный	Химическая полировка	ЭПП				
	0	2,0	0,5	1,0	3,0	5,0	10,0
Ti	16,0	13,7	17,2	16,6	17,4	16,1	17,9
O	74,6	76,1	78,1	79,3	78,9	80,4	78,3
Al	7,3	9,1	4,4	3,9	3,6	3,5	3,7
V	2,1	1,1	0,3	0,2	0,1	–	0,1

After EPP, the concentration of both aluminum and vanadium decreases from 7.3 to 3.5 at. % and from 2.1 to 0.1 at. %,. At the same time, energy-dispersive spectral (EDS) analysis showed that concentrations of Al and V are close to that of initial sample (9.7 and 2.9 at. %, respectively). Taking into account that the depth of XPS analysis is several nanometers, and the depth of EDS analysis is about 1–2 μm, it can be concluded that the elemental composition changes only in a thin near-surface layer. Such an effect of EPP can be explained as follows. The composition of the electrolyte includes a complexing agent, which forms stable complexes with both titanium and aluminum and vanadium. During the treatment, all free metal ions formed on the surface are bound to complex compounds and removed from the region of the reactions to the electrolyte volume.

Thus, as a result of the work carried out, the electrolyte composition for electrolytic plasma polishing was developed and treatment regimes were established ensuring low roughness, gloss and cleanliness of the surface of implants made of titanium and titanium alloys.

References

1. **Kulikov I.S., Vazhenko S.V., Kamenev A.Y.** Electrolytic plasma treatment of materials. (2010). Minsk: Belarusian Science, 232 p. (In Russian).
2. **Mirzoev R.A., Styrov M.I., Stepanova N.I., et al**. RU Patent 2168565 C25F3/16 2003.06.10.
3. **Smyslov A.M., Tamindarov D.R., Mingajev A.D., et. al.** RU Patent 2495967 C1 C25F 3/16 2013.10.20.
4. **Kulikov I.S., Kamenev A.Ja., Klimova L.A.** BY Patent 7570 C25F 3/20 2003.03.06.
5. **Muzgin V.N., Hamzina L.B., Zolotavin V.L., et. al**. Analytical chemistry of vanadium (1981). Moscow: Science, 216 p. (In Russian).

DBD-PLASMA TREATMENT OF PHOTOCATALYST IMPREGNATED WITH SILVER NANOPARTICLES

N.A. Savastenko[1], I.I. Filatova[2], V.A. Lyushkevich[2], N.I. Chubrik[2], N. D. Strekal[3], A.A. Shcherbovich[1], S.A. Maskevich[1]

[1]Belorussian State University, International Sakharov Environmental Institute BSU, 23 Dolgobrodskaya Str., 220070 Minsk, Belarus, nataliesavastenko@iseu.by
[2]B.I. Stepanov Institute of Physics, National Academy of Sciences of Belarus, 68 Nezavisimosti Ave., 220072 Minsk, Belarus, filatova@presidium.bas-net.by
[3] Yanka Kupala State University of Grogno, 22 Ozheshko Str., 230023 Grodno, Belarus, nat@grsu.by

During last decades, low temperature plasma treatment has been proposed as an alternative route for catalysts preparation /1/. Traditional way for supported catalysts preparation includes three main steps: impregnation with the active phase, drying and activation by thermochemical. Thermochemical treatment includes heat treatment in either oxidizing or reducing atmosphere. As it is well known, the activities of supported catalysts are strongly dependent upon size, shape and dispersion of the active phase on the. On the other hand, heat treatment can cause the undesirable morphological changes on the surface of the catalyst, such as sintering, particle size growth etc. To overcome this problem, a plasma-assisted method has been proposed for catalyst preparation /1/.

In this paper, dielectric barrier discharge (DBD) plasma treatment was applied to modify the ZnO-based photocatalyst impregnated with silver nanoparticle (Ag-NP). Semiconductor-metal nanocomposites have widely used in catalysis /2/. Effect of plasma treatment on the performance of metal doped photocatalysts has been also investigated /3/.Here we report a combinational effect of metal nanoparticles coating and plasma treatment on the performance of semiconductor photocatalyst. The performances of plasma-treated and untreated Ag-NPs impregnated ZnO-based catalysts were compared with that of commercially available catalysts. The catalysts were characterized by photoluminescence (PL) spectroscopy. The presence of silver in ZnO was established by inductively coupled plasma atomic emission spectrometry (ICP-AES) technique. The MO concentration in solution was measured spectrophotometrically (UV-Vis spectrophotometry).

Commercial (ECOS-1, Russia, GR pure) ZnO powder was employed as a catalyst support. The synthesis procedure can be divided into three parts. One is the preparation of colloidal suspension of silver nanoparticles in water. The second one was the impregnation of ZnO powders with silver nanoparticles. Finally, the silver impregnated catalyst was treated by plasma. Colloidal silver

nanoparticles were prepared according to the method documented in reference /4, 5/. A certain amount of ZnO powders was introduced in an aqueous solution containing silver nanoparticles. The silver loading was calculated to be 1 wt%. Then, the excess of solution was removed by the means of evaporation at room temperature. The product was denoted ZnO-Ag. After drying, a half amount of silver impregnated catalyst was treated by DBD plasma. This catalyst was marked as ZnO-Ag-DBD. The discharge was generated between a rod electrode (Ø: 20 mm) and a plate electrode (10x10 cm). The upper rode electrode was covered by 2.0 mm quartz glass layer and connected to a 1 kHz AC high voltage source, while the lower electrode is connected to earth through a resistor R (75 Ω) or a capacitor C (850 pF). The distance between upper electrode and treated sample was 4 mm. The applied voltage (peak-to-peak value) was of 35 kV range. The samples to be treated were located on the grounded electrode. Plasma treatment was carried out in air at atmospheric pressure for treatments times of 25 min. The electric energy (E_{el}) consumed by DBD during one cycle of the DBD was calculated, using voltage-versus-charge Lissajous figures /6/. The measured values were of the order: 35 kV peak-to-peak voltage, 6.5 mJ/cycle energy (E_{el}). As the frequency of feeding voltage was of 1 kHz, the electric power P_{el} was calculated to be 6.5 W. Untreated ZnO powder was used as reference catalyst (ZnO).

The actual contents of Ag in the catalysts samples was determined by ICP-OES. The amount of Ag was slightly decreased after plasma treatment. The silver content was of 0.7 and 0.63 wt% in untreated and DBD-plasma treated samples, respectively.

For photocatalytic activity studies, 10 mg of powder sample was dispersed in 5 ml of aqueous solution of methyl orange with a concentration of 50 mg/L. The dispersion was irradiated by UV-light using a 240 W high-pressure Hg lamp (DRT-240) with stirring. Aliquots were collected at various time intervals to monitor the photodegradation of dye. In the absorption spectra of methyl orange water solution, there are two main peaks, one is color peak at ~465 nm, and another is characteristic peak of benzyl at ~192 nm. The photocatalytic reaction was monitored spectrophotometrically by observing absorbance of methyl orange at the peak absorbance wavelength ($\lambda_{\max}$ =465 nm). The spectra were taken with UV-Vis spectrophotometer (SOLAR PB 2200, Belarus). Prior to the experiments, the UV-Vis spectrophotometer was calibrated in order to determine the linear range of the absorbance-concentration relationship.

The rate of methyl orange decomposition (C_r) was calculated as

$$C_r = \frac{\mathrm{C}}{\mathrm{C}_0} \cdot 100\% = \frac{A_t^{465}}{A_o^{465}} \cdot 100\% \,, \qquad (1)$$

where C_0 is initial concentration of dye solution, C is concentration of dye solution at any time t after photoirradiation, A_0^{465} and A_t^{465} are the initial absorption and absorption at photoirradiation time t at the λ_{max}=465 nm.

Prior to photocatalytic experiments, direct photolysis of MO solution was studied by UV-irradiation in the absence of the photocatalyst for 1 h. It was found no observable color removal due to direct photolysis. Dye adsorption on the surface of the photocatalyst was also studied. Aqueous solutions of MO mixed with photocatalysts were stirred in dark for 1 h to observe whether there was any color removal due to adsorption. The rate of non-photocatalytic decolorization (i.e. adsorption capacity of catalysts) was determined with respect to the change in intensity at 462 nm. It was found that plasma treated Ag impregnated catalyst (ZnO-Ag-DBD) had a higher adsorption capacity for MO (not shown). Plasma treated pure ZnO catalyst exhibited a similar behavior in dark experiments as untreated ZnO. These results imply that Ag-NPs as dopants may act as active sites for pollutant adsorption on the surface of plasma treated catalysts. This, in turn, can facilitate the reaction of photocatalytic degradation of MO.

Fig. 1 shows the result from photodegradation of MO for various ZnO-based catalysts. The order of photodegradation efficiency of various catalysts was ZnO-Ag-DBD > ZnO > ZnO-Ag. The rate of MO degradation was improved appreciable by using plasma treated Ag-NPs loaded ZnO (ZnO-Ag-DBD) instead of pure catalyst (ZnO). The photocatalytic activity, expressed in term of rate constants, was 2.9 times higher for plasma treated Ag-NPs loaded sample than that for pure ZnO catalyst. The rate constants (k) were found to be $1.4 \cdot 10^{-3}$ s^{-1} and $4.0 \cdot 10^{-3}$ s^{-1} for pure ZnO and Ag-NPs loaded ZnO, correspondently. On the other hand, a diminished catalytic activity was observed after impregnation of zinc oxide with Ag-NPs (ZnO-Ag). The rate constant was of the order of $1.3 \cdot 10^{-3}$ s^{-1} for the ZnO-Ag sample. The decrease in catalytic efficiency is most likely due to a surface coverage of ZnO with Ag nanoparticles. The results of the experiments imply that silver nanoparticles cannot be used as active sites until they are treated by DBD plasma. Fig. 2 shows the PL spectra of the catalysts with an excitation wavelength of 330 nm. In the PL spectra of ZnO, typically there are emission bands in the UV and visible regions /7/. The UV peak is a characteristic emission of ZnO. It is attributed to the near-band-edge (NBE) emission through exciton-exciton collision processes. The emission in visible region are dominantly considered to be due to electron-hole recombination caused by surface or intrinsic defects, e. g. zinc interstitials and oxygen vacancies. The green PL emission at around of 530 (deep-level emission, DL) can be originated from the oxygen vacancies while the violet emission (~425 nm) can be attributed to the electronic transition from the defect level, corresponding to Zn interstitials, to the valence band. As

can be seen from the Fig. 2, all samples exhibited two emission bands centred at 385 and 530 nm. The NBE-to-DL emission ratio was found to be of 0.6 and 0.8 for pure ZnO and for both Ag impregnated ZnO, respectively. The increase in NBE-to-DL emission ratio can be attributed to the surface plasmon resonance effect of the Ag NPS /8/.

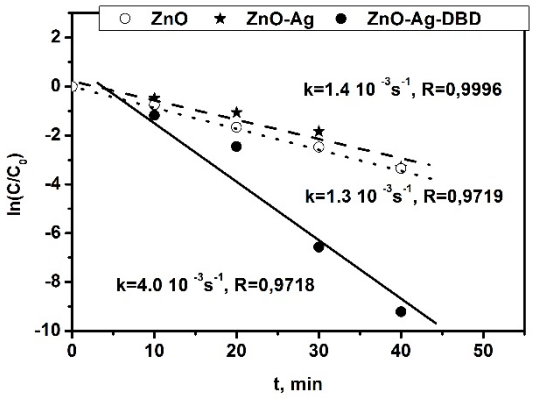

Fig. 1 – Kinetics of the degradation of MO under UV-irradiation

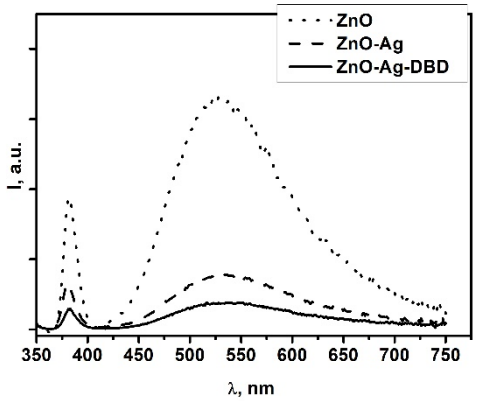

Fig. 2 – PL spectra of catalysts

In conclusion, the results suggest that nonthermal DBD plasma treatment is very effective way to manipulate catalyst surface properties and to enhance the performance of ZnO-based photocatalysts impregnated with silver nanoparticles. An approximately 3-fold improvement of the photocatalytic activity for decomposition of methyl orange was achived by DBD-plasma treatment of ZnO powder impregnated with silver nanoparticles for 25 min. The results imply that Ag-NPs as dopants may act as active sites for pollutant adsorption on the surface of plasma treated catalysts. This, in turn, can facilitate the reaction of photocatalytic degradation of MO.

Acknowledgements. This work was financially supported by the Belorussian Republican Foundation for Fundamental Research (grant No F17-076).

References

1. **Liu C.J., et al.** Appl. Catal. 47 (2004) 95-100.
2. **Feng Zh.C.** Handbook of Zinc Oxide and Related Materials. Volume One. Materials. Boca Raton: CRC Press (2013).
3. **Filatova I.I., et al.** High Temperature Material Processes 19 (2015) 221-229.
4. **Rivas L., et al.** Langmuir 16 (2000) 9722-9728.
5. **Lee P. C., and Meisel D**. J. Phys. Chem. 86 (1982) 3391-3395.
6. **Wagner H.-E., et al.** Vacuum 71(2003) 417–436.
7. **Li Y., et al.** Mater. Res. Soc. Symp. Proc. 1206 (2010) M13-03P1–P6.

EFFECT OF ELECTRICAL CHARACTERISTICS OF DBD ON THE PERFORMANCE OF DBD PLASMA TREATED ZnO-BASED PHOTOCATALYSTS

N.A. Savastenko[1], I.I. Filatova[2], V.A. Lyushkevich[2], N.I. Chubrik[2], S.A. Maskevich[1]

[1]Belorussian State University, International Sakharov Environmental Institute BSU, 23 Dolgobrodskaya Str., 220070 Minsk, Belarus, nataliesavastenko@iseu.by
[2]B.I. Stepanov Institute of Physics, National Academy of Sciences of Belarus, 68 Nezavisimosti Ave., 220072 Minsk, Belarus, filatova@presidium.bas-net.by

The application of plasma technologies in the preparation of catalysts is a developing area /1,2/. In this work, plasma treatments of ZnO-based photocatalysts have been conducted to study the effect of plasma characteristics on the performance of catalysts. Atmospheric-pressure air plasma generated by dielectric barrier discharge (DBD) is applied to treat commercial available ZnO powders. To elucidate the plasma treatment effect, DRIFTS technique (Diffuse Reflectance Infrared Fourier Transform Spectroscopy) has been used for catalysts characterization. The photocatalytic activities of untreated and plasma treated ZnO powders were evaluated by measuring the photodegradatation of methyl orange (MO).

A schematic diagram of the DBD plasma reactor built in-house is shown in Fig. 1. Electrode system was created from two metal electrodes. The bottom electrode was square-shaped with a side length of 100 mm. It was made of stainless steel and connected to the earth. As an upper electrode two types of electrode were used. A rode with 2 cm diameter and 10 cm length was used as a first-type of upper electrode. It was covered by 2.0 mm quartz glass layer mm and connected to an AC power source. The electrode was movable in the horizontal direction. A rod-plate electrode configuration is further denoted as DBD-RP. Second type of electrode (disk-grid, stainless steel mesh, D=98 mm) was glued to Petri dish. A disk-plate electrode configuration is further denoted as DBD-DP. The applied voltage (peak-to-peak value) was up to 35 kV. The distance between upper electrode and bottom one was 4 mm. Plasma was generated in the gap between electrodes. The samples to be treated were located on the grounded electrode. The plasma treatment time varied in the range 5-25 min.

The electric operation parameters of DBD such as discharge voltage U, discharge current I_d, transferred charge Q, consumed electric energy (discharge energy) E_{el} were estimated as described in /3/. For the degradation experiments, the absorption spectra were recorded and rate of decomposition of MO ($C_r(t)$)

was observed in terms of change in intensity at the peak absorbance wavelength λ_{max}, i.e., 465 nm, for maximum sensitivity.

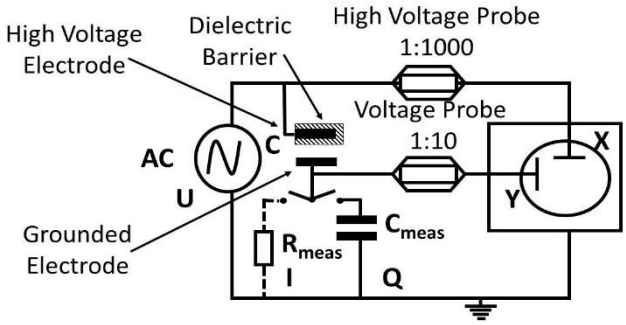

Fig. 1 – Experimental setup for voltage, current and charge transfer measurements

Diffuse reflectance infrared Fourier transform (DRIFT) spectra of samples were recorded on a Nicolet NEXUS FT-IR Spectrometer (Triad Scientific, USA) in the range of 400 to 4,000 cm^{-1} at room temperature.

Fig. 2a and b show waveforms of the voltage applied to the reactor U(t) and the associated discharge current I(t) for the DBD-RP and DBD-DP electrode configurations, respectively. Fig. 2c and d depict the Lissajous figure to be used for calculation of the electric energy (E_{el}) consumed by DBD for the DBD-RP and DBD-DP electrode configurations, respectively.

The consumed energy E_{el} was found to be 6.5 and 10.6 mJ for the DBD-RP and DBD-DP electrode configurations, respectively.

Fig. 3 shows the results from photodegradation of MO for ZnO-based catalysts treated for 25, 15, 10 and 5 min (catalysts ZnO DBD_RP_25_1, ZnO DBD_DP_25_1 ZnO DBD_DP_15_1, ZnO DBD_DP_10_1, ZnO DBD_DP_05_1, ZnO DBD_DP_05_500) by DBD plasma with an applied frequencies of 1 kHz (catalysts ZnO DBD_RP_25_1, ZnO DBD_DP_25_1 ZnO DBD_DP_15_1, ZnO DBD_DP_10_1, ZnO DBD_DP_05_1) and 500 Hz (catalyst ZnO DBD_DP_05_500) .

It can be clearly seen from the Fig. 3, that plasma treatment at E_{el} =6.5 and 10.6 mJ for 25 and 15 min resulted in similar activity of catalysts. For DBD-DP plasma with E_{el} =10.6 mJ and applied frequency of 1 kHz, decrease in treatment time from 25 to 5 min led to enhancement of catalysts performance. Further decrease in effective energy consumed by sample (i.e. plasma treatment for 5 min with E_{el} =10.6 mJ and applied frequency of 500 Hz) resulted in decrease in catalytic activity.

Fig. 4 shows the DRIFT spectra of untreated and plasma treated photocatalysts. There appeared some new peaks around 3570, 3604, 3481, 3442 2412 , 1637, 1760 and 1780 cm^{-1} after plasma treatment. For the double band at

approximately 1400 cm^{-1}, there were also some changes in peak form.

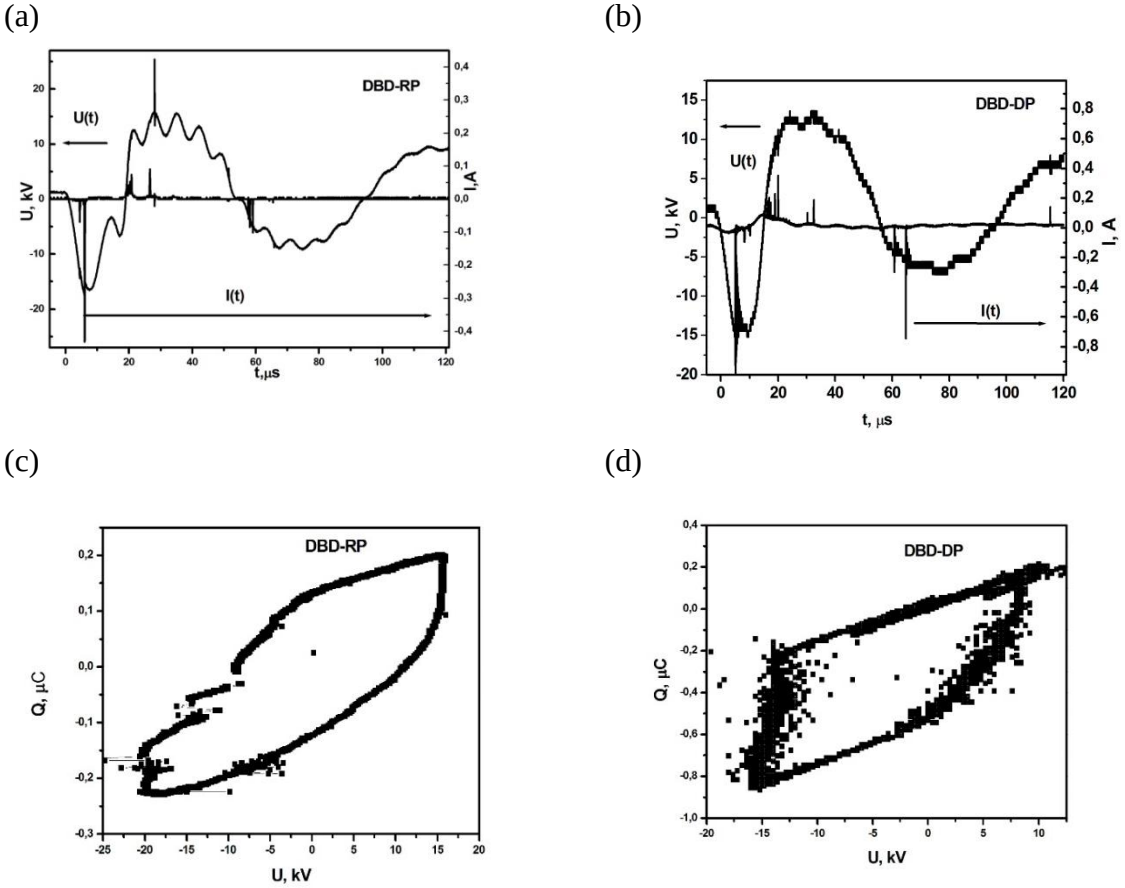

Fig. 2 – Voltage-current waveform (a, b), and Q-V Lissajous figure (c,d)

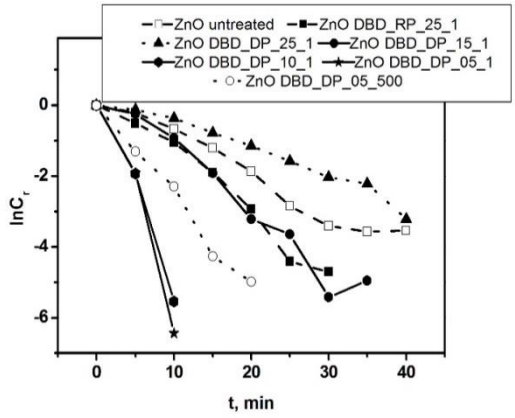

Figure 3 – Kinetics of the degradation of MO under UV-irradiation

In general, the peak intensities depended on the energy of DBD and treatment time. There was a weak correlation between peak area in the region of 1400 – 1600 cm^{-1} and activity of the catalysts. The catalysts activity is expressed as an amount of MO decomposed after 10 min of UV-light irradiation.

In summary, the most active catalyst was ZnO DBD_DP_05_1. It was treated for 5 min in DBD plasma with energy E_{el} =10.6 mJ. A weak correlation was found between the performance of the catalysts and peak area in DRIFT spectra in the region of 1400 – 1600 cm^{-1}.

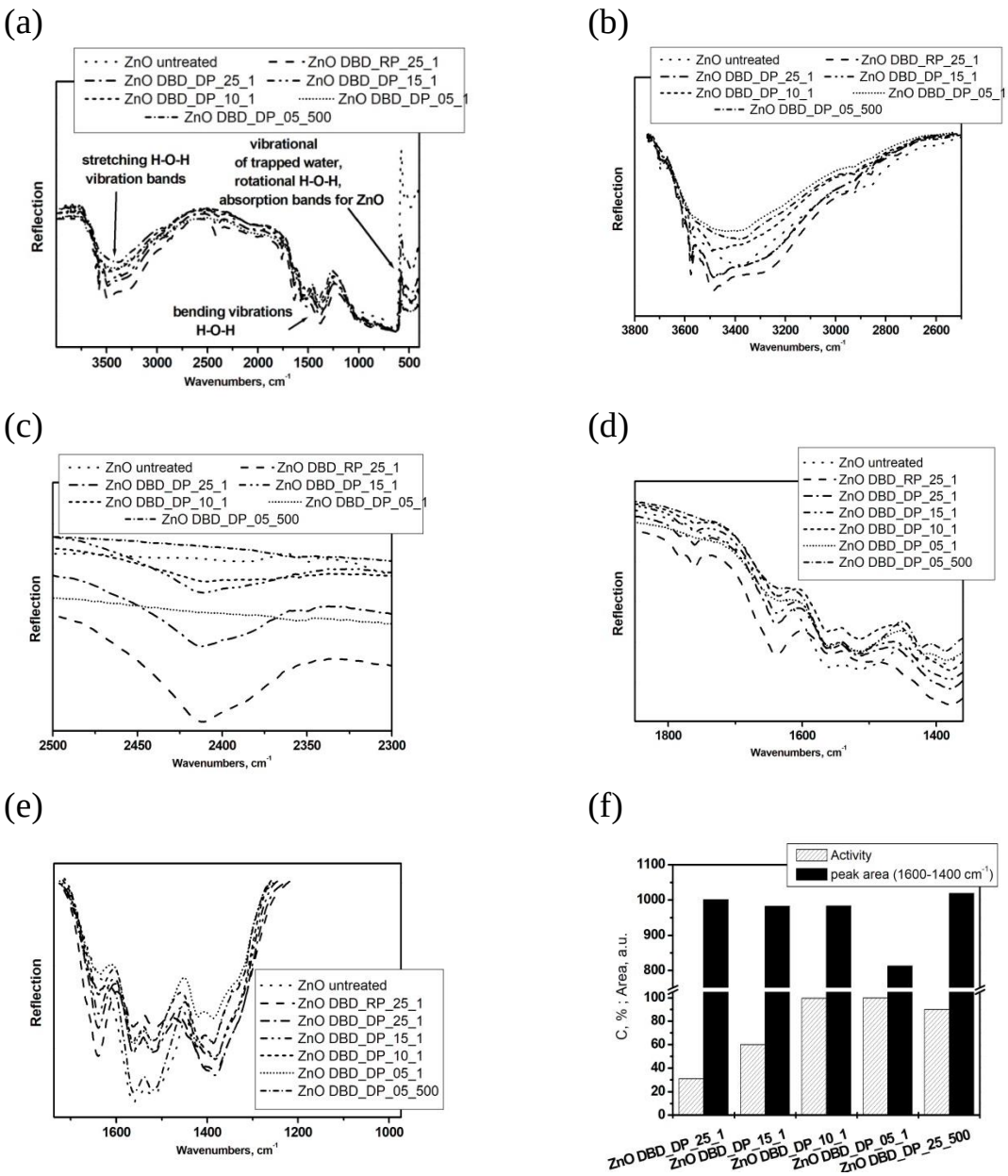

Fig. 4 – DRIFT spectra of untreated and plasma treated ZnO-based photocatalysts (a-e) and peak areas in the range of 1600-1400 cm^{-1} (f)

Acknowledgements. This work was financially supported by the Belorussian Republican Foundation for Fundamental Research (grant No F17-076).

References

1. **Liu C.J., et al.** Appl. Catal. 47 (2004) 95-100.
2. **Bartolomeu R., et al.** Catalysis Today 176 (2011) 234-238.
3. **Wagner H.-E., et al.** Vacuum 71(2003) 417–436.

PLASMA-ASSISTED SYNTHESIS OF POLYMER-CAPPED DYE-SENSITISED TiO_2-BASED PHOTOCATALYSTS FOR METHYL ORANGE PHOTODECOMPOSITION

N.A. Savastenko[1], V. Brüser[2], S.A. Maskevich[1]

[1]Belorussian State University, International Sakharov Environmental Institute BSU, 23 Dolgobrodskaya Str., 2 20070 Minsk, Belarus, nataliesavastenko@iseu.by
[2]Leibniz-Institute for Plasma Science and Technology, 2 Felix-Hausdorff-Strasse, 17489 Greifswald, Germany

Titanium oxide is the most widely researched photocatalyst. TiO_2 is an n-type semiconductor with chemical and thermal stability, and non-toxicity to human beings and environment. To date, titanium oxide is considered to be the best photocatalytic material for the photodegradation of organic contaminants. A wide variety of organic pollutants are introduced into the environmental because of the disposal of industrial wastes into the water /1, 2/. One of the major source of these pollutants is the waste rising from the industrial processes, which utilizes dyes to color fibers, paper and plastic. In the industry, a substantial amount of dyestuff are azo dyes /2/. Azo dyes are supposed to be carcinogens because they can be decomposed to amines /2/. Therefore decomposition of azo dyes has an important environmental significance. TiO_2 not only degrades organic compounds including organic dyes but also mineralizes them to CO_2, H_2O and mineral acids /1-3/.

Despite the many known advantages of using TiO_2, it suffers from the shortcoming of having a low efficiency in visiable range and narrow light response range. Titanium oxide has a large band gap (~3.2 eV) which restricts its use to the ultraviolet region. Since more than 40% of solar energy consists of visible light, it is more suitable to use visible light than UV light /4/. Therefore, new methods should be developed to overcome these problems. The photosensitization is considered to be a promising method to extend the light absorption /3, 5, 6/. It was shown that meso-tetraphenyl metalloporphyrins (Fe, Co, Mn and Cu) adsorbed on TiO_2 were efficient for the degradation of MO aqueous solution under visible and ultraviolet (UV) light irradiation /4/. Porphyrin-photosensitizers were found to be efficient for the degradation of 4-nitrophenol (4-NP) and atrazine under visible light irradiation /5, 6/.

In previous work /7/, the performance of Ru dye sensitized TiO_2 nanopowders was tested for photocatalytic H_2 evolution. An insufficient catalytic activity was observed after impregnation of TiO_2 with Ru dye as a result of poor bonding of the dye molecule to the surface of the nanopowders and self-aggregation of the dye. The performance of the catalysts was improved

by the encapsulation of the Ru dye-TiO_2 assembly in a polyamine layer anchored to titanium oxide.

In this study, the polymer-capped Ru sensitised TiO_2 nanopowders were employed for photocatalytic degradation of methyl orange (MO). MO was chosen as a model compound as it belongs to one of the most important classes of commercial azo dyes and is widely used in the printing and textile industries and chemical laboratories /8/.

TiO_2 anatase nanopowder (Aldrich, < 25 nm, 99.7%) was used as the photocatalyst powder. A Ru dye solution (0.3 mM) was prepared by dissolving commercially available N3 ($C_{26}H_{16}N_6O_8RuS_2$, Aldrich) in absolute ethanol with stirring overnight at room temperature to ensure the complete dissolution of all solids. The dye solution was then adsorbed onto the surface of the anatase nanopowder with stirring at room temperature for 24 h. In the final step, the solvent was evaporated and the sample was dried at 60° C. The plasma polymer coatings were deposited onto both pure and N3 impregnated TiO_2 anatase nanopowder using a low-pressure RF plasma polymerization process with allyl alcohol as precursor and argon as carrier gas. A rotating drum reactor 'Piccolo' (Plasma Electronic GmbH, Neuenburg) was used as device for plasma polymer deposition. The following process parameters have been set: RF plasma power 300 W, 13,56 MHz, deposition time 15 min, gas composition 20 sccm Ar and approx.1,5 sccm allyl alcohol, pressure 15 Pa.

The catalytic tests were carried out by irradiating the aqueous solutions of MO dye containing photocatalysts with UV and visible light. For each experiment, 10 mg of photocatalysts was added to 5 mL of 50 mg/l solution of MO. The suspension was subjected to irradiation under UV light for a fixed interval of time. A UV lamp (mercury vapor lamp with a quartz envelope, 240 W, DRT-240) was used as light source. The typical UV lamp spectrum is shown in Figure1.

At different time intervals, an aliquot was taken out. Then absorption spectra were recorded and rate of decomposition of MO ($C_r(t)$) was observed in terms of change in intensity at the peak absorbance wavelength λ_{max}, i.e., 465 nm, for maximum sensitivity.

$$C_r(t) = \frac{C(t)}{C_0} \cdot 100\% = \frac{A_t^{465}}{A_0^{465}} \cdot 100\%, \qquad (1)$$

where C_0 is initial concentration of dye solution, C(t) is concentration of dye solution at any time t after photoirradiation, A_0^{465} and A_t^{465} are the initial absorption and absorption after photoirradiation time t at the λ_{max}=465 nm.

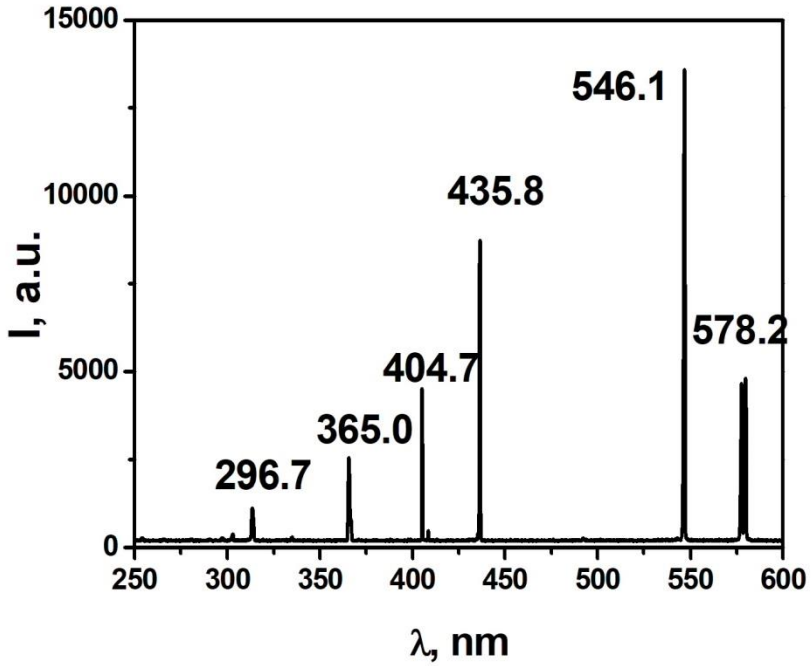

Fig. 1 – Spectrum of UV lamp (DRT-240)

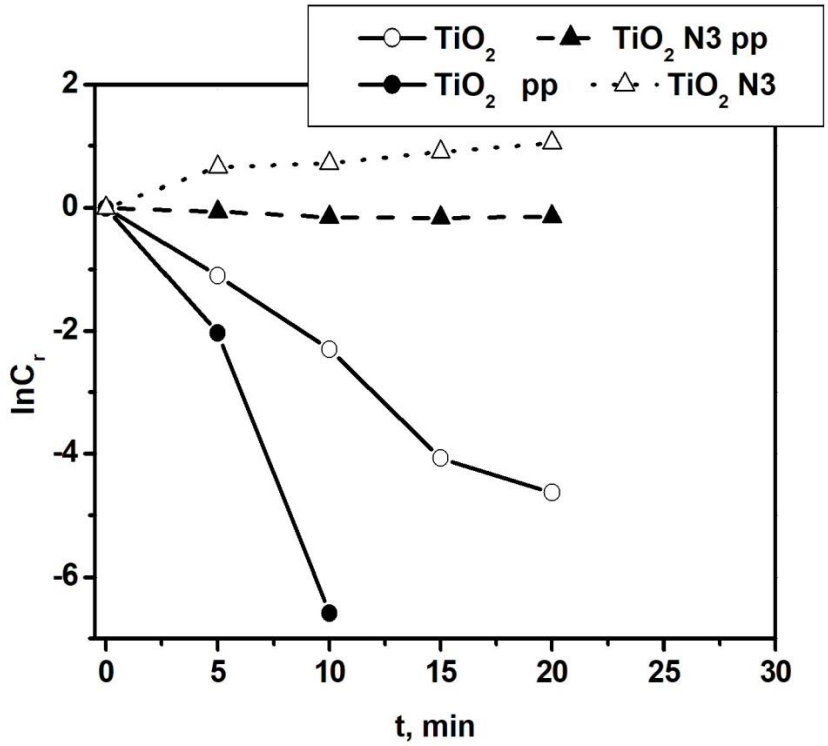

Fig. 2 – Kinetics of the degradation of MO under UV-irradiation

Fig. 2 shows the result from photodegradation of MO for various TiO_2-based catalysts. Bare TiO_2 nanopowders is denoted as TiO_2. Impregnated with Ru dye TiO_2 nanopowders is denoted as TiO_2 N3. Polymer capped Ru dye impregnated photoatalyst is denoted as TiO_2 N3 pp. TiO_2 nanopowders covered with polyallyalkohol layer is denoted as TiO_2 pp.

The order of photodegradation efficiency of various catalysts was TiO_2 pp > TiO_2 > TiO_2 N3 pp > TiO_2 N3. As can be seen in figure 2, polymer capped Ru dye impregnated titania nanopowders (TiO_2 N3 pp) is almost non-active. Approximately 86 % of MO was left after 10 min of irradiation. No further photodegradation of MO was observed. For polymer capped Ru dye impregnated photoatalyst (TiO_2 N3), the value of A_t^{465} increased with time. It might be caused by the absorbtion of Ru dye that was deleted from the surface of the TiO_2 nanopowders. For bare TiO_2, approximatelly 99% of MO was degradeted after 20 min of irradiation. Covering of TiO_2 with polymer layer led to enhancement of catalyst perfromans. For TiO_2 pp catalyst, less then 0,1% of MO was left after 10 min of irradiation.

Further work will be carried out to elucidate the origin of the catalytic activity of TiO_2 nanopowders covered with polymer layer.

Acknowledgements. This work was partially financially supported by the Belorussian Republican Foundation for Fundamental Research (grant No F17-076).

References

1. **Umar M. and Aziz H.A.** in Organic Pollutants - Monitoring, Risk and Treatment. IntechOpen (2013) 195 208.
2. **Kansal S.K., at al.** J. Hazard. Mater. 141 (2007) 581-590.
3. **Zhou X.-T., at al.** Molecules 17 (2012) 1149-1158.
4. **Fox M.A. and Dulay M.T**. Chem. Rev. 93 (1993) 341-347.
5. **Wang C., et al.** Appl. Catal. B 76 (2007) 218-226.
6. **Granados-Oliveros G. et al.,** Appl. Catal. B 89 (2009) 448-454.
7. **Kruth A. et al.** ChemSusChem. 6 (2013) 152-159.
8. **Kodom T., et al.** Intern. J. Chem. Technol. 4 (2012) 45-56.

Effect of seeds treatment by low pressure and atmospheric pressure plasma on the infection level and length of winter wheat seedlings

I.I. Filatova[1], V.A. Lyushkevich[1], S.V. Goncharik[1], N.I. Chubrik[1], A.G. Zhukovsky[2], N.A. Krupenko[2], N.G. Poplavskaya[2], Najeeb-ur-Rehman[3]

[1]B.I. Stepanov Institute of Physics, National Academy of Sciences of Belarus, 68-2 Nezavisimosti Ave., 220072 Minsk, Belarus, v.lyushkevich@ifanbel.bas-net.by
[2]RUE "Institute of Plant Protection", 2 Mira Str., 223011 Priluki, Minsk District, Belarus,
[3]COMSATS Institute of Information Technology, Park Road, 45550, Islamabad, Pakistan

Introduction

The cold plasma is one of the fastest emerging technologies in the food processing. Presently, cold plasma technology was now used for sterilization, functionalization, inactivation of enzymes, altering the hydrophilic/hydrophobic properties /1/. In order to prevent or decrease the damage caused by fungi, different physical or chemical methods can be used. Since some of them can lead to changes in the physicochemical properties of the seeds, decontamination of seeds without decreasing the seed or food quality is very important. Plasma treatment has synergistic effects as it increases germination rate, increase/decrease in enzymatic activity along with the microbial inactivation and breakdown the seed dormancy /2,3/. It is reported that grain and legume yields were significantly increased by cold plasma /4,5/. Carvalho /3/ showed that seed coating with thin films obtained by plasma polymerization protected grains and seeds and enhance seed germination. In additional, plasma treatment effectively reduces the cooking time of food products /6/.

In this paper, the effect of plasma treatment of seeds on the infection level and length of winter wheat seedlings is reported. The results of seed treatment under different experimental conditions, using gas plasma generated under two different systems, atmospheric pressure plasma and low pressure plasma are discussed.

Experimental

Special experiments were carried out in laboratory conditions to study the efficiency of plasma processing under conditions of artificial infectious background. For this, the seeds of winter wheat and oats were inoculated with a spore suspension of the fungus *Fusarium culmorum* - one of the most pathogenic species on the root system of cereals with a titer of 1.5×10^4 spores/ml. Seeds were treated by the resulting suspensions, dried at room temperature, and then treatment by plasma.

The treatment of seeds by low pressure plasma (RF plasma) was carried out in a planar geometry capacitively coupled 5.28 MHz plasma reactor consisting of two plane-parallel electrodes placed in a vacuum chamber. All treatments were performed in air at a pressure of 200 Pa. The power density was not more than 0.45 W/cm^3. The duration of plasma exposure was 5 and 10 min.

In case of treatment of seeds by atmospheric pressure plasma (DBD plasma), the upper grid electrode with 10 cm diameter was covered by 2.0 mm quartz glass layer and connected to an AC power source. The lower plate electrode (10x10 cm) was made of stainless steel and connected to the earth. The distance between upper electrode and treated sample was 4 mm. The applied voltage (peak-to-peak value) was of 30 kV range. The applied voltage frequency was of 1 kHz. The samples to be treated were located on the grounded electrode. Plasma treatment was carried out in air at atmospheric pressure for treatments times of 1 and 2 min.

Seed germination tests and determination of infection level were carried out using controlled conditions in the Institute of Plant Protection.

Results and discussion

The results of experiments demonstrate that pre-sowing plasma treatment of artificially infected winter wheat seeds promote to increase in germination energy and decrease in the infection of seeds with fungi *Fusarium* spp. and *Alternaria* spp. (Fig.1,2).

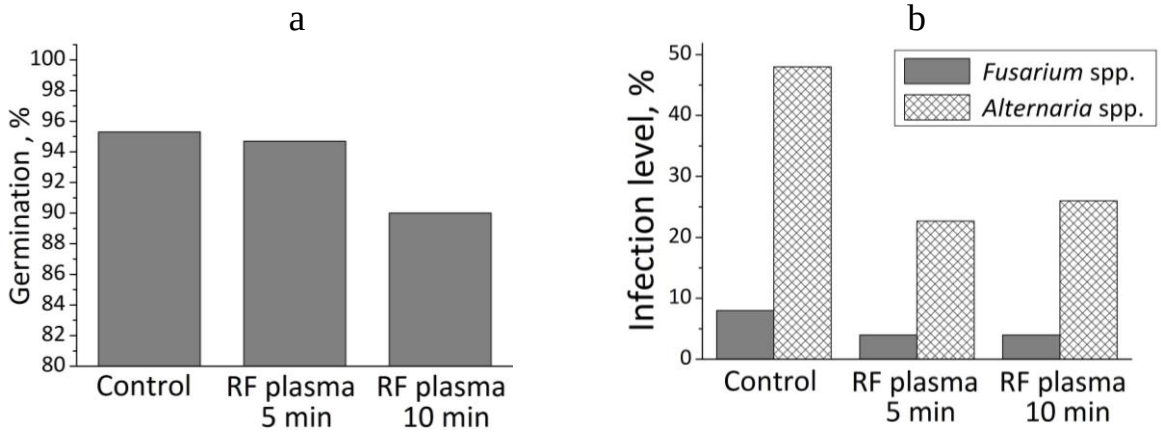

Fig. 1. – Germination (a) and infection level (b) of winter wheat after treatment of seeds by RF plasma.

The fungal loads of the seeds decreased for winter wheat seeds after plasma treatment, depending on exposure time and source of plasma. The positive or negative effect depended not only on plasma exposure time but also on the natural germination capacity of individual plant species and also on the size of seeds and their surface morphology, seed coat hardness and thickness of

endosperm /7/.

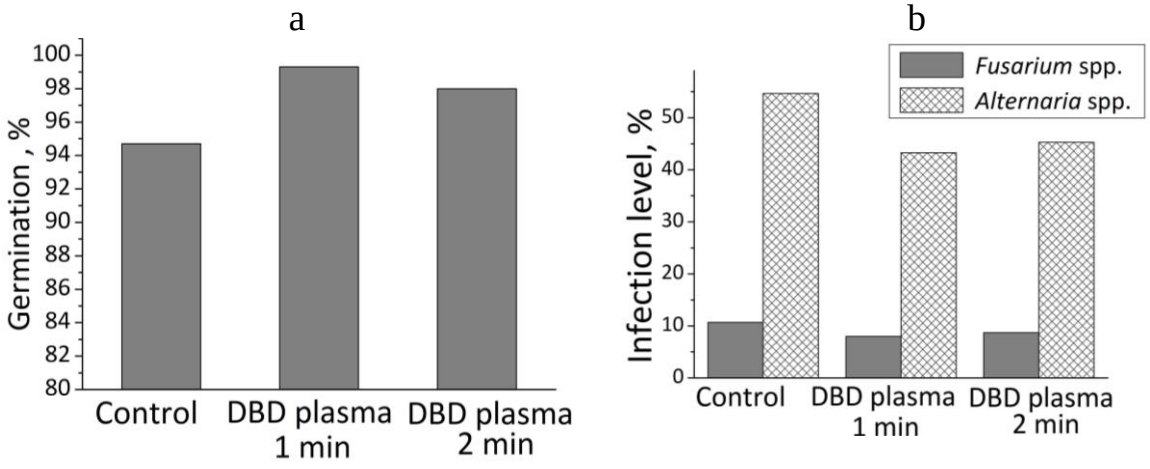

Fig. 2. – Germination (a) and infection level (b) of winter wheat after treatment of seeds by DBD plasma.

Treatment by low pressure plasma leaded to improvement of morphometric characteristics of wheat. A significant increase in the length of sprouts and roots of wheat was observed for 5 min treatment (Fig. 3). Thus, influence of RF plasma leaded to increase in the length of sprouts and roots of wheat by 19.5 and 13.4 mm respectively.

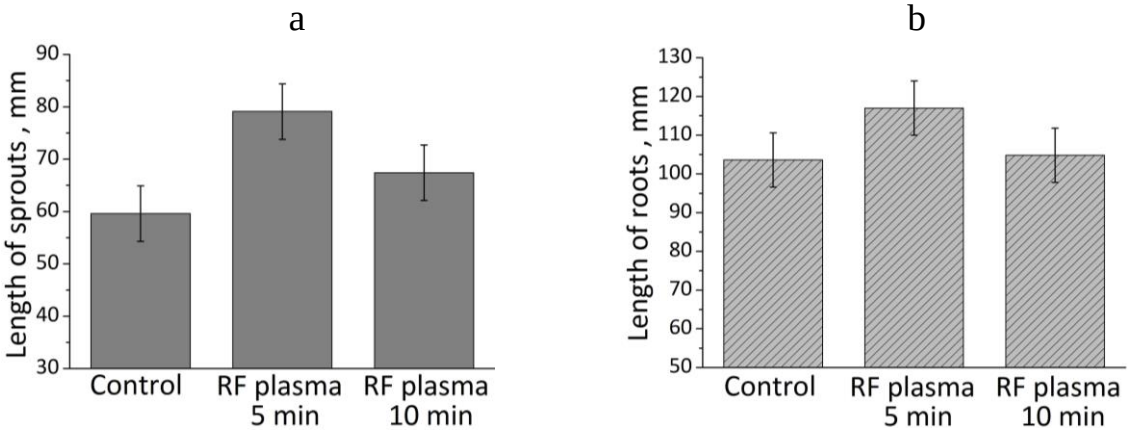

Fig. 3. – Morphometric characteristics of winter wheat after treatment of seeds by RF plasma: length of sprouts (a); length of roots (b).

Greater results were achieved for treatment of seeds by atmospheric pressure plasma. The length of sprouts and roots of wheat increased by 43.7 and 27.9 mm respectively (Fig.4).

These results suggest that cold plasma may be considered as alternative methods for disinfestations of crop seeds due to its strong potential for microbial inactivation and for stimulation of germination of crop seeds

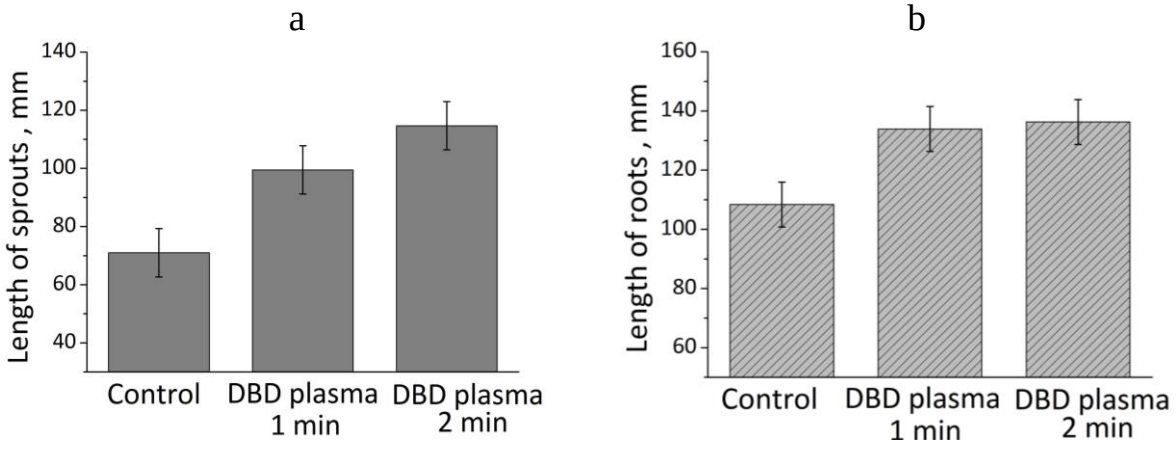

Fig. 4. – Morphometric characteristics of winter wheat after treatment of seeds by DBD plasma: length of sprouts (a); length of roots (b).

.

Conclusions

The results of seed treatment under different experimental conditions, using gas plasma generated under two different systems, atmospheric pressure plasma and low pressure plasma were obtained. It is shown that pre-sowing plasma treatment of artificially infected winter wheat seeds promote to increase in germination energy and decrease in the infection of seeds with fungi *Fusarium* spp. and *Alternaria* spp. Treatment by low pressure plasma leaded to increase in the length of sprouts and roots of wheat by 19.5 and 13.4 mm respectively. In case of treatment by atmospheric pressure plasma, the length of sprouts and roots of wheat increased by 43.7 and 27.9 mm respectively.

Acknowledgements. This work is partly supported by the Belarusian Republican Foundation for Fundamental Research under the grant No Ф17ПАКГ-001.

References

1. **Misra N.N et al.** Trends in Food Science & Technology, 55 (2016) 39–47.
2. **Zivkovic. S, Puac. N, Giba. Z, et al**. Seed Sci. Tech-nol., 32 (2004) 693-701.
3. **Carvalho R. A. et al**. Quim. Nova, 28 (2005) 1006-1009.
4. **Jiang J. F. et al**. Plasma Sci. Technol., 16 (2014) 54-58.
5. **Selcuk M. et al**. Bioresource Technol., 99 (2008) 5104-5109.
6. **Sarangapani C. et al**. LWT - Food Science and Technology, 63 (2015) 452-460.
7. **Zahoranova A**. **et al**, Plasma Chem Plasma Process., 36 (2016) 397-414.

STABILITY OF ZrSiN NANOCOMPOSITE FILMS AT AIR ANNEALING

I.A. Saladukhin[1], G. Abadias[2], V.V. Uglov[1], S.V. Zlotski[1]

[1] Dpt. of Solid State Physics, Belarusian State University, 4 Nezavisimosti ave., 220030 Minsk, BELARUS, solodukhin@bsu.by
[2] Institut P', Université de Poitiers-CNRS-ENSMA, SP2MI, Téléport 2, F86962 Chasseneuil-Futuroscope, FRANCE, gregory.abadias@univ-poitiers.fr

Introduction Thin films on the basis of nitrides of transitional metals (TM) are widely used as hard protective coatings in the industry. One of the most important properties of the coatings for their practical application is their resistance to high temperature oxidation. For such severe conditions, most of the mononitride films cease to perform their protective function. For example, TiN coatings are rapidly oxidized at temperatures as low as 550 °C /1/. Increase in their thermal stability, oxidation and wear resistance is promoted by adding either metallic elements (Al, Zr, Ta, etc.) or nonmetallic elements such as Si or C. The incorporation of Si atoms into TiN, ZrN or CrN contributes to grain size refinement and the formation of a nanocomposite structure (grains of TM nitride surrounded by an amorphous SiNx phase), resulting in modification of mechanical properties together with enhanced thermal stability /2-4/. Unlike the Ti-Si-N system, the Zr-Si-N and Cr-Si-N films are less studied.

Preparation of thin films Nanocomposite ZrSiN films were grown by reactive magnetron sputter-deposition in a high vacuum chamber (base pressure < 10-5 Pa) equipped with three confocal targets configuration. Films were deposited on Si substrates covered with 10 nm thick thermally grown SiO2 layer. A constant bias voltage of –60 V was applied to the substrate during deposition. Monolithic ZrN and Si3N4 films were also deposited as the reference films.

Water-cooled, 7.62-cm-diameter Zr (99.92 % purity), Si (99.995% purity, p-type doped) and Si3N4 (99.99 % purity) targets, located at 18 cm from the substrate holder, were used under Ar + N2 plasma discharges at constant power mode. The Zr and Si target were operated in magnetically unbalanced configuration using a DC power supply, while a RF power supply was used for the Si3N4 target in balanced mode. The total working pressure was 0.21 Pa, as measured using a Baratron® capacitance gauge. The Ar/N2 flow ratio was optimized to obtain stoichiometric nitrogen content in the films based on earlier results.

Nanocomposite ZrSiN films were deposited by co-sputtering from Zr and Si targets at the substrate temperature of 600 °C. The Si content in the films was varied by changing the DC power supply of the Si target, from 0 up to 200 W,

while maintaining the DC power supply of Zr targets constant. As a result, the coatings with Si content (CSi) ranging from 0 to 22.1 at.% were synthesized, as determined from elemental probe microanalysis. The total film thickness was ~ 300 nm.

Structure and phase composition of as-deposited nanocomposite ZrSiN films The analysis of ZrSiN films by TEM method allowed to conclude that their microstructure changes from nanocrystalline columnar grains ($0 \leq$ CSi ≤ 3.2 at.%) to a dual-phase structure characterized by the presence of grains included into a surrounding matrix (CSi = 12.3 at.% and CSi = 17.2 at.%) with increasing Si content. The cross-section TEM image for the case of CSi = 12.3 at.% is presented in Fig. 1a. The SAED pattern, shown in the insert, displays well-defined rings that can be indexed as 111, 200, 220 and 311 rings of a cubic (Na-Cl type) structure with a lattice parameter equal to 0.465 ± 0.005 nm, slightly higher than that of ZrN. When CSi increases up to 22.1 at. % the structure becomes close to amorphous (see Fig. 1b). However, the presence of diffuse rings indicates that short-range ordering is present for this sample (Fig. 1b, insert).

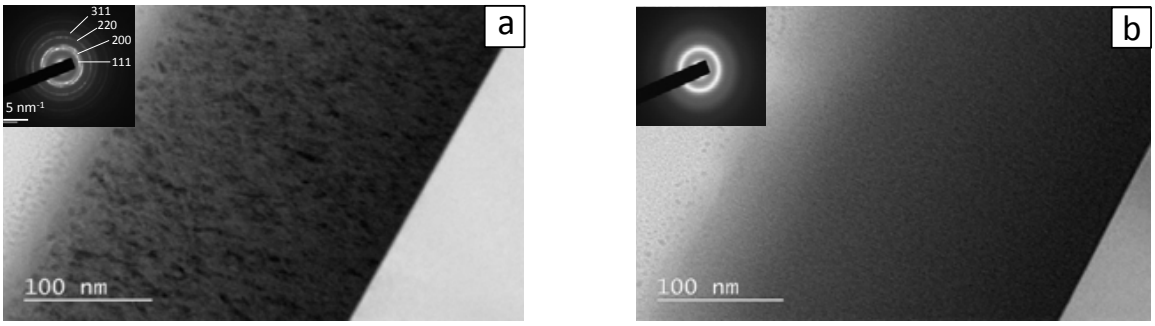

Fig. 1 - Cross-sectional bright field TEM micrographs of ZrSiN nanocomposite films with different silicon content: (a) CSi = 12.3 at.% and (b) CSi = 22.1 at.%. SAED patterns are shown in the insets.

Based on XPS data of the Si 2p emission lines for the ZrSiN films, the nature of the matrix which surrounds the ZrN grains in ZrSiN nanocomposite films with $C_{Si} \geq 12.3$ at.% was clarified. The Si 2p spectrum exhibits a main

peak centered at 101.85 eV, and a smaller one located near 98.4 eV. These two peaks can be assigned to Si $2p_{3/2}$ and Si $2p_{1/2}$ lines of amorphous silicon nitride (a-SiN_x) compound.

The results of XRD analysis for ZrN and ZrSiN films with different silicon content are given in Fig. 2 (see lower patterns corresponding to as-deposited state). The (111) preferred orientation prevails for ZrN reference film (Fig. 2a). When increasing C_{Si}, the strong decrease in 111 peak intensity and the concomitant increase in 200 peak intensity are observed (Fig. 2b,c). At the same time the broadening of peaks of zirconium nitride takes place. The crystallite size of ZrN phase decreases from 23 nm (ZrN film) down to 4-6 nm (ZrSiN film with 12.3 at.% $\leq C_{Si} \leq$ 17.2 at.%) as it was extracted from XRD line broadening of 200 peak using Scherrer approximation. For ZrSiN film with C_{Si} = 22.1 at.% the size of the crystalline grains cannot any longer be estimated since it is X-ray amorphous.

From the obtained results, it is possible to infer about the formation of ZrSiN nanocomposite films representing bi-phase systems consisting of a-SiN_x amorphous matrix and cubic ZrN grains included into it.

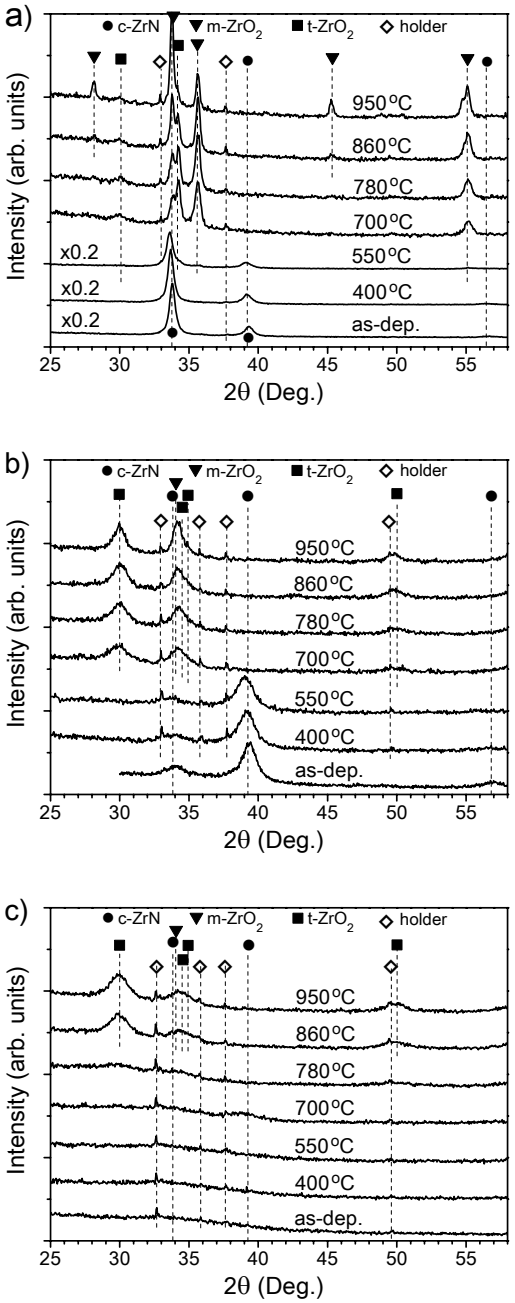

Fig. 2 - Evolution of XRD patterns under air annealing for ZrN reference film (a) and ZrSiN films with different silicon content: (b) C_{Si} = 12.3 at.% and (c) C_{Si} = 22.1 at.%.

Oxidation resistance of nanocomposite ZrSiN films under air annealing The appearance of crystalline oxide phases for ZrSiN nanocomposite films is revealed at higher temperatures in comparison with ZrN film (Fig. 2).

For ZrN film, the formation of tetragonal t-ZrO2 oxide is already registered at the temperature of 550 °C (Fig. 2a). For ZrSiN nanocomposite films, the

oxidation starts at 700-780 °C (Fig. 2b-c). It should be mentioned that after annealing at the maximum temperature (950 °C) only t-ZrO2 phase is revealed in ZrSiN films composition, unlike ZrN film where m-ZrO2 phase is mainly present. The presence of the sole t-ZrO2 phase for ZrSiN films could reflect that the oxidation process is not completed for these coatings, at least in the oxidation temperature and time ranges investigated here.

One can see for the ZrN reference film a high density of corrosion sites (Fig. 3), the presence of which leads to a coating swelling (Fig. 3a). The surface topography of the air-annealed Si_3N_4 coating exhibits extensive folded regions characteristic of blistering (Fig. 3b).

ZrSiN films retain a better surface integrity and there are no pronounced corrosion sites after air annealing at 950°C (Fig. 3c-d). However, these films tend to crack in consequence of constrained molar volume expansion associated with oxide formation during annealing.

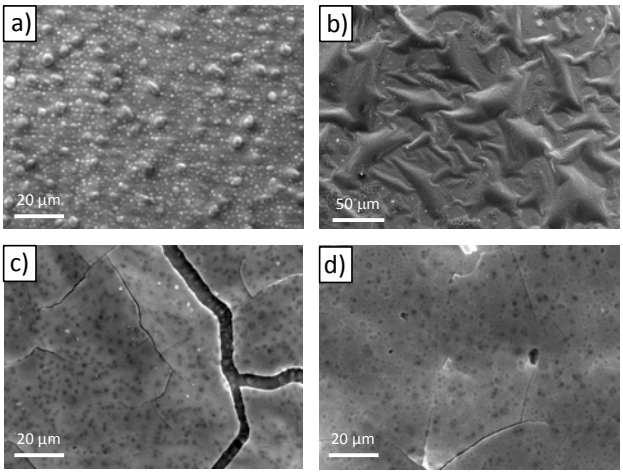

Fig. 3 - SEM micrographs of ZrN (a) and Si_3N_4 (b) reference films and ZrSiN nanocomposite films with C_{Si} = 12.3 at.% (c) and C_{Si} = 17.2 at.% (d) after air annealing at 950 °C.

Based on the obtained results one can conclude that with the increase of silicon content in ZrSiN films their resistance to high-temperature oxidation improves. However, after annealing at the maximum temperature of 950 °C, the cracking of these coatings occurs that interferes with retention of their protective properties.

Acknowledgments This work was supported by the project of Belarusian Republican Foundation for Fundamental Research (No. Ф18МС-027).

References

1. **Abadias G., et.al.** Thin Solid Films, 538 (2013) 56–70.
2. **Barshilia H.C., et.al.** Surf. Coat. Technol., 201 (2006) 329–337.
3. **Freitas F.G.R., et.al.** Materials Research, 18 (2015) 30–34.
4. **Lin J., et.al.** Surf. Coat. Technol., 216 (2013) 251–258.

50 WATT PULSED PLASMA THRUSTER SYSTEM

L. Potabachniy, R. Emlin, F. Kazankin, L. Yashnov, P. Morozov

Institute of Electrophysics UD RAS, 620016, Yekaterinburg, 106 Amundsena street
NIIMash, 624740, N.Salda, 72 Stroiteley str.
lfd@iep.uran.ru

The Research Institute of machine-building (NIIMash) in cooperation with the Institute of Electrophysics UD RAS (IEP) are sequentially working on creation of PPT and propulsion modules (PPTS) based on them for satellites. The work in this direction was based on the results of investigations on breakdown of solids and liquid dielectrics, supervised by corresponding member of RAS Yu. N. Vershinin /1/ using high-voltage (100-200 kV) generators of nanosecond pulses. The results of that works including vacuum flashover of Teflon in co-axial electrodes «anode centre – cathode case» gave the average velocity of carbon and fluorine ions' flow in order of 100 km/s at the high-voltage stage of formation of discharge gap overlap /2/.

The presence of arc phase of discharge process, generating low-rate plasma at the final (high-current, low-voltage) stage of discharge process, was minimized by decreasing duration of voltage pulse from the generator and by the size of discharge gap. When the discharge process in gap between the electrodes at the initial phase propagated from anode to cathode («anode breakdown»), it was called as electronic detonation (by analogy with the process of explosive materials' detonation) propagating in electronic subsystem of solid body. The detonation characteristic in this process is provided by reduction of width of dielectric's forbidden band E_g under the influence of high pressure ahead of the high-speed front of propagating zone of high conductivity (zone of development of discharge process).

Several patents for the elaborated variants of PPT using this type of discharge were taken out /3/. Comparatively low power efficiency of nanosecond generators (30 - 40%), their substantial mass (inner volume filled with transformer oil), poor resistance to mechanic overload and large sizes kept back the construction of PPT (and PPTS based on them) having mass and size characteristics surpassing the present-day levels. Therefore NIIMash holds subsequent search of technical solutions directed to upgrading of the characteristics of PPT and propulsion modules.

One of the results of this research is realized in demonstrational PPTS tested on test equipment of NIIMash and IEP. It is the substitution of solid fluorocarbon (PTFE) as a propellant in PPT for a liquid-phase dielectric with low value of saturated vapors for example the vacuum oils (brands BM-1 or BM- 5) that were deposited in a thin layer on the surface of rotating dielectric

ceramic disk with $\zeta \geq 200$, which moves about stationary electrode system «anode – cathode». Such approach means elaboration of a mechanism of strictly dosed supply of liquid propellant (LP) to the discharge gap zone. In fact, lack of liquid in discharge zone causes scorching and disturbance of surface geometry of the mobile disk underlayer , and excess of LP leads to unproductive losses, provoking drops release of liquid into inter-electrode zone during PPT operation. To provide stable work of PPT, the thickness of LP film is optimized not only in inter-electrode zones, but separately in the so called triple point «electrode – film – underlayer». Presently this problem solution is plotted in the variant of construction of the system of LP supply that provides not only delivery (inflow) of LP to pre-discharge zone limited by electrodes «anode – cathode», but also reception outflow of excess liquid from after-discharge zone. This technical solution (Fig. 1) is based on the introduction of double-channel pump of peristaltic type having a common electric rotation supply with the mobile solid ceramic disc as base, into the system of LP supply. This allows synchronizing of ceramic surface movement with the rate of supply of reaction substances (propellants). In this variant, elastic pipes of the pump are filled with wettable material of fuse type; one end of the pipe connected with a liquid in storage tank, and the second end contacts with the rotating disk underlayer for deposition (delivery) of liquid and removal of the excess LP /3/. The second important result of the search for constructive solutions of PPT is using of standard commercial high-voltage module. This module is loaded on capacitive energy storage based on ceramic strontium titanate capacitors (as the КВИ-3), on its cylindrical surface where discharge gaps of PPT are mounted and LP film is deposed.

Using of ceramics with $\zeta \geq 200$ permitted acute (proportional to ζ) enhancement of charge cumulating in the zones near electrodes in discharge gaps increase of efficiency of the process of breakdown initiation. This promoted breakdown and ionizing of the gaseous products of LP outflow at sufficiently lower values of discharge voltage than if the discharge gap was formed on underlayer of usual dielectric having a low dielectric penetrability.

By the way, such approach allowed to broaden downward the diapason of operating voltages for PPTS feeding from the sources on board the satellite down to level of 12 V without worsening the characteristics for devices. For the control of the ignition module a multivibrator or its adjustable analogue with of control pulses rates for each discharge arm till 500 Hz is used.

The diagram of storage and LP supply to the discharge is shown on Fig.1. To improve the temporal characteristics and to achieve discharge current of non-periodic form, the discharge gaps of PPT are electrically connected in daisy chain by analogy with multigap gas dischargers of capacitor type as applied to

vacuum. In multigap discharger the total time of discharge gaps overlap is mainly determined by the time of overlap of the first (single) discharge gap.

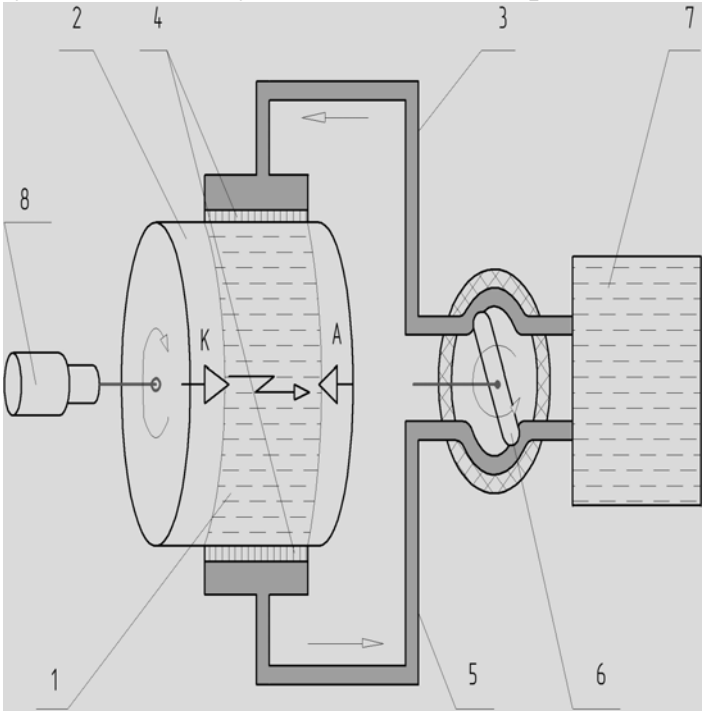

Fig.1 – The schematic diagram of storage and supply of LP to the discharge gap

1 – the surface of dielectric ceramic wetted by liquid propellant; «C – A» – cathode and anode of discharge gap; 2 – rotating ceramic underlayer; 3 – duct for supply of liquids to discharge gap; 4 – elastic dumpers for LP; 5 – duct for sucking out of excess liquid from discharge gap; 6 – double-channel pump; 7 – storage tank for liquid propellant; 8 – rotation gear of the underlayer.

vacuum. In multigap discharger the total time of discharge gaps overlap is mainly determined by the time of overlap of the first (single) discharge gap.

Measurements of electrophysical parameters of the discharge cell process as well as model testing were fulfilled in IEP with vacuum chamber of 2.5 m^3 volume. In the process of development of the construction, measurements of discharge current and voltage were done. Measurement of recoil momentum of plasma jet was made on torsion balances with hanging target 25 x 32 cm^2 in size. Period of oscillations of the balances is 17 sec, inertia is 25 000 $g \cdot cm^2$. After 400 discharges during one second the angular amplitude of oscillations of light indicator on the scale makes 1^0, giving second impulse of target recoil 75μN*s and, correspondingly, thrust about 0.18 μN*s per single discharge.

The technical solutions introduced in this work were legalized in applications for a patent /4, 5/. The offered scheme allows to realize in PPT a discharge characteristically close to electronic-detonation type, at sufficiently lower levels of voltages (in order of 15-25 kV) and energies near 0.05 - 0.10 J.

Basing on these development works, we managed to realize PPTS with substantially reduced mass and sizes in comparison with present analogues and considerably simplify the feeding and control of PPTS (Fig. 2). By the way, there appeared a possibility to attach rotation to whole electrode block of discharge gaps and organize its adjustment by thrust vector in 180^0 sector /6/.

What are the advantages of PPTS using LP concerning introduced constructive features over the analogues of ablation PPT type:

- Low level of power consumption (50 watt and less) with stable outlet characteristics;

- possibility of operation of PPTS when on-board supply drops to 12 V without worsening of characteristics;

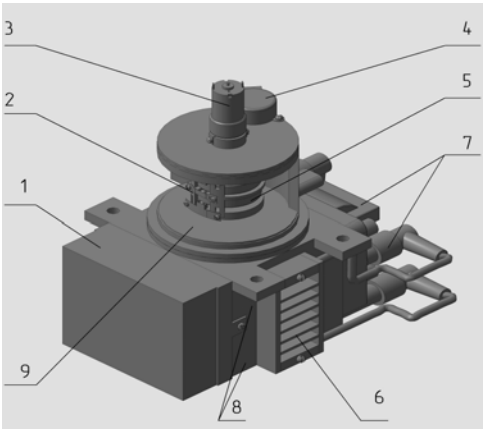

Fig.2 – General view of demonstrational PPTS

1 – stabilization and control block; 2 –system of electrodes; 3 – rotator drive for wetting of capacitors block и and two-channel pump of liquid propellant; 4 – step drive for control of electrode system position; 5 – movable double-capacitors block; 6 –rectifier unit; 7 – high voltage transformer; 8 – tank (container) with liquid propellant; 9 –thrust module housing.

- high velocity of products outflow (in order of 20 km/s) allows to reduce the reaction mass stock and the total mass of PPTS;

- absence of noticeable heating of the constructive elements of PPTS;

- possibility of adjustment of the thrust by means of change of operation frequency till 1kHz when a single thrust impulse has order of $2 \cdot 10^{-7}$ N·s.

We can forecast the use of such PPTS with total impulse of thrust till 1000 N·s for triaxial system of orientation as a part of a cosmic apparatus. Mounting of two such propulsion modules on board the satellite with adjustment of thrust vector in 180^0 sector will permit not only correction the orbit along three axes, but also usage of such PPTS for acceleration of cosmic apparatuses of classes “mini” and “micro”.

References

/1/ **Vershinin Yu. N.** Electron-detonation processes at electric breakdown of solid dielectrics. Yekaterinburg, 2000.

/2/ **Morozov P. A., Punanov I. F., Emlin R. V., Gilev A. S.** Measurement of Parameters of Particle Beams Generated by High-Voltage Surface Vacuum Discharge in Coaxial and Linear Electrode Geometry. Plasma Science, IEEE Transactions on plasma sciences, 41 (2013) 2145 — 2149.

/3/ **Potabachniy L., Emlin R., Kazankin F., Vershinin Yu**. Pulsed Electro-reactive Thruster. The patent of RF № 2211952 with priority от10.09.2003.

/4/ The patent of RF № 2615306 with priority on 19.01.2015 was taken out for this solution.

/5/ Application № 2016 114 646 on 14.04.2016 for a RF patent.

/6/ Application № 2017 128 269 for a patent on 07.08.2017.

LASER SYNTHESIS OF COLLOIDAL NANOPARTICLES FOR LASER ABLATION PROPULSING THRUSTER

M.I. Nedelko, V.V. Kiris, A.N. Chumakov, N.N. Tarasenka,
A.A. Nevar, N.V.Tarasenko

B.I. Stepanov Institute of Physics of National Academy of Sciences of Belarus , 68 Nezalezhnasti Ave., 220072 Minsk, Belarus

Abstract

A method is proposed for the production of colloidal carbon nanoparticles in vacuum oil for the use as a liquid working medium of laser micromotors. Colloidal nanoparticles were synthesized by laser sputtering of a graphite target above the surface of the oil under reduced-pressure helium atmosphere.

Introduction

To control small space satellites, micromotors are required that can ensure stable operation at low thrust levels. This can be provided by a micromotor based on the evaporation of a solid or liquid working medium by laser radiation in a pulse-periodic mode /1/. Liquid working medium must have set of physicochemical characteristics: low saturated vapor density, high absorption coefficient at the laser generation wavelength, high wettability coefficient, chemical inertness, stability to degradation of the local optical density, and some others. A number of known substances, for example, vacuum oils, ionic liquids are suitable for several parameters to solve this problem, but low values of their optical density will not provide the necessary parameters of laser micromotors. One way to increase the absorption coefficient of the above substances is to add to them certain additives that enhance the absorption of radiation.

1. Experimental

The experimental setup (Fig. 1) for the synthesis of liquid working medium of laser micromotors consists of a 1 – solid LS-2137U laser with second and third harmonics; 2 – the radiation converter into the fourth and fifth harmonics; 3 – focusing lens; 4 – the vacuum chamber; 5 – cuvette with liquid (oils, ionic liquids, etc.); 6 – target; 7 – gas pumping and inleting systems; 8 – manometer.

The design of the device ensures the movement of the target in three mutually perpendicular directions to focus the laser beam on its surface. The converter of laser radiation to the fourth and fifth harmonics is designed to shift the radiation frequency to the ultraviolet region, in which the light absorption coefficient increases for the of most materials, that enhances the synthesis efficiency.

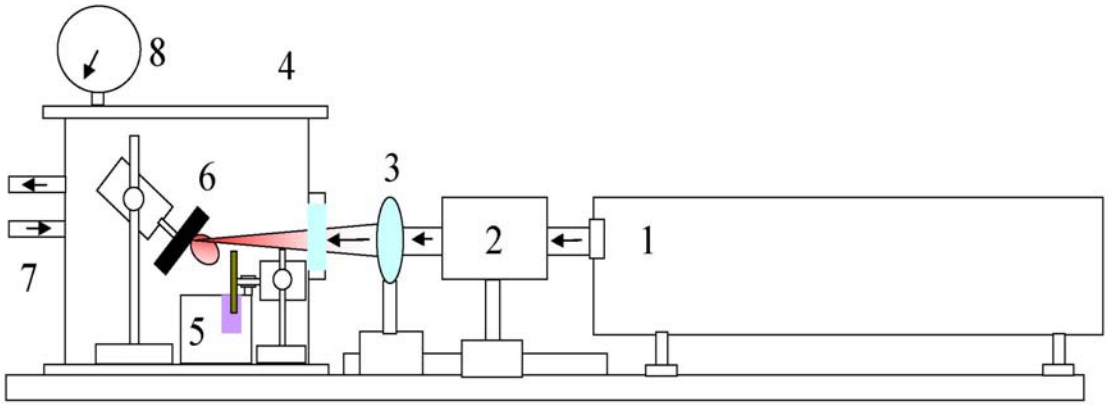

Fig. 1 – Experimental setup for the synthesis of colloidal nanoparticles: 1 –LS-2137U laser with second and third harmonics; 2 – the radiation converter into the fourth and fifth harmonics; 3 – focusing lens; 4 – the vacuum chamber; 5 – cuvette with liquid (oils, ionic liquids, etc.); 6 – target; 7 – gas pumping and inleting systems; 8 – manometer

The target was placed above the surface of the liquid to which the laser radiation was directed. To eliminate the influence of the atmosphere on the formation of nanoparticles, the target and the vessel with the liquid were placed in a vacuum chamber. The vacuum chamber was connected to a pumping system. A manometer was used to control the gas pressure. Helium of high purity was fed into the chamber from the gas cylinder with a reducer through a flexible hose and a vacuum valve. A sealed current lead was provided to supply two micromotors with a reducer, designed to rotate the target and mix the liquid. The vacuum chamber was evacuated by a fore-vacuum pump to a pressure of 0.05 Torr and was filled with helium to a pressure of 50 - 100 Torr. The laser radiation was directed to a graphite target through the lens and the window of the vacuum chamber at the angle of 45° to its surface. The erosion plasma flows propagated perpendicular to the target plane and were directed to the moving substrate covered with an oil film. Rotation of the moving platform provided the renewal of the oil film to prevent agglomeration of the carbon nanoparticles and mixing them in the cuvette. Preliminary experiments were conducted to select the optimal distance between the target surface and the movable substrate. The distance should provide a possibility to easily scan the beam along the surfaces. On the other hand, removal of the cuvette from the sputtered target led to a sharp drop in the efficiency of nanoparticles collecting, the concentration of which was monitored by measuring the optical density of the solution. Based on the results of the experiments, the optimal distance between the surface of the target and the movable substrate was estimated to be 12 mm so in all the following experiments the cuvette and the target were fixed at this distance.

2. Results and Discussion

The interaction of pulsed laser radiation with a solid target leads to the plasma formation with rapidly changing parameters above the target surface. The duration of the radiating stage of laser-induced plasma is small (several milliseconds). Some of the condensation products are deposited on the surface of the liquid, forming nanosized particles whose parameters are ultimately determined by the thermodynamic state of the decaying plasma (its temperature, density of atoms and ions). The nature of the processes of nanoparticles nucleation and growth depends on the component composition of the laser plasma. One way to control the size of the formed nanoparticles is to vary the energy density of the laser radiation and its wavelength. The size of the luminous zone of the erosion plume is strongly dependent on the radiation power density at the target, the pressure of the inert gas, and the surface relief of the target. In the chosen mode of the target ablation by the fourth harmonic of the Nd:YAG laser with the pulse energy of 15 mJ, repetition of 10 Hz and exposure time of 30 min, it was found that the size of the glowing zone of the plume in the longitudinal direction was approximately equal to 4 mm. The colloidal carbon nanoparticles were prepared in vacuum oil BM-1c.

Using the Cary-500 spectrophotometer, the optical density of the resulting colloidal nanoparticles in a 1-mm-thick cuvette was measured. Graphs of the optical density dependence on the wavelength are shown in Fig. 2.

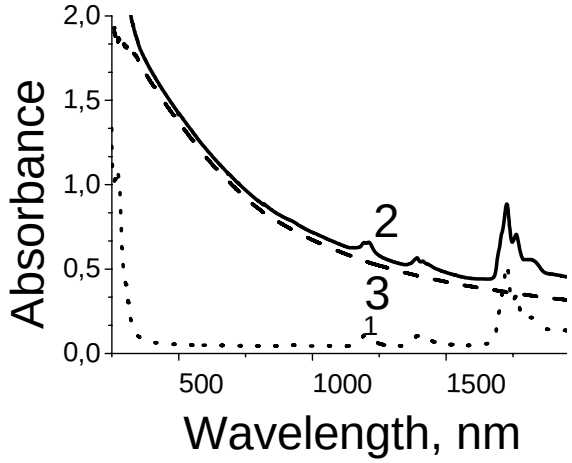

Fig. 2 – Absorption spectra of: 1) BM-1c vacuum oil; 2) carbon nanoparticles in vacuum oil 3) difference spectrum

Absorption of carbon nanoparticles can be substantially enhanced by their surface modification via introducing the functional groups having characteristic absorption bands at the wavelength of the ablation laser. At the generation wavelength of the erbium laser (1.5 μm), OH, R-H and R-NH_2 radicals have

suitable absorption bands. Fig. 3 shows the absorption spectra of the suspension of carbon nanoparticles in vacuum oil obtained by adding ethylenediamine to the resulting solution at various concentrations. The initial concentration of carbon nanoparticles in the solution was reduced to prevent the absorption saturation. It is established that an the dependence of the optical density of suspensions on the operating time is linear, and the particle production rate is 5 times higher for laser ablation at 266 nm compared to the ablation at 1064 nm under comparable conditions. It is shown that in order to avoid agglomeration of nanoparticles in the course of their formation in the gaseous phase with the deposition of the working substance onto the substrate surface (vacuum oils, ionic liquids) the stirring of the used liquid is necessary.

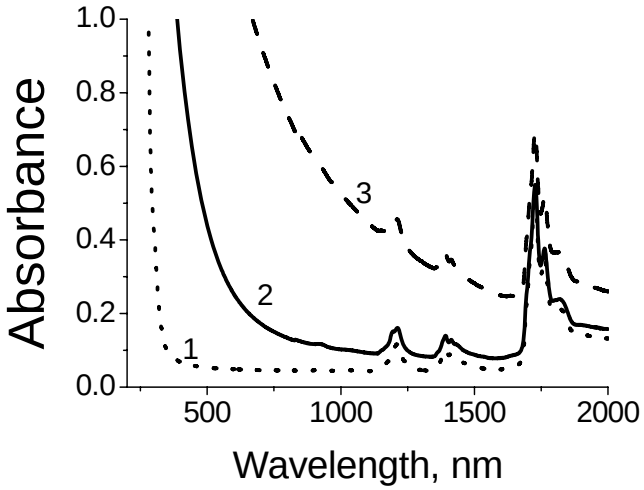

Fig. 3 – Absorption spectra of 1) BM-1c vacuum oil; 2) vacuum oil with colloidal carbon nanoparticles; 3) vacuum oil with colloidal carbon nanoparticles treated in ethylenediamine

Conclusion

The operating range of the parameters of the experimental setup for the synthesis of the colloids by laser ablation in a gaseous medium are determined. Dependences of the colloid optical density at the laser wavelength, time of particle production, spatial positioning of the target and the vessel with the liquid were studied. It is established that the method of laser sputtering of carbon in a gas and its deposition on the surface of a vacuum oil allows the formation of nanoparticles suitable for use as an working liquid for laser micromotors.

References

1. F.N. Lyubchenko, A.V. Fedenev, N.A. Bosak, A.N. Chumakov [et al.] // Cosmonautics and rocket science. - 2009. - No. 3 (56), p. 62-74.

COMBINED LIBS-SPARK DISCHARGE TECHNIQUE FOR ANALYSIS CARBON IN STEEL

V. Kiris, R. Pakhomenko, N. Tarasenko.

Institute of Physics, National Academy of Sciences of Belarus,
68 Nezavisimosti Ave, 220072 Minsk, Belarus, tarasenko@ifanbel.bas-net.by

Laser-induced breakdown spectroscopy (LIBS) has been a powerful and useful element analysis technique [1]. This method is based on using a focused high power laser to induce plasmas on the target surface. The spectral analysis of the emission lines from the luminous plasma provides the elemental compositions of the target. Main advantages of LIBS for elemental analysis is the possibility to perform rapid almost non destructive multielemental analysis without significant requirements for sample preparation. But the low sensitivity of the analysis hinders the wide dissemination of the LIBS, especially in the analysis of nonmetallic elements with relatively high excitation energies, such as carbon.

Many methods have been developed to improve the sensitivity of LIBS, such as, laser dual pulses [2], combination of LIBS with laser induced fluorescence [3], confinement with magnetic field [4], microwave re-excitation [5]. However, such approaches involve complicated technical design and are associated with increased cost of the equipment and the measurements. Spark discharge (SD) has been proved to be an effective and simple way to enhance the signal of LIBS [6,7].

In this work we investigated the possibility of using LIBS-SD combination for the analysis of carbon in steel under air atmosphere. Resonance lines in the vacuum UV spectral region are ruled out for detection and monitoring of the carbon content in analysis specimens, the spectral line in the near IR range C I 909.48 nm is the best possible choice because of low intensity and interference with other lines of this element from the rich spectrum of iron, which is main component of steel. The indicated carbon line actually has the highest transition probability compared to the other spectral lines in the visible and near IR spectral regions and has a relatively low excitation energy.

Fig. 1 shows a scheme of the experimental setup. For ablation of the analyte sample material, we used the YAG:Nd laser (Model LS 2134U, Lotis TII). The parameters of the fundamental harmonic of the laser output were: wavelength 1064 nm; pulse energy 100 mJ; laser pulse duration 7–8 nsec divergence ≤0.8 mrad. The laser emission was sharply focused by a short-focus lens (50 mm) onto the surface of the target under the angle - 45º. Cone-shaped (cone angle 30º) tungsten wire electrode of 5 mm diameter was set at a distance of 1.5 mm from the sample surface. The laser ablation plume seals in the electric

circuit containing 20 μF impulse capacitor charged to 400 V and 5 mkH inductor.

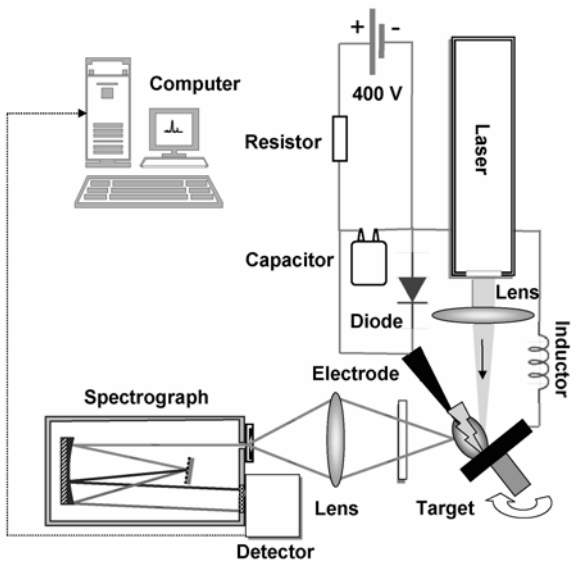

Fig. 1 – Scheme of experimental setup

The spark discharge was triggered by laser ablated plasma. To prevent capacitor recharging and oscillating discharge as would occur normally in that circuit, a high current diode is included across the capacitor. The steel samples are used as a cathode in a direct current discharge. This unipolar discharge provides the more efficient erosion of the analyzed material and reduces the destruction of the electrode. The discharge pulse current and voltage in the discharge gap was recorded by a digital oscilloscope using a low-resistance shunt and a 1:870 voltage divider. The oscillograms of the current and voltage in the discharge gap are shown in Fig. 2.

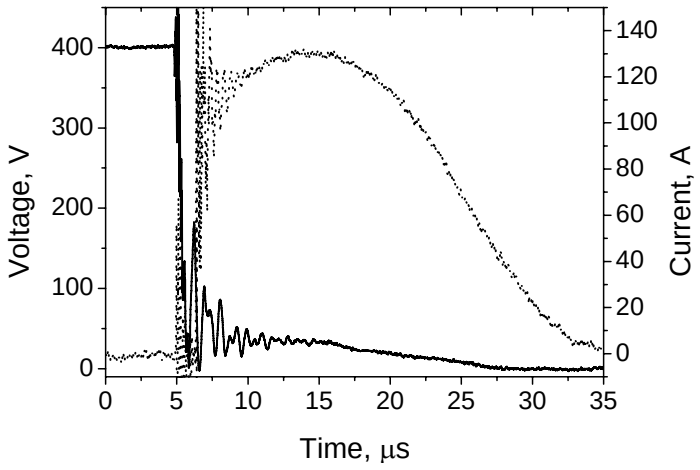

Fig. 2 – Time dependence of the discharge current (dotted) and voltage (solid)

The emitting plasma volume near sample surface has been 1:1 imaged by a lens (F=61mm) on the entrance slit of a grating (600 lines/mm) compact spectrometer having an aperture of 1:4.9 and a focal distance of 380 mm. A CCD array of 2048 pixels has been used to record the emission spectra.

The combined LIBS-SD regime with two tungsten electrodes set at a distance from the sample surface was previously investigated by us for the analysis of nonconducting materials such as soil and cement [6,7]. We have demonstrated that in this mode the electric discharge does not evaporate the analyzed material, but only excites the material evaporated by the laser pulse, the main reason of the increase in the intensity of line emission in the SD-LIBS mode as compared with conventional single-pulse LIBS is explained by the extended temporal evolution of the emission and the increase in the dimensions of the plasma volume. Thus, a significant increase in analytical time (with CCD detectors) and in analytical volume is achievable.

Since the steel is a conductive material, it is possible to connect the sample to be analyzed as a cathode in order to obtain additional ablation of the sample material by the action of an electric discharge Fig. 3.

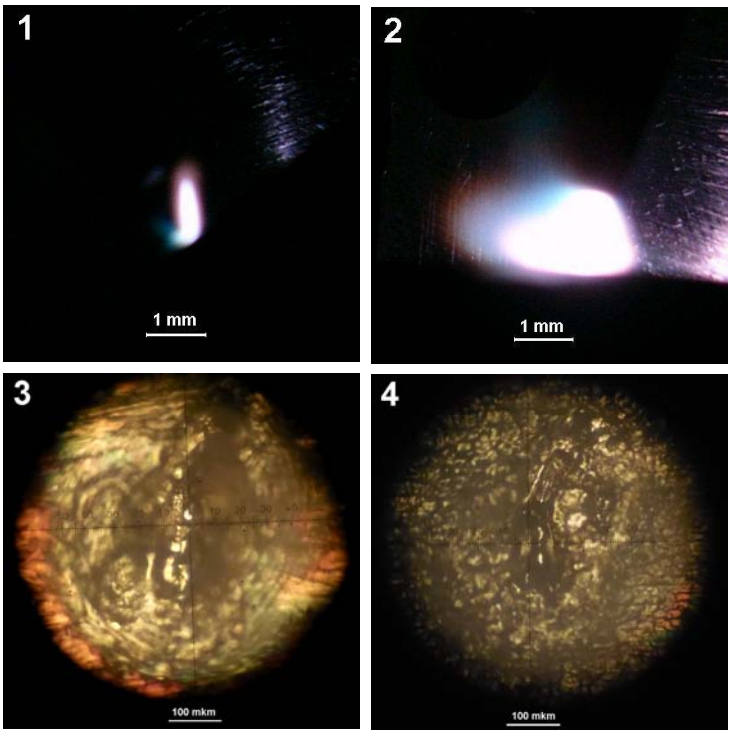

Fig.3 – Images of 1 - ablation plasma, 2 - the combined pulsed discharge-ablation plasma, 3 – ablation crater, 4 - combined pulsed discharge-ablation crater (250 pulses)

Figure 4 shows that when an electric discharge is applied, the carbon line C I 909.48 becomes available for measurement and in this case in a sample of steel

with a high carbon content, the line intensity is much higher. Thus, it can be concluded that at carbon concentrations characteristic for steels, the main contribution to the total intensity of the CI lines 909.48, Fe II 909.51, in the combined LIBS-SD regime, is provided by the carbon line.

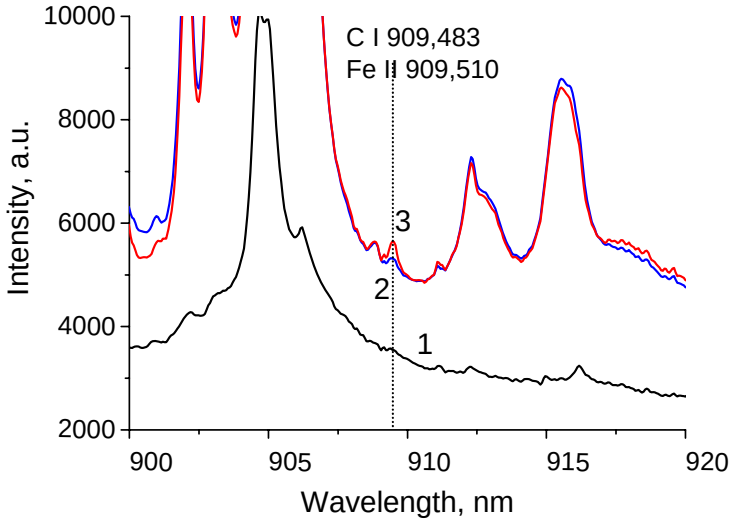

Fig. 4 – Spectrum of 1 - high carbon (1.2 %) steel in laser breakdown, 2 - low carbon (0.15 %) and 3 – high carbon steel in combined breakdown

Thus we have demonstrated a significant enhancement of spectral lines intensity of laser plasma with a electrical spark discharge. This enhanced plasma emission thereby will be helpful to improve the sensitivity of LIBS technique.

Acknowledgements. This work was supported by the by the National Academy of Sciences of Belarus under project «Convergence 2.4.06»

References

1. **Amy J. Ray Bauer and Steven G. Buckley** Applied Spectroscopy, 71 (2017) 553–566.
2. **Babushok, V. I. et.al.** Spectrochim. Acta B Atom.Spectros., 61 (2006) 999-1014.
3. **Jiaming Li et.al.** Analytical Chemistry, 89 (2017) 8134–8139.
4. **Hussain, A. et.al.** Plasma Sci.Technol., 17 (2015) 693-698.
5. **Liu, Y., Baudelet, M., Richardson M.** J.Anal. At. Spectrom., 25 (2010) 1316-1323.
6. **V. S. Burakov, V. V. Kiris, S. N. Raikov** Journal of Applied Spectroscopy, 74 (2007) 321-327.
7. **M. V. Bel'kov et.al.** Journal of Applied Spectroscopy, 75 (2008) 275-282.

THE IMPACT OF AN AIR PLASMA JET ON ISOLATES FROM HUMAN HABITAT OBJECTS

A.V. Kazak[1], O.A. Emeliyanova[2], L.V. Simonchik[1] and N.V. Dudchick[2]

[1] Institute of Physics of NAS of Belarus, 220072, Nezalezhnasci ave. 68-2, Minsk, Belarus, a.pavlova@ifanbel.bas-net.by
[2] Republican unitary enterprise «Scientific Practical Centre of Hygiene», 220072, Akademichnaya 8, Minsk, Belarus, lee616@yandex.by

To date, various sources of nonequilibrium plasma of atmospheric pressure have been developed, promising for biomedical applications /1/. The main field of plasma medicine is the direct application of cold atmospheric plasma on/or in the human body for therapeutic purposes. /1/ Among them, a special place is occupied by plasma jets, which allow processing objects of various shapes and sizes outside the closed discharge volume. The greatest bactericidal effectiveness is possessed by plasma jets that are formed in a discharge in the air environment /2/. In this article, we present the experimental results for inactivation of microbiota of medical institutions microorganisms by air plasma jet.

1. Experimental setup

The cold plasma jet (Fig. 1) is formed by direct current glow discharge /4/ in air at atmospheric pressure. The discharge chamber is composed of cylindrical 8 mm quartz tube inside of which a rod copper cathode of 6 mm in diameter is coaxially disposed. Flat copper anode (4 mm in thickness) with a central hole (1.5 mm in diameter) is located at the tube tip. Interelectrode gap is fixed at 0.7 mm. Discharge is maintained by DC or ripple current power supply with an output voltage up to 3 kV. A ballast resistor can be varied in the range of 1–300 kΩ. Air flow of 5 l/min into discharge chamber is provided through symmetrically arranged holes in cathode. Plasma generated in the discharge is blown out with the gas through anode hole into surrounding air. As a result, a glow of plasma jet of 2-3 mm in diameter and several centimeters in length is observed /5/.

Fig.1 – Photo of chamber and atmospheric pressure plasma jet in air

Determination of the concentration of long-living chemically active species in the plasma jet is performed by IR absorption spectroscopy. In the absorption spectra of air jet, NO, NO_2, $HNO_2$and N_2O bands are observed. Molar

fractions of these active species at the zone of the jet impact on the bacteria are 40 ppm, 20 ppm, 10 ppm and 2 ppm, correspondingly.

The suspension of microorganisms with an initial concentration of 10^6•CFU/ml is deposited uniformly onto the surface of a dense undifferentiated nutrient medium at the inactivation of bacteria in Petri dishes. Temperature of the plasma jet in the bacteria exposure zone did not exceed 30°C. The effect of the plasma jet was evaluated by inhibition zones on Petri dishes and in the concentrations of surviving microorganisms determined by colony counting method. The identity of bacteria growth on untreated and pretreated agar plates by plasma jet allows us to state that inactivation occurs due plasma impact on the cells and not due to changes in nutrient medium properties.

2. TREATMENT ISOLATES FROM HUMAN HABITAT OBJECTS

Clinically significant microbiota of medical institutions includes strains that have been isolated from the human habitat objects (for example, from food or personal care cosmetics) and strains that have been isolated directly from the sick person (for example, from the mucous membrane).

In that paragraph the efficiency of plasma exposure is estimated on strains of the planktonic microorganisms that have been isolated from the human habitat objects: gram-positive *Staphylococcus aureus*, *Bacillus subtilis*, gram-negative *Escherichia coli*, *Pseudomonas aeruginosa*, *Proteus mirabilis*, *Klebsiella pneumonia*, *Salmonella enterica*, spore *Candida albicans*.

The characteristic D-times of inactivation for all cultures were different. Monocultures of *S. aureus, P. aeruginosa, B. subtilis, Kl. pneumonia* had approximately equal inhibition zones (after 10 minutes of exposure this zone is about 50% of the total area of the Petri dish) with characteristic D-times of about 1.5 minutes. At the same time, D-times for *C. albicans, Pr. Mirabilis* and *E. coli*, were from 2.5 min with inhibition zones of 15-25%. The *Salmonella's* strain exhibited the greatest resistance with D-time more than 5 minutes with an inhibition zone of about 5%.

3. TREATMENT OF MEDICAL INSTITUTIONS MICROBIOTA

In addition to isolates taken from human habitats, we also used isolates taken directly from the mucous membrane of people who are chronically ill with pneumonia and bronchitis. These strains are highly aggressive and resistant to antibiotics. As samples were used isolates stains of *Enterobacter cloacae*, *Escherichia coli*, *Klebsiella oxytoca*, *Klebsiella pneumoniae*.

Samples were prepared in a similar manner (see section 1) and the efficiency of the plasma treatment was evaluated from the inhibition zones on Petri dishes.

Fig. 2 shows photos of the treated and untreated Petri dishes with the isolated strains. Petri dishes are treated for 10 minutes.

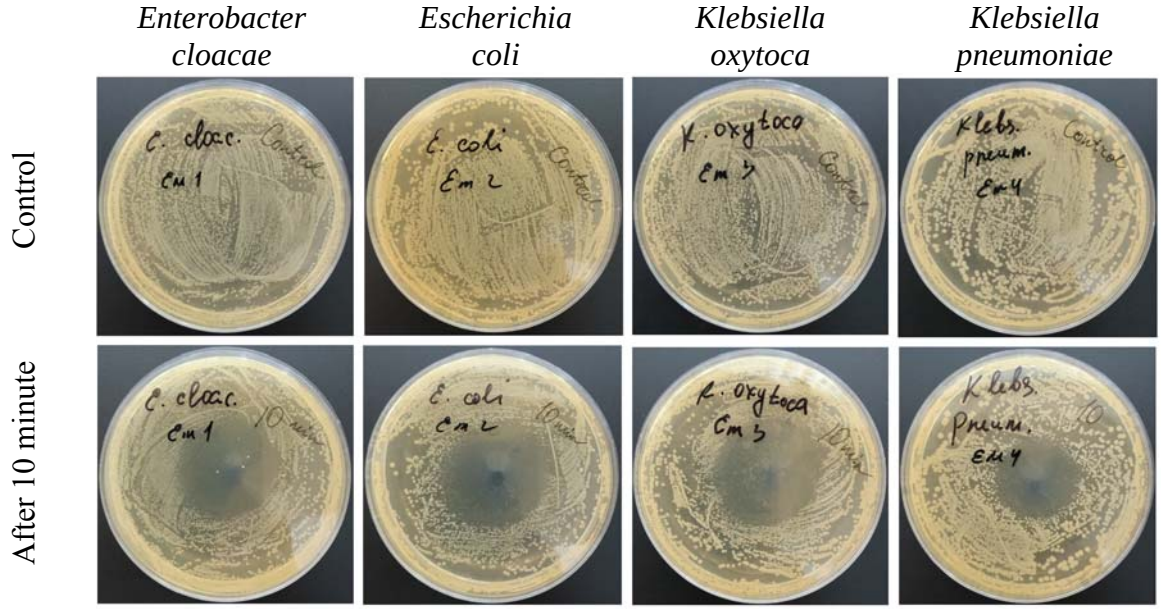

Fig. 2 – Photos of treated (down) and untreated (up) Petri dishes with monocultures of different isolates from sick people

These strains are more resistant to plasma effects, in contrast to the strains discussed above, but they also are demonstrated an inactivation effect. The appearance of an inhibition zones for all the strains examined is observed, which occupy from 12 % (*Klebsiella's stain*) to 27% (*Escherichia's stain*) of the total area of Petri dishes after 10 minutes of plasma treatment.

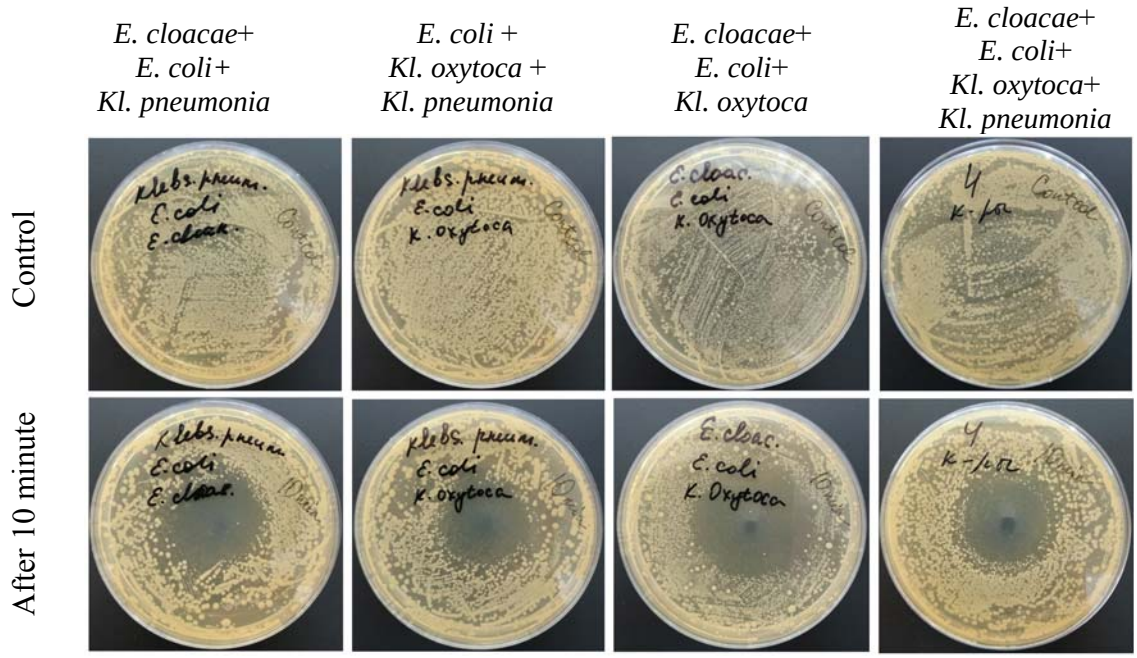

Fig. 3 – Photos of treated (down) and untreated (up) Petri dishes with consortiums from sick people

Usually these strains coexist among themselves in the organism in the form of consortiums and/or biofilms (concentration of microorganisms is more than 10^8 CFU/ml /5/), which makes them more resistant to various irritants and more dangerous for the human organism. Therefore, from the strains examined above, 4 different microorganisms consortiums were composed: *E. cloacae*+*E. coli*+ *Kl. pneumonia, E. coli* + *Kl. oxytoca* +*Kl. pneumonia, E. cloacae*+ *E. coli*+ *Kl. oxytoca*, *E. cloacae*+ *E. coli*+ *Kl. oxytoca*+ *Kl. pneumonia* (Figure 3). These compositions are found in people with chronic diseases. The total initial concentrations of microorganisms in Petri dishes are 10^6•CFU/ml. As in the cases discussed above, the Petri dishes were processed for 10 minutes. After 10 minutes, inhibition zones were formed on the treated Petri dishes.

The sizes of the formed inhibition zones were for the consortium *E. cloacae*+ *E. coli*+ *Kl. pneumonia* – 15%, for the consortium of *E. coli* + *Kl. oxytoca* +*Kl. pneumonia* – 10%, for the consortium *E. cloacae*+ *E. coli*+ *Kl. oxytoca* – 19% and the consortium *E. cloacae*+ *E. coli*+ *Kl. oxytoca*+ *Kl. pneumonia* – 8% of the total area of the Petri dish. From the obtained results, it can be concluded that the composition of the consortium has a significant effect on the stability of the consortium to the plasma effect.

Thus, it can be concluded that the air plasma jet under development is well suited for treatment a wide range of microorganisms, including active clinical epidemically significant microbiota of medical institutions.

Acknowledgements

This work was supported by the Belarusian Republican Foundation for Fundamental Research (grant No. F18SRBG-001).

REFERENCES

1. **Weltmann K.-D., Metelmann H.-R., Woedtke Th.** Europhysics News, 47(2016) 39–42.
2. **Lu X., Naidis G.V., Laroussi M., Reuter S., Graves D.B., Ostrikov K.,** Physics Reports , 630 (2016) 1–84
3. **Kirillov A.A., Paulava A.V., Safronau Y.A., Simonchik L.V., Dudchik N.V.** Prikladnaya fizika /Plasma Physics Reports/ 5(2013) 52-55.
4. **Kazak A.V., Kirillov A.A., Simonchik L.V., Nezhvinskaya O.E., Dudchik N.V.** Plasma medicine. 7 (2) (2017) 109 – 115.
5. **Olson M.E., Ceri H., Morck D.W., Buret A.G., and Read R.R.**. Can. J Vet. Res.; 66(2) (2002) 86–92.

APPLICATION OF SiO_2 NANO LIGUID GLASS ON PLASMA CLEANED SURFACES

O. Dogan

Necmettin Erbakan University, A.K. Education Faculty, Department of Physics, 42090, Konya, Turkey , E-mail: odogan@konya.edu.tr

Abstract:

Wetting state of a surface is characterized by the contact angle (CA). A surface with water contact angle greater than 90^o is usually referred to as hydrophobic, and one with water CA higher than 150^o is qualified as superhydrophobic. Plasma technology is used in the modification of surfaces. Plasma cleaned surfaces have hydrophobic properties under suitible conditions.

In this study, hydrophobicity value of SiO2 nano liquid glass was investigated on coated some surfaces cleaned with plasma technique and normal surfaces. SiO2 nano liquid glass solution was producted with sol-gel method in a special reactor. Nano liquid glass SiO_2 solutions produced by silicon-based nano powder is coated on the two kind of glass surface by using spray method. Surfaces were coated at the room temperature in air with the different spray nozzles. Surface of the firsth glass is cleaned with plazma technique and other glass is not cleaned. Contact angle on the surface was measured by using with Drop Shape Analysis System contact angle meter. Scanning Electron Microscope (SEM) was used for investigating microstructure of the coated surfaces. Roughness of surfaces was investigated using Atomic Force Microscopy (AFM).

The deposition of nanoparticles and their clusters onto the substrates provide high roughness, which is essential for hydrophobic properties. Contact angle measurements of the plasma cleaned surfaces were obtained 139-144^{o}and 122-127^o.

Key words: Plasma cleaning, SiO2 nano liquid glass, hydrophobic materials.

I. Introduction:

The maintenance and improvement of current properties and the creation of new material properties are the most important reasons for the functionalisation of textiles. The coating of textiles with chemically or physically modified silica sols with particle diameters smaller than 50 nm (“nanosols”) enables the manifold alteration of their physico-mechanical, optical, electrical and biological properties.

In present, preparation techniques of water repellent fabrics have several methods such as coating with paraffin wax, treating fiber surface with pyridinium compounds, silicone resin or fluorocarbon. The fluorochemicals are at present the most favorable due to their excellence with respect to water repellency /1,2/. Typically, the water contact angles between 120° and 130° are obtainable with

treatment using the fluorochemicals. Surface hydrophobicity modification using sol–gel method has been introduced as an alternative approach /3,4/. Particular interest was focused on the self organization of organosilane molecules which creates ordered hybrid materials with hydrophobic properties. The hybrid inorganic–organic nanocomposite coatings were produced using sol–gel reactions via hydrolysis and polycondensation of hexadecyltrimethoxysilane (HDTMS), tetraethoxyor-thosilicate (TEOS), and 3-glycidyloxypropyl-trimethoxysilane (GPTMS) mixture. It was reported that the water contact angle of 141° was achieved. The state of superhydrophobicity defined by the water contact angle above 140° was contributable to two main factors; (a) change in the surface geometry from smooth surface to rough surface and (b) hydrophobic properties of roughness surface /5/.

Wettability of surfaces with liquids is an important property of materials that is controlled by the chemical composition and the geometry of the surface/6/. Superhydrophobic surfaces that have a water contact angle □90° are attractive because of their importance in industrial applications/7/. Because of the minimized contact with water, chemical reactions or bond formation through water are limited for a superhydrophobic surface. Thus, various phenomena are expected to be inhibited on such a surface, for example, snow sticking, contamination, disease transmission, and current conduction. Recently, with the increasing demands toward functionality of materials that cannot withstand high temperatures, such as textiles and plastics, the control of surface wettability via low-temperature processing is particularly significant. Surface modification with hydrophobic properties using the sol–gel method has been investigated during recent years/8/. Although simple sol–gel reactions usually result in the formation of amorphous materials, self-organization of organosilane molecules offers an opportunity to create ordered hybrid materials with hydrophobic properties/9/. Previous studies have been focused on the use of fluoroalkyltrimethoxysilanes to control thechemical properties of surfaces, and the largest contact angle obtained for water has been 115°/10/. However, fluoroalkyl compounds have several economical and ecological disadvantages, such as high cost and potential risk for human health in case of skin contact and for the environment in case of emission of fluorine compounds during and after the coating process /11/.

Hence, some producers have stopped their production of water-repellent fluorine-containing compositions during the past few years. In addition to the environmental hazards associated with their production and application, a high-temperature process is usually required for their production. Therefore, the formation of nonfluorinated superhydrophobic surfaces at low temperatures is important for the fabrication of environmentally friendly coatings on substrates with low heat resistance. Transparency and durability of surface coatings are particular requirements for textiles. The durability of water-repellent coatings after washing, especially for those produced on cotton, remains a challenge, because a posttreatment is usually required to restore the hydrophobic properties /12/.

II. Experimental:

We prepared two glass samples. One of them is cleaned with plasma (OptoSense).OPT-PCO-2 plasma cleaning machine is single way gas input type. It's technical parameters are 1000W RF source power, 100 KHZ RF frequency, 0.3-1.0 MPa vacuum degree and 60-600 ml/min gas flow. The other sample is cleaned with acidic chemicals. All samples were coated layer by layer with spray methods at the room temperature in air. Different spray nozzles having of 1.4, 1, 0.8 mm used, keeping the spray gun at a working distance of 20 cm from the glass surfaces and fewer than 3.5 bar spray pressure. Coated samples were allowed to dry for 4hours, 12hours and 24hours various periods () at 50 ^{o}C in furnace.

Contact angles were measured with a deionized water droplet of 5 μL on instrument at room temperature. All the contact angles and roll-off angles were determined by averaging values measured at 4–5 different points on each sample surface. Roughness of surfaces was investigated using Atomic Force Microscopy (Park System-100).

The surface morphology of the treated samples was studied using a SU-1510 Hitachi Scanning Electron Microscope was used to perform elemental analysis. All samples fixed to conductive adhesive tapes and gold-metallized.

III. Results and Discussion:

Surfaces wettability were examined by contact angle measurements. The contact angle pictures are seen in Fig.1. There are seen the contact angle picturesfor plasma cleaned sample after the SiO_2 coating in Fig. 1(a) and with acidic cleaned sample after the SiO_2 coating in Fig. 1(b). The water static contact angles for the hydrophobized and plasma cleaned samples range from 139° to 144° for a 5 μL droplet, being completely water nonwettable whereas the contact angle for original cotton is 0°, because water drops spread instantly when placed on the surface of the substrate. And for the hydrophobized and acidic cleaned samples range is from 122° to 127° for a 5 μL droplet, being completely water nonwettable whereas the contact angle for original cotton is 0°, because water drops spread instantly when placed on the surface of the substrate. For a 50 μL water droplet, the roll-off angle ranges from 5° to 11° for samples.

When a water droplet sits on a hydrophobic glass surfaces, the wetting behavior can be described by the equation from Cassie and Baxter /13/ :

$$cos\theta_{CB}=f_{ls}cos\theta_0-f_{lv} \qquad (1)$$

where θ_{CB} is the observed water contact angle on a rough, porous surface, θ_0 is the intrinsic water contact angle on the corresponding smooth surface, f_{ls} is the liquid/solid contact area divided by the projected area, and f_{lv} is the liquid/vapor contact area divided by the projected area. Generally, water contact angle on smooth surfaces cannot exceed 120° through tailoring surface chemistry.

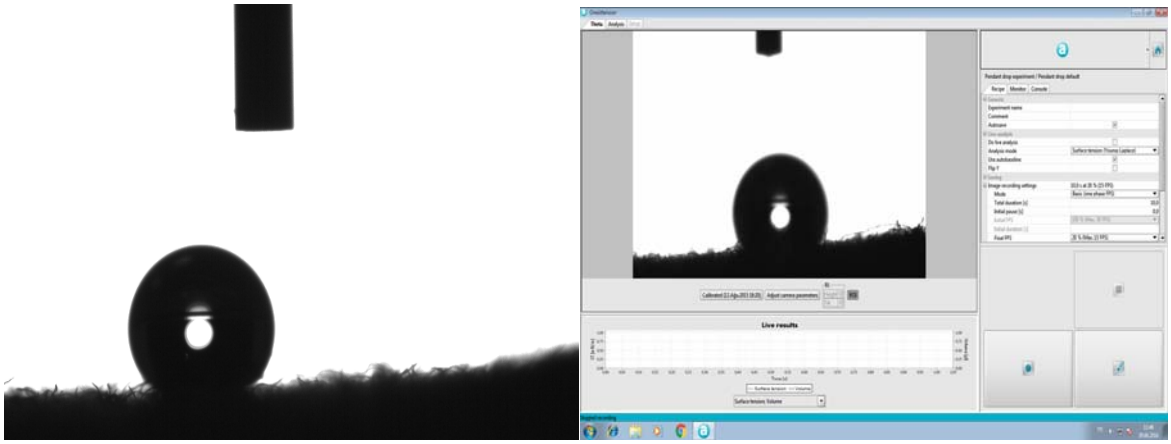

(a) (b)

Fig.1 – Contact angle images (a) Plasma cleaned sample after SiO_2 coating, (b) Acidic cleaned sample after SiO_2 coating

Roughness of surfaces was investigated using Atomic Force Microscopy (AFM). There are seen two AFM images for each samples in Fig.2. AFM image of roughness of the plasma cleaned surface is given in Fig. 2 (a) and for the other sample is given in Fig. 2(b).

SEM observations have been performed in order to assess the morphology of the surfaces after the spray treatments. When the surfaces are layer by layer sprayed, their surfaces appears covered, and the silica coating appeared rough and grainy on the surfaces as well evidenced. In general terms, it is possible to conclude that the plasma cleaned samples allows the formation of a more homogeneous and compact coating on the glass surfaces than acidic cleaned glass sample.

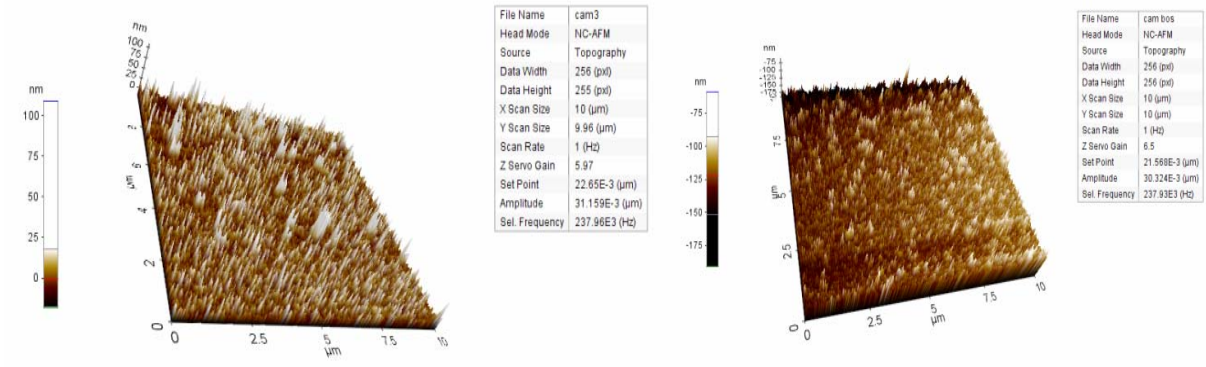

(a) (b)

Fig. 2 – AFM images for plasma cleaned sample(a) and acidic cleaned sample (b)

Conclusion:

In the present work, silica based coatings have been deposited on glass sufaces by layer by layer assembly. The effectiveness of layer by layer spray method and cleaning with plasma technique for homogeneously covering the glass surfaces has been assessed.

Acknowledgments:

This study was supported by the Necmettin Erbakan University Scientific Researh Project.

References

1 **Linemann R., Gorenberg A., Bar G., Cantow H.J., Mulhaupt R**. (1997) J Coating Technol 69(871):77–81

2 **Easter E.P., Ankenman B.E.** (2005) AATCC Rev 5(11):27–31

3 **Mahltig B., Bottcher H**. (2003) J Sol–Gel Sci Technol 27(1):43–52

4 **Yeh J.T., Chen C.L., Huang K.S.** (2007) J Appl Polym Sci 103(2):1140–1145

5 **Daoud W.A**, **Xin J.H, Tao X.M.** (2004) J Am Ceram Soc 87(9):1782–1784

6 **Adamson A. W**., "Contact Angle"; pp. 385–88 in Phys. Chem. of Surfaces, 5th Ed. Wiley, NY, 1990.

7 **Parker A. R.** and **Lawrence C. R.**, "Water Capture by a Desert Beetle," Nature, 414,33–34 (2001).

8 **Akamatsu Y., Makita K., Inaba H**., and **Minami T**., Thin Solid Films, 389 (1,2) 138–45 (2001).

9 **Shimojima A.** and **Kuroda K.**, Langmuir, 18 /4/ 1144–49 (2002).

10 **Yuasa A., Inaba H., Tadanaga K., Tatsumisago M.**, and **T. Minami**, Proc. Int. Congr. Glass, 17th, 4, 445–49 (1995).

11 **Wallington** T. J. and **Nielsen** O. J., "Handbook of Environmental Chemistry"; pp. 85–102. Springer, Berlin, Germany, 2002.

12 **Walid** A. **Daoud**, **John** H. **Xin**, and **Xiaoming Tao**, J. Am. Ceram. Soc., 87 (9) 1782–1784 (2004)

13 **Hoefnagels H.F., Wu D., de With G., Ming W**. Langmuir, 23 (2007), p. 13158

ABOUT MAGNETIZATION OF PARTICLES IN DUSTY PLASMA

V. Karasev, E. Dzlieva, S. Pavlov, L. Novikov, S. Tarasov

Saint Petersburg State University, 199034, Universitetskaya nab., 7/9, St. Petersburg, Russia,
e-mail: plasmadust@yandex.ru

Abstract. From a fundamental point of view, it is important to understand how the presence of a dust component can affect the properties of the plasma in magnetic field. By analogy with the effect on the operation of electrical probes, the presence of dust particles complicates the magnetization of the plasma components and affects dynamics of the particles.
The change in the characteristics of motion and diffusion of charged particles in a magnetic field occurs when critical values are reached by several parameters. When $\omega_e \tau_e = 1$, the electron circulates around the cyclotron circle of radius and is considered magnetized. Under typical conditions in experiments with a complex plasma, $\omega_e \tau_e = 1$ already in field of the order 10^{-2} T. The magnetization of ions depends on their type. For neon, the condition $\omega_e \tau_e = 1$ is satisfied in fields of the order $2 \cdot 10^{-1}$ T, and for helium of the order $5 \cdot 10^{-2}$ T.
The results of the studies of dust formations are presented with the magnetization of the plasma components in the lightest inert gases. For instance the experiment with helium is carried out in standard magnetic coils under reduced pressure to 0.1 Torr in the trap near the narrowing of the current channel. In preliminary observations, the conditions of magnetization are technically achieved.

The change in the characteristics of motion and diffusion of charged particles in a magnetic field occurs when several parameters reach critical values as the magnetic induction B increases. Consider an electron whose cyclotron radius r_{ce} is smaller than the characteristic size of the chamber (the radius of the discharge tube R). When $\omega_e \tau_e >> 1$, the electron makes a revolution or more along the cyclotron circle of radius $r_{ce} = m_e u_e / eB$ and is considered magnetized. Here ω_e is the cyclotron frequency, τ_e is the time between electron collisions, usually with the atoms of the discharge gas, m_e and u_e are the electron mass and velocity, e is the elementary charge. This magnetization condition depends on the ratio of the magnetic field and the gas pressure B/p. Under typical conditions of experiments with complex plasmas, we have $\omega_e \tau_e = 1$ already in a field of the order of 10^{-2} T. In the presence of a dust particle of radius a, the determination of the magnetization becomes more complicated. As is customary in the theory of an electric probe in a magnetic field /1-2/, for a significant change of the electron flow on the collecting surface of a probe (or a dust particle), the condition $r_{ce} = a$ is required. The magnetic field corresponding to this condition

$B = m_e u_e / ea$ does not depend on the pressure. For dust particles with a size of 10 μm, it is performed in fields of the order of 1 T.

The criterion for the magnetization of ions depends on their type. We give estimates for neon. The condition $\omega_i \tau_i = 1$ holds in fields of order $2 \cdot 10^{-1}$ T. We note that the condition $r_{ci}=R$ is satisfied at $B = 10^{-2}$ T. The total magnetization of the ion in the complex plasma is carried out under the condition $r_{ci} = a$ in the field $B = m_i u_i / ea$, here m_i and u_i are the ion mass and velocity. For dust particles with a size of a = 10 μm, it occurs in a magnetic field of the order of 10 T. In experiments this condition can be realized already today. In helium, an essentially smaller field B = 2.4 T is required for the magnetization of the ions.

In dusty plasma /3-6/, the magnetization criterion can hardly be performed under laboratory conditions. But their presence in a multicomponent plasma significantly changes the criteria for the magnetization of plasma particles, which is reflected in the dynamics of the dust subsystem when the key values $B = 10^{-2}$ and 1 T are attained by the magnetic field (at the appropriate gas and pressure), which are feasible in modern experiments.

In the experiments conducted, dust structures were created in dust traps in a glow discharge in a magnetic field at low gas pressures. Dust traps were used in the region of a high-voltage arc formed near a dielectric insert narrowing the discharge current channel /8/. For the lightest inert gas of helium, standard magnetic coils were used to create a magnetic field /7-8/. In this case, visual observations and videography were made with a large optical magnification. In the case of using neon, the magnetic field was created by a superconducting magnet placed in an extended cryostat. The scheme of the experiment was similar to the work /9-10/.

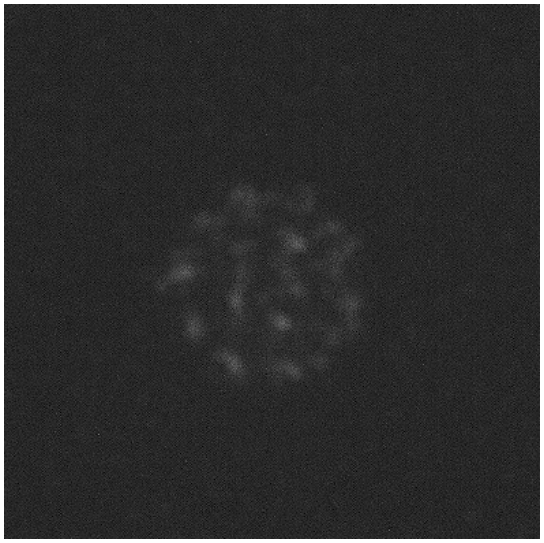

Fig. 1. The image of the horizontal section of the structure in the trap. Conditions: *He*, p = 0.1 Torr, i = 1.5 mA, particles MF, d = 1.1 μm. The value of the magnetic field corresponds to the magnetization of the ions. The horizontal image size is 3 mm.

Dust structures close to clusters in helium were created at a pressure $p = 0.1$ Torr in a magnetic field of 450 G, when the magnetization of helium ions is equal to 1. In the experiment, conditions were tested (selection of parameters) at which stable structures can be created. The particle arrangement and the particle distance were determined. An example of an image of a dust cluster under these conditions is given in Fig.1.

Dust structures in neon are obtained at a higher pressure $p = 0.4$ Torr in a magnetic field of about 1 T when the magnetization of the neon ion is close to 1. The same parameters were determined for helium as well as the speed of rotation of dust formation in a magnetic field. An example of an image of a dust cluster under these conditions is given in Fig.2.

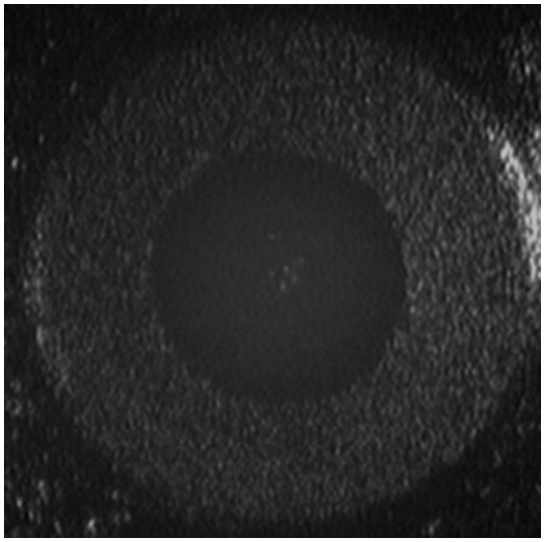

Fig. 2. The image of the horizontal section of the structure in the trap. Conditions: *Ne*, $p = 0.6$ Torr, i = 1.5 mA, quartz particles. The value of the magnetic field corresponds to the magnetization of the ions. The horizontal image size is 7 mm.

At present, these unique results are interpreted in accordance with the idea of dusty plasma in a magnetic field /13/.

Acknowledgements. Investigation of the magnetization in helium was supported by RFBR grant № 18-02-00113, the study of the magnetization in neon was supported by the RSF grant No. 18-12-00009.

References

1. **Chen F.F.** Electric probes. Plasma diagnostic techniques (New York: Academic Press) (1965).
2. **Chan P., Talbot L., Turian K.** Electrical Probes in Stationary and Flowing Plasmas, Theory and Application. (Springer-Verlag: Berlin, Heidelberg,

New York) (1975).
3. **Fortov V.E., Mofill G.E.** Complex and dusty plasmas: from laboratory to space. NewYork: Taylor & Francis Group (2010).
4. **Shukla P.K., Mamun A. A.** Introduction to Dusty Plasma Physics. Bristol: Institute of Physics Publishing (2002).
5. **Vladimirov S.V., Ostrikov K., and Samarian A.A.** Physics and Applications of Complex Plasmas (London: Imperial College Press) (2005).
6. **Tsytovich V.N., Morfill G.E., Vladimirov S.V., Thomas H.M.** Elementary Physics of complex plasmas (Berlin, NewYork: Springer) (2008).
7. **Dzlieva E.S., Karasev V.Y., Pavlov S.I.** Plasma Physics Reports 42 2 (2016) 147-154.
8. **Karasev V.Yu., Dzlieva E.S., Ivanov A.Yu. et al.** Phys. Rev. E 74 (2006) 066403.
9. **Vasiliev M.M., D'yachkov L.G., Antipov S.N., Huijink R., Petrov O.F., Fortov V.E.** Europhys. Lett. 93 (2011) 15001.
10. **Karasev V.Yu., Dzlieva E.S., Pavlov S.I., Novikov L.A., Maiorov S.A.** IEEE Transactions on Plasma Science 46 4 (2018) 727-730.
11. **Schwabe M., Konopka U., Morfill G.E. et al.** Phys. Rev. Lett. 106 (2011) 215004.
12. **E. Thomas Jr., Lynch B., Konopka U., Merlino R.L., and Rosenberg M.** Phys. Plasmas 22 (2015) 030701.
13. **Karasev V.Yu., Dzlieva E.S., and Pavlov S.I.** Laboratory dusty plasma in magnetic field (SPb: Svoyio izdatelstvo) (2016).

OBSERVATION OF THE ORDINARY WAVE ANOMALOUS ABSORPTION IN PLASMA FILAMENT

V.I. Arkhipenko[1], E.Z. Gusakov[2], L.V. Simonchik[1], M.S. Usachonak[1]

[1]Institute of Physics of NAS of Belarus, 68-2 Nezavisimosty Ave.,Minsk, Belarus
E-mail: m.usachonak@dragon.bas-net.by
[2]Ioffe Institute, 26 Politekhnicheskaya, St-Petersburg, Russia

1. Introduction

The electron cyclotron resonance heating (ECRH) systems launching powerful microwave beams into the plasma volume are widely utilized for the auxiliary heating and noninductive current drive in the current magnetic confinement experiments and will be used in ITER. However, during the last decade, different anomalous effects (anomalous backscattering, ion accelerating), that are reducing heating efficiency, were observed in the ECRH experiments at different toroidal devices [1-3], which had not been explained within the conventional paradigm based upon the linear wave propagation and absorption theory. For instance, theoretical model proposed recently [4] explains the anomalous backscattering as a result of the two upper-hybrid (UH) plasmons parametric decay (TUHPD) instability which has a very low threshold due to nonlinearly excited plasmons, which are trapped in the vicinity of the density maximum that accompanies the magnetic island. The theory [4] also predicts substantial (up to 25%) anomalous absorption due to this process. This makes important the detailed analysis of the parametric decay instabilities accompanying the O1-mode ECRH scenario, which is planned for utilization in ITER. The saturation regime of the low-power-threshold ordinary (O) wave parametric decay instability leading to the excitation of a localized upper hybrid (UH) wave and a low-hybrid wave was analyzed theoretically in [5]. In the present work the anomalous absorption of the O-wave in plasma filament is under investigation.

2. Experimental setup and results

Plasma filament was created in a glass tube with an internal diameter of 22 mm. The tube was passed through waveguide with cross-section 72×34 mm^2 perpendicular to the wide walls and located on the axis of electromagnet (2 on Fig. 1, *a*). The initial plasma was produced in argon (pressure of 1-2 Pa) under forcing of RF power (~100 W, frequency ~27 MHz). The RF power is supplied to the ring electrodes placed outside of the tube and disposed on both sides of the waveguide at a distance of about 30 cm. At the maximal RF power the averaged plasma density measured using the cavity diagnostics 6 (Fig. 1, *a*) is about 1.5×10^{10} cm^{-3}. It varies at the changing of the magnetic field from 0 to 45 mT by three times.

The O-mode microwave pulses (up to 200 W) were incident onto the plasma along the waveguide 3. Since the frequency of the launched waves f_0 = 2.35 GHz is much higher than the upper hybrid (UH) and electron cyclotron resonance (ECR) frequencies, it seems that there were no linear mechanisms of the wave-particle interaction. The temporal behavior of the transmitted and reflected microwave signal as well as the plasma luminosity is observed in the experiment. The radial distribution of integral plasma emission was registered with CCD-camera UC-14T32 and can be approximated by the function $(1 - (r/r_0)^2)^{1.6}$. Assuming the light intensity is proportional to the plasma density, the maximal density in the discharge is about 2.2×10^{10} cm^{-3}.

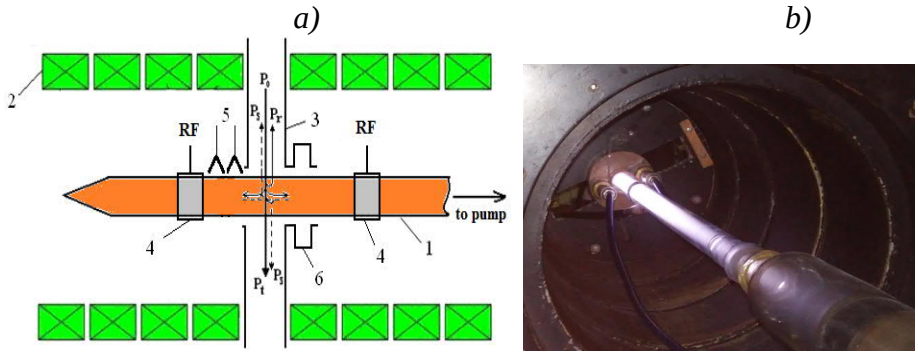

1 – quartz tube; 2 – magnetic system; 3 – waveguide; 4 – RF antenna; 5 – probing wave antenna; 6 – microwave cavity

Fig. 1. - Schematic of experimental setup (*a*) and photo of the plasma filament (*b*).

The observations of the microwave anomalous absorption are performed at the incident power of 160 W and magnetic field about 42 mT. Full microwave power balance is defined as following: $P_0 = P_t + P_r + P_h$, where P_0, P_t and P_r, are incident, transmitted and reflected powers, P_h is a power irradiated through holes in waveguide. According to experimental conditions the irradiation power was about several watts and we do not take it into account in subsequent experiments. It's seen (Fig. 2, *a*) that at the case when plasma is switched off, the microwave is mainly transmitted through waveguide, and envelopes for incident, transmitted and reflected pulses are sufficiently flat. After the plasma appearing the envelopes of reflected and transmitted pulses are sharply changed

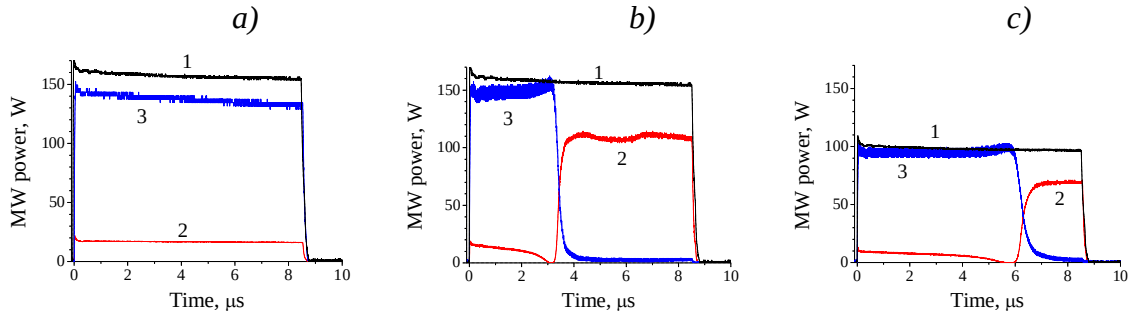

Fig. 2. - Waveforms of incident (1), reflected (2) and transmitted (3) pulses: *a* – without plasma and with plasma at different MW power levels 160 W (*b*) and 100 W (*c*).

(Fig. 2, *b*). The reduce of the incident wave power level leads to time delay increase of the pump power absorption appearing (Fig. 2, *c*).

The dependence of inverse time of the sharp microwave absorption appearing on the pump power level is presented in Figure 3. It is shown that the observed microwave absorption has threshold of about 30 W, that indicates the nonlinearity of the phenomenon. The time delay of the anomalous phenomenon appearance depends on the pump power, magnetic field and electron density of initial plasma similarly as in [6]. Increase of magnetic field or pressure leads to threshold decrease.

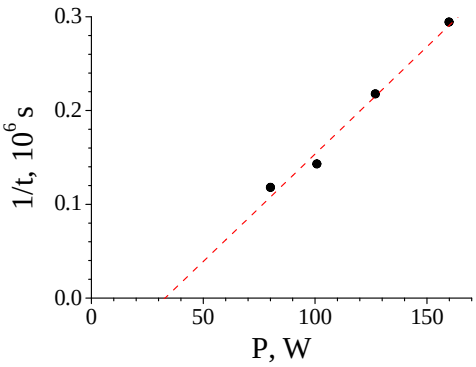

Fig. 3. - The dependence of inverse time of the microwave absorption appearing on the pump power level

In Figure 4, *a*, the plasma luminosity time dependence from the filament axis is presented. The absorption is accompanied by the sharp increase of the plasma luminosity. The plasma luminosity radial distribution was registered at different moments during the microwave pulse (Fig. 4, *b*). At the microwave pulse beginning a smooth increase of the plasma luminosity is observed (Fig. 4, *a*) and it is higher on right side of radial distribution, which is associated with collisional absorption in the plasma filament. At the moment of a sharp luminosity increase, the distribution becomes symmetric about the center of the plasma filament, which may be due to decay processes of O-wave. At the end of the microwave pulse, the distortion of the plasma luminosity is observed from right side on which microwaves incidents on plasma column.

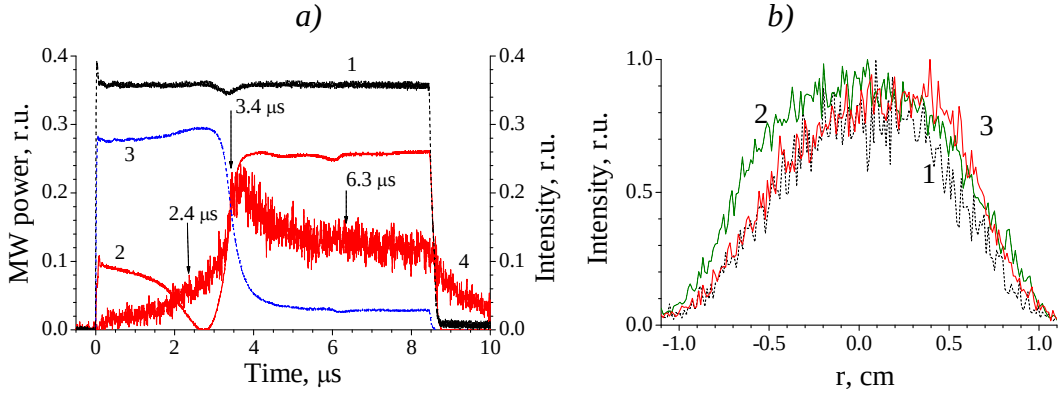

b) 1 – 2.4 μs; 2 – 3.4 μs; 3 – 6.3 μs

Fig. 4. - The envelopes of incident (1), transmitted (3), reflected (2) microwave pulses and the time dependence of the plasma luminosity from the filament axis (4) (*a*) and (*b*) the plasma luminosity radial distributions at different moments during the microwave pulse.

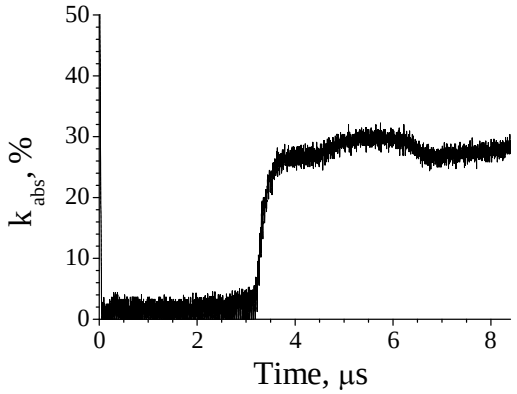

Fig. 5. - The time evaluation of the plasma absorption coefficient.

The efficiency of the microwave power absorption was determined at external magnetic field about 43 mT and averaged electron density in the filament about 1.5×10^{10} cm^{-3}. In the presence of the anomalous absorption of microwave waves, we must take into account the power absorbed by the plasma P_{abs} in the full power balance: $P_0 = P_t + P_r + P_h + P_{abs}$. Then an absorption coefficient k_{abs} can be expressed as $k_{abs} = 1 - (P_t + P_r + P_h)/P_0$. Absorption coefficient time dependence calculated using experimental data is shown in Figure 5. It is close to zero (small collisional absorption) from 0 to 3th microsecond, and reaches 30-35% at t > 3.5 th microsecond.

CONCLUSIONS

The anomalous absorption effect of O-wave in plasma filament was observed by means of optical and microwave diagnostics. It was shown that this effect has a threshold nature. The threshold of the absorption has been estimated experimentally at the level of incident power about 30 W. During the microwave pulse, the radial profile changing of plasma luminosity was demonstrated. The efficiency of the microwave power absorption was about 30-35%. The observed anomalous absorption effect of O-wave in plasma filament can be connected with parametric decay of O-mode pump wave in upper hybrid resonance and its further study is supposed.

Acknowledgements. The work was performed under support of the BRFBR under grant F18R-040 and RFBR under grant 18-52-00010 Bel_a.

References

[1] **E. Westerhof , et. al.**, Phys. Rev. Lett. 103, 125001 (2009).
[2] **A. N. Karpushov, S. Coda, and B. P. Duval**, in Proceedings of the 30th EPS Conference on Plasma Physics (2003), Vol. 27A(3), p. 123.
[3] **V. F. Andreev, et. al.**, Plasma Phys. Control. Fusion 46, 319–335 (2004).
[4] **E.Z. Gusakov and A.Yu. Popov**, Physics of Plasmas, **23,** 082503 (2016)
[5] **E.Z. Gusakov and A.Yu. Popov**, Physics of Plasmas, **25,** 082117 (2018)
[6] **A. Altukhov, et. al.**, EPJ Web of Conferences, 157, 03050 (2017).

AUTHOR INDEX

Научное издание

ФИЗИКА ПЛАЗМЫ И ПЛАЗМЕННЫЕ ТЕХНОЛОГИИ

IX Международная конференция
Минск, Беларусь, 17 – 21 сентября 2018 г.

Материалы конференции

На английском языке

Составители:

Тарасенко Николай Владимирович
Невар Елена Аркадьевна
Тарасенко Наталья Николаевна
Усачёнок Максим Сергеевич
Кирис Василий Владимирович

Ответственный за выпуск В.П. Кузьмин

Подписано в печать 06.09.2018.
Формат 60x84$^{1/16}$. Бумага офсетная. Печать цифровая.
Усл. печ. л.24,6. Уч. изд. л. 23,5.
Тираж 150 экз. Заказ 426.

ООО «Ковчег».
Свидетельство о государственной регистрации издателя, изготовителя,
распространителя печатных изданий № 1/381 от 1 июля 2014 г.
Ул. Л.Беды, 11/1-205, 220040 г. Минск
Тел./факс: (017) 284 19 81
kovcheg_info@tut.by

Planar XY Linear Stage

8MTL120XY

FEATURES

- Direct drive zero backlash system
- High resolution non-contact optical incremental encoder
- Integrated, low-profile, XY, linear motor stage
- High accuracy linear guide with crossed roller bearings, anti-creep
- Easy integration with metric/imperial opto-mechanical systems
- 5 arcsec orthogonality
- All measurement reports are included by default

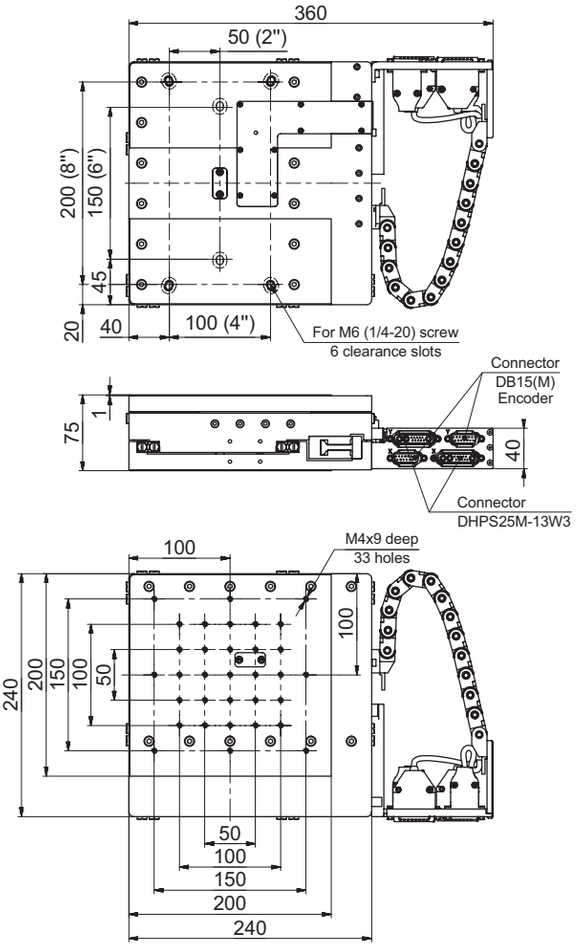

SPECIFICATIONS

Parameter	Value
Travel range	120 × 120 mm
Motor	Linear Ironless BLDC
Encoder type	Optical
Encoder resolution	any of the range: 25 nm to 5 µm
Bi-directional repeatability	(peak to peak) ± 0.15 µm
Bi-directional repeatability (RMS)	± 0.10 µm
Absolute accuracy	
before calibration	± 4.00 µm
after calibration	± 0.5 µm
Maximum velocity (load 4kg)	< 1 000 mm/s
Maximum acceleration (load 4kg)	< 20 000 mm/s^2
Load capacity (centrally placed)	30.00 kg
Recommended controllers	8SMC5-USB series or ACS Products Line

MOTORIZED PLANAR XY LINEAR STAGE

www.standa.LT

Manufacturer of Opto-Mechanical equipment for research, industry and education

Standa Ltd.
P.O.Box 377
LT 03012 Vilnius
LITHUANIA
Phone: +370-5-2651474
Fax: +370-5-2651483
E-mail: sales@standa.LT

LASER SYSTEMS

PULSED Nd:YAG LASERS

- Pulse energy up to 1.5 J
- Flat top beam profile
- PRR up to 100 Hz
- VIS and UV Harmonic generators
- MM, TEM_{00}, SLM operation modes

FEMTO- & PICOSECOND LASERS

- Pulsewidth from 120 fs to 10 ps
- Output power up to 10 W
- VIS and UV harmonic generators
- Laser diode pumping
- Tunable picosecond laser systems

TUNABLE LASERS

- Ti:Sapphire lasers, OPO and DFG systems
- Linewidth up to 0.1 cm^{-1}
- 0.2 ... 20 µm tuning range
- Pulse energy up to 100 mJ

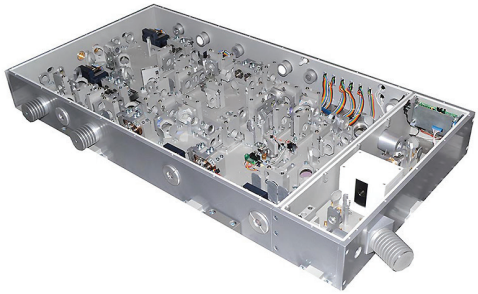

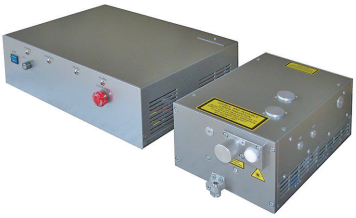

DPSS LASERS

- Compact and dustproof design
- Air cooling
- Pulsed energy up to 200 mJ at 1064 nm/20 Hz
- Output power up to 3W at 355 nm/50 kHz
- VIS and UV Harmonic generators

SOLAR LASER SYSTEMS

SOLAR Laser Systems, 4 Stebenev lane, Minsk 220024, BELARUS,
Fax: +375 (17) 2019596, Phone: +375 (17) 2019590, e-mail: info@solarls.eu, www.solarlaser.com